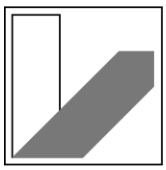

UNIVERSITÄT
BAYREUTH

Semiconductor quantum-dot–cavity systems as sources of highly nonclassical states of light

Von der Universität Bayreuth
zur Erlangung des Grades eines
Doktors der Naturwissenschaften (Dr. rer. nat.)
genehmigte Abhandlung

von
Michael Cosacchi
aus Hof (Saale)

1. Gutachter: Prof. Dr. V. M. Axt
2. Gutachter: Prof. Dr. S. Kümmel
3. Gutachter: Prof. Dr. T. Kuhn

Tag der Einreichung: 22. Dezember 2021
Tag des Kolloquiums: 25. April 2022

UNIVERSITÄT
BAYREUTH

Semiconductor quantum-dot–cavity systems as sources of highly nonclassical states of light

Von der Universität Bayreuth
zur Erlangung des Grades eines
Doktors der Naturwissenschaften (Dr. rer. nat.)
genehmigte Abhandlung

von

Michael Cosacchi
aus Hof (Saale)

1. Gutachter: Prof. Dr. V. M. Axt
2. Gutachter: Prof. Dr. S. Kümmel
3. Gutachter: Prof. Dr. T. Kuhn

Tag der Einreichung: 22. Dezember 2021
Tag des Kolloquiums: 25. April 2022

A·M·D·G

Abstract

At the turning point from the digital to the quantum era, research on technologically viable quantum systems is active as never before. Many innovative ideas in all areas of quantum sciences and technologies, ranging from quantum metrology, quantum communication and quantum cryptography to quantum computation, are based on the exchange of information between different systems. As photons, being the quanta of light, travel at the highest possible speed, using them is an attractive pathway to encode information. Semiconductor systems are particularly interesting candidates for sources of such quanta of light, since they are expected to be directly integrable into existing semiconductor technologies.

This cumulative thesis theoretically explores the suitability of self-assembled semiconductor quantum dots (QDs) in microcavities as sources of nonclassical photonic states and thus contributes to this fast-growing research area. In contrast to atomic devices, a QD is embedded in a solid-state bulk material and is therefore prone to its temperature-dependent vibrations called phonons once they are quantized. Even at cryogenic temperatures of a few kelvin, at which QDs are commonly operated, the phonon influence is known to have a profound impact on the QD state dynamics. Understanding the effect of this environment of longitudinal acoustic phonons on the joint QD electronic and cavity photonic dynamics is a prerequisite for harnessing these systems to generate specific photon states on demand. To this end, a numerically exact path-integral formalism is employed that does not rely on any further approximations, once the model is stated. Thus, all system–environment correlations are fully accounted for, thereby clearly going beyond a Born–Markov treatment of the phonon environment.

This thesis is organized following the increasing complexity of exemplary photonic states as measured by the contributing photon number. Starting out with single photons, a phonon enhancement of their quality is reported and a protocol to store single photons in a QD–cavity system is proposed. Entanglement, being one of the most notorious consequences of quantum theory, is investigated in terms of polarization-entangled photon pairs. The generation of different types of Bell-state entanglement is discussed and a protocol to switch between them in a time-dependent manner is suggested. The analysis of the preparation of higher-order Fock states and N-photon bundles in QD–cavity systems showcases the different impact phonons might have on a protocol's success. The influence of phonons on the shape-changing of photon number distributions due to varying excitation conditions of the QD is discussed. The

investigation is closed by a proposal to generate Schrödinger-cat states in QD–cavity systems.

These studies are framed by two methodological considerations. While the analysis of the accuracy of the quantum regression theorem applied to photonic figures of merit in QD–cavity systems provides a groundwork, the discussion of a new numerically exact method to simulate arbitrary open quantum systems gives an outlook for future studies.

Kurzfassung

Am Wendepunkt zwischen dem digitalen und dem Quantenzeitalter ist die Forschung an technologisch praktikablen Quantensystemen so aktiv wie niemals zuvor. Da Photonen die Quanten des Lichts sind und sich mit dessen Geschwindigkeit fortbewegen, ist deren Gebrauch zur Informationskodierung ein attraktiver Weg, um innovative Ideen in allen Bereichen der Quantenwissenschaften und -technologien zu realisieren: von der Quantenmetrologie über die Quantenkommunikation und -kryptographie bis hin zum Quantencomputing. Halbleitersysteme sind besonders interessante Kandidaten als Quellen solcher Quantenzustände des Lichts, da sie voraussichtlich direkt in existierende Halbleitertechnologien integrierbar sind.

Diese kumulative Dissertation untersucht theoretisch die Eignung von selbstorganisierten Halbleiterquantenpunkten (im folgenden QP genannt) in Mikroresonatoren als Quellen nichtklassischer Photonzustände und trägt so zu diesem schnell wachsenden Forschungsfeld bei. Im Gegensatz zu Geräten, die auf atomaren Systemen beruhen, ist ein QP in ein Festkörpermaterial eingebettet und daher den temperaturabhängigen Schwingungen ausgesetzt, die nach ihrer Quantisierung Phononen genannt werden. Selbst bei kryogenen Temperaturen von wenigen Kelvin, bei denen ein QP üblicherweise verwendet wird, haben die Phononen bekannterweise einen großen Einfluss auf die Dynamik der QP-Zustände. Letztere interagieren wiederum mit den Resonatorphotonen. Das Verständnis des Einflusses einer Umgebung longitudinal akustischer Phononen auf diese gemeinsame Dynamik ist eine Voraussetzung zur Nutzbarmachung solcher Systeme zur Erzeugung von bestimmten Photonzuständen auf Abruf.

Zu diesem Zweck wird ein numerisch exakter Pfadintegralformalismus verwendet, der sich auf keine weiteren Näherungen stützt, sobald das Modell formuliert ist. Alle Korrelationen zwischen dem System und der Umgebung werden also vollständig berücksichtigt, so dass diese Theoriestufe klar über eine Behandlung der Phononumgebung im Rahmen einer Born-Markov-Näherung hinausgeht.

Die vorliegende Dissertation ist anhand der wachsenden Komplexität beispielhafter Photonzustände aufgebaut, die durch die beitragende Photonzahl gemessen wird. Beginnend mit einzelnen Photonen wird eine Erhöhung deren Qualität durch Phononen vorhergesagt und ein Protokoll zur Speicherung von einzelnen Photonen in QP-Resonator-Systemen vorgeschlagen. Verschränkung als eine der bekanntesten Folgen der Quantentheorie wird anhand polarisationsverschränkter Photonpaare eruiert. Die Erzeugung von verschiedenen Typen einer Bell-

Zustandsverschränkung wird diskutiert und ein Protokoll zum zeitabhängigen Schalten zwischen ihnen vorgeschlagen. Die Analyse der Gewinnung von Fockzuständen höherer Ordnung und N-Photon-Bündeln in QP-Resonator-Systemen unterstreicht den unterschiedlichen Einfluss, den Phononen auf den Erfolg eines Protokolls haben können. Ein veränderlicher Phononeinfluss auf formverändernde Photonzahlverteilungen, abhängig von den Anregungsbedingungen des QPs, wird diskutiert und die Untersuchung durch den Vorschlag eines Protokolls zur Erzeugung von Schrödinger-Katzen-Zuständen in QP-Resonator-Systemen abgeschlossen.

Zwei methodische Überlegungen rahmen diese Studien ein:

Während die Analyse der Genauigkeit des Quantenregressionstheorems, angewandt auf photonische Kennzahlen in QP-Resonator-Systemen, eine Grundlage dieser Arbeit bildet, gibt die Diskussion einer neuen, numerisch exakten Methode zur Simulation von beliebigen offenen Quantensystemen einen Ausblick auf künftige Untersuchungen.

Contents

1 Introduction to the field **1**

1.1 Motivation – a popular introduction . . . 1

1.2 Self-assembled semiconductor quantum dots . . . 2

1.2.1 The driven two-level QD . . . 2

1.2.2 The Jaynes–Cummings coupling to individual cavity modes . . . 3

1.2.3 Phenomenological losses . . . 4

1.3 The phonon environment . . . 4

1.4 The dynamical equation . . . 5

1.5 The numerically exact path-integral method . . . 6

1.5.1 Expectation values . . . 6

1.5.2 Two-time correlation functions . . . 7

1.5.3 Comparison with other methods . . . 8

2 A guide for the publications **13**

2.1 The quantum regression theorem and beyond . . . 14

2.2 Quantum dots and single photons . . . 17

2.2.1 Phonon-enhanced single-photon sources . . . 18

2.2.2 Deterministic storage and readout of a single photon . . . 20

2.3 Polarization-entangled photon pairs . . . 22

2.4 Multiphoton states and structures . . . 25

2.4.1 Higher-order Fock states . . . 25

2.4.2 N-photon bundles . . . 27

2.4.3 Shape-shifting photon number distributions . . . 29

2.4.4 Schrödinger-cat states . . . 31

2.5 Methodological outlook and perspectives . . . 33

3 Summary and outlook **37**

Bibliography **39**

Acknowledgments **49**

Publications **51**

List of publications as referred to in this thesis 51

Further publications contributed to by the author 53

Conference and seminar contributions 54

Eidesstattliche Versicherung

1 Introduction to the field

1.1 Motivation – a popular introduction

Novel technologies permeate our world in ways unimaginable only a few decades ago. The advent of online communication via various social media platforms roughly twenty years ago heralded a society so reliant on their proper functioning, that a six-hour outage of products and services of Facebook Inc. in October 2021 affected 3.5 billion users[1]. The shift of large sections of infrastructure to cyberspace critical even to national security has led US president Biden in a summit with Russian president Putin in June 2021 to define red lines of cyberwarfare, which once crossed would trigger an offline military response[2]. The ongoing COVID-19 pandemic forced a large portion of the global workforce into home office to a degree that some companies consider maintaining this mode of employment even after the pandemic[3], thus fostering the global online interconnectedness.

All of these developments increase the demand on computational and communication hardware dramatically. In sharp contrast, Moore's law predicting the doubling of the on-chip transistor density every two years was officially abandoned in 2016, while the CPU clock speeds have already been capped to limit heat since 2004[4]. There are various propositions to overcome this tradeoff situation. Tackling the problem of heat would be possible using millivolt switches like spintronic materials[5], that would consume less power while still operating in the digital realm.

A fundamental paradigm shift to solve some problems of the binary is to go quantum. Quantum computation allows certain tasks to be solved exponentially faster, while quantum cryptography could base communication security on physical laws, in essence creating unbreakable codes[6]. Awareness of the qualitative changes to all aspects of our modern society that quantum innovation and quantum technologies will herald, has risen to such a degree that various governments started investing significantly in research and development in recent years. Examples are the US 'National Quantum Initiative Act'[7] pledging $1.2 billion, the 'Quantum Flagship' of the European Commission[8] with a budget of €1 billion, and the German 'Quantum Technologies Federal Government Framework Programme'[9] investing €650 million.

This thesis focuses on light quanta, the photons, as the carrier of quantum information. Nonclassical quantum states of light are at the heart of many innovative applications in the quantum

information sciences, covering quantum communication [10,11] and cryptography [12,13], quantum metrology [14–16], and quantum computation [17–20]. Self-assembled semiconductor quantum dots (QDs) in microcavities are widely discussed as on-demand, deterministic sources of such states of light. These nanostructures are often called 'artificial atoms' because of their discrete spectrum arising from their confinement in all three spatial directions. While they are versatile in terms of the energetic level structure established during the growth process, their embedding in the surrounding solid-state crystal matrix introduces a special kind of environment. Even at cryogenic temperatures of a few kelvin, a QD is coupled to a continuum of longitudinal acoustic phonons, which has been shown to be the main source of decoherence in the QD's quantum few-level system [21–25].

1.2 Self-assembled semiconductor quantum dots

Semiconductor quantum dots (QDs) are nanostructures that are strongly confined in space [26]. Self-assembled QDs that are grown by the Stranski-Krastanov mechanism [27] are typically up to about 10 nm in diameter. These self-organized three-dimensional lens-shaped islands spontaneously form due to strain out of a thin film deposited on a bulk material with a similar but slightly different lattice constant. Predominantly, InAs QDs grown on GaAs bulk materials are considered in this thesis.

Due to the strong spatial confinement, the carrier wave functions are highly localized and their corresponding energies are discrete and well separated. Therefore, it is often sufficient to take the lowest conduction band and the highest valence (heavy-hole) band state into account. Excitons form as pairs of an s-like conduction band electron and a p-like valence band heavy hole. Since both the light-hole and the split-off band are energetically detuned from the heavy-hole band and transitions into them are thus unlikely, only the heavy-hole band is taken into account.

Because of the heavy-hole spin component of $S_z^{\mathrm{h}} = \pm\frac{3}{2}$, pairing up with a spin-$\frac{1}{2}$ electron leads to two types of excitons: the optically active *bright* excitons with spin ±1 and the dipole-*dark* states with spin ±2. For the description of most optical experiments, the latter can be neglected due to their lack of direct optical addressability. Furthermore, there is a bound state composed of two bright excitons called the biexciton that has a typical binding energy E_{B} of a few meV.

1.2.1 The driven two-level QD

This state space can be further reduced when external driving of a defined circular polarization is considered. For typical fine-structure splittings of a few tens of μeV [28] between the two bright states with spin ±1, only the ground state $|G\rangle$ without any excitations and the bright

exciton $|X\rangle$ with a spin corresponding to the circular polarization of the external driving need to be considered [29,30].

Thus, one arrives at a two-level model for the electronic subspace of a QD, which is the description predominantly used in this thesis. For certain applications, though, the biexciton state, the dark exciton, and energetically higher lying exciton states are taken into account (cf., [Pub 3, Pub 4, Pub 5, Pub 6]). Including the external driving into the model as a classical amplitude, the Hamiltonian of the driven two-level QD is

$$H_{\mathrm{QD}} = -\hbar\Delta\omega_{\mathrm{LX}}|X\rangle\langle X| - \frac{\hbar}{2}f(t)\left(\sigma_{\mathrm{X}} + \sigma_{\mathrm{X}}^{\dagger}\right) , \tag{1.1}$$

where the dipole and rotating wave approximations have been used. The ground state is chosen as the zero point of the energy scale, the energy of the exciton is $\hbar\omega_{\mathrm{X}}$, the polarization operator describing the transition between the exciton and the ground state is defined as $\sigma_{\mathrm{X}} := |G\rangle\langle X|$, and the Hamiltonian is written down in a frame co-rotating with the frequency of the external driving laser ω_{L}. $f(t)$ denotes the real envelope function of the laser and $\Delta\omega_{\mathrm{LX}} := \omega_{\mathrm{L}} - \omega_{\mathrm{X}}$ the laser-exciton detuning.

1.2.2 The Jaynes–Cummings coupling to individual cavity modes

When electron and hole recombine radiatively and the QD transitions from the exciton to the ground state, a photon is created in the continuum of the electromagnetic field coupled to the QD. In this sense, the polarization operator σ_{X} can be interpreted as the source of a photon (cf., [Pub 1]). In cavity quantum electrodynamics (cQED), though, the interaction between a few-level quantum system and well-separated individual electromagnetic field modes is of interest. The coupling of the two-level QD to a single mode of a solid-state microcavity [31] is well described within the rotating wave approximation using the Jaynes-Cummings model [32]

$$H_{\mathrm{C}} = \hbar\Delta\omega_{\mathrm{CL}}a^{\dagger}a + \hbar g\left(a^{\dagger}\sigma_{\mathrm{X}} + a\sigma_{\mathrm{X}}^{\dagger}\right) , \tag{1.2}$$

where $a^{\dagger}$ (a) creates (annihilates) a photon with the cavity mode frequency ω_{C}. The coupling strength is given by $\hbar g$ and the cavity-laser detuning is defined as $\Delta\omega_{\mathrm{CL}} := \omega_{\mathrm{C}} - \omega_{\mathrm{L}}$. This Hamiltonian is again written in a rotating frame with the laser frequency as reference.

If two modes of opposite polarization simultaneously interact with the QD, a Jaynes-Cummings model can be used for each mode. In particular, this extension is necessary when considering the biexciton-exciton cascade in a cavity or discussing the influence of a finite fine-structure splitting (cf., [Pub 4, Pub 5, Pub 6]).

1.2.3 Phenomenological losses

A realistic model for an experimental setup needs to account for inevitable imperfections of the system. The most important ones in cQED are the losses of the microcavity with rate κ due to, e.g., non-unity reflectance, and the radiative decay of the few-level emitter orthogonal to the cavity into the continuum of the electromagnetic field with rate γ. This geometry reflects the driving of the QD, which is performed orthogonal to the cavity [33], whereas the detection takes place on the axis distinguished by the cavity.

These processes are well described phenomenologically using a Markovian Lindblad superoperator [34–36] acting on the density matrix ρ of the QD–cavity system

$$\mathcal{L}_{O,\Gamma}\rho = \Gamma\left(O\rho O^\dagger - \frac{1}{2}\left\{\rho, O^\dagger O\right\}_+\right). \tag{1.3}$$

The action of the loss process is captured by the corresponding system operator O and loss rate Γ. The anti-commutator between operators A and B is denoted as $\{A,B\}_+$.

1.3 The phonon environment

QDs are embedded in a surrounding solid-state crystal matrix. Even at cryogenic temperatures of a few kelvin, this leads to a coupling of the QD excitations to a phonon continuum. The deformation potential coupling to longitudinal acoustic (LA) phonons is the most important decoherence mechanism in QDs [21,23,25,37]. This interaction is of the so-called pure-dephasing type and has the form [21–24]

$$H_{\mathrm{Ph}} = \hbar\sum_{\mathbf{q}}\omega_{\mathbf{q}} b_{\mathbf{q}}^\dagger b_{\mathbf{q}} + \hbar\sum_{\mathbf{q}}\left(\gamma_{\mathbf{q}}^{\mathrm{X}} b_{\mathbf{q}}^\dagger + \gamma_{\mathbf{q}}^{\mathrm{X}*} b_{\mathbf{q}}\right)|X\rangle\langle X|. \tag{1.4}$$

The bosonic operator $b_{\mathbf{q}}$ ($b_{\mathbf{q}}^\dagger$) annihilates (creates) a phonon of energy $\hbar\omega_{\mathbf{q}}$ in mode $\mathbf{q}$ with the coupling strength $\gamma_{\mathbf{q}}^{\mathrm{X}}$. As the initial condition of the dynamics, the QD–cavity and the phonon subsystems are assumed to factorize, while the latter is in thermal equilibrium at temperature T. Note that bulk phonon modes are considered rather than modes confined in the QD [21], since the elastic properties of the QD and substrate materials are similar in self-assembled QDs.

Several important phenomena arise from this interaction, such as the appearance of phonon sidebands in the emission spectrum [21,23,38], the damping of Rabi oscillations [39–43] and the renormalization of their frequency [44,45], a dynamic decoupling of electronic and phononic subsystems [46,47], and the degradation of the quality of emitted photons [48]. Note that in strongly polar materials like GaN, the piezoelectric coupling becomes important [23,37], but in the GaAs structures considered in this thesis it is negligible. Furthermore, optical phonons that interact with the QD via the Fröhlich coupling have typical energies of a few 10 meV. Their contribution

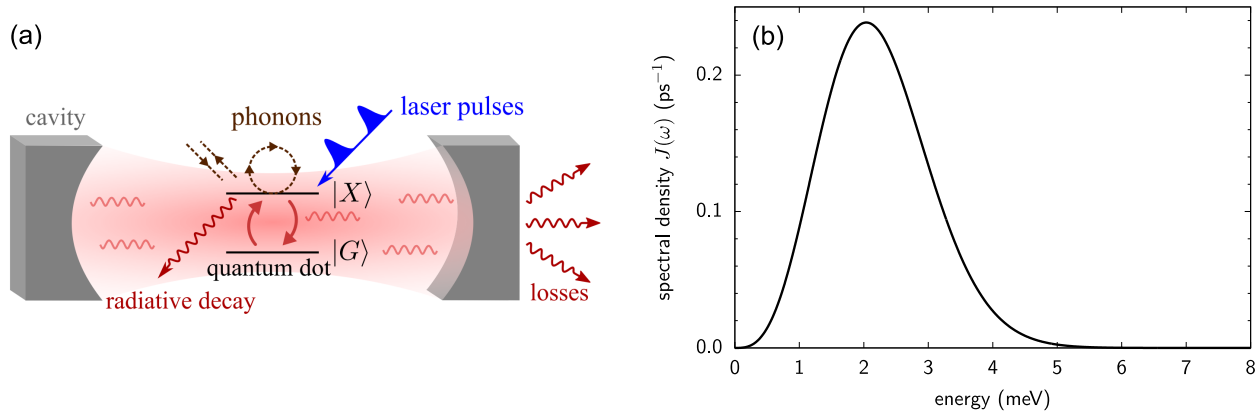

Figure 1.1: [(a) taken from [Pub 2]] (a) Sketch of the QD–cavity system. (b) The phonon spectral density $J(\omega)$ according to Eq. (1.5) for GaAs material parameters and an electron confinement length of $a_e = 3\,\mathrm{nm}$.

to the dephasing in QDs has been shown to be rather minor[23].

The coupling constant $\gamma_{\mathbf{q}}^{\mathrm{X}}$ in Eq. (1.4) determines the phonon spectral density $J(\omega) = \sum_{\mathbf{q}} |\gamma_{\mathbf{q}}^{\mathrm{X}}|^2 \delta(\omega - \omega_{\mathbf{q}})$. Under the assumptions of a spherically symmetric potential, a harmonic confinement, and a linear dispersion $\omega_{\mathbf{q}} = c_s|\mathbf{q}|$ with sound velocity c_s, an expression for $J(\omega)$ can be obtained, which contains only geometric and material parameters:

$$J(\omega) = \frac{\omega^3}{4\pi^2 \rho_D \hbar c_s^5} \left(D_e e^{-\omega^2 a_e^2/(4c_s^2)} - D_h e^{-\omega^2 a_h^2/(4c_s^2)} \right)^2 . \tag{1.5}$$

ρ_D is the density of the material, D_e (D_h) the electron (hole) deformation potential, and a_e (a_h) the electron (hole) confinement length. The parameter values for GaAs, which is the predominantly considered substrate material in this thesis, are listed in Refs. [37,49] and are repeated in Tab. I in the supplementary material of [Pub 1]. When identical confinement potentials for electrons and holes are presumed, the confinement ratio is fixed by the effective masses as $a_h = a_e/1.15$. Therefore, the electron confinement length a_e is the only free parameter in Eq. (1.5). It is interpreted as a measure for the size of the QD. Values between 3 nm and 5 nm have produced results in good agreement with experiment[46,50,51]. Exemplarily, the spectral density is shown in Fig. 1.1(b) for $a_e = 3\,\mathrm{nm}$.

1.4 The dynamical equation

The QD–cavity model described in Secs. 1.2 and 1.3 is comprised of a Hamiltonian part for the subsystem of interest $H_{\mathrm{S}} := H_{\mathrm{QD}} + H_{\mathrm{C}}$, a Hamiltonian part for the phonon environment H_{Ph}, and a Lindbladian part for the phenomenological description of losses. A sketch of this system is shown in Fig. 1.1(a). The dynamics of the QD–cavity system is fully determined by

the Liouville–von Neumann equation for the density matrix ρ

$$\frac{\partial}{\partial t}\rho = -\frac{i}{\hbar}\{H_{\mathrm{S}}, \rho\}_- - \frac{i}{\hbar}\{H_{\mathrm{Ph}}, \rho\}_- + \mathcal{L}_{a,\kappa}\rho + \mathcal{L}_{\sigma_X,\gamma}\rho\,. \tag{1.6}$$

The commutator between operators A and B is denoted as $\{A, B\}_-$.

Due to the sum in Eq. (1.4), the pure-dephasing coupling to LA phonons expands the Hilbert space of the problem infinitely. Analytical solutions for arbitrary external driving $f(t)$ are not known. Nonetheless, this phonon Hamiltonian can be treated in an numerically exact way using an iterative real-time path-integral method, presented in the following section.

1.5 The numerically exact path-integral method

1.5.1 Expectation values

In order to solve Eq. (1.6) for the QD–cavity subsystem dynamics using an iterative real-time path-integral method, first the propagator defined by the dynamical equation has to be discretized into small chunks of Δt. Then, the phonon subspace is traced out analytically, yielding a solution for the reduced density matrix (RDM) $\bar{\rho}(t) := \mathrm{Tr}_{\mathrm{Ph}}\left[\rho(t)\right]$ of the subsystem. This derivation is correct up to $\mathcal{O}\left(\Delta t^2\right)$.

The cost of this simplification is a memory kernel induced by the phonon environment that renders the subsystem dynamics non-local in time. The memory kernel for an InAs/GaAs QD with a confinement length of 3 nm decays to zero in roughly $\tau_{\mathrm{mem}} = 3\,\mathrm{ps}$[52]. Since this memory depth is on the same order of magnitude as the dynamical scale of the QD–cavity subsystem, it cannot be neglected using a Markov approximation, for which a phenomenological description using a Lindbladian would be sufficient.

The crucial point is the fact that the memory depth for a QD is not negligible, but finite. Thus, the system at time $t + \Delta t$ is fully determined by the knowledge of the system in the time interval $[t - \tau_{\mathrm{mem}}, t]$. This insight allows for an iterative formulation of the solution[52–54] in the form of the so-called augmented density matrix (ADM). The ADM contains all the information about the subsystem during the length of the memory, which is discretized as $\tau_{\mathrm{mem}} = n_{\mathrm{mem}}\Delta t$. It is thus a $2n_{\mathrm{mem}}$-rank tensor, which is propagated according to[55]

$$\bar{\rho}^{\mu_n \ldots \mu_{n-n_{\mathrm{mem}}+1}}_{\nu_n \ldots \nu_{n-n_{\mathrm{mem}}+1}} = \mathcal{M}^{\nu_{n-1}\mu_{n-1}}_{\nu_n\mu_n} \sum_{\substack{\nu_{n-n_{\mathrm{mem}}} \\ \mu_{n-n_{\mathrm{mem}}}}} \exp\left(\sum_{l=n-n_{\mathrm{mem}}}^{n} S_{\nu_n\nu_l\mu_n\mu_l}\right) \bar{\rho}^{\mu_{n-1}\ldots\mu_{n-n_{\mathrm{mem}}}}_{\nu_{n-1}\ldots\nu_{n-n_{\mathrm{mem}}}}\,. \tag{1.7}$$

The object $\mathcal{M}^{\nu_{n-1}\mu_{n-1}}_{\nu_n\mu_n}$ is the subsystem propagator, including the non-Hamiltonian Lindblad contributions, and $S_{\nu_n\nu_l\mu_n\mu_l}$ is the phonon influence functional. For a detailed definition of both objects cf., Ref. [55]. The subsystem state μ and ν at the j-th time step is described by the

indices μ_j and ν_j, respectively. The RDM at time $t = n\Delta t$ is retrieved by tracing out the memory contained in the ADM

$$\bar{\rho}_{\nu_n\mu_n} = \sum_{\substack{\nu_{n-1}\cdots\nu_{n-n_{\mathrm{mem}}+1} \\ \mu_{n-1}\cdots\mu_{n-n_{\mathrm{mem}}+1}}} \bar{\rho}^{\mu_n\cdots\mu_{n-n_{\mathrm{mem}}+1}}_{\nu_n\cdots\nu_{n-n_{\mathrm{mem}}+1}} \,. \tag{1.8}$$

The dynamics of every (single-time) expectation value of any subsystem observable can be obtained with the knowledge of the RDM. Only two parameters can introduce errors to this solution: (i) the time discretization Δt and (ii) the memory depth τ_{mem} taken into account. Both convergence parameters are easily controllable. A solution is denoted as numerically exact, when decreasing Δt or increasing τ_{mem} leads to no noticeable change. In particular, it follows that no further approximations are necessary to obtain a solution for the time evolution of the QD–cavity system once the model is stated in terms of a Hamiltonian and a Lindbladian.

While the iterative formulation allows for long-time studies of a few-level system, the investigation of multi-level systems remains illusive with Eq. (1.7), since the number of ADM elements to be stored during computation scales exponentially as $N_{\mathrm{S}}^{2n_{\mathrm{mem}}}$ with the subsystem's dimension N_{S}. Calculations including up to 20 photons require the treatment of a 41-dimensional subsystem. With $n_{\mathrm{mem}} = 7$ and $\Delta t = 0.5\,\mathrm{ps}$, which typically leads to converged results for a 3 nm-InAs/GaAs QD, roughly 3.8×10^{22} ADM elements have to be stored – a number completely out of reach for current computational equipment.

In a QD–cavity system, only the QD states couple to the phonons[49]. This observation allows for an organization of the states into groups with identical phonon coupling. Then, the ADM can be partially summed within each group[49], such that the number of elements to be iterated scales as $N_{\mathrm{S}}^2 N_{\mathrm{g}}^{(2n_{\mathrm{mem}}-1)}$ with the number of groups N_{g} – two in the case of a two-level QD. In the example above, this decreases the ADM elements to roughly 6.9×10^6. Only this reduction of more than 15 orders of magnitude in computational demand makes the numerically exact study of realistic QD–cavity systems possible.

1.5.2 Two-time correlation functions

Properties of a photon source and the generated state of light are often characterized in coincidence experiments. A famous example is the Hanbury Brown–Twiss setup[56], which yields a measure for the multiphoton component of the analyzed photonic state. Glauber formulated a model for this setup[57], yielding a second-order two-time correlation function of the electrical field operators, i.e., the cavity photon operators in a QD–cavity system

$$G^{(2)}(t,\tau) = \langle a^\dagger(t)a^\dagger(t+\tau)a(t+\tau)a(t)\rangle \,, \tag{1.9}$$

where t is the real time of the experiment and τ is the delay time between detector clicks.

A numerically exact path-integral scheme for a multitime correlation function as in Eq. (1.9) has been derived in [FPub 2]. First, the ADM is propagated until time $t = n\Delta t$. Here, the operators evaluated at this time are multiplied to produce a modified ADM (MADM):

$$\bar{\rho}_{aa^\dagger \nu_n \ldots \nu_{n-n_{\mathrm{mem}}+1}}^{\mu_n \cdots \mu_{n-n_{\mathrm{mem}}+1}} = \sum_{\nu_n' \mu_n'} (a)_{\nu_n \nu_n'} \mathcal{M}_{\nu_n' \mu_n'}^{\nu_{n-1} \mu_{n-1}} (a^\dagger)_{\mu_n' \mu_n} \sum_{\substack{\nu_{n-n_{\mathrm{mem}}} \\ \mu_{n-n_{\mathrm{mem}}}}} \exp\left(\sum_{l=n-n_{\mathrm{mem}}}^{n} S_{\nu_n \nu_l \mu_n \mu_l} \right) \bar{\rho}_{\nu_{n-1} \ldots \nu_{n-n_{\mathrm{mem}}}}^{\mu_{n-1} \ldots \mu_{n-n_{\mathrm{mem}}}} . \tag{1.10}$$

For the subsequent m steps until $t + \tau$ with $\tau = m\Delta t$, the MADM is iterated instead of the ADM. Finally, the operators evaluated at time $t+\tau$ are multiplied and the correlation function is obtained by performing the trace over the memory

$$G^{(2)}(t, \tau) = \sum_{\substack{\nu_{n+m} \ldots \nu_{n+m-n_{\mathrm{mem}}+1} \\ \mu_{n+m} \ldots \mu_{n+m-n_{\mathrm{mem}}+1}}} \left[a^\dagger a \right]_{\mu_{n+m} \nu_{n+m}} \bar{\rho}_{aa^\dagger \nu_{n+m} \ldots \nu_{n+m-n_{\mathrm{mem}}+1}}^{\mu_{n+m} \cdots \mu_{n+m-n_{\mathrm{mem}}+1}} . \tag{1.11}$$

This scheme ensures that the memory accumulated during the t-propagation is properly transferred to the τ-propagation. Thus, this numerically exact method reaches clearly beyond the so-called quantum regression theorem (QRT)[35,36], which is the most widely used tool to calculate multitime correlation functions, even in non-Markovian situations[38,48].

1.5.3 Comparison with other methods

Taking the phonon-induced memory into account beyond a Born–Markov approximation is possible without having to resort to the above presented numerically exact path-integral (PI) formalism. In this section, two state-of-the-art approximative methods are presented that yield accurate predictions of the QD–phonon dynamics in many cases with less numerical demand: the polaron master equation (PME) approach and a fourth-order correlation expansion (CE4). During the studies presented in this thesis both methods have been employed either to conduct methodological comparisons or in cooperation with the theoretical physics group on 'Ultrafast Optics in Nanostructured Solids' headed by D. E. Reiter at the University of Münster. The PME approach is applied in [Pub 1] to discuss the frame dependence of the quantum regression theorem, while the CE4 method is used in [FPub 4] and for extensive parameter studies in the aftermath of [FPub 5]. Finally, a motivation is given why nonetheless the PI formalism is employed throughout the studies discussed in this thesis.

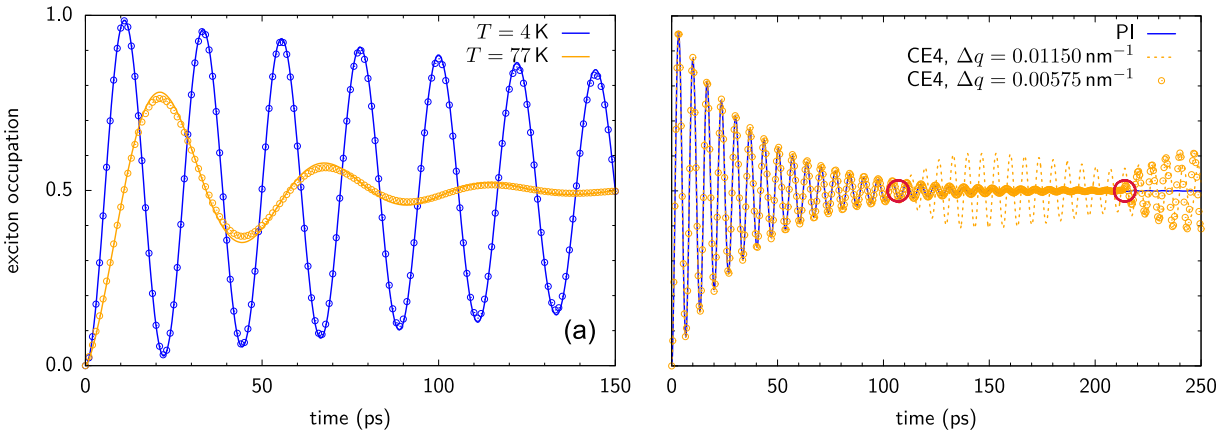

Figure 1.2: [(b) Data on the CE4 method kindly provided by T. K. Bracht, Reiter group, University of Münster] Two-level QD of size 3 nm driven by a constant external laser and coupled to a phonon environment. (a) Path-integral (PI) results (solid lines) compared with PME results (open circles) for two different temperatures $T = 4\,\mathrm{K}$ and $T = 77\,\mathrm{K}$ for a driving strength of $\hbar f = 0.2\,\mathrm{meV}$. (b) PI results (blue solid line) compared with CE4 results for a driving strength of $f = 1\,\mathrm{ps}^{-1}$ at $T = 4\,\mathrm{K}$. The orange dotted line corresponds to 200 grid points and orange open circles to 400 within the considered phonon wave vector interval. Red circles indicate the time $T_{\max}$ at which the CE4 method is predicted to break down for the respective discretization.

The polaron master equation

The transformation of the system into the polaron frame is at the heart of the PME approach[58–60], which is given by

$$H' = e^{S} H e^{-S} \tag{1.12a}$$

$$S = \sigma_{\mathrm{X}}^{\dagger}\sigma_{\mathrm{X}} \sum_{\mathbf{q}} \frac{1}{\omega_{\mathbf{q}}} \left(\gamma_{\mathbf{q}}^{X} b_{\mathbf{q}}^{\dagger} - \gamma_{\mathbf{q}}^{X*} b_{\mathbf{q}} \right) . \tag{1.12b}$$

A time-local master equation for the reduced system dynamics is derived in this frame employing a Born–Markov approximation (explicitly given in, e.g., the supplemental material of Ref. [49]). This procedure allows for the consideration of a variety of non-Markovian features beyond a Born–Markov treatment in the original laboratory frame, e.g., the prediction of the phonon sidebands in the QD emission spectra (cf., Fig. 1 in the supplement of [Pub 1]). A validity analysis in Ref. [61] suggests that the exploration of the strong-driving regime is possible as long as the QD–phonon coupling is rather weak or the temperature T low and vice versa. In Fig. 1.2(a) PI and PME results are compared with each other for a two-level QD of size 3 nm driven by a constant external laser and coupled to a phonon environment. A strong driving of $\hbar f = 0.2\,\mathrm{meV}$ is chosen here. Nonetheless, the results coincide at $T = 4\,\mathrm{K}$. At a higher temperature of 77 K, though, differences become visible consolidating the validity claims in Ref. [61].

A strict quantitative limit of the PME validity is elusive, though, as the authors of Ref. [61] concede. Thus, one should be wary of using the PME approach in strongly-pulsed systems at high temperatures. Moreover, the phonon influence might be overestimated when the pulse length is of the same order or shorter than the phonon-induced memory[62]. The reason is the time-local property of the PME method. The gradual buildup of the phonon influence during the memory time is not captured by this approach.

Therefore, exploring a parameter space where it is a priori unclear whether the PME approach is accurate is ill-advised. Since both strong and short pulses, high temperatures, and strong QD–phonon coupling are cases of interest in the studies discussed in this thesis, the numerically exact path-integral method is advantageous. When the convergence parameters are taken care of, the entire parameter space can be studied without methodological restrictions.

The correlation expansion

Deriving equations of motion for the exciton occupation and the polarisation of a two-level QD using the Heisenberg equation and subsequently taking expectation values yields no closed set, as is common for many-body problems. Rather, expectation values of the type $\langle \sigma_{\mathrm{X}} b_{\mathbf{q}} \rangle$ appear as sources on the right-hand side of the differential equations. Factorizing these as

$$\langle \sigma_{\mathrm{X}} b_{\mathbf{q}} \rangle = \langle \sigma_{\mathrm{X}} \rangle \langle b_{\mathbf{q}} \rangle + \delta \langle \sigma_{\mathrm{X}} b_{\mathbf{q}} \rangle \tag{1.13}$$

introduces the correlation $\delta \langle \sigma_{\mathrm{X}} b_{\mathbf{q}} \rangle$ as a new dynamical variable, which is defined by Eq. (1.13) and for which an additional equation of motion has to be derived. This procedure leads to an infinite hierarchy of equations of motions. To render this hierarchy numerically tractable, a truncation is necessary, the expectation being that the importance of higher-order correlations decreases.

In the fourth-order correlation expansion (CE4) formalism[44,63], five-point correlations are neglected. Thus, the CE4 method takes two-phonon processes into account, which yields good agreement with experiment[46]. In contrast to the PI or the PME approaches, which both rely on a trace over the environment, the CE4 formalism can access the phonon dynamics. For example, it is possible to observe the propagation of a phonon wave packet after excitation of the QD[64]. Even the phenomenon of phonon squeezing can be described using the CE4 method[65]. One drawback of this method is the inverse connection between the $\mathbf{q}$-discretization of the phonon environment and the stable simulation time, which can be derived from the energy-time uncertainty relation[66]. This property of the CE4 method is demonstrated in Fig. 1.2(b) for a two-level QD driven by a laser of strength $f = 1\,\mathrm{ps}^{-1}$. While both methods perfectly agree at the beginning of the simulation, after a maximum time predicted by $T_{\max} = 1.23/\Delta q\,\mathrm{ps\,nm}^{-1}$ for GaAs parameters[66], the CE4 results strongly deviate from the PI dynamics. Red circles

indicate the values of $T_{\max}$ for the respective discretizations Δq given in the figure's legend.

Thus, with reasonable computational demand, the simulation of a few hundred picoseconds is feasible, but the nanosecond-regime remains out of reach. Therefore, long-time studies as necessary for modeling coincidence experiments are challenging using the CE4 formalism. An iterative scheme as the PI method has thus a clear advantage in this regard.

2 A guide for the publications

In this thesis, the phonon influence on the preparation of quantum states of light in QD–cavity systems as described in Chap. 1 is studied. The number of photons that constitute the various photonic states under scrutiny is chosen as the leitmotif of the following investigation, starting from single photons and progressing to more and more complex multiphoton states. Here, a guide shall be given to concisely connect the publications that are at the heart of this thesis by picking the highlights of each one of them.

The overall storyline of this work is the following. The on-demand generation of single photons is technologically very important, in particular, in quantum communication and cryptography. After a section devoted to this task (Sec. 2.2.1), a QD single-photon buffer is proposed to store the generated photon for a predetermined amount of time in Sec. 2.2.2. Pairs of entangled photons allow for both advanced technological applications and fundamental questions regarding the quantum theory. The corresponding section (Sec. 2.3) explores the possibility to generate different types of Bell-state entanglement in diamond-shaped four-level emitters and proposes a time-dependent protocol to deterministically switch between them. Higher-order Fock states are the simplest kind of multiphoton states. Discussing the possibility to prepare them in QD–cavity systems is taken as the starting point of the studies on multiphoton states and structures presented in Sec. 2.4. N-photon bundles are related to higher-order Fock states, insofar as they are connected to the emission properties of a cavity. This trait results in a characteristic fingerprint in the photon number distribution, which is exploited in the corresponding analysis. Photon number distributions as such are interesting tools to analyze multiphoton states. In particular, a vast variety of qualitative shape changes can be found depending on the excitation condition. The interplay with the phonon environment is of special interest here. A section devoted to the preparation of Schrödinger-cat states in QD–cavity systems crowns the investigation of multiphoton states. These prime examples of nonclassical, purely quantum states are worth studying both from a technological and a fundamental point of view.

Two methodological studies frame this storyline. The investigation of the accuracy of the quantum regression theorem can be considered a groundwork for the characterization of single photons in terms of coincidence experiments and is therefore the topic of the first section (Sec. 2.1). The last section (Sec. 2.5) is devoted to the question of additivity concerning multiple environments on the one hand, while giving an outlook using a new numerically exact

method on the other hand.

2.1 The quantum regression theorem and beyond

A single-photon source is commonly characterized in terms of three quantities, the so-called figures of merit: the single-photon purity $\mathcal{P}$, which is a measure for the multiphoton contribution present in the detected state, the indistinguishability $\mathcal{I}$ of two successively emitted photons, and the brightness $\mathcal{B}$, which is the amount of photons generated by the source. If all three quantities equal unity, the source produces perfect single photons. Models and definitions of these quantities are given in Eqs. (1)–(5) in [Pub 1], respectively. Note that this specific definition of the indistinguishability incorporates the effect of a non-unity single-photon purity. The consequence is a codomain of $\mathcal{I} \in [0.5, 1]$[67].

Two of these quantities, $\mathcal{P}$ and $\mathcal{I}$, contain two-time correlation functions in their definitions. The QRT is the most widely used tool to obtain multitime correlation functions in an open quantum system setting[35,36]. It is a prescription to use the same dynamical equation for the propagation of a correlation function in both the real time t and the delay time τ. A density matrix modified by multiplying the operators evaluated at time t is taken as the initial value for the τ-propagation. This procedure presumes a factorization of system and environment for $\tau = 0$, i.e., for every t. It is therefore quite probable that the QRT breaks down in a system exhibiting strong non-Markovian features.

Interestingly, the QRT is commonly used in the analysis of the photonic properties of a QD, where the coupling to the LA phonon environment requires the consideration of non-Markovian effects[48,68,69]. It was shown in Ref. [38] that naively applying the QRT to the calculation of a QD emission spectrum results in the prediction of the phonon sideband on the energetically wrong side of the zero phonon line (ZPL). This qualitatively false result on the one hand and the still widespread usage of the QRT on the other hand call for a detailed discussion of the accuracy of the QRT, which is provided in [Pub 1].

To enable a direct comparison between numerically exact results and the QRT, an implementation of the latter within the path-integral formalism has to be formulated. To this end, the memory contained in the ADM is traced out as in Eq. (1.8) after the time $t = n\Delta t$ is reached. Then, a modified RDM (MRDM) is introduced

$$\bar{\rho}_{aa^\dagger}{}^{\mu_n}_{\nu_n} = \sum_{\nu'_n \mu'_n} (a)_{\nu_n \nu'_n} \bar{\rho}_{\nu'_n \mu'_n} (a^\dagger)_{\mu'_n \mu_n} \tag{2.1}$$

and used as the initial RDM for the subsequent m steps of propagation in the delay time argument τ. This procedure captures the essence of the QRT to neglect the memory accumulated during the t-propagation at the switch between real time and delay time, while ensuring the

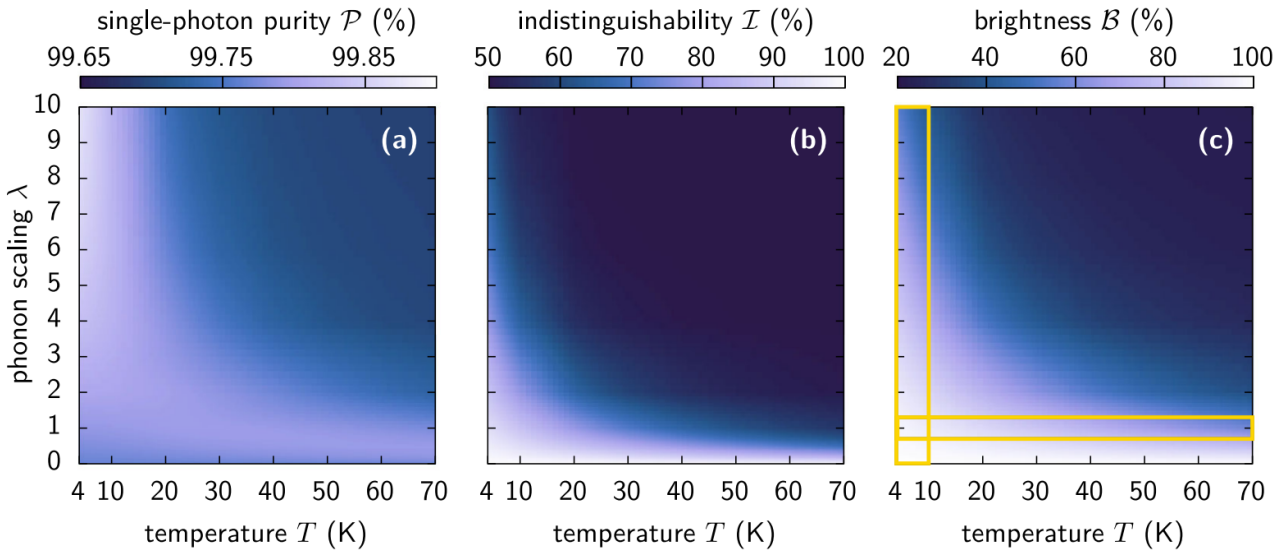

Figure 2.1: [Taken from [Pub 1]] Photonic figures of merit of a two-level QD single-photon source using the numerically exact path-integral formalism: (a) the single-photon purity, (b) the indistinguishability, and (c) the brightness. Their dependencies on the temperature T and the phonon scaling λ (cf., main text) are shown. Yellow boxes highlight the physically most interesting parameter region around $\lambda = 1$ for GaAs material parameters and the low-temperature regime below 10 K.

incorporation of all memory effects during the respective single-time propagations. In order to test the validity of this implementation, the prediction of the phonon sideband on the wrong side of the ZPL when using the QRT [38] is successfully reproduced in Fig. 1 in the supplement of [Pub 1].

In order to keep this rather fundamental methodological analysis as simple and transparent as possible, a two-level QD without the coupling to a cavity is studied in [Pub 1]. The driving pulse train consists of resonant π pulses of 3 ps length with Gaussian envelopes. The QD's polarization operator is considered as the source of photon emissions. Therefore, the cavity operators are replaced in all correlation functions necessary to obtain $\mathcal{P}$, $\mathcal{I}$, and $\mathcal{B}$ by QD operators.

Furthermore, to analyze the influence of the strength of the non-Markovian coupling to the phonon environment, a scaling parameter λ is introduced as a prefactor to the phonon spectral density $J(\omega)$. Thus, the coupling constant $\gamma_{\mathbf{q}}^{\mathrm{X}}$ in Eq. (1.4) is scaled by $\sqrt{\lambda}$. While a scaling of $\lambda = 0$ models a situation without a phonon environment and $1 < \lambda \leq 10$ provides a rough estimate for stronger couplings as in piezoelectric materials like GaN [37], the full GaAs model is recovered for $\lambda = 1$.

The dependence of the three figures of merit $\mathcal{P}$, $\mathcal{I}$, and $\mathcal{B}$ on the temperature T and the phonon scaling λ is shown in Fig. 2.1 using the numerically exact path-integral approach. All three quantities decrease for high temperatures and large coupling. The highest values of $\mathcal{I}$

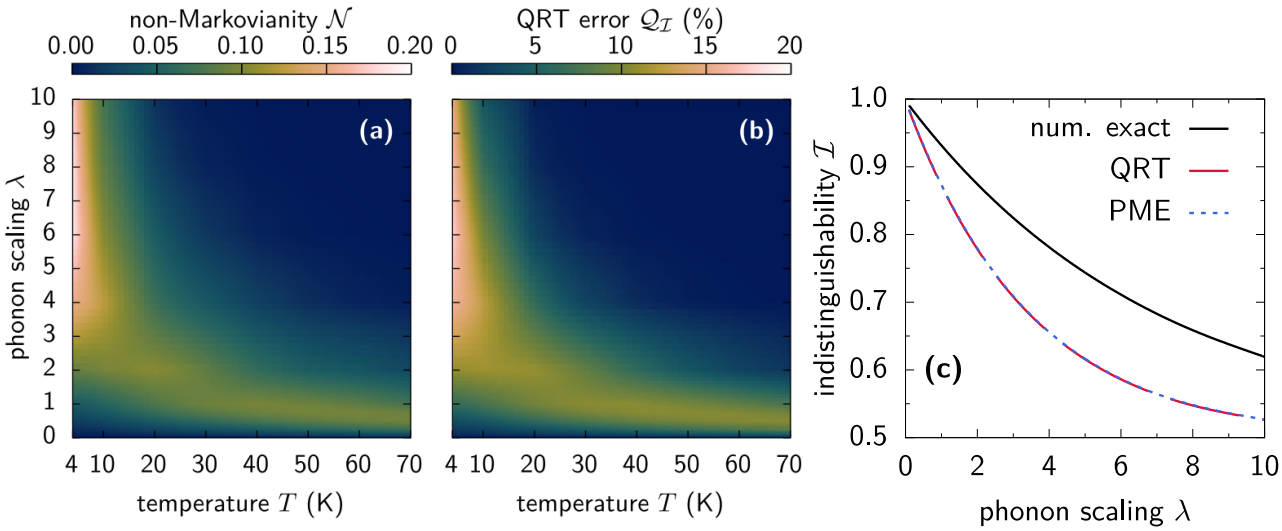

Figure 2.2: [Adapted from [Pub 1]] (a) The non-Markovianity measure $\mathcal{N}$, (b) the error $\mathcal{Q}_\mathcal{I}$ introduced by the QRT, and (c) the indistinguishability at $T = 4\,\mathrm{K}$ as a function of the phonon scaling λ. The latter is calculated using the numerically exact approach (num. exact), the QRT applied in the lab frame (QRT), and the QRT applied in a polaron transformed frame (PME).

and $\mathcal{B}$ are found in the limit of weak coupling and low temperatures, confirming previous observations of a degrading influence of the phonon environment on photonic properties[48]. The single-photon purity shows a slightly different behavior compared with the indistinguishability or the brightness in the region of interest [marked by yellow boxes in Fig. 2.1(c)]. It is nonmonotonic as a function of λ at higher temperatures with large values around $\lambda = 1$ [cf., Fig. 2.1(a)] and reaches its maximum value at large scalings and low temperatures. Phonons inhibit the full preparation of the QD exciton. Therefore, the reexcitation of the QD during the length of the pulse is suppressed even more. This leads to a lower multiphoton component explaining the higher single-photon purity. It is possible to take this phenomenon even further by using phonon-assisted off-resonant excitation, which can lead to phonon-enhanced single-photon purities. The mechanism of this enhancement is the topic of [Pub 2] outlined in Sec. 2.2.

The relative error of a figure of merit M introduced by using the QRT $\mathcal{Q}_M$ is taken as a measure for the accuracy of the QRT. Fig. 2.2(b) shows this quantity with respect to the indistinguishability $\mathcal{Q}_\mathcal{I}$. In the physically interesting region marked by yellow boxes in Fig. 2.1 it is particularly high and reaches up to 18 %. In the race for a perfect single-photon source[70] where improvements in the sub-per mill regime matter[71], this is a huge value.

In order to explain the physical origin of this error, a non-Markovianity measure $\mathcal{N}$ is introduced to assess the relevant parameter space. Its definition is stated in Eq. (8) of [Pub 1] and taken from Refs. [38,72–74] and its most important property is the implication of the indivisibility of the underlying dynamical map when $\mathcal{N} \neq 0$. This is a fundamental aspect of

non-Markovianity. Consequently, $\mathcal{N} = 0$ implies Markovian dynamics. Thus, the appearance of memory effects in the system dynamics can be traced using this measure.

The temperature and phonon scaling dependence of $\mathcal{N}$ is shown in Fig. 2.2(a) alongside the error $\mathcal{Q}_{\mathcal{I}}$ introduced by the QRT. Qualitatively, it exhibits exactly the same behavior, fostering the conclusion that the breakdown of the QRT is related to the non-Markovianity of the system dynamics. This connection, though, is highly dependent on the considered quantity: the error $\mathcal{Q}_{\mathcal{P}}$ regarding the single-photon purity is of the order of 10^{-4} for the entire parameter range studied in [Pub 1]. The physical origin of this finding is explained ibidem.

Interestingly, using the QRT one consistently overestimates the phonon influence on the indistinguishability, shown in Fig. 2.2(c) as a function of the phonon scaling λ for a slice at $T = 4\,\mathrm{K}$. Therefore, the numerically exact path-integral method shows that the theoretical upper bound for the indistinguishability of photons from a QD source is higher than previously predicted by studies using the QRT.

The polaron transform captures many essential features of the non-Markovian dynamics induced by the phonon environment, as explained in Sec. 1.5.3. It is therefore quite surprising that the accuracy of the QRT does not depend on the frame. Applying it not in the lab frame, but in a polaron transformed frame using the PME technique[58–60], the prediction of the indistinguishability does not improve at all [cf., Fig. 2.2(c)]. The reason is the following: The PME approach captures the phonon influence on the dynamics of (single-time) expectation values as the exciton occupation extremely well for the considered temperature and phonon scaling parameters [cf., Fig. (2) in the Erratum to [Pub 1]]. Therefore, a comparable error enters the calculation at the switch between the t- and the τ-propagation, when the memory is traced out, regardless of the frame. While using the QRT in the polaron frame can, in fact, predict the phonon sideband on the correct side of the ZPL in contrast to its lab frame counterpart, this sign flip does not affect the indistinguishability, which is why the application of the QRT in both frames produces agreeing results. Technical details concerning this finding are explained in the Erratum to [Pub 1].

To summarize, the accuracy of the QRT in a fundamentally non-Markovian system is not known a priori, although it can be applied in specific settings or for the calculation of specific quantities like the single-photon purity. Therefore, all subsequent studies are undertaken using the path-integral formalism[FPub 2].

2.2 Quantum dots and single photons

Single photons are a key building block in many innovative applications, in particular, in quantum communication and cryptography[12,75]. Generating them on demand with high brightness and vanishing multiphoton component is key to these technologies. QDs are widely discussed

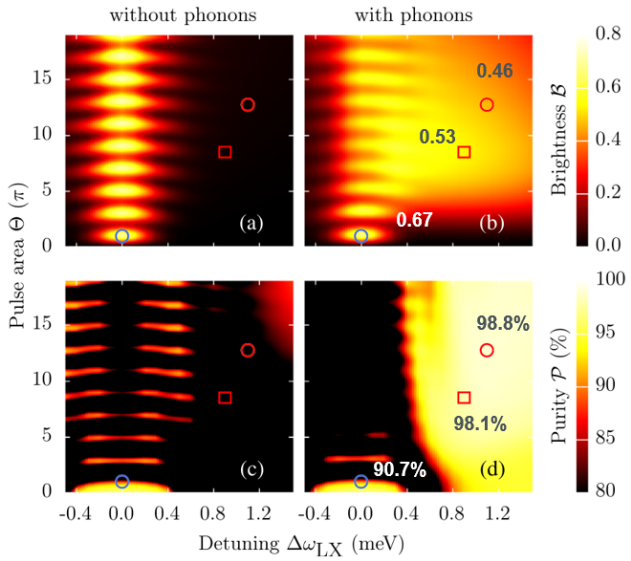

Figure 2.3: [Adapted from [Pub 2]] The brightness [panels (a) and (b)] and the single-photon purity [panels (c) and (d)] of a QD–cavity single-photon source as functions of the laser-exciton detuning and the laser pulse area. Calculations with phonons [panels (b) and (d)] are compared with phonon-free results [panels (a) and (c)]. Blue circle: the case of resonant π-pulse excitation. Red circle: the point of maximum single-photon purity including phonons. Red square: simultaneous optimization of the single-photon purity and brightness.

as a candidate system that satisfies these requirements[71,76–80]. After discussing the phonon influence on the single-photon purity in QD–cavity systems, in this section, a protocol is proposed to store the generated photon deterministically. Such buffering devices are necessary for synchronization in quantum networks.

2.2.1 Phonon-enhanced single-photon sources

The interaction with the LA phonon environment is often stigmatized as a purely destructive phenomenon regarding the technological usage of QDs. In particular, limits of the single-photon quality due to the phonon coupling have been predicted[48].

In [Pub 2], it is discovered that on the contrary, phonons can play a beneficial role. Using off-resonant phonon-assisted excitation of the QD exciton, an enhancement of the single-photon purity compared with the resonant case under otherwise identical conditions is found. In Fig. 2.3, single-photon figures of merit are shown for a QD–cavity system under various excitation conditions. The center frequency of the Gaussian-shaped pulses is varied with respect to the two-level QD transition frequency as measured by the laser-exciton detuning $\Delta\omega_{LX} := \omega_L - \omega_X$. Furthermore, their pulse area is chosen as a second parameter freely adjustable in experiment. The pulse width is kept fixed at 7 ps. The pulsed-excitation technique ascertains that the QD–cavity system is an on-demand source. The photon emission is triggered by the arrival of the external pulse in contrast to, e.g., sources exploiting spontaneous parametric down conversion (SPDC)[81].

In the case without phonons [panels (a) and (c) in Fig. 2.3] both the brightness and the single-photon purity are symmetric with respect to the detuning and display Rabi rotations with respect to the pulse area. This is expected since at all odd multiples of π the QD is inverted and has therefore the capacity to emit a photon. The phonon influence [panels (b)

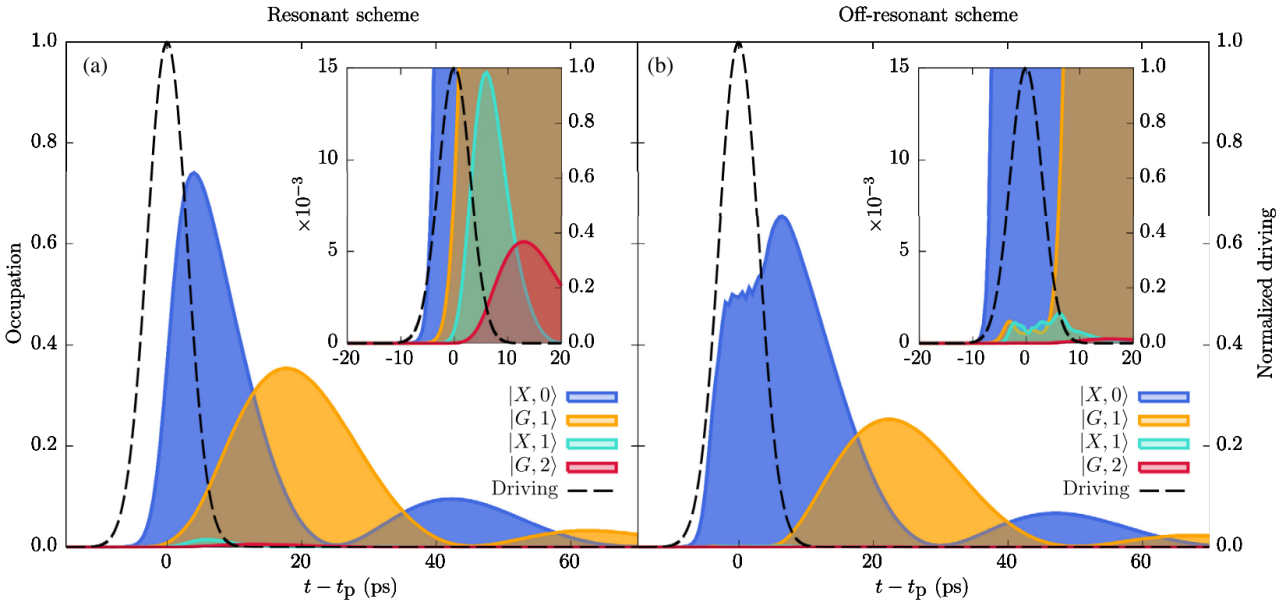

Figure 2.4: [Taken from [Pub 2]] Occupation dynamics of the QD–cavity states during and after the pulse (driving). The resonant (a) (cf., blue circle in Fig. 2.3) and the off-resonant phonon-assisted excitation schemes (b) (cf., red circle in Fig. 2.3) are compared with each other. The latter exhibits a two-step process in the exciton occupation (blue line) of phonon-induced relaxation in the dressed-state basis and subsequent adiabatic undressing.

and (d) in Fig. 2.3] renders the picture completely asymmetric. The reason is the asymmetry of phonon emission and absorption at low temperatures. While the former is always possible, the latter is less probable due to the absence of phonon occupation at temperatures of a few kelvin. A large parameter regime appears for $\Delta\omega_{\mathrm{LX}} > 0$, where both the brightness and the single-photon purity take on high values. This phonon impact even significantly enhances the single-photon purity compared with the resonant π-pulse excitation [blue circle in Fig. 2.3(d)]. Its maximum value of 98.8 % [red circle in Fig. 2.3(d)] is comparable to experimentally obtained values for the optimum-case resonant excitation, which is found for shorter pulse lengths of around 3 ps, namely 98.8 %[78] and 99.1 %[79].

The vital advantage of the off-resonant scheme compared with its resonant counterpart lies in its robustness against small fluctuations of pulse parameters, such as the central frequency or the area (cf., Fig. 2.3). Furthermore, off-resonant excitation allows for a spectral separation of pump and signal, thus providing a background-free single-photon source.

The reason for this finding is the two-step nature of the phonon-assisted exciton preparation. During the pulse, the phonons induce a relaxation in the dressed-state basis, the eigenbasis of the laser-driven two-level problem, into the lower-energy dressed state. In the original bare-state basis, this means that the exciton is only occupied by half [cf., Fig. 2.4(b)]. When switching off the pulse, the system is adiabatically undressed[82], yielding a boost of the exciton occupation only at a time when the pulse amplitude has essentially vanished [cf., Fig. 2.4(b)].

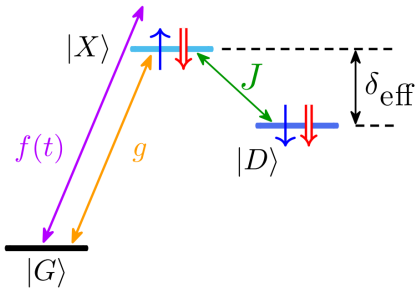

Figure 2.5: [Taken from [Pub 3]] Sketch of the Λ-type three-level system. The left arm is coupled to a cavity and is driven by an off-resonant AC-Stark pulse. The right arm is coupled by the flip-flop term that induces simultaneous spin flips of the electron (blue arrows) and the Mn spin. The red arrows represent the hole spin, which is pinned in a pure heavy-hole system.

Therefore, reexcitation of the QD and subsequently the possibility of multiphoton emission are strongly suppressed. The dynamics of the QD–cavity state occupations in the off-resonant case is compared with the resonant one in Fig. 2.4.

2.2.2 Deterministic storage and readout of a single photon

To technologically use a single photon in an optical quantum network, synchronization is paramount. Therefore, buffering a single photon to control the exact emission time is necessary. In [Pub 3], a QD-based single-photon buffering device is proposed.

Buffering, i.e., temporary storage and readout can be achieved by exploiting a metastable state. The dipole-dark exciton states with a total spin of ± 2 are interesting candidates for this application, since their decay time is about two orders of magnitude longer than that of the bright exciton. To this end, the model of the two-level QD has to be expanded.

In particular, a mechanism is needed that allows for optically addressing the dark state. Introducing a single magnetic atom as a dopand couples the bright and dark states via the exchange interaction. Manganese (Mn) stands out because of its large spin of $\frac{5}{2}$. To enable isoelectric doping, this analysis is performed for a CdTe/ZnTe QD.

Assuming the Mn spin to be initially prepared in the state with orientation $M_z = -\frac{5}{2}$ and a circular polarization of the external laser of -1, the QD can be modeled as a Λ-type three-level system. Using the projection of the total spin of the electronic excitation and the Mn spin orientation as labels, the three product states are the ground state $|G\rangle := |0, -\frac{5}{2}\rangle$, the bright exciton $|X\rangle := |-1, -\frac{5}{2}\rangle$, and the dark exciton $|D\rangle = |-2, -\frac{3}{2}\rangle$.

A sketch of the corresponding level scheme including its couplings is shown in Fig. 2.5. The transition between the ground and the bright state interacts with a single-mode microcavity. The electron-Mn exchange interaction leads to a coupling between the bright and the dark state. These two states are split by δ_{eff}, consisting of a material dependent intrinsic splitting due to the electron-hole exchange interaction and a splitting arising from an Ising-term contribution to the carrier-Mn exchange. By applying an external magnetic field in Faraday configuration, δ_{eff} can be tuned.

To obtain full-amplitude oscillations between the two exciton states and thus facilitate an

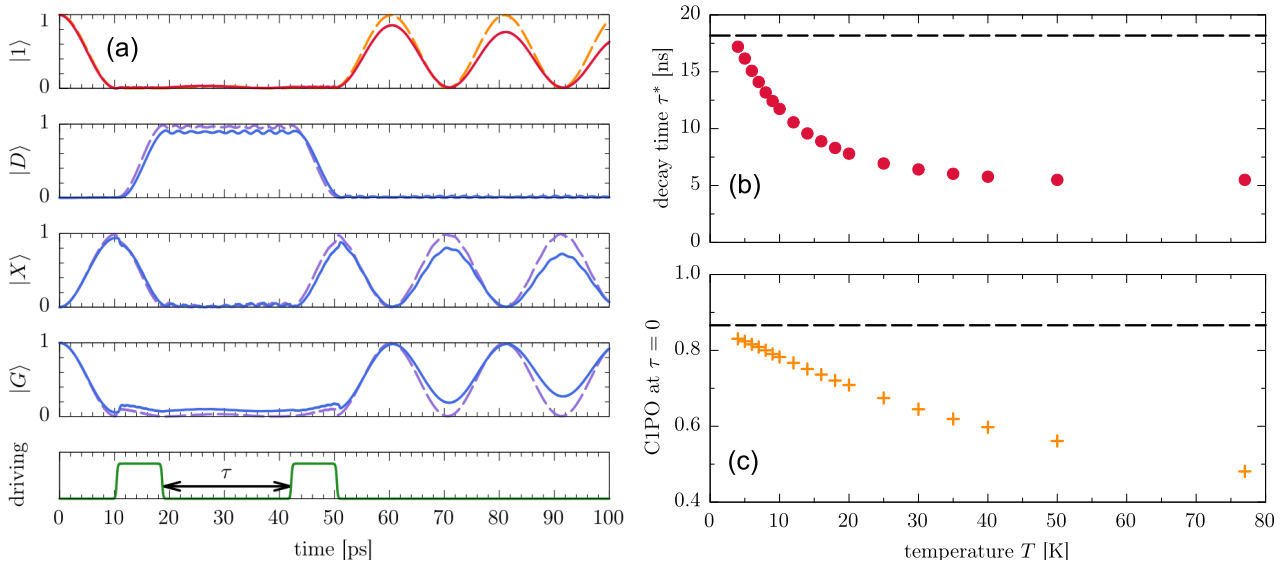

Figure 2.6: [Adapted from [Pub 3]] (a) The occupation dynamics of the QD states and the single-photon Fock state. The bottom panel shows the two AC-Stark pulses to write the excitation to the dark state and then read it out again after the storage time τ. The ideal case without phonons and losses (dashed lines) is compared with the case including radiative decay and cavity losses (solid lines). (b) The decay time τ^* and (c) the maximum captured 1-photon occupation (C1PO) at $\tau = 0$ depending on the temperature T. The dashed lines mark the phonon-free value.

excitation transfer, they need to be brought into resonance for half an oscillation period. To enable this energetic shift on such fast timescales, the optical or AC-Stark effect is exploited. An external laser driving the transition between the ground and the bright state off-resonantly induces an energetic shift [FPub 4]. Choosing a rectangular pulse with appropriate specifications, the effective splitting δ_{eff} can be canceled during the plateau time of the pulse [cf., Sec. IV.A. in [Pub 3]].

Suppose that the cavity contains a single photon that needs to be buffered. The initial state of the dynamics is thus $|G, 1\rangle$. In Fig. 2.6(a), the occupation dynamics of the three QD states and the single-photon Fock state of the cavity are shown. After half a Rabi oscillation between the cavity and the QD, the bright state $|X\rangle$ is occupied. Then, an AC-Stark pulse, the *writing* pulse, is switched on, such that $|X\rangle$ and $|D\rangle$ are effectively put to resonance. The exchange coupling J leads to the occupation of the dark state $|D\rangle$. After the storage time τ, a second *readout* pulse reverses the entire writing process to eventually put back the excitation to the cavity as a single photon, which then oscillates with the bright exciton. In the ideal case without losses and phonons [dashed lines in Fig. 2.6(a)], the first maximum after the readout pulse is close to unity, thus proving the concept of the buffering device.

This maximum captured 1-photon occupation (C1PO) after the readout pulse is now taken as a measure for the performance of the protocol. Its value at $\tau = 0$ shows how much of the

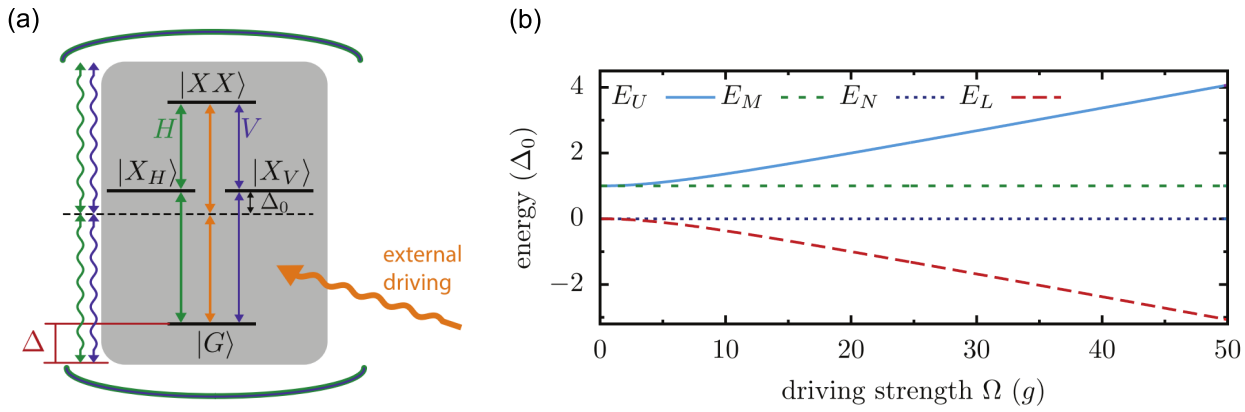

Figure 2.7: [(a) Taken from [Pub 5], (b) taken from [Pub 4]] (a) Sketch of the four-level emitter (FLE) coupled to two oppositely polarized cavity modes. The two-photon resonance of the FLE is driven externally. (b) The energies of the four laser-dressed states depending on the driving strength.

excitation initially present in the cavity is lost during writing and readout. The dashed line in Fig. 2.6(c) displays its value including radiative and cavity loss effects, but without taking phonons into account. The yellow points show its temperature dependence. While it is well above 80 % for low temperatures, more than 50 % of the excitation is lost at 77 K only because of the writing and readout processes.

Simulating the storage time dependence C1PO(τ) and fitting an exponential function yields a decay time τ^* that can be interpreted as a characteristic length for which storage is reasonably possible. At $T = 4\,\mathrm{K}$, this value reaches 17 ns and at high temperatures it is still around 5 ns. Thus, even under realistic conditions, the proposed buffering device can store a single photon about two orders of magnitude longer than state-of-the-art high-quality microcavities alone.

2.3 Polarization-entangled photon pairs

Entanglement is a phenomenon entirely native to the quantum realm. It is a feature of quantum mechanics which is at the heart of many innovative applications, predominantly in quantum communication [10,11] and cryptography [12,13]. Moreover, from the point of view of basic research, it allows for the inspection of Bell's inequalities [83,84], thus ultimately testing the fundamental principles of quantum mechanics itself.

Polarization-entangled photon pairs are a particularly interesting realization of an entangled bipartite system because of their traveling with the velocity of light and their robustness against environmental disturbance. An attractive platform to generate such pairs are diamond-shaped four-level emitters (FLEs). A sketch of an FLE coupled to two degenerate modes of opposite polarization in a cavity is shown in Fig. 2.7(a). In addition to the ground state and two

oppositely polarized excited states, there is a doubly excited state $|XX\rangle$, which typically has an energy less than twice the excited-state energy. In a QD, this is the biexciton state, a bound state composed of two excitons, which leads to a biexciton binding energy E_B corresponding to the reduction of its energy.

The two different types of Bell states (BS) are famous examples of maximally entangled states

$$\Phi_\pm = \frac{1}{\sqrt{2}}\left(|HH\rangle \pm |VV\rangle\right) \tag{2.2a}$$

$$\Psi_\pm = \frac{1}{\sqrt{2}}\left(|HV\rangle \pm |VH\rangle\right) , \tag{2.2b}$$

henceforth called ΦBS and ΨBS, respectively. H (V) denotes a horizontally (vertically) polarized photon and the order of their notation in Eq. (2.2) corresponds to the temporal order of their detection.

Preparing the state $|XX\rangle$ and subsequently leaving the system to cascaded decay has been demonstrated as a pathway to generate ΦBS in numerous works[11,84–90]. The addition of a constant external driving [cf., Fig. 2.7(a)] opens up the possibility to create ΨBS using the presented FLE[91]. Driving the two-photon resonance leaves two free parameters, the cavity-laser detuning Δ and the driving strength Ω.

[Pub 4] is devoted to analyzing this parameter space and predicting the type of the resulting entanglement. To this end, a discussion in terms of the laser-dressed states turns out to be beneficial. The eigenenergies of the driven electronic subsystem are depicted in Fig. 2.7(b). The four states are denoted as the upper (U), middle (M), null (N), and lower (L) state. While the energies of M and N do not depend on the driving strength, U and L exhibit such a dependency [cf., Eqs. (10)–(12) in [Pub 4]]. Now, the emission of an entangled photon pair is connected to two-photon transitions in the FLE system. Its probability in the driven case is highest when the dressed states offer a two-photon transition, i.e., when twice the photon energy matches the energy difference between two laser-dressed states. Combinatorially, this state of affairs presents numerous opportunities of entanglement generation.

Technically, one measure to quantify the degree of entanglement is the concurrence[92] [for a formal definition, cf., Eqs. (19) and (20) in [Pub 4]], which is widely accepted to characterize an entangled bipartite system. The input quantity for this measure is the two-photon density matrix, which is reconstructed in experiment using quantum state tomography[93] and modeled by two-time correlation functions [cf., Eqs. (16)–(18) in [Pub 4]], which are obtained following the phonon-free method in [FPub 2]. The qualitatively most important point of this definition is the fact that the concurrence has a monotonic relation to the entanglement of formation[94] and can thus be considered a direct measure for the entanglement of the given bipartite system in its own right.

[Pub 4] delivers a detailed analysis of the different two-photon resonances. Analytic approx-

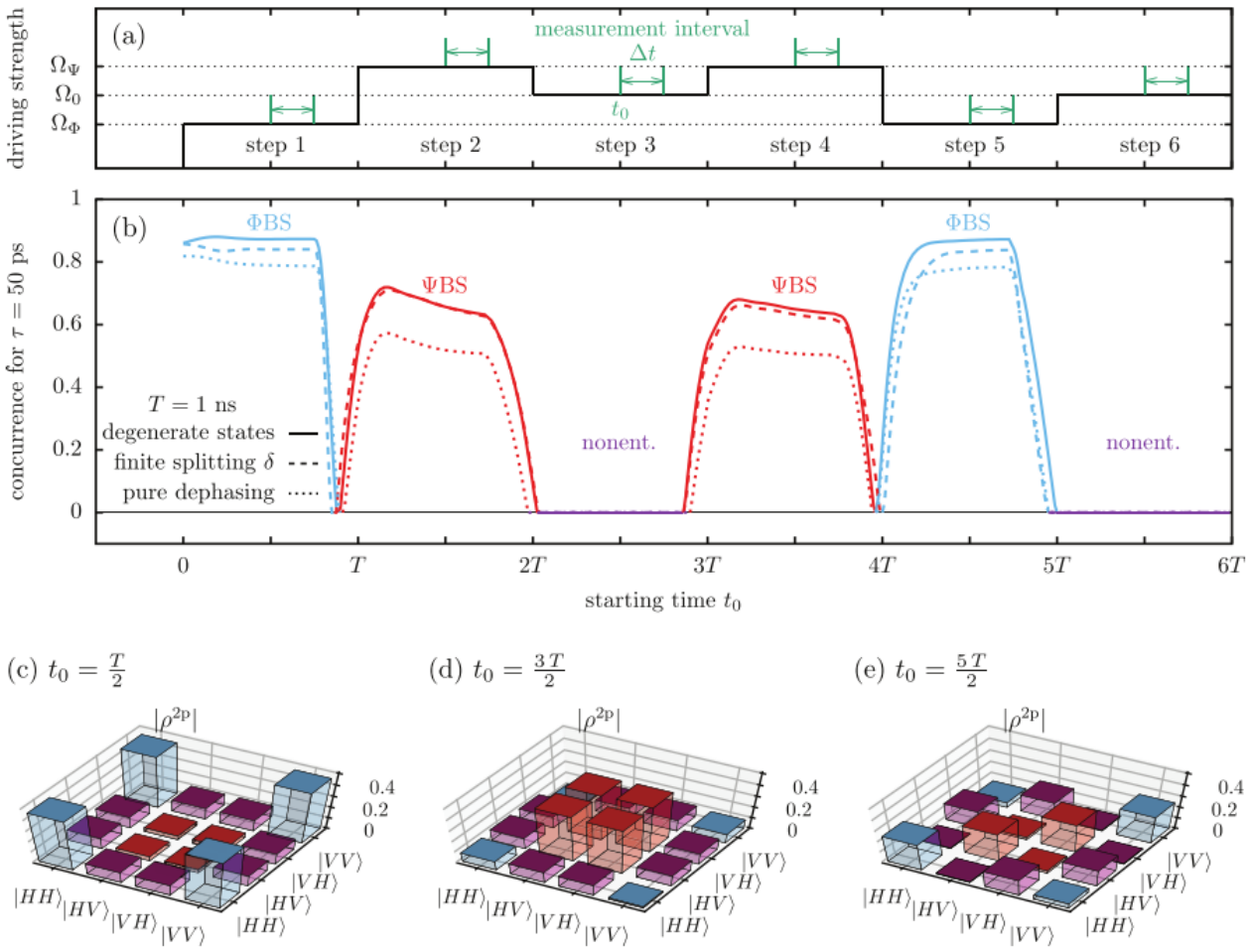

Figure 2.8: [Taken from [Pub 5]] (a) Time-dependent step-like protocol to achieve entanglement switching. (b) Concurrence depending on the starting time t_0 of the coincidence measurement. The entanglement type is color-coded. (c)–(e) Two-photon density matrices corresponding to the different types of entanglement as measured at the respective t_0.

imations are found in terms of the Schrieffer-Wolff transformation, which reduces the problem to the subspace of the most relevant states. Thus, for each resonance and combination of laser parameters, a prediction is possible, whether the system exhibits entanglement at all and, if so, whether the entanglement type is ΦBS or ΨBS. The numerical results confirm these predictions.

While the entanglement type could be changed after the generation of the photon pair using waveplates or polarization filters, in a chosen basis, the two types are clearly distinguishable. Targeting each type in a given basis by just adding external driving thus allows for the time-dependent switching between the entanglement types by adjusting the laser parameters. In [Pub 5], a step-like protocol is proposed that realizes this idea.

In experiment, the reconstructed two-photon density matrix depends on three measurement parameters: the starting time of the measurement t_0, its real-time length Δt, and the delay-time window τ of the coincidence experiment. Thus, the concurrence also depends on these

parameters. Fig. 2.8(b) shows the concurrence as a function of t_0 for fixed τ and Δt, while the driving protocol is displayed in panel (a) of the same figure. Clearly, high ΦBS and ΨBS entanglement is achieved deterministically depending on the external driving. Also, for a certain laser parameter set, a nonentangled state is found. Furthermore, this switching does not depend on the order, which is demonstrated in steps 4 to 6 in Fig. 2.8(a) and (b). The corresponding two-photon density matrices are shown in Fig. 2.8(c)–(e). For ΦBS, the occupations and coherences between the states $|HH\rangle$ and $|VV\rangle$ clearly dominate, while the corresponding values of the states $|HV\rangle$ and $|VH\rangle$ are high for ΨBS. In the nonentangled case, the density matrix is close to a mixed state, which exhibits no entanglement.

To analyze the stability of this protocol against small disturbances of the system, a finite splitting δ between the two exited states is introduced. In QDs, this splitting is known as the fine-structure splitting. Choosing a value realistically encountered in QDs, the concurrence is decreased only slightly [cf., dashed line in Fig. 2.8(b)]. Furthermore, including a phenomenological dephasing model with a rate observed in QDs at low temperatures leads to a quantitative reduction of the concurrence, while the qualitative feature of the switching process is preserved [cf., dotted line in Fig. 2.8(b)].

2.4 Multiphoton states and structures

Having started with QDs as single-photon sources and discussed the generation of entangled photon pairs, the investigation of multiphoton states and structures ensues. While the simplest multiphoton state is a higher-order Fock state, N-photon bundles are their close relatives, since they are created by the cascaded emission from a cavity starting with the Fock state $|N\rangle$. This process leaves a characteristic fingerprint in the photon number distribution, which is used as an identifying feature in the corresponding analysis. The utility of photon number distributions in studying multiphoton states is further demonstrated, when transiently and qualitatively changing overall shapes are observed for different excitation conditions of the QD, in particular, under consideration of the phonon environment. This section culminates with the proposal of QDs as sources of photonic Schrödinger-cat states.

2.4.1 Higher-order Fock states

Inspired from the field of atomic physics, [Pub 6] transfers existing protocols to prepare higher-order Fock states from the atomic to the solid-state realm and proposes an additional one specific to the solid state. The general idea for atoms in cavities is a limitation of the atom–cavity coupling to the time of flight through the cavity[95–97]: an excited atom is sent through a cavity, to which it couples resonantly. The velocity is adjusted such that its time of flight is

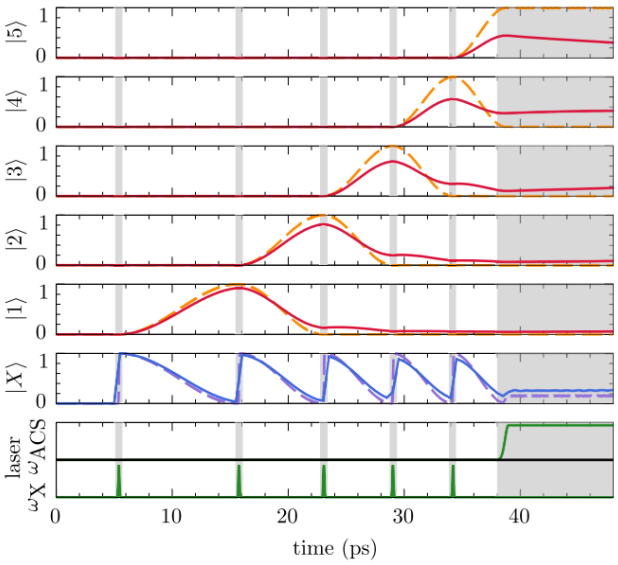

Figure 2.9: [Taken from [Pub 6]] Dynamics of the protocol with uninterrupted coupling (PUC). The exciton occupation and the fidelities to the Fock states with $n = 1, 2, ..., 5$ are shown. Dashed lines: ideal case without phonons or losses. Solid lines: results including phonon effects as well as cavity and radiative losses at 4 K. The lowest panels show the envelope functions of the driving lasers.

exactly half a Rabi oscillation between atom and cavity. Repeating this process subsequently increases the order of the Fock state created inside the cavity.

Since a QD has a fixed location in space, the temporal coupling has to be achieved otherwise. In [Pub 6], an off-resonant AC-Stark pulse is used to bridge the detuning between the QD and the cavity. The length of the pulse controls the time interval, in which the excitation transfer from the QD to the cavity takes place. This protocol with interrupted coupling (PIC) yields a 5-photon Fock state with a fidelity of 96.3 % in the ideal case without taking loss or phonon effects into account. Including both at $T = 4\,\mathrm{K}$ reduces this number to 38.5 %.

In superconducting qubits placed in microwave cavities, the preparation of higher-order Fock states has been demonstrated[98]. Although Ref. [98] gives no value for the fidelity, an estimation is possible by reproducing their experimental result in the simulations yielding roughly 20 %. Higher-order Fock states have also been prepared using SPDC[81] with fidelities not exceeding 50 % regarding the state $|5\rangle$. Thus, the PIC result is competitive with existing schemes on other platforms. The advantage of the PIC in QDs is its on-demand character compared with SPDC sources. Furthermore, a cooling to the mK-regime as in superconducting qubits is not necessary.

Exploiting the spatial localization of the QD, a protocol with uninterrupted coupling (PUC) is proposed in [Pub 6]. A QD grown on resonance with the single cavity mode is assumed. The preparation of the exciton is accomplished by an ultrashort 100 fs-pulse. Thus, the timescales of the preparation and the cavity coupling are separated, such that during the preparation process the cavity coupling can be neglected. The lowest panels of Fig. 2.9 show the PUC to prepare a 5-photon Fock state. The exciton occupation and the fidelities to the Fock states $|n\rangle$ with $n \in \{1, 2, 3, 4, 5\}$ are displayed in the upper panels. Only at the end of the protocol an AC-Stark pulse is needed to effectively decouple the QD from the cavity to preserve the

target state there without interference from the QD. In the ideal case (dashed lines), a fidelity to the state $|5\rangle$ of 99.4 % is achieved. Including phonon effects at $T = 4\,\mathrm{K}$ as well as realistic cavity loss and radiative decay rates yields a fidelity of 45.1 %, which is 17 % higher than the PIC result. The reason is the 15 % shorter runtime of the PUC compared with the PIC, which leaves the loss processes less time to act on the QD–cavity system.

To analyze the robustness of the PUC against the two-level approximation, a variety of extended models is discussed in [Pub 6]. Using ultrashort pulses to excite the QD could lead to the excitation of higher-energetic exciton states (HEES) due to the large spectral width of the pulses. A finite exchange coupling between the two oppositely circularly polarized excitons can introduce the biexciton to the system dynamics. Furthermore, a linearly polarized excitation can address the biexciton directly as a parasitic state. It is shown in [Pub 6] that the influence of a HEES and a finite exchange coupling on the PUC is only minor. While the inclusion of the parasitic biexciton state when linearly polarized lasers are used is quite detrimental, a simple pulse-shaping technique can salvage a nonzero fidelity.

2.4.2 N-photon bundles

An N-photon bundle is a recently proposed[99] quantum structure of light related to Fock states that is defined by its temporal emission properties. Bundle emission takes place as a cascade over successive Fock states starting from $|N\rangle$ in the stationary case of a constantly driven cQED system. Since a Fock state $|n\rangle$ effectively decays with $n\kappa$ in a resonator with loss rate κ, the temporal spacing between the photons forming the bundle is a direct consequence of the outcoupling process. The corresponding photon statistics reflects this property

$$P_N(n) = \begin{cases} 1 - \frac{\langle n\rangle}{N} \sum_{j=1}^{N} \frac{1}{j} & n = 0 \\ \frac{\langle n\rangle}{N} \frac{1}{n} & 1 \leq n \leq N \\ 0 & n > N \end{cases} \tag{2.3}$$

and can thus be considered a fingerprint of an N-photon bundle. Here, $\langle n\rangle$ is the stationary mean photon number.

In [Pub 7], the suitability of solid-state implementations of the generic cQED system discussed in Ref. [99] is investigated, in particular a QD–cavity system. The analysis is focused on the case $N = 2$, using Eq. (2.3) as the defining property to characterize the bundle. This implies a number distribution, where the Fock state $|2\rangle$ has half the occupation of the state $|1\rangle$, while all higher-order Fock states are not occupied at all.

For the numerical studies, system parameters, in particular the cavity loss and radiative decay rates, are chosen such that they are realistically achievable with current equipment. While the

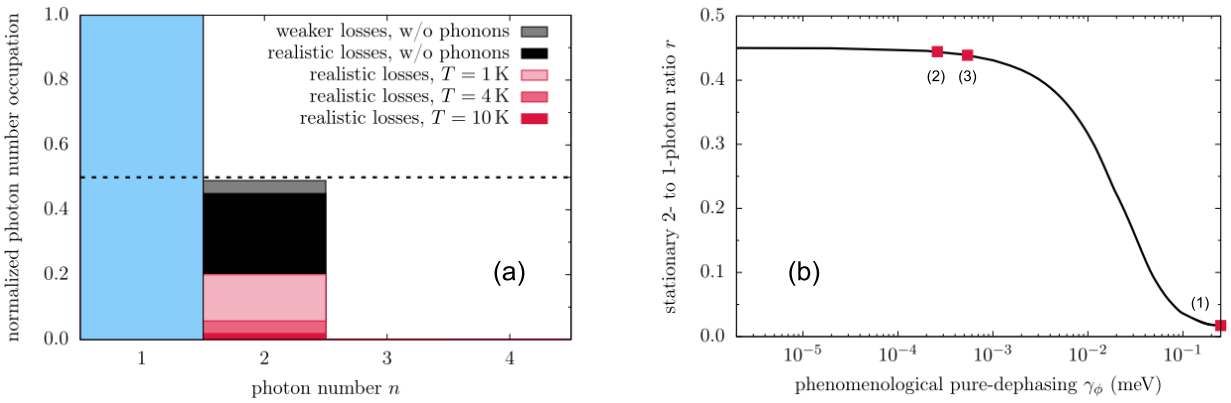

Figure 2.10: [Adapted from [Pub 7]] (a) The photon number distribution normalized to the 1-photon Fock state. The value 0.5, indicative of a 2-photon bundle, is marked by a dashed line. (b) Stationary 2- to 1-photon ratio r as a function of a pure-dephasing rate, when a Lindbladian model is used instead of the full microscopic phonon Hamiltonian. Red squares mark special cases of model calibrations, cf., main text.

bundle statistics is reasonably observable in the phonon-free case [cf., black bar in Fig. 2.10(a)], choosing a set of weaker loss parameters as in Ref. [99] yields a ratio r of the stationary 2- to 1-photon occupation closer to the target $r = 0.5$ [cf., gray bar in Fig. 2.10(a)]. Including the phonon coupling leads to a number distribution, which can no longer be considered to characterize a 2-photon bundle. Already at $T = 1\,\mathrm{K}$, the ratio drops to $r = 0.2$.

In contrast to the analysis of the phonon impact in [Pub 7] based on the microscopic model H_{Ph} [cf., Eq. (1.4)], in Ref. [99] the impact of pure dephasing on the generation of N-photon bundles is studied in terms of a Lindbladian $\mathcal{L}_{|X\rangle\langle X|,\gamma_\phi}$. Therefore, this case constitutes an opportunity to investigate the range of validity of a Lindbladian model compared with the full microscopic analysis. To this end, the ratio r is calculated for different values of the phenomenological pure-dephasing rate γ_ϕ in Fig. 2.10(b) by exchanging the microscopic phonon model H_{Ph} for a Lindblad contribution $\mathcal{L}_{|X\rangle\langle X|,\gamma_\phi}$ to the Liouville–von Neumann equation, Eq. (1.6).

In the limit of vanishing γ_ϕ, the value $r = 0.45$ is reclaimed [cf., black bar in Fig. 2.10(a)]. A large plateau region is found where the addition of $\mathcal{L}_{|X\rangle\langle X|,\gamma_\phi}$ has only a marginal effect on the bundle generation. Therefore, the question arises which value of γ_ϕ best approximates the full microscopic model. For this purpose, the Lindbladian is calibrated to three different cases, where the microscopic model H_{Ph} is used, indicated by red squares in Fig. 2.10(b): (1) a driven Jaynes-Cummings model with $|G, 0\rangle$ as the initial state, (2) Jaynes-Cummings model without driving with the initial state $|G, 1\rangle$, and (3) Jaynes-Cummings model again without driving, but with $|G, 2\rangle$ as the initial state. This comparison is performed for the all-resonant case at $T = 4\,\mathrm{K}$ without taking cavity and radiative losses into account, in order to compare the pure phonon influence without interference from other effects. The exciton dynamics is compared for varying γ_ϕ until the envelopes of the two results agree.

Case (1) is the closest approximation to the full model, where the calibration yields a large pure-dephasing rate of the order of 0.1 meV. As the full microscopic model, the phenomenological Lindbladian predicts the destruction of the bundle in terms of a nearly vanishing ratio r when the rate γ_ϕ is chosen properly. Often, rates in the μeV regime are quoted when a rough estimate of the phonon influence in QD–cavity systems is sought after. From the above calibration, it becomes clear that such a rate is valid only when the system is not driven. Furthermore, care has to be taken concerning multiphoton states and structures, since the rate turns out to depend on the photon number inside the cavity [cf., cases (2) and (3)].

Thus, for special *a posteriori* justified cases, the use of a phenomenological Lindbladian model instead of the full microscopic one is possible. To freely roam the parameter space of a QD–cavity system, though, it is advisable to use the full model lest *a priori* elusive dependencies are overlooked.

2.4.3 Shape-shifting photon number distributions

Photon number distributions are a versatile tool to visualize superpositions of many Fock states. Although they contain no information on the coherences, number distributions allow for a quick overview over some important features of the state. In particular, the qualitative shape of such a distribution and its evolution in time are the topic of [Pub 8].

Rough features of a number distribution can be captured using just a few numbers like the mean photon number $\langle n \rangle$ and the Mandel parameter

$$Q := \left(\langle \Delta n \rangle^2 - \langle n \rangle \right) / \langle n \rangle \,. \tag{2.4}$$

The latter measures the normalized deviation of the mean-square fluctuation $\langle \Delta n \rangle^2$ from the mean photon number $\langle n \rangle$. For Poissonian distributions corresponding to coherent states, which are considered to be the closest to the classical realm, the Mandel parameter vanishes, thus drawing a line between the super-Poissonian regime with $Q > 0$ and the sub-Poissonian regime for $Q < 0$, which implies a quantum state since there is no classical analog to this situation [100].

In [Pub 8], the excitation of a two-level QD in a cavity with chirped laser pulses is studied, i.e., pulses with frequencies changing linearly in time. The shape of number distributions and its evolution are investigated for various excitation conditions, in particular, the pulse length and the sign of the chirp, which determines a linearly increasing or decreasing pulse frequency.

The pulse length has a profound impact on the distribution, which is first analyzed using chirp-free pulses. For short pulses around a few picoseconds, the result is known from the usage of QD–cavity systems as single-photon sources: The single-photon component Rabi-oscillates with the vacuum, which translates to an oscillating mean photon number [cf., orange line in Fig. 2.11(a)]. The Mandel parameter, shown in Fig. 2.11(b), oscillates between at most −1

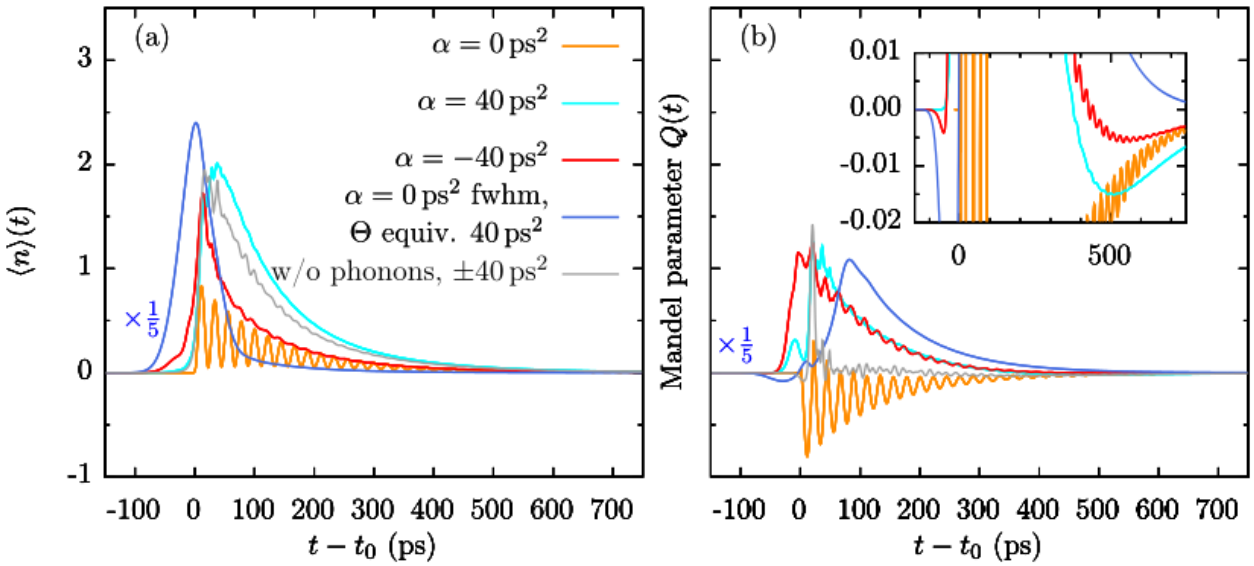

Figure 2.11: [Taken from [Pub 8]] (a) Mean photon number and (b) Mandel parameter for different excitation conditions. The pulse with chirp α has its maximum at $t = t_0$. Phonon effects at $T = 4\,\mathrm{K}$ are taken into account, unless noted otherwise. Choosing a chirp-free pulse with pulse area and length corresponding to the effective values obtained after passing the chirp filter results in the blue lines. Note that these results are scaled down by a factor of 5.

and basically 0, thus indicating the quantumness of the investigated state. This implication is correct, since two Fock states perform an oscillatory dynamics. For longer pulses around 100 ps with larger pulse area, a bell-shaped distribution moves up and down the Jaynes-Cummings ladder, while keeping its shape (cf., Fig. 1 in [Pub 8]). Thus, it reaches large mean photon numbers [cf., blue line in Fig. 2.11(a)]. This is qualitatively different from the situation with shorter pulses.

Sending a Gaussian pulse through a chirp filter results in adjusted pulse parameters [cf., Eq. (11) in [Pub 8]]. Most importantly, the pulse length is effectively prolonged. The parameters in [Pub 8] are chosen such that after applying the chirp filter, both the effective pulse area and length correspond to the parameters of the long pulse considered in the chirp-free case. Thus, the influence of a linearly changing frequency is distilled from all other effects.

In the phonon-free case, chirped excitation leads to distributions that stay close to the vacuum, instead of moving up and down the Jaynes-Cummings ladder, as monitored by the much lower mean photon number [cf., gray line in Fig. 2.11(a)]. Moreover, the shape changes dynamically: Distributions with two smooth peaks as well as jagged shapes with multiple maxima are observed [cf., Figs. 2(a) and (b) in [Pub 8]]. The dynamics is symmetric with respect to the sign of the chirp. The phonons have an asymmetric influence on the distributions depending on this sign. While the jaggedness is smoothed out for positive chirp, the distribution thermalizes for a negative sign [cf., Figs. 2(c) and (d) in [Pub 8]]. The reason is the asymmetry of phonon

emission and absorption at low temperatures. Analyses in terms of laser- and cavity-dressed states described in detail in [Pub 8] yield insights into the behavior of the mean photon number shortly before and after the pulse maximum as well as the origin of the double-peaked shape.

Notably, in all considered cases the Mandel parameter assumes a value of zero at some point of the time evolution. Interestingly, though, the corresponding shape of the distribution might be far off the bell shape of a Poissonian. Already at about 40 ps, Q is close to zero in the phonon-free case with chirped excitation [cf., gray line in Fig. 2.11(b)]. Often, this finding is taken as an indication of the Poissonian nature of the distribution. In [Pub 8], it is shown that the corresponding distribution has a jagged shape with two maxima, thus being far from having a Poissonian bell shape. It is therefore an important conclusion that there are physically relevant situations, where the Mandel parameter fails as a measure for the deviation from a Poissonian distribution.

2.4.4 Schrödinger-cat states

Time and time again, effects were predicted on the basis of the quantum theory that were considered to be absurd and thus prove quantum mechanics wrong, just before being experimentally observed and backing precisely these absurd aspects of the theory and nature itself. A famous example is Schrödinger's gedankenexperiment of the cat in a box[101] supposedly being alive and dead simultaneously

$$|\mathrm{cat}\rangle = \mathcal{N}\left(|\mathrm{alive}\rangle + e^{i\varphi}|\mathrm{dead}\rangle\right) , \tag{2.5}$$

where $\mathcal{N}$ is the normalization and φ a phase. Such Schrödinger-cat states $|\mathrm{cat}\rangle$ are interesting both from a technological[18,102–104] and a fundamental point of view to understand the quantum-to-classical transition[105].

A possible implementation of a Schrödinger-cat state in quantum optics is the coherent superposition of two macroscopically distinguishable states. In [Pub 9], two protocols to generate Schrödinger cats in QD–cavity systems are analyzed, one driving the QD, thus indirectly transferring excitations to the cavity, and the other driving the cavity directly. The dot-driven protocol (DOD) targets the superposition of two coherent states and is adapted from a protocol first proposed by Law and Eberly[106] employed in a QD–cavity setup. Indeed, in the ideal case without phonons and losses, this protocol yields a Schrödinger cat with near-unity fidelity. Its Wigner function [cf., Fig. 2.12(a)] is a textbook example of a Schrödinger-cat state's: two packets representing the two coherent states are coherently superposed, which is indicated by the oscillations to negative values between them. Note that there is no classical analog for a negative-valued Wigner function, which is why it can be used to define a nonclassicality measure δ[107] [cf., Eq. (9) in [Pub 9]]. While considering radiative decay of the QD and cavity losses

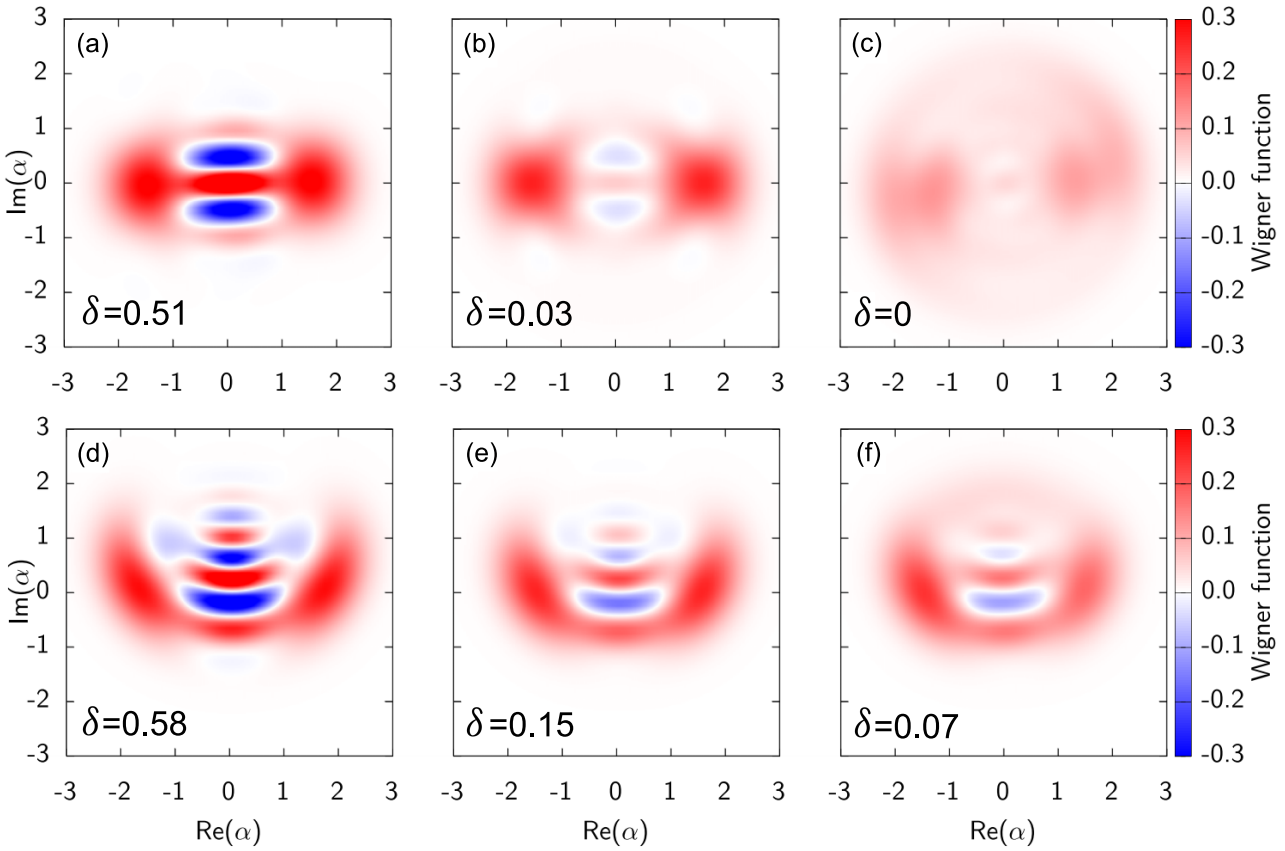

Figure 2.12: [Adapted from [Pub 9]] (a) Optical Wigner functions of the photonic states at the times of their respective preparation after the DOD [panels (a), (b), and (c)] and the CAD [panels (d), (e), and (f)]. Their argument is the complex coherent amplitude α [cf., Eq. (B1) in [Pub 9]]. Three different model cases are shown: [(a), (d)] the ideal case without losses or phonons, [(b), (e)] including radiative decay and cavity losses, [(c), (f)] considering both, loss and phonon effects at $T = 4\,\mathrm{K}$. For each Wigner function, the corresponding nonclassicality measure δ is given.

reduces the nonclassicality [cf., Fig. 2.12(b)], already at $T = 4\,\mathrm{K}$ the phonon influence destroys the superposition completely. Indeed, the corresponding Wigner function in Fig. 2.12(c) is positive-valued and resembles the incoherent superposition of two macroscopically distinguishable states.

The cavity-driven protocol (CAD) is based on an observation in Refs. [108,109]: In the textbook collapse-and-revival phenomenon of the Jaynes-Cummings model a Schrödinger-cat state emerges at half the revival time in the limit $\langle n\rangle \to \infty$, at which the two-level system and the cavity even factorize. To harness this feature, a suitable initial state has to be prepared in the cavity and an appropriate $\langle n\rangle$ has to be found that yields a high fidelity to the target Schrödinger cat. The resulting CAD in [Pub 9] is a one-pulse protocol, compared with the ten pulses necessary in the DOD, that yields a Schrödinger cat not only in the ideal case [cf., Fig. 2.12(d)]. Including losses and even phonons [cf., Figs. 2.12(e) and (f)] diminishes the

amplitude of the oscillations to negative values in the Wigner function without damping them out completely. In particular, the nonclassicality as measured by δ is finite. Note that an AC-Stark pulse is necessary in both protocols to effectively decouple the QD from the cavity to preserve the target state directly after its preparation, exactly as in Sec. 2.4.1.

Thus, the Wigner function in Fig. 2.12(f) predicts the possibility of preparing a Schrödinger-cat state in QD–cavity systems under realistic conditions. This discovery crowns and concludes the study of multiphoton states and structures in QD–cavity systems under phonon influence.

2.5 Methodological outlook and perspectives

In all previous studies of this thesis, a numerically exact iterative real-time path-integral method including Markovian loss effects by Lindblad superoperators in Liouville space has been applied, which is also known as the iterative quasi-adiabatic path integral (iQUAPI). In particular, the phonon environment has been treated, fully accounting for the system-environment correlations and the finite memory time, while the electromagnetic environment is assumed to be flat justifying the Born-Markov approximation used in deriving the Lindblad term, both for radiative decay and cavity losses. This clear distinction between baths presumes an additive coupling of each environment to the system, i.e., the dynamics induced by the baths are assumed not to interfere with each other.

In [Pub 10], a numerically exact method is presented that is suitable for arbitrary environments using the so-called automated compression of environments (ACE). In particular, it can treat multiple environments on the same microscopic level. The only prerequisite is the environment Hamiltonian to be composed of non-interacting degrees of freedom. Thus, ACE gives a methodological outlook beyond the diagonal pure-dephasing type coupling tractable by iQUAPI. Bosonic, fermionic, and spin environments, environments ranging from infinite to Markovian memory, strong and weak system-environment correlations, Gaussian and non-Gaussian environments, linear and non-linear system-environment coupling: All can be treated numerically exactly within the single method ACE. This renders ACE a general-purpose tool for open quantum systems.

Writing an expression for the system's RDM in analogy to Eqs. (1.7) and (1.8) (but without a memory cutoff) for a general set of independent environmental modes yields a generalized influence functional called the process tensor (PT) [cf., Eq. (1) in [Pub 10]], which has the form of a matrix product operator (MPO). While the MPO form contains the dimensionality of the environmental Liouville space as the dimension of the so called inner indices, standard MPO compression algorithms using singular value decomposition automatically select the most important environment modes.

To showcase each claim about the generality of ACE, [Pub 10] features a variety of physi-

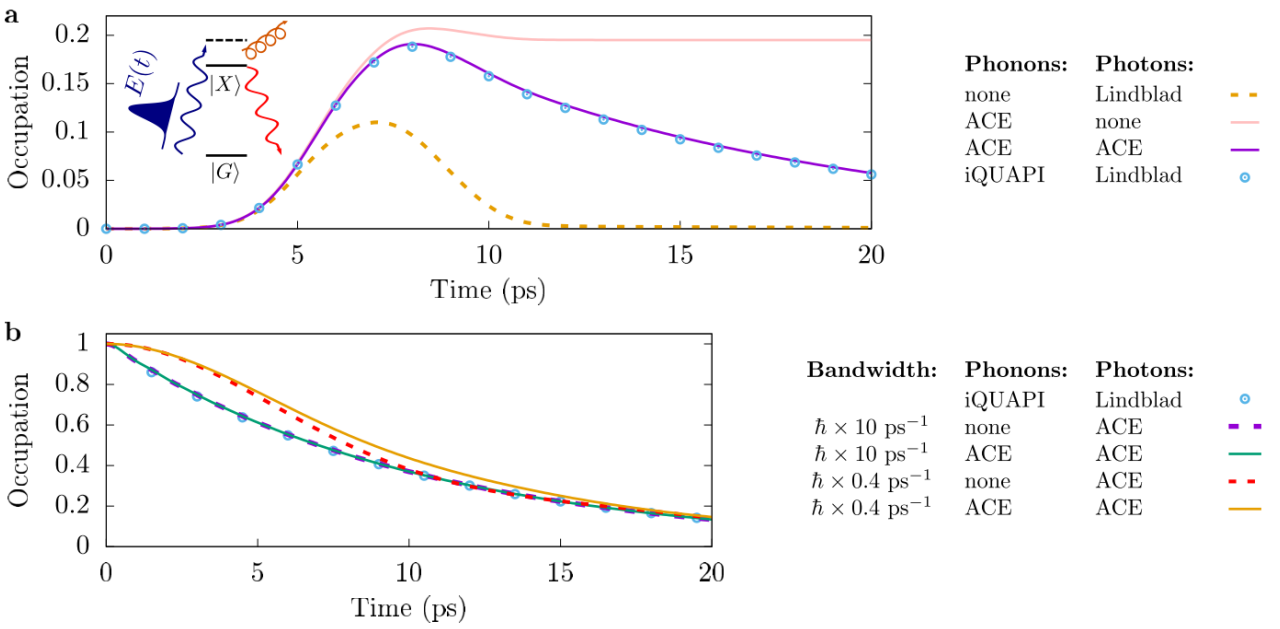

Figure 2.13: [Taken from [Pub 10]] (a) Phonon-assisted exciton preparation in a two-level QD without cavity. Different theory levels accounting for the phonon and electromagnetic environment are compared, where the latter is assumed flat. (b) Dynamics of an initially fully occupied exciton without driving. Results of different theory levels are shown for two bandwidths of the electromagnetic environment. The smaller bandwidth induces a photon memory time comparable to the phononic one.

cal systems to which ACE is applied: electron transport between localized states, central spin dynamics, coupling of a two-level system to an anharmonic Morse-type environment, superradiance of two quantum emitters, and dispersive coupling of a two-level system to a multi-mode cavity. Extensive analyses of the numerical convergence and computational performance are provided. In particular, limits of the method are discussed in detail.

One important constraint are environments that intrinsically do not allow for a selection of relevant modes, when all modes might potentially contribute equally significantly. Then, convergence within ACE is hard to achieve [cf., the coupling of a central spin to an environment of randomly oriented, unpolarized spins in [Pub 10]]. The most important limitation of ACE concerning applications in QD–cavity systems is its simulation time. While lengths around 100 ps are possible, the non-iterative nature of the algorithm prohibits long-time studies in the nanosecond-regime necessary to obtain multitime correlation functions in setups using pulse trains. Nonetheless, numerically exact studies of phenomena manageable within a 100 ps simulation time are feasible using ACE.

Fig. 2.13(a) shows the off-resonant LA phonon-assisted excitation of a two-level QD without a cavity treated on different theory levels concerning the phonon and the photon environment. Since the latter is assumed flat in this example, ACE and iQUAPI should yield the same

result. In the case without considering phonons and treating the photonic environment on the Lindblad level, only a transient occupation is observed, since there are no phonons to assist the excitation scheme. Treating the phonons with ACE without considering photons yields a finite, stationary exciton occupation as expected from phonon-assisted preparation. Including both environments yields an additional exponential decay due to losses to the electromagnetic bath. No noteworthy difference is observed between treating both baths with ACE and using iQUAPI for the phonons and a Lindblad term for the photons. This observation underlines the additivity of the two environments when the photonic one is flat.

The initial value problem of an excited QD without driving further strengthens this argument in the case of a finite, but large bandwidth, shown in Fig. 2.13(b). For a bandwidth of $\hbar\times 10\,\mathrm{ps}^{-1}$ no cross-interaction between baths is observed, such that iQUAPI with a Lindblad term for the photons is employable. When decreasing the bandwidth, though, to $\hbar \times 0.4\,\mathrm{ps}^{-1}$, the photon environment acquires a memory similar to the phononic one. The influence on the exciton dynamics is rendered non-additive: including the phonon influence slows the decay compared with the case, where only the photon bath is accounted for.

3 Summary and outlook

Self-assembled semiconductor quantum dots (QDs) in microcavities are indeed a versatile platform for the generation of highly nonclassical states of light. In this thesis, QD–cavity systems have been discussed as on-demand high-quality single-photon sources. The influence of environmental longitudinal acoustic (LA) phonons often considered to be detrimental to the preparation of quantum states could even be exploited to enhance the single-photon purity. QDs have been proposed as a candidate for a single-photon buffering device. To this end, a single Mn atom as a dopant has been suggested to facilitate a coupling between the optically bright and dipole-dark excitons, the latter being a metastable state used in the storage scheme.

The generation of different types of entanglement in a driven four-level emitter inside a cavity has been discussed, QD–cavity systems being a possible candidate for experimental realization. A protocol to switch between the two types of Bell-state entanglement time-dependently has been proposed. The generation of multiphoton states and structures in QD–cavity systems has been investigated, in particular, the LA phonon influence on various preparation protocols. While the generation of higher-order Fock states up to $n = 5$ could be shown to be feasible, the emission of N-photon bundles in QD–cavity systems does not seem to be possible. Transiently changing photon number distributions due to different excitation conditions, in particular, a frequency chirp have been studied. The phonon influence has been shown to be grave when the chirp is finite. Finally, two protocols to prepare optical Schrödinger-cat states have been compared. While the phonon influence renders the preparation of these textbook examples of purely quantum states impossible, if the QD-driven protocol is being used, the cavity-driven protocol yields a Schrödinger-cat state with reasonable fidelity and nonclassicality.

The core result of the application-oriented part of this thesis is therefore the prediction of the possibility to generate various nonclassical states of light in QD–cavity systems, even under realistic conditions, in particular, regarding the phonon environment. Especially the prediction that the single-photon purity following from LA phonon-assisted excitation benefits from phonon enhancement such that values at least as high as for resonant excitation are encountered, can be considered an important step both from an experimental point of view and regarding the physical explanation of the underlying mechanism. Above all, this prediction was recently confirmed in experiment [110,111]. Furthermore, an ongoing cooperation of the main supervisor's group with the Universities of Vienna and Stuttgart explores the advantages of single photons

generated in LA phonon-assisted schemes for quantum cryptographic applications. Finally, it is noteworthy that equipment available to groups in Vienna, Linz, Innsbruck, or Paderborn might permit proof-of-principle experiments on the presented multiphoton states in the near future.

Methodologically, the impact of using the quantum regression theorem (QRT) on the prediction of single-photon figures of merit has been analyzed. Benchmarking the QRT to the numerically exact path-integral method has brought a systematic overestimation of the phonon influence on the indistinguishability using the QRT to light, while the impact on the single-photon purity has turned out to be negligible. This finding pushes the phonon-imposed limits on the single-photon source quality beyond previous estimates and gives fresh impetus to future experimental work, which is why it can be considered a key methodological result of this thesis.

Finally, a new general-purpose formalism to simulate open quantum systems has been discussed. The ACE algorithm has provided a microscopic justification of the assumption used throughout this thesis that the phonon and a flat electromagnetic field environment couple additively. But ACE allows for the exploration of new physics beyond current frontiers. The influence of placing a QD inside a structured electromagnetic environment provided by a photonic crystal has become accessible, to name an example already studied in the first supervisor's group. Various other experimentally and technologically relevant open quantum systems are now laid open to numerically exact investigation owing to ACE.

Thus, it seems to be true as ever before to be extraordinarily wary of complacency, as encountered at the end of the 19th century, when Albert Michelson stated in 1894[112]:

> "An eminent physicist has remarked that the future truths of Physical Science are to be looked for in the sixth place of decimals."

On the contrary, at this turning point from the digital to a quantum age, a quote attributed to Isaac Newton is more appropriate:

> "What we know is a drop, what we don't know is an ocean."

Bibliography

[1] S. Patnaik, E. Mathews, S. Dang. 'Facebook blames 'faulty configuration change' for nearly six-hour outage'. Reuters (2021), URL: https://www.reuters.com/article/facebook-outages-idCAKBN2GU1TV. Accessed: 2021-10-19.

[2] V. Soldatkin, H. Pamuk. 'Biden tells Putin certain cyberattacks should be 'off-limits''. Reuters (2021), URL: https://www.reuters.com/technology/biden-tells-putin-certain-cyber-attacks-should-be-off-limits-2021-06-16/. Accessed: 2021-10-19.

[3] A. Saphir. 'Sticking with remote work? Businesses are betting on it'. Reuters (2021), URL: https://www.reuters.com/business/sticking-with-remote-work-businesses-are-betting-it-2021-05-03/ (2021). Accessed: 2021-10-21.

[4] M. M. Waldrop. 'The chips are down for Moore's law'. *Nature* **530**, 144–147 (2016).

[5] S. Datta, B. Das. 'Electronic analog of the electro-optic modulator'. *Appl. Phys. Lett.* **56**, 665 (1990).

[6] C. H. Bennett, D. P. DiVincenzo. 'Quantum information and computation'. *Nature* **404**, 247 (2000).

[7] J. L. Lee. 'U.S. to spend $625 million in five quantum information research hubs'. Reuters (2021), URL: https://www.reuters.com/article/us-usa-quantum-funding-idUSKBN25M0Y9 (2020). Accessed: 2021-10-19.

[8] 'Quantum Technologies Flagship'. Research and innovation initiative by the European Commission, URL: https://digital-strategy.ec.europa.eu/en/policies/quantum-technologies-flagship. Accessed: 2021-10-19.

[9] 'Quantentechnologien – von den Grundlagen zum Markt'. Rahmenprogramm der Bundesregierung, URL: https://www.quantentechnologien.de/. Accessed: 2021-10-19.

[10] L.-M. Duan, M. D. Lukin, J. I. Cirac, P. Zoller. 'Long-distance quantum communication with atomic ensembles and linear optics'. *Nature* **414**, 413 (2001).

[11] D. Huber, M. Reindl, J. Aberl, A. Rastelli, R. Trotta. 'Semiconductor quantum dots as an ideal source of polarization-entangled photon pairs on-demand: a review'. *J. Opt.* **20**, 073002 (2018).

[12] N. Gisin, G. Ribordy, W. Tittel, H. Zbinden. 'Quantum cryptography'. *Rev. Mod. Phys.* **74**, 145 (2002).

[13] H.-K. Lo, M. Curty, K. Tamaki. 'Secure quantum key distribution'. *Nat. Photonics* **8**, 595 (2014).

[14] M. J. Holland, K. Burnett. 'Interferometric detection of optical phase shifts at the Heisenberg limit'. *Phys. Rev. Lett.* **71**, 1355 (1993).

[15] T. Nagata, R. Okamoto, J. L. O'Brien, K. Sasaki, S. Takeuchi. 'Beating the standard quantum limit with four-entangled photons'. *Science* **316**, 726 (2007).

[16] S. Slussarenko, M. M. Weston, H. M. Chrzanowski, L. K. Shalm, V. B. Verma, S. W. Nam, G. J. Pryde. 'Unconditional violation of the shot-noise limit in photonic quantum metrology'. *Nat. Photonics* **11**, 700 (2017).

[17] Y. Yamamoto, H. A. Haus. 'Preparation, measurement and information capacity of optical quantum states'. *Rev. Mod. Phys.* **58**, 1001 (1986).

[18] T. C. Ralph, A. Gilchrist, G. J. Milburn, W. J. Munro, S. Glancy. 'Quantum computation with optical coherent states'. *Phys. Rev. A* **68**, 042319 (2003).

[19] A. P. Lund, T. C. Ralph, H. L. Haselgrove. 'Fault-tolerant linear optical quantum computing with small-amplitude coherent states'. *Phys. Rev. Lett.* **100**, 030503 (2008).

[20] M. Mirrahimi, Z. Leghtas, V. V. Albert, S. Touzard, R. J. Schoelkopf, L. Jiang, M. H. Devoret. 'Dynamically protected cat-qubits: a new paradigm for universal quantum computation'. *New J. Phys.* **16**, 045014 (2014).

[21] L. Besombes, K. Kheng, L. Marsal, H. Mariette. 'Acoustic phonon broadening mechanism in single quantum dot emission'. *Phys. Rev. B* **63**, 155307 (2001).

[22] P. Borri, W. Langbein, S. Schneider, U. Woggon, R. L. Sellin, D. Ouyang, D. Bimberg. 'Ultralong dephasing time in InGaAs quantum dots'. *Phys. Rev. Lett.* **87**, 157401 (2001).

[23] B. Krummheuer, V. M. Axt, T. Kuhn. 'Theory of pure dephasing and the resulting absorption line shape in semiconductor quantum dots'. *Phys. Rev. B* **65**, 195313 (2002).

[24] V. M. Axt, T. Kuhn, A. Vagov, F. M. Peeters. 'Phonon-induced pure dephasing in exciton-biexciton quantum dot systems driven by ultrafast laser pulse sequences'. *Phys. Rev. B* **72**, 125309 (2005).

[25] D. E. Reiter, T. Kuhn, V. M. Axt. 'Distinctive characteristics of carrier-phonon interactions in optically driven semiconductor quantum dots'. *Adv. Phys. X* **4**, 1655478 (2019).

[26] D. Bimberg, M. Grundmann, N. N. Ledentsov. *Quantum Dot Heterostructures*. John Wiley & Sons, Hoboken, New Jersey (1998).

[27] E. Bauer. 'Phänomenologische Theorie der Kristallabscheidung an Oberflächen. I'. *Zeitschrift für Kristallographie - Crystalline Materials* **110**, 372 (1958).

[28] S. Bounouar, C. de la Haye, M. Strauß, P. Schnauber, A. Thoma, M. Gschrey, J.-H. Schulze, A. Strittmatter, S. Rodt, S. Reitzenstein. 'Generation of maximally entangled states and coherent control in quantum dot microlenses'. *Appl. Phys. Lett.* **112**, 153107 (2018).

[29] S. Lüker, T. Kuhn, D. E. Reiter. 'Direct optical state preparation of the dark exciton in a quantum dot'. *Phys. Rev. B* **92**, 201305 (2015).

[30] S. Lüker, T. Kuhn, D. E. Reiter. 'Phonon-assisted dark exciton preparation in a quantum dot'. *Phys. Rev. B* **95**, 195305 (2017).

[31] K. Hennessy, A. Badolato, M. Winger, D. Gerace, M. Atatüre, S. Gulde, S. Fält, E. L. Hu, A. Imamoğlu. 'Quantum nature of a strongly coupled single quantum dot–cavity system'. *Nature* **445**, 896 (2007).

[32] E. Jaynes, F. Cummings. 'Comparison of quantum and semiclassical radiation theories with application to the beam maser'. *P. IEEE* **51**, 89 (1963).

[33] R. Proux, M. Maragkou, E. Baudin, C. Voisin, P. Roussignol, C. Diederichs. 'Measuring the photon coalescence time window in the continuous-wave regime for resonantly driven semiconductor quantum dots'. *Phys. Rev. Lett.* **114**, 067401 (2015).

[34] G. Lindblad. 'On the generators of quantum dynamical semigroups'. *Commun. Math. Phys.* **48**, 119 (1976).

[35] H. Carmichael. *An open systems approach to quantum optics*. Springer, Berlin (1993).

[36] H. Breuer, F. Petruccione. *The theory of open quantum systems*. Oxford University Press, Oxford (2002).

[37] B. Krummheuer, V. M. Axt, T. Kuhn, I. D'Amico, F. Rossi. 'Pure dephasing and phonon dynamics in GaAs- and GaN-based quantum dot structures: Interplay between material parameters and geometry'. *Phys. Rev. B* **71**, 235329 (2005).

[38] D. P. S. McCutcheon. 'Optical signatures of non-Markovian behavior in open quantum systems'. *Phys. Rev. A* **93**, 022119 (2016).

[39] J. Förstner, C. Weber, J. Danckwerts, A. Knorr. 'Phonon-assisted damping of Rabi oscillations in semiconductor quantum dots'. *Phys. Rev. Lett.* **91**, 127401 (2003).

[40] P. Machnikowski, L. Jacak. 'Resonant nature of phonon-induced damping of Rabi oscillations in quantum dots'. *Phys. Rev. B* **69**, 193302 (2004).

[41] A. Vagov, V. M. Axt, T. Kuhn, W. Langbein, P. Borri, U. Woggon. 'Nonmonotonous temperature dependence of the initial decoherence in quantum dots'. *Phys. Rev. B* **70**, 201305(R) (2004).

[42] A. Vagov, M. D. Croitoru, V. M. Axt, T. Kuhn, F. M. Peeters. 'Nonmonotonic field dependence of damping and reappearance of Rabi oscillations in quantum dots'. *Phys. Rev. Lett.* **98**, 227403 (2007).

[43] A. J. Ramsay, A. V. Gopal, E. M. Gauger, A. Nazir, B. W. Lovett, A. M. Fox, M. S. Skolnick. 'Damping of exciton Rabi rotations by acoustic phonons in optically excited InGaAs/GaAs quantum dots'. *Phys. Rev. Lett.* **104**, 017402 (2010).

[44] A. Krügel, V. M. Axt, T. Kuhn, P. Machnikowski, A. Vagov. 'The role of acoustic phonons for Rabi oscillations in semiconductor quantum dots'. *Appl. Phys. B* **81**, 897 (2005).

[45] A. J. Ramsay, T. M. Godden, S. J. Boyle, E. M. Gauger, A. Nazir, B. W. Lovett, A. M. Fox, M. S. Skolnick. 'Phonon-induced Rabi-frequency renormalization of optically driven single InGaAs/GaAs quantum dots'. *Phys. Rev. Lett.* **105**, 177402 (2010).

[46] T. Kaldewey, S. Lüker, A. V. Kuhlmann, S. R. Valentin, J.-M. Chauveau, A. Ludwig, A. D. Wieck, D. E. Reiter, T. Kuhn, R. J. Warburton. 'Demonstrating the decoupling regime of the electron-phonon interaction in a quantum dot using chirped optical excitation'. *Phys. Rev. B* **95**, 241306 (2017).

[47] S. Lüker, D. E. Reiter. 'A review on optical excitation of semiconductor quantum dots under the influence of phonons'. *Semicond. Sci. Tech.* **34**, 063002 (2019).

[48] J. Iles-Smith, D. P. S. McCutcheon, A. Nazir, J. Mørk. 'Phonon scattering inhibits simultaneous near-unity efficiency and indistinguishability in semiconductor single-photon sources'. *Nat. Photonics* **11**, 521 (2017).

[49] M. Cygorek, A. M. Barth, F. Ungar, A. Vagov, V. M. Axt. 'Nonlinear cavity feeding and unconventional photon statistics in solid-state cavity QED revealed by many-level real-time path-integral calculations'. *Phys. Rev. B* **96**, 201201(R) (2017).

[50] S. Bounouar, M. Müller, A. M. Barth, M. Glässl, V. M. Axt, P. Michler. 'Phonon-assisted robust and deterministic two-photon biexciton preparation in a quantum dot'. *Phys. Rev. B* **91**, 161302 (2015).

[51] J. H. Quilter, A. J. Brash, F. Liu, M. Glässl, A. M. Barth, V. M. Axt, A. J. Ramsay, M. S. Skolnick, A. M. Fox. 'Phonon-assisted population inversion of a single InGaAs/GaAs quantum dot by pulsed laser excitation'. *Phys. Rev. Lett.* **114**, 137401 (2015).

[52] A. Vagov, M. D. Croitoru, M. Glässl, V. M. Axt, T. Kuhn. 'Real-time path integrals for quantum dots: Quantum dissipative dynamics with superohmic environment coupling'. *Phys. Rev. B* **83**, 094303 (2011).

[53] N. Makri, D. E. Makarov. 'Tensor propagator for iterative quantum time evolution of reduced density matrices. I. Theory'. *J. Chem. Phys.* **102**, 4600 (1995).

[54] N. Makri, D. E. Makarov. 'Tensor propagator for iterative quantum time evolution of reduced density matrices. II. Numerical methodology'. *J. Chem. Phys.* **102**, 4611 (1995).

[55] A. M. Barth, A. Vagov, V. M. Axt. 'Path-integral description of combined Hamiltonian and non-Hamiltonian dynamics in quantum dissipative systems'. *Phys. Rev. B* **94**, 125439 (2016).

[56] R. Hanbury Brown, R. Q. Twiss. 'A test of a new type of stellar interferometer on Sirius'. *Nature* **178**, 1046 (1956).

[57] R. J. Glauber. *Quantum theory of optical coherence: Selected papers and lectures.* Wiley (2007).

[58] C. Roy, S. Hughes. 'Influence of electron–acoustic-phonon scattering on intensity power broadening in a coherently driven quantum-dot–cavity system'. *Phys. Rev. X* **1**, 021009 (2011).

[59] A. Nazir, D. P. S. McCutcheon. 'Modelling exciton–phonon interactions in optically driven quantum dots'. *J. Phys.: Condens. Matter* **28**, 103002 (2016).

[60] J. Iles-Smith, A. Nazir. 'Quantum correlations of light and matter through environmental transitions'. *Optica* **3**, 207 (2016).

[61] D. P. S. McCutcheon, A. Nazir. 'Quantum dot Rabi rotations beyond the weak exciton–phonon coupling regime'. *New J. Phys.* **12**, 113042 (2010).

[62] M. Cosacchi. 'Phonon impact on photonic characteristics of quantum dot-cavity systems using path integral methods'. Master's thesis, Bayreuth (2018).

[63] F. Rossi, T. Kuhn. 'Theory of ultrafast phenomena in photoexcited semiconductors'. *Rev. Mod. Phys.* **74**, 895 (2002).

[64] S. Lüker, T. Kuhn, D. E. Reiter. 'Phonon impact on optical control schemes of quantum dots: Role of quantum dot geometry and symmetry'. *Phys. Rev. B* **96**, 245306 (2017).

[65] D. Wigger, S. Lüker, V. M. Axt, D. E. Reiter, T. Kuhn. 'Squeezed phonon wave packet generation by optical manipulation of a quantum dot'. *Photonics* **2**, 214 (2015).

[66] S. Lüker. 'Einfluss akustischer Phononen auf die optische Kontrolle von Halbleiter-Quantenpunkten'. Diploma thesis, Münster (2012).

[67] K. A. Fischer, K. Müller, K. G. Lagoudakis, J. Vučković. 'Dynamical modeling of pulsed two-photon interference'. *New J. Phys.* **18**, 113053 (2016).

[68] R. Manson, K. Roy-Choudhury, S. Hughes. 'Polaron master equation theory of pulse-driven phonon-assisted population inversion and single-photon emission from quantum-dot excitons'. *Phys. Rev. B* **93**, 155423 (2016).

[69] C. Gustin, S. Hughes. 'Pulsed excitation dynamics in quantum-dot–cavity systems: Limits to optimizing the fidelity of on-demand single-photon sources'. *Phys. Rev. B* **98**, 045309 (2018).

[70] S. Thomas, P. Senellart. 'The race for the ideal single-photon source is on'. *Nat. Nanotechnol.* **16**, 367 (2021).

[71] L. Schweickert, K. D. Jöns, K. D. Zeuner, S. F. Covre da Silva, H. Huang, T. Lettner, M. Reindl, J. Zichi, R. Trotta, A. Rastelli, V. Zwiller. 'On-demand generation of background-free single photons from a solid-state source'. *Appl. Phys. Lett.* **112**, 093106 (2018).

[72] G. Guarnieri, A. Smirne, B. Vacchini. 'Quantum regression theorem and non-Markovianity of quantum dynamics'. *Phys. Rev. A* **90**, 022110 (2014).

[73] H.-P. Breuer, E.-M. Laine, J. Piilo. 'Measure for the degree of non-Markovian behavior of quantum processes in open systems'. *Phys. Rev. Lett.* **103**, 210401 (2009).

[74] S. Wißmann, A. Karlsson, E.-M. Laine, J. Piilo, H.-P. Breuer. 'Optimal state pairs for non-Markovian quantum dynamics'. *Phys. Rev. A* **86**, 062108 (2012).

[75] G. Brassard, N. Lütkenhaus, T. Mor, B. C. Sanders. 'Limitations on practical quantum cryptography'. *Phys. Rev. Lett.* **85**, 1330 (2000).

[76] P. Michler, A. Kiraz, C. Becher, W. V. Schoenfeld, P. M. Petroff, L. Zhang, E. Hu, A. Imamoğlu. 'A quantum dot single-photon turnstile device'. *Science* **290**, 2282 (2000).

[77] C. Santori, D. Fattal, J. Vuckovic, G. S. Solomon, Y. Yamamoto. 'Indistinguishable photons from a single-photon device'. *Nature* **419**, 594 (2002).

[78] Y.-M. He, Y. He, Y.-J. Wei, D. Wu, M. Atatüre, C. Schneider, S. Höfling, M. Kamp, C.-Y. Lu, J.-W. Pan. 'On-demand semiconductor single-photon source with near-unity indistinguishability'. *Nat. Nanotechnol.* **8**, 213 (2013).

[79] X. Ding, Y. He, Z.-C. Duan, N. Gregersen, M.-C. Chen, S. Unsleber, S. Maier, C. Schneider, M. Kamp, S. Höfling, C.-Y. Lu, J.-W. Pan. 'On-demand single photons with high extraction efficiency and near-unity indistinguishability from a resonantly driven quantum dot in a micropillar'. *Phys. Rev. Lett.* **116**, 020401 (2016).

[80] N. Somaschi, V. Giesz, L. De Santis, J. C. Loredo, M. P. Almeida, G. Hornecker, S. L. Portalupi, T. Grange, C. Antón, J. Demory, C. Gómez, I. Sagnes, N. D. Lanzillotti-Kimura, A. Lemaítre, A. Auffeves, A. G. White, L. Lanco, P. Senellart. 'Near-optimal single-photon sources in the solid state'. *Nat. Photonics* **10**, 340 (2016).

[81] J. Tiedau, T. J. Bartley, G. Harder, A. E. Lita, S. W. Nam, T. Gerrits, C. Silberhorn. 'Scalability of parametric down-conversion for generating higher-order Fock states'. *Phys. Rev. A* **100**, 041802 (2019).

[82] A. M. Barth, S. Lüker, A. Vagov, D. E. Reiter, T. Kuhn, V. M. Axt. 'Fast and selective phonon-assisted state preparation of a quantum dot by adiabatic undressing'. *Phys. Rev. B* **94**, 045306 (2016).

[83] A. Orieux, M. A. M. Versteegh, K. D. Jöns, S. Ducci. 'Semiconductor devices for entangled photon pair generation: a review'. *Rep. Prog. Phys.* **80**, 076001 (2017).

[84] N. Akopian, N. H. Lindner, E. Poem, Y. Berlatzky, J. Avron, D. Gershoni, B. D. Gerardot, P. M. Petroff. 'Entangled photon pairs from semiconductor quantum dots'. *Phys. Rev. Lett.* **96**, 130501 (2006).

[85] R. M. Stevenson, R. J. Young, P. Atkinson, K. Cooper, D. A. Ritchie, A. J. Shields. 'A semiconductor source of triggered entangled photon pairs'. *Nature* **439**, 179 (2006).

[86] A. Muller, W. Fang, J. Lawall, G. S. Solomon. 'Creating polarization-entangled photon pairs from a semiconductor quantum dot using the optical Stark effect'. *Phys. Rev. Lett.* **103**, 217402 (2009).

[87] H. Wang, H. Hu, T.-H. Chung, J. Qin, X. Yang, J.-P. Li, R.-Z. Liu, H.-S. Zhong, Y.-M. He, X. Ding, Y.-H. Deng, Q. Dai, Y.-H. Huo, S. Höfling, C.-Y. Lu, J.-W. Pan. 'On-demand semiconductor source of entangled photons which simultaneously has high fidelity, efficiency, and indistinguishability'. *Phys. Rev. Lett.* **122**, 113602 (2019).

[88] A. Dousse, J. Suffczynski, A. Beveratos, O. Krebs, A. Lemaître, I. Sagnes, J. Bloch, P. Voisin, P. Senellart. 'Ultrabright source of entangled photon pairs'. *Nature* **466**, 217 (2010).

[89] R. M. Stevenson, C. L. Salter, J. Nilsson, A. J. Bennett, M. B. Ward, I. Farrer, D. A. Ritchie, A. J. Shields. 'Indistinguishable entangled photons generated by a light-emitting diode'. *Phys. Rev. Lett.* **108**, 040503 (2012).

[90] O. Benson, C. Santori, M. Pelton, Y. Yamamoto. 'Regulated and entangled photons from a single quantum dot'. *Phys. Rev. Lett.* **84**, 2513 (2000).

[91] C. S. Muñoz, F. P. Laussy, C. Tejedor, E. del Valle. 'Enhanced two-photon emission from a dressed biexciton'. *New J. Phys.* **17**, 123021 (2015).

[92] W. K. Wootters. 'Entanglement of formation of an arbitrary state of two qubits'. *Phys. Rev. Lett.* **80**, 2245 (1998).

[93] D. F. V. James, P. G. Kwiat, W. J. Munro, A. G. White. 'Measurement of qubits'. *Phys. Rev. A* **64**, 052312 (2001).

[94] W. K. Wootters. 'Entanglement of formation and concurrence'. *Quantum Info. Comput.* **1**, 27–44 (2001).

[95] F. W. Cummings, A. K. Rajagopal. 'Production of number states of the electomagnetic field'. *Phys. Rev. A* **39**, 3414 (1989).

[96] B. T. H. Varcoe, S. Brattke, M. Weidinger, H. Walther. 'Preparing pure photon number states of the radiation field'. *Nature* **403**, 743 (2000).

[97] X. Zhou, I. Dotsenko, B. Peaudecerf, T. Rybarczyk, C. Sayrin, S. Gleyzes, J. M. Raimond, M. Brune, S. Haroche. 'Field locked to a Fock state by quantum feedback with single photon corrections'. *Phys. Rev. Lett.* **108**, 243602 (2012).

[98] M. Hofheinz, E. M. Weig, M. Ansmann, R. C. Bialczak, E. Lucero, M. Neeley, A. D. O'Connell, H. Wang, J. M. Martinis, A. N. Cleland. 'Generation of Fock states in a superconducting quantum circuit'. *Nature* **454**, 310 (2008).

[99] C. S. Muñoz, E. del Valle, A. G. Tudela, K. Müller, S. Lichtmannecker, M. Kaniber, C. Tejedor, J. J. Finley, F. P. Laussy. 'Emitters of N-photon bundles'. *Nat. Photonics* **8**, 550 (2014).

[100] W. Vogel, D.-G. Welsch. *Quantum Optics*. Wiley-VCH, Weinheim (2006).

[101] E. Schrödinger. 'Die gegenwärtige Situation in der Quantenmechanik'. *Naturwissenschaften* **23**, 807 (1935).

[102] A. Facon, E.-K. Dietsche, D. Grosso, S. Haroche, J.-M. Raimond, M. Brune, S. Gleyzes. 'A sensitive electrometer based on a Rydberg atom in a Schrödinger-cat state'. *Nature* **535**, 262 (2016).

[103] S. J. van Enk, O. Hirota. 'Entangled coherent states: Teleportation and decoherence'. *Phys. Rev. A* **64**, 022313 (2001).

[104] N. Ofek, A. Petrenko, R. Heeres, P. Reinhold, Z. Leghtas, B. Vlastakis, Y. Liu, L. Frunzio, S. M. Girvin, L. Jiang, M. Mirrahimi, M. H. Devoret, R. J. Schoelkopf. 'Extending the lifetime of a quantum bit with error correction in superconducting circuits'. *Nature* **536**, 441 (2016).

[105] M. Brune, E. Hagley, J. Dreyer, X. Maître, A. Maali, C. Wunderlich, J. M. Raimond, S. Haroche. 'Observing the progressive decoherence of the "meter" in a quantum measurement'. *Phys. Rev. Lett.* **77**, 4887 (1996).

[106] C. K. Law, J. H. Eberly. 'Arbitrary control of a quantum electromagnetic field'. *Phys. Rev. Lett.* **76**, 1055 (1996).

[107] A. Kenfack, K. Życzkowski. 'Negativity of the Wigner function as an indicator of non-classicality'. *J. Opt. B-Quantum S. O.* **6**, 396 (2004).

[108] J. Gea-Banacloche. 'Collapse and revival of the state vector in the Jaynes-Cummings model: An example of state preparation by a quantum apparatus'. *Phys. Rev. Lett.* **65**, 3385 (1990).

[109] J. Gea-Banacloche. 'Atom- and field-state evolution in the Jaynes-Cummings model for large initial fields'. *Phys. Rev. A* **44**, 5913 (1991).

[110] M. Reindl, J. H. Weber, D. Huber, C. Schimpf, S. F. Covre da Silva, S. L. Portalupi, R. Trotta, P. Michler, A. Rastelli. 'Highly indistinguishable single photons from incoherently excited quantum dots'. *Phys. Rev. B* **100**, 155420 (2019).

[111] S. E. Thomas, M. Billard, N. Coste, S. C. Wein, Priya, H. Ollivier, O. Krebs, L. Tazaïrt, A. Harouri, A. Lemaitre, I. Sagnes, C. Anton, L. Lanco, N. Somaschi, J. C. Loredo, P. Senellart. 'Bright polarized single-photon source based on a linear dipole'. *Phys. Rev. Lett.* **126**, 233601 (2021).

[112] S. Weinberg. *Dreams of a final theory: The scientist's search for the ultimate laws of nature*. Knopf Doubleday Publishing Group, New York (2011).

Acknowledgments

First of all, I have to thank my doctoral adviser, Vollrath Martin Axt, who taught me the spirit of physics as I practice it. The unconditional commitment to truth, knowledge, and science that he embodies without question even in the face of one's own disadvantage is a rare beacon of principle in this unprincipled world. During the time in his group, I learned a lot about the scientific background of any topic we touched, thrived in the discussions about physics, science as a business, politics, philosophy, art and beyond. By granting me far-reaching independence in planning and executing all projects that are summarized in this thesis, he managed to strengthen my trust in my own skills. And, on a very practical note, he obtained the funding in the shape of a DFG grant that allowed me to work in his group in the first place.

A particularly heartfelt thank-you goes to Doris Reiter, who cosupervised my work in general and my papers in particular. From her, I learned the intricacies of convincing scientific presentation, the art of making eye-catching sketches, and verbally highlighting the most important aspects in a paper. Most of all, I thank her for the many pleasant conversations during conferences and later - after the pandemic had hit - via Zoom.

I thank Stephan Kümmel and Tilmann Kuhn for their time and effort to evaluate my thesis in detail and create two very thoughtful reports.

Without organizational and administrative backup, the life of a doctoral candidate in the maze of bodies of university and the IT network would be hell. Therefore, I would like to thank Monika Birkelbach and Susanne Süss for their continued and patient support in all questions concerning administration as well as Markus Hilt for his invaluable help with the large and little aches and pains of our machines and networks, especially during the transition to home office at the beginning of the pandemic.

Without a scientific network, practicing physics is neither successful nor fun. For always providing a fruitful and productive atmosphere at work, I thank all past and present members of the chair for Theoretical Physics III - Quantum Theory of Condensed Matter. The countless coffee breaks, conversations, and joint projects will not be forgotten.

In particular, I thank my doctoral brother Tim Seidelmann. Working together with him on joint projects was always both professional and fun. We breathed life into the DFG project and led it to success together. Beyond that, I would not have emerged from the pandemic sanely without the close virtual contact with Tim during the 18 months of lockdown and home office.

Extraordinary times indeed called for extraordinary measures and our almost-daily phone calls made work bearable during this time and kept the motivation alive.

A very special thanks goes to Florian Ungar and Adam Mielnik-Pyszczorski, my two partners in crime. The coffee, tea, and laughter will always remain an integral part of my years in that one office facing the Festival Theater. Physics in daylight and PhysX in darkness indeed forged a long-lasting friendship beyond our times at university.

I would not have come far in physics without Rebecca Benelli, Timo Lebeda, and Sebastian Krauß. Our studying group built in the first weeks as first-year students taught me that together anything is possible. Productive teamwork in physics and beyond even today, three years after the end of our studies, is characteristic to us four and hopefully will remain so.

A special thanks goes to Stefan Ansorg, my high school physics teacher. He saw a talent for physics in me at a time when I could not even imagine doing science as a job. Using a plethora of popular scientific books he fostered my interest in mathematics and physics early on. Without him, I would not have embarked on the journey that led me here.

For the unconditional support in all aspects of life, the continued warmth and guidance I thank my parents. Always letting me do stuff and find out the consequences for myself, while cushioning the cases when things went wrong, cultivated a curiosity essential to physics.

And most importantly, I thank my lovely wife. Antonia, you show me how to live every day, to seize the moment, to marvel at the beauty of nature and all living beings. With you, life is always fun, even on dark days. Thank you!

Publications

List of publications as referred to in this thesis

[Pub 1] **M. Cosacchi**, T. Seidelmann, M. Cygorek, A. Vagov, D. E. Reiter, V. M. Axt.
Accuracy of the quantum regression theorem for photon emission from a quantum dot.
Phys. Rev. Lett. **127**, 100402 (2021).
& Erratum: arXiv:2103.13100 (2021), submitted to *Physical Review Letters*.
Note: As of the publication date of this thesis, the Erratum is published as
Phys. Rev. Lett. **128**, 079901 (2022).

[Pub 2] **M. Cosacchi**, F. Ungar, M. Cygorek, A. Vagov, V. M. Axt.
Emission-frequency separated high quality single-photon sources enabled by phonons.
Phys. Rev. Lett. **123**, 017403 (2019).

[Pub 3] **M. Cosacchi**, T. Seidelmann, A. Mielnik-Pyszczorski, M. Neumann, T. K. Bracht, M. Cygorek, A. Vagov, D. E. Reiter, V. M. Axt.
Deterministic photon storage and readout in a semimagnetic quantum dot–cavity system doped with a single Mn ion
arXiv:2110.07576 (2021), under review at *Advanced Quantum Technologies*.
Note: As of the publication date of this thesis, the Article is published as
Adv. Quantum Technol. **5**, 2100131 (2022).

[Pub 4] T. Seidelmann, **M. Cosacchi**, M. Cygorek, D. E. Reiter, A. Vagov, V. M. Axt.
Different types of photon entanglement from a constantly driven quantum emitter inside a cavity.
Adv. Quantum Technol. **4**, 2000108 (2021).

[Pub 5] T. Seidelmann, D. E. Reiter, **M. Cosacchi**, M. Cygorek, A. Vagov, V. M. Axt.
Time-dependent switching of the photon entanglement type using a driven quantum emitter–cavity system.
Appl. Phys. Lett. **118**, 164001 (2021).

[Pub 6] **M. Cosacchi**, J. Wiercinski, T. Seidelmann, M. Cygorek, A. Vagov, D. E. Reiter, V. M. Axt.
On-demand generation of higher-order Fock states in quantum-dot–cavity systems.
Phys. Rev. Research **2**, 033489 (2020).

[Pub 7] **M. Cosacchi**, A. Mielnik-Pyszczorski, T. Seidelmann, M. Cygorek, A. Vagov, D. E. Reiter, V. M. Axt.
Suitability of solid-state platforms as sources of N-photon bundles.
arXiv:2108.03967 (2021), under review at *Quantum*.
Note: As of the publication date of this thesis, the Article is under review at *Physical Review B*.

[Pub 8] **M. Cosacchi**, T. Seidelmann, F. Ungar, M. Cygorek, A. Vagov, V. M. Axt.
Transiently changing shape of the photon number distribution in a quantum-dot–cavity system driven by chirped laser pulses.
Phys. Rev. B **101**, 205304 (2020).

[Pub 9] **M. Cosacchi**, T. Seidelmann, J. Wiercinski, M. Cygorek, A. Vagov, D. E. Reiter, V. M. Axt.
Schrödinger cat states in quantum-dot-cavity systems.
Phys. Rev. Research **3**, 023088 (2021).

[Pub 10] M. Cygorek, **M. Cosacchi**, A. Vagov, V. M. Axt, B. W. Lovett, J. Keeling, E. M. Gauger.
Numerically exact open quantum systems simulations for arbitrary environments using automated compression of environments.
arXiv:2101.01653 (2021), under review at *Nature Physics*.
Note: As of the publication date of this thesis, the Article is published in
Nat. Phys. (2022).

Further publications contributed to by the author

[FPub 1] **M. Cosacchi**, M. Cygorek, F. Ungar, and V. M. Axt.
Nonexponential spin decay in a quantum kinetic description of the D'yakonov-Perel' mechanism mediated by impurity scattering.
Phys. Rev. B **95**, 195313 (2017).

[FPub 2] **M. Cosacchi**, M. Cygorek, F. Ungar, A. M. Barth, A. Vagov, and V. M. Axt.
Path-integral approach for nonequilibrium multitime correlation functions of open quantum systems coupled to Markovian and non-Markovian environments.
Phys. Rev. B **98**, 125302 (2018), selected as *Editors' Suggestion.*

[FPub 3] F. Trybel, **M. Cosacchi**, T. Meier, V. M. Axt, and G. Steinle-Neumann.
Proton dynamics in high-pressure ice-VII from density functional theory.
Phys. Rev. B **102**, 184310 (2020).

[FPub 4] M. Neumann, F. Kappe, T. K. Bracht, **M. Cosacchi**, T. Seidelmann, V. M. Axt, G. Weihs, and D. E. Reiter.
Optical Stark shift to control the dark exciton occupation of a quantum dot in a tilted magnetic field.
Phys. Rev. B **104**, 075428 (2021).

[FPub 5] T. K. Bracht, **M. Cosacchi**, T. Seidelmann, M. Cygorek, A. Vagov, V. M. Axt, T. Heindel, and D. E. Reiter.
Swing-up of quantum emitter population using detuned pulses.
PRX Quantum **2**, 040354 (2021), selected as *Editors' Suggestion.*

Conference and seminar contributions

The author attended the following conferences during his time as a doctoral candidate, presenting parts of this work or other research as posters or contributed talks:

- GRC Spin Dynamics in Nanostructures, Les Diablerets, Switzerland (2019)
- OECS 2019, St. Petersburg, Russia (2019)
- OPON 2020, Warsaw, Poland (2020)
- QD 2020, Munich, Germany (2020) [online format due to the COVID-19 pandemic]

Furthermore, the author was invited by D. R. Gulevich, Department of Phyics, ITMO University, St. Petersburg, Russia, to give an on-site seminary talk on the iterative real-time path integral formalism in September 2019.

Publication 1

Accuracy of the quantum regression theorem for photon emission from a quantum dot.

M. Cosacchi, T. Seidelmann, M. Cygorek, A. Vagov, D. E. Reiter, V. M. Axt.

Phys. Rev. Lett. **127**, 100402 (2021).

DOI: 10.1103/PhysRevLett.127.100402

&

Erratum: Accuracy of the quantum regression theorem for photon emission from a quantum dot.

M. Cosacchi, T. Seidelmann, M. Cygorek, A. Vagov, D. E. Reiter, V. M. Axt.

arXiv:2103.13100 (2021), submitted to *Physical Review Letters*.

arXiv:2103.13100 (2021)

Author contributions

The author had the original idea to use photonic characteristics of a two-level system for a comparison of numerically exact calculations with results obtained using the quantum regression theorem and to compare it with a non-Markovianity measure. He has designed the concept of this study, in particular, he has performed the data generation and analysis, has provided the interpretation of the results, and has written the first draft of the paper. He has moderated all discussions and revision requests of the draft, has organized the correspondence with the editor and referees, and has provided the first drafts of answers to the referees.

T. Seidelmann has assisted in the numerical implementation of the quantum regression theorem and the convergence tests, has discussed the results in detail with the author, thus contributing to the interpretation, and has contributed to revisions of the draft and the answers to the referees.

M. Cygorek, A. Vagov, and D. E. Reiter have cosupervised this work, in particular, they have participated in the discussion and interpretation of the results. They have contributed to the optimization of the presentation as well as revisions of the draft and the answers to the referees.

V. M. Axt has advised the author throughout his work as the main supervisor. He has obtained the funding for this work and has participated in the discussion and interpretation of the results. He has contributed to the optimization of the presentation as well as revisions of the draft and the answers to the referees.

Accuracy of the Quantum Regression Theorem for Photon Emission from a Quantum Dot

M. Cosacchi,[1] T. Seidelmann,[1] M. Cygorek,[2] A. Vagov,[1,3] D. E. Reiter,[4] and V. M. Axt[1]
[1]Theoretische Physik III, Universität Bayreuth, 95440 Bayreuth, Germany
[2]Heriot-Watt University, Edinburgh EH14 4AS, United Kingdom
[3]ITMO University, St. Petersburg 197101, Russia
[4]Institut für Festkörpertheorie, Universität Münster, 48149 Münster, Germany

(Received 25 March 2021; accepted 3 August 2021; published 31 August 2021)

The quantum regression theorem (QRT) is the most widely used tool for calculating multitime correlation functions for the assessment of quantum emitters. It is an approximate method based on a Markov assumption for environmental coupling. In this Letter we quantify properties of photons emitted from a single quantum dot coupled to phonons. For the single-photon purity and the indistinguishability, we compare numerically exact path-integral results with those obtained from the QRT. It is demonstrated that the QRT systematically overestimates the influence of the environment for typical quantum dots used in quantum information technology.

DOI: 10.1103/PhysRevLett.127.100402

To be used as photon sources for quantum information technology [1,2], semiconductor quantum dots (QDs) must deliver photons with high-quality characteristics such as a high brightness, a perfect single-photon purity, and indistinguishability. However, due to the electron-phonon interaction in QDs these quantities can be degraded [3,4]. In the current race for the perfect single-photon source [5,6] with achieved purities and indistinguishabilities close to unity [4,7–12], it is crucial to understand the influence of the phonon-induced dephasing on the properties of emitted photons. The coupling to environmental phonons has been shown to lead to several important phenomena like the phonon sidebands [13,14], damping of Rabi oscillations [15–19], and the possibility for a dynamic decoupling of electronic and phononic subsystems [20,21], or degradation of photon properties [22].

The quantum regression theorem (QRT) known from quantum optics is probably the most widely used standard tool to investigate the above photon properties [23]. In essence, the QRT prescribes to calculate the two- (or multi-) time correlation functions using the same dynamical equation for both the (real-) time and the delay-time arguments, which is used to determine the time evolution of the single-time correlations. Solving an initial value problem for the delay-time propagation as done in the QRT disregards the memory that has build up until the start of the propagation, and thus, the use of the QRT may become critical when used for non-Markovian dynamics. With the help of the QRT, multitime correlation functions yielding, e.g., the purity and indistinguishability can be deduced. The QRT can be extended such that it also accounts for the electron-phonon interaction [24–28]. For our current study it is most important that phonons are known to induce non-Markovian dynamics [24,26,29–32] which provides a situation where the QRT may come to its limits [33–37]. Because the QRT is an approximation it is not always clear, whether the assumptions made in the derivation are fulfilled.

Testing the limits of the QRT has recently become possible by a path-integral approach to calculate multitime photon correlation functions [38]. This approach is numerically exact meaning that the time-dependent solution to the many-body Hamiltonian model is obtained without any further approximations, and thus the phonon influence including its non-Markovian part is fully taken into account [39–41]. The accuracy of the result is controlled by choosing an appropriate time discretization and memory length.

In this Letter, we explore the limits of the QRT approximation for calculating multitime correlation functions using a QD coupled to phonons as an example. To compare numerically exact results with the QRT approximation in the most transparent way, we implement the QRT directly within the path-integral method. Since apart from the QRT no further approximations are involved, this approach offers a direct way to evaluate the influence of the QRT on the multitime correlations. Details of the implementations are found in the Supplemental Material [42].

We demonstrate that the QRT systematically overestimates the phonon impact on the indistinguishability, in particular for standard GaAs QDs relevant for technological applications [51–58]. We show that this is connected to the non-Markovian part of the dynamics. In contrast, the QRT yields quantitatively correct results for the purity.

We consider a model where a two-level QD can emit photons and interacts with environmental longitudinal acoustic (LA) phonons [14,32,59]. For the calculations we consider GaAs QDs of radius 3 nm and standard material parameters for the phonon coupling with the

exception that we introduce a scaling factor λ modifying the overall coupling amplitude. Details of the model are found in the Supplemental Material [42]. We assume that this scaling is a variable in the interval $\lambda \in [0, 10]$, where 0 means the absence of phonons, 1 corresponds to the GaAs QDs, and larger values allow us to explore strongly coupled QD-phonon systems [39,60]. Larger couplings $1 < \lambda \leq 10$ can be found in piezoelectric materials like GaN [61]. We further account for the radiative decay of the QD exciton by introducing a Lindblad superoperator, setting the radiative decay rate to $\gamma = 1\ \mathrm{ns}^{-1}$. The QD is excited by an external laser pulse with a Gaussian envelope. We consider a resonant [62] excitation scheme with a π pulse of 3 ps length (full width at half maximum) [63] to prepare the excited state in the QD [7,28]. Using this model, we can then calculate the photonic properties.

The single-photon purity $\mathcal{P}$ is defined as

$$\mathcal{P} = 1 - p \quad \text{with} \quad p = \frac{\int_{-T_{\mathrm{Pulse}}/2}^{T_{\mathrm{Pulse}}/2} d\tau G^{(2)}(\tau)}{\int_{T_{\mathrm{Pulse}}/2}^{3T_{\mathrm{Pulse}}/2} d\tau G^{(2)}(\tau)}. \tag{1}$$

T_{Pulse} is the separation of the pulses in the excitation pulse train, and

$$G^{(2)}(\tau) \coloneqq \lim_{T\to\infty} \frac{1}{T} \int_{-T}^{T} dt G^{(2)}(t,\tau), \tag{2a}$$

$$G^{(2)}(t,\tau) \coloneqq \langle \sigma_X^\dagger(t)\sigma_X^\dagger(t+\tau)\sigma_X(t+\tau)\sigma_X(t)\rangle \tag{2b}$$

with σ_X describing the QD transition from the excited to the ground state. $\mathcal{P}$ is a measure for the single-photon component of the photonic state [1,7,8,64–68]. It is measured using a Hanbury Brown-Twiss setup [69], which is a coincidence measurement and can thus be modeled with a second-order two-time correlation function $G^{(2)}(\tau)$. $\mathcal{P} = 1$ implies a perfect single-photon purity. The quantity has no lower bound, $-\infty < \mathcal{P} \leq 1$, since p can be larger than 1 in the case of bunching instead of antibunching behavior.

The indistinguishability $\mathcal{I}$ of two successively emitted photons is obtained as

$$\mathcal{I} = 1 - p_{\mathrm{HOM}} \quad \text{with} \quad p_{\mathrm{HOM}} = \frac{\int_{-T_{\mathrm{Pulse}}/2}^{T_{\mathrm{Pulse}}/2} d\tau\, G^{(2)}_{\mathrm{HOM}}(\tau)}{\int_{T_{\mathrm{Pulse}}/2}^{3T_{\mathrm{Pulse}}/2} d\tau\, G^{(2)}_{\mathrm{HOM}}(\tau)} \tag{3}$$

with the correlation functions [28,70,71]

$$G^{(2)}_{\mathrm{HOM}}(\tau) \coloneqq \lim_{T\to\infty} \frac{1}{T} \int_{-T}^{T} dt\, G^{(2)}_{\mathrm{HOM}}(t,\tau) \tag{4a}$$

$$G^{(2)}_{\mathrm{HOM}}(t,\tau) \coloneqq \frac{1}{2}[\langle \sigma_X^\dagger(t)\sigma_X(t)\rangle\langle \sigma_X^\dagger(t+\tau)\sigma_X(t+\tau)\rangle - |\langle \sigma_X^\dagger(t+\tau)\sigma_X(t)\rangle|^2 + G^{(2)}(t,\tau)], \tag{4b}$$

where the last term in Eq. (4b) accounts for nonunity single-photon purities. This quantity is measured in a Hong-Ou-Mandel setup [72]. Perfect indistinguishability corresponds to $\mathcal{I} = 1$, and using the definition Eq. (4b) it is bounded by $0.5 \leq \mathcal{I} \leq 1$ [71]. We note that other definitions of $\mathcal{I}$ are often used which are not applicable when the single-photon purity deviates from unity and where the lower bound is 0 rather than 0.5 [22,73].

The brightness $\mathcal{B}$ of a photon source is defined as the number of photons emitted per excitation laser pulse [8]. It is given as [28,74]

$$\mathcal{B} \coloneqq \gamma \int_{t_0 - T_{\mathrm{Pulse}}/2}^{t_0 + T_{\mathrm{Pulse}}/2} dt\ \langle \sigma_X^\dagger(t)\sigma_X(t)\rangle, \tag{5}$$

where t_0 is the center time of the pulse and $0 \leq \mathcal{B} \leq \gamma T_{\mathrm{Pulse}}$. A value of $\mathcal{B}$ of 100% corresponds to the ideal case of a delta-pulse excitation.

To calculate these quantities we use the path-integral method both without and with the QRT. The path-integral method propagates the augmented density matrix that contains the information about the memory induced by the environment to the QD dynamics. Since the phonon-induced memory depth is finite, a memory window is formed in each time step. To implement the QRT, the augmented density matrix is traced over all memory-related variables at the end of the t propagation to yield a new initial reduced density matrix before the subsequent τ propagation. Thus, the accumulated phonon memory is discarded for the τ propagation. Therefore, the τ propagation becomes independent from the past evolution in t, which is the central assumption of the QRT. We have checked the validity of this approach by comparing our results with a standard implementation of the QRT as discussed in Ref. [26] and verify the finding therein that the QRT yields the phonon sidebands in emission spectra on the energetically wrong side, cf., Fig. 2 in the Supplemental Material [42].

Using the path-integral method, we calculate the photon properties $\mathcal{P}$, $\mathcal{I}$, and $\mathcal{B}$ for a wide parameter range as shown in Fig. 1, which displays the results using the path-integral approach without the QRT approximation. In the phonon-free case, $\lambda = 0$, the excitation of the QD leads to a near-optimal single-photon source with $\mathcal{P} = 99.76\%$, $\mathcal{I} = 99.76\%$, and $\mathcal{B} = 99.82\%$. Slight deviations ($< 0.3\%$) from the perfect source can be traced back to the finite pulse length.

While the single-photon purity is close to unity for the entire parameter range under consideration, for a finite phonon scaling λ, the indistinguishability rapidly deteriorates with rising temperature T, such that for $\lambda = 1$ it falls below 70% when $T > 30$ K. For large phonon scalings, the indistinguishability cannot exceed 60% even at $T = 4$ K. At higher temperatures and for large phonon scaling, the indistinguishability decreases to its lowest possible value of

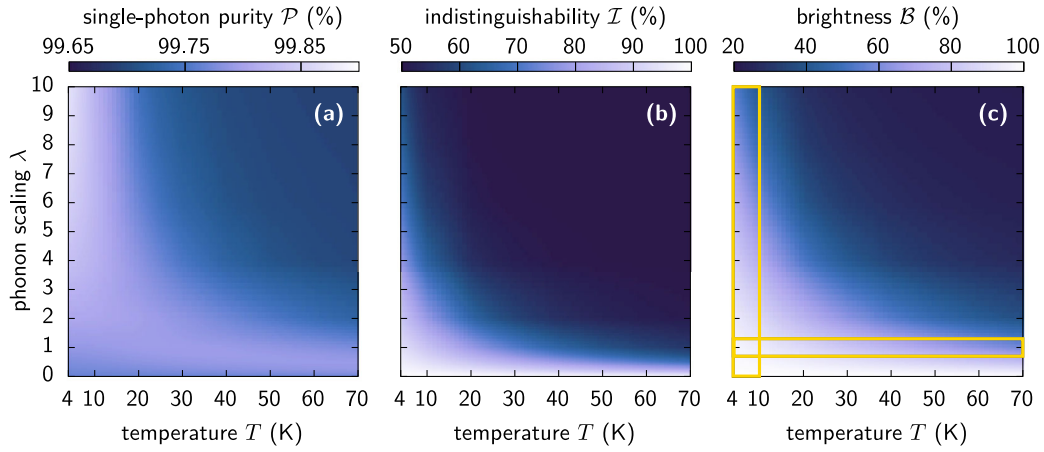

FIG. 1. The single-photon purity (a), the indistinguishability of two successively emitted photons (b), and their brightness (c) in a two-level QD for a temperature range between 4 and 70K and phonon scalings from 0 to 10. Yellow rectangles in panel (c) mark the physically important parameter regime of GaAs around $\lambda = 1$ for different temperatures and different phonon scalings for temperatures below 10K.

50%. Nonetheless, the corresponding brightness is nonvanishing, such that the QD becomes a source of distinguishable single photons in this regime of higher temperatures and stronger QD-phonon coupling.

We have marked the most physically relevant regions with yellow boxes in Fig. 1(c). They correspond to the low-temperature regime in which experiments are typically conducted for different QD materials from GaAs to GaN modeled here by different scalings λ (vertical box) as well as over a temperature range between liquid helium and nitrogen temperatures (horizontal box) for GaAs ($\lambda = 1$). In the parameter range of highest interest, i.e., where the boxes overlap at $\lambda = 1$ and $T = 4$ K, we find $\mathcal{P} = 99.79\%$, $\mathcal{I} = 93.16\%$, and $\mathcal{B} = 96.75\%$.

We now evaluate how the QRT approximation changes these results. It is usually conjectured that the QRT might fail when the dynamics is non-Markovian, i.e., when memory effects are nonnegligible [34,35]. Furthermore, there is a class of environmental couplings for which the QRT cannot be accurately applied, even when the single-time dynamics is Markovian [36]. In order to describe the contribution of the memory effects quantitatively, we consider a non-Markovianity measure for our system.

In contrast to classical Markovian stochastic processes, in open quantum systems there is no single definition of Markovianity (or non-Markovianity) that is agreed upon. Rather, there are different measures that capture different aspects of Markovian quantum dynamics [75–81], one of

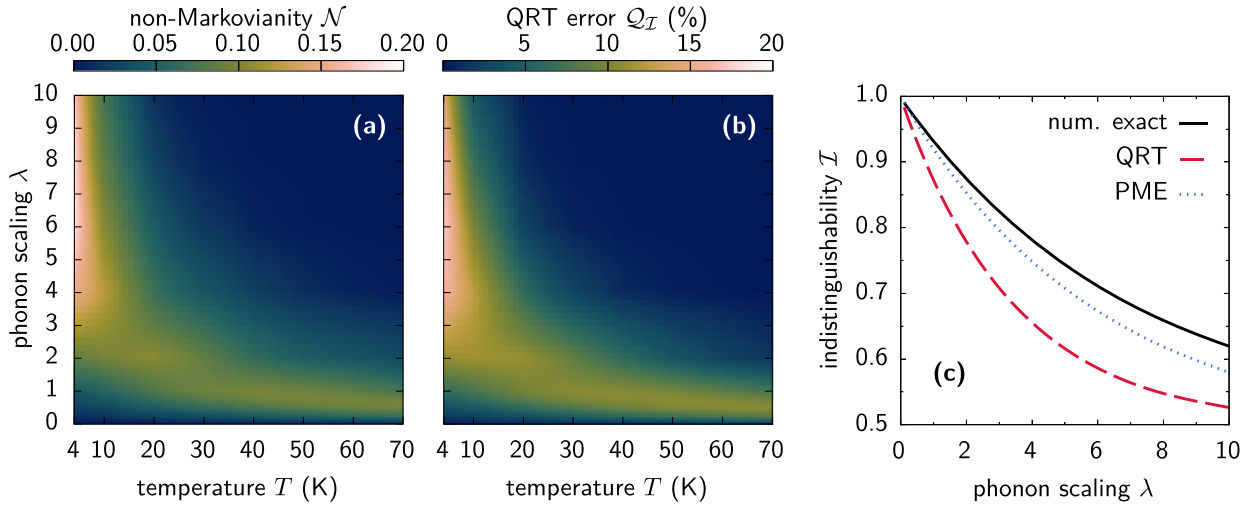

FIG. 2. The non-Markovianity measure $\mathcal{N}$ (a) and the relative error $\mathcal{Q}_\mathcal{I}$ for the indistinguishability (b) as a function of temperature T and phonon scaling λ. (c) The indistinguishability as a function of the phonon scaling parameter l at 4K, calculated with the numerically exact path-integral method (num. exact), by using the QRT in the lab frame (QRT), and by applying the QRT in the polaron transformed frame within the PME approach (PME).

which is the trace distance measure. The trace distance between two states described by the reduced density matrices ρ_1 and ρ_2 is defined as

$$D[\rho_1(t),\rho_2(t)] \coloneqq \frac{1}{2}||\rho_1(t)-\rho_2(t)||_1 = \frac{1}{2}\sum_k |x_k(t)|, \quad (6)$$

where $x_k(t)$ are the eigenvalues of the difference matrix $\rho_1(t)-\rho_2(t)$. In our case, ρ_1 and ρ_2 correspond to arbitrary states chosen on the Bloch sphere of the two-level QD.

For Markovian dynamics, this quantity is a contraction:

$$\frac{d}{dt}D[\rho_1(t),\rho_2(t)] \leq 0. \quad (7)$$

The intuitive explanation for this behavior lies in the loss of information in a Markovian system: two originally distinct states monotonically lose their distinguishability over time. Only in a non-Markovian system, information can flow back from the environment to the system, making the trace distance a nonmonotonic function of time. Therefore, the non-Markovianity of a system can be quantified as [26,36,75]

$$\mathcal{N} \coloneqq \max_{\rho_1,\rho_2}\int_{\Omega_+}\frac{d}{dt}D[\rho_1(t),\rho_2(t)]dt. \quad (8)$$

Ω_+ is the union of the intervals on which $(d/dt)D[\rho_1(t),\rho_2(t)] > 0$. The maximum is taken over all pairs of possible initial states. Fortunately, only the subset of those states, which are orthogonal to each other, needs to be considered [82]. For our two-level system, this means that the corresponding Bloch sphere needs to be sampled only for pairs of opposing points on its surface.

While $\mathcal{N}=0$ implies Markovianity, it is important to realize that $\mathcal{N}\neq 0$ implies that the underlying dynamical map is *indivisible* [36]. Therefore, the measure $\mathcal{N}$ captures the appearance of memory effects in the dynamics of the system, which is a fundamental aspect of non-Markovianity both in classical stochastic processes and open quantum systems.

To quantify the deviations introduced by the QRT, we define the relative error of evaluating a target quantity M using the QRT as a measure for the validity of the QRT with respect to M:

$$\mathcal{Q}_M = \left|\frac{M-M_{\mathrm{QRT}}}{M}\right|, \quad (9)$$

where M is calculated numerically exact and M_{QRT} using the QRT.

The QRT states that the same dynamical map that is used to evolve the density matrix and, in extension, expectation values of any subsystem operator, can be used for the time evolution of multitime correlation functions used in Eqs. (2b) and (4b). In particular, the differential equation propagating the density matrix in the real time t is reused for the propagation in the delay time τ [83,84]. This assumption presumes that the initial factorization of subsystem and environment common in the description of open quantum systems is also used at the beginning of the τ dynamics. In other words, this factorization is assumed for every t.

Now, we examine the impact of the QRT approximation on the photon source characteristics considered above. The non-Markovianity measure $\mathcal{N}$ and the relative error $\mathcal{Q}_\mathcal{I}$ for the indistinguishability are depicted in Figs. 2(a) and 2(b) as a function of T and λ. We see large values of $\mathcal{N}$ and $\mathcal{Q}_\mathcal{I}$, in particular, in the physically relevant parameter regimes, i.e., at $\lambda = 1$ and low temperatures. The largest $\mathcal{N}$ is found for $\lambda > 1$ and $T < 10$ K [cf., Fig. 2(a)], where the error introduced by using the QRT also rises up to roughly 18%. This behavior can be related to the connection between Markovianity and the QRT. Interestingly, there are also parameter ranges with a nonzero $\mathcal{N}$, where the QRT error is insignificant, e.g., at $\lambda = 10$ and $T = 20$ K, where $\mathcal{N} = 0.0125$, while $\mathcal{Q}_\mathcal{I} = 0.3\%$. This means that there are parameter sets where the QRT approximation is valid to a better degree than a Markovian description. This is unexpected since the former imposes more restrictive conditions on the system dynamics: for the QRT to hold, the subsystem and environment have to factorize for all times t, not only at the initial time. In the entire parameter regime considered here, the QRT overestimates the phonon influence on $\mathcal{I}$, that is $\mathcal{I} > \mathcal{I}_{\mathrm{QRT}}$, cf., Fig. 2(c) for a slice at 4K.

In contrast, the error $\mathcal{Q}_\mathcal{P}$ introduced by the QRT to the single-photon purity is negligible, and the brightness is unaffected by the QRT, since its definition in Eq. (5) contains only expectation values at a single time. Surprisingly, $\mathcal{Q}_\mathcal{P}$ is also extraordinarily small, being on the order of 10^{-4} for all considered parameter values (not shown), in contrast to $\mathcal{Q}_\mathcal{I}$.

In order to understand this, we examine the multitime correlation functions. While the purity contains only the second-order correlation $G^{(2)}(t,\tau)$, the indistinguishability also includes the correlation $G^{(1)}(t,\tau) \coloneqq \langle\sigma_X^\dagger(t+\tau)\sigma_X(t)\rangle$. In $G^{(2)}(t,\tau)$ the operators $\sigma_X^\dagger$ and σ_X appear in pairs at each time t and $t+\tau$, respectively, hence modeling intensity-intensity correlation measurements, i.e., the correlation between occupations. In $G^{(1)}(t,\tau)$ on the other hand, $\sigma_X^\dagger$ and σ_X appear as stand-alone operators for each time argument in $G^{(1)}(t,\tau)$. Therefore, this function correlates coherences rather than occupations. Because the coupling to the LA phonon environment has a stronger impact on coherences than on occupations, it becomes clear why the approximations introduced by the QRT have a significantly stronger impact on $\mathcal{I}$ than on $\mathcal{P}$.

This finding implies two consequences: first, the single-photon purity can be calculated using the QRT with

negligible error, even for those parameters, where the dynamics is clearly non-Markovian according to the measure $\mathcal{N}$ [cf., Fig. 2(a)]. Second, one cannot use $\mathcal{Q}_{\mathcal{P}}$ as a *general* measure for the validity of the QRT. Using it in such a way would imply the validity of the QRT, which is misleading since in the same parameter regimes considered, the indistinguishability is off by up to 18% when evaluating with the QRT.

Finally, we analyze the frame dependence of the QRT by applying it in a polaron transformed frame. This technique is widely used in the polaron master equation approach (PME) [85–87] (see also Supplemental Material [42]). In Fig. 2(c), the indistinguishability is shown for a varying phonon scaling parameter λ at $T = 4$ K. The numerically exact result (black solid line) is compared with the calculation using the QRT in the lab frame (red dashed line) and the PME approach applying the QRT in the polaron frame (blue dotted line). While all methods yield qualitatively the same dependency, the PME produces results closer to the numerically exact calculation. While the largest relative error encountered in the slice shown in Fig. 2(c) is 18% for the QRT in the lab frame (red dashed line), it is only 6% when the QRT is applied in the polaron frame within the PME. The better performance of the PME is expected because due to the transformation to the polaron frame a variety of, but not all, non-Markovian effects are captured. Therefore, changing the frame improves the usage of the QRT, but still a significant systematic overestimation of phonon effects on the photon indistinguishability is obtained.

In summary, assessing the validity of the commonly used QRT is dependent on the target quantity that is calculated. In particular, there is no single measure by which the validity of the QRT could be estimated for all possible figures of merit derived from multitime correlation functions. Using a numerically exact path-integral method to calculate the properties of photons emitted from a QD coupled to LA phonons enabled us to explore the boundaries of the QRT, showing that the phonon effect on photon indistinguishability is systematically overestimated by the QRT, while the purity can be safely calculated using the QRT. Unlike what is found for other systems [36], the QRT induces errors in the photon emission from QDs typically only when the dynamics is non-Markovian. Though we show that due to the phonons the photon properties are limited close to but below unity in typical cases, there is still room for improvement, e.g., by placing the QD in a cavity. Furthermore, our results should be applicable to a broad range of physical two-level systems, such as defects in diamonds [88–93], silicon [94,95], hexagonal boron nitride [96,97], or other solid-state emitters [98] coupled to a continuum of environmental oscillators.

This work was funded by the Deutsche Forschungsgemeinschaft (DFG, German Research Foundation) Project No. 419036043.

[1] P. Michler, A. Kiraz, C. Becher, W. V. Schoenfeld, P. M. Petroff, L. Zhang, E. Hu, and A. Imamoglu, A quantum dot single-photon turnstile device, Science **290**, 2282 (2000).
[2] P. Senellart, G. Solomon, and A. White, High-performance semiconductor quantum-dot single-photon sources, Nat. Nanotechnol. **12**, 1026 (2017).
[3] S. Gerhardt, J. Iles-Smith, D. P. S. McCutcheon, Y.-M. He, S. Unsleber, S. Betzold, N. Gregersen, J. Mørk, S. Höfling, and C. Schneider, Intrinsic and environmental effects on the interference properties of a high-performance quantum dot single-photon source, Phys. Rev. B **97**, 195432 (2018).
[4] B.-Y. Wang, E. V. Denning, U. M. Gür, C.-Y. Lu, and N. Gregersen, Micropillar single-photon source design for simultaneous near-unity efficiency and indistinguishability, Phys. Rev. B **102**, 125301 (2020).
[5] H. Vural, S. L. Portalupi, and P. Michler, Perspective of self-assembled ingaas quantum-dots for multi-source quantum implementations, Appl. Phys. Lett. **117**, 030501 (2020).
[6] S. Thomas and P. Senellart, The race for the ideal single-photon source is on, Nat. Nanotechnol. **16**, 367 (2021).
[7] X. Ding, Y. He, Z.-C. Duan, N. Gregersen, M.-C. Chen, S. Unsleber, S. Maier, C. Schneider, M. Kamp, S. Höfling, C.-Y. Lu, and J.-W. Pan, On-Demand Single Photons with High Extraction Efficiency and Near-Unity Indistinguishability from a Resonantly Driven Quantum Dot in a Micropillar, Phys. Rev. Lett. **116**, 020401 (2016).
[8] N. Somaschi *et al.*, Near-optimal single-photon sources in the solid state, Nat. Photonics **10**, 340 (2016).
[9] Y. Arakawa and M. J. Holmes, Progress in quantum-dot single photon sources for quantum information technologies: A broad spectrum overview, Appl. Phys. Rev. **7**, 021309 (2020).
[10] N. Tomm, A. Javadi, N. O. Antoniadis, D. Najer, M. C. Löbl, A. R. Korsch, R. Schott, S. R. Valentin, A. D. Wieck, A. Ludwig, and R. J. Warburton, A bright and fast source of coherent single photons, Nat. Nanotechnol. **16**, 399 (2021).
[11] S. E. Thomas, M. Billard, N. Coste, S. C. Wein, Priya, H. Ollivier, O. Krebs, L. Tazaïrt, A. Harouri, A. Lemaitre, I. Sagnes, C. Anton, L. Lanco, N. Somaschi, J. C. Loredo, and P. Senellart, Bright Polarized Single-Photon Source Based on a Linear Dipole, Phys. Rev. Lett. **126**, 233601 (2021).
[12] L. Zhai, G. N. Nguyen, C. Spinnler, J. Ritzmann, M. C. Lbl, A. D. Wieck, A. Ludwig, A. Javadi, and R. J. Warburton, Quantum interference of identical photons from remote quantum dots, arXiv:2106.03871.
[13] L. Besombes, K. Kheng, L. Marsal, and H. Mariette, Acoustic phonon broadening mechanism in single quantum dot emission, Phys. Rev. B **63**, 155307 (2001).
[14] B. Krummheuer, V. M. Axt, and T. Kuhn, Theory of pure dephasing and the resulting absorption line shape in semiconductor quantum dots, Phys. Rev. B **65**, 195313 (2002).
[15] J. Förstner, C. Weber, J. Danckwerts, and A. Knorr, Phonon-Assisted Damping of Rabi Oscillations in Semiconductor Quantum Dots, Phys. Rev. Lett. **91**, 127401 (2003).
[16] P. Machnikowski and L. Jacak, Resonant nature of phonon-induced damping of Rabi oscillations in quantum dots, Phys. Rev. B **69**, 193302 (2004).
[17] A. Vagov, V. M. Axt, T. Kuhn, W. Langbein, P. Borri, and U. Woggon, Nonmonotonous temperature dependence of the

initial decoherence in quantum dots, Phys. Rev. B **70**, 201305(R) (2004).
[18] A. Vagov, M. D. Croitoru, V. M. Axt, T. Kuhn, and F. M. Peeters, Nonmonotonic Field Dependence of Damping and Reappearance of Rabi Oscillations in Quantum Dots, Phys. Rev. Lett. **98**, 227403 (2007).
[19] A. J. Ramsay, A. V. Gopal, E. M. Gauger, A. Nazir, B. W. Lovett, A. M. Fox, and M. S. Skolnick, Damping of Exciton Rabi Rotations by Acoustic Phonons in Optically Excited InGaAs/GaAs Quantum Dots, Phys. Rev. Lett. **104**, 017402 (2010).
[20] T. Kaldewey, S. Lüker, A. V. Kuhlmann, S. R. Valentin, J.-M. Chauveau, A. Ludwig, A. D. Wieck, D. E. Reiter, T. Kuhn, and R. J. Warburton, Demonstrating the decoupling regime of the electron-phonon interaction in a quantum dot using chirped optical excitation, Phys. Rev. B **95**, 241306 (R) (2017).
[21] S. Lüker and D. E. Reiter, A review on optical excitation of semiconductor quantum dots under the influence of phonons, Semicond. Sci. Technol. **34**, 063002 (2019).
[22] J. Iles-Smith, D. P. S. McCutcheon, A. Nazir, and J. Mørk, Phonon scattering inhibits simultaneous near-unity efficiency and indistinguishability in semiconductor single-photon sources, Nat. Photonics **11**, 521 (2017).
[23] H. Breuer and F. Petruccione, *The Theory of Open Quantum Systems* (Oxford University Press, New York, 2002).
[24] P. Kaer, P. Lodahl, A.-P. Jauho, and J. Mork, Microscopic theory of indistinguishable single-photon emission from a quantum dot coupled to a cavity: The role of non-Markovian phonon-induced decoherence, Phys. Rev. B **87**, 081308(R) (2013).
[25] K. Roy-Choudhury and S. Hughes, Quantum theory of the emission spectrum from quantum dots coupled to structured photonic reservoirs and acoustic phonons, Phys. Rev. B **92**, 205406 (2015).
[26] D. P. S. McCutcheon, Optical signatures of non-Markovian behavior in open quantum systems, Phys. Rev. A **93**, 022119 (2016).
[27] J. Iles-Smith, D. P. S. McCutcheon, J. Mørk, and A. Nazir, Limits to coherent scattering and photon coalescence from solid-state quantum emitters, Phys. Rev. B **95**, 201305(R) (2017).
[28] C. Gustin and S. Hughes, Pulsed excitation dynamics in quantum-dot–cavity systems: Limits to optimizing the fidelity of on-demand single-photon sources, Phys. Rev. B **98**, 045309 (2018).
[29] P. Kaer, T. R. Nielsen, P. Lodahl, A.-P. Jauho, and J. Mørk, Non-Markovian Model of Photon-Assisted Dephasing by Electron-Phonon Interactions in a Coupled Quantum-Dot-Cavity System, Phys. Rev. Lett. **104**, 157401 (2010).
[30] D. P. S. McCutcheon and A. Nazir, Quantum dot Rabi rotations beyond the weak exciton–phonon coupling regime, New J. Phys. **12**, 113042 (2010).
[31] A. Carmele and S. Reitzenstein, Non-Markovian features in semiconductor quantum optics: Quantifying the role of phonons in experiment and theory, Nanophotonics **8**, 655 (2019).
[32] D. E. Reiter, T. Kuhn, and V. M. Axt, Distinctive characteristics of carrier-phonon interactions in optically driven semiconductor quantum dots, Adv. Phys. **4**, 1655478 (2019).
[33] T. Renger and R. A. Marcus, On the relation of protein dynamics and exciton relaxation in pigmentprotein complexes: An estimation of the spectral density and a theory for the calculation of optical spectra, J. Chem. Phys. **116**, 9997 (2002).
[34] H.-P. Breuer, E.-M. Laine, J. Piilo, and B. Vacchini, Colloquium: Non-Markovian dynamics in open quantum systems, Rev. Mod. Phys. **88**, 021002 (2016).
[35] I. de Vega and D. Alonso, Dynamics of non-Markovian open quantum systems, Rev. Mod. Phys. **89**, 015001 (2017).
[36] G. Guarnieri, A. Smirne, and B. Vacchini, Quantum regression theorem and non-Markovianity of quantum dynamics, Phys. Rev. A **90**, 022110 (2014).
[37] A. Kurt, Two-time correlation functions beyond quantum regression theorem: Effect of external noise, Quantum Inf. Process. **20**, 238 (2021).
[38] M. Cosacchi, M. Cygorek, F. Ungar, A. M. Barth, A. Vagov, and V. M. Axt, Path-integral approach for nonequilibrium multitime correlation functions of open quantum systems coupled to Markovian and non-Markovian environments, Phys. Rev. B **98**, 125302 (2018).
[39] A. Vagov, M. D. Croitoru, M. Glässl, V. M. Axt, and T. Kuhn, Real-time path integrals for quantum dots: Quantum dissipative dynamics with superohmic environment coupling, Phys. Rev. B **83**, 094303 (2011).
[40] A. M. Barth, A. Vagov, and V. M. Axt, Path-integral description of combined Hamiltonian and non-Hamiltonian dynamics in quantum dissipative systems, Phys. Rev. B **94**, 125439 (2016).
[41] M. Cygorek, A. M. Barth, F. Ungar, A. Vagov, and V. M. Axt, Nonlinear cavity feeding and unconventional photon statistics in solid-state cavity QED revealed by many-level real-time path-integral calculations, Phys. Rev. B **96**, 201201(R) (2017).
[42] See Supplemental Material at http://link.aps.org/supplemental/10.1103/PhysRevLett.127.100402 for a complete definition of our model, in particular the phonon coupling, and a detailed explanation of the numerical procedure. Additionally, further details on the QRT in a polaron transformed frame are presented. It includes Refs. [43–50] in addition to other references already cited in the main text.
[43] P. Borri, W. Langbein, S. Schneider, U. Woggon, R. L. Sellin, D. Ouyang, and D. Bimberg, Ultralong Dephasing Time in InGaAs Quantum Dots, Phys. Rev. Lett. **87**, 157401 (2001).
[44] P. Machnikowski, V. M. Axt, and T. Kuhn, Quantum-information encoding in dressed qubits, Phys. Rev. A **75**, 052330 (2007).
[45] M. Florian, P. Gartner, C. Gies, and F. Jahnke, Phonon-mediated off-resonant coupling effects in semiconductor quantum-dot lasers, New J. Phys. **15**, 035019 (2013).
[46] A. Nysteen, P. Kaer, and J. Mork, Proposed Quenching of Phonon-Induced Processes in Photoexcited Quantum Dots due to Electron-Hole Asymmetries, Phys. Rev. Lett. **110**, 087401 (2013).
[47] D. P. S. McCutcheon and A. Nazir, Model of the Optical Emission of a Driven Semiconductor Quantum Dot:

Phonon-Enhanced Coherent Scattering and Off-Resonant Sideband Narrowing, Phys. Rev. Lett. **110**, 217401 (2013).

[48] D. E. Reiter, T. Kuhn, M. Glssl, and V. M. Axt, The role of phonons for exciton and biexciton generation in an optically driven quantum dot, J. Phys. Condens. Matter **26**, 423203 (2014).

[49] M. Reindl, K. D. Jöns, D. Huber, C. Schimpf, Y. Huo, V. Zwiller, A. Rastelli, and R. Trotta, Phonon-assisted two-photon interference from remote quantum emitters, Nano Lett. **17**, 4090 (2017).

[50] A. Strathearn, P. Kirton, D. Kilda, J. Keeling, and B. W. Lovett, Efficient non-Markovian quantum dynamics using time-evolving matrix product operators, Nat. Commun. **9**, 3322 (2018).

[51] S. Hepp, F. Hornung, S. Bauer, E. Hesselmeier, X. Yuan, M. Jetter, S. L. Portalupi, A. Rastelli, and P. Michler, Purcell-enhanced single-photon emission from a strain-tunable quantum dot in a cavity-waveguide device, Appl. Phys. Lett. **117**, 254002 (2020).

[52] L. Bremer, K. Weber, S. Fischbach, S. Thiele, M. Schmidt, A. Kaganskiy, S. Rodt, A. Herkommer, M. Sartison, S. L. Portalupi, P. Michler, H. Giessen, and S. Reitzenstein, Quantum dot single-photon emission coupled into single-mode fibers with 3D printed micro-objectives, APL Photonics **5**, 106101 (2020).

[53] P. Holewa, M. Burakowski, A. Musiał, N. Srocka, D. Quandt, A. Strittmatter, S. Rodt, S. Reitzenstein, and G. Sęk, Thermal stability of emission from single InGaAs/GaAs quantum dots at the telecom O-band, Sci. Rep. **10**, 21816 (2020).

[54] N. Srocka, P. Mrowiski, J. Groe, M. Schmidt, S. Rodt, and S. Reitzenstein, Deterministically fabricated strain-tunable quantum dot single-photon sources emitting in the telecom O-band, Appl. Phys. Lett. **117**, 224001 (2020).

[55] C. L. Phillips, A. J. Brash, D. P. S. McCutcheon, J. Iles-Smith, E. Clarke, B. Royall, M. S. Skolnick, A. M. Fox, and A. Nazir, Photon Statistics of Filtered Resonance Fluorescence, Phys. Rev. Lett. **125**, 043603 (2020).

[56] A. J. Brash, J. Iles-Smith, C. L. Phillips, D. P. S. McCutcheon, J. O'Hara, E. Clarke, B. Royall, L. R. Wilson, J. Mørk, M. S. Skolnick, A. M. Fox, and A. Nazir, Light Scattering from Solid-State Quantum Emitters: Beyond the Atomic Picture, Phys. Rev. Lett. **123**, 167403 (2019).

[57] E. Schöll, L. Schweickert, L. Hanschke, K. D. Zeuner, F. Sbresny, T. Lettner, R. Trivedi, M. Reindl, S. F. Covre da Silva, R. Trotta, J. J. Finley, J. Vučković, K. Müller, A. Rastelli, V. Zwiller, and K. D. Jöns, Crux of Using the Cascaded Emission of a Three-Level Quantum Ladder System to Generate Indistinguishable Photons, Phys. Rev. Lett. **125**, 233605 (2020).

[58] S. Manna, H. Huang, S. F. C. da Silva, C. Schimpf, M. B. Rota, B. Lehner, M. Reindl, R. Trotta, and A. Rastelli, Surface passivation and oxide encapsulation to improve optical properties of a single GaAs quantum dot close to the surface, Appl. Surf. Sci. **532**, 147360 (2020).

[59] V. M. Axt, T. Kuhn, A. Vagov, and F. M. Peeters, Phonon-induced pure dephasing in exciton-biexciton quantum dot systems driven by ultrafast laser pulse sequences, Phys. Rev. B **72**, 125309 (2005).

[60] S. Lüker, T. Kuhn, and D. E. Reiter, Phonon impact on optical control schemes of quantum dots: Role of quantum dot geometry and symmetry, Phys. Rev. B **96**, 245306 (2017).

[61] B. Krummheuer, V. M. Axt, T. Kuhn, I. D'Amico, and F. Rossi, Pure dephasing and phonon dynamics in GaAs- and GaN-based quantum dot structures: Interplay between material parameters and geometry, Phys. Rev. B **71**, 235329 (2005).

[62] Note that the excitation has to be resonant to the polaron shifted exciton energy, when phonons are taken into account.

[63] For resonant excitation, this value has been shown both experimentally Ding2016 and theoretically [28] to be a favorable value concerning the photonic figures of merit.

[64] C. Santori, M. Pelton, G. Solomon, Y. Dale, and Y. Yamamoto, Triggered Single Photons from a Quantum Dot, Phys. Rev. Lett. **86**, 1502 (2001).

[65] C. Santori, D. Fattal, J. Vuckovic, G. S. Solomon, and Y. Yamamoto, Indistinguishable photons from a single-photon device, Nature (London) **419**, 594 (2002).

[66] Y.-M. He, Y. He, Y.-J. Wei, D. Wu, M. Atatüre, C. Schneider, S. Höfling, M. Kamp, C.-Y. Lu, and J.-W. Pan, On-demand semiconductor single-photon source with near-unity indistinguishability, Nat. Nanotechnol. **8**, 213 (2013).

[67] Y.-J. Wei, Y.-M. He, M.-C. Chen, Y.-N. Hu, Y. He, D. Wu, C. Schneider, M. Kamp, S. Höfling, C.-Y. Lu, and J.-W. Pan, Deterministic and robust generation of single photons from a single quantum dot with 99.5% indistinguishability using adiabatic rapid passage, Nano Lett. **14**, 6515 (2014).

[68] L. Schweickert, K. D. Jöns, K. D. Zeuner, S. F. Covre da Silva, H. Huang, T. Lettner, M. Reindl, J. Zichi, R. Trotta, A. Rastelli, and V. Zwiller, On-demand generation of background-free single photons from a solid-state source, Appl. Phys. Lett. **112**, 093106 (2018).

[69] R. Hanbury Brown and R. Q. Twiss, A test of a new type of stellar interferometer on sirius, Nature (London) **178**, 1046 (1956).

[70] A. Kiraz, M. Atatüre, and A. Imamoğlu, Quantum-dot single-photon sources: Prospects for applications in linear optics quantum-information processing, Phys. Rev. A **69**, 032305 (2004).

[71] K. A. Fischer, K. Müller, K. G. Lagoudakis, and J. Vučković, Dynamical modeling of pulsed two-photon interference, New J. Phys. **18**, 113053 (2016).

[72] C. K. Hong, Z. Y. Ou, and L. Mandel, Measurement of Subpicosecond Time Intervals between Two Photons by Interference, Phys. Rev. Lett. **59**, 2044 (1987).

[73] R. Manson, K. Roy-Choudhury, and S. Hughes, Polaron master equation theory of pulse-driven phonon-assisted population inversion and single-photon emission from quantum-dot excitons, Phys. Rev. B **93**, 155423 (2016).

[74] M. Cosacchi, F. Ungar, M. Cygorek, A. Vagov, and V. M. Axt, Emission-Frequency Separated High Quality Single-Photon Sources Enabled by Phonons, Phys. Rev. Lett. **123**, 017403 (2019).

[75] H.-P. Breuer, E.-M. Laine, and J. Piilo, Measure for the Degree of Non-Markovian Behavior of Quantum Processes in Open Systems, Phys. Rev. Lett. **103**, 210401 (2009).

[76] A. Rivas, S. F. Huelga, and M. B. Plenio, Entanglement and Non-Markovianity of Quantum Evolutions, Phys. Rev. Lett. **105**, 050403 (2010).
[77] X.-M. Lu, X. Wang, and C. P. Sun, Quantum Fisher information flow and non-Markovian processes of open systems, Phys. Rev. A **82**, 042103 (2010).
[78] S. Lorenzo, F. Plastina, and M. Paternostro, Geometrical characterization of non-Markovianity, Phys. Rev. A **88**, 020102(R) (2013).
[79] Á. Rivas, S. F. Huelga, and M. B. Plenio, Quantum non-Markovianity: Characterization, quantification and detection, Rep. Prog. Phys. **77**, 094001 (2014).
[80] D. Chruścińskiand S. Maniscalco, Degree of Non-Markovianity of Quantum Evolution, Phys. Rev. Lett. **112**, 120404 (2014).
[81] L. Li, M. J. Hall, and H. M. Wiseman, Concepts of quantum non-Markovianity: A hierarchy, Phys. Rep. **759**, 1 (2018).
[82] S. Wißmann, A. Karlsson, E.-M. Laine, J. Piilo, and H.-P. Breuer, Optimal state pairs for non-Markovian quantum dynamics, Phys. Rev. A **86**, 062108 (2012).
[83] W. H. Louisell, *Quantum Statistical Properties of Radiation* (Wiley, New York, 1973).
[84] H. Carmichael, *An Open Systems Approach to Quantum Optics* (Springer, Berlin, 1993).
[85] C. Roy and S. Hughes, Influence of Electron—Acoustic-Phonon Scattering on Intensity Power Broadening in a Coherently Driven Quantum-Dot—Cavity System, Phys. Rev. X **1**, 021009 (2011).
[86] A. Nazir and D. P. S. McCutcheon, Modelling exciton-phonon interactions in optically driven quantum dots, J. Phys. Condens. Matter **28**, 103002 (2016).
[87] J. Iles-Smith and A. Nazir, Quantum correlations of light and matter through environmental transitions, Optica **3**, 207 (2016).
[88] D. Englund, B. Shields, K. Rivoire, F. Hatami, J. Vučković, H. Park, and M. D. Lukin, Deterministic coupling of a single nitrogen vacancy center to a photonic crystal cavity, Nano Lett. **10**, 3922 (2010).
[89] K. Beha *et al.*, Diamond nanophotonics, Beilstein J. Nanotechnol. **3**, 895 (2012).
[90] I. Aharonovich, D. Englund, and M. Toth, Solid-state single-photon emitters, Nat. Photonics **10**, 631 (2016).
[91] K. G. Fehler, A. P. Ovvyan, N. Gruhler, W. H. P. Pernice, and A. Kubanek, Efficient coupling of an ensemble of nitrogen vacancy center to the mode of a high-Q, Si_3N_4 photonic crystal cavity, ACS Nano **13**, 6891 (2019).
[92] E. Janitz, M. K. Bhaskar, and L. Childress, Cavity quantum electrodynamics with color centers in diamond, Optica **7**, 1232 (2020).
[93] P. P. J. Schrinner, J. Olthaus, D. E. Reiter, and C. Schuck, Integration of diamond-based quantum emitters with nanophotonic circuits, Nano Lett. **20**, 8170 (2020).
[94] J. C. Lee, I. Aharonovich, A. P. Magyar, F. Rol, and E. L. Hu, Coupling of silicon-vacancy centers to a single crystal diamond cavity, Opt. Express **20**, 8891 (2012).
[95] K. G. Fehler, A. P. Ovvyan, L. Antoniuk, N. Lettner, N. Gruhler, V. A. Davydov, V. N. Agafonov, W. H. Pernice, and A. Kubanek, Purcell-enhanced emission from individual SiV- center in nanodiamonds coupled to a Si_3N_4-based, photonic crystal cavity, Nanophotonics **9**, 3655 (2020).
[96] N. V. Proscia, H. Jayakumar, X. Ge, G. Lopez-Morales, Z. Shotan, W. Zhou, C. A. Meriles, and V. M. Menon, Microcavity-coupled emitters in hexagonal boron nitride, Nanophotonics **9**, 2937 (2020).
[97] J. E. Fröch, S. Kim, N. Mendelson, M. Kianinia, M. Toth, and I. Aharonovich, Coupling hexagonal boron nitride quantum emitters to photonic crystal cavities, ACS Nano **14**, 7085 (2020).
[98] S. Rodt, S. Reitzenstein, and T. Heindel, Deterministically fabricated solid-state quantum-light sources, J. Phys. Condens. Matter **32**, 153003 (2020).

Supplement: Accuracy of the quantum regression theorem for photon emission from a quantum dot

M. Cosacchi,[1] T. Seidelmann,[1] M. Cygorek,[2] A. Vagov,[1,3] D. E. Reiter,[4] and V. M. Axt[1]

[1] *Theoretische Physik III, Universität Bayreuth, 95440 Bayreuth, Germany*
[2] *Heriot-Watt University, Edinburgh EH14 4AS, United Kingdom*
[3] *ITMO University, St. Petersburg, 197101, Russia*
[4] *Institut für Festkörpertheorie, Universität Münster, 48149 Münster, Germany*

I. HAMILTONIAN AND MODEL EQUATION

Our model Hamiltonian reads as:

$$H = H_{\mathrm{QD}} + H_{\mathrm{Ph}} + H_{\mathrm{driving}}\,. \tag{1}$$

The two-level quantum dot (QD) has an excited state $|X\rangle$ at energy $\hbar\omega_X$ and the energy of the ground state $|G\rangle$ is set to zero. In a frame co-rotating with the laser frequency ω_L the corresponding Hamiltonian is

$$H_{\mathrm{QD}} = \hbar\Delta\omega_{XL}|X\rangle\langle X| \tag{2}$$

with the exciton-laser detuning $\Delta\omega_{XL} = \omega_X - \omega_L$. The QD interacts with an environment of longitudinal acoustic (LA) phonons via a pure-dephasing coupling Hamiltonian [1–5]

$$H_{\mathrm{Ph}} = \hbar\sum_{\mathbf{q}}\omega_{\mathbf{q}}b^\dagger_{\mathbf{q}}b_{\mathbf{q}} + \hbar\sqrt{\lambda}\sum_{\mathbf{q}}\left(\gamma^{\mathrm{X}}_{\mathbf{q}}b^\dagger_{\mathbf{q}} + \gamma^{\mathrm{X}*}_{\mathbf{q}}b_{\mathbf{q}}\right)|X\rangle\langle X|\,, \tag{3}$$

where $b_{\mathbf{q}}$ ($b^\dagger_{\mathbf{q}}$) annihilates (creates) a phonon in the mode $\mathbf{q}$ with energy $\hbar\omega_{\mathbf{q}}$. The coupling strength to the QD is denoted by $\gamma^{\mathrm{X}}_{\mathbf{q}}$. In order to analyze the impact of the phonon coupling, we introduce a scaling parameter λ, with $0 \leq \lambda \leq 10$. $\lambda = 0$ describes the phonon-free case, $\lambda = 1$ the coupling in a GaAs QD. $1 < \lambda \leq 10$ roughly estimates the stronger phonon coupling in piezoelectric materials like GaN [6]. λ is referred to as the phonon scaling in the main text. Note that we followed the standard way to write the phonon coupling in Eq. (3) to the exciton state $|X\rangle$ only. But in fact, it can be written to the ground state $|G\rangle$ without any influence on the stationary emission spectrum, which we checked numerically by calculating the QRT spectrum in Fig. 1 (red dashed line) both ways.

The QD is driven by an external laser pulse described by

$$H_{\mathrm{driving}} = -\frac{\hbar}{2}f_{\mathrm{p}}(t)\left(\sigma_X + \sigma_X^\dagger\right)\,. \tag{4}$$

$\sigma_X := |G\rangle\langle X|$ is the operator for the transition between $|X\rangle$ and the ground state $|G\rangle$. $f_{\mathrm{p}}(t)$ is the real envelope function of the external laser pulse. Throughout the main text, we consider a Gaussian pulse with an area of π and pulse duration as measured by the full width at half maximum $\tau_{\mathrm{FWHM}} = 3\,\mathrm{ps}$ resonant to the polaron shifted QD transition energy. We further account for the radiative decay of the QD exciton by introducing a Lindblad superoperator acting on the density matrix ρ to our model

$$\mathcal{L}_{\sigma_X,\gamma}\rho = \gamma\left(\sigma_X\rho\sigma_X^\dagger - \frac{1}{2}\left\{\rho, \sigma_X^\dagger\sigma_X\right\}_+\right)\,, \tag{5}$$

where $\{A,B\}_+$ denotes the anti-commutator of operators A and B and γ the radiative decay rate set to a typical value of $1\,\mathrm{ns}^{-1}$ unless noted otherwise.

In this model the QD environment consists of two parts: the coupling to photon modes which is responsible for the radiative decay and the coupling to phonons. Since the radiative decay is modeled by a Markovian rate, it is not expected to limit the validity of the QRT. Phonons are known to influence the QD dynamics profoundly [1, 7–18] and to be the origin of non-Markovian behavior [5, 19–23], which might entail errors of the QRT.

While the Hamiltonian in Eq. (1) defines the model, the corresponding Liouville-von Neumann equation for the density matrix ρ reads

$$\frac{\partial}{\partial t}\rho = -\frac{i}{\hbar}\{H,\rho\}_- + \mathcal{L}_{\sigma_X,\gamma}\rho \tag{6}$$

TABLE I. Parameters typical for GaAs QDs [6].

Electron deformation potential	D_e (eV)	7.0
Hole deformation potential	D_h (eV)	-3.5
Density	ρ_D (kg/m^3)	5370
Sound velocity	c_s (m/s)	5110
Electron-to-hole confinement ratio	a_e/a_h	1.15
Electron confinement radius	a_e (nm)	3.0

with the commutator $\{A,B\}_-$ of operators A and B. This equation is solved in a numerically exact way for the time evolution of the QD subsystem's reduced density matrix $\bar{\rho} = \mathrm{Tr}_{\mathrm{Ph}}[\rho]$, where the trace is taken over the phonon subspace, by employing an iterative real-time path-integral formalism (details are explained in Refs. 24–26).

The deformation potential coupling of the QD to LA phonons influences the reduced electronic density matrix via the phonon spectral density $J(\omega) = \sum_{\mathbf{q}} |\gamma_{\mathbf{q}}^X|^2 \delta(\omega - \omega_{\mathbf{q}})$. Note that the sign or even the phase of the coupling has no influence on the electronic dynamics, since only the absolute square enters the spectral density. Assuming a linear dispersion $\omega_{\mathbf{q}} = c_s|\mathbf{q}|$ with sound velocity c_s and Gaussian wave functions for both electrons and holes with radii a_e and a_h, the spectral density becomes [24, 26, 27]

$$J(\omega) = \frac{\omega^3}{4\pi^2 \rho_D \hbar c_s^5} \left(D_e e^{-\omega^2 a_e^2/(4c_s^2)} - D_h e^{-\omega^2 a_h^2/(4c_s^2)} \right)^2 . \tag{7}$$

We use typical GaAs parameters for a QD with radius $a_e = 3.0\,\mathrm{nm}$ listed in Tab. I. Note that scaling the phonon coupling $\gamma_{\mathbf{q}}^X$ with $\sqrt{\lambda}$ as in Eq. (3) implies that the spectral density $J(\omega)$ is scaled with λ.

The low-frequency behavior of this spectral density is given by $J(\omega) \propto \omega^s$ with $s = 3$. Spectral densities with such a power law dependence are classified as super-Ohmic, in contrast to the Ohmic case, for which $s = 1$, and the sub-Ohmic case with $0 \leq s < 1$. The super-Ohmic case is known to result in a nonexponential and only partial polarization decay [3] which is a clear signature of non-Markovian dynamics. Rather generally, the low-frequency behavior has been shown to potentially play a decisive role for the relation between Markovianity and QRT errors [28].

II. EVALUATION OF $G^{(2)}(t,\tau)$

Numerically Exact Evaluation To evaluate the two-time correlation function introduced in the main text $G^{(2)}(t,\tau) = \langle \sigma_X^\dagger(t)\sigma_X^\dagger(t+\tau)\sigma_X(t+\tau)\sigma_X(t)\rangle$ within the path-integral formalism, first, we assume a time discretization of n equidistant time steps with length Δt for the interval $[0,t]$ and of another m time steps of the same length to cover $[t,t+\tau]$, i.e., $t = n\Delta t$ and $\tau = m\Delta t$. The object propagated in time is the augmented density matrix (ADM), a $2n_c$-rank tensor that contains all the information induced by the $n_c\Delta t$ long memory. The iterative propagation of the ADM is summarized as [25]:

$$\bar{\rho}^{\mu_n \ldots \mu_{n-n_c+1}}_{\nu_n \ldots \nu_{n-n_c+1}} = \mathcal{M}^{\nu_{n-1}\mu_{n-1}}_{\nu_n \mu_n} \sum_{\substack{\nu_{n-n_c} \\ \mu_{n-n_c}}} \exp\left(\sum_{l=n-n_c}^{n} S_{\nu_n \nu_l \mu_n \mu_l} \right) \bar{\rho}^{\mu_{n-1}\ldots\mu_{n-n_c}}_{\nu_{n-1}\ldots\nu_{n-n_c}} , \tag{8}$$

where $\mathcal{M}^{\nu_{n-1}\mu_{n-1}}_{\nu_n\mu_n}$ is the subsystem propagator and $S_{\nu_n\nu_l\mu_n\mu_l}$ the phonon influence functional. The indices μ_j and ν_j describe the subsystem state μ and ν, respectively, at the time step j. The subsystem's reduced density matrix at time $n\Delta t$, which is the quantity necessary to calculate any expectation value of observables within the subsystem, is obtained by tracing out the memory contained in the ADM, i.e.,

$$\bar{\rho}_{\nu_n\mu_n} = \sum_{\substack{\nu_{n-1}\ldots\nu_{n-n_c+1} \\ \mu_{n-1}\cdots\mu_{n-n_c+1}}} \bar{\rho}^{\mu_n\cdots\mu_{n-n_c+1}}_{\nu_n\ldots\nu_{n-n_c+1}} . \tag{9}$$

In order to calculate the two-time correlation function $G^{(2)}(t,\tau)$, the ADM is propagated for the first n steps, after

which the operators evaluated at time t are multiplied to produce a modified ADM (MADM):

$$\bar{\rho}_{\sigma_X\sigma_X^\dagger\nu_n\ldots\nu_{n-n_c+1}}^{\mu_n\cdots\mu_{n-n_c+1}} = \sum_{\nu'_n\mu'_n} (\sigma_X)_{\nu_n\nu'_n} \mathcal{M}_{\nu'_n\mu'_n}^{\nu_{n-1}\mu_{n-1}} (\sigma_X^\dagger)_{\mu'_n\mu_n} \sum_{\substack{\nu_{n-n_c}\\ \mu_{n-n_c}}} \exp\left(\sum_{l=n-n_c}^{n} S_{\nu_n\nu_l\mu_n\mu_l}\right) \bar{\rho}_{\nu_{n-1}\ldots\nu_{n-n_c}}^{\mu_{n-1}\cdots\mu_{n-n_c}}, \tag{10}$$

The MADM follows the same recursion as the ADM, such that for the subsequent m steps until $t+\tau$, the MADM is iterated instead of the ADM. Finally, the two-time correlation function is obtained by multiplying the operators evaluated at time $t+\tau$ and the trace is performed to yield

$$G^{(2)}(t,\tau) = \sum_{\substack{\nu_{n+m}\cdots\nu_{n+m-n_c+1}\\ \mu_{n+m}\cdots\mu_{n+m-n_c+1}}} \left[\sigma_X^\dagger\sigma_X\right]_{\mu_{n+m}\nu_{n+m}} \bar{\rho}_{\sigma_X\sigma_X^\dagger\nu_{n+m}\ldots\nu_{n+m-n_c+1}}^{\mu_{n+m}\cdots\mu_{n+m-n_c+1}}. \tag{11}$$

A derivation of this scheme with detailed explanations can be found in Ref. [29]. Note that the first-order correlation function $\langle\sigma_X^\dagger(t+\tau)\sigma_X(t)\rangle$ appearing in the main text can be obtained using the same method by simply exchanging $\sigma_X^\dagger(t)$ and $\sigma_X(t+\tau)$ with identity operators in $G^{(2)}(t,\tau)$.

QRT Evaluation To implement the QRT within this framework, one traces out the memory of the ADM after reaching the time $n\Delta t$ as in Eq. (9) to obtain the reduced density matrix (RDM) $\bar{\rho}_{\nu_n\mu_n}$. Then, a modified RDM (MRDM) which is defined as

$$\bar{\rho}_{\sigma_X\sigma_X^\dagger\nu_n}^{\mu_n} = \sum_{\nu'_n\mu'_n} (\sigma_X)_{\nu_n\nu'_n} \bar{\rho}_{\nu'_n\mu'_n} (\sigma_X^\dagger)_{\mu'_n\mu_n} \tag{12}$$

is used as the new initial RDM for the next m time steps, which now describe the propagation in τ. The essential difference to the exact propagation scheme is that here the memory acquired until the time t is discarded for the subsequent τ-propagation. As for the initial (real) time $t=0$, the phonon subspace is assumed to be in equilibrium at a temperature of T at the time $n\Delta t$, when the propagation of the MRDM begins. The statistical operator of the total system is approximated by the QRT at the beginning of the τ-propagation by a product of the statistical operators for the two-level system and the environment, thus ignoring the entanglement between these subsystems that has been built up during the t-propagation due to their mutual interaction [30].

III. EMISSION SPECTRA AND QRT IMPLEMENTATION

The emission spectrum $S(\omega)$ is obtained in a stationary nonequilibrium state of the system. To this end, the first-order two-time correlation function $G^{(1)}(t,\tau) = \langle\sigma_X^\dagger(t+\tau)\sigma_X(t)\rangle$ is considered in the limit $t\to\infty$. After subtraction of the coherent part of the emission [29, 31] $\lim_{t,\tau\to\infty} G^{(1)}(t,\tau)$ the Fourier transform is taken:

$$S(\omega) = \mathrm{Re}\left[\int_{-\infty}^{\infty} d\tau \lim_{t\to\infty}\left(G^{(1)}(t,\tau) - \lim_{\tau\to\infty} G^{(1)}(t,\tau)\right) e^{-i\omega\tau}\right]. \tag{13}$$

In Fig. 1 QD emission spectra calculated for a constantly driven QD with a field strength of $\hbar f_\mathrm{p}(t) = 0.079\,\mathrm{meV}$ and a radiative decay rate of $\gamma = 0.01\,\mathrm{ps}^{-1}$ at $T = 10\,\mathrm{K}$ are shown. As a reference, the phonon-free result, i.e., for $\lambda = 0$, is depicted (orange dashed-dotted line), where no sidebands appear. The inset in Fig. 1 shows the same data zoomed in on the energy scale and zoomed out on the intensity axis. On this scale, the Mollow triplet becomes visible with the peaks at $\pm\hbar f_\mathrm{p}$, which corresponds to the Rabi splitting. For finite temperature, the peaks shift to smaller energies and broaden slightly, which corresponds to the phonon-induced renormalization of the Rabi frequency and its damping, respectively. Note that the numerically exact result at 10 K has been obtained by employing a matrix-product-state representation of the iterative path-integral method [32] to enable calculations with very fine time discretization.

We stress that there is a clear physical picture that the phonon sideband has to be on the left side of the zero phonon line (ZPL). At low temperatures, phonon emission is strongly favored over phonon absorption. Therefore, the energies of the emitted photon and of the emitted phonon have to add up to the QD transition energy due to energy conservation. Accordingly, in an emission spectrum, the energy of the emitted photon after phonon emission has to be smaller than the QD transition energy. This results in the phonon emission sideband being on the energetically lower side of the ZPL.

The numerically exact approach (black solid line) gives the physically correct results showing the phonon sideband on the energetically lower side of the ZPL. In contrast, when the QRT is applied, the phonon sideband appears on

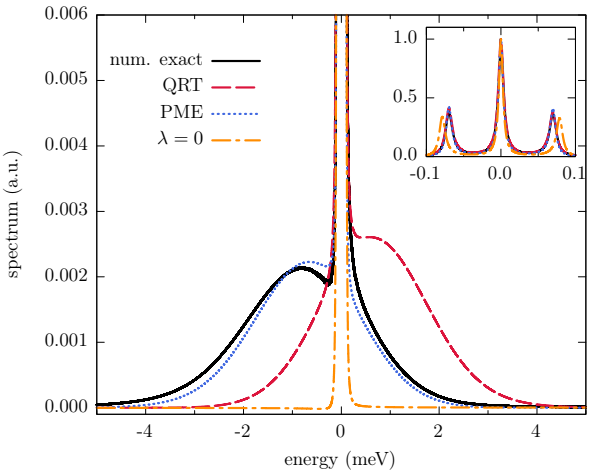

FIG. 1. The QD emission spectrum [29] calculated for a constantly driven QD with $\hbar f_{\mathrm{p}}(t) = 0.079\,\mathrm{meV}$ and a radiative decay rate of $\gamma = 0.01\,\mathrm{ps}^{-1}$ at $T = 10\,\mathrm{K}$. The numerically exact result (num. exact) is compared with results obtained using the QRT in the lab frame (QRT) and in the polaron frame (PME). As a reference, the phonon-free case $\lambda = 0$ is also shown. The inset depicts the same data on a different scale, where the Mollow triplet becomes visible.

the energetically higher side (red dashed line). This wrong outcome of the QRT was already discussed in Ref. 22, where it was explicitly shown that by neglecting correlations resulting in memory effects, physically wrong results are obtained. We consider our implementation of the QRT as verified, since it reproduces this result of Ref. 22, which was obtained within a completely different methodological framework. When including said correlations and memory effects on the other hand, as they are in our numerically exact path-integral approach, the physically correct picture of a phonon sideband at the lower energy side of the emission spectrum is found.

IV. THE QRT IN THE POLARON TRANSFORMED FRAME

An approximate method to account for the coupling to the LA phonon environment is the polaron master equation approach (PME) [33–35]. The core idea of this method is to transform the system into the polaron frame by

$$H' = e^{S} H e^{-S} \tag{14a}$$

$$S = \sigma_X^\dagger \sigma_X \sum_{\mathbf{q}} \frac{\sqrt{\lambda}}{\omega_{\mathbf{q}}} \left(\gamma_{\mathbf{q}}^X b_{\mathbf{q}}^\dagger - \gamma_{\mathbf{q}}^{X*} b_{\mathbf{q}}\right) . \tag{14b}$$

Only then the Markov approximation is employed to obtain a time-local master equation for the reduced subsystem dynamics. This method becomes exact in the weak-driving limit. Since we consider strong pulsed excitation, it is not a priori clear if this condition is fulfilled. The PME approach captures a variety of non-Markovian features that would be lost if the Markov approximation had been used in the original laboratory frame.

Therefore, the question arises whether the QRT is also frame dependent. Indeed, QD emission spectra calculated within the PME approach by employing the QRT in the polaron frame show the correct phonon sidebands [36], cf., blue dotted line in Fig. 1.

In the following, we describe the procedure to compare the effect of using the QRT in the lab and the polaron frame on the indistinguishability, cf., Fig. 2(c) in the main text. To obtain the indistinguishability in the lab frame within the PME approach, one has to transform it back after using the QRT in the polaron frame. In this transformation, all $\sigma_X^\dagger$ (σ_X) operators acquire a B_+ (B_-) operator with $B_\pm = \exp\left[\pm \sum_{\mathbf{q}} (\sqrt{\lambda}/\omega_{\mathbf{q}})(\gamma_{\mathbf{q}}^{X*} b_{\mathbf{q}} - \gamma_{\mathbf{q}}^X b_{\mathbf{q}}^\dagger)\right]$. Hence, whenever the two transition operators appear in pairs at equal times as in the second-order correlation function $G^{(2)}(t,\tau)$ the back transform is the identity operation. In contrast, the function $G^{(1)}(t,\tau)$ is influenced by the back transform. In particular, a term $\langle B_+(\tau) B_-(0)\rangle$ appears, which is simplified to $\langle B\rangle^2 e^{\phi(\tau)}$ [37]. The so-called Franck-Condon factor

[16] $\langle B\rangle$ is defined as

$$\langle B\rangle = \langle B_{\pm}\rangle = \exp\left[-\frac{1}{2}\int_0^{\infty} d\omega \frac{J(\omega)}{\omega^2}\coth\left(\hbar\omega/(2k_BT)\right)\right], \tag{15}$$

where k_B denotes the Boltzmann constant. The phonon correlation function is

$$\phi(\tau) = \int_0^{\infty} d\omega \frac{J(\omega)}{\omega^2}[\coth\left(\hbar\omega/(2k_BT)\right)\cos\left(\omega\tau\right) - i\sin\left(\omega\tau\right)]. \tag{16}$$

[1] L. Besombes, K. Kheng, L. Marsal, H. Mariette. 'Acoustic phonon broadening mechanism in single quantum dot emission'. *Phys. Rev. B* **63**, 155307 (2001). doi:10.1103/PhysRevB.63.155307.

[2] P. Borri, W. Langbein, S. Schneider, U. Woggon, R. L. Sellin, D. Ouyang, D. Bimberg. 'Ultralong dephasing time in InGaAs quantum dots'. *Phys. Rev. Lett.* **87**, 157401 (2001). doi:10.1103/PhysRevLett.87.157401.

[3] B. Krummheuer, V. M. Axt, T. Kuhn. 'Theory of pure dephasing and the resulting absorption line shape in semiconductor quantum dots'. *Phys. Rev. B* **65**, 195313 (2002). doi:10.1103/PhysRevB.65.195313.

[4] V. M. Axt, T. Kuhn, A. Vagov, F. M. Peeters. 'Phonon-induced pure dephasing in exciton-biexciton quantum dot systems driven by ultrafast laser pulse sequences'. *Phys. Rev. B* **72**, 125309 (2005). doi:10.1103/PhysRevB.72.125309.

[5] D. E. Reiter, T. Kuhn, V. M. Axt. 'Distinctive characteristics of carrier-phonon interactions in optically driven semiconductor quantum dots'. *Adv. Phys.: X* **4**, 1655478 (2019). doi:10.1080/23746149.2019.1655478.

[6] B. Krummheuer, V. M. Axt, T. Kuhn, I. D'Amico, F. Rossi. 'Pure dephasing and phonon dynamics in GaAs- and GaN-based quantum dot structures: Interplay between material parameters and geometry'. *Phys. Rev. B* **71**, 235329 (2005). doi:10.1103/PhysRevB.71.235329.

[7] J. Förstner, C. Weber, J. Danckwerts, A. Knorr. 'Phonon-assisted damping of rabi oscillations in semiconductor quantum dots'. *Phys. Rev. Lett.* **91**, 127401 (2003). doi:10.1103/PhysRevLett.91.127401.

[8] P. Machnikowski, L. Jacak. 'Resonant nature of phonon-induced damping of Rabi oscillations in quantum dots'. *Phys. Rev. B* **69**, 193302 (2004). doi:10.1103/PhysRevB.69.193302.

[9] A. Vagov, V. M. Axt, T. Kuhn, W. Langbein, P. Borri, U. Woggon. 'Nonmonotonous temperature dependence of the initial decoherence in quantum dots'. *Phys. Rev. B* **70**, 201305(R) (2004). doi:10.1103/PhysRevB.70.201305.

[10] A. Vagov, M. D. Croitoru, V. M. Axt, T. Kuhn, F. M. Peeters. 'Nonmonotonic field dependence of damping and reappearance of Rabi oscillations in quantum dots'. *Phys. Rev. Lett.* **98**, 227403 (2007). doi:10.1103/PhysRevLett.98.227403.

[11] A. J. Ramsay, A. V. Gopal, E. M. Gauger, A. Nazir, B. W. Lovett, A. M. Fox, M. S. Skolnick. 'Damping of exciton Rabi rotations by acoustic phonons in optically excited InGaAs/GaAs quantum dots'. *Phys. Rev. Lett.* **104**, 017402 (2010). doi:10.1103/PhysRevLett.104.017402.

[12] M. Florian, P. Gartner, C. Gies, F. Jahnke. 'Phonon-mediated off-resonant coupling effects in semiconductor quantum-dot lasers'. *New J. Phys.* **15**, 035019 (2013). doi:10.1088/1367-2630/15/3/035019.

[13] A. Nysteen, P. Kaer, J. Mork. 'Proposed quenching of phonon-induced processes in photoexcited quantum dots due to electron-hole asymmetries'. *Phys. Rev. Lett.* **110**, 087401 (2013). doi:10.1103/PhysRevLett.110.087401.

[14] D. P. S. McCutcheon, A. Nazir. 'Model of the optical emission of a driven semiconductor quantum dot: Phonon-enhanced coherent scattering and off-resonant sideband narrowing'. *Phys. Rev. Lett.* **110**, 217401 (2013). doi:10.1103/PhysRevLett.110.217401.

[15] D. E. Reiter, T. Kuhn, M. Glässl, V. M. Axt. 'The role of phonons for exciton and biexciton generation in an optically driven quantum dot'. *Journal of Physics: Condensed Matter* **26**, 423203 (2014). doi:10.1088/0953-8984/26/42/423203.

[16] J. Iles-Smith, D. P. S. McCutcheon, A. Nazir, J. Mørk. 'Phonon scattering inhibits simultaneous near-unity efficiency and indistinguishability in semiconductor single-photon sources'. *Nature Photonics* **11**, 521 (2017). doi:10.1038/nphoton.2017.101.

[17] T. Kaldewey, S. Lüker, A. V. Kuhlmann, S. R. Valentin, J.-M. Chauveau, A. Ludwig, A. D. Wieck, D. E. Reiter, T. Kuhn, R. J. Warburton. 'Demonstrating the decoupling regime of the electron-phonon interaction in a quantum dot using chirped optical excitation'. *Phys. Rev. B* **95**, 241306 (2017). doi:10.1103/PhysRevB.95.241306.

[18] M. Reindl, K. D. Jöns, D. Huber, C. Schimpf, Y. Huo, V. Zwiller, A. Rastelli, R. Trotta. 'Phonon-assisted two-photon interference from remote quantum emitters'. *Nano Lett.* **17**, 4090 (2017). doi:10.1021/acs.nanolett.7b00777.

[19] P. Kaer, T. R. Nielsen, P. Lodahl, A.-P. Jauho, J. Mørk. 'Non-Markovian Model of Photon-Assisted Dephasing by Electron-Phonon Interactions in a Coupled Quantum-Dot-Cavity System'. *Phys. Rev. Lett.* **104**, 157401 (2010). doi:10.1103/PhysRevLett.104.157401.

[20] D. P. S. McCutcheon, A. Nazir. 'Quantum dot Rabi rotations beyond the weak exciton–phonon coupling regime'. *New Journal of Physics* **12**, 113042 (2010). doi:10.1088/1367-2630/12/11/113042.

[21] P. Kaer, P. Lodahl, A.-P. Jauho, J. Mork. 'Microscopic theory of indistinguishable single-photon emission from a quantum dot coupled to a cavity: The role of non-Markovian phonon-induced decoherence'. *Phys. Rev. B* **87**, 081308 (2013). doi:10.1103/PhysRevB.87.081308.

[22] D. P. S. McCutcheon. 'Optical signatures of non-Markovian behavior in open quantum systems'. *Phys. Rev. A* **93**, 022119 (2016). doi:10.1103/PhysRevA.93.022119.

[23] A. Carmele, S. Reitzenstein. 'Non-Markovian features in semiconductor quantum optics: quantifying the role of phonons in experiment and theory'. *Nanophotonics* **8**, 655 (2019). doi:doi:10.1515/nanoph-2018-0222.
[24] A. Vagov, M. D. Croitoru, M. Glässl, V. M. Axt, T. Kuhn. 'Real-time path integrals for quantum dots: Quantum dissipative dynamics with superohmic environment coupling'. *Phys. Rev. B* **83**, 094303 (2011). doi:10.1103/PhysRevB.83.094303.
[25] A. M. Barth, A. Vagov, V. M. Axt. 'Path-integral description of combined Hamiltonian and non-Hamiltonian dynamics in quantum dissipative systems'. *Phys. Rev. B* **94**, 125439 (2016). doi:10.1103/PhysRevB.94.125439.
[26] M. Cygorek, A. M. Barth, F. Ungar, A. Vagov, V. M. Axt. 'Nonlinear cavity feeding and unconventional photon statistics in solid-state cavity QED revealed by many-level real-time path-integral calculations'. *Phys. Rev. B* **96**, 201201(R) (2017). doi:10.1103/PhysRevB.96.201201.
[27] S. Lüker, T. Kuhn, D. E. Reiter. 'Phonon impact on optical control schemes of quantum dots: Role of quantum dot geometry and symmetry'. *Phys. Rev. B* **96**, 245306 (2017). doi:10.1103/PhysRevB.96.245306.
[28] G. Guarnieri, A. Smirne, B. Vacchini. 'Quantum regression theorem and non-Markovianity of quantum dynamics'. *Phys. Rev. A* **90**, 022110 (2014). doi:10.1103/PhysRevA.90.022110.
[29] M. Cosacchi, M. Cygorek, F. Ungar, A. M. Barth, A. Vagov, V. M. Axt. 'Path-integral approach for nonequilibrium multitime correlation functions of open quantum systems coupled to Markovian and non-Markovian environments'. *Phys. Rev. B* **98**, 125302 (2018). doi:10.1103/PhysRevB.98.125302.
[30] P. Machnikowski, V. M. Axt, T. Kuhn. 'Quantum-information encoding in dressed qubits'. *Phys. Rev. A* **75**, 052330 (2007). doi:10.1103/PhysRevA.75.052330.
[31] H. Carmichael. *An open systems approach to Quantum Opt.* Springer, Berlin (1993).
[32] A. Strathearn, P. Kirton, D. Kilda, J. Keeling, B. W. Lovett. 'Efficient non-Markovian quantum dynamics using time-evolving matrix product operators'. *Nat. Commun.* **9**, 3322 (2018). doi:10.1038/s41467-018-05617-3.
[33] C. Roy, S. Hughes. 'Influence of electron–acoustic-phonon scattering on intensity power broadening in a coherently driven quantum-dot–cavity system'. *Phys. Rev. X* **1**, 021009 (2011). doi:10.1103/PhysRevX.1.021009.
[34] A. Nazir, D. P. S. McCutcheon. 'Modelling exciton-phonon interactions in optically driven quantum dots'. *J. Phys.: Condens. Matter* **28**, 103002 (2016). doi:10.1088/0953-8984/28/10/103002.
[35] J. Iles-Smith, A. Nazir. 'Quantum correlations of light and matter through environmental transitions'. *Optica* **3**, 207 (2016). doi:10.1364/OPTICA.3.000207.
[36] K. Roy-Choudhury, S. Hughes. 'Quantum theory of the emission spectrum from quantum dots coupled to structured photonic reservoirs and acoustic phonons'. *Phys. Rev. B* **92**, 205406 (2015). doi:10.1103/PhysRevB.92.205406.
[37] C. Gustin, S. Hughes. 'Pulsed excitation dynamics in quantum-dot–cavity systems: Limits to optimizing the fidelity of on-demand single-photon sources'. *Phys. Rev. B* **98**, 045309 (2018). doi:10.1103/PhysRevB.98.045309.

Erratum: Accuracy of the quantum regression theorem for photon emission from a quantum dot

M. Cosacchi, T. Seidelmann, M. Cygorek, A. Vagov, D. E. Reiter, and V. M. Axt

In our Letter, the main investigation was a comparison between a numerically exact path-integral (PI) method and the quantum regression theorem (QRT) to model photonic figures of merit in quantum-dot–cavity systems obtained from two-time correlation functions. As a side aspect, we discussed the dependence of applying the quantum regression theorem in different frames, in particular, the lab frame and the polaron frame. The latter was achieved by considering the polaron master equation (PME) approach. Upon closer inspection of our numerical analysis, we have found a parameter error as explained below that affects the results obtained within the PME approach. We stress that the results do not affect the majority and the main message of the Letter, namely that the QRT overestimates the phonon influence on the indistinguishability. Nonetheless, the corrected results give rise to a number of additional insights regarding the PME approach that we would like to present in the following.

Concerning Fig. 2(c) of our original Letter, the numerically exact results and the ones obtained by using the QRT in the lab frame were calculated for a quantum dot (QD) with an electron confinement radius of $a_e = 3\,\mathrm{nm}$ (as defined in Tab. 1 in the supplemental material). In contrast, the PME results were erroneously calculated for $a_e = 4.175\,\mathrm{nm}$, which prohibits a meaningful comparison of the different methods. In Fig. 1, the corresponding PME results for a 3 nm QD are shown (blue dotted line).

As was stated in the original Letter, both the QRT applied in the lab frame and in the polaron frame systematically overestimate the phonon influence on the indistinguishability. In contrast to the previous comparison, though, quite unexpectedly the correct PME results basically coincide with the QRT results (cf., Fig. 1). Therefore, applying the QRT in the polaron frame does not improve the accuracy of the indistinguishability. This new insight calls for a more detailed explanation, which we would like to provide in the following in two subsequent steps: the comparison of numerically exact and PME results concerning single-time observables and then a discussion of the two-time correlation function $G^{(1)}(t,\tau) := \langle \sigma_X^+(t+\tau)\sigma_X\rangle$, which enters the definitions of both the QD emission spectrum and the indistinguishability $\mathcal{I}$.

In Fig. 2 the dynamics of the exciton occupation after resonant π-pulse excitation is shown. The numerically exact results are compared with the PME approach for two different phonon scalings $\lambda = 1$ and $\lambda = 10$. In the PME community, two different ways to account for the radiative decay by a phenomenological Lindblad term are

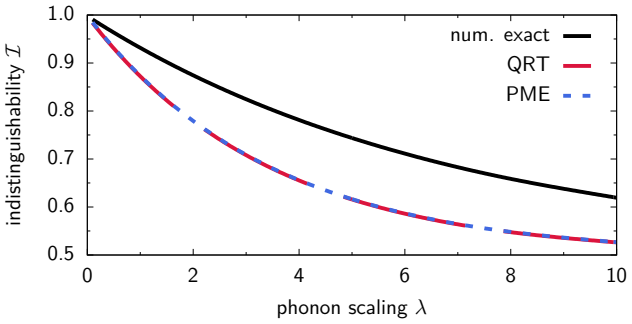

FIG. 1. The indistinguishability as a function of the phonon scaling parameter λ at 4 K, calculated with the numerically exact path-integral method (num. exact), by using the QRT in the lab frame (QRT), and by applying the QRT in the polaron transformed frame within the PME approach (PME).

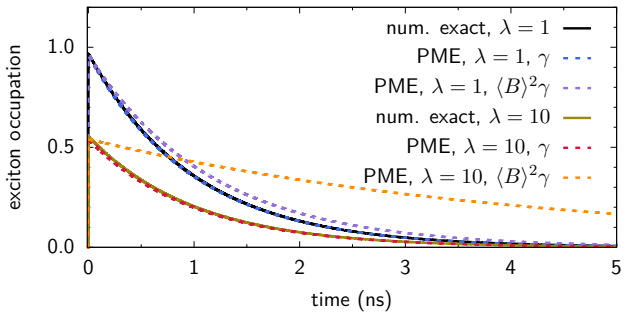

FIG. 2. The QD exciton dynamics at $T = 4\,\mathrm{K}$ after a Gaussian π-pulse of length $\tau_{\mathrm{fwhm}} = 3\,\mathrm{ps}$ centered around $t_0 = 0$. Numerically exact results are compared with PME results that either use a radiative decay rate of γ or $\langle B\rangle^2\gamma$. The cases of two different phonon scalings λ are shown.

being used: either the corresponding rate is scaled by a factor $\langle B\rangle^2$ (as done in, e.g., Ref. [85] of our Letter) or not (as done in, e.g., Ref. [87] of our Letter), where $\langle B\rangle$ is the phonon Franck-Condon factor as given in Eq. (15) in the supplemental material of our Letter. In the calculations shown in our Letter, we had scaled the radiative decay rate by the factor $\langle B\rangle^2$.

Now, we show results for the exciton occupation obtained by both versions in Fig. 2. It becomes clear that the PME results without the additional factor $\langle B\rangle^2$ agree with the numerically exact path-integral results for both phonon scalings λ. Therefore, both methods take into account the phonon influence equally accurately concerning (single-time) expectation values. Since both the QRT

applied in the lab frame (labeled QRT in Fig. 1) and in the polaron frame (labeled PME in Fig. 1) introduce the same approximation to the method, this finding gives a first hint at the agreement between the two-time results obtained in the two frames.

Returning to Fig. 2, taking into account a rate $\langle B\rangle^2\gamma$ leads to results far off the path-integral calculations with an increasing difference for increasing phonon scaling λ. The underlying assumption that the radiative decay of the QD into a spectrally flat electromagnetic field environment is not affected by the phonon environment has recently been confirmed by taking into account both environements microscopically within the numerically exact algorithm ACE [M. Cygorek *et. al.*, arXiv:2101.01653 (2021)]. Therefore, we continue here without using the factor $\langle B\rangle^2$. (Note that the PME results in Fig. 1 are already calculated without $\langle B\rangle^2$. This different scaling, though, has only a marginal influence on the corresponding results for our parameters. The different QD size a_e is responsible for the larger contribution to the change of the results.)

In Fig. 3, which corresponds to Fig. 1 in the supplemental material of our Letter, we show an emission spectrum obtained within the PME formalism without the factor $\langle B\rangle^2$ (blue dotted line). All other curves are the same as in the original figure. Strikingly, the PME spectrum is now almost a mirror image of the spectrum obtained by applying the QRT in the lab frame (red dashed line) similar to what was found earlier by a perturbative approach (cf., Ref. [26] of our Letter). Since the emission spectrum is essentially the Fourier transform of the two-time correlation function $G^{(1)}(t,\tau)$ [cf., Eq. (13) in the supplemental material of our Letter], this finding implies that using the QRT in the lab or in the polaron frame affects essentially only the sign of the imaginary part of $G^{(1)}(t,\tau)$. We stress that there is a sizable quantitative difference between the spectra resulting from the numerically exact and the PME approaches. This difference arises because the QRT applied in the polaron frame is overestimating the phonon influence on the correlation function $G^{(1)}(t,\tau)$.

With the conclusions drawn from Figs. 2 and 3, we can now explain, why the QRT applied in the lab and in the polaron frame agree concerning the indistinguishability $\mathcal{I}$ in Fig. 1. The indistinguishability is based upon the Hong-Ou-Mandel correlation function

$$G^{(2)}_{\mathrm{HOM}}(t,\tau) := \frac{1}{2}\big[\langle\sigma_X^\dagger(t)\sigma_X(t)\rangle\langle\sigma_X^\dagger(t+\tau)\sigma_X(t+\tau)\rangle - \big|\langle\sigma_X^\dagger(t+\tau)\sigma_X(t)\rangle\big|^2 + G^{(2)}(t,\tau)\big] \quad (1)$$

[cf., Eqs. (3) and (4) in our Letter]. We now look at each term of this expression and compare their derivation within the different methods. The factors in the first term are both (single-time) expectation values of the exciton occupation. Fig. 2 gives a compelling argument that the

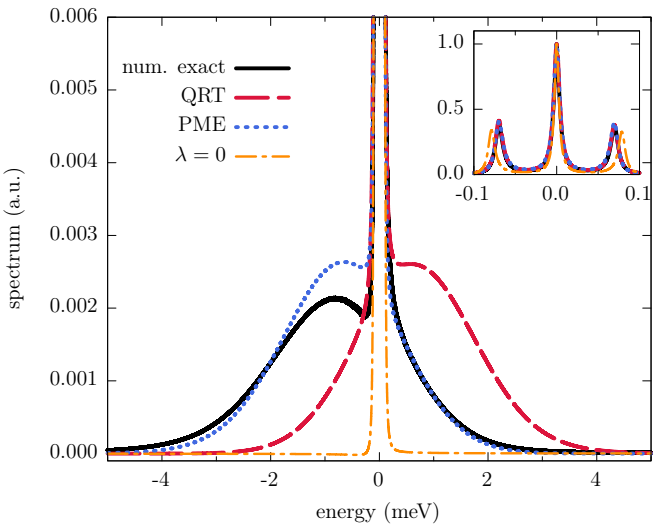

FIG. 3. The QD emission spectrum calculated for a constantly driven QD with $\hbar f_{\mathrm{p}}(t) = 0.079\,\mathrm{meV}$ and a radiative decay rate of $\gamma = 0.01\,\mathrm{ps}^{-1}$ at $T = 10\,\mathrm{K}$. The numerically exact result (num. exact) is compared with results obtained using the quantum regression theorem in the lab frame (QRT) and in the polaron frame (PME). In the latter, an unscaled radiative decay rate γ is used instead of a factor $\langle B\rangle^2\gamma$ as in the original plot (Fig. 1 in the supplemental material of our Letter). As a reference, the phonon-free case $\lambda = 0$ is also shown. The inset depicts the same data on a different scale, where the Mollow triplet becomes visible.

PME approach agrees well with the path-integral method regarding the exciton occupation for the parameters concerned. The last term is the second-order two-time correlation function $G^{(2)}(t,\tau)$, upon which the single-photon purity $\mathcal{P}$ is based. In our Letter, we found that the QRT introduces basically no error to this quantity compared with the numerically exact evaluation of the two-time function. The second term $\big|\langle\sigma_X^\dagger(t+\tau)\sigma_X(t)\rangle\big|^2$ is the absolute square of the first-order correlation function $G^{(1)}(t,\tau)$. Fig. 3 implies that the QRT and PME results differ basically only by the sign of the imaginary part of this correlation function, which does not affect the absolute square. Thus, we find that for all three terms there is no difference between the QRT and the PME. This is the reason why the QRT and PME results of the indistinguishability $\mathcal{I}$ are in such good agreement in Fig. 1. However, the large difference between the numerically exact results and the QRT approximation remains. It stems from the already noticed quantitative difference in the $G^{(1)}(t,\tau)$ function as observed earlier in the spectra. This implies that the only error resulting in a reduced indistinguishability is caused solely by the application of the QRT, regardless of the frame it is used in.

Therefore, our correction sheds new light on the PME formalism: For the considered parameters, the PME re-

sults concerning (single-time) expectation values match the numerically exact path-integral calculations well. Nonetheless, a large difference is found regarding the indistinguishability, which is based upon two-time correlation functions, the highest relative error being 18 % in the parameter space under scrutiny. Finally, the impact of the application of the QRT on the indistinguishability is independent of the frame: Applying the QRT in the polaron frame does not yield an improvement of the prediction of the indistinguishability.

Publication 2

Emission-frequency separated high quality single-photon sources enabled by phonons.

M. Cosacchi, F. Ungar, M. Cygorek, A. Vagov, V. M. Axt.

Phys. Rev. Lett. **123**, 017403 (2019).

DOI: 10.1103/PhysRevLett.123.017403

Author contributions

The author had the original idea to explain the mechanism that leads to phonon-enhanced single-photon purities. He has designed the concept of this study, in particular, he has performed the data generation and analysis, has provided the interpretation of the results, and has written the first draft of the paper. He has moderated all discussions and revision requests of the draft, has organized the correspondence with the editor and referees, and has provided the first drafts of answers to the referees.

F. Ungar has discussed the results in detail with the author, thus assisting in the interpretation of the physical origin of the discussed effect and has contributed to designing the figures. He has contributed to revisions of the draft and the answers to the referees and assisted in the correspondence with the editors and referees.

M. Cygorek and A. Vagov have cosupervised this work, in particular, they have participated in the discussion and interpretation of the results. They have contributed to the optimization of the presentation as well as revisions of the draft and the answers to the referees.

V. M. Axt has advised the author throughout his work as the main supervisor. He has obtained the funding for this work and has participated in the discussion and interpretation of the results. He has contributed to the optimization of the presentation as well as revisions of the draft and the answers to the referees.

Emission-Frequency Separated High Quality Single-Photon Sources Enabled by Phonons

M. Cosacchi,[1] F. Ungar,[1] M. Cygorek,[2] A. Vagov,[1,3] and V. M. Axt[1]
[1]Theoretische Physik III, Universität Bayreuth, 95440 Bayreuth, Germany
[2]Department of Physics, University of Ottawa, Ottawa, Ontario, Canada K1N 6N5
[3]ITMO University, St. Petersburg, 197101, Russia

(Received 19 February 2019; published 3 July 2019)

We demonstrate theoretically that the single-photon purity of photons emitted from a quantum dot exciton prepared by phonon-assisted off-resonant excitation can be significantly higher in a wide range of parameters than that obtained by resonant preparation for otherwise identical conditions. Despite the off-resonant excitation, the brightness stays on a high level. These surprising findings exploit the fact that the phonon-assisted preparation is a two-step process where phonons first lead to a relaxation between laser-dressed states while high exciton occupations are reached only with a delay to the laser pulse maximum by adiabatically undressing the dot states. Due to this delay, possible subsequent processes, in particular multiphoton excitations, appear at a time when the laser pulse is almost gone. The resulting suppression of reexcitation processes increases the single-photon purity. Due to the spectral separation of the signal photons from the laser frequencies this enables the emission of high quality single photons not disturbed by a laser background while taking advantage of the robustness of the phonon assisted scheme.

DOI: 10.1103/PhysRevLett.123.017403

On-demand single-photon sources continue to gain attention as key building blocks in quantum technological applications, ranging from novel metrology over quantum communication to quantum computing. Semiconductor quantum dots (QDs) have proven to be suitable single-photon emitters [1–8] that, due to their high compatibility with existing semiconductor technology, are promising candidates for device applications. In contrast to atomic systems, these nanoscale structures are prone to the influence of the surrounding solid state crystal matrix. Longitudinal acoustic (LA) phonons are the main source of decoherence of excitons in semiconductor QDs even at cryogenic temperatures of a few kelvin [9–13]. Nevertheless, phonon-assisted off-resonant QD excitations have been shown to provide a robust alternative to resonant exciton preparation schemes [14–18]. In this Letter, we demonstrate theoretically that, quite unexpectedly, the coupling to LA phonons combined with off-resonant driving can be extremely beneficial for a single-photon source based on a QD-cavity system, allowing for the generation of high-quality single-photons that are easily detectable due to their spectral separation from the laser pulses used for the excitation of the QD.

Placing a QD in a cavity strongly enhances the photon emission by enlarging the effective dot-cavity coupling and by setting a preferable emission axis. When exciting the QD exciton resonantly, the frequencies of the excitation and the signal are identical—separating the two is a formidable experimental challenge. In fact, spectral separability is achievable, e.g., by wetting layer excitation or by exciting the biexciton via the two-photon resonance and subsequently exploiting the biexciton-exciton cascade [8,19]. But while the former introduces a time jitter that reduces the on-demand character of the photon source, the latter is sensitive to small fluctuations of excitation parameters such as the laser energy and the pulse area. Both problems are overcome by an off-resonant excitation of the quantum dot, which is thus extremely advantageous. Indeed, it has recently been shown that the robustness of off-resonant excitation schemes paves the way to excite two spatially separated QDs with different transition energies simultaneously with the same laser pulse, which is a milestone towards the scalability of complex quantum networks [20].

The quality of a QD-cavity system as an on-demand single-photon source is typically quantified by several key figures of merit, such as the single-photon purity $\mathcal{P}$ and the brightness $\mathcal{B}$. While the former measures whether indeed a single photon is emitted by the source, the latter characterizes its total photon yield [5]. When $\mathcal{P} = \mathcal{B} = 1$, the source emits a single photon with a probability of unity at every excitation pulse via the cavity. The single-photon purity (SPP) can be extracted from a Hanbury Brown–Twiss coincidence experiment [3,7,8,21–24], which gives a conditional probability to detect a second photon when a first one has already been detected. Suppressing this probability is possible, e.g., by parametric down-conversion, which enhances the SPP, albeit at the cost of a severely reduced brightness of the photon source [25]. Maximizing both SPP and brightness is of utmost importance to create efficient single-photon emitters.

Simultaneously large $\mathcal{P}$ and $\mathcal{B}$ in a QD-cavity system can be achieved by exciting the dot resonantly by ultrashort

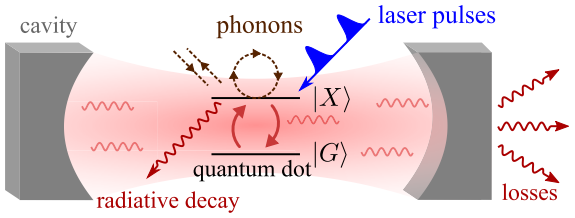

FIG. 1. Sketch of the system under consideration. A two-level QD with a ground state $|G\rangle$ and an exciton state $|X\rangle$ is coupled to a lossy single-mode microcavity. The $|G\rangle \rightarrow |X\rangle$ transition is driven by external laser pulses and the exciton state is coupled to LA phonons in a pure-dephasing manner. Finally, the dot can decay radiatively.

laser pulses [3,4,7]. However, shortening the pulse duration is equivalent to widening it spectrally. The detrimental influence of exciting higher-lying states, especially the biexciton state of the QD by short pulses is discussed in Ref. [26]. In view of the various advantages of phonon-assisted off-resonant excitations listed above, the question arises how photonic characteristics such as SPP and brightness perform under off-resonant schemes. In short, we want to explore whether all of the advantages of phonon-assisted off-resonant schemes come at the cost of severely reduced photonic properties.

It is expected that driving a QD off-resonantly is much less efficient. For longer and stronger pulses the resulting quantum state of a QD-cavity system contains an admixture of multiphoton states, which reduces the SPP. Phonon-induced dephasing is expected to degrade the quantum state even further. But paradoxically quite the opposite can take place: a combination of off-resonant driving with the phonon-induced relaxation between laser-dressed QD states leads eventually to high exciton occupations in a subsequent adiabatic undressing process [27]. In this Letter, we demonstrate that the delay of the exciton creation caused by the undressing suppresses the probability for multiphoton generation. Therefore, comparing off-resonant and resonant excitation with otherwise same conditions may, quite unexpectedly, yield enhanced SPPs in the off-resonant case. The best values predicted in this Letter are even comparable to the best values obtained so far within resonant schemes addressing the exciton.

We model the QD-cavity system as a laser-driven two-level system with a ground state $|G\rangle$ and an excited state $|X\rangle$, $H_{\mathrm{DL}} = -\hbar\Delta\omega_{\mathrm{LX}}|X\rangle\langle X| - (\hbar/2)f(t)(|X\rangle\langle G| + |G\rangle\langle X|)$, coupled to a single-mode microcavity (cf., Fig. 1), $H_{\mathrm{C}} = \hbar\Delta\omega_{\mathrm{CL}}a^\dagger a + \hbar g(a^\dagger|G\rangle\langle X| + a|X\rangle\langle G|)$, which is on resonance with the QD exciton. Here, $\Delta\omega_{\mathrm{LX}}$ and $\Delta\omega_{\mathrm{CL}}$ are the laser-exciton and cavity-laser detuning, respectively, and a is the photon annihilation operator in the cavity, which is coupled to the dot by the coupling constant g. A train of Gaussian pulses is assumed represented by the laser envelope function $f(t)$. The excitation can leave the system either via radiative decay or cavity losses modeled by Lindblad rates γ and κ, respectively. Finally, the exciton is coupled to a continuum of LA phonons in a pure-dephasing manner [28], $H_{\mathrm{Ph}} = \hbar\sum_{\mathbf{q}}\omega_{\mathbf{q}}b_{\mathbf{q}}^\dagger b_{\mathbf{q}} + \hbar\sum_{\mathbf{q}}(\gamma_{\mathbf{q}}^{\mathrm{X}}b_{\mathbf{q}}^\dagger + \gamma_{\mathbf{q}}^{\mathrm{X}*}b_{\mathbf{q}})|X\rangle\langle X|$. $b_{\mathbf{q}}$ annihilates a phonon in the mode $\mathbf{q}$ coupled to the dot by the coupling constant $\gamma_{\mathbf{q}}^{\mathrm{X}}$. Full details of the model and of our numerical approach are given in the Supplemental Material [29]. It is worthwhile to note that we use path-integral methods for our simulations that allow us to perform all simulations without approximation to the model [29,36–38].

For the calculations, standard GaAs parameters are used [39] for a QD of 6 nm diameter (for details on the phonon coupling consider the Supplemental Material [29]). If not stated otherwise, the excitation pulse full width at half maximum is set to 7 ps, the cavity mode is resonant with the QD transition, the dot-cavity coupling is $\hbar g = 50\ \mu$eV, the radiative decay rate is $\hbar\gamma = 20\ \mu$eV, and the cavity loss rate is $\hbar\kappa = 50\ \mu$eV. This corresponds to a Purcell factor of $F_{\mathrm{P}} = g^2/(\gamma\kappa) = 2.5$. The initial phonon distribution is assumed to be thermal with a temperature of $T = 4.2$ K.

The main target quantities of interest in this Letter, the SPP $\mathcal{P}$ and the brightness $\mathcal{B}$, are obtained from path-integral simulations of the two-time photonic correlation function $G^{(2)}(t,\tau) = \langle a^\dagger(t)a^\dagger(t+\tau)a(t+\tau)a(t)\rangle$ and the time dependent photon occupation $\langle a^\dagger a\rangle(t)$, respectively. In order to express the SPP in terms of $G^{(2)}(t,\tau)$ one first needs to take the average over the first time argument t, i.e., $G^{(2)}(\tau) = \int_{-\infty}^{\infty} dt G^{(2)}(t,\tau)$, which yields a function with the delay time τ of the coincidence measurement as its single argument. The probability p of detecting a second photon during the same excitation pulse after a first one has already been emitted thus can be obtained by

$$p = \frac{\int_{-T_{\mathrm{Pulse}}/2}^{T_{\mathrm{Pulse}}/2} d\tau G^{(2)}(\tau)}{\int_{T_{\mathrm{Pulse}}/2}^{3T_{\mathrm{Pulse}}/2} d\tau G^{(2)}(\tau)}, \tag{1}$$

where T_{Pulse} is the separation of the pulses in the pulse train. The SPP is then defined as $\mathcal{P} = 1 - p$. Note that $-\infty < \mathcal{P} \leq 1$, where the lack of a lower bound is due to the possibility of bunching instead of antibunching.

In this Letter, the brightness of the source is modeled as the integrated leakage of the average photon number during the duration of one pulse, i.e., $\mathcal{B} = \kappa\int_{-T_{\mathrm{Pulse}}/2}^{T_{\mathrm{Pulse}}/2} dt\langle a^\dagger a\rangle(t)$. Due to the definition, this quantity formally ranges in $0 \leq \mathcal{B} < \infty$ without an upper bound since in principal infinitely many photons can exist in a single electromagnetic field mode.

In Fig. 2(a) the brightness simulated without phonons is shown as a function of the detuning $\Delta\omega_{\mathrm{LX}}$ between the central laser frequency and the transition frequency connecting the ground and the exciton state of the QD as well as the pulse area Θ. An oscillatory behavior as a function of the pulse area with maxima at odd multiples of π is observed [cf., Fig. 2(a)]. This is a consequence of the well-known Rabi rotation of the exciton occupation since

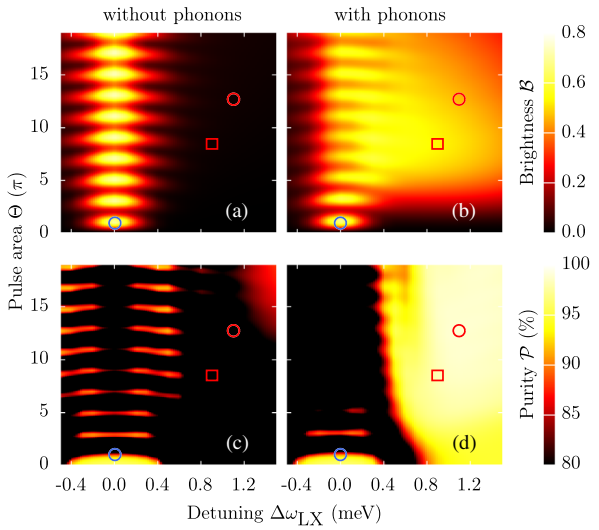

FIG. 2. Brightness $\mathcal{B}$ [panels (a) and (b)] and SPP $\mathcal{P}$ [panels (c) and (d)] as a function of the laser-exciton detuning $\Delta\omega_{LX}$ and the excitation pulse area Θ of a pulse in the pulse train. The left column (a), (c) is the result of a phonon-free calculation, the right column (b), (d) includes the coupling to a continuum of LA phonons. Blue circle: resonant π-pulse excitation. Red circle: maximal SPP (with phonons). Red square: optimal SPP and brightness for off-resonant excitation (with phonons).

the exciton feeds the cavity photons, which in turn are measured by the brightness. As a function of the detuning, the regions of high brightness are confined to a fairly small range around resonance. The inclusion of phonons drastically changes this picture [cf., Fig. 2(b)]. Through off-resonant excitation with detunings that can be bridged by the emission of LA phonons, a nonvaninshing brightness can be obtained in a previously dark region. Note that the asymmetry with respect to the sign of the detuning is due to the low temperature of $T = 4.2$ K considered here where phonon absorption is largely suppressed.

The SPP in the phonon-free case [cf., Fig. 2(c)] also displays Rabi rotational behavior but decreases with rising pulse area close to resonance, which is due to a reexcitation of the QD during the same laser pulse. This leads to the emission of more than one photon per pulse, thus diminishing the SPP. Although a SPP can always be calculated, one should be aware that it constitutes a physically meaningful quantity only for finite brightness. Therefore, the area of increased SPP in the upper right corner of Fig. 2(c) is of no physical relevance.

It is intuitively expected that the continuum of LA phonons reduces the quantum correlations of the system and thus the SPP by inducing a manifold of transitions between its quantum states. However, contrary to these expectations Fig. 2(d) reveals a huge systematic increase in $\mathcal{P}$ at $\Delta\omega_{LX} \gtrsim 0.5$ meV. Moreover, the maximum $\mathcal{P}_{max} = 98.8\%$ (red circle) is even larger than 90.7% obtained for the resonantly driven system (blue circle). Combined with an appreciably large $\mathcal{B}$, this indicates a possibility to have a good quality single-photon source in the off-resonant excitation regime. Note that $\mathcal{B} = 0.46$ observed at the point of $\mathcal{P}_{max}$ [cf., red circle in Fig. 2(b)] is not much smaller than the maximal value of 0.67 achieved in the resonantly driven case [cf., blue circle in Fig. 2(b)]. It is also noteworthy that it is possible to obtain a significantly larger brightness at the cost of a slight decrease in the SSP. For example, if we choose a trade-off by maximizing the sum of the squares of the two figures of merit in the off-resonant regime, we obtain $\mathcal{B} = 0.53$ and $\mathcal{P} = 98.1\%$ (red square). This value for $\mathcal{P}$ is close to typical experimental values obtained for resonant excitation of the quantum dot exciton (98.8% [4], 99.1% [7]) even though the pulse lengths in Refs. [4,7] have been slightly shorter [40].

To explain the mechanism behind this observation, one needs to consider the dynamics of the QD-cavity states. In Fig. 3, the time dependent occupations in the resonant and the off-resonant case (cf., the blue and red circles in Fig. 2, respectively) are compared. The considered states are product states between the QD states and a photon state with photon number n. After resonant π-pulse excitation [cf., Fig. 3(a)], the exciton state $|X, 0\rangle$ without photons is occupied (blue curve). The cavity coupling rotates the dot back to its ground state and produces one photon in the cavity (orange curve). Because the driving is still nonzero at this point, the dot is reexcited to produce an occupation of the state $|X, 1\rangle$ (green curve), which is shown in the inset of Fig. 3(a). Finally, the cavity coupling leads to an occupation of the ground state with two photons $|G, 2\rangle$ (red curve), such that the SPP is diminished.

In contrast to the π-pulse induced rotation of the Bloch vector, the off-resonant excitation scheme exploits an effect called adiabatic undressing [27]. Switching on the laser transforms the dot states to a new energy eigenbasis commonly known as laser-dressed states, the gap between which can be bridged by LA phonons with typical energies of a few meV. At low temperatures, the lower dressed state becomes occupied via phonon emission. However, the phonon-induced relaxation is only efficient when both dressed states have roughly equal exciton components. Thus, the exciton state exhibits typically occupations of the order of 50% after the relaxation is completed [27]. When the laser is turned off adiabatically, the lower dressed state is subsequently transformed to the exciton state in the original basis provided the detuning is positive (otherwise the ground state is reached [27]). This adiabatic undressing of the dot states therefore boosts the exciton occupation only at the end of the pulse [cf., the blue curve in Fig. 3(b)]. This in turn means that during the phase of phonon relaxation no photon can be put into the cavity efficiently [cf., the orange curve in Fig. 3(b)]. When finally the adiabatic undressing-induced exciton boost occurs, the occupation of $|G, 1\rangle$ follows [cf., Fig. 3(b)]. Since the excitation pulse is basically gone by then, the reexcitation of the QD is strongly

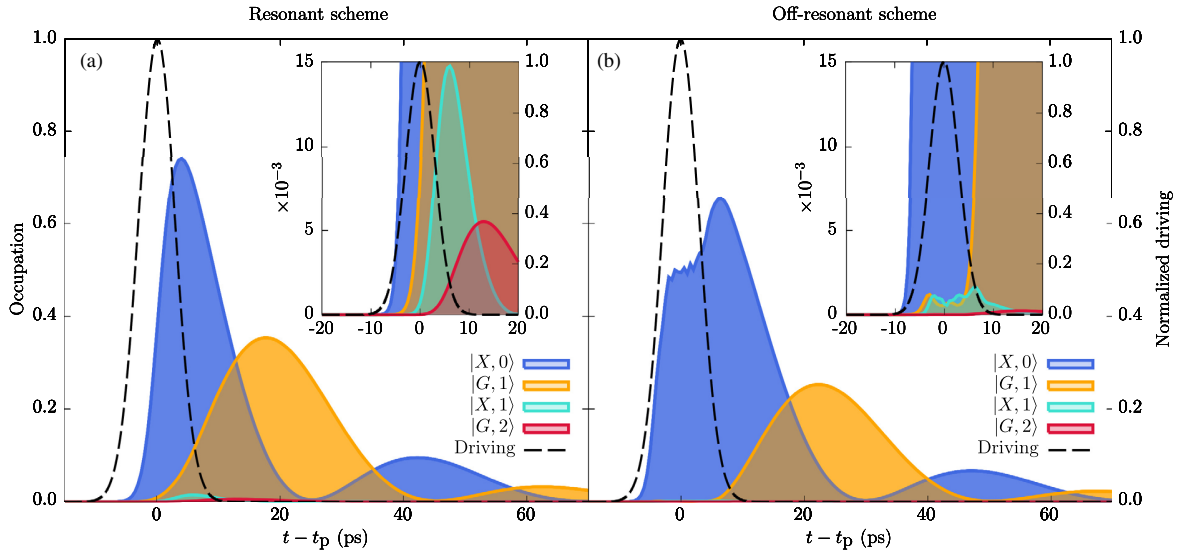

FIG. 3. Time-dependent occupations: (a) after resonant π-pulse excitation (cf., blue circle in Fig. 2) and (b) in the off-resonant phonon-assisted case (cf., red circle in Fig. 2). The occupations of the states $|X,0\rangle$, $|G,1\rangle$, $|X,1\rangle$, and $|G,2\rangle$ are shown as colored filled curves. The Gaussian envelope of the laser driving pulse normalized to its maximum value centered at t_p is shown as a black dashed line. The insets show the same curves, respectively, on an enlarged scale for the occupations.

suppressed (green curve), such that effectively no second photon can be put into the cavity (red curve). This implies a far higher SPP than in the resonant counterpart, as is observed in Fig. 2(d). In summary, the delay of the exciton occupation caused by the two-step procedure of first relaxing to a dressed state via phonon emission and then reaching the exciton by adiabatic undressing is responsible for the enhancement of the SPP.

To quantify the robustness of the phonon-induced SPP enhancement against variations of other system parameters,

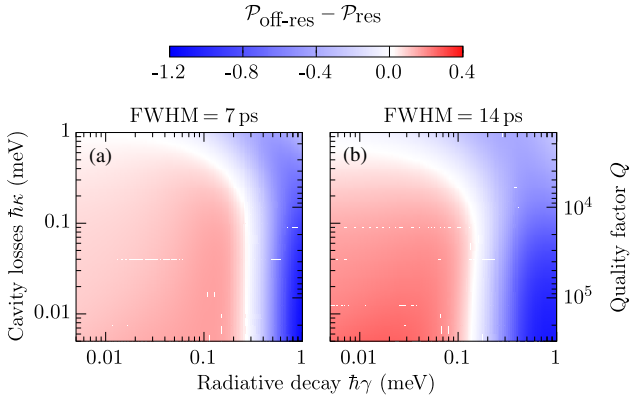

FIG. 4. The difference between the SPP after off-resonant phonon-assisted excitation $\mathcal{P}_{\text{off-res}}$ and after resonant π-pulse rotation $\mathcal{P}_{\text{res}}$ is shown for two different pulse lengths (FWHM), namely: (a) 7 ps and (b) 14 ps, as a function of radiative decay $\hbar\gamma$ and cavity losses $\hbar\kappa$. The cavity quality factor $Q = \omega_c/\kappa$ is obtained via the cavity losses assuming a cavity single-mode energy of $\hbar\omega_c = 1.5$ eV. The pulse area is set to 12.75π and $\Delta\omega_{LX} = 1.1$ meV.

the difference between the SPP after off-resonant excitation and after the resonant one is shown as a function of the radiative decay γ and the cavity loss rate κ in Fig. 4. A positive value (reddish shade) indicates a set of parameters where the SPP is enhanced for off-resonant excitation. We find such an enhancement for a wide parameter regime in κ and γ that is experimentally well accessible. Also, changing the pulse length from 7 ps in Fig. 4(a) to 14 ps in Fig. 4(b) does not change the phonon-induced SPP enhancement qualitatively. The reason why the SPP for off-resonant excitation falls below the resonant one in the bad cavity limit and/or in the limit of high radiative losses is that relaxation processes limit the time available for the adiabatic undressing which eventually becomes incomplete.

In conclusion, we have presented a seemingly paradoxical scheme for the phonon-assisted operation of a QD-cavity system as a single-photon source, where the excitation is spectrally separated from the generated photons. Two factors that would separately lead to a quality degradation—off-resonant driving and dot-phonon coupling—in combination result in a huge boost in critical characteristics of a single-photon source. We have demonstrated that the achievable single-photon purity can be noticeably higher than for resonant excitation while the brightness is still at an acceptable level. The physical mechanism of this enhancement—the adiabatic undressing—is realized in a wide interval of physically accessible parameters.

M. Cy. thanks the Alexander-von-Humboldt foundation for support through a Feodor Lynen fellowship. A. V. acknowledges the support from the Russian Science Foundation under the Project No. 18-12-00429, which

was used to study dynamical processes nonlocal in time by the path integral approach. This work was also funded by the Deutsche Forschungsgemeinschaft (DFG, German Research Foundation)—Project No. 419036043.

[1] P. Michler, A. Kiraz, C. Becher, W. V. Schoenfeld, P. M. Petroff, L. Zhang, E. Hu, and A. Imamoglu, Science **290**, 2282 (2000).
[2] C. Santori, M. Pelton, G. Solomon, Y. Dale, and Y. Yamamoto, Phys. Rev. Lett. **86**, 1502 (2001).
[3] C. Santori, D. Fattal, J. Vuckovic, G. S. Solomon, and Y. Yamamoto, Nature (London) **419**, 594 (2002).
[4] Y.-M. He, Y. He, Y.-J. Wei, D. Wu, M. Atatüre, C. Schneider, S. Höfling, M. Kamp, C.-Y. Lu, and J.-W. Pan, Nat. Nanotechnol. **8**, 213 (2013).
[5] N. Somaschi, V. Giesz, L. De Santis, J. C. Loredo, M. P. Almeida, G. Hornecker, S. L. Portalupi, T. Grange, C. Antón, J. Demory, C. Gómez, I. Sagnes, N. D. Lanzillotti-Kimura, A. Lemaítre, A. Auffeves, A. G. White, L. Lanco, and P. Senellart, Nat. Photonics **10**, 340 (2016).
[6] Y.-J. Wei, Y.-M. He, M.-C. Chen, Y.-N. Hu, Y. He, D. Wu, C. Schneider, M. Kamp, S. Höfling, C.-Y. Lu, and J.-W. Pan, Nano Lett. **14**, 6515 (2014).
[7] X. Ding, Y. He, Z.-C. Duan, N. Gregersen, M.-C. Chen, S. Unsleber, S. Maier, C. Schneider, M. Kamp, S. Höfling, C.-Y. Lu, and J.-W. Pan, Phys. Rev. Lett. **116**, 020401 (2016).
[8] L. Schweickert, K. D. Jöns, K. D. Zeuner, S. F. Covre da Silva, H. Huang, T. Lettner, M. Reindl, J. Zichi, R. Trotta, A. Rastelli, and V. Zwiller, Appl. Phys. Lett. **112**, 093106 (2018).
[9] J. Förstner, C. Weber, J. Danckwerts, and A. Knorr, Phys. Rev. Lett. **91**, 127401 (2003).
[10] A. Vagov, M. D. Croitoru, V. M. Axt, T. Kuhn, and F. M. Peeters, Phys. Rev. Lett. **98**, 227403 (2007).
[11] A. J. Ramsay, A. V. Gopal, E. M. Gauger, A. Nazir, B. W. Lovett, A. M. Fox, and M. S. Skolnick, Phys. Rev. Lett. **104**, 017402 (2010).
[12] P. Kaer, T. R. Nielsen, P. Lodahl, A.-P. Jauho, and J. Mørk, Phys. Rev. Lett. **104**, 157401 (2010).
[13] D. E. Reiter, Phys. Rev. B **95**, 125308 (2017).
[14] M. Glässl, A. M. Barth, and V. M. Axt, Phys. Rev. Lett. **110**, 147401 (2013).
[15] P.-L. Ardelt, L. Hanschke, K. A. Fischer, K. Müller, A. Kleinkauf, M. Koller, A. Bechtold, T. Simmet, J. Wierzbowski, H. Riedl, G. Abstreiter, and J. J. Finley, Phys. Rev. B **90**, 241404 (2014).
[16] D. E. Reiter, T. Kuhn, M. Glässl, and V. M. Axt, J. Phys. Condens. Matter **26**, 423203 (2014).
[17] S. Bounouar, M. Müller, A. M. Barth, M. Glässl, V. M. Axt, and P. Michler, Phys. Rev. B **91**, 161302 (2015).
[18] J. H. Quilter, A. J. Brash, F. Liu, M. Glässl, A. M. Barth, V. M. Axt, A. J. Ramsay, M. S. Skolnick, and A. M. Fox, Phys. Rev. Lett. **114**, 137401 (2015).
[19] L. Hanschke, K. A. Fischer, S. Appel, D. Lukin, J. Wierzbowski, S. Sun, R. Trivedi, J. Vučković, J. J. Finley, and K. Müller, npj Quantum Inf. **4**, 43 (2018).
[20] M. Reindl, K. D. Jns, D. Huber, C. Schimpf, Y. Huo, V. Zwiller, A. Rastelli, and R. Trotta, Nano Lett. **17**, 4090 (2017).
[21] R. Hanbury Brown and R. Q. Twiss, Nature (London) **178**, 1046 (1956).
[22] C. Bentham, D. Hallett, N. Prtljaga, B. Royall, D. Vaitiekus, R. J. Coles, E. Clarke, A. M. Fox, M. S. Skolnick, I. E. Itskevich, and L. R. Wilson, Appl. Phys. Lett. **109**, 161101 (2016).
[23] N. Prtljaga, C. Bentham, J. O'Hara, B. Royall, E. Clarke, L. R. Wilson, M. S. Skolnick, and A. M. Fox, Appl. Phys. Lett. **108**, 251101 (2016).
[24] M. Weiß, S. Kapfinger, T. Reichert, J. J. Finley, A. Wixforth, M. Kaniber, and H. J. Krenner, Appl. Phys. Lett. **109**, 033105 (2016).
[25] J.-W. Pan, Z.-B. Chen, C.-Y. Lu, H. Weinfurter, A. Zeilinger, and M. Żukowski, Rev. Mod. Phys. **84**, 777 (2012).
[26] C. Gustin and S. Hughes, Phys. Rev. B **98**, 045309 (2018).
[27] A. M. Barth, S. Lüker, A. Vagov, D. E. Reiter, T. Kuhn, and V. M. Axt, Phys. Rev. B **94**, 045306 (2016).
[28] B. Krummheuer, V. M. Axt, and T. Kuhn, Phys. Rev. B **65**, 195313 (2002).
[29] See Supplemental Material at http://link.aps.org/supplemental/10.1103/PhysRevLett.123.017403 for a complete definition of our model, in particular the phonon coupling, and the numerical procedure used. It includes Refs. [30–35] in addition to other references already cited in the main text.
[30] L. Besombes, K. Kheng, L. Marsal, and H. Mariette, Phys. Rev. B **63**, 155307 (2001).
[31] P. Borri, W. Langbein, S. Schneider, U. Woggon, R. L. Sellin, D. Ouyang, and D. Bimberg, Phys. Rev. Lett. **87**, 157401 (2001).
[32] A. Vagov, M. D. Croitoru, M. Glässl, V. M. Axt, and T. Kuhn, Phys. Rev. B **83**, 094303 (2011).
[33] N. Makri and D. E. Makarov, J. Chem. Phys. **102**, 4600 (1995).
[34] N. Makri and D. E. Makarov, J. Chem. Phys. **102**, 4611 (1995).
[35] D. P. S. McCutcheon, Phys. Rev. A **93**, 022119 (2016).
[36] A. M. Barth, A. Vagov, and V. M. Axt, Phys. Rev. B **94**, 125439 (2016).
[37] M. Cygorek, A. M. Barth, F. Ungar, A. Vagov, and V. M. Axt, Phys. Rev. B **96**, 201201(R) (2017).
[38] M. Cosacchi, M. Cygorek, F. Ungar, A. M. Barth, A. Vagov, and V. M. Axt, Phys. Rev. B **98**, 125302 (2018).
[39] B. Krummheuer, V. M. Axt, T. Kuhn, I. D'Amico, and F. Rossi, Phys. Rev. B **71**, 235329 (2005).
[40] Note that other system parameters in these experiments are also different from the ones used here, e.g., the Purcell factor reported in Ref. [7] is 6.3 compared with 2.5 in our case.

Supplement: Emission-frequency separated high quality single-photon sources enabled by phonons

M. Cosacchi,[1] F. Ungar,[1] M. Cygorek,[2] A. Vagov,[1,3] and V. M. Axt[1]

[1] *Theoretische Physik III, Universität Bayreuth, 95440 Bayreuth, Germany*
[2] *Department of Physics, University of Ottawa, Ottawa, Ontario, Canada K1N 6N5*
[3] *ITMO University, St. Petersburg, 197101, Russia*

MODEL AND NUMERICAL METHOD

In this supplement we specify in detail the model used in the main paper and outline the numerical procedure used for our simulations. We represent the quantum dot (QD)-cavity system by a Hamiltonian comprising three parts:

$$H = H_{\mathrm{DL}} + H_C + H_{\mathrm{Ph}}, \tag{1}$$

where H_{DL} describes the QD driven by an external laser, H_C accounts for the coupling of the QD to a quantized cavity mode, while H_{Ph} represent the interaction with a continuum of longitudinal acoustic (LA) phonons.

Within the usual dipole and rotating wave approximations, the dot-laser Hamiltonian takes the form

$$H_{\mathrm{DL}} = -\hbar\Delta\omega_{\mathrm{LX}}|X\rangle\langle X| - \frac{\hbar}{2}f(t)\left(|X\rangle\langle G| + |G\rangle\langle X|\right) \tag{2}$$

in a frame co-rotating with the laser frequency ω_{L}. Here, $|G\rangle$ denotes the QD ground state and $|X\rangle$ is the exciton state and a detuning between the laser and exciton frequency $\Delta\omega_{\mathrm{LX}} := \omega_{\mathrm{L}} - \omega_{\mathrm{X}}$ is introduced. $\mathbf{d}$ is the transition dipole and $\mathbf{E}(t)$ the laser field, such that $-\mathbf{d}\cdot\mathbf{E}(t) = -\hbar f(t)/2\,\exp\left(-i\omega_{\mathrm{L}}t\right)$, where $f(t)$ denotes the real envelope function of the exciting laser. $f(t)$ is taken to be a pulse train consisting of Gaussian functions, where each Gaussian has an area Θ and a pulse length measured by the full-width-at-half-maximum (FWHM). Every T_{Pulse} the maximum of a Gaussian hits the QD. The dot is coupled to a single-mode microcavity via

$$H_{\mathrm{C}} = \hbar\Delta\omega_{\mathrm{CL}}a^\dagger a + \hbar g\left(a^\dagger|G\rangle\langle X| + a|X\rangle\langle G|\right). \tag{3}$$

The single-mode photons of the cavity are created (annihilated) by the bosonic operator $a^\dagger$ (a) and are detuned by $\Delta\omega_{\mathrm{CL}} := \omega_{\mathrm{C}} - \omega_{\mathrm{L}}$ with respect to the laser frequency. The coupling strength between the QD and the microcavity is denoted by $\hbar g$. Furthermore, the pure dephasing-type coupling [1–3] between the QD and a continuum of longitudinal acoustic (LA) phonons is modeled as

$$H_{\mathrm{Ph}} = \hbar\sum_{\mathbf{q}}\omega_{\mathbf{q}}b^\dagger_{\mathbf{q}}b_{\mathbf{q}} + \hbar\sum_{\mathbf{q}}\left(\gamma^{\mathrm{X}}_{\mathbf{q}}b^\dagger_{\mathbf{q}} + \gamma^{\mathrm{X}*}_{\mathbf{q}}b_{\mathbf{q}}\right)|X\rangle\langle X|, \tag{4}$$

where the bosonic operator $b^\dagger_{\mathbf{q}}$ ($b_{\mathbf{q}}$) creates (destroys) phonons with frequency $\omega_{\mathbf{q}}$. $\gamma^{\mathrm{X}}_{\mathbf{q}}$ denotes the deformation-potential-type coupling constant between the exciton state and the $\mathbf{q}$-th bosonic mode, which is obtained as the difference between the electron-phonon and hole-phonon constants, $\gamma^{\mathrm{X}}_{\mathbf{q}} = \gamma^{\mathrm{e}}_{\mathbf{q}} - \gamma^{\mathrm{h}}_{\mathbf{q}}$. We consider bulk-phonon modes with linear dispersion, $\omega_{\mathbf{q}} = v_s|\mathbf{q}|$, with the sound velocity v_s. With these assumptions the coupling constants take on the form

$$\gamma^{\mathrm{e(h)}}_{\mathbf{q}} = \Psi^{\mathrm{e(h)}}(\mathbf{q})\frac{|\mathbf{q}|D_{\mathrm{e(h)}}}{\sqrt{2V\rho\hbar\omega_{\mathbf{q}}}}, \tag{5}$$

where ρ is the density of the material, V the sample volume, $D_{\mathrm{e(h)}}$ the deformation potential constant, and $\Psi^{\mathrm{e(h)}}(\mathbf{q})$ the form factor that is obtained as the Fourier transform of the absolute square of the confined carrier wave functions. The coupling constant enters the phonon spectral density

$$J(\omega) = \sum_{\mathbf{q}}\left|\gamma^{\mathrm{X}}_{\mathbf{q}}\right|^2\delta(\omega - \omega_{\mathbf{q}}), \tag{6}$$

which in turn determines the depth of the phonon-induced memory [4]. Assuming a spherical dot with harmonic confinement yields

$$J(\omega) = \frac{\omega^3}{4\pi^2\rho\hbar v_s^5}\left\{D_{\mathrm{e}}\exp\left(-\frac{\omega^2a_{\mathrm{e}}^2}{4v_s^2}\right) - D_{\mathrm{h}}\exp\left(-\frac{\omega^2a_{\mathrm{h}}^2}{4v_s^2}\right)\right\}^2, \tag{7}$$

where $a_{\mathrm{e(h)}}$ denotes the electron (hole) confinement length.

For the calculations in the main text, we use values that are typical for GaAs self-assembled QDs [5]: $D_{\mathrm{e}} = 7.0\,\mathrm{eV}$, $D_{\mathrm{h}} = -3.5\,\mathrm{eV}$, $\rho = 5370\,\mathrm{kg/m^3}$, $v_s = 5110\,\mathrm{m/s}$, $a_{\mathrm{e}}/a_{\mathrm{h}} = 1.15$. This leaves only the dot diameter as a free parameter in the shape of the electron confinement length, i.e., $6\,\mathrm{nm} = 2a_{\mathrm{e}}$, as quoted in the main text.

Finally, radiative decay of the QD exciton as well as cavity losses are included via Lindblad-type superoperators $\mathcal{L}_{|G\rangle\langle X|,\gamma}\bullet$ and $\mathcal{L}_{a,\kappa}\bullet$, respectively, with

$$\mathcal{L}_{O,\Gamma}\bullet = \Gamma\left(O\bullet O^\dagger - \frac{1}{2}\left\{\bullet, O^\dagger O\right\}_+\right). \tag{8}$$

Here, $\{\cdot,\cdot\}_+$ denotes the anti-commutator, O is a system operator, and Γ the decay rate of the associated loss process.

We solve the Liouville-von Neumann equation

$$\dot{\rho} = -\frac{i}{\hbar}\{H,\rho\}_- + \mathcal{L}\rho \tag{9}$$

with $H = H_{\mathrm{DL}} + H_C + H_{\mathrm{Ph}}$ and $\mathcal{L}\bullet = \mathcal{L}_{|G\rangle\langle X|,\gamma}\bullet + \mathcal{L}_{a,\kappa}\bullet$, where $\{\cdot,\cdot\}_-$ is the commutator. The density matrix ρ is assumed to initially factorize into a subsystem part corresponding to the dot-cavity system (DL+C) and a phonon part (Ph). The phonon part is initially taken to be a thermal distribution. We employ an iterative real-time path integral method [6, 7] to obtain the time-dependent reduced density matrix $\bar{\rho} = \mathrm{Tr}_{\mathrm{Ph}}[\rho]$. To the best of our knowledge this method is so far the only one where accounting for the influence of the infinitely many LA phonon modes has been realized in a numerically complete way, i.e., without any further approximations to the model described above, since all phonon contributions can be integrated out analytically. Furthermore, recent developments within this formalism allow for the consistent and natural inclusion of Lindblad-type losses [8] and the consideration of more subsystem levels beyond the few-level limit due to an exact reformulation of the iterative scheme [9]. In fact, the reformulation presented in the supplement of Ref. [9] reduces the numerical demand in our present application by many orders of magnitude without which the simulations presented in the main text would have been impossible. Finally, the two-time photonic correlation function $G^{(2)}(t,\tau) = \langle a^\dagger(t)a^\dagger(t+\tau)a(t+\tau)a(t)\rangle$ necessary for the calculation of the single-photon purity is obtained following a numerically complete algorithm that has been proposed recently [10]. In particular, this algorithm avoids the quantum regression theorem, which is valid only when all bath interactions are Markovian [11]. Indeed, it is known that the coupling to LA phonons induces a memory of several picoseconds [4] and thus a Markovian treatment of the QD-phonon interaction would not be adequate.

[1] L. Besombes, K. Kheng, L. Marsal, and H. Mariette, Phys. Rev. B **63**, 155307 (2001).
[2] P. Borri, W. Langbein, S. Schneider, U. Woggon, R. L. Sellin, D. Ouyang, and D. Bimberg, Phys. Rev. Lett. **87**, 157401 (2001).
[3] B. Krummheuer, V. M. Axt, and T. Kuhn, Phys. Rev. B **65**, 195313 (2002).
[4] A. Vagov, M. D. Croitoru, M. Glässl, V. M. Axt, and T. Kuhn, Phys. Rev. B **83**, 094303 (2011).
[5] B. Krummheuer, V. M. Axt, T. Kuhn, I. D'Amico, and F. Rossi, Phys. Rev. B **71**, 235329 (2005).
[6] N. Makri and D. E. Makarov, The J. Chem. Phys. **102**, 4600 (1995).
[7] N. Makri and D. E. Makarov, The J. Chem. Phys. **102**, 4611 (1995).
[8] A. M. Barth, A. Vagov, and V. M. Axt, Phys. Rev. B **94**, 125439 (2016).
[9] M. Cygorek, A. M. Barth, F. Ungar, A. Vagov, and V. M. Axt, Phys. Rev. B **96**, 201201(R) (2017).
[10] M. Cosacchi, M. Cygorek, F. Ungar, A. M. Barth, A. Vagov, and V. M. Axt, Phys. Rev. B **98**, 125302 (2018).
[11] D. P. S. McCutcheon, Phys. Rev. A **93**, 022119 (2016).

Publication 3

Deterministic photon storage and readout in a semimagnetic quantum dot–cavity system doped with a single Mn ion

M. Cosacchi, T. Seidelmann, A. Mielnik-Pyszczorski, M. Neumann, T. K. Bracht, M. Cygorek, A. Vagov, D. E. Reiter, V. M. Axt.

arXiv:2110.07576 (2021), under review at *Advanced Quantum Technologies*.

arXiv:2110.07576 (2021)

Author contributions

The author has designed the concept of this study, in particular, he has performed the data generation and analysis, has provided the interpretation of the results, and has written the first draft of the paper. He has moderated all discussions and revision requests of the draft and has organized the correspondence with the editor.

T. Seidelmann has discussed the results in detail with the author, thus contributing to the interpretation. In particular, he has proposed the analytic approximation leading to Eq. (19). He has contributed to revisions of the draft.

A. Mielnik-Pyszczorski has discussed the results in detail with the author, thus contributing to the interpretation. He has provided an extensive literature search for and the first draft of the introduction. He has contributed to revisions of the draft.

M. Neumann has provided detailed discussions concerning the background of the proposed scheme, in particular, the preparation of the dark state. Her valuable input on the AC-Stark pulse parameter space resulted in the considered set of values. She has contributed to revisions of the draft.

T. K. Bracht has assisted in the convergence tests by providing reference calculations with the correlation expansion method. He has provided details concerning the preparation of the dark state. He has contributed to revisions of the draft.

M. Cygorek, A. Vagov, and D. E. Reiter have cosupervised this work, in particular, they have participated in the discussion and interpretation of the results. They have contributed to revisions of the draft and optimized the presentation.

V. M. Axt has advised the author throughout his work as the main supervisor. He has obtained the funding for this work and has participated in the discussion and interpretation of the results and has contributed to revisions of the draft and the optimization of the presentation.

Deterministic photon storage and readout in a semimagnetic quantum dot–cavity system doped with a single Mn ion

Michael Cosacchi*,[1] Tim Seidelmann,[1] Adam Mielnik-Pyszczorski,[1,2] Miriam Neumann,[3] Thomas K. Bracht,[3] Moritz Cygorek,[4] Alexei Vagov,[1,5] Doris E. Reiter,[3] and Vollrath M. Axt[1]

[1] *Lehrstuhl für Theoretische Physik III, Universität Bayreuth, Universitätsstraße 30, 95447 Bayreuth, Germany**

[2] *Department of Theoretical Physics, Wrocław University of Science and Technology, 50-370 Wrocław, Poland*

[3] *Institut für Festkörpertheorie, Universität Münster, Wilhelm-Klemm-Straße 10, 48149 Münster, Germany*

[4] *Institute of Photonics and Quantum Sciences, Heriot-Watt University, Edinburgh EH14 4AS, United Kingdom*

[5] *ITMO University, Kronverksky Pr. 49, St. Petersburg, 197101, Russia*

Light trapping is a crucial mechanism for synchronization in optical communication. Especially on the level of single photons, control of the exact emission time is desirable. In this paper, we theoretically propose a single-photon buffering device composed of a quantum dot doped with a single Mn atom in a cavity. We present a method to detain a single cavity photon as an excitation of the dot. The storage scheme is based on bright to dark exciton conversion performed with an off-resonant external optical field and mediated via a spin-flip with the magnetic ion. The induced Stark shift brings both exciton states to resonance and results in an excitation transfer to the optically inactive one. The stored photon can be read out on demand in the same manner by repopulating the bright state, which has a short lifetime. Our results indicate the possibility to suspend a photon for almost two orders of magnitude longer than the lifetime of the bright exciton.

I. INTRODUCTION

Self-assembled quantum dots (QDs) are optically active and allow the control of electronic states with light.[1–4] In return, they can serve as photon sources, which makes them attractive for quantum communication devices.[5,6] A QD–cavity system greatly increases light emission efficiency due to the Purcell effect[7] and has a favored direction of emission in contrast to a standalone QD, providing easier in- and outcoupling. While QDs in cavities are a suitable platform for quantum information processing devices,[8] the realization requires the synchronization of signals,[9] for which a photon buffer is desirable.

In all-optical systems, buffers were realized with fibers and waveguides.[9–12] Another proposed realization of an optical memory cell is a three-level Λ system, which gives the possibility to store information in a dark state.[13] Extremely long light storage was achieved in atomic systems, where the slow light effect is commonly based on electromagnetically induced transparency (EIT). Adequate coupling in the Λ system highly reduces the group velocity of light and results in slow propagation of a beam through atoms or even reversible trapping of light in atomic excitations.[13–16] Recent experiments were performed even on the single-photon level,[17–19] raising hopes for use in quantum communication. Atomic systems were also used to store time-entangled solitons in a cavity, representing a step towards multiplexed quantum communication.[20]

In solid-state systems, photons may be absorbed and stored as excitons. However, the typical lifetime of a bright exciton is short (typically a few hundred ps up to one ns). Therefore, a separated electron-hole pair, the indirect exciton, was used in coupled nanostructures to extend the storage time.[21–29] On the other hand, in a single QD–cavity system, the lifetime of an exciton may be increased by the Stark shift, which decouples the exciton from the cavity mode.[30] A more attractive direction for storing excitations in a QD is to use a dark state, which lives for at least an order of magnitude longer than the bright one. For a long time, dark excitons were beyond much interest as they are not optically active and hence not directly accessible.

Recent progress allows for indirectly accessing the dark exciton with light[31,32] or other complexes,[33] but all-optical control of the dark state using an intermediate biexciton state has also been proposed for the use as a long-lived qubit.[31,34–37] Another possibility is the coupling of bright and dark states using micromechanical resonators, making the dark state addressable by light.[38] Still, it is much easier to excite the bright state. Hence, a method to realize the bright-to-dark conversion for excitation storage was already proposed for colloidal systems.[39] Yet, they cannot be easily integrated on-chip. A dark state was also used as a microsecond valley polarization memory in transition metal dichalcogenides.[40] More recently, a controllable occupation transfer between bright and dark excitons in a QD–cavity system was suggested.[41]

Our method facilitates QDs with a single magnetic dopant, which can be deterministically fabricated for several years,[42] with dopand atoms like Manganese (Mn),[43,44] Cromium,[45] Iron,[46] or Cobalt.[47] Interestingly, the spin state of the dopant can be changed via optical control.[48–52]

Here, we choose a Mn doped CdTe/ZnTe QD in a microcavity.[53] The exchange coupling between the Mn and the electron spin enables a coupling between bright

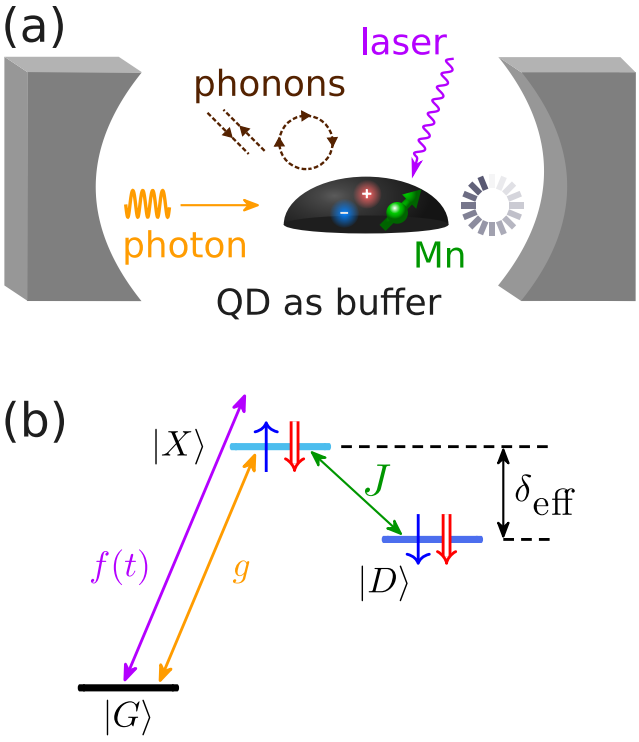

FIG. 1. (a) Sketch of the QD–cavity system. The Mn ion provides the magnetic field necessary to facilitate the storage of a single cavity photon. An off-resonant external laser controls both the storage and the release time and thus the entire buffering procedure deterministically. (b) The Λ-type three-level model of the QD. The spin configuration of the two exciton states is symbolized by arrows.

and dark excitons in the quantum dot under the simultaneous flip of the Mn spin.[48,54] Given a spin state, the states can be interpreted as a Λ-type three-level system, as specified in the next section. The main advantage of using a magnetically doped QD is its intrinsic property to couple bright and dark excitons, such that no external magnetic field needs to be applied as in other studies.[41,55,56]

The buffering scheme relies on storing the photon in the dark state. After the photon is converted to the bright exciton state, an AC-Stark pulse is utilized to facilitate the conversion of the bright into a dark exciton. We stress that the Stark pulse is the only external pulse which is used in the buffering scheme.

II. MN-DOPED QUANTUM DOT SYSTEM

We consider a self-assembled CdTe quantum dot (QD) doped by a single Mn ion inside a ZnTe micropillar cavity. Due to the strong spatial confinement of the carriers in the QD, only the lowest conduction band state and the uppermost valence band state need to be considered, namely electrons in the s-like conduction band and holes in the p-like heavy-hole band.

Excitons form as pairs of conduction band electrons and valence band heavy holes. Having a spin component of $S_z^{\text{h}} = \pm\frac{3}{2}$, heavy holes can form two types of excitons with the spin-$\frac{1}{2}$ electrons: the optically active *bright* states with a circular polarization of ±1 and the dipole-*dark* states with ±2. For typical fine-structure splittings of a few tens of μeV[57] between the two bright exciton states of opposite circular polarization, only excitons of one polarization need to be considered, if the external driving has a defined circular polarization.[55,58,59]

Doping such a QD system with a single Mn ion, which has a spin of $\frac{5}{2}$, introduces an additional state space, namely the six possible orientations of its spin. The Mn spin interacts with electrons and holes via the exchange interaction[43,48,62,72–74]

$$H_{\text{ex}} = j_{\text{e}}\boldsymbol{M}\cdot\boldsymbol{S}^{\text{e}} + j_{\text{h}}\boldsymbol{M}\cdot\boldsymbol{S}^{\text{h}}\,, \tag{1}$$

where $\boldsymbol{M}$ denotes the spin of the Mn ion. $\boldsymbol{S}^{\text{e}}$ ($\boldsymbol{S}^{\text{h}}$) is the operator of the electron (hole) spin in the QD. $j_{\text{e/h}} = J_{\text{e/h}}\left|\Psi_0^{\text{e/h}}(\boldsymbol{r}_{\text{Mn}})\right|^2$ are composed of the coupling constants $J_{\text{e/h}}$ between the electon/hole and the Mn spin (cf., **Table I**) and the carrier ground state wave function Ψ_0 at the position $\boldsymbol{r}_{\text{Mn}}$ of the Mn atom. Modelling the QD with a hard wall cubic potential[74,75] with in-plane widths of 6 nm and a height of 2 nm, the coupling strengths $j_{\text{e/h}}$ depends on the position of the Mn atom.

For a more intuitive understanding of the exchange Hamiltonian, it can be rewritten as

$$\begin{aligned} H_{\text{ex}} = {} & j_{\text{e}}M_zS_z^{\text{e}} + \frac{j_{\text{e}}}{2}\left(M_+S_-^{\text{e}} + M_-S_+^{\text{e}}\right) \\ & + j_{\text{h}}M_zS_z^{\text{h}} + \frac{j_{\text{h}}}{2}\left(M_+S_-^{\text{h}} + M_-S_+^{\text{h}}\right) \end{aligned} \tag{2}$$

with $M_\pm := M_x \pm iM_y$ and $S_\pm^{\text{e/h}} := S_x^{\text{e/h}} \pm iS_y^{\text{e/h}}$. The Ising terms[1] arising from the z-component of the interaction lead to energy shifts of the exciton states with different spin configuration. These contributions lead to the characteristic splitting of the exciton line into six lines even at zero magnetic field.[42–44,73] The electron flip-flop term[2] on the other hand results in a coupling between the excitonic bright state with total spin ±1 and the excitonic dark state with ±2 via simultaneous spin flip. While usually the flip-flop term is much weaker than the energetic splitting, for an applied magnetic field in Faraday configuration, this coupling is seen as anti-crossing in the optical spectrum at a field of several Tesla. Note that the flip-flop term regarding the hole[3] can be neglected since the hole spin is pinned in a pure heavy-hole system.[48]

Assuming the Mn spin to be initially prepared in the state $M_z = -\frac{5}{2}$, we can reduce our system to a three-level system. This preparation can be achieved by thermal occupation at low temperatures: by applying a magnetic field, it becomes the energetically lowest state.[48] Then, the three states are: the ground state without an

TABLE I. Parameters used for the simulations.

Electron-Mn coupling	J_e [meV nm^3]	-15	[60]
Hole-Mn coupling	J_h [meV nm^3]	60	[60]
Intrinsic dark-bright splitting	δ_{XD} [meV]	0.95	[61]
Mn g-factor	g_{Mn}	2.0075	[62]
Electron g-factor	g_{e}	-1.5	[43]
QD–cavity coupling	$\hbar g$ [meV]	0.1	[63]
Cavity loss rate	κ [ns^{-1}]	8.5	[64]
Radiative decay rate of $\lvert X\rangle$	γ_{X} [ns^{-1}]	2.4	[63]
Residual decay rate of $\lvert D\rangle$	γ_{D} [ns^{-1}]	0.01	[65]
Electron deformation potential	D_e [eV]	-5	[66]
Hole deformation potential	D_h [eV]	1	[66]
Density	ρ_D [kg m^{-3}]	5510	[66]
Sound velocity	c_s [m s^{-1}]	4000	[66]
Electron-to-hole confinement ratio	a_e/a_h	1.38	[67,68]
Electron confinement radius	a_e [nm]	3.0	[69–71]

electronic excitation $|G\rangle := |0, -\frac{5}{2}\rangle$, the bright exciton $|X\rangle := |-1, -\frac{5}{2}\rangle$, and the dark exciton $|D\rangle := |-2, -\frac{3}{2}\rangle$. Here, the first entry denotes the total spin of the electronic excitation and the second one the Mn spin orientation. Note that a circular polarization of the external laser of -1 is assumed, from which the sign of the bright exciton spin follows.

III. MODEL OF THE Λ-TYPE THREE-LEVEL SYSTEM

In the basis of the three states $|G\rangle$, $|X\rangle$, and $|D\rangle$ the Hamiltonian reads as follows:

$$H = H_{\mathrm{QD}} + H_{\mathrm{flip}} + H_{\mathrm{driv}}(t) + H_{\mathrm{C}} + H_{\mathrm{Ph}}\,, \qquad (3)$$

consisting of the QD part H_{QD} and the flip-flop term H_{flip} as introduced in Equation (2). In addition, we account for the driving of the system with an external laser pulse $H_{\mathrm{driv}}(t)$, the coupling to a single-mode cavity H_{C}, and the coupling to longitudinal acoustic (LA) phonons H_{Ph}. A sketch of the system and its level structure is shown in **Figure 1**.

The QD part is composed of

$$H_{\mathrm{QD}} = \hbar\omega_{\mathrm{X}}|X\rangle\langle X| + (\hbar\omega_{\mathrm{X}} - \delta_{\mathrm{eff}})\,|D\rangle\langle D|\,, \qquad (4)$$

where the energy of the ground state is set to zero, the bright exciton has the energy $\hbar\omega_{\mathrm{X}}$, and the effective dark-bright splitting is δ_{eff}. Three contributions enter the latter quantity: the intrinsic splitting δ_{XD} due to the electron-hole exchange interaction, the splitting arising from the Ising terms in Eq. (2), and a Zeeman splitting due to an external magnetic field in Faraday configuration $\boldsymbol{B} = B_z\boldsymbol{e}_z$

$$\delta_{\mathrm{eff}} = \delta_{\mathrm{XD}} - 2j_{\mathrm{e}} + \frac{3}{2}j_{\mathrm{h}} + (g_{\mathrm{Mn}} - g_{\mathrm{e}})\,\mu_{\mathrm{B}}B_z\,. \qquad (5)$$

g_{Mn} and g_{e} denote the Mn and the electron g-factors (cf., Table I), respectively, and μ_{B} is the Bohr magneton.

One arm of the Λ-type system is coupled by the flip-flop term

$$H_{\mathrm{flip}} = -\frac{1}{2}J\left(|X\rangle\langle D| + |D\rangle\langle X|\right)\,. \qquad (6)$$

The interaction strength results from calculating the corresponding matrix elements in the three-level basis as $J = -\sqrt{5}j_{\mathrm{e}}$. We assume the position of the Mn atom to be 30 % away from the QD edge in both x and y direction and 13 % in z direction. This results in a coupling strength of $J = 0.25\,\mathrm{meV}$. This value can be interpreted as the Mn spin providing an effective magnetic field for the excitons with a strength of roughly 3 T.

The other arm of the Λ-type system, i.e., the ground to bright exciton state transition is driven by an external laser classically described by the function $f(t) = f_{\mathrm{ACS}}(t)e^{-i\omega_{\mathrm{ACS}}t}$ with the real envelope function $f_{\mathrm{ACS}}(t)$ and the off-resonant AC-Stark frequency ω_{ACS} [cf., Figure 1(b)]. Although the AC-Stark pulse is off-resonant, the parameters are chosen such that the conditions for the usual dipole and rotating wave approximations still hold and the corresponding coupling can be written as:[76,77]

$$H_{\mathrm{driv}}(t) = -\frac{\hbar}{2}\left(f^*(t)|G\rangle\langle X| + f(t)|X\rangle\langle G|\right)\,. \qquad (7)$$

The coupling to the single-mode cavity with strength g [cf., Figure 1(b)] is described by a Jaynes-Cummings model

$$H_{\mathrm{C}} = \hbar\omega_{\mathrm{C}}a^\dagger a + \hbar g\left(a|X\rangle\langle G| + a^\dagger|G\rangle\langle X|\right)\,, \qquad (8)$$

where a ($a^\dagger$) is the annihilation (creation) operator for a photon at the cavity frequency ω_{C}, which is assumed to be on resonance with the bright state ω_{X}.

To model the decoherence in the QD, we consider that the QD is coupled to an environment of LA phonons in the bulk material [cf., Figure 1(a)][66,78–82]

$$H_{\rm Ph} = \hbar \sum_{\boldsymbol{q}} \omega_{\boldsymbol{q}} b_{\boldsymbol{q}}^\dagger b_{\boldsymbol{q}} + \hbar \sum_{\boldsymbol{q}} \left(\gamma_{\boldsymbol{q}} b_{\boldsymbol{q}}^\dagger + \gamma_{\boldsymbol{q}}^* b_{\boldsymbol{q}}\right) \left(|X\rangle\langle X| + |D\rangle\langle D|\right) . \quad (9)$$

$b_{\boldsymbol{q}}$ ($b_{\boldsymbol{q}}^\dagger$) annihilates (creates) a phonon in the mode $\boldsymbol{q}$ with the frequency $\omega_{\boldsymbol{q}}$. Both exciton states are assumed to couple to the environment with the same strength $\gamma_{\boldsymbol{q}}$. The role of phonons in QD–cavity systems is typically considered to be detrimental to the preparation of photonic quantum states, e.g., single photons[83–91] or entangled photon pairs.[92–98] Nonetheless, in specific situations a phonon enhancement of the single-photon purity is found.[99,100] Also, a boost in the entanglement of two photons has been predicted to be a result of the phonon interaction.[101]

Furthermore, we account for cavity losses ($\mathcal{L}_{a,\kappa}$) as well as radiative decay of the bright exciton ($\mathcal{L}_{|G\rangle\langle X|,\gamma_{\rm X}}$) and losses of the dark exciton ($\mathcal{L}_{|G\rangle\langle D|,\gamma_{\rm D}}$) using Lindblad superoperators acting on the density matrix ρ as

$$\mathcal{L}_{O,\Gamma}\rho = \Gamma \left(O\rho O^\dagger - \frac{1}{2}\left\{\rho, O^\dagger O\right\}_+ \right) , \quad (10)$$

where $\{A,B\}_+$ is the anti-commutator of operators A and B. These superoperators describe phenomenologically loss processes with rate Γ on a dissipation channel O.

We use an interaction picture representation of this Hamiltonian for the numerics as well as the physical discussion, in order to eliminate fast oscillating terms in the dynamics resulting from transition energies in the eV range. The noninteracting Hamiltonian used for this transform is[41]

$$H_0 = -\hbar\Delta\omega_{\rm AX}|G\rangle\langle G| + \hbar\omega_{\rm X}\left(|X\rangle\langle X| + |D\rangle\langle D|\right) + \hbar\omega_{\rm ACS} a^\dagger a . \quad (11)$$

Here, the detuning between the laser and bright exciton frequencies $\Delta\omega_{\rm AX} := \omega_{\rm ACS} - \omega_{\rm X}$ has been introduced. Then, the transformed Hamiltonian is $H_I = U^\dagger(H - H_0)U$ with $U = \exp\left[-(i/\hbar)H_0 t\right]$.

We choose parameters from the experimental literature, in order to perform simulations as realistic as possible. The values are given in Table I together with corresponding references.

The dynamics is obtained as the solution of the Liouville-von Neumann equation

$$\frac{\partial}{\partial t}\rho = -\frac{i}{\hbar}\{H,\rho\}_- + \mathcal{L}_{a,\kappa}\rho + \mathcal{L}_{|G\rangle\langle X|,\gamma_{\rm X}}\rho + \mathcal{L}_{|G\rangle\langle D|,\gamma_{\rm D}}\rho \quad (12)$$

with the commutator $\{A,B\}_-$ of operators A and B. We treat the phonon Hamiltonian in a numerically exact way using a path-integral formalism.[69,102–105] By numerically exact we denote a solution that depends only on the time discretization and the memory length as the sole convergence parameters. Beyond these two convergence parameters, no approximations enter the solution for the QD–cavity dynamics.

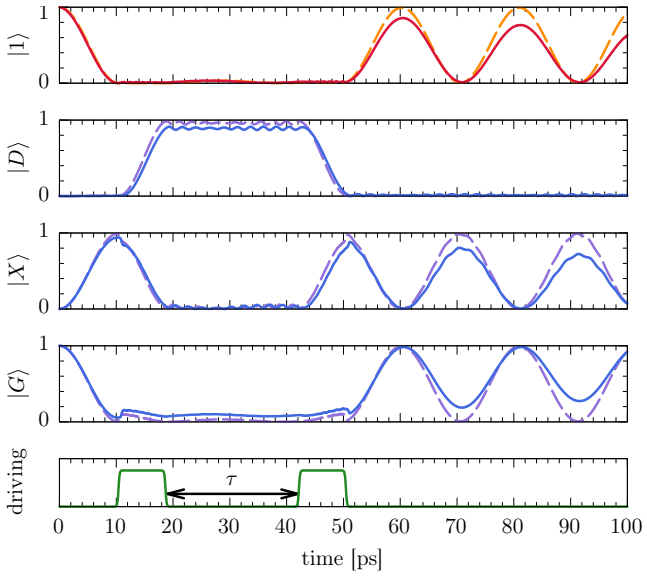

FIG. 2. A single cavity photon is stored in the dark exciton state of the QD using a first writing AC-Stark pulse (bottom panel). The occupations of the ground state $|G\rangle$, the bright exciton $|X\rangle$, the dark exciton $|D\rangle$, and the 1-photon Fock state $|1\rangle$ are depicted: ideal case without phonons and losses (dashed lines); including radiative and cavity loss effects (solid lines). A second readout AC-Stark pulse retrieves the single photon. The time between the pulses is the buffer time τ.

Physically, the phonon influence is fully captured by the phonon spectral density $J(\omega) = \sum_{\boldsymbol{q}} |\gamma_{\boldsymbol{q}}|^2 \delta(\omega - \omega_{\boldsymbol{q}})$. Assuming harmonic confinement and a linear dispersion $\omega_{\boldsymbol{q}} = c_s|\boldsymbol{q}|$ with sound velocity c_s, the spectral density reads

$$J(\omega) = \frac{\omega^3}{4\pi^2\rho_D\hbar c_s^5}\left(D_e e^{-\omega^2 a_e^2/(4c_s^2)} - D_h e^{-\omega^2 a_h^2/(4c_s^2)}\right)^2 , \quad (13)$$

where we have considered deformation potential coupling which is usually the dominant coupling mechanism.[79] Here, ρ_D is the density of the material, D_e (D_h) the electron (hole) deformation potential, and a_e (a_h) the electron (hole) confinement radius, listed in Table I.

IV. BUFFERING PROTOCOL

A. General idea

We propose a protocol to buffer a single cavity photon deterministically using the Λ-type three-level system described in Section III. Initially, we assume the QD to be

in its ground state $|G\rangle$ and one photon to be present in the cavity, i.e., the initial state of the QD–cavity dynamics is $|G,1\rangle$ (cf., **Figure 2**), where we have introduced the notation $|\chi,n\rangle$ for the QD–cavity product space with $\chi \in \{G,X,D\}$ and the photon number n. Due to the QD–cavity coupling, the cavity photon is absorbed into the bright state $|X\rangle$ after half a coherent Rabi oscillation. Then, the dark state $|D\rangle$ is prepared using a recently proposed protocol relying on the optical Stark shift.[41] The transfer of the excitation from the bright to the dark state is triggered deterministically using an off-resonant AC-Stark pulse, which shifts the bright state energy such that the bright and dark states are effectively in resonance. The pulse duration is chosen such that exactly half a Rabi oscillation between the two exciton states is possible.

To present a physically clear picture of the processes involved in the buffering scheme, we use rectangular pulses with smoothed edges for the AC-Stark pulse envelopes, following Ref. 41

$$f_{\mathrm{ACS}}(t) = \frac{f_0}{\left(1+e^{-\alpha(t-t_{\mathrm{on}})}\right)\left(1+e^{-\alpha(t_{\mathrm{ACS}}-(t-t_{\mathrm{on}}))}\right)}\,. \tag{14}$$

Here, α determines the rise time of the pulse, which we set to $10\,\mathrm{ps}^{-1}$, t_{on} is the switch-on time, and t_{ACS} the pulse duration. The pulse amplitude f_0 is determined by the effective dark-bright splitting δ_{eff}, which needs to be bridged, and the pulse duration t_{ACS} by the oscillation frequency J.

During the pulse, when the amplitude is essentially f_0, the induced optical Stark shift is

$$\Delta E_{\mathrm{Stark}} = \frac{\hbar}{2}\left(\sqrt{\Delta\omega_{\mathrm{AX}}^2+f_0^2}-\Delta\omega_{\mathrm{AX}}\right) \tag{15}$$

for $\Delta\omega_{\mathrm{AX}} > 0$.[41] By setting $\Delta E_{\mathrm{Stark}} = \delta_{\mathrm{eff}}$, the pulse amplitude necessary to bridge the dark-bright splitting is determined to be

$$f_0 = \sqrt{\left(2\frac{\delta_{\mathrm{eff}}}{\hbar}+\Delta\omega_{\mathrm{AX}}\right)^2-\Delta\omega_{\mathrm{AX}}^2}\,. \tag{16}$$

The length t_{ACS} of the pulse has to correspond to half a Rabi oscillation between the two exciton states mediated by the spin-flip coupling[41]

$$t_{\mathrm{ACS}} = \frac{2\pi\hbar}{2\sqrt{J^2+\left(\delta_{\mathrm{eff}}-\Delta E_{\mathrm{Stark}}\right)^2}}\,, \tag{17}$$

which simplifies to $t_{\mathrm{ACS}} = \pi\hbar/J$ for $\Delta E_{\mathrm{Stark}} = \delta_{\mathrm{eff}}$.

This leaves only the detuning with respect to the bright exciton frequency $\Delta\omega_{\mathrm{AX}}$ as a free parameter. For a dark-bright splitting in the order of a meV, it has been shown that a detuning of $\Delta\omega_{\mathrm{AX}} = 15\,\mathrm{meV}$ is favorable for the transfer of the excitation from the bright to the dark state.[41]

Since the dark state is not optically active, it is a metastable state. This is reflected in its decay rate γ_{D} being about two orders of magnitude smaller than the radiative decay rate γ_{X} of the bright state (cf., Table I). Therefore, in an ideal system free of losses and decoherence, the excitation is expected to stay in the dark state indefinitely. The release of the photon is facilitated by the reverse process with a second AC-Stark pulse.

The time evolution of this protocol in the ideal case (without taking phenomenological losses or phonons into account) is presented in Figure 2 (dashed lines), which shows the occupation of the three states together with the occupation of the 1-photon state and the applied laser pulses as functions of time. The dynamics behaves as predicted by the *writing* scheme described above. Indeed, the occupation of the dark state after the first writing pulse is close to unity. Small-amplitude oscillations appear due to the residual coupling to the bright state, which depend both on the coupling J and the splitting δ_{eff} between the bright and the dark state.

To release the photon after the buffering time τ (23.5 ps in the example shown in Figure 2), a second *readout* AC-Stark pulse is required (cf., bottom panel of Figure 2). When the excitation is transferred back to the single-photon state, Rabi oscillations between the cavity mode and the bright exction are observed. These oscillations are undamped in the ideal case, where no phonon coupling and no phenomenological loss processes are considered (cf., dashed lines in Figure 2). The maximum occupation of the 1-photon state $|1\rangle$ is 99.95 %, implying a close to perfect writing and readout of the buffered single photon in the ideal case.

V. STORAGE PERFORMANCE

The key quantity of interest in a buffering scheme is the retrievable percentage of the stored photon after the buffering time τ. Therefore, we here discuss the dependence of this captured 1-photon occupation on the buffering time τ and various system parameters, including the dark-bright coupling J, the splitting δ_{eff}, and the temperature T. An example of the influence of phenomenological losses on the buffering scheme is shown in Figure 2(b) (solid lines). We find that the scheme is degraded and here we quantify the amount of storage which is still achievable. Since damped Rabi oscillations between the bright exciton and the cavity occur in the protocol proposed in Section IV after the readout AC-Stark pulse when including phenomenological losses, we take the maximum captured 1-photon occupation (C1PO) after the readout pulse as a measure of the retrievable percentage of the stored photon.

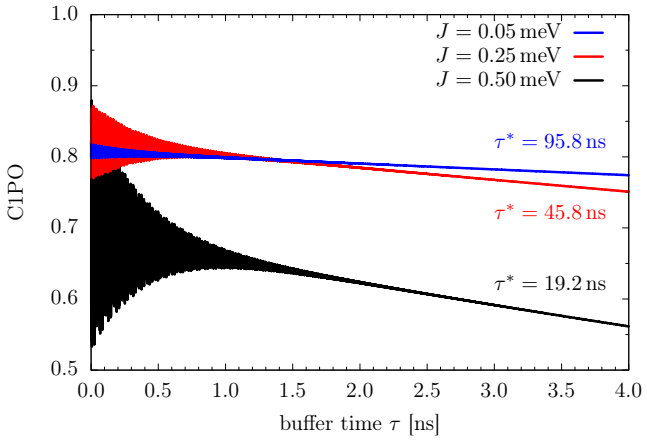

FIG. 3. The maximum captured 1-photon occupation (C1PO) after the second AC-Stark pulse as a function of the buffering time τ, i.e., the delay time between the two pulses. The dependence is shown for different coupling strengths J between the bright and the dark state. Labels indicate the decay time τ^* extracted from fitting an exponential function to the corresponding curve (cf., main text for detailed explanation).

A. Influence of the dark-bright coupling J

Figure 3 shows the dependence of the C1PO on the buffering time τ, i.e., the delay time between the two AC-Stark pulses. These calculations are performed considering phenomenological losses, but without taking phonons into account. The red line corresponds to the coupling $J = 0.25\,\text{meV}$. After initial oscillations, the C1PO decreases exponentially. The oscillations are a direct consequence of the dark-bright coupling with strength J, which is off-resonant due to the dark-bright splitting δ_{eff}. This off-resonance leads to low-amplitude high-frequency oscillations of the dark state occupation in between the writing and readout pulses (cf., Figure 2). When the second AC-Stark pulse arrives during a minimum of this oscillation, the corresponding value of the C1PO also becomes minimal.

The damping of these oscillations and the subsequent exponential decay shown in Figure 3 is a result of the decay of the dark state $|D\rangle$. While its decay rate γ_{D} corresponds to a lifetime of 100 ns, the residual off-resonant coupling to the bright state, which decays two orders of magnitude faster, leads to a much faster effective decay of the dark state.

Fitting an exponential function of the form

$$\text{C1PO}_{\text{fit}}(\tau) = c\, e^{-\tau/\tau^*} \tag{18}$$

using the scaling constant c and the decay time τ^* as free parameters, one obtains a decay time of $\tau^* = 45.8\,\text{ns}$. This value corresponds exactly to the effective decay time of the dark state (not shown here), corroborating the conclusion that the storage performance between writing and readout only depends on the decay of the dark state $|D\rangle$.

Increasing J while keeping all the other parameters fixed, yields a shorter decay time τ^* (cf., black line in Figure 3) and thus a worse performance of the storage protocol. The reason is the increased oscillation amplitude between $|D\rangle$ and $|X\rangle$ stemming from the larger dark-bright coupling. Therefore, the interaction with the faster-decaying bright state is more effective. The higher oscillation amplitude is reflected in the larger initial oscillation amplitude of C1PO. The reverse argument holds for a smaller coupling strength J and indeed for $J = 0.05\,\text{meV}$ (cf., blue line in Figure 3) $\tau^* = 95.8\,\text{ns}$ is already close to the lifetime of 100 ns of the dark exciton without exchange coupling to the bright exciton.

Overall, decay times on the order of a few tens of ns suggest a high storage performance. In comparison, a single photon inside a high-Q cavity with a quality factor of $2.68 \cdot 10^5$,[64] corresponding to our value of κ (cf., Table I), has a decay time of $\kappa^{-1} = 118\,\text{ps}$. Therefore, the buffering protocol presented here facilitates a storage time roughly two orders of magnitude longer.

Note that changing the dark-bright coupling J experimentally means that the location of the Mn atom $\boldsymbol{r}_{\text{Mn}}$ needs to be changed, thus requiring different QD samples. Changing the Mn position also changes the shifts induced by the carrier-Mn Ising terms. Therefore, an additional magnetic field in Faraday configuration would be necessary to keep δ_{eff} constant [cf., Eq. (5)].

B. Influence of the dark-bright splitting δ_{eff}

In the previous section, it became clear that the main loss channel during the storage time is the effective decay of the dark state. This in turn depends on the residual coupling to the bright state, which is determined by J and δ_{eff}. In this section, we analyze the influence of the latter by repeating the calculations of C1PO(τ) by varying δ_{eff} and fitting Eq. (18) to the resulting curves, in analogy to Figure 3. We keep the dark-bright coupling fixed at $J = 0.25\,\text{meV}$.

The dependence of the decay time τ^* on the effective dark-bright splitting δ_{eff} is shown in **Figure 4**(a). Without an external magnetic field in Faraday configuration, the splitting is 1.85 meV and the decay time τ^* corresponds to the red line in Figure 3.

By applying a field with magnitude B_z, the effective splitting is changed [cf., second axis in Figure 4(a)]. At constant J, a higher splitting means that the residual coupling of the dark to the bright state is weaker. This closes the corresponding radiative loss channel more and more, such that τ^* converges to the intrinsic decay time of the dark state $\gamma_{\text{D}}^{-1} = 100\,\text{ns}$. The opposite argument holds for smaller splittings. Without any splitting, the two exciton states would perform coherent full-amplitude Rabi oscillations with a frequency corresponding to J, such that the radiative decay channel would diminish the storage performance maximally.

Assuming $g \ll \delta_{\text{eff}}$ and $J \ll \delta_{\text{eff}}$, which holds well for

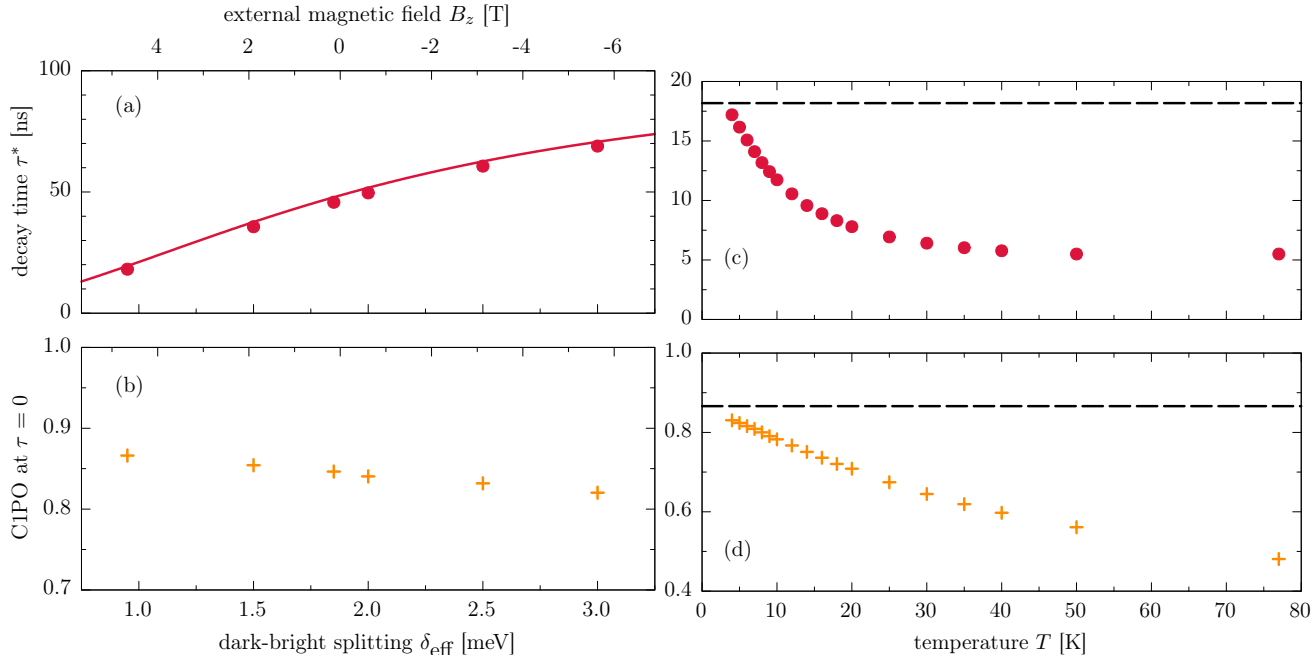

FIG. 4. The dependencies of the decay time τ^* and the C1PO at $\tau = 0$ on the effective splitting δ_{eff} between the dark and bright state [panels (a) and (b)] without taking phonons into account and on the temperature T [panels (c) and (d)] including phonon effects. The red solid line in panel (a) is the approximate analytical prediction from Equation (19). For the temperature dependent study, the splitting is set to $\delta_{\text{eff}} = \delta_{\text{XD}} = 0.95\,\text{meV}$.

the parameters considered in Figure 4(a), an analytical approximation of the following form can be derived:

$$\tau^*(\delta_{\text{eff}}) = \left[\left(\frac{J}{2\delta_{\text{eff}}}\right)^2 (\gamma_{\text{X}} - \gamma_{\text{D}}) + \gamma_{\text{D}}\right]^{-1}. \qquad (19)$$

This function is plotted in **Figure 4**(a) as a red solid line, reproducing the numerically obtained data well.

To analyze the performance of the writing and reading process separately from the losses during storage, we take the C1PO for $\tau = 0$ as a measure, i.e., the writing and readout pulses merge to a single pulse of length $2t_{\text{ACS}}$. This value indicates, what percentage of the initially present photon can be retrieved after writing it to the dark state and immediately reading it out again. Note that due to the initial oscillations of C1PO(τ) (cf., data shown in Figure 3), the fit parameter c in Eq. (18) does not necessarily correspond to the value of C1PO($\tau = 0$).

The results are shown in Figure 4(b). Overall, the losses during writing and readout are restricted to values between 10 % and 20 %, originating from the loss rates γ_{X} and κ.

C. Temperature dependence

Including the coupling of both the bright and the dark exciton states to LA phonons as described by Equation (9) leads to a faster decay of the initial oscillations of C1PO(τ) and a faster subsequent exponential decay. We perform this analysis for a dark-bright splitting of $\delta_{\text{eff}} = \delta_{\text{XD}} = 0.95\,\text{meV}$, i.e., for the intrinsic splitting due to the electron-hole exchange, with a coupling of $J = 0.25\,\text{meV}$.

The resulting decay times τ^* and values of C1PO($\tau = 0$) are shown in Figure 4(c) and (d), respectively. The phonon-free results are marked by dashed black lines. At $T = 4\,\text{K}$, the decay time is close to its phonon-free counterpart. With rising temperature, though, the decay times become drastically shorter. At $T = 77\,\text{K}$, it is only roughly a quarter of the phonon-free value. The reason is the asymmetry of phonon absorption and emission at low temperatures that vanishes at higher temperatures. During storage, the state $|D, 0\rangle$ is mostly occupied. The state $|G, 1\rangle$ lies $\delta_{\text{eff}} = 0.95\,\text{meV}$ above it and thus cannot be reached by phonon emission, which is predominant at low temperatures. In contrast, at higher temperatures, δ_{eff} can be bridged by phonon absorption. Thus, an additional decay channel of the dark state $|D, 0\rangle$ opens during storage. Reducing the residual coupling during storage by means of smaller J or a δ_{eff} much larger than the maximum of the phonon spectral density should therefore weaken the phonon influence, too.

The losses due to writing and readout are also hardly influenced at low temperatures, while they become stronger with rising T. This means that the preparation of the dark state during writing is already incomplete. The reason lies in the fact that the phonon interaction dampens the Rabi oscillations between the bright state

and the cavity to an extent that already the transfer from the single-photon state to the bright exciton (before the writing pulse) is incomplete.

VI. STORAGE OF A SINGLE PHOTON OUT OF THE STATE $|n\rangle$ WITH $n > 1$

We have demonstrated the buffering capacity of our protocol concerning a single-photon state. Now, the question arises how it performs, when higher-order Fock states are present in the cavity. To this end, we consider the state $|G, 2\rangle$ as the initial value of the QD–cavity system and buffer one of the two photons present in the cavity using the presented protocol. The occupation dynamics is shown in **Figure 5**(a) for a fixed $\tau = 15.5\,\mathrm{ps}$. The analysis is performed for $J = 0.25\,\mathrm{meV}$ and $\delta_{\mathrm{eff}} = \delta_{\mathrm{XD}} = 0.95\,\mathrm{meV}$ as before. Dashed lines show the ideal case, while solid lines depict the case including phenomenological losses.

We consider both the C1PO and the captured 2-photon occupation (C2PO) after the buffering time τ in Figure 5(b) (black and red lines, respectively). All loss processes and the phonon influence at $T = 4\,\mathrm{K}$ are taken into account in these results. The C2PO decays exponentially. The rate corresponds exactly to the cavity loss rate κ. Since one of the two initially present photons is stored in the dark state, the remaining single photon can leave the cavity via the cavity loss channel. Retrieving the other photon from the dark state and recombining it with the remaining one to yield the initial Fock state $|2\rangle$ is only possible, when the remaining one has not left the cavity yet.

Nonetheless, the effective buffering of the 2-photon Fock state outperforms the case, where the state $|2\rangle$ decays without using a storage scheme. The reason is the fact that the Fock state $|n\rangle$ decays with an effective rate of $n\kappa$. Therefore, our single-photon buffering protocol can reduce this effective rate to $(n-1)\kappa$, as shown here for the case $n = 2$. Meanwhile, the dependence of the C1PO on the buffering time corresponds again to the effective lifetime of the dark state of about $\sim 20\,\mathrm{ns}$. Interestingly, the dependence of the C1PO on τ is, even when disregarding the high-frequency oscillations in the beginning, nonmonotonous. The reason is the photon that remains in the cavity: the Rabi frequency of the oscillations between the bright state and the cavity depends on the number of photons present in the cavity. Since the frequencies for the different photon numbers are incommensurable, changes in the amplitude and therefore the nonmonotonicity of the C1PO are the consequence.

VII. TOWARDS EXPERIMENTAL REALIZATION

To present a clear and well understandable physical picture of the buffering scheme, we used rectangular pulses with smoothed edges as model AC-Stark pulses [cf., Eq. (14)]. While such pulses can be generated using fast electro-optical modulators to cut the desired envelopes out of a continuous wave laser,[41] the rise time of $1/\alpha = 0.1\,\mathrm{ps}$ assumed in Section IV A in combination with the pulse length necessary for the protocol is out of reach with current state-of-the-art equipment.[41] Experimentally, it is a far lesser challenge to use pulses with Gaussian envelopes.

The AC-Stark pulses are needed for the excitation transfer from the bright to the dark state for the writing and vice versa for the readout procedure. Therefore, we compare the storage capacity of differently shaped pulses by using the maximum occupation of the dark state $|D\rangle$ after the first (writing) pulse (cf., Figure 2) as a target quantity in the following. Note that any losses experienced during writing occur again at readout, thus influencing the C1PO two times. Nonetheless, the pulse shape should not have any influence on the decay time τ^* during storage, since there are no pulses in the time interval between writing and readout.

Using Gaussian pulses of the form

$$f_{\mathrm{ACS}}(t) = \frac{\Theta}{\sqrt{2\pi}\,\sigma} e^{-\frac{(t-t_0)^2}{2\sigma^2}}\,, \tag{20}$$

three parameters have to be determined: the pulse area Θ, the standard deviation σ, which is connected to the full width at half maximum via $\mathrm{FWHM} = 2\sqrt{2\ln 2}\,\sigma$, and the time t_0, where the maximum of the pulse occurs. While the three parameters f_0, t_{ACS}, and t_{on} can be determined from analytical considerations for rectangular pulses from Ref. 41, predicting an optimal set of Gaussian pulse parameters is not straightforward. Therefore, we numerically search for the maximum occupation of $|D\rangle$ in the parameter space spanned by Θ, σ, and t_0 by discretizing all three parameters. At $T = 4\,\mathrm{K}$ for example, this optimum is given by $\Theta = 33.77\pi$, $\mathrm{FWHM} = 7.14\,\mathrm{ps}$, and $t_0 = 15.01\,\mathrm{ps}$. We perform this optimization for the parameters used in the last two sections, namely $J = 0.25\,\mathrm{meV}$ and $\delta_{\mathrm{eff}} = \delta_{\mathrm{XD}} = 0.95\,\mathrm{meV}$.

Figure 6 shows the results depending on the temperature T. Although the rectangular pulses consistently outperform the Gaussian ones, the loss in occupation due to the experimentally easier to implement Gaussian shape is only around 5 percentage points for all considered temperatures. Therefore, the presented buffering protocol also works with Gaussian instead of rectangular pulses. This provides a path to an experimental realization in the near future.

Finally, let us comment on the usage of a semimagnetic QD for this protocol. The dark-bright coupling provided by the Mn atom is crucial for the operation of the protocol. The advantage of the Mn doping is that the dark-bright interaction is provided by an intrinsic degree of freedom of the QD. Nonetheless, this coupling could also be provided by an additional external magnetic field in Voigt configuration without using the Mn atom as a mediator.[41] Therefore, our proposed storage

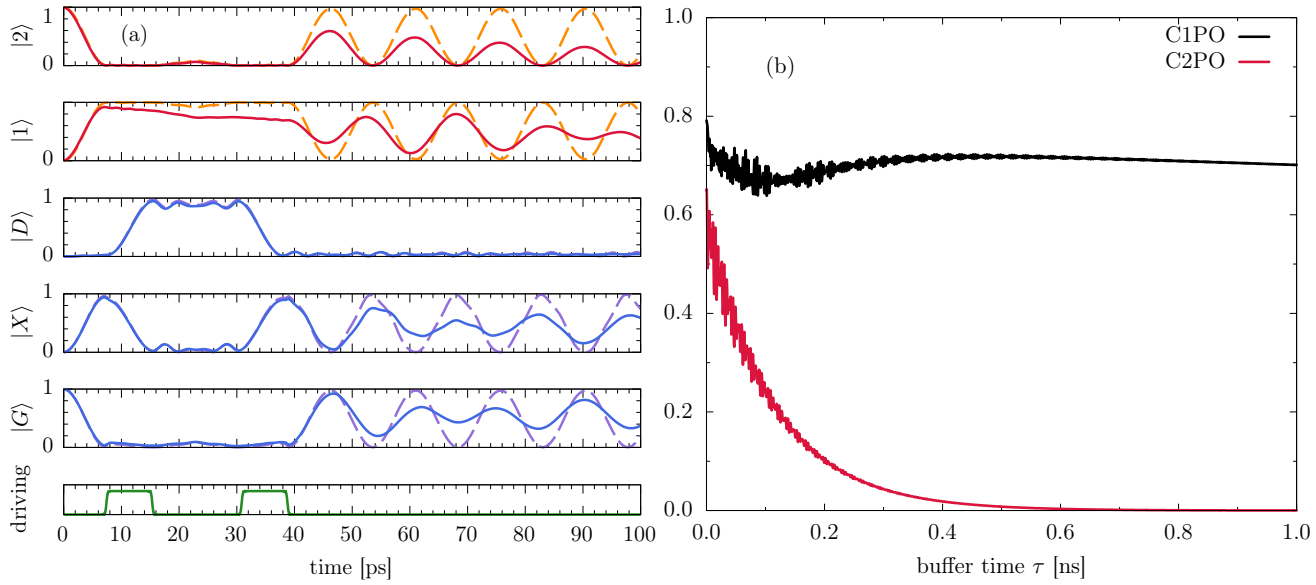

FIG. 5. (a) Same protocol as in Figure 2, but for an initial QD–cavity state of $|G, 2\rangle$. While one of the photons is stored in the dark state, the remaining one can leave the cavity, when cavity losses are taken into account. Ideal case without phonons and losses (dashed lines); including radiative and cavity loss effects (solid lines) (b) The maximum captured photon occupation after the second AC-Stark pulse as a function of the buffering time τ. Here, both phenomenological loss effects and the phonon influence at $T = 4\,\mathrm{K}$ are taken into account.

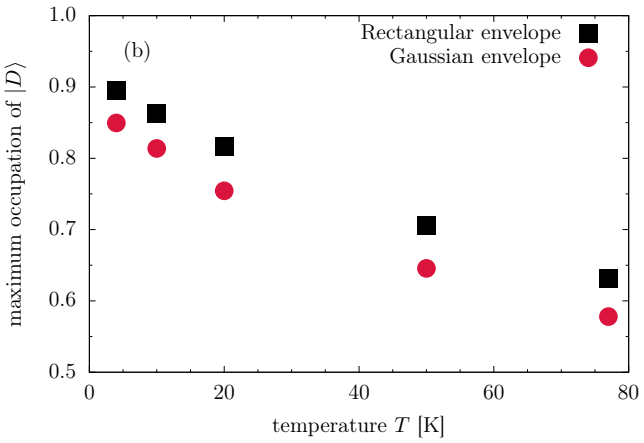

FIG. 6. The maximum occupation of the dark exciton $|D\rangle$ after the storage pulse depending on temperature. Pulses with rectangular envelope are compared with Gaussian pulses.

protocol should in principle also work in nonmagnetic QDs.

VIII. CONCLUSION

We proposed a protocol to deterministically write and read a single photon in a QD–cavity system. Assuming a CdTe QD isoelectrically doped with a single Mn ion yields a Λ-type three-level system consisting of a ground state and two exciton states, one optically active bright state and one that is dipole dark. The storage protocol relies on a coherent transfer of the photon occupation to the bright exciton due to Rabi oscillations. Then, an AC-Stark pulse shifts the bright state to be in resonance with the dark exciton. A coherent excitation transfer during the length of the pulse prepares the dark state, which due to its optical inactivity is a metastable state with long lifetime. The readout procedure is exactly the reverse process.

We analyzed the influence of the dark-bright coupling strength J and the effective dark-bright splitting δ_{eff} on the performance of the protocol as well as its dependence on temperature. During storage in the dark state, its residual coupling to the bright state and thus to faster loss channels is controlled by J and δ_{eff}. Reducing this residual coupling by decreasing J or increasing δ_{eff} leads to a better overall performance of the buffering scheme. At rising temperatures, the phonon environment acts on the coupling between the bright state and the cavity. Thus, an additional loss channel during storage has to be considered, which again can be influenced by adjusting the residual coupling of the dark to the bright exciton. Furthermore, phonons have a rather strong influence on the writing and readout procedure. At high enough temperatures, already the transfer of the photon to the bright exciton before writing becomes incomplete.

Nonetheless, for all considered parameter sets the overall storage time as measured by τ^* ranges from a few to tens of ns. Thus, it is two orders of magnitude longer than the lifetime of a photon in a high-Q cavity with a quality factor of $2.68 \cdot 10^5$.[64]

Furthermore, we have shown that the proposed scheme can store a single photon out of a higher-order Fock state $|n\rangle$ with $n > 1$. Thus, the lifetime of the state $|n\rangle$, which is $(n\kappa)^{-1}$ in a cavity with loss rate κ, can be extended to $[(n-1)\kappa]^{-1}$ (for $\gamma_{\mathrm{D}} \ll \kappa$).

Finally, we discussed the possibility of using Gaussian pulses for the buffering protocol instead of rectangular ones, which are experimentally out of reach with current equipment for the pulse characteristics needed for the protocol. For optimal pulse parameters, Gaussian pulses can be used successfully. Pulses of rectangular shape are only ~ 5 percentage points better concerning the dark state occupation after the writing procedure.

Thus, we expect the proposed scheme to be realizable with state-of-the-art equipment. After QDs have long been discussed as on-demand single-photon sources, this work paves the way for them to also be used as storage components. Such a QD buffering device for single photons could serve as a building block in more complex QD quantum information processing devices.

ACKNOWLEDGMENTS

This work was funded by the Deutsche Forschungsgemeinschaft (DFG, German Research Foundation) – project No. 419036043. M.Co. gratefully acknowledges support by the Studienstiftung des Deutschen Volkes.

* michael.cosacchi@uni-bayreuth.de

[1] A. J. Ramsay, Semiconductor Science and Technology **25**, 103001 (2010).
[2] A. Greilich, R. Oulton, E. A. Zhukov, I. A. Yugova, D. R. Yakovlev, M. Bayer, A. Shabaev, A. L. Efros, I. A. Merkulov, V. Stavarache, D. Reuter, and A. Wieck, Physical Review Letters **96**, 227401 (2006).
[3] M. Kroner, K. M. Weiss, B. Biedermann, S. Seidl, S. Manus, A. W. Holleitner, A. Badolato, P. M. Petroff, B. D. Gerardot, R. J. Warburton, and K. Karrai, Physical Review Letters **100**, 156803 (2008).
[4] M. V. G. Dutt, J. Cheng, B. Li, X. Xu, X. Li, P. R. Berman, D. G. Steel, A. S. Bracker, D. Gammon, S. E. Economou, R.-B. Liu, and L. J. Sham, Physical Review Letters **94**, 227403 (2005).
[5] K. D. Greve, D. Press, P. L. McMahon, and Y. Yamamoto, Reports on Progress in Physics **76**, 092501 (2013).
[6] W. B. Gao, A. Imamoglu, H. Bernien, and R. Hanson, Nature Photonics **9**, 363 (2015).
[7] E. M. Purcell, H. C. Torrey, and R. V. Pound, Phys. Rev. **69**, 37 (1946).
[8] K. Hennessy, A. Badolato, M. Winger, D. Gerace, M. Atatüre, S. Gulde, S. Fält, E. L. Hu, and A. Imamoğlu, Nature **445**, 896 (2007).
[9] H. Takesue, N. Matsuda, E. Kuramochi, W. J. Munro, and M. Notomi, Nature Communications **4**, 2725 (2013).
[10] W. Liu, B. Romeira, M. Li, R. S. Guzzon, E. J. Norberg, J. S. Parker, L. A. Coldren, and J. Yao, Journal of Lightwave Technology **34**, 3466 (2016).
[11] S. Clemmen, A. Farsi, S. Ramelow, and A. L. Gaeta, Optics Letters **43**, 2138 (2018).
[12] Y. Lai, M. S. Mohamed, B. Gao, M. Minkov, R. W. Boyd, V. Savona, R. Houdré, and A. Badolato, Scientific Reports **8**, 14811 (2018).
[13] C. Liu, Z. Dutton, C. H. Behroozi, and L. V. Hau, Nature **409**, 490 (2001).
[14] L. V. Hau, S. E. Harris, Z. Dutton, and C. H. Behroozi, Nature **397**, 594 (1999).
[15] Y. O. Dudin, L. Li, and A. Kuzmich, Physical Review A **87**, 031801 (2013).
[16] O. Katz and O. Firstenberg, Nature Communications **9**, 2074 (2018).
[17] H. de Riedmatten, M. Afzelius, M. U. Staudt, C. Simon, and N. Gisin, Nature **456**, 773 (2008).
[18] M. T. Rakher, R. J. Warburton, and P. Treutlein, Physical Review A **88**, 053834 (2013).
[19] E. Saglamyurek, T. Hrushevskyi, L. Cooke, A. Rastogi, and L. J. LeBlanc, Physical Review Research **1**, 022004 (2019).
[20] D. D. M. Welakuh and A. M. Dikandé, Optics Communications **403**, 27 (2017).
[21] T. Lundstrom, W. Schoenfeld, H. Lee, and P. M. Petroff, Science **286**, 2312 (1999).
[22] B. Song-Bao, T. Yan, L. Gui-Rong, L. Yue-Xia, Y. Fu-Hua, Z. Hou-Zhi, and Z. Yi-Ping, Chinese Physics Letters **20**, 1362 (2003).
[23] A. G. Winbow, A. T. Hammack, L. V. Butov, and A. C. Gossard, Nano Letters **7**, 1349 (2007).
[24] A. G. Winbow, L. V. Butov, and A. C. Gossard, Journal of Applied Physics **104**, 063515 (2008).
[25] A. A. High, E. E. Novitskaya, L. V. Butov, M. Hanson, and A. C. Gossard, Science **321**, 229 (2008).
[26] A. M. Fischer, V. L. Campo, M. E. Portnoi, and R. A. Römer, Physical Review Letters **102**, 096405 (2009).
[27] J. Simonin, C. R. Proetto, M. Pacheco, and Z. Barticevic, Physical Review B **89**, 075304 (2014).
[28] J. I. Climente and J. Planelles, Applied Physics Letters **104**, 193101 (2014).
[29] F. Tseng, E. Simsek, and D. Gunlycke, Journal of Physics: Condensed Matter **28**, 034005 (2015).
[30] R. Johne and A. Fiore, Physical Review A **84**, 053850 (2011).
[31] E. Poem, Y. Kodriano, C. Tradonsky, N. H. Lindner, B. D. Gerardot, P. M. Petroff, and D. Gershoni, Nature Physics **6**, 993 (2010).
[32] M. Zieliński, Physical Review B **102**, 245423 (2020).
[33] J. McFarlane, P. A. Dalgarno, B. D. Gerardot, R. H. Hadfield, R. J. Warburton, K. Karrai, A. Badolato, and P. M. Petroff, Applied Physics Letters **94**, 093113 (2009).
[34] I. Schwartz, D. Cogan, E. R. Schmidgall, L. Gantz, Y. Don, M. Zieliński, and D. Gershoni, Physical Review B **92**, 201201 (2015).
[35] I. Schwartz, E. R. Schmidgall, L. Gantz, D. Cogan, E. Bordo, Y. Don, M. Zielinski, and D. Gershoni, Physical Review X **5**, 011009 (2015).

[36] T. Heindel, A. Thoma, I. Schwartz, E. R. Schmidgall, L. Gantz, D. Cogan, M. Strauß, P. Schnauber, M. Gschrey, J.-H. Schulze, A. Strittmatter, S. Rodt, D. Gershoni, and S. Reitzenstein, APL Photonics **2**, 121303 (2017).

[37] E. R. Schmidgall, I. Schwartz, D. Cogan, L. Gantz, Y. Don, and D. Gershoni, in *Quantum Dots for Quantum Information Technologies*, Nano-Optics and Nanophotonics, edited by P. Michler (Springer International Publishing, Cham, 2017) pp. 123–164.

[38] R. Ohta, H. Okamoto, T. Tawara, H. Gotoh, and H. Yamaguchi, Physical Review Letters **120**, 267401 (2018).

[39] R. M. Kraus, P. G. Lagoudakis, A. L. Rogach, D. V. Talapin, H. Weller, J. M. Lupton, and J. Feldmann, Physical Review Letters **98**, 017401 (2007).

[40] C. Jiang, W. Xu, A. Rasmita, Z. Huang, K. Li, Q. Xiong, and W.-b. Gao, Nature Communications **9**, 753 (2018).

[41] M. Neumann, F. Kappe, T. K. Bracht, M. Cosacchi, T. Seidelmann, V. M. Axt, G. Weihs, and D. E. Reiter, Phys. Rev. B **104**, 075428 (2021).

[42] J. Kobak, T. Smoleński, M. Goryca, M. Papaj, K. Gietka, A. Bogucki, M. Koperski, J.-G. Rousset, J. Suffczyński, E. Janik, M. Nawrocki, A. Golnik, P. Kossacki, and W. Pacuski, Nature Communications **5**, 3191 (2014).

[43] L. Besombes, Y. Léger, L. Maingault, D. Ferrand, H. Mariette, and J. Cibert, Phys. Rev. Lett. **93**, 207403 (2004).

[44] M. Goryca, P. Plochocka, T. Kazimierczuk, P. Wojnar, G. Karczewski, J. A. Gaj, M. Potemski, and P. Kossacki, Phys. Rev. B **82**, 165323 (2010).

[45] A. Lafuente-Sampietro, H. Utsumi, H. Boukari, S. Kuroda, and L. Besombes, Phys. Rev. B **95**, 035303 (2017).

[46] T. Smoleński, T. Kazimierczuk, J. Kobak, M. Goryca, A. Golnik, P. Kossacki, and W. Pacuski, Nature Communications **7**, 10484 (2016).

[47] J. Kobak, A. Bogucki, T. Smoleński, M. Papaj, M. Koperski, M. Potemski, P. Kossacki, A. Golnik, and W. Pacuski, Phys. Rev. B **97**, 045305 (2018).

[48] D. E. Reiter, T. Kuhn, and V. M. Axt, Phys. Rev. Lett. **102**, 177403 (2009).

[49] M. Goryca, T. Kazimierczuk, M. Nawrocki, A. Golnik, J. A. Gaj, P. Kossacki, P. Wojnar, and G. Karczewski, Phys. Rev. Lett. **103**, 087401 (2009).

[50] C. Le Gall, L. Besombes, H. Boukari, R. Kolodka, J. Cibert, and H. Mariette, Phys. Rev. Lett. **102**, 127402 (2009).

[51] D. E. Reiter, V. M. Axt, and T. Kuhn, Phys. Rev. B **87**, 115430 (2013).

[52] A. Lafuente-Sampietro, H. Utsumi, H. Boukari, S. Kuroda, and L. Besombes, Applied Physics Letters **109**, 053103 (2016), https://doi.org/10.1063/1.4959243.

[53] W. Pacuski, T. Jakubczyk, C. Kruse, J. Kobak, T. Kazimierczuk, M. Goryca, A. Golnik, P. Kossacki, M. Wiater, P. Wojnar, G. Karczewski, T. Wojtowicz, and D. Hommel, Crystal Growth & Design **14**, 988 (2014).

[54] D. E. Reiter, T. Kuhn, and V. M. Axt, Phys. Rev. B **85**, 045308 (2012).

[55] S. Lüker, T. Kuhn, and D. E. Reiter, Phys. Rev. B **92**, 201305(R) (2015).

[56] S. Lüker, T. Kuhn, and D. E. Reiter, Phys. Rev. B **95**, 195305 (2017).

[57] S. Bounouar, C. de la Haye, M. Strauß, P. Schnauber, A. Thoma, M. Gschrey, J.-H. Schulze, A. Strittmatter, S. Rodt, and S. Reitzenstein, Applied Physics Letters **112**, 153107 (2018), https://doi.org/10.1063/1.5020242.

[58] S. Lüker, T. Kuhn, and D. E. Reiter, Phys. Rev. B **95**, 195305 (2017).

[59] M. Cosacchi, J. Wiercinski, T. Seidelmann, M. Cygorek, A. Vagov, D. E. Reiter, and V. M. Axt, Phys. Rev. Research **2**, 033489 (2020).

[60] J. K. Furdyna, Journal of Applied Physics **64**, R29 (1988), https://doi.org/10.1063/1.341700.

[61] L. Besombes, K. Kheng, L. Marsal, and H. Mariette, Phys. Rev. B **65**, 121314 (2002).

[62] Y. Léger, L. Besombes, L. Maingault, D. Ferrand, and H. Mariette, Phys. Rev. Lett. **95**, 047403 (2005).

[63] T. Jakubczyk, W. Pacuski, T. Smoleński, A. Golnik, M. Florian, F. Jahnke, C. Kruse, D. Hommel, and P. Kossacki, Applied Physics Letters **101**, 132105 (2012), https://doi.org/10.1063/1.4754078.

[64] C. Schneider, P. Gold, S. Reitzenstein, S. Höfling, and M. Kamp, Applied Physics B **122**, 19 (2016).

[65] J. McFarlane, P. A. Dalgarno, B. D. Gerardot, R. H. Hadfield, R. J. Warburton, K. Karrai, A. Badolato, and P. M. Petroff, Applied Physics Letters **94**, 093113 (2009), https://doi.org/10.1063/1.3086461.

[66] L. Besombes, K. Kheng, L. Marsal, and H. Mariette, Phys. Rev. B **63**, 155307 (2001).

[67] China Rare Metal Material Co., Ltd., "Cadmium Telluride (CdTe)," (2021), accessed: 2021-07-26.

[68] S. Lüker, T. Kuhn, and D. E. Reiter, Phys. Rev. B **96**, 245306 (2017).

[69] M. Cygorek, A. M. Barth, F. Ungar, A. Vagov, and V. M. Axt, Phys. Rev. B **96**, 201201(R) (2017).

[70] J. H. Quilter, A. J. Brash, F. Liu, M. Glässl, A. M. Barth, V. M. Axt, A. J. Ramsay, M. S. Skolnick, and A. M. Fox, Phys. Rev. Lett. **114**, 137401 (2015).

[71] S. Bounouar, M. Müller, A. M. Barth, M. Glässl, V. M. Axt, and P. Michler, Phys. Rev. B **91**, 161302 (2015).

[72] Y. Léger, L. Besombes, L. Maingault, and H. Mariette, Phys. Rev. B **76**, 045331 (2007).

[73] L. Besombes, Y. Leger, J. Bernos, H. Boukari, H. Mariette, J. P. Poizat, T. Clement, J. Fernández-Rossier, and R. Aguado, Phys. Rev. B **78**, 125324 (2008).

[74] D. E. Reiter, V. M. Axt, and T. Kuhn, physica status solidi (b) **246**, 779 (2009), https://onlinelibrary.wiley.com/doi/pdf/10.1002/pssb.200880622.

[75] J. Fernández-Rossier, Phys. Rev. B **73**, 045301 (2006).

[76] E. Jaynes and F. Cummings, Proceedings of the IEEE **51**, 89 (1963).

[77] B. W. Shore and P. L. Knight, Journal of Modern Optics **40**, 1195 (1993), https://doi.org/10.1080/09500349314551321.

[78] P. Borri, W. Langbein, S. Schneider, U. Woggon, R. L. Sellin, D. Ouyang, and D. Bimberg, Phys. Rev. Lett. **87**, 157401 (2001).

[79] B. Krummheuer, V. M. Axt, and T. Kuhn, Phys. Rev. B **65**, 195313 (2002).

[80] V. M. Axt, T. Kuhn, A. Vagov, and F. M. Peeters, Phys. Rev. B **72**, 125309 (2005).

[81] D. E. Reiter, T. Kuhn, M. Glässl, and V. M. Axt, J. Phys.: Condens. Matter **26**, 423203 (2014).

[82] D. E. Reiter, T. Kuhn, and V. M. Axt, Advances in Physics: X **4**, 1655478 (2019).

[83] P. Michler, A. Kiraz, C. Becher, W. V. Schoenfeld, P. M. Petroff, L. Zhang, E. Hu, and A. Imamoglu, Science **290**, 2282 (2000).

[84] C. Santori, M. Pelton, G. Solomon, Y. Dale, and Y. Yamamoto, Phys. Rev. Lett. **86**, 1502 (2001).

[85] C. Santori, D. Fattal, J. Vuckovic, G. S. Solomon, and Y. Yamamoto, Nature **419**, 594 (2002).

[86] Y.-M. He, Y. He, Y.-J. Wei, D. Wu, M. Atatüre, C. Schneider, S. Höfling, M. Kamp, C.-Y. Lu, and J.-W. Pan, Nat. Nanotechnol. **8**, 213 (2013).

[87] Y.-J. Wei, Y.-M. He, M.-C. Chen, Y.-N. Hu, Y. He, D. Wu, C. Schneider, M. Kamp, S. Höfling, C.-Y. Lu, and J.-W. Pan, Nano Lett. **14**, 6515 (2014).

[88] X. Ding, Y. He, Z.-C. Duan, N. Gregersen, M.-C. Chen, S. Unsleber, S. Maier, C. Schneider, M. Kamp, S. Höfling, C.-Y. Lu, and J.-W. Pan, Phys. Rev. Lett. **116**, 020401 (2016).

[89] N. Somaschi, V. Giesz, L. De Santis, J. C. Loredo, M. P. Almeida, G. Hornecker, S. L. Portalupi, T. Grange, C. Antón, J. Demory, C. Gómez, I. Sagnes, N. D. Lanzillotti-Kimura, A. Lemaítre, A. Auffeves, A. G. White, L. Lanco, and P. Senellart, Nat. Photonics **10**, 340 (2016).

[90] L. Schweickert, K. D. Jöns, K. D. Zeuner, S. F. Covre da Silva, H. Huang, T. Lettner, M. Reindl, J. Zichi, R. Trotta, A. Rastelli, and V. Zwiller, Appl. Phys. Lett. **112**, 093106 (2018).

[91] L. Hanschke, K. A. Fischer, S. Appel, D. Lukin, J. Wierzbowski, S. Sun, R. Trivedi, J. Vučković, J. J. Finley, and K. Müller, npj Quantum Inf. **4** (2018).

[92] N. Akopian, N. H. Lindner, E. Poem, Y. Berlatzky, J. Avron, D. Gershoni, B. D. Gerardot, and P. M. Petroff, Phys. Rev. Lett. **96**, 130501 (2006).

[93] R. M. Stevenson, R. J. Young, P. Atkinson, K. Cooper, D. A. Ritchie, and A. J. Shields, Nature **439**, 179 (2006).

[94] R. Hafenbrak, S. M. Ulrich, P. Michler, L. Wang, A. Rastelli, and O. G. Schmidt, New J. Phys. **9**, 315 (2007).

[95] A. Dousse, J. Suffczynski, A. Beveratos, O. Krebs, A. Lemaître, I. Sagnes, J. Bloch, P. Voisin, and P. Senellart, Nature **466**, 217 (2010).

[96] E. del Valle, New J. Phys **15**, 025019 (2013).

[97] M. Müller, S. Bounouar, K. D. Jöns, M. Glässl, and P. Michler, Nat. Photonics **8**, 224 (2014).

[98] A. Orieux, M. A. M. Versteegh, K. D. Jöns, and S. Ducci, Rep. Prog. Phys. **80**, 076001 (2017).

[99] M. Cosacchi, F. Ungar, M. Cygorek, A. Vagov, and V. M. Axt, Phys. Rev. Lett. **123**, 017403 (2019).

[100] S. E. Thomas, M. Billard, N. Coste, S. C. Wein, Priya, H. Ollivier, O. Krebs, L. Tazaïrt, A. Harouri, A. Lemaitre, I. Sagnes, C. Anton, L. Lanco, N. Somaschi, J. C. Loredo, and P. Senellart, Phys. Rev. Lett. **126**, 233601 (2021).

[101] T. Seidelmann, F. Ungar, A. M. Barth, A. Vagov, V. M. Axt, M. Cygorek, and T. Kuhn, Phys. Rev. Lett. **123**, 137401 (2019).

[102] N. Makri and D. E. Makarov, J. Chem. Phys. **102**, 4600 (1995).

[103] N. Makri and D. E. Makarov, J. Chem. Phys. **102**, 4611 (1995).

[104] A. Vagov, M. D. Croitoru, M. Glässl, V. M. Axt, and T. Kuhn, Phys. Rev. B **83**, 094303 (2011).

[105] A. M. Barth, A. Vagov, and V. M. Axt, Phys. Rev. B **94**, 125439 (2016).

Publication 4

Different types of photon entanglement from a constantly driven quantum emitter inside a cavity.

T. Seidelmann, **M. Cosacchi**, M. Cygorek, D. E. Reiter, A. Vagov, V. M. Axt.

Adv. Quantum Technol. **4**, 2000108 (2021).

DOI: 10.1002/qute.202000108

Author contributions

T. Seidelmann has designed the concept of this study, in particular, he has performed the data generation and analysis, has provided the interpretation of the results, and has written the first draft of the paper. He has moderated all discussions and revision requests of the draft, has organized the correspondence with the editor and referees, and has provided the first drafts of answers to the referees.

The author has assisted in the numerical implementation. He has discussed the results in detail with T. Seidelmann, thus contributing to the interpretation, and has contributed to revisions of the draft and the answers to the referees.

M. Cygorek, D. E. Reiter, and A. Vagov have cosupervised this work, in particular, they have participated in the discussion and interpretation of the results. They have contributed to the optimization of the presentation as well as revisions of the draft and the answers to the referees.

V. M. Axt has advised T. Seidelmann throughout his work as the main supervisor. He has obtained the funding for this work and has participated in the discussion and interpretation of the results. He has contributed to the optimization of the presentation as well as revisions of the draft and the answers to the referees.

ADVANCED QUANTUM TECHNOLOGIES
www.advquantumtech.com

Different Types of Photon Entanglement from a Constantly Driven Quantum Emitter Inside a Cavity

Tim Seidelmann, Michael Cosacchi, Moritz Cygorek, Doris E. Reiter, Alexei Vagov, and Vollrath M. Axt*

Bell states are the most prominent maximally entangled photon states. In a typical four-level emitter, like a semiconductor quantum dot, the photon states exhibit only one type of Bell state entanglement. By adding an external driving to the emitter system, also other types of Bell state entanglement are reachable without changing the polarization basis. In this work, it is shown under which conditions the different types of entanglement occur and analytical equations are given to explain these findings. Furthermore, special points are identified, where the concurrence, being a measure for the degree of entanglement, drops to zero, while the coherences between the two-photon states stay strong. Results of this work pave the way to achieve a controlled manipulation of the entanglement type in practical devices.

1. Introduction

Entanglement of quantum states is one of the most remarkable and interesting physical effects that separate the quantum mechanical from the classical world.[1,2] Entanglement can be used to test quantum mechanical principles on a fundamental level, for example, by revealing violations of Bell inequalities.[2,3] Furthermore, many fascinating and innovative applications, for example, in quantum cryptography,[4,5] quantum communication,[6,7] or quantum information processing and computing,[8–11] rely on entangled photon pairs.

T. Seidelmann, M. Cosacchi, Dr. A. Vagov, Prof. V. M. Axt
Lehrstuhl für Theoretische Physik III
Universität Bayreuth
Universitätsstraße 30, 95447 Bayreuth, Germany
E-mail: tim1.seidelmann@uni-bayreuth.de

Dr. M. Cygorek
Institute of Photonics and Quantum Sciences
Heriot-Watt University
Edinburgh EH14 4AS, UK

Dr. D. E. Reiter
Institut für Festkörpertheorie
Universität Münster
Wilhelm-Klemm-Straße 10, 48149 Münster, Germany

Dr. A. Vagov
ITMO University
Kronverksky Pr. 49, St. Petersburg 197101, Russia

The ORCID identification number(s) for the author(s) of this article can be found under https://doi.org/10.1002/qute.202000108

DOI: 10.1002/qute.202000108

The defining property of an entangled bipartite system is that its quantum mechanical state cannot be factorized into parts corresponding to the constituent subsystems. There are four prominent states, which are maximally entangled and known as the Bell states, established for two entangled photons with horizontal H polarization and vertical V polarization

$$|\Phi_{\pm}\rangle = \frac{1}{\sqrt{2}}(|HH\rangle \pm |VV\rangle), \tag{1}$$

$$|\Psi_{\pm}\rangle = \frac{1}{\sqrt{2}}(|HV\rangle \pm |VH\rangle). \tag{2}$$

In the following we will refer to these states as Φ Bell state (ΦBS) and ΨBS. To create maximally entangled states, one of the best established routes is via the cascaded relaxation in few-level systems like atoms, semiconductor quantum dots or F-centers.[12–15]

In this paper, we study under which driving conditions, a four-level emitter (FLE) placed in a microcavity produces entangled photons being either in a ΦBS or ΨBS. We demonstrate that a constantly driven FLE undergoes a sharp transition between regions of high ΦBS and ΨBS entanglement for a certain two-photon resonance. At the transition the degree of entanglement drops to zero at a special point, because the quantum state of the system becomes factorizable. We will further study all two-photon resonances revealing a rich variety of different scenarios with or without switching the type of entanglement and with or without special points of zero concurrence.

2. Generation of Entangled States

The generation procedure of entangled photons in a typical (non-driven) four-level system is as follows [see also **Figure 1** (left)]: In a first step the uppermost state is prepared, for example, by using two-photon resonant or near-resonant excitation with short coherent pulses[16–24] or adiabatic rapid passage protocols.[25–28] The excited emitter then decays into a superposition of the two intermediate states which can be reached from the uppermost state by emission of either a horizontally or vertically polarized photon. In the subsequent decay to the ground state a second photon is emitted. Since a component in the superposition that was created by emitting a photon with a given polarization gives rise to a second photon having the same polarization a ΦBS two-photon state is generated. Experiments and theoretical studies in semiconductor quantum dots demonstrated the possibility to generate ΦBS entanglement.[3,16,29–50]

The situation changes profoundly when the few-level system is continuously driven by an external laser. Then additionally, it becomes possible to create ΨBS entanglement. A possible mechanism could be that the uppermost state emits a horizontally polarized photon via one path way, is then re-excited by the laser and then emits a vertically polarized photon via the other path. Since the sequence of emission of a pair of *H, V* or *V, H* polarized photons is identical, this process results in an entangled ΨBS. Note that the states $|HV\rangle$ and $|VH\rangle$ are distinguished by the temporal order of the *H* or *V* polarized photon emissions. Indeed, Sánchez Muñoz et al. found that under specific conditions the resulting two-photon state is close to the ΨBS.[51] Here we will show that ΨBS entanglement occurs under various conditions, but also ΦBS entanglement is supported by a driven FLE system. The key is adjusting the cavity modes to two-photon transitions between the emerging laser-dressed states of the FLE. The situation of constant driving was also studied experimentally,[52,53] where the emission spectra clearly demonstrated the transition from the bare states toward the laser-dressed states.

To create entangled photon states in an optimal way, the FLE is embedded inside a microcavity. By this, the coupling to the cavity enhances the light-collection efficiency and the photon emission rate due to the Purcell effect.[42,54] Additionally, the energetic placement of the cavity modes can have a profound impact on the resulting degree of entanglement. By placing the cavity modes in resonance with a two-photon transition of the emitter[29,32,33,47,51,55] direct two-photon emission processes dominate over sequential single-photon ones. Since the direct two-photon emission is much less affected by a possible which-path information this configuration results in a high degree of entanglement of the emitted photon pairs,[32,33] at least at low temperature.[29]

3. Driven Four-Level Emitter

3.1. Bare State Picture

We consider an externally driven FLE embedded inside a microcavity, adopting the model from ref. [51]. The FLE comprises the energetic ground state $|G\rangle$ at energy 0, two degenerate intermediate states $|X_{H/V}\rangle$ with energy $\hbar\omega_X$, and the upper state $|XX\rangle$ at energy $2\hbar\omega_X - E_B$. Note that it is quite common to find the state $|XX\rangle$ not exactly at twice the energy of the single excited states, which in quantum dots is known as the biexciton binding energy.[2,55,56] Optical transitions which involve the state $|X_H\rangle$ ($|X_V\rangle$) are evoked by horizontally (vertically) polarized light. Following ref. [51], we assume the fine-structure splitting between these two intermediate states to be zero. A sketch of the FLE is shown in Figure 1 (left). The Hamiltonian of the FLE reads

$$\hat{H}_{\mathrm{FLE}} = \hbar\omega_X\left(|X_H\rangle\langle X_H| + |X_V\rangle\langle X_V|\right) + \left(2\hbar\omega_X - E_B\right)|XX\rangle\langle XX|. \tag{3}$$

The FLE is continuously driven by an external laser with frequency ω_L and driving strength Ω. The laser driving is assumed to be linearly polarized, such that the *H* and *V* polarized transitions are driven with equal strength ensuring that there is no preferred polarization and, consequently, no which-path

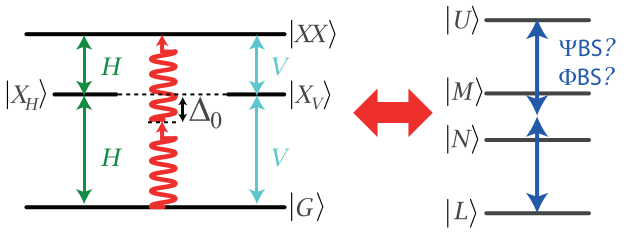

Figure 1. Left: Sketch of the FLE including optical selection rules for transitions with either horizontally (*H*) or vertically (*V*) polarized light. In addition, an external laser field excites the system. Right: Sketch of the laser-dressed states.

information is introduced by the external laser. In the frame co-rotating with the laser frequency ω_L the corresponding Hamiltonian reads

$$\hat{H}_L = \Omega\left(\hat{\sigma}_D + \hat{\sigma}_D^\dagger\right); \qquad \hat{\sigma}_D = \left(\hat{\sigma}_H + \hat{\sigma}_V\right)/\sqrt{2} \tag{4}$$

with the transition operators

$$\hat{\sigma}_H = |G\rangle\langle X_H| + |X_H\rangle\langle XX|, \tag{5a}$$

$$\hat{\sigma}_V = |G\rangle\langle X_V| + |X_V\rangle\langle XX|. \tag{5b}$$

We fix the laser frequency to $\hbar\omega_L = (2\hbar\omega_X - E_B)/2$, such that the energetic detuning between emitter transitions and laser is set to

$$\Delta_0 := \hbar\left(\omega_X - \omega_L\right) = \frac{E_B}{2}. \tag{6}$$

By this, we resonantly drive the two-photon transition between ground state $|G\rangle$ and upper state $|XX\rangle$.

The FLE is embedded inside a microcavity and coupled to two orthogonal linearly polarized cavity modes with energies $\hbar\omega_H^c$ and $\hbar\omega_V^c$, which we assume to be energetically degenerate, that is, $\omega_c := \omega_H^c = \omega_V^c$. The cavity mode is best defined with respect to the driving laser frequency (or the two-photon resonance to $|XX\rangle$) via the cavity laser detuning

$$\Delta := \hbar\left(\omega_c - \omega_L\right) = \hbar\omega_c - \left(\hbar\omega_X - \Delta_0\right). \tag{7}$$

The Hamiltonian describing the cavity modes and their interaction with the FLE reads

$$\hat{H}_c = \sum_{\ell=H,V} \Delta\hat{a}_\ell^\dagger\hat{a}_\ell + \hat{H}_{\mathrm{FLE\text{-}c}}. \tag{8}$$

In matrix form, using the basis $|XX\rangle$, $|X_H\rangle$, $|X_V\rangle$, and $|G\rangle$, the interaction Hamiltonian is given as

$$\hat{H}_{\mathrm{FLE\text{-}c}} = \begin{pmatrix} 0 & g\hat{a}_H & g\hat{a}_V & 0 \\ g\hat{a}_H^\dagger & 0 & 0 & g\hat{a}_H \\ g\hat{a}_V^\dagger & 0 & 0 & g\hat{a}_V \\ 0 & g\hat{a}_H^\dagger & g\hat{a}_V^\dagger & 0 \end{pmatrix}, \tag{9}$$

where the emitter-cavity coupling constant *g* is assumed equal for all transitions. The bosonic operators $\hat{a}_{H/V}^\dagger$ ($\hat{a}_{H/V}$) create (annihilate) one cavity photon with frequency ω_c and H/V polarization.

Note that $\hat{H}_c$ is again written in the rotating frame. From the interaction Hamiltonian we can already see that in the un-driven situation the cascade from the state $|XX\rangle$ into the state $|G\rangle$ can only go via the emission of two H or two V polarized photons and therefore can result exclusively in the generation of ΦBS entanglement.

3.2. Laser-Dressed States

The creation of entangled two-photon states is facilitated by resonant transitions between quantum states of the FLE with the emission of two photons. Further analysis of the system dynamics reveals that such transitions take place not between the original FLE basis states but between the dressed states of the laser driven FLE, obtained by diagonalizing $\hat{H}_{\mathrm{FLE}} + \hat{H}_{\mathrm{L}}$. For the diagonalization we go into a frame rotating with the laser frequency ω_{L}. The eigenenergies of the dressed states read

$$E_{\mathrm{U}} = \frac{1}{2}\left(\Delta_0 + \sqrt{\Delta_0^2 + 8\Omega^2}\right) \tag{10a}$$

$$E_{\mathrm{M}} = \Delta_0 \tag{10b}$$

$$E_{\mathrm{N}} = 0 \tag{10c}$$

$$E_{\mathrm{L}} = \frac{1}{2}\left(\Delta_0 - \sqrt{\Delta_0^2 + 8\Omega^2}\right) \tag{10d}$$

and the corresponding laser-dressed states are

$$|U\rangle = c(|G\rangle + |XX\rangle) + \tilde{c}\left(|X_{\mathrm{H}}\rangle + |X_{\mathrm{V}}\rangle\right) \tag{11a}$$

$$|M\rangle = \frac{1}{\sqrt{2}}\left(|X_{\mathrm{H}}\rangle - |X_{\mathrm{V}}\rangle\right) \tag{11b}$$

$$|N\rangle = \frac{1}{\sqrt{2}}(|G\rangle - |XX\rangle) \tag{11c}$$

$$|L\rangle = \tilde{c}(|G\rangle + |XX\rangle) - c\left(|X_{\mathrm{H}}\rangle + |X_{\mathrm{V}}\rangle\right) \tag{11d}$$

with the coefficients

$$c = \frac{2\Omega}{\sqrt{8\Omega^2 + \left(\Delta_0 + \sqrt{\Delta_0^2 + 8\Omega^2}\right)^2}}, \quad \tilde{c} = \sqrt{\frac{1}{2} - c^2}. \tag{12}$$

A sketch of the four laser-dressed states is given in Figure 1 (right panel). The dependence of the dressed state energies on the driving strength Ω is illustrated in **Figure 2**. The uppermost $|U\rangle$ and the lowest $|L\rangle$ states have contributions of all four original (bare) FLE states. In the limiting case of strong driving the contribution coefficients c and $\tilde{c}$ approach 1/2. On the other hand, the composition and energies of the intermediate dressed states $|M\rangle$ ("middle") and $|N\rangle$ ("null") are independent of Ω. In general, the laser-dressed states and the transition energies between them are functions of Ω. Therefore, also the cavity frequency associated with a two-photon resonance between two given dressed states depends on the driving strength, the only exception being the resonance between the states $|M\rangle$ and $|N\rangle$.

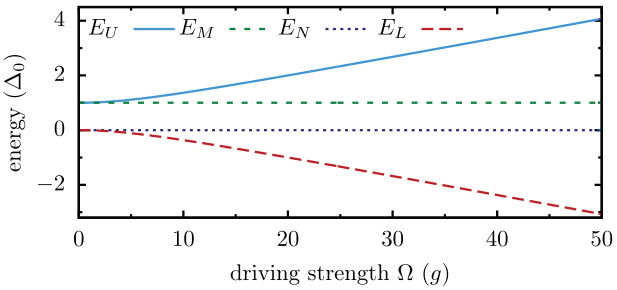

Figure 2. Energies of the laser dressed states (in the units of the emitter-laser detuning Δ_0) as a function of the driving strength Ω (in the units of the emitter-cavity coupling strength g).

The Hamiltonian describing the coupling to the cavity also changes profoundly by using the dressed state basis and now reads in the basis $|U\rangle$, $|M\rangle$, $|N\rangle$, $|L\rangle$

$$\hat{H}_{\mathrm{DS\text{-}c}} = g\begin{pmatrix} 2\sqrt{2}c\tilde{c}\,\hat{a}_{\mathrm{D}}^\dagger & c\,\hat{a}_{\mathrm{A}}^\dagger & -\tilde{c}\,\hat{a}_{\mathrm{D}}^\dagger & \sqrt{2}(\tilde{c}^2 - c^2)\hat{a}_{\mathrm{D}}^\dagger \\ c\,\hat{a}_{\mathrm{A}}^\dagger & 0 & \frac{-1}{\sqrt{2}}\hat{a}_{\mathrm{A}}^\dagger & \tilde{c}\,\hat{a}_{\mathrm{A}}^\dagger \\ \tilde{c}\,\hat{a}_{\mathrm{D}}^\dagger & \frac{1}{\sqrt{2}}\hat{a}_{\mathrm{A}}^\dagger & 0 & -c\,\hat{a}_{\mathrm{D}}^\dagger \\ \sqrt{2}(\tilde{c}^2 - c^2)\hat{a}_{\mathrm{D}}^\dagger & \tilde{c}\,\hat{a}_{\mathrm{A}}^\dagger & c\,\hat{a}_{\mathrm{D}}^\dagger & -2\sqrt{2}c\tilde{c}\,\hat{a}_{\mathrm{D}}^\dagger \end{pmatrix} + c.c. \tag{13}$$

with $\hat{a}_{\mathrm{D}}^\dagger = (\hat{a}_{\mathrm{H}}^\dagger + \hat{a}_{\mathrm{V}}^\dagger)/\sqrt{2}$ and $\hat{a}_{\mathrm{A}}^\dagger = (\hat{a}_{\mathrm{H}}^\dagger - \hat{a}_{\mathrm{V}}^\dagger)/\sqrt{2}$ being the creation operators in the diagonal and anti-diagonal polarization, respectively.

One notes that the two-photon transitions between the dressed states can follow different pathways that connect those states. Considering as an example the transition from $|U\rangle$ to $|L\rangle$, one path is to emit two photons with anti-diagonal polarization A via the intermediate state $|M\rangle$, while another path is a self interaction within $|U\rangle$ and then a direct transition to $|L\rangle$ via emission of two diagonally D-polarized photons. This already indicates that due to the constant optical driving it is not clear a priori, which entanglement type occurs. We will show below that new types of entanglement become possible and analyze their respective strength.

3.3. Cavity Losses and Radiative Decay

To account for cavity losses and radiative decay, present in every FLE-cavity system, we introduce Lindblad-type operators

$$\mathcal{L}_{\hat{O},\Gamma}\,\hat{\rho} = \frac{\Gamma}{2}\left(2\hat{O}\hat{\rho}\hat{O}^\dagger - \hat{\rho}\hat{O}^\dagger\hat{O} - \hat{O}^\dagger\hat{O}\hat{\rho}\right), \tag{14}$$

where $\hat{O}$ is the system operator associated with a loss process with corresponding loss rate Γ in the bare state system. The dynamics of the statistical operator of the system $\hat{\rho}$ is then determined by the Liouville-von Neumann equation

$$\frac{\mathrm{d}}{\mathrm{d}t}\hat{\rho} = \mathcal{L}\hat{\rho} := -\frac{i}{\hbar}\left[\hat{H}, \hat{\rho}\right] + \sum_{\ell=H,V}\left\{\mathcal{L}_{\hat{a}_\ell,\kappa} + \mathcal{L}_{|G\rangle\langle X_\ell|,\gamma} + \mathcal{L}_{|X_\ell\rangle\langle XX|,\gamma}\right\}\hat{\rho}, \tag{15}$$

Table 1. Fixed system parameters used in the calculations.

Parameter		Value
Emitter-cavity coupling strength	g	0.051 meV
Detuning	Δ_0	$20 \times g = 1.02$ meV
Cavity loss rate	κ	$0.1 \times g/\hbar \approx 7.8$ ns^{-1}
Radiative decay rate	γ	$0.01 \times g/\hbar \approx 0.78$ ns^{-1}

where $[\cdot,\cdot]$ denotes the commutator, κ is the cavity loss rate, and γ the radiative decay rate. The complete system Hamiltonian $\hat{H}$ includes all contributions discussed in Section 3.1. The system is assumed initially in the ground state $|G\rangle$ without any cavity photons. Note that we performed all numerical calculations in the rotating frame with the laser frequency ω_L and use the bare state system, while for the interpretation the dressed state picture is advantageous.

The parameter values used in our simulations are listed in **Table 1**, where we followed ref. [51]. The frequency of the cavity mode is taken to $\hbar\omega_c = 1.5$ eV. The adopted parameter values correspond to a high quality cavity resonator with $Q = 1.5 \times 10^5$.

4. Photon Entanglement

4.1. Two-Photon Density Matrix

The basis for quantifying the degree of entanglement is the determination of the two-photon density matrix ρ^{2p}. Experimentally, ρ^{2p} can be reconstructed using methods of quantum state tomography,[57] a technique based on polarization-resolved two-time coincidence measurements. The detected signals are proportional to the two-time correlation functions

$$G^{(2)}_{jk,lm}(t,\tau) = \left\langle \hat{a}^\dagger_j(t)\hat{a}^\dagger_k(t+\tau)\hat{a}_m(t+\tau)\hat{a}_l(t)\right\rangle, \tag{16}$$

where $\{j,k,l,m\} \in \{H,V\}$, t is the real time when the first photon is detected, and τ the delay time between the detection of the first and the second photon. Note that in experiments one typically measures photons that have already left the cavity. However, considering the out-coupling of light out of the cavity to be a Markovian process, Equation (16) can also describe $G^{(2)}_{jk,lm}(t,\tau)$ measured outside the cavity.[10,30]

In experiments data is typically averaged over finite real time and delay time windows. Thus, the experimentally reconstructed two-photon density matrix is calculated as [30,51]

$$\rho^{2p}_{jk,lm}(\tau) = \frac{\overline{G}^{(2)}_{jk,lm}(\tau)}{\mathrm{Tr}\left\{\overline{G}^{(2)}(\tau)\right\}}, \tag{17}$$

where $\overline{G}^{(2)}$ is the time-averaged correlation with

$$\overline{G}^{(2)}_{jk,lm}(\tau) = \frac{1}{\Delta t\,\tau}\int_{t_0}^{t_0+\Delta t} \mathrm{d}t \int_0^\tau \mathrm{d}\tau' G^{(2)}_{jk,lm}(t,\tau'). \tag{18}$$

Here, τ (Δt) is the delay time (real time) window used in the coincidence measurement and t_0 is its starting time. The trace $\mathrm{Tr}\{\cdot\}$ is introduced for normalization. For simplicity we refer to ρ^{2p} as the two-photon density matrix in the following.

Throughout this work we calculate the two-photon density matrix for the system that reached its steady state so that the t-average is independent of t_0 and Δt. The steady state of the system $\hat{\rho}_s$ is defined by $\frac{\mathrm{d}}{\mathrm{d}t}\hat{\rho}_s = \mathcal{L}\hat{\rho}_s = 0$. This state is obtained numerically by letting the system evolve in time until its density matrix becomes stationary. We will further set $\tau = 50$ ps, which is a realistic value for the delay time window used in experiment.[58] More details on the calculation of the two-time correlation functions for systems including Markovian loss processes can be found in ref. [60].

4.2. Concurrence

Using the two-photon density matrix we determine the corresponding concurrence C,[59] which is a widely accepted measure for the degree of entanglement of a bipartite system. The concurrence is calculated from a given two-photon density matrix ρ^{2p} according to [47,57,59]

$$C = \max\left\{0, \sqrt{\lambda_1} - \sqrt{\lambda_2} - \sqrt{\lambda_3} - \sqrt{\lambda_4}\right\} \tag{19}$$

where λ_j are the (real and positive) eigenvalues in decreasing order, $\lambda_1 \geq \lambda_2 \geq \lambda_3 \geq \lambda_4$, of the matrix

$$M = \rho^{2p}\, T\, (\rho^{2p})^*\, T, \tag{20}$$

where T is an anti-diagonal matrix of rank 4 with elements $\{-1,1,1,-1\}$ and $(\rho^{2p})^*$ is the complex conjugated two-photon density matrix. In the standard situation without driving, where only a ΦBS $|\Phi_\pm\rangle$ can be generated, the full expression for the concurrence reduces to $C = 2|\rho^{2p}_{HH,VV}|$. Thus, the degree of entanglement is closely related to the corresponding coherences in the two-photon density matrix. Note that like the two-photon density matrix $\rho^{2p}(\tau)$ also the concurrence $C(\tau)$ depends on the measurement window τ. A finite delay time window τ is necessary for the detection of ΨBS entanglement since the two contributions that build up $|\Psi_+\rangle$ in Equation (2) can only be distinguished if the two photons are detected at different times.[51]

For the numerical calculation of the concurrence we use the following procedure: First, following ref. [60], the averaged two-time photon correlation $\overline{G}^{(2)}$ is calculated. This quantity is then used to obtain the time-averaged two-photon density matrix in Equation (17). Finally from the two-photon density matrix the concurrence is determined according to Equation (19). Note that we do not use any further approximations in the calculation of $\overline{G}^{(2)}$.

5. Two-Photon Transition Between Upper and Lower Dressed State

The emission of entangled two-photon states is associated with two photon transitions between the dressed FLE states. The dressed FLE states feature two-photon emissions, which are

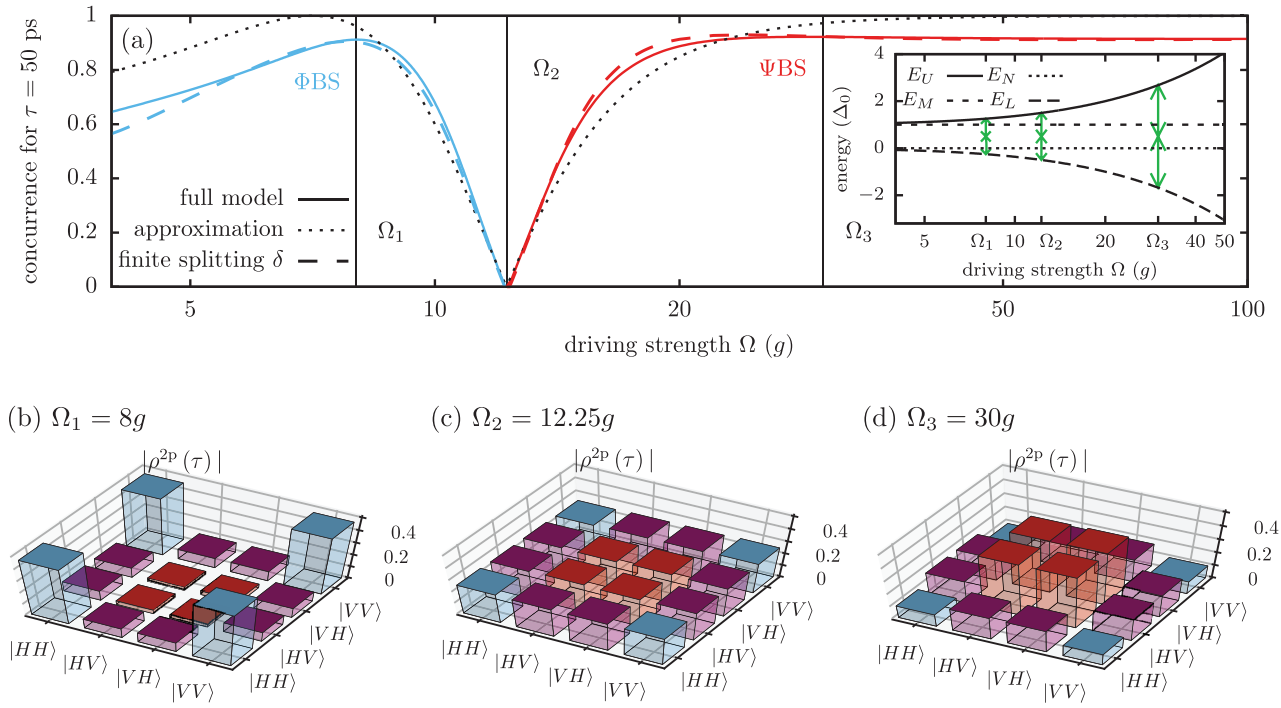

Figure 3. a) Concurrence as function of the laser driving strength Ω for the full model (solid line), the analytic approximation $C(r)$ presented in Equation (29) (dotted line), and with a finite fine-structure splitting $\delta = 0.1\Delta_0$ (dashed line). Inset: Dressed state energies as a function of the driving strength and the two-photon resonant cavity modes (green arrows) for three selected Ω values. b–d) Absolute value of the two-photon density matrix $|\rho^{2p}(\tau)|$ for driving strength (b) $\Omega_1 = 8 \times g$, (c) $\Omega_2 = 12.25 \times g$, and (d) $\Omega_3 = 30 \times g$ (indicated by vertical lines in (a)).

largest every time the cavity frequency is tuned in resonance with a possible two-photon transition, that is, when twice the photon energy (here Δ) is equal to the transition energy between the dressed state pairs. Therefore, the analysis is focused on these resonant situations.

We start our analysis with the case where the cavity photons are in resonance with the transition between the states $|U\rangle$ and $|L\rangle$, that is, the cavity frequency is always tuned such that

$$\Delta = \frac{E_U - E_L}{2} = \frac{1}{2}\sqrt{\Delta_0^2 + 8\Omega^2}. \tag{21}$$

Notice, that keeping this condition requires the cavity frequency ω_c to change with the driving strength Ω. This resonance for a driven FLE was considered in earlier works,[51] where a possibility to achieve a high degree of ΨBS entanglement was demonstrated. Here we demonstrate that ΨBS entanglement is not the only type of two-photon entanglement that can be obtained. It will be shown that by varying the driving strength (while keeping the system at the considered resonance) the FLE can reach the domain of ΦBS entanglement, separated from that of the ΨBS by a special critical point of zero concurrence.

5.1. Transition Between ΦBS and ΨBS Entanglement

The concurrence as a function of the driving strength Ω is shown in **Figure 3**a, where the inset illustrates the resonance in question. In full agreement with earlier calculations[51] one observes ΨBS entanglement when the driving is strong. However, when the driving strength is lowered the entanglement changes its type to ΦBS entanglement. A sharp transition between the two types occurs at a special critical point $\Omega \approx 12.25 \times g$ where the concurrence is exactly zero. The ΦBS entanglement obtained for weak driving reflects the fact that for small Ω the system approaches the undriven case. Recalling that ΨBS entanglement has been found in ref. [51] for higher Ω, it is clear that a transition has to take place in between.

More insight into the entanglement change is obtained by calculating the corresponding two-photon density matrices as presented in Figure 3b for the driving strength $\Omega_1 = 8 \times g$ and Figure 3d $\Omega_3 = 30 \times g$. At Ω_1 the occupations of the states $|HH\rangle$ and $|VV\rangle$ and their coherence clearly dominate over the remaining elements representing ΦBS entanglement. A very different behavior is found at $\Omega_3 = 30 \times g$, where the occupations of the states $|HV\rangle$ and $|VH\rangle$ and the corresponding coherences exhibit the highest values and, consequently, are associated with ΨBS entanglement.

Let us now focus on the special point at $\Omega_2 = 12.25 \times g$. The two-photon density matrix at the special point, shown in Figure 3c, reveals that the concurrence does not vanish because of the absence of coherences. On the contrary, all coherences are close to their maximal possible value of about 0.25. Further analysis reveals that the corresponding two-photon state is

$$\begin{aligned} |\psi_{sp}\rangle &= \frac{1}{2}(|HH\rangle - |HV\rangle - |VH\rangle + |VV\rangle) \\ &= \frac{1}{\sqrt{2}}(|H_1\rangle - |V_1\rangle)\frac{1}{\sqrt{2}}(|H_2\rangle - |V_2\rangle). \end{aligned} \tag{22}$$

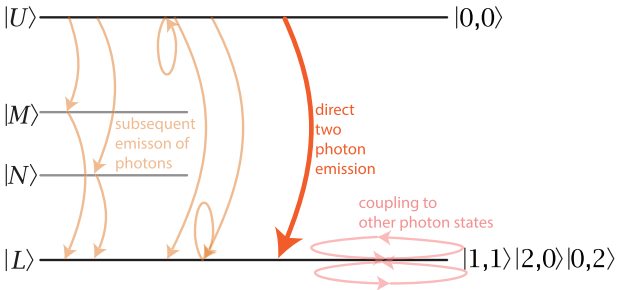

Figure 4. Schematic depiction of the possible transitions connecting $|U, 0, 0\rangle$ to the two-photon states $|L, 1, 1\rangle$, $|L, 2, 0\rangle$, and $|L, 0, 2\rangle$. All but the direct two-photon emission process (bold orange arrow) are eliminated in the Schrieffer–Wolff transformation.

Remarkably, this is a pure state and $|\psi_{sp}\rangle$ can be factorized into a product of two one-photon states describing the first and second detected photon, respectively (indicated by 1 and 2). Since $|\psi_{sp}\rangle$ can be factorized, it is not entangled and, thus, the concurrence vanishes at this point. Therefore, instead of a direct transition from high ΦBS to high ΨBS entanglement the system passes through this special point with vanishing degree of entanglement.

We note that the special point occurs at a distinct resonance condition. Beside the two-photon transition between the two outermost dressed states, also the one-photon process between the intermediate states $|M\rangle$ and $|N\rangle$ becomes resonant.

5.2. Effective Hamiltonian of the System at the Resonance

In order to understand the underlying physics of the crossover between the entanglement types we derive an effective Hamiltonian that describes the most relevant transition processes involving the $|U\rangle$ and $|L\rangle$ states. To be more specific, we account only for the uppermost state without photons $|U, 0, 0\rangle$ and the lowest states with two photons $|L, 1, 1\rangle$, $|L, 2, 0\rangle$, and $|L, 0, 2\rangle$. Here, $|\chi, n_H, n_V\rangle$ is the product state of $|\chi\rangle \in \{|U\rangle, |M\rangle, |N\rangle, |L\rangle\}$ and the photon number state for H and V polarization.

Besides the direct two-photon transitions, there are several other possibilities to go from the initial to the final states. One example are subsequent one photon transitions, either going via one of the intermediate states or by a self-interaction and then a one-photon process. Also, from the final states, a sequential photon emission and absorption (or the other way around) can take place. These processes are depicted in **Figure 4**. Therefore, the states mentioned above are coupled to a bunch of other states, namely the one-photon states $|\chi, 1, 0\rangle$, $|\chi, 0, 1\rangle$ and the three-photon states $|\chi, 3, 0\rangle$, $|\chi, 2, 1\rangle$, $|\chi, 1, 2\rangle$, and $|\chi, 0, 3\rangle$ (with $\chi \in \{U, M, N, L\}$), while the latter can be reached in sequential emission/absorption processes.

Using a Schrieffer–Wolff transformation, it is now possible to encode these transitions into a single matrix, acting only within the basis spanned by the direct two-photon transitions, that is, $|U, 0, 0\rangle$, $|L, 1, 1\rangle$, $|L, 2, 0\rangle$, and $|L, 0, 2\rangle$.[61,62] A Schrieffer–Wolff transformation thereby performs a block-diagonalization, which decouples the desired states from the rest. This is reasonable, because the removed states are strongly off-resonant in this situation and, thus, represent a small perturbation. More details on the Schrieffer–Wolff transformation can be found in Appendix A.

After the Schrieffer–Wolff transformation, which is treated within the photon number states, we afterward perform additionally a basis transformation to rotate the system partially into the Bell basis with $\{|U, 0, 0\rangle, |L, 1, 1\rangle, |L, \Phi_+\rangle, |L, \Phi_-\rangle\}$. In this representation $|L, 1, 1\rangle$ corresponds to the possibility of ΨBS entanglement, where two photons are generated such that one is H- and the other V-polarized. However, without further analysis, we cannot distinguish between $\Psi_\pm$BS entanglement. The effective Schrieffer–Wolff Hamiltonian is then given by

$$\hat{H}^{(2)}_{UL} = g^2 \begin{pmatrix} \delta^{UL} & \gamma_1^{UL} & -\gamma_2^{UL} & 0 \\ \gamma_1^{UL} & -\delta^{UL} & \alpha^{UL} & 0 \\ -\gamma_2^{UL} & \alpha^{UL} & -\delta^{UL} & 0 \\ 0 & 0 & 0 & -\delta^{UL} \end{pmatrix} \tag{23}$$

with

$$\begin{aligned} \delta^{UL} &= \left(\tilde{c}^2 - c^2\right)\left(\frac{2}{\Delta_0} + \frac{4}{\Delta_{UL}}\right) \\ \gamma_1^{UL} &= 4c\tilde{c}\frac{1}{\Delta_0} - 16c\tilde{c}\left(\tilde{c}^2 - c^2\right)\frac{1}{\Delta_{UL}} \\ \gamma_2^{UL} &= 16c\tilde{c}\left(\tilde{c}^2 - c^2\right)\frac{1}{\Delta_{UL}} \\ \alpha^{UL} &= \frac{1}{\Delta_0} - \left(1 - 16c^2\tilde{c}^2\right)\frac{1}{\Delta_{UL}}, \end{aligned} \tag{24}$$

where $\Delta_{UL} = E_U - E_L$. The given expressions contain only the most important contributions. The full expressions can be found in Appendix A.1. It is interesting to note that the coefficients $\gamma^{UL}_{1/2}$ stem from the subsequent emission of two single photons (faded orange arrows in Figure 4) and simultaneous two-photon emission, while α^{UL} accounts for the fact that from the two photon states, coupling to higher (lower) photon states can take place and therefore couple different types of two-photon states (faded red arrows in Figure 4). An example for the latter case is the coupling of $|L, 2, 0\rangle \rightarrow |L, 2, 1\rangle$, followed by a photon number reduction via $|L, 2, 1\rangle \rightarrow |L, 1, 1\rangle$ illustrating why different two-photon states are coupled.

From this Hamiltonian, we can now deduce which type of entanglement is created: First of all we find that the state $|L, \Phi_-\rangle$ is decoupled, such that we see that photons with this type of entanglement are not created. In contrast, the initial state $|U, 0, 0\rangle$ is coupled to the $|L, \Phi_+\rangle$ state via γ_2^{UL} and to the state $|L, 1, 1\rangle$ via γ_1^{UL}. Therefore in principle both ΦBS and ΨBS entanglement can be created. The different types of entangled states are coupled via the coefficient α^{UL}, however, we will for now neglect this coupling (see discussion at the end of the next section). Which type of entanglement dominates depends on the ratio

$$r = \frac{\gamma_1^{UL}}{\gamma_2^{UL}} = 4\left(\frac{\Omega}{\Delta_0}\right)^2 - \frac{1}{2}. \tag{25}$$

This means, we obtain preferably ΦBS entanglement, when $\gamma_2^{UL} > \gamma_1^{UL}$ (or $|r| < 1$), and preferably ΨBS entanglement if

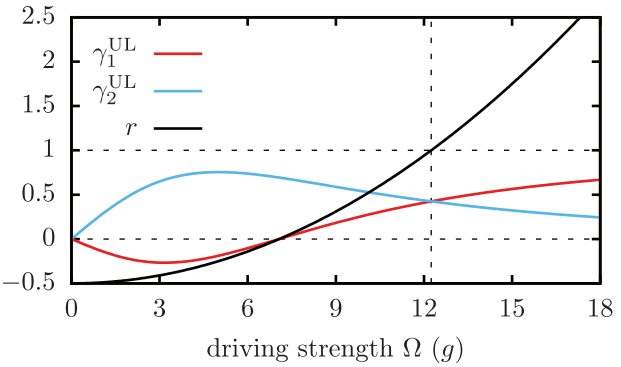

Figure 5. Effective coupling constants γ_1^{UL} and γ_2^{UL} and the ratio $r = \gamma_1^{UL}/\gamma_2^{UL}$ as function of the driving strength Ω.

$\gamma_2^{UL} < \gamma_1^{UL}$ (or $|r| > 1$). **Figure 5** displays the ratio r as well as the couplings γ_1^{UL} and γ_2^{UL} as a function of the driving strength Ω. Indeed, $r = 1$ corresponds to $\Omega_{sp} = \sqrt{3/8}\Delta_0$ and we obtain our special point, when both types of entanglement are occurring with equal weight and we have zero concurrence since their superposition results in a factorizable state.

5.3. Approximate Two-Photon Density Matrix

Further insight is obtained by calculating the two-photon density matrix assuming the delay window τ is small and can be neglected so that

$$\rho^{2p}_{jk,lm}(\tau) \approx \mathcal{N}\mathrm{Tr}\left\{\hat{a}_m\,\hat{a}_l\,\hat{\rho}_s\,\hat{a}_j^\dagger\,\hat{a}_k^\dagger\right\} \tag{26}$$

where $\mathcal{N}$ is a normalization constant and $\hat{\rho}_s$ describes the steady state of the system. Note that only states with at least two photons inside the cavity contribute to the two-photon density matrix. Neglecting the coupling α^{UL} in the effective Hamiltonian (23) and performing another basis transformation, one finds that the only two-photon state coupled to $|U,0,0\rangle$ is

$$|\psi_s\rangle = \frac{1}{\sqrt{\left(\gamma_1^{UL}\right)^2 + \left(\gamma_2^{UL}\right)^2}}\left(\gamma_1^{UL}|L,1,1\rangle - \gamma_2^{UL}|L,\Phi_+\rangle\right). \tag{27}$$

Therefore, in this approximation, also the contribution to the steady state which contains two photons inside the cavity should be proportional to $|\psi_s\rangle$. Consequently, the approximate normalized two-photon density matrix can be calculated by inserting $\rho_s = |\psi_s\rangle\langle\psi_s|$ into Equation (26) which results in

$$\rho^{2p}_{approx} = \frac{1}{2(1+r^2)}\begin{pmatrix} 1 & -r & -r & 1 \\ -r & r^2 & r^2 & -r \\ -r & r^2 & r^2 & -r \\ 1 & -r & -r & 1 \end{pmatrix}, \tag{28}$$

For this simplified density matrix, we can analytically calculate the concurrence C [Equation (19)] to

$$C(r) = \frac{|1-r^2|}{1+r^2}. \tag{29}$$

In Figure 3a the approximate result $C(r)$ is included as a dotted line. The approximate solution agrees quite well with the numerical results. This underlines the idea that the concurrence depends essentially on the ratio r. Also for the approximate solution we have the special point at $r = 1$ and the regions of high entanglement and the corresponding type of entanglement can be directly extracted from the analytical result. Below the special point we have $|r| < 1$, therefore, $r^2 < |r|$, resulting in a density matrix of ΦBS entanglement. The maximum concurrence value appears around $\Omega = \frac{1}{2\sqrt{2}}\Delta_0 \approx 7.1 \times g$ where the ratio r passes through zero. Above Ω_{sp}, we have $r \geq 1$ and $r^2 > r$. Thus, in this regime one obtains ΨBS entanglement in the two-photon density matrix.

We now discuss the deviations between the numerical and the approximate result for the concurrence. One obvious reason for the difference is the obmission of the coupling between the two-photon states (via one- or three-photon states), as indicated by α^{UL} in Equation (23). This coupling mixes ΦBS and ΨBS, such that in the full model, the total obtained concurrence is reduced. Nonetheless, neglecting α^{UL} for the analysis is reasonable, when taking the cavity losses into account. By analyzing the values of α^{UL} and γ^{UL}, we find that these are always smaller than the cavity loss rate κ. This means that the losses relax the system before the coupling between the different photon states becomes efficient. Another reason for the deviations is that for low driving strength values, other transitions between the laser-dressed states besides the discussed direct two-photon one become important as they get closer to resonance.

5.4. Influence of a Finite Fine-Structure Splitting

So far only the situation of degenerate intermediate bare states $|X_H\rangle$ and $|X_V\rangle$ has been analyzed. However, an often discussed asymmetry in the system is a possible finite fine-structure splitting δ between these two intermediate states.[29,32,41,45,46] A finite fine-structure splitting introduces which-path information into the system and can, therefore, result in a reduced degree of entanglement.[3,29,32]

In Figure 3a the influence of a finite splitting δ on the concurrence is shown, where $\delta = \hbar\omega_{X_H} - \hbar\omega_{X_V}$ is the difference between the energies of the horizontally and vertically polarized intermediate state $\hbar\omega_{X_{H/V}} = \hbar\omega_X \pm \delta/2$. Even in the case of a rather large splitting $\delta = 0.1\Delta_0$, the resulting degree of entanglement as measured by the concurrence is only weakly influenced by the fine-structure splitting. Furthermore, all main features discussed before remain unchanged: A sharp transition between regions of high ΦBS and ΨBS entanglement takes place at a special point of vanishing concurrence. Note that the chosen parameters reflect the often realized situation where the fine-structure splitting is one order of magnitude smaller than the binding energy.[3,16,41,45] Thus, the energies of the laser-dressed states and their character do not change significantly. Therefore, also the resonance conditions and optical selection rules stay roughly the same leading to very similar results. Consequently, the resulting two-photon state and its degree of entanglement are robust against a possible fine-structure splitting.

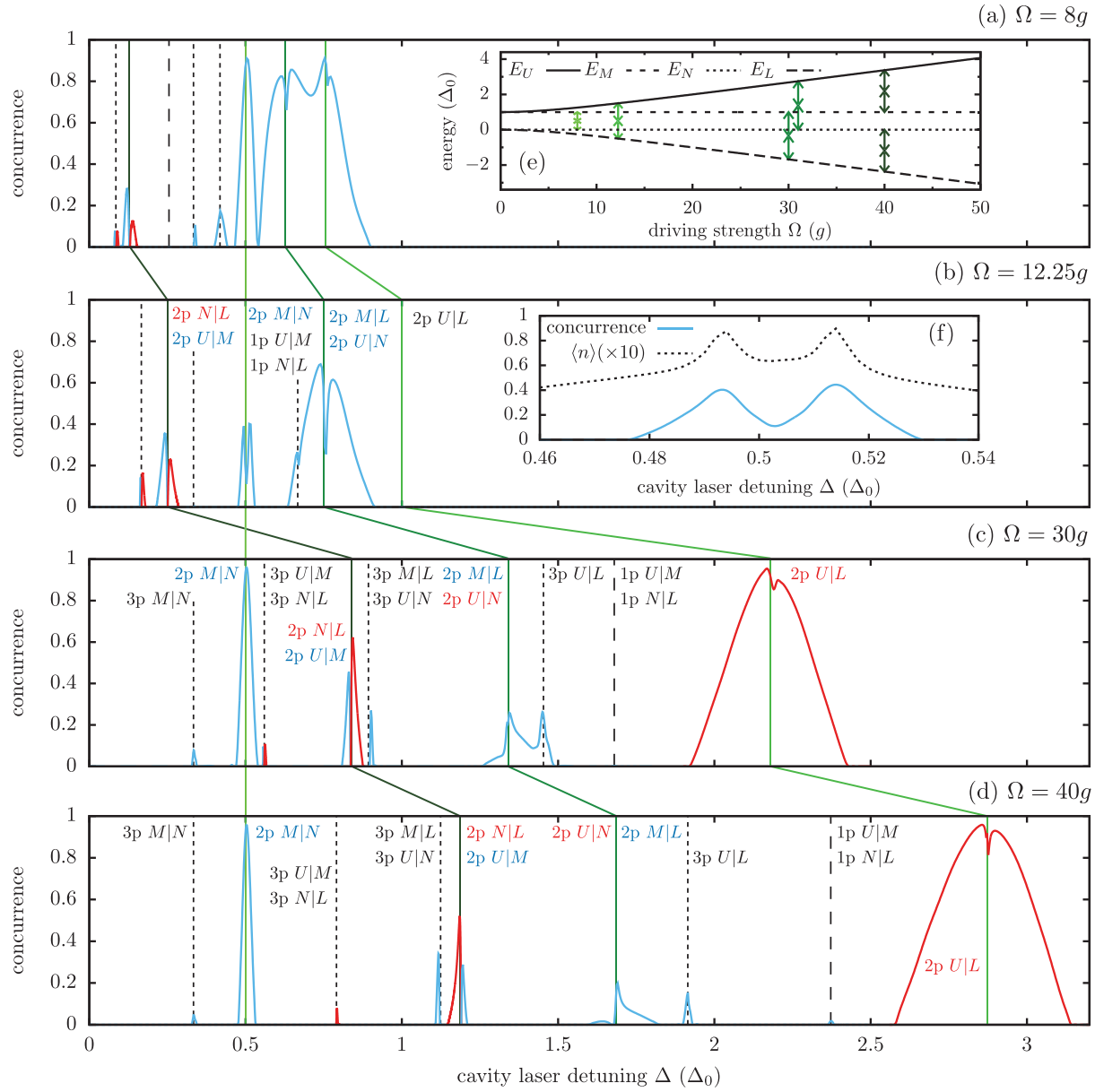

Figure 6. Concurrence as function of the cavity laser detuning Δ for fixed values of the external laser driving a) $\Omega = 8 \times g$, b) $\Omega = 12.25 \times g$, c) $\Omega = 30 \times g$, and d) $\Omega = 40 \times g$. The color code indicates the type of entanglement: blue curves symbolize ΦBS and red curves are ΨBS entanglement. The vertical lines mark the position of photon resonances labeled by $np\ \chi_1|\chi_2$. e) Energy of the laser-dressed states as a function of the driving strength Ω marking the four selected two-photon resonance conditions which correspond to the two-photon resonances of the same color in panels (a)–(d). f) Concurrence and mean photon number $\langle n \rangle$ for $\Omega = 12.25 \times g$ in the vicinity of $\Delta = \Delta_{MN}/2$.

6. Entanglement at the Other Two-Photon Transitions

Having discussed the transition between $|U\rangle$ and $|L\rangle$, we now want to examine the behavior of the other two-photon resonances. In particular, there are three other two-photon resonances matching the transitions between the corresponding dressed states (given by $\Delta_{\chi_1\chi_2} = E_{\chi_1} - E_{\chi_2}$) in the system at

$$\frac{\Delta_{UM}}{2} = \frac{\Delta_{NL}}{2} = \frac{1}{4}\left(\sqrt{\Delta_0^2 + 8\Omega^2} - \Delta_0\right)$$

$$\frac{\Delta_{UN}}{2} = \frac{\Delta_{ML}}{2} = \frac{1}{4}\left(\sqrt{\Delta_0^2 + 8\Omega^2} + \Delta_0\right)$$

$$\frac{\Delta_{MN}}{2} = \frac{\Delta_0}{2}. \tag{30}$$

Therefore, to sweep through the respective resonances, we now fix the driving strength and vary the cavity laser detuning Δ. The corresponding concurrence is calculated and the results are shown in **Figure 6** for four different driving strength values $\Omega = 8 \times g$, $12.25 \times g$, $30 \times g$, and $40 \times g$.

The type of entanglement is encoded in the color: Blue lines are for ΦBS and red lines for ΨBS entanglement. On first sight, we find that both types of entanglement occur when we vary Δ. In addition to a strong concurrence at the four two-photon resonances, we find several other cavity detuning values with non-vanishing concurrence. We can attribute these to the one-photon resonances $U|M$ and $N|L$ and several three-photon resonances, which occur between the respective states. Accordingly, we have labeled all resonances by np $\chi_1|\chi_2$, which denotes the n-photon resonances between the laser-dressed states $|\chi_1\rangle$ and $|\chi_2\rangle$.

Figure 6e shows the dressed states as a function of the driving strength and we used colored arrows to mark the different two-photon resonances. The same colors are used to indicate the position of the two-photon resonances in Figure 6a–d. Before we will go through the two-photon resonances one-by-one (note that we already discussed the 2p $U|L$ resonance), let us briefly remark some general findings:

While some n-photon transitions are always associated with the same type of entanglement, others can change from one to the other. This change may happen as a result of changing the cavity laser detuning or the driving strength. Furthermore, in between some of the resonance conditions the concurrence value stays at a finite level, whereas it passes through zero in other situations. A striking feature is the appearance of a second special point with vanishing concurrence between regions of high entanglement when the cavity laser detuning is approximately $\Delta \approx \Delta_{\mathrm{UM}}/2 = \Delta_{\mathrm{NL}}/2$, which we will discuss in detail in Section 6.2.

Next, we will go through the two-photon resonances one-by-one. For each two-photon resonance we perform a Schrieffer–Wolff transformation, followed by a rotation of the states, such that each Hamiltonian in the following is given in the basis

$$\{|\chi_1, 0, 0\rangle, |\chi_2, 1, 1\rangle, |\chi_2, \Phi_+\rangle, |\chi_2, \Phi_-\rangle\} \tag{31}$$

with χ_1 being the higher energy state and χ_2 being the lower energy state of the 2p $\chi_1|\chi_2$ resonance. More details on the Schrieffer–Wolff transformation are given in Appendix A.

6.1. Two-Photon $M|N$ Resonance

We start by looking at 2p $M|N$, which is the only two-photon transition for which the resonance condition does not depend on the driving strength. The corresponding transitions are marked by a light green line in Figure 6. At this resonance the concurrence always displays ΦBS entanglement. While the concurrence is mostly maximal at the resonance, we find a decrease in strength at the maximum at $\Omega = 12.25 \times g$.

We use the Schrieffer–Wolff transformation to obtain the effective Hamiltonian

$$\hat{H}^{(2)}_{\mathrm{MN}} = g^2 \begin{pmatrix} \delta^{\mathrm{MN}} & 0 & 0 & \gamma_2^{\mathrm{MN}} \\ 0 & -\delta^{\mathrm{MN}} & -\delta^{\mathrm{MN}} & 0 \\ 0 & -\delta^{\mathrm{MN}} & -\delta^{\mathrm{MN}} & 0 \\ \gamma_2^{\mathrm{MN}} & 0 & 0 & -\delta^{\mathrm{MN}} \end{pmatrix} \tag{32}$$

with

$$\delta^{\mathrm{MN}} = 2\left(\tilde{c}^2 - c^2\right)\frac{1}{\Delta_{\mathrm{UL}}}$$

$$\gamma_2^{\mathrm{MN}} = -4\, c\, \tilde{c}\, \frac{1}{\Delta_{\mathrm{UL}}}. \tag{33}$$

Note that these are shortened expressions and the full expressions can be found in Appendix A.2. From the Hamiltonian, it is obvious that the initial state is only coupled to the final state $|N, \Phi_-\rangle$, while the other two-photon states become uncoupled. This is in agreement with Figure 6, where we only find ΦBS entanglement at the 2p $M|N$ resonance.

The smaller height in concurrence at $\Omega = 12.25 \times g$ (see also Figure 6f), can be traced back to the occurrence of several resonance conditions at the same driving strength, in particular the one-photon transitions 1p $U|M$ and 1p $N|L$. This is confirmed by looking at the mean photon number $\langle n\rangle = \langle \hat{a}_{\mathrm{H}}^\dagger \hat{a}_{\mathrm{H}} + \hat{a}_{\mathrm{V}}^\dagger \hat{a}_{\mathrm{V}}\rangle$ as displayed in Figure 6f. The alignment of several resonance conditions causes the peak to split into two separate resonances, as indicated by the mean photon number. Due to the additional one-photon resonances three-photon states with all four possible combinations of polarized photons gain a noticeable population and the extracted (two-photon) coherence $\rho^{\mathrm{2p}}_{\mathrm{HH,VV}}$ reaches only about half the value of the occupations $\rho^{\mathrm{2p}}_{\mathrm{HH,HH}}$ and $\rho^{\mathrm{2p}}_{\mathrm{VV,VV}}$. As a result, the degree of entanglement is strongly reduced.

6.2. Two-Photon $U|M$ and Two-Photon $N|L$ Resonance

Next we consider the two-photon resonances between the laser-dressed states $|U\rangle$ and $|M\rangle$, and between $|N\rangle$ and $|L\rangle$, which have the same energy. In Figure 6, these resonances are indicated by a dark green line. From Figure 6, we see that here always a sharp transition between ΦBS and ΨBS entanglement takes place. This is highlighted in **Figure 7**a, which presents a closer look at this resonance condition for $\Omega = 30 \times g$. Figure 7b–d display the corresponding two-photon density matrices for three selected detuning values. With rising cavity laser detuning the entangled state created inside the cavity changes from ΦBS to ΨBS entanglement, passing through a special point at $\Delta \approx 0.836\Delta_0$ where the concurrence drops to zero.

Here, we have two transitions, for which the corresponding Schrieffer–Wolff analysis yields the Hamiltonians

$$\hat{H}^{(2)}_{\mathrm{UM}} = g^2 \begin{pmatrix} \delta_1^{\mathrm{UM}} - \delta_2^{\mathrm{UM}} & 0 & 0 & \gamma_2^{\mathrm{UM}} \\ 0 & \delta_3^{\mathrm{UM}} & \alpha^{\mathrm{UM}} & 0 \\ 0 & \alpha^{\mathrm{UM}} & \delta_3^{\mathrm{UM}} & 0 \\ \gamma_2^{\mathrm{UM}} & 0 & 0 & \delta_3^{\mathrm{UM}} \end{pmatrix} \tag{34}$$

and

$$\hat{H}^{(2)}_{\mathrm{NL}} = g^2 \begin{pmatrix} \delta_1^{\mathrm{UM}} - \delta_2^{\mathrm{UM}} & \gamma_1^{\mathrm{NL}} & \gamma_2^{\mathrm{NL}} & 0 \\ \gamma_1^{\mathrm{NL}} & \delta_3^{\mathrm{NL}} & \alpha^{\mathrm{NL}} & 0 \\ \gamma_2^{\mathrm{NL}} & \alpha^{\mathrm{NL}} & \delta_3^{\mathrm{NL}} & 0 \\ 0 & 0 & 0 & \delta_3^{\mathrm{NL}} \end{pmatrix} \tag{35}$$

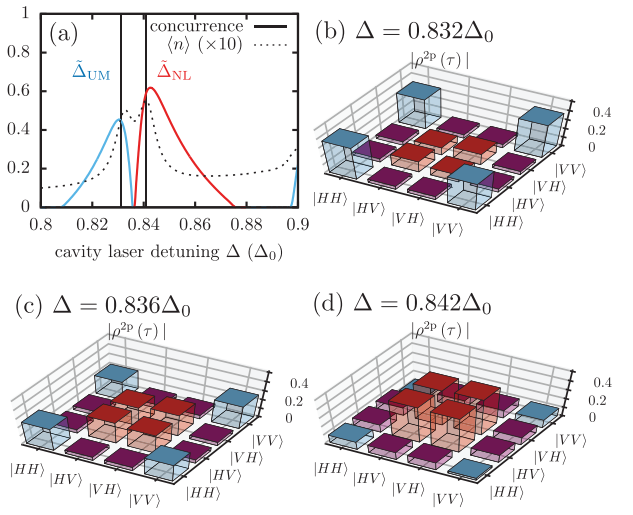

Figure 7. a) Concurrence and mean photon number $\langle n\rangle$ for $\Omega = 30\times g$. Vertical lines indicate the position of $\tilde{\Delta}_{UM}$ (Equation (37)) and $\tilde{\Delta}_{NL}$ (Equation (38)). b–d) Absolute values of the two-photon density matrices $|\rho^{2p}(\tau)|$ for Δ as indicated.

with the coefficients given in Appendix A.3. While the Hamiltonian $\hat{\tilde{H}}^{(2)}_{UM}$ has the same form as $\hat{\tilde{H}}^{(2)}_{MN}$ in Equation (32), the Hamiltonian $\hat{\tilde{H}}^{(2)}_{NL}$ has a form similar to $\hat{\tilde{H}}^{(2)}_{UL}$ in Equation (23).

From the effective Hamiltonian, it is evident that the isolated 2p $U|M$ resonance supports only ΦBS entanglement, while the isolated 2p $N|L$ resonance has competing channels for both ΦBS and ΨBS entanglement. From the coefficients, we can deduce the strengths of the competing channels, finding that

$$|\gamma_1^{NL}| = |\gamma_2^{NL}| + \frac{2\sqrt{2}\tilde{c}}{2\Delta_0 + \Delta_{UM}}. \tag{36}$$

Therefore the ratio $\gamma_1^{NL}/\gamma_2^{NL}$ is always larger than 1 and the preferred type of entanglement for the 2p $N|L$ resonance is always ΨBS entanglement.

A zoom in around the two-photon transition at $\Delta = \Delta_{UM}/2$, presented in Figure 7a for $\Omega = 30\times g$, shows clearly that two peaks appear, a ΦBS one and a ΨBS one. The approximate position of these peaks can be determined by the diagonal elements of the Schrieffer–Wolff Hamiltonians in Equation (34) and Equation (35). Due to the transformation, diagonal elements appear encoded by $\delta_j^{\chi_1\chi_2}$, which slightly shift the resulting resonance, such that now we have the resonances for the 2p $U|M$ transition with ΦBS entanglement at

$$\tilde{\Delta}_{UM} = \frac{1}{2}\left(\Delta_{UM} + (\delta_1^{UM} - \delta_2^{UM}) - \delta_3^{UM}\right) \tag{37}$$

and the 2p $N|L$ transition with ΨBS entanglement at

$$\tilde{\Delta}_{NL} = \frac{1}{2}\left(\Delta_{UM} + (\delta_1^{UM} - \delta_2^{UM}) - \delta_3^{NL}\right). \tag{38}$$

The values of the different $\delta_j^{\chi_1\chi_2}$ are given in Appendix A.3. Indeed, the position of the peak maxima visible in Figure 7 agree well with these shifted resonances (indicated by vertical lines). This interpretation is confirmed by the mean photon number $\langle n\rangle$ (dotted line in Figure 7) which also displays two separate maxima, indicating two close-by resonances (confer Figure 7a).

Also, the $\delta_j^{\chi_1\chi_2}$ depend sensibly on the driving strength Ω. For a driving strength being smaller than $\Omega_m = \sqrt{3}\Delta_0 \approx 34.6\times g$ we find that $\tilde{\Delta}_{UM} < \tilde{\Delta}_{NL}$, while for $\Omega > \Omega_m$ this order is reversed. Therefore, in Figure 6d for a driving strength $\Omega = 40\times g$ the arrangement of ΨBS and ΦBS entanglement is swapped.

In between the regions of ΦBS and ΨBS entanglement we have the special point at $(\tilde{\Delta}_{UM} + \tilde{\Delta}_{NL})/2$. From the density matrix at this special point (confer Figure 7c), we see that the concurrence does not vanish due to the lack of coherences. We find that at the special point the generated two-photon state is essentially the superposition of the two density matrices created by each transition individually with

$$\rho^{2p}_{sp2} = \frac{1}{2}\left[\frac{1}{2}\begin{pmatrix}0&0&0&0\\0&1&1&0\\0&1&1&0\\0&0&0&0\end{pmatrix} + \frac{1}{2}\begin{pmatrix}1&0&0&-1\\0&0&0&0\\0&0&0&0\\-1&0&0&1\end{pmatrix}\right] \tag{39}$$

This can be rewritten into

$$\rho^{2p}_{sp2} = \frac{1}{2}|\psi^{(+)}_{sp2}\rangle\langle\psi^{(+)}_{sp2}| + \frac{1}{2}|\psi^{(-)}_{sp2}\rangle\langle\psi^{(-)}_{sp2}|, \tag{40}$$

with

$$|\psi^{(\pm)}_{sp2}\rangle = \frac{1}{\sqrt{2}}\left(|H_1\rangle \pm i|V_1\rangle\right)\frac{1}{\sqrt{2}}\left(|H_2\rangle \pm i|V_2\rangle\right). \tag{41}$$

Thus, the density matrix can be written as a mixed state, where both contributing states are products of two one-photon states, that is, the states are factorizable states, and, accordingly, the corresponding concurrence vanishes.

We emphasize that this is a different type of special point than the one discussed in Section 5.1 where the system approaches a pure factorizable state. Another difference in comparison to the 2p $U|L$ resonance can be found in the limit $\Omega\to\infty$. While the concurrence obtained at the 2p $U|L$ resonance approaches a high finite value and becomes independent of the driving strength, the concurrence for the 2p $U|M$ and 2p $N|L$ resonances approach zero. In the limiting case the difference $\tilde{\Delta}_{UM} - \tilde{\Delta}_{NL}$ vanishes and, therefore, the two resonances merge together and the different types of entanglement cancel each other.

6.3. Two-Photon $U|N$ and Two-Photon $M|L$ Resonance

Finally, we analyze the remaining two resonances 2p $U|N$ and 2p $M|L$. In Figure 6 we see that always ΦBS occurs at this transition.

The analysis with the Schrieffer–Wolff transformation results in a similar situation as discussed in the previous subsection 6.2: The Hamiltonian of the 2p $M|L$ transition has the same form as the 2p $U|M$ transition [Equation (34) or also Equation (32)] and therefore promotes exclusively ΦBS entanglement. On the other hand, the Hamiltonian of the 2p $U|N$ transition has the same form as the 2p $N|L$ transition [Equation (35) or also Equation (23)] and therefore promotes both ΦBS and ΨBS entanglement. The

Table 2. Various scenarios: Similarities and differences at the different two-photon resonances.

Resonance	Small driving Ω	Large driving Ω	Special point	Limit $\Omega \to \infty$
2p $U\|L$	$\Omega < 12.25 \times g$: ΦBS	$\Omega > 12.25 \times g$: ΨBS	for $\Omega \approx 12.25 \times g$	high ΨBS ent.
2p $M\|N$	always ΦBS		none	high ΦBS ent.
2p $U\|M$	always ΦBS		in between the two close-by resonances	resonances coincide and ent. vanishes
2p $N\|L$	always ΨBS		in between the two close-by resonances	resonances coincide and ent. vanishes
2p $U\|N$	$\Omega < 20 \times g$: ΦBS	$\Omega > 20 \times g$: ΨBS	not observed for $\Omega \leq 40 \times g$	resonances coincide and ent. vanishes
2p $M\|L$	ΦBS (irrelevant)	ΦBS (dominant)	not observed for $\Omega \leq 40 \times g$	resonances coincide and ent. vanishes

dominating type of entanglement depends on the ratio of γ_1^{UN} to γ_2^{UN}, but also on the splitting from the other resonances given by the diagonal elements $\delta_j^{\chi_1\chi_2}$. For small driving strength values $\Omega < 20 \times g$ the 2p $U|N$ transition dominates the dynamics and the resulting entanglement is ΦBS entanglement. For larger Ω both two-photon resonances become of equal importance and a transition between ΦBS and ΨBS entanglement is expected, similar to the results presented in Section 6.2. But, in contrast to the previous section, here, the splitting of the two peaks is too small for the given driving strength values, therefore, we only observe ΦBS entanglement in Figure 6. The corresponding Hamiltonians and constants are given in Appendix A.4.

By investigating the various two-photon resonances we are able to understand the origins of all regions of high entanglement observable in Figure 3 and 6. We stress that, we find a rich variety of different scenarios depending on the considered resonance condition, which are all equally fascinating. For example, at the 2p $M|N$ resonance one always obtains a high ΦBS entanglement. In contrast to this, in case of the 2p $U|L$ transition, the type of entanglement undergoes a sharp transition at a special point of vanishing concurrence when the driving strength is varied. Additionally, a second type of special point can occur between two close-by resonances, as demonstrated by the 2p $U|M$ and 2p $N|L$ resonances. Table 2 provides a short overview over the similarities and differences between the various scenarios at the different two-photon resonances. Using the same analytic formalism based on a Schrieffer–Wolff transformation, we are able to successfully predict the resulting type of entanglement at all two-photon resonances, and even more important, we can also explain these various features.

7. Conclusion

In conclusion, we have investigated the possible types of entanglement generated by a driven four-level emitter-cavity system. We found that two different types of entanglement can occur, which we classified as ΦBS and ΨBS entanglement.

By adjusting the driving strength as well as the cavity detuning, we found a rich picture showing a finite concurrence at various transitions. Using a Schrieffer–Wolff transformation, we were able to give analytical insight into the occurrence of the different types of entanglement showing that either ΦBS or a mixture of ΦBS and ΨBS is promoted at the two-photon transitions. Most excitingly, we found special points, where the concurrence, a measure for the entanglement, drops to zero, though the corresponding coherences in the two-photon density matrix are not absent. Instead, factorizable (and therefore not entangled states) are reached.

In principle, the resulting type of Bell state could also be changed afterward, for example, by the use of waveplates or polarization filters. But these additional components often lead to a significant loss of photon yield. These kinds of losses can be avoided when the target photonic state is generated directly. Furthermore, although ΦBS and ΨBS entanglement can be converted into each other by postprocessing, they are clearly distinguishable in a fixed basis and reflect the systems ability to get entangled in more than one fashion. Seeing that entanglement, being one of the most remarkable and interesting physical effects that separates the quantum mechanical from the classical world, can change its character by just adding an external driving to a few-level emitter is exciting from a fundamental point of view and can also lead to new possibilities for using few-level emitters in quantum information technology.

Appendix A: Schrieffer–Wolff Transformation

For the Schrieffer–Wolff transformation we consider the FLE-cavity system without losses and use the states $|\chi, n_{\mathrm{H}}, n_{\mathrm{V}}\rangle$ where $|\chi\rangle \in \{|U\rangle, |M\rangle, |N\rangle, |L\rangle\}$ is one of the four laser-dressed states defined in Section 3.2 and n_{H} (n_{V}) denotes the number of photons present in the horizontally (vertically) polarized cavity mode. The direct two-photon transition from $|\chi_1\rangle$ to $|\chi_2\rangle$ involves only the states

$$A : |\chi_1, 0, 0\rangle, |\chi_2, 1, 1\rangle, |\chi_2, 2, 0\rangle, |\chi_2, 0, 2\rangle. \tag{A.1}$$

As discussed in Section 5.2, there are also several other paths to create the two-photon states, thereby coupling the aforementioned states. These processes are depicted in Figure 4 and include the states

$$B : |\chi, 1, 0\rangle, |\chi, 0, 1\rangle, \\ |\chi, 3, 0\rangle, |\chi, 2, 1\rangle, |\chi, 1, 2\rangle, |\chi, 0, 3\rangle, \tag{A.2}$$

where the one- and three-photon states include all four bare states, that is, $|\chi\rangle = |U\rangle, |M\rangle, |N\rangle, |L\rangle$. This results in a 28×28 matrix. To reduce this to a 4×4 matrix for the relevant states in subset A [see Equation (A.1)], we use a Schrieffer–Wolff transformation.[61,62] In the transformation, we perform a

block-diagonalization of the system Hamiltonian via the unitary transformation

$$e^{-\hat{S}}\hat{H}e^{\hat{S}}, \tag{A.3}$$

where $\hat{S}$ is an anti-Hermitian operator.[61] After the decoupling procedure, the states in set B [see Equation (A.2)] can be disregarded as they are insignificant for the system dynamics. This formalism can be applied here since, for a given two-photon resonance, where the cavity laser detuning matches half the transition energy between the states $|\chi_1\rangle$ and $|\chi_2\rangle$, one-photon transition processes between the laser-dressed states are typically strongly off-resonant.

In second order the effective Hamiltonian for the states in set A is then given by $\hat{H}^{(2)}_{\chi_1\chi_2} = \{H^{(2)}_{a,a'}\}_{\chi_1\chi_2}$ with the matrix elements[61]

$$H^{(2)}_{a,a'} = H_{a,a'} + \frac{1}{2}\left\{\sum_b H_{a,b}H_{b,a'}\left[\frac{1}{E_a - E_b} + \frac{1}{E_{a'} - E_b}\right]\right\}, \tag{A.4}$$

where a runs over the states in subset A, the index b runs over the states in B, and

$$E_j = \langle j|\hat{H}|j\rangle = E_\chi + \left(n_\mathrm{H} + n_\mathrm{V}\right)\Delta \tag{A.5}$$

is the energy of the state $|j\rangle = |\chi, n_\mathrm{H}, n_\mathrm{V}\rangle \in A, B$. The matrix elements are calculated from the system Hamiltonian with

$$H_{a,a'} = E_a\delta_{a,a'}, \tag{A.6}$$

This term can be dropped since it represents a constant energy shift as the four states in set A are energetically degenerate. The remaining matrix elements for $a \neq b$ are given by the coupling Hamiltonian in the dressed state basis [Equation (13)] with

$$H_{a,b} = \langle a|\hat{H}_{\mathrm{DS\text{-}c}}|b\rangle \tag{A.7}$$

After the Schrieffer–Wolff transformation we perform a rotation to the basis

$$|\chi_1, 0, 0\rangle, |\chi_2, 1, 1\rangle, |\chi_2, \Phi_+\rangle, |\chi_2, \Phi_-\rangle \tag{A.8}$$

using

$$\hat{\tilde{H}}^{(2)}_{\chi_1\chi_2} = T^\dagger \hat{H}^{(2)}_{\chi_1\chi_2} T \text{ with } T = \begin{pmatrix} 1 & 0 & 0 & 0 \\ 0 & 1 & 0 & 0 \\ 0 & 0 & \frac{1}{\sqrt{2}} & \frac{1}{\sqrt{2}} \\ 0 & 0 & \frac{1}{\sqrt{2}} & -\frac{1}{\sqrt{2}} \end{pmatrix} \tag{A.9}$$

We performed this procedure for all two-photon resonances.

A.1. Effective Hamiltonian for the 2p U|L Resonance

The effective Hamiltonian is

$$\hat{\tilde{H}}^{(2)}_{\mathrm{UL}} = g^2 \times \begin{pmatrix} \delta^{\mathrm{UL}} & \gamma_1^{\mathrm{UL}} & -\gamma_2^{\mathrm{UL}} & 0 \\ \gamma_1^{\mathrm{UL}} & -\delta^{\mathrm{UL}} - \delta_3^{\mathrm{UL}} & \alpha^{\mathrm{UL}} & 0 \\ -\gamma_2^{\mathrm{UL}} & \alpha^{\mathrm{UL}} & -\delta^{\mathrm{UL}} - \delta_3^{\mathrm{UL}} & 0 \\ 0 & 0 & 0 & -\delta^{\mathrm{UL}} - \delta_3^{\mathrm{UL}} \end{pmatrix} \tag{A.10}$$

in the basis $|U, 0, 0\rangle$, $|L, 1, 1\rangle$, $|L, \Phi_+\rangle$ and $|L, \Phi_-\rangle$ with

$$\begin{aligned}
\delta^{\mathrm{UL}} &= \left(\tilde{c}^2 - c^2\right)\left(\frac{2}{\Delta_0} + \frac{4}{\Delta_{\mathrm{UL}}}\right) \\
\delta_3^{\mathrm{UL}} &= \frac{8\left(\tilde{c}^2 - c^2\right)^2}{3\Delta_{\mathrm{UL}}} + \frac{2\tilde{c}^2}{\Delta_{\mathrm{UL}} + \Delta_0/2} + \frac{2c^2}{\Delta_{\mathrm{UL}} - \Delta_0/2} \\
\gamma_1^{\mathrm{UL}} &= 4c\tilde{c}\frac{1}{\Delta_0} - 16c\tilde{c}\left(\tilde{c}^2 - c^2\right)\frac{1}{\Delta_{\mathrm{UL}}} \\
\gamma_2^{\mathrm{UL}} &= 16c\tilde{c}\left(\tilde{c}^2 - c^2\right)\frac{1}{\Delta_{\mathrm{UL}}} \\
\alpha^{\mathrm{UL}} &= \frac{1}{\Delta_0} - \left(1 - 16c^2\tilde{c}^2\right)\frac{1}{\Delta_{\mathrm{UL}}} - \frac{1}{2}\delta_3^{\mathrm{UL}} + \frac{2\tilde{c}^2}{\Delta_{\mathrm{UL}} + \Delta_0/2}.
\end{aligned} \tag{A.11}$$

A.2. Effective Hamiltonian for the 2p M|N Resonance

The effective Hamiltonian is

$$\hat{\tilde{H}}^{(2)}_{\mathrm{MN}} = g^2 \times \begin{pmatrix} \delta^{\mathrm{MN}} & 0 & 0 & \gamma_2^{\mathrm{MN}} \\ 0 & -\delta^{\mathrm{MN}} + \delta_3^{\mathrm{MN}} & \alpha^{\mathrm{MN}} & 0 \\ 0 & \alpha^{\mathrm{MN}} & -\delta^{\mathrm{MN}} + \delta_3^{\mathrm{MN}} & 0 \\ \gamma_2^{\mathrm{MN}} & 0 & 0 & -\delta^{\mathrm{MN}} + \delta_3^{\mathrm{MN}} \end{pmatrix} \tag{A.12}$$

in the basis $|M, 0, 0\rangle$, $|N, 1, 1\rangle$, $|N, \Phi_+\rangle$ and $|N, \Phi_-\rangle$ with

$$\begin{aligned}
\delta^{\mathrm{MN}} &= 2\left(\tilde{c}^2 - c^2\right)\frac{1}{\Delta_{\mathrm{UL}}} \\
\delta_3^{\mathrm{MN}} &= -\frac{4\tilde{c}^2}{2\Delta_0 + \Delta_{\mathrm{UL}}} - \frac{2}{3\Delta_0} - \frac{4c^2}{2\Delta_0 - \Delta_{\mathrm{UL}}} \\
\gamma_2^{\mathrm{MN}} &= -4\,c\,\tilde{c}\frac{1}{\Delta_{\mathrm{UL}}} \\
\alpha^{\mathrm{MN}} &= -\delta^{\mathrm{MN}} + \frac{1}{2}\delta_3^{\mathrm{MN}} + \frac{1}{3\Delta_0}.
\end{aligned} \tag{A.13}$$

A.3. Effective Hamiltonians for the 2p U|M and 2p N|L Resonance

The effective Hamiltonian for the 2p $U|M$ resonance is

$$\hat{\tilde{H}}^{(2)}_{\mathrm{UM}} = g^2 \times \begin{pmatrix} \delta_1^{\mathrm{UM}} - \delta_2^{\mathrm{UM}} & 0 & 0 & \gamma_2^{\mathrm{UM}} \\ 0 & \delta_3^{\mathrm{UM}} & \alpha^{\mathrm{UM}} & 0 \\ 0 & \alpha^{\mathrm{UM}} & \delta_3^{\mathrm{UM}} & 0 \\ \gamma_2^{\mathrm{UM}} & 0 & 0 & \delta_3^{\mathrm{UM}} \end{pmatrix} \text{for} \begin{matrix} |U,0,0\rangle \\ |M,1,1\rangle \\ |M,\Phi_+\rangle \\ |M,\Phi_-\rangle \end{matrix} \tag{A.14}$$

where

$$\delta_1^{\mathrm{UM}} = -\frac{16c^2\tilde{c}^2}{\Delta_{\mathrm{UM}}} + \frac{2\tilde{c}^2}{2\Delta_0 + \Delta_{\mathrm{UM}}} + \frac{4(\tilde{c}^2 - c^2)^2}{2\Delta_0 + 3\Delta_{\mathrm{UM}}}$$

$$\delta_2^{\mathrm{UM}} = -\frac{2c^2}{\Delta_{\mathrm{UM}}} + \frac{1}{2\Delta_0 + \Delta_{\mathrm{UM}}} + \frac{2\tilde{c}^2}{2\Delta_0 + 3\Delta_{\mathrm{UM}}}$$

$$\delta_3^{\mathrm{UM}} = -\frac{4c^2}{3\Delta_{\mathrm{UM}}} + \frac{2}{2\Delta_0 - \Delta_{\mathrm{UM}}} + \frac{4\tilde{c}^2}{2\Delta_0 + \Delta_{\mathrm{UM}}}$$

$$\gamma_2^{\mathrm{UM}} = -\frac{4\sqrt{2}c^2\tilde{c}}{\Delta_{\mathrm{UM}}} - \frac{\sqrt{2}\tilde{c}}{2\Delta_0 + \Delta_{\mathrm{UM}}} + \frac{2\sqrt{2}(\tilde{c}^2 - c^2)\tilde{c}}{2\Delta_0 + 3\Delta_{\mathrm{UM}}}$$

$$\alpha^{\mathrm{UM}} = -\delta_2^{\mathrm{UM}} - \frac{1}{2}\delta_3^{\mathrm{UM}} \tag{A.15}$$

The effective Hamiltonian for the two-photon transition between the states $|N\rangle$ and $|L\rangle$ is given by

$$\hat{\tilde{H}}^{(2)}_{\mathrm{NL}} = g^2 \times \begin{pmatrix} \delta_1^{\mathrm{UM}} - \delta_2^{\mathrm{UM}} & \gamma_1^{\mathrm{NL}} & \gamma_2^{\mathrm{NL}} & 0 \\ \gamma_1^{\mathrm{NL}} & \delta_3^{\mathrm{NL}} & \alpha^{\mathrm{NL}} & 0 \\ \gamma_2^{\mathrm{NL}} & \alpha^{\mathrm{NL}} & \delta_3^{\mathrm{NL}} & 0 \\ 0 & 0 & 0 & \delta_3^{\mathrm{NL}} \end{pmatrix} \text{for} \begin{matrix} |N,0,0\rangle \\ |L,1,1\rangle \\ |L,\Phi_+\rangle \\ |L,\Phi_-\rangle \end{matrix} \tag{A.16}$$

with

$$\delta_3^{\mathrm{NL}} = -\frac{32c^2\tilde{c}^2}{\Delta_{\mathrm{UM}}} - \frac{4c^2}{3\Delta_{\mathrm{UM}}} - \frac{8(\tilde{c}^2 - c^2)}{2\Delta_0 + 5\Delta_{\mathrm{UM}}} - \frac{4\tilde{c}^2}{2\Delta_0 + 3\Delta_{\mathrm{UM}}}$$

$$\gamma_1^{\mathrm{NL}} = \gamma_2^{\mathrm{UM}}$$

$$\gamma_2^{\mathrm{NL}} = \gamma_2^{\mathrm{UM}} + \frac{2\sqrt{2}\tilde{c}}{2\Delta_0 + \Delta_{\mathrm{UM}}}$$

$$\alpha^{\mathrm{NL}} = -\delta_1^{\mathrm{UM}} + \frac{1}{2}\delta_3^{\mathrm{NL}} + \frac{4\tilde{c}^2}{2\Delta_0 + \Delta_{\mathrm{UM}}} + \frac{4\tilde{c}^2}{2\Delta_0 + 3\Delta_{\mathrm{UM}}} \tag{A.17}$$

A.4. Effective Hamiltonians for the 2p U|N and 2p M|L Resonance

For the 2p $U|N$ transition we obtain

$$\hat{\tilde{H}}^{(2)}_{\mathrm{UN}} = g^2 \times \begin{pmatrix} \delta_1^{\mathrm{UN}} - \delta_2^{\mathrm{UN}} & \gamma_1^{\mathrm{UN}} & \gamma_2^{\mathrm{UN}} & 0 \\ \gamma_1^{\mathrm{UN}} & \delta_3^{\mathrm{UN}} & \alpha^{\mathrm{UN}} & 0 \\ \gamma_2^{\mathrm{UN}} & \alpha^{\mathrm{UN}} & \delta_3^{\mathrm{UN}} & 0 \\ 0 & 0 & 0 & \delta_3^{\mathrm{UN}} \end{pmatrix} \text{for} \begin{matrix} |U,0,0\rangle \\ |N,1,1\rangle \\ |N,\Phi_+\rangle \\ |N,\Phi_-\rangle \end{matrix} \tag{A.18}$$

The energies and coupling strengths are

$$\delta_1^{\mathrm{UN}} = -\frac{16c^2\tilde{c}^2}{\Delta_{\mathrm{UN}}} + \frac{2c^2}{\Delta_{\mathrm{UN}} - 2\Delta_0} + \frac{4(\tilde{c}^2 - c^2)^2}{3\Delta_{\mathrm{UN}} - 2\Delta_0}$$

$$\delta_2^{\mathrm{UN}} = -\frac{2\tilde{c}^2}{\Delta_{\mathrm{UN}}} + \frac{1}{\Delta_{\mathrm{UN}} - 2\Delta_0} + \frac{2c^2}{3\Delta_{\mathrm{UN}} - 2\Delta_0}$$

$$\delta_3^{\mathrm{UN}} = -\frac{4\tilde{c}^2}{3\Delta_{\mathrm{UN}}} - \frac{2}{2\Delta_0 + \Delta_{\mathrm{UN}}} - \frac{4c^2}{2\Delta_0 - \Delta_{\mathrm{UN}}}$$

$$\gamma_1^{\mathrm{UN}} = -\frac{4\sqrt{2}c\tilde{c}^2}{\Delta_{\mathrm{UN}}} - \frac{\sqrt{2}c}{\Delta_{\mathrm{UN}} - 2\Delta_0} - \frac{2\sqrt{2}(\tilde{c}^2 - c^2)c}{3\Delta_{\mathrm{UN}} - 2\Delta_0}$$

$$\gamma_2^{\mathrm{UN}} = \gamma_1^{\mathrm{UN}} + \frac{2\sqrt{2}c}{\Delta_{\mathrm{UN}} - \Delta_0}$$

$$\alpha^{\mathrm{UN}} = \delta_2^{\mathrm{UN}} + \frac{1}{2}\delta_3^{\mathrm{UN}} - \frac{2}{\Delta_{\mathrm{UN}} - 2\Delta_0} + \frac{2}{2\Delta_0 + \Delta_{\mathrm{UN}}}. \tag{A.19}$$

For the 2p $M|L$ transition we have

$$\hat{\tilde{H}}^{(2)}_{\mathrm{ML}} = g^2 \times \begin{pmatrix} \delta_1^{\mathrm{UN}} - \delta_2^{\mathrm{UN}} & 0 & 0 & \gamma_1^{\mathrm{UN}} \\ 0 & \delta_3^{\mathrm{ML}} & \alpha^{\mathrm{ML}} & 0 \\ 0 & \alpha^{\mathrm{ML}} & \delta_3^{\mathrm{ML}} & 0 \\ \gamma_1^{\mathrm{UN}} & 0 & 0 & \delta_3^{\mathrm{ML}} \end{pmatrix} \text{for} \begin{matrix} |M,0,0\rangle \\ |L,1,1\rangle \\ |L,\Phi_+\rangle \\ |L,\Phi_-\rangle \end{matrix} \tag{A.20}$$

with

$$\delta_3^{\mathrm{ML}} = \frac{8(\tilde{c}^2 - c^2)^2}{2\Delta_0 - 5\Delta_{\mathrm{UN}}} - \frac{4\tilde{c}^2}{3\Delta_{\mathrm{UN}}} + \frac{4c^2}{2\Delta_0 - 3\Delta_{\mathrm{UN}}} - \frac{32c^2\tilde{c}^2}{\Delta_{\mathrm{UN}}}$$

$$\alpha^{\mathrm{ML}} = -\delta_1^{\mathrm{UN}} + \frac{1}{2}\delta_3^{\mathrm{ML}} + \frac{4\tilde{c}^2}{3\Delta_{\mathrm{UN}}}. \tag{A.21}$$

Acknowledgements

M.Cy. thanks the Alexander-von-Humboldt foundation for support through a Feodor Lynen fellowship. A.V. acknowledges the support from the Russian Science Foundation under the Project 18-12-00429 which was used to study dynamical processes leading to two-photon entanglement. D.E.R. acknowledges support by the Deutsche Forschungsgemeinschaft (DFG) via the project 428026575. The authors are further greatful for support by the Deutsche Forschungsgemeinschaft (DFG, German Research Foundation) via the project 419036043.

Open access funding enabled and organized by Projekt DEAL.

Conflict of Interest

The authors declare no conflict of interest.

Keywords

entangled quantum states, optical cavities, quantum emitters, quantum entanglement, quantum optics

Received: September 28, 2020
Revised: November 3, 2020
Published online: December 14, 2020

[1] R. Horodecki, P. Horodecki, M. Horodecki, K. Horodecki, *Rev. Mod. Phys.* **2009**, *81*, 865.
[2] A. Orieux, M. A. M. Versteegh, K. D. Jöns, S. Ducci, *Rep. Prog. Phys.* **2017**, *80*, 076001.
[3] N. Akopian, N. H. Lindner, E. Poem, Y. Berlatzky, J. Avron, D. Gershoni, B. D. Gerardot, P. M. Petroff, *Phys. Rev. Lett.* **2006**, *96*, 130501.
[4] N. Gisin, G. Ribordy, W. Tittel, H. Zbinden, *Rev. Mod. Phys.* **2002**, *74*, 145.
[5] H.-K. Lo, M. Curty, K. Tamaki, *Nat. Photonics* **2014**, *8*, 595.
[6] L.-M. Duan, M. D. Lukin, J. I. Cirac, P. Zoller, *Nature* **2001**, *414*, 413.
[7] D. Huber, M. Reindl, J. Aberl, A. Rastelli, R. Trotta, *J. Opt.* **2018**, *20*, 073002.
[8] J.-W. Pan, Z.-B. Chen, C.-Y. Lu, H. Weinfurter, A. Zeilinger, M. Żukowski, *Rev. Mod. Phys.* **2012**, *84*, 777.
[9] C. H. Bennett, D. P. DiVincenzo, *Nature* **2000**, *404*, 247.
[10] S. C. Kuhn, A. Knorr, S. Reitzenstein, M. Richter, *Opt. Express* **2016**, *24*, 25446.
[11] A. Zeilinger, *Phys. Scr.* **2017**, *92*, 072501.
[12] K. Edamatsu, *Jpn. J. Appl. Phys.* **2007**, *46*, 7175.
[13] S. J. Freedman, J. F. Clauser, *Phys. Rev. Lett.* **1972**, *28*, 938.
[14] J. Wen, S. Du, Y. Zhang, M. Xiao, M. H. Rubin, *Phys. Rev. A* **2008**, *77*, 033816.
[15] J. Park, T. Jeong, H. Kim, H. S. Moon, *Phys. Rev. Lett.* **2018**, *121*, 263601.
[16] M. Müller, S. Bounouar, K. D. Jöns, M. Glässl, P. Michler, *Nat. Photonics* **2014**, *8*, 224.
[17] L. Hanschke, K. A. Fischer, S. Appel, D. Lukin, J. Wierzbowski, S. Sun, R. Trivedi, J. Vučković, J. J. Finley, K. Müller, *npj Quantum Inf.* **2018**, *4*, 43.
[18] D. Huber, M. Reindl, Y. Huo, H. Huang, J. S. Wildmann, O. G. Schmidt, A. Rastelli, R. Trotta, *Nat. Commun.* **2017**, *8*, 15506.
[19] M. Reindl, K. D. Jöns, D. Huber, C. Schimpf, Y. Huo, V. Zwiller, A. Rastelli, R. Trotta, *Nano Lett.* **2017**, *17*, 4090.
[20] P.-L. Ardelt, L. Hanschke, K. A. Fischer, K. Müller, A. Kleinkauf, M. Koller, A. Bechtold, T. Simmet, J. Wierzbowski, H. Riedl, G. Abstreiter, J. J. Finley, *Phys. Rev. B* **2014**, *90*, 241404(R).
[21] S. Bounouar, M. Müller, A. M. Barth, M. Glässl, V. M. Axt, P. Michler, *Phys. Rev. B* **2015**, *91*, 161302(R).
[22] M. Glässl, A. M. Barth, V. M. Axt, *Phys. Rev. Lett.* **2013**, *110*, 147401.
[23] A. M. Barth, S. Lüker, A. Vagov, D. E. Reiter, T. Kuhn, V. M. Axt, *Phys. Rev. B* **2016**, *94*, 045306.
[24] D. E. Reiter, T. Kuhn, M. Glässl, V. M. Axt, *J. Phys.: Condens. Matter* **2014**, *26*, 423203.
[25] A. Debnath, C. Meier, B. Chatel, T. Amand, *Phys. Rev. B* **2013**, *88*, 201305(R).
[26] M. Glässl, A. M. Barth, K. Gawarecki, P. Machnikowski, M. D. Croitoru, S. Lüker, D. E. Reiter, T. Kuhn, V. M. Axt, *Phys. Rev. B* **2013**, *87*, 085303.
[27] T. Kaldewey, S. Lüker, A. V. Kuhlmann, S. R. Valentin, A. Ludwig, A. D. Wieck, D. E. Reiter, T. Kuhn, R. J. Warburton, *Phys. Rev. B* **2017**, *95*, 161302(R).
[28] D. E. Reiter, T. Kuhn, V. M. Axt, *Adv. Phys.: X* **2019**, *4*, 1655478.
[29] T. Seidelmann, F. Ungar, M. Cygorek, A. Vagov, A. M. Barth, T. Kuhn, V. M. Axt, *Phys. Rev. B* **2019**, *99*, 245301.
[30] M. Cygorek, F. Ungar, T. Seidelmann, A. M. Barth, A. Vagov, V. M. Axt, T. Kuhn, *Phys. Rev. B* **2018**, *98*, 045303.
[31] T. Seidelmann, F. Ungar, A. M. Barth, A. Vagov, V. M. Axt, M. Cygorek, T. Kuhn, *Phys. Rev. Lett.* **2019**, *123*, 137401.
[32] S. Schumacher, J. Förstner, A. Zrenner, M. Florian, C. Gies, P. Gartner, F. Jahnke, *Opt. Express* **2012**, *20*, 5335.
[33] D. Heinze, A. Zrenner, S. Schumacher, *Phys. Rev. B* **2017**, *95*, 245306.
[34] A. Carmele, A. Knorr, *Phys. Rev. B* **2011**, *84*, 075328.
[35] R. M. Stevenson, R. J. Young, P. Atkinson, K. Cooper, D. A. Ritchie, A. J. Shields, *Nature* **2006**, *439*, 179.
[36] R. J. Young, R. M. Stevenson, P. Atkinson, K. Cooper, D. A. Ritchie, A. J. Shields, *New J. Phys.* **2006**, *8*, 29.
[37] A. Muller, W. Fang, J. Lawall, G. S. Solomon, *Phys. Rev. Lett.* **2009**, *103*, 217402.
[38] D. Huber, M. Reindl, S. F. Covre da Silva, C. Schimpf, J. Martín-Sánchez, H. Huang, G. Piredda, J. Edlinger, A. Rastelli, R. Trotta, *Phys. Rev. Lett.* **2018**, *121*, 033902.
[39] H. Wang, H. Hu, T.-H. Chung, J. Qin, X. Yang, J.-P. Li, R.-Z. Liu, H.-S. Zhong, Y.-M. He, X. Ding, Y.-H. Deng, Q. Dai, Y.-H. Huo, S. Höfling, C.-Y. Lu, J.-W. Pan, *Phys. Rev. Lett.* **2019**, *122*, 113602.
[40] J. Liu, R. Su, Y. Wei, B. Yao, S. F. C. d. Silva, Y. Yu, J. Iles-Smith, K. Srinivasan, A. Rastelli, J. Li, X. Wang, *Nat. Nanotechnol.* **2019**, *14*, 586.
[41] S. Bounouar, C. de la Haye, M. Strauß, P. Schnauber, A. Thoma, M. Gschrey, J.-H. Schulze, A. Strittmatter, S. Rodt, S. Reitzenstein, *Appl. Phys. Lett.* **2018**, *112*, 153107.
[42] A. Dousse, J. Suffczyński, A. Beveratos, O. Krebs, A. Lemaître, I. Sagnes, J. Bloch, P. Voisin, P. Senellart, *Nature* **2010**, *466*, 217.
[43] R. Winik, D. Cogan, Y. Don, I. Schwartz, L. Gantz, E. R. Schmidgall, N. Livneh, R. Rapaport, E. Buks, D. Gershoni, *Phys. Rev. B* **2017**, *95*, 235435.
[44] A. Fognini, A. Ahmadi, M. Zeeshan, J. T. Fokkens, S. J. Gibson, N. Sherlekar, S. J. Daley, D. Dalacu, P. J. Poole, K. D. Jöns, V. Zwiller, M. E. Reimer, *ACS Photonics* **2019**, *6*, 1656.
[45] R. Hafenbrak, S. M. Ulrich, P. Michler, L. Wang, A. Rastelli, O. G. Schmidt, *New J. Phys.* **2007**, *9*, 315.
[46] A. J. Bennett, M. A. Pooley, R. M. Stevenson, M. B. Ward, R. B. Patel, A. Boyer de la Giroday, N. Sköld, I. Farrer, C. A. Nicoll, D. A. Ritchie, A. J. Shields, *Nat. Phys.* **2010**, *6*, 947.
[47] E. del Valle, *New J. Phys.* **2013**, *15*, 025019.
[48] F. Troiani, J. I. Perea, C. Tejedor, *Phys. Rev. B* **2006**, *74*, 235310.
[49] R. M. Stevenson, C. L. Salter, J. Nilsson, A. J. Bennett, M. B. Ward, I. Farrer, D. A. Ritchie, A. J. Shields, *Phys. Rev. Lett.* **2012**, *108*, 040503.
[50] O. Benson, C. Santori, M. Pelton, Y. Yamamoto, *Phys. Rev. Lett.* **2000**, *84*, 2513.
[51] C. Sánchez Muñoz, F. P. Laussy, C. Tejedor, E. del Valle, *New J. Phys.* **2015**, *17*, 123021.
[52] P.-L. Ardelt, M. Koller, T. Simmet, L. Hanschke, A. Bechtold, A. Regler, J. Wierzbowski, H. Riedl, J. J. Finley, K. Müller, *Phys. Rev. B* **2016**, *93*, 165305.
[53] F. Hargart, M. Müller, K. Roy-Choudhury, S. L. Portalupi, C. Schneider, S. Höfling, M. Kamp, S. Hughes, P. Michler, *Phys. Rev. B* **2016**, *93*, 115308.
[54] A. Badolato, K. Hennessy, M. Atatüre, J. Dreiser, E. Hu, P. M. Petroff, A. Imamoğlu, *Science* **2005**, *308*, 1158.
[55] Y. Ota, S. Iwamoto, N. Kumagai, Y. Arakawa, *Phys. Rev. Lett.* **2011**, *107*, 233602.
[56] Q. Mermillod, D. Wigger, V. Delmonte, D. E. Reiter, C. Schneider, M. Kamp, S. Höfling, W. Langbein, T. Kuhn, G. Nogues, J. Kasprzak, *Optica* **2016**, *3*, 377.
[57] D. F. V. James, P. G. Kwiat, W. J. Munro, A. G. White, *Phys. Rev. A* **2001**, *64*, 052312.
[58] R. M. Stevenson, A. J. Hudson, A. J. Bennett, R. J. Young, C. A. Nicoll, D. A. Ritchie, A. J. Shields, *Phys. Rev. Lett.* **2008**, *101*, 170501.
[59] W. K. Wootters, *Phys. Rev. Lett.* **1998**, *80*, 2245.
[60] M. Cosacchi, M. Cygorek, F. Ungar, A. M. Barth, A. Vagov, V. M. Axt, *Phys. Rev. B* **2018**, *98*, 125302.
[61] R. Winkler, *Spin-Orbit Coupling Effects in Two-Dimensional Electron and Hole Systems*, Springer Tracts in Modern Physics, Vol. *191*, Springer, Berlin **2003**.
[62] S. Bravyi, D. P. DiVincenzo, D. Loss, *Ann. Phys.* **2011**, *326*, 2793.

Publication 5

Time-dependent switching of the photon entanglement type using a driven quantum emitter–cavity system.

T. Seidelmann, D. E. Reiter, **M. Cosacchi**, M. Cygorek, A. Vagov, V. M. Axt.

Appl. Phys. Lett. **118**, 164001 (2021).

DOI: 10.1063/5.0045377

Author contributions

T. Seidelmann has designed the concept of this study, in particular, he has performed the data generation and analysis, has provided the interpretation of the results, and has written the first draft of the paper. He proposed a feasible protocol to realize time-dependent entanglement switching. He has moderated all discussions and revision requests of the draft, has organized the correspondence with the editor and referees, and has provided the first drafts of answers to the referees.

D. E. Reiter has provided the opportunity of a contribution in this journal through her invitation. She has optimized the presentation of the results. She has participated in the discussion and interpretation of the results and has contributed to revisions of the draft and the answers to the referees.

The author has discussed the results in detail with T. Seidelmann, thus contributing to the interpretation, and has contributed to revisions of the draft and the answers to the referees.

M. Cygorek and A. Vagov have cosupervised this work, in particular, they have participated in the discussion and interpretation of the results. They have contributed to the optimization of the presentation as well as revisions of the draft and the answers to the referees.

V. M. Axt has advised T. Seidelmann throughout his work as the main supervisor. He has obtained the funding for this work and has participated in the discussion and interpretation of the results. He has contributed to the optimization of the presentation as well as revisions of the draft and the answers to the referees.

Time-dependent switching of the photon entanglement type using a driven quantum emitter–cavity system

Cite as: Appl. Phys. Lett. **118**, 164001 (2021); https://doi.org/10.1063/5.0045377
Submitted: 26 January 2021 . Accepted: 31 March 2021 . Published Online: 20 April 2021

T. Seidelmann, D. E. Reiter, M. Cosacchi, et al.

Applied Physics Letters ARTICLE scitation.org/journal/apl

Time-dependent switching of the photon entanglement type using a driven quantum emitter–cavity system

Cite as: Appl. Phys. Lett. **118**, 164001 (2021); doi: 10.1063/5.0045377
Submitted: 26 January 2021 · Accepted: 31 March 2021 ·
Published Online: 20 April 2021

T. Seidelmann,[1,a] D. E. Reiter,[2,b] M. Cosacchi,[1] M. Cygorek,[3] A. Vagov,[1,4] and V. M. Axt[1]

AFFILIATIONS

[1]Lehrstuhl für Theoretische Physik III, Universität Bayreuth, 95440 Bayreuth, Germany
[2]Institut für Festkörpertheorie, Universität Münster, 48149 Münster, Germany
[3]Heriot-Watt University, Edinburgh EH14 4AS, United Kingdom
[4]ITMO University, St. Petersburg 197101, Russia

Note: This paper is part of the APL Special Collection on Non-Classical Light Emitters and Single-Photon Detectors.
[a]**Author to whom correspondence should be addressed:** tim.seidelmann@uni-bayreuth.de
[b]**Electronic mail:** doris.reiter@uni-muenster.de

ABSTRACT

The cascaded decay in a four-level quantum emitter is a well-established mechanism to generate polarization-entangled photon pairs, the building blocks of many applications in quantum technologies. The four most prominent maximally entangled photon pair states are the Bell states. In a typical experiment based on an undriven emitter, only one type of Bell state entanglement can be observed in a given polarization basis. Other types of Bell state entanglement in the same basis can be created by continuously driving the system by an external laser. In this work, we propose a protocol for time-dependent entanglement switching in a four-level quantum emitter–cavity system that can be operated by changing the external driving strength. By selecting different two-photon resonances between the laser-dressed states, we can actively switch back and forth between the different types of Bell state entanglement in the same basis as well as between entangled and nonentangled photon pairs. This remarkable feature demonstrates the possibility to achieve a controlled, time-dependent manipulation of the entanglement type that could be used in many innovative applications.

Entangled qubits are the building blocks for fascinating applications in many innovative research fields, like quantum cryptography,[1,2] quantum communication,[3,4] or quantum information processing and computing.[5–8] Besides possible applications, the phenomenon of entanglement is also important from a fundamental point of view, being a genuine quantum effect. Especially, attractive realizations of two entangled qubits are polarization-entangled photon pairs, because they travel at the speed of light and are hardly influenced by the environment.[9]

The most prominent maximally entangled states, established for polarization-entangled photons pairs, are the four Bell states (BS)

$$|\Phi_{\pm}\rangle = \frac{1}{\sqrt{2}}(|HH\rangle \pm |VV\rangle), \tag{1a}$$

$$|\Psi_{\pm}\rangle = \frac{1}{\sqrt{2}}(|HV\rangle \pm |VH\rangle), \tag{1b}$$

where H and V denote horizontally and vertically polarized photons, respectively. The order corresponds to the order of photon detection: in a Φ Bell state (ΦBS), the first and second detected photon exhibit the same polarization, whereas in a Ψ Bell state (ΨBS), the two detected photons have exactly the opposite polarization.

A well-established mechanism for the creation of these maximally entangled Bell states is the cascaded decay that takes place in a four-level quantum emitter (FLE) after an initial excitation. Such an FLE can be realized by a variety of systems, including F-centers, semiconductor quantum dots, or atoms.[10–13] Employing a FLE, ΦBS entanglement in the chosen basis of linearly polarized photons was demonstrated for various conditions in both theoretical and experimental studies.[14–37] In contrast, ΨBS entanglement in the same linearly polarized basis has only been predicted in the case of continuous laser driving.[38,39] For the driven FLE, laser-dressed states emerge, which have been observed experimentally.[40,41] By embedding the FLE

inside a microcavity with cavity modes tuned in resonance with the desired emission process, certain two-photon emission processes between the laser-dressed states can be favored.[38,39] The emerging type and degree of entanglement depend strongly on the dominant two-photon emission path between the laser-dressed states, which, in turn, can be tuned by the external driving strength.[39]

Based on these findings, we propose a protocol for time-dependent entanglement switching using a driven FLE-cavity system. Simply changing the external driving strength in a step-like manner enables one to actively switch between the generation of ΦBS and ΨBS entanglement as well as between entangled and nonentangled photon pairs. Therefore, different entangled states can be generated from the same source without further processing the photons to change the entanglement, e.g., by wave plates.

We consider an externally driven FLE-cavity system, which has been presented in detail in Refs. 38 and 39. Figure 1 depicts a sketch of this system. A generic FLE comprises the ground state $|G\rangle$, two degenerate intermediate single-excited states $|X_{\mathrm{H/V}}\rangle$, and the upper state $|XX\rangle$. Typically, $|XX\rangle$ is not found at twice the energy of the single-excited states but is shifted by the value E_{B}, e.g., in quantum dots, E_{B} is referred to as the biexciton binding energy.[9,42] Transitions between the FLE states that involve the state $|X_{\mathrm{H/V}}\rangle$ are coupled to horizontally/vertically polarized light. If the $|XX\rangle$ state has been prepared,[29,43–45] cascaded photon emission takes place when the FLE relaxes to its ground state resulting in the typical ΦBS.

An external laser with driving strength Ω is used to excite the FLE. The laser frequency is adjusted such that the two-photon transition between the ground state $|G\rangle$ and $|XX\rangle$ is driven resonantly, resulting in a fixed energetic detuning $\Delta_0 = E_{\mathrm{B}}/2$ between the single-excitation transitions and the laser (cf. Fig. 1). The laser polarization is chosen to be linear with equal components of the H and V polarization. The FLE is placed inside a microcavity and coupled to its two energetically degenerate linearly polarized modes, H and V. The energetic placement of the cavity modes is described by the cavity laser detuning Δ, i.e., the difference between the cavity mode and laser energy. In typical setups, the fabrication process determines Δ, and it cannot be changed afterward. Accordingly, we fix the cavity laser detuning to $\Delta = 0.8\Delta_0$. The coupling strength g between cavity and FLE is assumed to be equal for all FLE transitions.

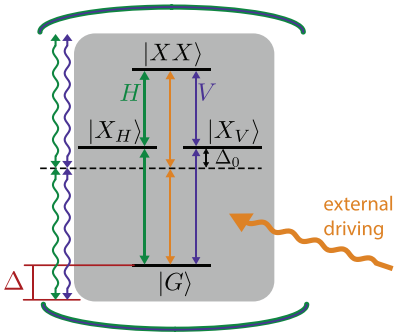

FIG. 1. Sketch of the driven FLE-cavity system. The FLE consists of the states $|G\rangle$, $|X_{\mathrm{H/V}}\rangle$, and $|XX\rangle$, which are coupled via optical transitions by horizontally/vertically polarized light (green/purple straight arrows). The FLE is driven by an external laser at the two-photon resonance, which results in a detuning of Δ_0 to the intermediate states (orange arrows). The FLE is embedded into a cavity with two energetically degenerate but orthogonal horizontally/vertically polarized cavity modes (green/purple wavy arrows) detuned by Δ to the laser energy.

Furthermore, important loss processes, i.e., radiative decay with rate γ and cavity losses with rate κ, are included using Lindblad-type operators.[39,46] The time evolution of the statistical operator of the system and two-time correlation functions are calculated by numerically solving the resulting Liouville–von Neumann equation.[47] The system parameters for the calculations are displayed in Table I.[38,39] Initially, the system is in the FLE ground state $|G\rangle$ without any cavity photons. For the Hamiltonian and details on the calculations, we refer to Ref. 39.

The entanglement characterization relies on the standard two-time correlation functions

$$G^{(2)}_{jk,lm}(t,\tau') = \langle \hat{a}^\dagger_j(t)\hat{a}^\dagger_k(t+\tau')\hat{a}_m(t+\tau')\hat{a}_l(t)\rangle, \tag{2}$$

with $\{j,k,l,m\} \in \{H,V\}$.[15] Here, t is the real time of the first photon detection and τ' is the delay time between this detection event and the detection of the second photon. The operator $\hat{a}^\dagger_{\mathrm{H/V}}$ creates one horizontally/vertically polarized cavity photon.[48] In realistic two-time coincidence experiments, the data are always obtained by averaging the signal over finite real time and delay time intervals. Consequently, we use averaged correlation functions that depend on the starting time of the coincidence measurement t_0, the used real time measurement interval Δt, and the delay time window τ (see also Ref. 39).

A measure to classify the entanglement is the two-photon density matrix $\rho^{2\mathrm{p}}$, from which the resulting type of entanglement can be extracted directly from its form. In standard experiments, $\rho^{2\mathrm{p}}$ is reconstructed employing quantum state tomography,[49] and, consequently, it is obtained from the averaged correlation functions as detailed in Ref. 39.

To quantify the degree of entanglement, we use the concurrence C, which can be calculated directly from the two-photon density matrix.[34,39,49–51] Note that both, the two-photon density matrix and the concurrence, depend on the parameters of the coincidence measurements: t_0, Δt, and τ. Throughout this article, a delay time window $\tau = 50$ ps is assumed.[52]

Before presenting the switching protocol, we study the behavior of the constantly driven FLE-cavity system as a function of the driving strength for a fixed selected cavity laser detuning. The resulting type of entanglement and its degree depend on the cavity laser detuning Δ and the driving strength Ω, as demonstrated in Ref. 39. In particular, a high degree of ΦBS or ΨBS entanglement is only possible, when the cavity modes are close to or in resonance with a direct two-photon transition between the laser-dressed states of the FLE. In the present setup, we have fixed all frequencies and detunings, such that the only free tuning parameter is the driving strength Ω.

TABLE I. Fixed system parameters used in the calculations.

Parameter		Value
Coupling strength	g	0.051 meV
Detuning	Δ_0	$20g = 1.02$ meV
Cavity laser detuning	Δ	$0.8\Delta_0 = 0.816$ meV
Cavity loss rate	κ	$0.1g/\hbar \approx 7.8\ \mathrm{ns}^{-1}$
Radiative decay rate	γ	$0.01g/\hbar \approx 0.78\ \mathrm{ns}^{-1}$

The constant driving of the FLE results in a mixing of the bare states $|G\rangle$, $|X_{H/V}\rangle$, and $|XX\rangle$, such that the new eigenstates are the laser-dressed states, which we label by $|U\rangle$, $|M\rangle$, $|N\rangle$, and $|L\rangle$. Their respective energies are given by[39]

$$E_U = \frac{1}{2}\left(\Delta_0 + \sqrt{\Delta_0^2 + 8\Omega^2}\right), \tag{3a}$$

$$E_M = \Delta_0, \tag{3b}$$

$$E_N = 0, \tag{3c}$$

$$E_L = \frac{1}{2}\left(\Delta_0 - \sqrt{\Delta_0^2 + 8\Omega^2}\right). \tag{3d}$$

Both the state mixing and the energies depend on the driving strength Ω, which we will now use to tune certain two-photon transitions in resonance with the cavity modes.

Figure 2 depicts the dressed state energies [panel (a)], the mean photon number $\langle n\rangle = \langle \hat{a}_H^\dagger \hat{a}_H + \hat{a}_V^\dagger \hat{a}_V\rangle$ [panel (b)], and the concurrence [panel (c)] as functions of the driving strength Ω. All quantities are calculated at times where the system has reached its steady state, i.e., it is assumed that the coincidence measurements necessary to determine ρ^{2p} and C are performed after the steady state in the system

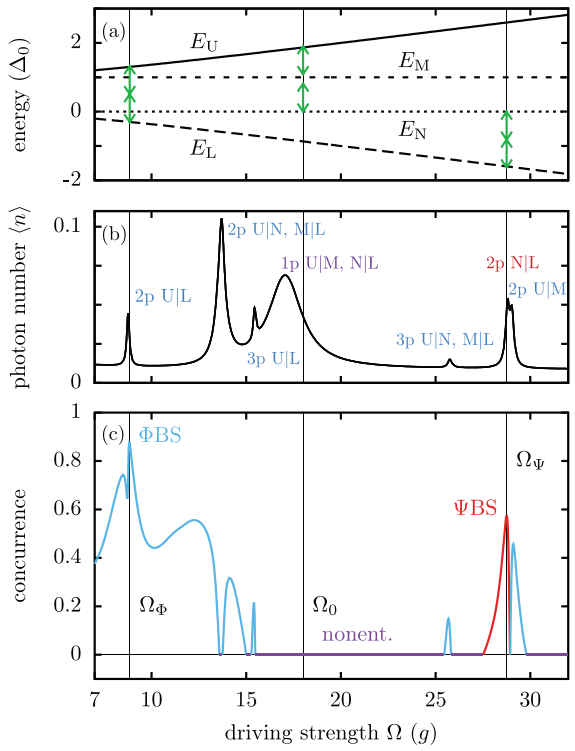

FIG. 2. (a) Energies of the four laser-dressed states as function of Ω (in units of g). Green double-headed arrows symbolize the cavity mode energy. (b) Mean photon number $\langle n\rangle$ and (c) concurrence as functions of the driving strength Ω for a cavity laser detuning $\Delta = 0.8\Delta_0$. n-photon resonances between the dressed states $|\chi_1\rangle$ and $|\chi_2\rangle$ are labeled by np $\chi_1|\chi_2$. The type of entanglement is color-coded: blue = ΦBS entanglement, red = ΨBS entanglement, purple = no entanglement. Straight lines mark the driving strengths used for switching in Fig. 3.

dynamics has been achieved.[53] A color code is used to distinguish among ΦBS (blue) entanglement, ΨBS (red) entanglement, and non-entangled photon pairs (purple).

The mean photon number exhibits a series of differently shaped peaks related to n-photon transitions between the four laser-dressed states. An n-photon transition between a pair of dressed states $|\chi_1\rangle$ and $|\chi_2\rangle$, labeled as np $\chi_1|\chi_2$ in Fig. 2(b), is in resonance with the cavity modes when n-times the cavity laser detuning Δ matches the transition energy $E_{\chi_1} - E_{\chi_2}$. Based on this condition, all peaks of enhanced photon production can be linked to one-, two-, or three-photon resonances between the dressed states. In particular, two-photon resonances manifest themselves as high and narrow peaks, e.g., for $\Omega \approx 9g$, $14g$, or $29g$.

Turning to the concurrence, presented in Fig. 2(c), one obtains again a peak-like structure and both types of Bell state entanglement occur. By comparing the concurrence and $\langle n\rangle$, one notes that the regions of high entanglement are associated with two-photon resonances. A more detailed analysis reveals that the features observable for $\Omega \approx 14g$ ($29g$) are actually caused by two closely spaced resonances, 2p U|N and 2p M|L (2p U|M and 2p N|L), which result in a double peak in the concurrence. A particularly high degree of ΦBS entanglement is obtained for $\Omega_\Phi = 8.85g$ when the cavity mode is almost at resonance with the two-photon transition between the dressed states $|U\rangle$ and $|L\rangle$, while at $\Omega_\Psi = 28.75g$, a high ΨBS entanglement occurs at the two-photon transition between $|N\rangle$ and $|L\rangle$. This behavior can be well understood using an analysis based on a Schrieffer–Wolff transformation.[39] Additionally, three-photon resonances lead to small peaks in the concurrence and in the mean photon number.

Besides the regions of high ΦBS and ΨBS entanglement, also a wide regime of vanishing concurrence is found, between $\Omega = 16g, \ldots, 25g$, where the cavity modes do not match any multi-photon transition process, cf. Fig. 2. Note that the vanishing degree of entanglement in this parameter regime is not due to a lack of emitted photons. On the contrary, the photon generation can be comparatively high due to the proximity to one-photon resonances, cf. Fig. 2(b). Therefore, in this parameter regime, the measurement detects two subsequent photons that are not entangled.

According to our findings, we choose three driving strengths Ω_j with similar photon number, but different types of entanglement for the switching protocol: at $\Omega_\Phi = 8.85g$, we have a strong ΦBS entanglement, at $\Omega_0 = 18.00g$, we have no entanglement, and at $\Omega_\Psi = 28.75g$, we have a strong ΨBS entanglement.

We propose a step-like excitation protocol to demonstrate time-dependent entanglement switching. The results are presented in Fig. 3. A schematic sketch of the protocol is depicted in Fig. 3(a). The basic idea is to change between three different driving strengths Ω_j that, in the stationary case, are associated with different types of entangled photon pairs. During the protocol, the FLE is continuously driven with a constant driving strength Ω_j for a fixed time period T, and then Ω changes step-like to one of the other two values. Accordingly, the resulting time-dependent laser driving has a step-like structure with step length T. In order to allow for a time resolved detection of the entanglement type, measurements with measurement interval $\Delta t = T/4$, delay time window $\tau = 50$ ps, and varying starting times t_0 are performed.

Figure 3(b) displays the calculated concurrence for each measurement as a function of its respective starting time t_0, where a step length

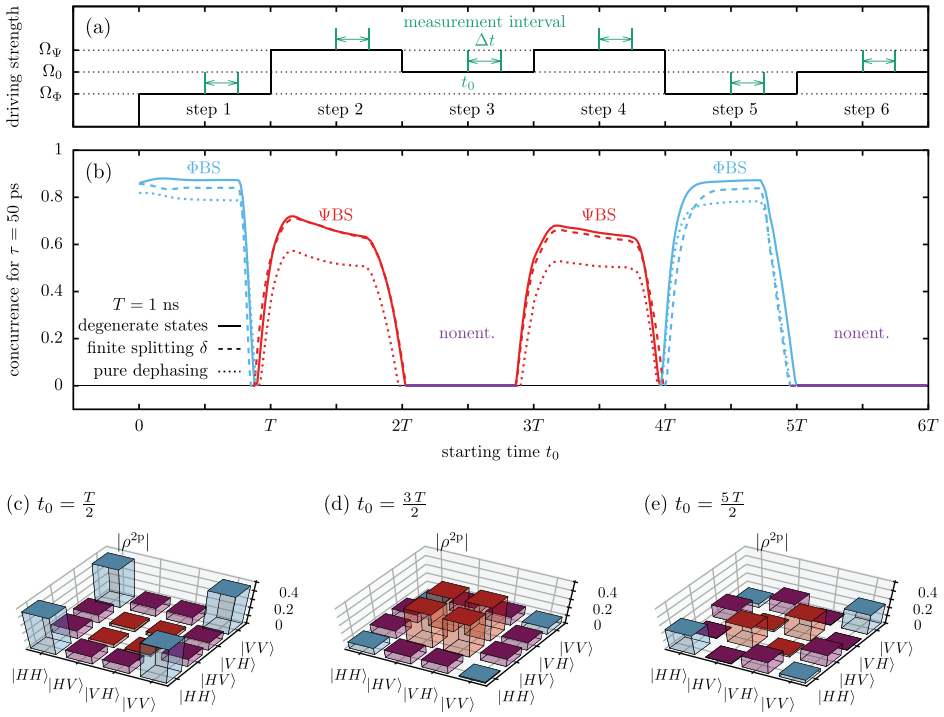

FIG. 3. (a) The proposed protocol that enables time-dependent entanglement switching. The driving strength is changed instantaneously between the three values Ω_Φ, Ω_Ψ, and Ω_0 after a time interval T, resulting in a step-like time-dependent laser driving with step length T. During each step j, coincidence measurements with starting time t_0, measurement interval $\Delta t = T/4$, and delay time window $\tau = 50$ ps can be performed. (b) Concurrence calculated for the respective measurements as a function of the starting time t_0 for a step length $T = 1$ ns. Results are calculated for degenerate intermediate states $|X_{H/V}\rangle$ (solid line), for the finite fine-structure splitting $\delta = 0.1\Delta_0$ between them (dashed line), and including pure dephasing with $\hbar\gamma_{PD} = 3$ μeV (dotted line). The cavity laser detuning is set to $\Delta = 0.8\Delta_0$, and the driving strength values $\Omega_\Phi = 8.85\,g$, $\Omega_\Psi = 28.75\,g$, and $\Omega_0 = 18\,g$ are used. A color code indicates ΦBS (blue) and ΨBS (red) entanglement as well as nonentangled photon pairs (purple). (c)–(e) Corresponding two-photon density matrices ρ^{2p} obtained for the measurements performed at $t_0 = T/2$, $3T/2$, and $5T/2$ for the case of degenerate intermediate states.

of $T = 1$ ns is assumed. As before, the entanglement type is color coded: blue (red) indicates ΦBS (ΨBS) entanglement and purple symbolizes nonentangled photon pairs. The corresponding two-photon density matrices for the measurements performed at $t_0 = T/2$, $3T/2$, and $5T/2$ are depicted in Figs. 3(c)–3(e).

The protocol starts with the driving strength Ω_Φ, and indeed, ΦBS entanglement with a high concurrence is obtained. The corresponding two-photon density matrix shown in Fig. 3(c) represents a two-photon state close to a maximally entangled ΦBS. We find that the occupations of the states with two equally polarized photons, $|HH\rangle$ and $|VV\rangle$, and the coherence between them dominate ρ^{2p} such that their absolute values are close to 1/2. In the second step, we switch to Ω_Ψ and obtain a high concurrence related to ΨBS entanglement. In the two-photon density matrix, presented in Fig. 3(d), the states $|HV\rangle$ and $|VH\rangle$ display the highest occupations and coherence values. In the third step with Ω_0, the entanglement is switched off with zero concurrence. The corresponding, reconstructed density matrix is similar to a statistical mixture, where the coherences needed for an entangled Bell state are practically absent, resulting in a vanishing degree of entanglement.

Having demonstrated that all types of entanglement can be created, we continue the protocol demonstrating that the order of switching does not play a role. Accordingly, in step 4, we switch into ΨBS entanglement; in step 5, we switch into ΦBS entanglement; and in step 6, back to no entanglement. The obtained concurrence is similar to that in steps 1–3. We also checked that density matrices ρ^{2p} obtained in the middle of steps 4, 5, and 6 are almost identical to those presented in Figs. 3(c)–3(e) for the respective driving strength (not shown).

It is also interesting to look at the case when the measurements start in the vicinity of switching times jT, where $j \in \{1, 2, \ldots, 5\}$. Here, one observes a continuous transition between the different entanglement types. This transition begins when the measurement starting at t_0 extends into the next step, i.e., when $t_0 \geq jT - \Delta t$. During this transition process, the degree of entanglement, as measured by the concurrence, passes through zero when one switches between ΦBS and ΨBS entanglement, or vice versa. After a short transition interval, the measured concurrence enters either a plateau of high entanglement associated with the used driving strength or remains zero, when the driving strength is Ω_0.

An important question is how sensitive the proposed protocol is to parameter variations. The main requirement is that different types of entanglement can be obtained at different driving strength values. While regions of high ΦBS entanglement can be found rather easily, ΨBS entanglement occurs not so often. Only the two-photon transition 2p N|L always features ΨBS entanglement, while for high driving strengths, it can be found also at the 2p U|L resonance.[39] Furthermore, the necessary precondition to obtain ΨBS entanglement at these resonances is a finite detuning Δ_0. In principle, in these situations, one can then switch between the different entanglement types using any finite cavity laser detuning Δ. Hence, we expect that the protocol also works for different values of Δ_0 and Δ. However, a more elaborate analysis suggests that high concurrence values for both entanglement types are only obtained if Δ and Δ_0 are of the same order.

Another possible perturbation is an energy difference between the single-excited states $|X_{H/V}\rangle$, which, in quantum dots, is known as the fine-structure splitting (FSS). A finite FSS, defined as $\delta = \hbar\omega_{X_H} - \hbar\omega_{X_V}$, between the energies of the intermediate bare states $|X_{H/V}\rangle$, is regarded as a main obstacle for entanglement generation,[14,17,26,32,33] because it introduces which-path information and, thus, reduces the degree of entanglement.[14,17,31]

To consider the effect of a FSS on the switching protocol and entangled photon pair generation, we included an FSS of $\delta = 0.1\Delta_0$ in our calculations [dashed line in Fig. 3(b)], which is a typical value being one order of magnitude smaller than the binding energy.[26,29,31,32] We find that this rather large FSS only marginally reduces the concurrence compared with the previous results. The reason is that the transitions in the driven system take place between the laser-dressed states. The FSS affects the energies of the laser-dressed states and their composition only weakly such that the resonance conditions and optical selection rules hold. This implies that the generated photonic states are practically the same, and the proposed protocol is robust with respect to a nonzero FSS.

By adding a phenomenological rate model[17,35]

$$\mathcal{L}_{\mathrm{PD}}\hat{\rho} = -\frac{1}{2}\sum_{\substack{\chi,\chi'\\ \chi\neq\chi'}} \gamma_{\mathrm{PD}}|\chi\rangle\langle\chi|\hat{\rho}|\chi'\rangle\langle\chi'|, \tag{4}$$

with rate γ_{PD} and $\chi, \chi' \in \{G, X_{\mathrm{H}}, X_{\mathrm{V}}, XX\}$ acting on the statistical operator $\hat{\rho}$, we, furthermore, consider the influence of pure dephasing. Using a realistic value for quantum dots at low temperatures,[17] $\hbar\gamma_{\mathrm{PD}} = 3\ \mu\mathrm{eV}$, we find that, although the concurrence is reduced, all essential features are unaffected. In particular, one can still switch between different entanglement types with corresponding concurrence $C \geq 0.5$ [dotted line in Fig. 3(b)].

In conclusion, this work presents a protocol for time-dependent entanglement switching based on a driven four-level emitter–cavity system. The protocol is operated by simply switching between different driving strengths in a step-like manner. Depending on the driving strength, one obtains either ΦBS entanglement, ΨBS entanglement, or nonentangled photon pairs in the respective measurements. Thus, this work demonstrates a possibility to actively switch between different types of entanglement using a time-dependent external laser excitation. The protocol is also robust against a possible FSS. It is stressed that the protocol enables one to achieve different types of entanglement within the same basis and without further post-processing of the generated photons.

The proposed protocol is, therefore, a suitable candidate for the realization of time-dependent entanglement switching, which is an important step toward future applications.

D. E. Reiter acknowledges support from the Deutsche Forschungsgemeinschaft (DFG) via the Project No. 428026575. We are further grateful for support from the Deutsche Forschungsgemeinschaft (DFG, German Research Foundation) via the Project No. 419036043.

DATA AVAILABILITY

The data that support the findings of this study are available from the corresponding author upon reasonable request.

REFERENCES

[1]N. Gisin, G. Ribordy, W. Tittel, and H. Zbinden, Rev. Mod. Phys. **74**, 145 (2002).
[2]H.-K. Lo, M. Curty, and K. Tamaki, Nat. Photonics **8**, 595 (2014).
[3]L.-M. Duan, M. D. Lukin, J. I. Cirac, and P. Zoller, Nature **414**, 413 (2001).
[4]D. Huber, M. Reindl, J. Aberl, A. Rastelli, and R. Trotta, J. Opt. **20**, 073002 (2018).
[5]J.-W. Pan, Z.-B. Chen, C.-Y. Lu, H. Weinfurter, A. Zeilinger, and M. Żukowski, Rev. Mod. Phys. **84**, 777 (2012).
[6]C. H. Bennett and D. P. DiVincenzo, Nature **404**, 247 (2000).
[7]S. C. Kuhn, A. Knorr, S. Reitzenstein, and M. Richter, Opt. Express **24**, 25446 (2016).
[8]A. Zeilinger, Phys. Scr. **92**, 072501 (2017).
[9]A. Orieux, M. A. M. Versteegh, K. D. Jöns, and S. Ducci, Rep. Prog. Phys. **80**, 076001 (2017).
[10]K. Edamatsu, Jpn. J. Appl. Phys., Part 1 **46**, 7175 (2007).
[11]S. J. Freedman and J. F. Clauser, Phys. Rev. Lett. **28**, 938 (1972).
[12]J. Wen, S. Du, Y. Zhang, M. Xiao, and M. H. Rubin, Phys. Rev. A **77**, 033816 (2008).
[13]J. Park, T. Jeong, H. Kim, and H. S. Moon, Phys. Rev. Lett. **121**, 263601 (2018).
[14]T. Seidelmann, F. Ungar, M. Cygorek, A. Vagov, A. M. Barth, T. Kuhn, and V. M. Axt, Phys. Rev. B **99**, 245301 (2019).
[15]M. Cygorek, F. Ungar, T. Seidelmann, A. M. Barth, A. Vagov, V. M. Axt, and T. Kuhn, Phys. Rev. B **98**, 045303 (2018).
[16]T. Seidelmann, F. Ungar, A. M. Barth, A. Vagov, V. M. Axt, M. Cygorek, and T. Kuhn, Phys. Rev. Lett. **123**, 137401 (2019).
[17]S. Schumacher, J. Förstner, A. Zrenner, M. Florian, C. Gies, P. Gartner, and F. Jahnke, Opt. Express **20**, 5335 (2012).
[18]D. Heinze, A. Zrenner, and S. Schumacher, Phys. Rev. B **95**, 245306 (2017).
[19]A. Carmele and A. Knorr, Phys. Rev. B **84**, 075328 (2011).
[20]R. M. Stevenson, R. J. Young, P. Atkinson, K. Cooper, D. A. Ritchie, and A. J. Shields, Nature **439**, 179 (2006).
[21]R. J. Young, R. M. Stevenson, P. Atkinson, K. Cooper, D. A. Ritchie, and A. J. Shields, New J. Phys. **8**, 29 (2006).
[22]A. Muller, W. Fang, J. Lawall, and G. S. Solomon, Phys. Rev. Lett. **103**, 217402 (2009).
[23]D. Huber, M. Reindl, S. F. Covre da Silva, C. Schimpf, J. Martín-Sánchez, H. Huang, G. Piredda, J. Edlinger, A. Rastelli, and R. Trotta, Phys. Rev. Lett. **121**, 033902 (2018).
[24]H. Wang, H. Hu, T.-H. Chung, J. Qin, X. Yang, J.-P. Li, R.-Z. Liu, H.-S. Zhong, Y.-M. He, X. Ding, Y.-H. Deng, Q. Dai, Y.-H. Huo, S. Höfling, C.-Y. Lu, and J.-W. Pan, Phys. Rev. Lett. **122**, 113602 (2019).
[25]J. Liu, R. Su, Y. Wei, B. Yao, S. F. C. d Silva, Y. Yu, J. Iles-Smith, K. Srinivasan, A. Rastelli, J. Li, and X. Wang, Nat. Nanotechnol. **14**, 586 (2019).
[26]S. Bounouar, C. de la Haye, M. Strauß, P. Schnauber, A. Thoma, M. Gschrey, J.-H. Schulze, A. Strittmatter, S. Rodt, and S. Reitzenstein, Appl. Phys. Lett. **112**, 153107 (2018).
[27]A. Dousse, J. Suffczyński, A. Beveratos, O. Krebs, A. Lemaître, I. Sagnes, J. Bloch, P. Voisin, and P. Senellart, Nature **466**, 217 (2010).
[28]R. Winik, D. Cogan, Y. Don, I. Schwartz, L. Gantz, E. R. Schmidgall, N. Livneh, R. Rapaport, E. Buks, and D. Gershoni, Phys. Rev. B **95**, 235435 (2017).
[29]M. Müller, S. Bounouar, K. D. Jöns, M. Glässl, and P. Michler, Nat. Photonics **8**, 224 (2014).
[30]A. Fognini, A. Ahmadi, M. Zeeshan, J. T. Fokkens, S. J. Gibson, N. Sherlekar, S. J. Daley, D. Dalacu, P. J. Poole, K. D. Jöns, V. Zwiller, and M. E. Reimer, ACS Photonics **6**, 1656 (2019).
[31]N. Akopian, N. H. Lindner, E. Poem, Y. Berlatzky, J. Avron, D. Gershoni, B. D. Gerardot, and P. M. Petroff, Phys. Rev. Lett. **96**, 130501 (2006).
[32]R. Hafenbrak, S. M. Ulrich, P. Michler, L. Wang, A. Rastelli, and O. G. Schmidt, New J. Phys. **9**, 315 (2007).
[33]A. J. Bennett, M. A. Pooley, R. M. Stevenson, M. B. Ward, R. B. Patel, A. B. de la Giroday, N. Sköld, I. Farrer, C. A. Nicoll, D. A. Ritchie, and A. J. Shields, Nat. Phys. **6**, 947 (2010).
[34]E. del Valle, New J. Phys. **15**, 025019 (2013).
[35]F. Troiani, J. I. Perea, and C. Tejedor, Phys. Rev. B **74**, 235310 (2006).
[36]R. M. Stevenson, C. L. Salter, J. Nilsson, A. J. Bennett, M. B. Ward, I. Farrer, D. A. Ritchie, and A. J. Shields, Phys. Rev. Lett. **108**, 040503 (2012).
[37]O. Benson, C. Santori, M. Pelton, and Y. Yamamoto, Phys. Rev. Lett. **84**, 2513 (2000).
[38]C. Sánchez Muñoz, F. P. Laussy, C. Tejedor, and E. del Valle, New J. Phys. **17**, 123021 (2015).
[39]T. Seidelmann, M. Cosacchi, M. Cygorek, D. E. Reiter, A. Vagov, and V. M. Axt, Adv. Quantum Technol. **4**, 2000108 (2021).
[40]P.-L. Ardelt, M. Koller, T. Simmet, L. Hanschke, A. Bechtold, A. Regler, J. Wierzbowski, H. Riedl, J. J. Finley, and K. Müller, Phys. Rev. B **93**, 165305 (2016).

[41]F. Hargart, M. Müller, K. Roy-Choudhury, S. L. Portalupi, C. Schneider, S. Höfling, M. Kamp, S. Hughes, and P. Michler, Phys. Rev. B **93**, 115308 (2016).
[42]Q. Mermillod, D. Wigger, V. Delmonte, D. E. Reiter, C. Schneider, M. Kamp, S. Höfling, W. Langbein, T. Kuhn, G. Nogues, and J. Kasprzak, Optica **3**, 377 (2016).
[43]D. E. Reiter, T. Kuhn, M. Glässl, and V. M. Axt, J. Phys. **26**, 423203 (2014).
[44]M. Reindl, K. D. Jöns, D. Huber, C. Schimpf, Y. Huo, V. Zwiller, A. Rastelli, and R. Trotta, Nano Lett. **17**, 4090 (2017).
[45]L. Hanschke, K. A. Fischer, S. Appel, D. Lukin, J. Wierzbowski, S. Sun, R. Trivedi, J. Vucković, J. J. Finley, and K. Müller, npj Quantum Inf. **4**, 43 (2018).
[46]G. Lindblad, Commun. Math. Phys. **48**, 119 (1976).
[47]M. Cosacchi, M. Cygorek, F. Ungar, A. M. Barth, A. Vagov, and V. M. Axt, Phys. Rev. B **98**, 125302 (2018).
[48]Note that in typical experiments the measurements are performed on photons which have already left the cavity. Nevertheless, when the out-coupling of light out of the cavity is considered to be a Markovian process, Eq. (2) can be used to describe $G^{(2)}(t,\tau')$ as measured outside of the cavity (cf. Refs. 7 and 15).
[49]D. F. V. James, P. G. Kwiat, W. J. Munro, and A. G. White, Phys. Rev. A **64**, 052312 (2001).
[50]W. K. Wootters, Phys. Rev. Lett. **80**, 2245 (1998).
[51]$C = \max\{\sqrt{\lambda_1} - \sqrt{\lambda_2} - \sqrt{\lambda_3} - \sqrt{\lambda_4}, 0\}$ where $\lambda_j \geq \lambda_{j+1}$ are the eigenvalues of $\rho^{2p} T \rho^{2p*} T$ in decreasing order and T is the antidiagonal matrix with elements $\{-1, 1, 1, -1\}$.
[52]R. M. Stevenson, A. J. Hudson, A. J. Bennett, R. J. Young, C. A. Nicoll, D. A. Ritchie, and A. J. Shields, Phys. Rev. Lett. **101**, 170501 (2008).
[53]Note that in the steady state situation with constant continuous driving, ρ^{2p} and C do not depend on Δt since the statistical operator and the Hamiltonian $\hat{H}$ are constant during the measurement process.

Publication 6

On-demand generation of higher-order Fock states in quantum-dot–cavity systems.

M. Cosacchi, J. Wiercinski, T. Seidelmann, M. Cygorek, A. Vagov, D. E. Reiter, V. M. Axt.

Phys. Rev. Research **2**, 033489 (2020).

DOI: 10.1103/PhysRevResearch.2.033489

Author contributions

The author has designed the concept of this study, in particular, he has performed the data generation and analysis, has provided the interpretation of the results, and has written the first draft of the paper. He has moderated all discussions and revision requests of the draft, has organized the correspondence with the editor and referees, and has provided the first drafts of answers to the referees.

J. Wiercinski has analyzed and optimized both Fock state preparation protocols for the two-level model in the phonon-free case. He has demonstrated the limits of the implicit model that includes the AC-Stark pulse indirectly. He has participated in the discussion and interpretation of the results and has contributed to revisions of the draft and the answers to the referees.

T. Seidelmann has discussed the results in detail with the author, thus contributing to the interpretation, and has contributed to revisions of the draft and the answers to the referees.

M. Cygorek, A. Vagov, and D. E. Reiter have cosupervised this work, in particular, they have participated in the discussion and interpretation of the results. They have contributed to the optimization of the presentation as well as revisions of the draft and the answers to the referees.

V. M. Axt has advised the author throughout his work as the main supervisor. He has obtained the funding for this work and has participated in the discussion and interpretation of the results. He has contributed to the optimization of the presentation as well as revisions of the draft and the answers to the referees.

On-demand generation of higher-order Fock states in quantum-dot–cavity systems

M. Cosacchi,[1] J. Wiercinski,[1] T. Seidelmann,[1] M. Cygorek,[2] A. Vagov,[1,3] D. E. Reiter,[4] and V. M. Axt[1]

[1]*Theoretische Physik III, Universität Bayreuth, 95440 Bayreuth, Germany*

[2]*Heriot-Watt University, Edinburgh EH14 4AS, United Kingdom*

[3]*ITMO University, St. Petersburg, 197101, Russia*

[4]*Institut für Festkörpertheorie, Universität Münster, 48149 Münster, Germany*

(Received 26 June 2020; accepted 1 September 2020; published 24 September 2020)

The on-demand preparation of higher-order Fock states is of fundamental importance in quantum information sciences. We propose and compare different protocols to generate higher-order Fock states in solid state quantum-dot–cavity systems. The protocols make use of a series of laser pulses to excite the quantum dot exciton and off-resonant pulses to control the detuning between dot and cavity. Our theoretical studies include dot and cavity loss processes as well as the pure-dephasing type coupling to longitudinal acoustic phonons in a numerically complete fashion. By going beyond the two-level approximation for quantum dots, we study the impact of a finite exchange splitting, the impact of a higher energetic exciton state, and an excitation with linearly polarized laser pulses leading to detrimental occupations of the biexciton state. We predict that under realistic conditions, a protocol which keeps the cavity at resonance with the quantum dot until the desired target state is reached is able to deliver fidelities to the Fock state $|5\rangle$ well above 40%.

DOI: 10.1103/PhysRevResearch.2.033489

I. INTRODUCTION

Semiconductor quantum-dot–cavity (QDC) systems are widely discussed as candidates for highly integrable on-demand emitters of nonclassical states of light. They have been successfully proven to be reliable sources of high quality single photons [1–10] as well as entangled photon pairs [11–18]. Nonetheless, the preparation of higher-order Fock states remains a challenge. These states find vast applications in quantum metrology [19–21], as building blocks for more complex quantum states of light such as Schrödinger cat states [22], and in quantum computing [23].

While schemes to prepare higher-order Fock states have been known in atomic cavity systems for decades [24–26], these protocols rely on properties specific to atoms, such as the finite time of flight through a resonator, which cannot be translated straightforwardly to a locally fixed solid state qubit as encountered in quantum dots (QDs). Nonetheless, this protocol has been applied to a superconducting qubit coupled to a microwave cavity [27]. In this setup, coupling the qubit and the cavity only temporarily is achieved by changing the structure of the potential with an external flux bias and thus directly tuning the resonance frequency of the qubit. This is not possible in QDCs after the growth process is completed and thus the confinement potential set. Furthermore, protocols involving parametric down-conversion have achieved remarkable fidelities to the targeted higher-order Fock states [28]. A huge challenge in such setups to be solved is the on-demand character of these sources.

In this work, we propose protocols for the preparation of higher-order Fock states in QDCs and explore their feasibility up to $n = 5$. The protocols rely on the application of a series of ultrashort laser pulses combined with off-resonant laser pulses to induce an AC-Stark effect. In contrast to atoms, QDs are solid state systems and are therefore affected by the electron-phonon interaction. The pure-dephasing type coupling of the excitonic states to longitudinal acoustic phonons is known as the main source of decoherence in QDs even at cryogenic temperatures of a few Kelvin [29–33]. Accordingly, we study the influence of phonons as well as of cavity and radiative losses on the proposed protocols. Because we use ultrashort pulses, we further calculate the influence of higher energetic excitons on the preparation schemes. In neutral QDs, the approximation of the QD as a two-level system is often reasonable. In particular, this is the case when transitions to the biexciton are forbidden by selection rules. Note that this sets constraints on the polarization of the driving laser as well as on the resonantly coupled cavity modes. Furthermore, the two-level approximation holds well, when the fine-structure splitting (FSS) happens to be absent or is suppressed, e.g., by external fields, strain, or by fabricating highly symmetrical QDs [12,34–37]. We study the respective influences by extending our system to a three- or four-level system.

We show that even under these realistic conditions, our preparation schemes can reach fidelities to the Fock state $|5\rangle$ well above 40%. To put this value into perspective, let us compare it to other works. Hofheinz *et al.* [27] prepared Fock states with up to six photons in their superconducting qubit

setup but do not report a value for the fidelity. To be able to compare our results with theirs, we simulated the experiment described in Ref. [27] to reproduce the figures therein, while giving an estimate for the preparation fidelity of their setup. For the fidelity to the state $|5\rangle$ our estimate yields $\approx$20%. Tiedau *et al.* [28] use heralded parametric down-conversion to generate higher-order Fock states. Their best fidelities to Fock states with $n \geqslant 5$ do not exceed 50%. Therefore our QDC protocol is competitive with other means to prepare higher-order Fock states. Compared with superconducting qubits, QDCs have the advantage of being in an energetic regime corresponding to the ps- rather than the nanosecond timescale, thus making the total preparation time for the Fock state $|5\rangle$ about three orders of magnitude faster.

In the following, we start our analysis with a simple two-level QD-model and subsequently shift our focus to more complex situations by taking into account levels present in a QD that might have adverse effects on the preparation fidelity of higher-order Fock states.

II. PROTOCOLS FOR A TWO-LEVEL SYSTEM

In atomic cavities, protocols for the preparation of higher-order Fock states have been successfully employed in the 1980s. A well known example is the so called micromaser setup, where a highly excited Rydberg atom is brought to resonance with a single-mode cavity only during its time of flight through the resonator [24–26]. Sending excited atoms subsequently through the cavity fills the latter with one more photon at a time, thus preparing a higher-order Fock state. While earlier experiments [25] succeeded in the preparation of up to $n = 2$, recent results yield states with up to seven photons [26]. This technique was translated to a solid state platform by Hofheinz *et al.* [27]. In that work, a superconducting qubit is coupled to a single mode of a microwave cavity. The transition frequency of the former can be tuned to bring it to resonance with the resonator frequency only during a finite time window, in which half a Rabi oscillation transfers the excitation from the qubit to a cavity photon. This procedure simulates the finite dwell time of an atom in a cavity with a locally fixed superconducting qubit.

In the QDC case, there are several differences to the atomic situation. Firstly, the interaction between the QD and the cavity cannot be turned off by removing the QD from the cavity. Secondly, the transition frequency of the QD is set once the nanostructure is grown. Nonetheless, preparation schemes similar to those used in atomic cavities can be realized also in QDCs using the mechanisms sketched in Fig. 1. An interchange between exciting the QD with a sequence of π-pulses and controlling the effective cavity-QD coupling by inducing AC-Stark shifts lies at the heart of the two schemes we present here. The difference between them is the way the AC-Stark pulses are used: in the first scheme, they lead to a cavity-QD coupling, while in the second one, they decouple the two subsystems at the end of the protocol. Note that inducing ultrafast Stark shifts is also possible by electrical, rather than optical manipulation of the system [38].

We start by assuming that the QD can be modelled as a two-level system, while we will discuss more realistic QD models in Sec. III. This approximation holds very well for

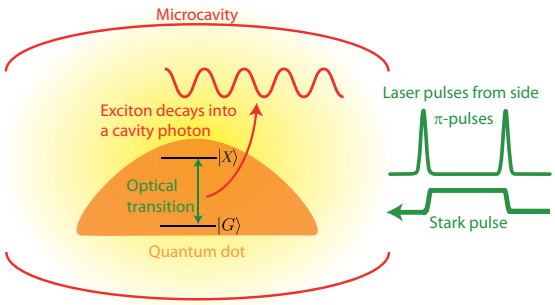

FIG. 1. Sketch of the QDC system, where photons are created by recombination of the QD exciton. A Stark pulse from the side controls the photon emission such that Fock states can be generated on demand.

strongly confined charged QDs where the ground state is coupled to a trion state and higher excited states are energetically well separated. But it can also be realized in neutral QDs where, however, it entails constraints on the FSS, the polarizations of the driving laser, and the cavity modes.

The Hamiltonian for the two-level QD coupled to a single cavity mode and driven by external laser pulses reads

$$\begin{aligned} H_{\mathrm{2LS}} &= \hbar\omega_X |X\rangle\langle X| + \hbar\omega_C a^\dagger a + \hbar g(a\sigma_X^\dagger + a^\dagger \sigma_X) \\ &\quad - \frac{\hbar}{2}(f_X^*(t)\sigma_X + f_X(t)\sigma_X^\dagger), \\ f_X(t) &= f^{\mathrm{pulses}}(t) + f^{\mathrm{AC\text{-}Stark}}(t), \end{aligned} \tag{1}$$

where $|X\rangle$ is the exciton state at energy $\hbar\omega_X$ and $\sigma_X := |G\rangle\langle X|$ is the operator for the transition between $|X\rangle$ and the ground state $|G\rangle$. The energy of the latter is set to zero. a denotes the photonic annihilation operator. The QDC is described by the Jaynes-Cummings model and the exciting and Stark laser pulses are represented by the function $f_X(t)$, which is specified in Appendix A 1, in particular its two parts $f^{\mathrm{pulses}}(t)$ and $f^{\mathrm{AC\text{-}Stark}}(t)$. The cavity frequency is denoted by ω_C and its coupling to the QD by g. We further account for the pure-dephasing type interaction with longitudinal acoustic (LA) phonons [29–33], the radiative decay of the QD excitons, and cavity losses. In this work, whenever we consider phononic effects, the phonons are assumed to be initially in thermal equilibrium at a temperature of $T = 4$ K. We solve the corresponding Liouville equation in a numerically complete manner by employing a path-integral formalism (for details see Refs. [39–41] and Appendix A 1). The parameters for the calculation are given in Appendix A 2.

A. Protocol with interrupted coupling (PIC)

In a first step, we would like to translate the protocol known from atomic cavities as closely as possible to our solid state platform. Therefore we assume that the QD transition and the cavity mode are off-resonant. In particular, we assume that $\Delta\omega_{\mathrm{CX}} := \omega_{\mathrm{C}} - \omega_{\mathrm{X}} > 0$, i.e., the QD line lies below the cavity. In order to enable the efficient generation of a single photon in the cavity we apply an AC-Stark pulse tuned below the exciton line to bring the QD in resonance with the cavity.

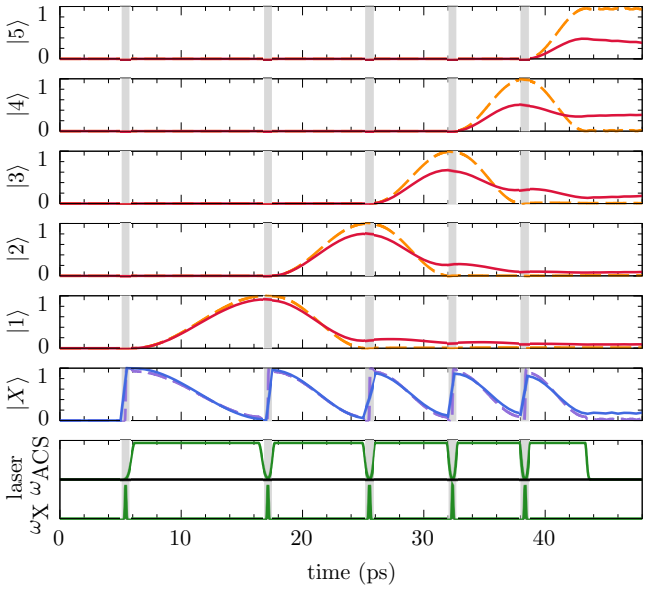

FIG. 2. Dynamics of a QDC for the PIC. Panels from bottom to top: series of ultrafast π-pulses and off-resonant AC-Stark pulses (green); the occupation of the exciton $|X\rangle$ (blue), occupation of the photon states $|n\rangle = |1\rangle, |2\rangle, \ldots, |5\rangle$ (red/orange). Dashed lines: without phonons and without losses. Solid lines with phonons as well as cavity losses and radiative decay.

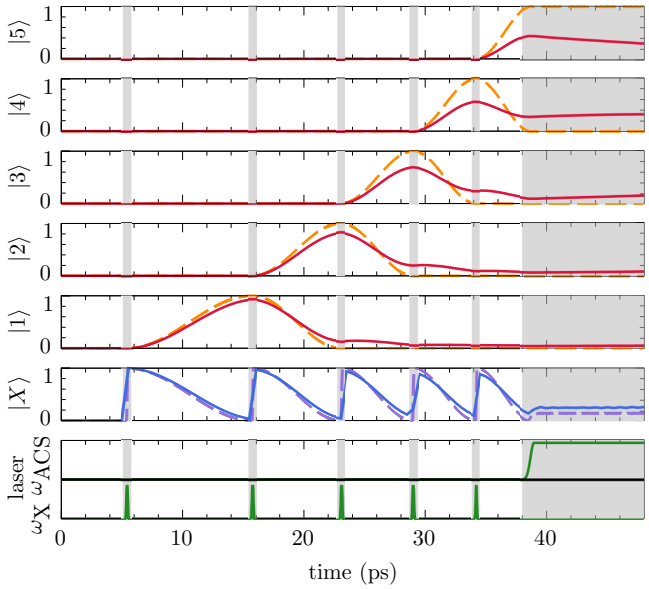

FIG. 3. Dynamics of the QDC for the PUC. Panels and line types as in Fig. 2

Each Stark pulse is a rectangular pulse with softened edges [cf., Eq. (A3)]. Whilst in resonance, the QD exciton can emit a photon. Before a re-absorption of this photon occurs, we switch off the AC-Stark pulse, thus effectively interrupting the coupling of QD and cavity. Now these steps can be repeated to reach any desired photon state. In the following, we refer to this scheme as *protocol with interrupted coupling* (PIC).

The corresponding dynamics of the PIC is displayed in Fig. 2. The panels from bottom to top show the laser pulses (green), the occupation of the exciton $|X\rangle$ (blue), and the occupation of the photon states $|n\rangle = |1\rangle, |2\rangle, \ldots, |5\rangle$ (red/orange). We use our procedure of alternating π- and AC-Stark pulses five times until the Fock state $|5\rangle$ is prepared. The dashed lines show the protocol in the ideal case of a two-level system without phonons and losses. Here, every Fock state is reached with a near-unity fidelity of 96.3% (cf., Sec. II C for a formal definition of this quantity). Because the Rabi frequency depends on the number of photons already present in the cavity, the length of the AC-Stark pulses for each step is reduced by $1/\sqrt{n}$ compared to the first Stark pulse.

When taking both the phonon Hamiltonian and Markovian loss processes into account, both the exciton occupation and the occupation of the photon states are reduced (solid lines in Fig. 2) and the fidelity of the protocol diminishes considerably. Nonetheless, we are still able to address each Fock state with our protocol. We note that cavity losses are responsible for the refilling of the Fock state with $n-1$ photons during the preparation of the state with n leading to an additional loss of fidelity. Moreover, this effect yields second local maxima in the fidelity after the first ones intended by the preparation.

Even when considering all loss channels, we find a fidelity of 38.5%, which is in good comparison with other protocols [27,28]. A further advantage of the PIC is that the preparation is on-demand, which is a challenge in setups relying on parametric down-conversion.

B. Protocol with uninterrupted coupling (PUC)

In contrast to the previous situation, now we consider the case that the QD and the cavity shall be grown such that they are on-resonance ($\Delta\omega_{CX} = 0$). Such systems are nowadays common in QDCs [42,43]. If now a series of resonant π-pulses hits the QD, such that the exciton performs half a Rabi oscillation in the time between the pulses, a number of photons according to the number of π-pulses is created. Since in this scheme the coupling between QD and cavity is kept at resonance until the final state is reached, we refer to it as *protocol with uninterrupted coupling* (PUC). Note that like for the PIC the delay between the pulses has to be scaled by $1/\sqrt{n}$. Only when the target state has been reached, an AC-Stark pulse decouples the QD and the cavity to store the desired number state.

Figure 3 shows the dynamics of the participating quantities for the PUC. In the phonon- and loss-free case (dashed lines in Fig. 3), the fidelity to the five-photon state is 99.4% which is even slightly higher than in the PIC, where we only reached 96.3%. Including the influence of phonons and losses, qualitatively the same effects as in the PIC can be observed, in particular the refilling of lower number states due to the cavity losses (solid lines in Fig. 3). We achieve a fidelity including phonons and Markovian losses of 45.1%.

C. Comparison of the two protocols

The striking difference between the two protocols is their total duration. The PUC is roughly 15% faster than its PIC counterpart. This minimizes the time when losses can influence the dynamics.

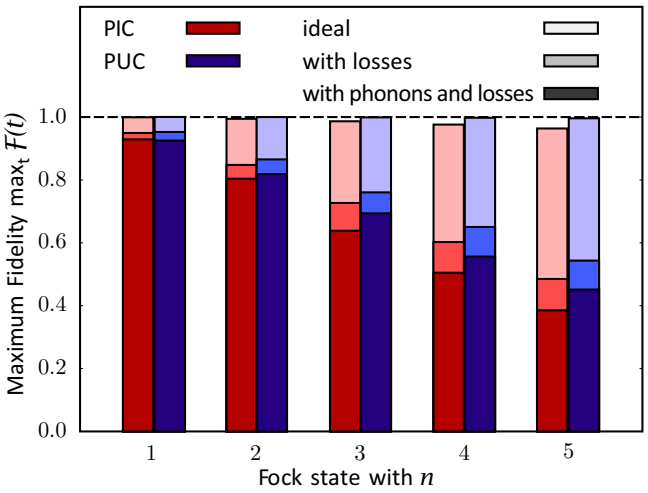

FIG. 4. The maximum fidelity over time to the Fock states $|n\rangle$, $n \in \{1, 2, \ldots, 5\}$ for the PIC (left bars, red) and PUC (right bars, blue) for the cases without phonons and without losses (light colors), without phonons and with losses (middle colors), and with phonons and with losses (dark colors).

We summarize our findings by looking at the maximum fidelity over time for each Fock state in Fig. 4 for the different levels of approximation. The fidelity is a generalization of the overlap projection between two pure states to mixed states first introduced by Jozsa [44]. For two arbitrary density matrices ρ_1 and ρ_2, it is defined as

$$\mathcal{F}(\rho_1, \rho_2) = \left[\mathrm{Tr}\left(\sqrt{\sqrt{\rho_1}\rho_2\sqrt{\rho_1}}\right)\right]^2. \tag{2}$$

It is bounded between zero and unity and symmetric in its two arguments. In our case, we consider the photonic reduced density matrix $\rho_1 = \mathrm{Tr}_{\mathrm{QD}}[\mathrm{Tr}_{\mathrm{Ph}}(\rho)]$, which is the full density matrix ρ obtained as a solution of Eq. (A8) traced over the phononic (Ph) and the electronic (QD) subspaces. We compare this state to the target Fock states $|n\rangle$, i.e., $\rho_2 = |n\rangle\langle n|$. In this special case, the fidelity simplifies to the occupation of $|n\rangle$.

The red bars in Fig. 4 correspond to the PIC, while the blue bars are for the PUC. The lightly colored bars show the ideal case without phonons and without losses, the medium colored bars are without phonons, but with losses, and the dark colored bars are with phonons and with losses.

Looking at the fidelity of the Fock states, we can see several trends: The effect of cavity losses and radiative decay is more detrimental than the phonon influence. As an example, for the $n = 5$-Fock state prepared by the PIC, the losses reduce the fidelity from 96.3% to 48.5%, while the phonons further lower this value only to 38.5%. Note that this is a quantitative result for the considered GaAs/In(Ga)As QD at $T = 4$ K. In particular, this behavior might change in other materials or at higher temperatures. The PUC is better than the PIC for all cases. Overall, the 15% saving of time in the PUC yields a clear benefit. The maximum fidelity to the $n = 5$-Fock state including phonon and loss effects is now 45.1% (compared with 38.5% in the previous paragraph), a significant improvement by 17%. Furthermore, the PUC poses less demand on the experimental realization, since only one AC-Stark pulse is necessary to decouple the system at the end of the protocol. Even the field strength of this final pulse need not be precise, as required in the PIC, as long as it is large enough to effectively detune the dot from the cavity.

Therefore we conclude that our protocols both perform well in comparison with existing protocols to prepare higher-order Fock states [27,28]. The PUC outperforms the PIC with respect to the total duration as well as the fidelity as long as the conditions for using a two-level model are fulfilled.

III. PROTOCOLS FOR A MULTILEVEL QUANTUM DOT SYSTEM

For charged QDs, the transition between the residing electron and the trion state (i.e., the charged exciton) can be well modelled by a two-level system [45]. However, for a neutral QD, the assumption of a two-level system imposes further constraints. In particular, the single exciton manifold in a neutral QD comprises two states, which can be selectively addressed by circularly polarized laser pulses. A finite exchange interaction couples these states resulting in a finite FSS and corresponding new eigenstates that couple to linearly polarized light [32,46–49]. Also, there exists the biexciton, which can be addressed using linearly polarized pulses. Additionally, using ultrashort π-pulses, might lead to the excitation of higher energetic exciton states. Note that these states are also present in charged QDs, thus affecting the two-level approximation even in this favorable system. In the following, we study how these deviations from a two-level system affect the Fock state preparation fidelity.

A. Systems

(1) Four-level system (4LS). For modeling a neutral QD, we consider a four-level system accounting for the ground state $|G\rangle$, the left and right circularly polarized exciton $|X_L\rangle$ and $|X_R\rangle$ as well as the biexciton $|B\rangle$

$$\begin{aligned} H_{4\mathrm{LS}} &= \hbar\omega_X(|X_L\rangle\langle X_L| + |X_R\rangle\langle X_R|) \\ &+ \hbar\frac{V_{\mathrm{ex}}}{2}(|X_L\rangle\langle X_R| + |X_R\rangle\langle X_L|) \\ &+ (2\hbar\omega_X - E_B)|B\rangle\langle B| \\ &+ \sum_{j=L,R}[\hbar\omega_C a_j^\dagger a_j + \hbar g(a_j\sigma_j^\dagger + a_j^\dagger\sigma_j)] \\ &- \frac{\hbar}{2}(f_L^*(t)\sigma_L + f_L(t)\sigma_L^\dagger), \end{aligned} \tag{3}$$

$\hbar V_{\mathrm{ex}}$ is the exchange splitting between the linearly polarized exciton states, and E_B the biexciton binding energy. The allowed dipole selection rules lead to the following transition operator matrices:

$$\begin{aligned} \sigma_L &:= |G\rangle\langle X_L| + |X_R\rangle\langle B|, \\ \sigma_R &:= |G\rangle\langle X_R| + |X_L\rangle\langle B|. \end{aligned} \tag{4}$$

The exchange interaction couples the two oppositely polarized exciton states $|X_L\rangle$ and $|X_R\rangle$, thus opening up a path to occupy the biexciton state $|B\rangle$ even when the QD is driven by pulses $f_L(t)$ that all have the same circular polarization. The cavity

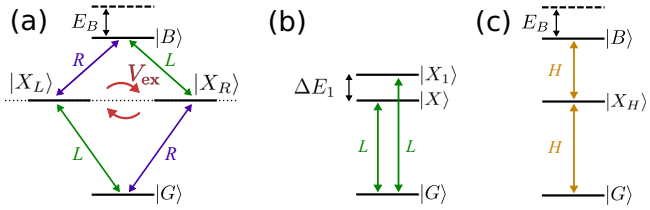

FIG. 5. Level schemes for: (a) the four-level system representing a neutral QD, (b) the system with a higher energetic exciton and (c) the three-level system for a neutral QD driven by linearly polarized light. Arrows denote the optically allowed transitions with the corresponding polarization.

modes are described by the photon annihilation operators a_L and a_R. Note that here two cavity modes are coupled which are assumed to be degenerate. The coupling strength is denoted by g and assumed to be equal for all modes. A sketch of the 4LS is shown in Fig. 5(a).

(2) Higher energetic exciton system (HEES). To account for a higher energetic exciton, we assume a three-level system consisting of the ground state $|G\rangle$, the lowest energetic exciton $|X\rangle$, and an additional higher energetic exciton state $|X_1\rangle$.

$$\begin{aligned} H_{\mathrm{HEES}} =& \hbar\omega_X |X\rangle\langle X| + (\hbar\omega_X + \Delta E_1)|X_1\rangle\langle X_1| \\ &+ \hbar\omega_C a^\dagger a + \hbar g(a\sigma_X^\dagger + a^\dagger\sigma_X) \\ &- \frac{\hbar}{2}(f_X^*(t)\sigma_X + f_X(t)\sigma_X^\dagger) \\ &- \frac{\hbar}{2}(f_X^*(t)\sigma_1 + f_X(t)\sigma_1^\dagger), \end{aligned} \tag{5}$$

where the higher energetic exciton lies few tens of meV above the exciton energy as denoted by ΔE_1. The corresponding transition operators in this system are

$$\begin{aligned} \sigma_X &:= |G\rangle\langle X|, \\ \sigma_1 &:= |G\rangle\langle X_1|. \end{aligned} \tag{6}$$

Because it is strongly off-resonant, we do not consider the coupling of σ_1 into the cavity mode. A sketch of the HEES is shown in Fig. 5(b).

(3) Three level system (3LS). The degeneracy of the two cavity modes in the 4LS implies that when driving with pulses all having the same linear polarization, one exciton becomes dark and the 4LS with two cavity modes reduces to a 3LS coupled only to a single linearly polarized mode as follows:

$$\begin{aligned} H_{\mathrm{3LS}} =& \hbar\omega_{\bar{X}} |X_H\rangle\langle X_H| + (2\hbar\omega_{\bar{X}} - E_B)|B\rangle\langle B| \\ &+ \hbar\omega_C a_H^\dagger a_H + \hbar g(a_H\sigma_H^\dagger + a_H^\dagger\sigma_H) \\ &- \frac{\hbar}{2}(f_H^*(t)\sigma_H + f_H(t)\sigma_H^\dagger), \end{aligned} \tag{7}$$

with the exciton energy lying at $\hbar\omega_{\bar{X}}$ and the transition operators

$$\sigma_H := |G\rangle\langle X_H| + |X_H\rangle\langle B|. \tag{8}$$

The cavity photon is annihilated by the operator a_H and the laser driving is described by the function $f_H(t)$. A sketch of the 3LS is shown in Fig. 5(c).

For all systems, we again take into account the electron-phonon coupling and losses as described in Appendix A 1.

B. Results

Now we analyze the different influences on our preparation protocols. Figure 6 shows the maximal fidelity over time for the Fock states in the different systems. The values obtained for different n are compared with the corresponding results of the PUC for an ideal two-level system accounting both for phonons and losses. This benchmark is displayed by a blue box around the bars.

1. Influence of a finite exchange splitting - 4LS

The leftmost (pink) bars in Fig. 6 show the maximal fidelities for the four-level system with an exchange splitting of $\hbar V_{\mathrm{ex}} = 20\ \mu$eV and a biexciton binding energy of $E_B = 2$ meV, which represents values typically encountered in QDs. We find that for all Fock states the deterioration of the fidelity due to the finite exchange coupling is nonessential. As example consider the fidelity to the five-photon Fock state, which reduces only to a value of 44.4%, i.e., only by 0.7%. For lower values of V_{ex} the fidelity becomes even higher. We conclude that, typical exchange splittings of up to 20 μeV encountered in QDs do not influence the performance of the protocol significantly when it is excited with a well defined circular polarization.

2. Influence of a higher energetic exciton state - HEES

The purple bars in Fig. 6 show the resulting fidelities for exciting the three-level system with $\Delta E_1 = 60$ meV, which is a typical value for strongly confined QDs [50]. Again, we find that the decrease of the fidelity is negligible. For $\Delta E_1 = 60$ meV, we obtain a five-photon fidelity of 43.8%, while for $\Delta E_1 = 40$ meV (not shown) the fidelity drops to 40.8%. This value is only 1.3% (or 4.3%) below the result of the two-level model. Therefore we conclude that the influence of the higher lying exciton state is not important as well as long as ΔE_1 is sufficiently large which is the case for strongly confined QDs.

It is interesting to note that an increase of the pulse length does not necessarily improve the performance of the protocol in this case, even though this would result in a sharper spectral width of the pulse. To understand this effect, imagine lengthening the excitation pulses in the two-level case. When the pulses are long enough so that the dynamics induced by the cavity coupling g sets in during the pulse, the exciton cannot reach its highest possible occupation anymore. Thus the photon occupation and therefore the fidelity both decrease. Therefore there is a competition between the detrimental influence of the simultaneous QD and cavity dynamics for longer pulses and the larger spectral width for shorter pulses which might lead to a spectral overlap with the higher lying exciton state for a given value of ΔE_1.

3. Linearly polarized excitation and pulse shaping—3LS

Finally, we study the 3LS representing a neutral QD driven by linearly polarized pulses. Here, $|B\rangle$ is the parasitic state with the difference that the energy spacing to be bridged is the

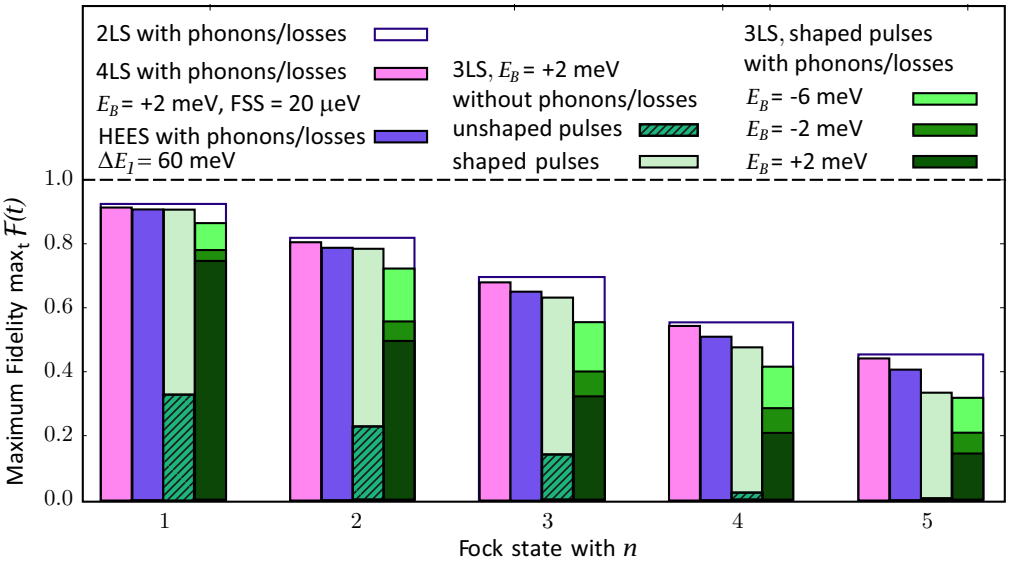

FIG. 6. The maximum fidelity over time to the Fock states $|n\rangle$, $n \in \{1, 2, \ldots, 5\}$ for different systems. The blue rectangles mark the values obtained for an ideal two-level system. From left to right: (pink) four-level system with circular polarization with finite exchange splitting of $\hbar V_{\mathrm{ex}} = 20\,\mu$eV and a biexciton binding energy of $E_B = 2$ meV. (Purple) Three-level system including an additional higher lying exciton state $|X_1\rangle$ excited at an energetic difference of $\Delta E_1 = 60$ meV. (green) Linearly excited biexcitonic three-level system using shaped or unshaped pulses (left) and shaped pulses for different biexciton binding energies $E_B = \pm 2$ and -6 meV (right). In all calculations, the PUC has been used.

biexciton binding energy E_B, which is an order of magnitude smaller than ΔE_1.

This case is often studied in the literature as a limiting factor in the operation of QDs, both with respect to photonic properties [51] and to the preparation of specific QD states [52]. Therefore we investigate this rather unusual case of linearly polarized excitation in more detail. Furthermore, this model is a prototype for a system with a parasitic state that is energetically close. Discussing a solution in such a situation is a key point of this paragraph.

The green bars in Fig. 6 display the results for a finite binding energy. For $E_B = 2$ meV already in the phonon- and loss-free case (lower left green bars), the PUC acting on this biexcitonic 3LS breaks down drastically and the fidelity to the state $|5\rangle$ drops below one percent. It is clear that the dynamics induced by significantly occupying the state $|B\rangle$ has a catastrophic effect on the success of the PUC.

To remedy this insufficiency, we employ shaped pulses that provide spectral holes at precisely the energies, where the parasitic states are found. A simple pulse shaping scheme for such purposes, proposed in Ref. [53], is based on a superposition of two Gaussian pulses with central frequencies separated by E_B with different widths s_1 and s_2 in the time domain. The corresponding envelope function, which is put into Eq. (A1), is

$$f_H^{\mathrm{p}}(t) = f_{H,0}\left(e^{-(\frac{t}{\sqrt{2}s_1})^2} - e^{-(\frac{t}{\sqrt{2}s_2})^2 + i\frac{E_B}{\hbar}t}\right) \tag{9}$$

with $f_{H,0} = [\sqrt{\pi}[\sqrt{2}s_1 - \sqrt{2}s_2 \exp\{-(\frac{E_B}{2\hbar}\sqrt{2}s_2)^2\}]]^{-1}$. The two free parameters s_1 and s_2 can now be used to tune the spectral maximum to the transition to be addressed and the spectral hole to the parasitic state, in our case $|B\rangle$. For a binding energy of $E_B = 2$ meV, this is achieved by setting $s_1 = 0.42$ ps and $s_2 = 0.18$ ps. The spectrum of this shaped pulse as well as the respective spectra of its two constituent Gaussians are depicted in Fig. 7.

The upper left green bars in Fig. 6 show the results for the pulse shaping protocol without phonons and losses. Remarkably, this simple pulse shaping technique boosts the five-photon fidelity from essentially zero back to 33.4%.

Next we study how phonons and losses affect the PUC with shaped pulses (right green bars in Fig. 6). We find a strong detrimental effect on the fidelity for $E_B = +2$ meV (lower right green bars), which reduces the fidelity to the five-photon state from 33.4% to 14.4%.

We have also considered negative binding energies of $E_B = -2$ meV (middle right green bars) and $E_B = -6$ meV (upper right green bars). QDs can be grown to have negative biexciton binding energies [54]. Alternatively, E_B can be tuned by

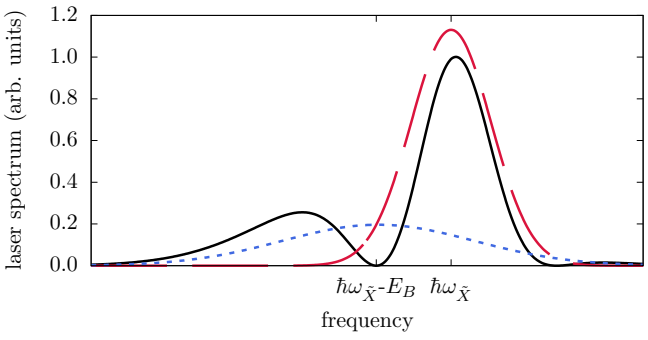

FIG. 7. The spectrum of the shaped laser pulse as in Eq. (9) (black solid line) as well as the respective spectra of its two constituent Gaussians (red dashed and blue dotted lines).

applying electrostatic fields [55,56] or biaxial strain [57], even to become negative. Clearly, the fidelities to the Fock states become higher for negative E_B. We notice that even larger negative binding energies give rise to higher fidelities.

A negative biexciton binding energy has the advantage that phonon emission processes that lead to an occupation of the biexciton state are suppressed since in a frame rotating with the laser frequency the biexciton state is not the energetically lowest one anymore [58]. Accordingly, we find for $E_B = -2$ meV that the fidelity is higher (20.9%) for $n = 5$ than what is obtained for the corresponding positive binding energy $E_B = 2$ meV. For the higher negative value of $E_B = -6$ meV (upper right green bars in Fig. 6) with the pulse shaping proposal (now with $s_1 = 0.21$ ps and $s_2 = 0.04$ ps) we obtain a five-photon fidelity of 31.8%.

Even though phonons always degrade the performance of the here proposed protocols, they suppress an unfavorable process when the sign of the binding energy is chosen accordingly. It is worthwhile to note that there are situations where phonons are even more beneficial [33]. Examples include phonon-assisted preparation schemes for excitons and biexcitons [59–64], the introduction of off-resonant QD-cavity couplings [65–73], the phonon-induced enhancement of photon purities [10] or the photon-pair entanglement [18] as well as enabling correlated emission from spatially remote QDs [64].

In summary, even in the worst case of linearly polarized excitation pulses, the fidelity to the five-photon Fock state can be enhanced from essentially zero to above 30% even when the phonon-induced and other loss mechanisms are present. This is made possible by a combination of shaping the spectral characteristics of the laser pulses and tuning the biexciton binding energy to negative values, taking advantage of the otherwise interfering LA phonon coupling.

IV. CONCLUSION

We have presented and investigated two protocols for the preparation of higher-order Fock states in QDCs. To this end, we adapted a standard protocol, developed for the atomic physics platform, to QDC-based devices. The basic ingredients of this scheme are a series of π-pulse excitations and effective energy shifts induced by AC-Stark pulses that effectively interrupt the coupling between the QD and the cavity. It turns out, however, that a protocol where the coupling is uninterrupted until the final target state is reached outperforms this standard scheme both in terms of duration and in terms of fidelity as long as it is justified to treat the system as a two-level system. In our analysis, we include radiative decay, cavity losses, and phonon effects, which are specific to solid state QDCs. We predicted in the two-level system a fidelity to the Fock state $|5\rangle$ of over 40% when the protocol with uninterrupted coupling is used. This value is comparable to results achieved in superconducting qubit setups as well as by parametric down-conversion. We have tested our protocol against the influence of the fine structure splitting and higher excited exciton states and have demonstrated that in all of these cases fidelities above 40% can be achieved. The advantage of using this protocol for a QDC platform is its total duration on a timescale of a few tens of picoseconds and its on-demand character.

We further discussed the excitation with linearly polarized pulses, which entails detrimental excitations of the biexciton in the QD. The coupling to the biexciton leads to a complete breakdown of our protocols already in the loss- and phonon-free case. Nonetheless, a combination of a pulse shaping technique, tuning the biexciton binding energy to negative values, and the influence of phonons is able to push the fidelity to $|5\rangle$ back to 31.8%.

With these easy to implement protocols, we are confident that also in solid state cavity systems the on-demand preparation of higher-order Fock states on the picosecond timescale becomes possible.

ACKNOWLEDGMENTS

M.Cy. thanks the Alexander-von-Humboldt foundation for support through a Feodor Lynen fellowship. This work was also funded by the Deutsche Forschungsgemeinschaft (DFG, German Research Foundation), Project No. 419036043.

APPENDIX: THEORETICAL MODEL

1. Coupling Hamiltonian

The external laser pulses are described by

$$f_j(t) = \underbrace{\sum_m f_j^{\mathrm{p}}(t-t_m)e^{-i\omega_{\mathrm{p}}(t-t_m)}}_{:=f^{\mathrm{pulses}}(t)} + \underbrace{\sum_n f_j^{\mathrm{ACS}}(t-t_n)e^{-i\omega_{\mathrm{ACS}}(t-t_n)}}_{:=f^{\mathrm{AC\text{-}Stark}}(t)}. \tag{A1}$$

$f_j^{\mathrm{p}}(t)$ and $f_j^{\mathrm{ACS}}(t)$ are the envelope functions of pump fields and AC-Stark pulses, respectively, with $j \in \{X, L, H\}$. ω_{p} and ω_{ACS} are the corresponding laser frequencies. The pump fields are Gaussian π-pulses

$$f_j^{\mathrm{p}}(t) = \frac{\pi}{\sqrt{2\pi}\sigma} e^{-\frac{t^2}{2\sigma^2}}, \tag{A2}$$

where σ denotes the standard deviation, which is connected to the full width at half maximum (fwhm) by $\mathrm{fwhm} = 2\sqrt{2\ln 2}\sigma$. We assume $\omega_{\mathrm{p}} = \omega_X$ for the 2LS, the HEES, and the 4LS and set $\omega_p = \omega_{\bar{X}}$ for the 3LS, i.e., the laser is in resonance with an exciton resonance in the 2LS, the HEES, and the 3LS cases while it is in the middle between the fine-structure split exciton resonances for the 4LS. The AC-Stark pulses are of rectangular shape with the edges smoothened by half Gaussians

$$f_j^{\mathrm{ACS}}(t) = \begin{cases} f_{j,s} e^{-(t+\frac{\tau_{\mathrm{length}}}{2})^2/(2\sigma_{\mathrm{on}}^2)} & t < -\frac{\tau_{\mathrm{length}}}{2} \\ f_{j,s} & -\frac{\tau_{\mathrm{length}}}{2} \leqslant t \leqslant \frac{\tau_{\mathrm{length}}}{2} \\ f_{j,s} e^{-(t-\frac{\tau_{\mathrm{length}}}{2})^2/(2\sigma_{\mathrm{off}}^2)} & t > \frac{\tau_{\mathrm{length}}}{2} \end{cases}, \tag{A3}$$

where $f_{j,s}$ denotes the field strength, i.e., the plateau height of the rectangular pulse, τ_{length} its length, and σ_{on} (σ_{off}) the width of the rise (fall) of the smoothened edges. Note that

by letting σ_{on} (σ_{off}) $\to 0$, high-frequency components disrupt the dynamics and thus the fidelity of the effective coupling of cavity and QD. We checked this by observing a decreasing fidelity to the Fock state $|1\rangle$ with lower values of σ_{on} (σ_{off}). We would like to stress that any smooth rise and fall of the rectangular pulse is sufficient, which we tested by using cosine edges instead. The key point is the modeling of a realistic rectangular pulse, which has never mathematically precise Heaviside-shaped edges.

Also, the precise shape of the pump pulses is of minor importance as a test with hyperbolic secant pulses showed. The main requirement is the shortness of the pulses compared with the timescale of the QDC dynamics. Furthermore, the pulses need not be phase-locked, as we checked by introducing random mutual phases between the pulses. This finding vastly reduces the experimental demand of realizing the proposed protocols.

In Sec. III B 3, the pump pulses $f_H^{\text{p}}(t)$ are shaped according to Eq. (9). The respective spectrum is depicted in Fig. 7 as a black solid line. The spectral hole at the biexciton binding energy E_B is clearly visible. The spectra of the constituent Gaussian pulses are plotted as red dashed and blue dotted lines.

The AC-Stark pulses are tuned below the exciton line by $\omega_{\text{ACS,X}} := \omega_{\text{ACS}} - \omega_{\text{X}}$ that is within the range of validity of the RWA. The resulting shift of the exciton line can be calculated from the energies of the laser dressed states. Matching the shift to $\Delta\omega_{\text{CX}}$, an AC-Stark pulse brings the exciton transition in resonance with the cavity provided that

$$\Delta\omega_{\text{CX}} = \Delta\omega_{\text{ACS,X}} + \sqrt{\Delta\omega_{\text{ACS,X}}^2 + f_s^2}\,. \tag{A4}$$

Note that tuning the coupling with an AC-Stark pulse is much more accurate than controlling the time of flight of an atom through a cavity. Any resonator has stray fields at its edges that depend on its geometry. Therefore the time dependent coupling of the atom to the resonator is not rectangular, but has smoothened edges that are fixed by the geometry. In contrast, a laser pulse can be shaped to vary the edge characteristics, which introduces additional dials for optimizing the protocol.

The QD is coupled to LA phonons in a pure dephasing-type manner [29–33]:

$$H_{\text{Ph}} = \sum_{\mathbf{q}} \hbar\omega_{\mathbf{q}} b_{\mathbf{q}}^\dagger b_{\mathbf{q}} + \sum_{\mathbf{q},\chi} n_\chi (\gamma_{\mathbf{q}} b_{\mathbf{q}}^\dagger + \gamma_{\mathbf{q}}^* b_{\mathbf{q}}) |\chi\rangle\langle\chi|\,, \tag{A5}$$

where $b_{\mathbf{q}}^\dagger$ and $b_{\mathbf{q}}$ are the phonon operators with wave vector $\mathbf{q}$ and energy $\hbar\omega_{\mathbf{q}}$. Bulk phonons with linear dispersion are considered that are coupled to the electronic states that are present in our respective systems $|\chi\rangle \in \{|X_L\rangle, |X_R\rangle, |X_1\rangle, |B\rangle\}$ by the deformation potential-type coupling constant $\gamma_{\mathbf{q}}$. n_χ is the number of electron-hole pairs present in the state $|\chi\rangle$.

Finally, we take radiative recombination of the excitons and cavity loss processes into account by introducing Markovian Lindblad-type operators

$$\mathcal{L}_{O,\Gamma}\bullet = \Gamma\big(O \bullet O^\dagger - \tfrac{1}{2}\big\{\bullet, O^\dagger O\big\}_+\big)\,, \tag{A6}$$

where $\{\cdot,\cdot\}_+$ denotes the anti-commutator. O is a system operator and Γ the decay rate of the associated loss process. We assume the radiative decay rate γ is the same for all electronic transitions and take the same cavity loss rate κ for both polarizations of the modes in the cavity.

The full Hamiltonian then reads as

$$H = H_j + H_{\text{Ph}} \tag{A7}$$

with the different system Hamiltonians H_j with $j \in \{\text{2LS, 4LS, HEES, 3LS}\}$ as defined in Sec. III A. The dynamics of these systems is then described by the Liouville-von Neumann equation

$$\frac{\partial}{\partial t}\rho = -\frac{i}{\hbar}\{H, \rho\}_- + \mathcal{L}\rho\,, \tag{A8}$$

where $\{\cdot,\cdot\}_-$ denotes the commutator. The superoperator $\mathcal{L}\bullet$ comprises all Lindblad-type contributions to the dynamics for each considered system as follows:

$$\mathcal{L}\bullet = \begin{cases} \mathcal{L}_{a,\kappa}\bullet + \mathcal{L}_{|G\rangle\langle X|,\gamma}\bullet & \text{for the 2LS} \\ \sum_{j=L,R}\left[\mathcal{L}_{a_j,\kappa}\bullet + \mathcal{L}_{|G\rangle\langle X_j|,\gamma}\bullet + \mathcal{L}_{|X_j\rangle\langle B|,\gamma}\bullet\right] & \text{for the 4LS} \\ \mathcal{L}_{a,\kappa}\bullet + \mathcal{L}_{|G\rangle\langle X|,\gamma}\bullet + \mathcal{L}_{|G\rangle\langle X_1|,\gamma}\bullet & \text{for the HEES} \\ \mathcal{L}_{a_H,\kappa}\bullet + \mathcal{L}_{|G\rangle\langle X_H|,\gamma}\bullet + \mathcal{L}_{|X_H\rangle\langle B|,\gamma}\bullet & \text{for the 3LS} \end{cases}. \tag{A9}$$

We solve Eq. (A8) in a numerically complete manner by employing a path-integral formalism [39,40,74,75] that allows for the analytical integration of the infinitely many phonon modes. Tracing the phonon degrees of freedom out yields a phonon induced memory kernel for the subsystem of interest. By the term "numerically complete," we denote a solution that does not change noticeably by making the time discretization finer and the memory taken into account longer. Recent advances within this method allows one to obtain solutions for systems with many quantum levels [41], which is paramount for the problem posed in this paper, since the relevant basis states to be considered are product states of the QD states and the number states of the two cavity modes.

2. Parameters

For the numerical calculations we use typical parameters for self-assembled strongly confined GaAs/In(Ga)As QDs [41,76]. The QD diameter is set to 6 nm. The cavity coupling is assumed to be $\hbar g = 0.1$ meV and the cavity losses are set to $\kappa = 0.0085\,\text{ps}^{-1}$. Assuming a mode frequency of $\hbar\omega_{\text{C}} = 1.5$ eV, this value of the loss rate corresponds to a cavity quality factor $Q \approx 268,000$, which was reported in Ref. [77] as an extremely high but experimentally achievable value in QDCs. The radiative decay rate of the QD exciton is set to $\gamma = 0.001\,\text{ps}^{-1}$. This corresponds to a typical lifetime of 1 ns. Whenever phonon effects are considered in this work,

the phonons are assumed to be initially in thermal equilibrium at a temperature of $T = 4$ K.

The detuning between the cavity and the QD is assumed to be $\hbar\Delta\omega_{\mathrm{CX}} = 5$ meV in the case of the PIC and the difference between the AC-Stark pulse and the QD is set to $\hbar\Delta\omega_{\mathrm{ACS,X}} = -40$ meV. Following from the condition Eq. (A4), the AC-Stark amplitude has to be $\hbar f_s = 21$ meV. Furthermore, the width of the smoothened edges is chosen to be $\sigma_{\mathrm{on}} = \sigma_{\mathrm{off}} = 0.28$ ps. The pump pulses are on-resonance with the QD exciton and have a width of fwhm $= 0.1$ ps.

3. Time discretization of the path-integral calculations

The phonon induced memory kernel for GaAs/In(Ga)As QDs of 6 nm diameter at $T = 4$ K decays on a timescale of $\approx$3 ps to zero [39–41]. Therefore numerically complete converged results are typically obtained for a discretization of $\Delta t_{\mathrm{Ph}} = 0.55$ ps and $n_m = 6$ memory steps. With these values, the memory kernel is well sampled. In this work, we use $\Delta t_{\mathrm{Ph}} = 0.5$ ps and $n_m = 7$.

To be able to resolve 0.1 ps-pulses, we first note that the dynamics induced by these ultrashort pulses is separated by one order of magnitude from the phonon timescale defined by the memory kernel. Thus, on this fast timescale, the phonon coupling has no influence on the system. Therefore a finer time discretization grid of $\Delta t = 0.01$ ps is put on top of the phonon discretization Δt_{Ph}. On this finer grid Δt, the dynamics is calculated using the phonon-free propagator. This two-grid strategy is necessary since the discretization of the phonon memory with a time step of $\Delta t = 0.01$ ps would make the numerics intractable.

4. Implicit model for the PIC

In the PIC presented in Sec. II A for the two-level case, a sequence of AC-Stark pulses that are highly off-resonant ($\hbar\Delta\omega_{\mathrm{ACS,X}} = -40$ meV) is the key ingredient. To study the phonon effect on this protocol, the double grid scheme explained in Appendix A 3 is not sufficient, since the fast oscillations induced by the AC-Stark pulses have to be sampled on the phonon discretization grid Δt_{Ph} to fully capture the energy shifts induced by the off-resonant nature of the pulses and their interplay with the phonon environment.

To this end, an implicit model is introduced that does not include the AC-Stark pulse explicitly, i.e., $f^{\mathrm{ACS}}(t) = 0$ in the driving term $f(t)$. Instead, in a frame co-rotating with the exciton frequency ω_X the detuning $\Delta\omega_{\mathrm{CX}}$ becomes effectively time-dependent when a sequence of AC-Stark pulses is applied. It is calculated according to Eq. (A4) by replacing f_s with $f^{\mathrm{ACS}}(t)$. Thus the largest detuning in the system is $|\hbar\Delta\omega_{\mathrm{CX}}| = 5$ meV in the implicit model compared with $|\hbar\Delta\omega_{\mathrm{ACS,X}}| = 40$ meV in the explicit incorporation of the AC-Stark pulses.

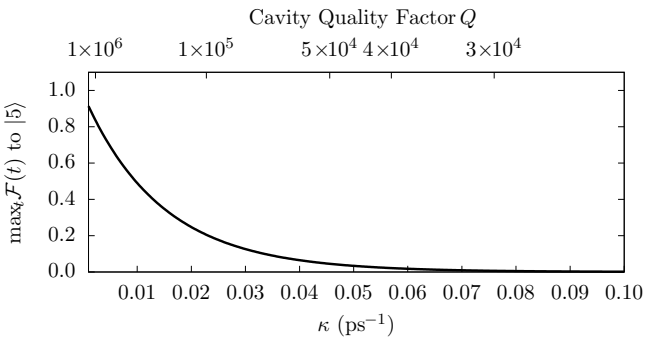

FIG. 8. Dependence of the maximum fidelity over time to the five-photon Fock state on the cavity loss rate. The cavity quality factor Q is calculated assuming a mode frequency of 1.5 eV. The radiative decay has been kept fixed at $\gamma = 0.001\,\mathrm{ps}^{-1}$ (cf., Appendix A 2), while phonon effects are not considered in this plot.

Comparing the implicit and the explicit model in the phonon-free case by studying the occupational dynamics of the system reveals that the amplitude of the oscillations is nearly identical, while their frequencies differ slightly for $\hbar\Delta\omega_{\mathrm{ACS,X}} \lesssim 10$ meV. For values greater than that and, in particular, in the limit $\Delta\omega_{\mathrm{ACS,X}} \to \infty$, the implicit and explicit models yield identical occupational dynamics.

5. Influence of the cavity losses

The analysis in the main text, in particular, Sec. II C and Fig. 4, shows that the most influential parameter concerning the preparation fidelity of the Fock states is the cavity loss rate, i.e., the cavity quality factor Q. Therefore it is clear that lower Q values worsen and higher Q improve the results. Nonetheless, it is of interest to quantify this effect due to its relevance for practical implementations of our scheme. Figure 8 displays the fidelity reached for the five-photon Fock state by the PUC as a function of the quality factor, which is varied by changing the cavity loss rate.

Indeed, the expectation that the fidelity to the five-photon Fock state monotonically increases with higher Q is fulfilled. The calculations shown are performed without considering phonon effects and keeping all the other parameters the same as in the main text. In particular we have kept the radiative decay at the finite value of $\gamma = 0.001\,\mathrm{ps}^{-1}$. This is the main reason why the fidelity stays noticeably below one in the limit of high Q values.

[1] P. Michler, A. Kiraz, C. Becher, W. V. Schoenfeld, P. M. Petroff, L. Zhang, E. Hu, and A. Imamoglu, Science **290**, 2282 (2000).
[2] C. Santori, M. Pelton, G. Solomon, Y. Dale, and Y. Yamamoto, Phys. Rev. Lett. **86**, 1502 (2001).
[3] C. Santori, D. Fattal, J. Vuckovic, G. S. Solomon, and Y. Yamamoto, Nature (London) **419**, 594 (2002).
[4] Y.-M. He, Y. He, Y.-J. Wei, D. Wu, M. Atatüre, C. Schneider, S. Höfling, M. Kamp, C.-Y. Lu, and J.-W. Pan, Nat. Nanotechnol. **8**, 213 (2013).
[5] Y.-J. Wei, Y.-M. He, M.-C. Chen, Y.-N. Hu, Y. He, D. Wu, C. Schneider, M. Kamp, S. Höfling, C.-Y. Lu, and J.-W. Pan, Nano Lett. **14**, 6515 (2014).

[6] X. Ding, Y. He, Z.-C. Duan, N. Gregersen, M.-C. Chen, S. Unsleber, S. Maier, C. Schneider, M. Kamp, S. Höfling, C.-Y. Lu, and J.-W. Pan, Phys. Rev. Lett. **116**, 020401 (2016).

[7] N. Somaschi, V. Giesz, L. De Santis, J. C. Loredo, M. P. Almeida, G. Hornecker, S. L. Portalupi, T. Grange, C. Antón, J. Demory, C. Gómez, I. Sagnes, N. D. Lanzillotti-Kimura, A. Lemaítre, A. Auffeves, A. G. White, L. Lanco, and P. Senellart, Nat. Photonics **10**, 340 (2016).

[8] L. Schweickert, K. D. Jöns, K. D. Zeuner, S. F. Covre da Silva, H. Huang, T. Lettner, M. Reindl, J. Zichi, R. Trotta, A. Rastelli, and V. Zwiller, Appl. Phys. Lett. **112**, 093106 (2018).

[9] L. Hanschke, K. A. Fischer, S. Appel, D. Lukin, J. Wierzbowski, S. Sun, R. Trivedi, J. Vučković, J. J. Finley, and K. Müller, npj Quantum Inf. **4**, 43 (2018).

[10] M. Cosacchi, F. Ungar, M. Cygorek, A. Vagov, and V. M. Axt, Phys. Rev. Lett. **123**, 017403 (2019).

[11] N. Akopian, N. H. Lindner, E. Poem, Y. Berlatzky, J. Avron, D. Gershoni, B. D. Gerardot, and P. M. Petroff, Phys. Rev. Lett. **96**, 130501 (2006).

[12] R. M. Stevenson, R. J. Young, P. Atkinson, K. Cooper, D. A. Ritchie, and A. J. Shields, Nature (London) **439**, 179 (2006).

[13] R. Hafenbrak, S. M. Ulrich, P. Michler, L. Wang, A. Rastelli, and O. G. Schmidt, New J. Phys. **9**, 315 (2007).

[14] A. Dousse, J. Suffczynski, A. Beveratos, O. Krebs, A. Lemaître, I. Sagnes, J. Bloch, P. Voisin, and P. Senellart, Nature (London) **466**, 217 (2010).

[15] E. del Valle, New J. Phys. **15**, 025019 (2013).

[16] M. Müller, S. Bounouar, K. D. Jöns, M. Glässl, and P. Michler, Nat. Photonics **8**, 224 (2014).

[17] A. Orieux, M. A. M. Versteegh, K. D. Jöns, and S. Ducci, Rep. Prog. Phys. **80**, 076001 (2017).

[18] T. Seidelmann, F. Ungar, A. M. Barth, A. Vagov, V. M. Axt, M. Cygorek, and T. Kuhn, Phys. Rev. Lett. **123**, 137401 (2019).

[19] M. J. Holland and K. Burnett, Phys. Rev. Lett. **71**, 1355 (1993).

[20] T. Nagata, R. Okamoto, J. L. O'Brien, K. Sasaki, and S. Takeuchi, Science **316**, 726 (2007).

[21] S. Slussarenko, M. M. Weston, H. M. Chrzanowski, L. K. Shalm, V. B. Verma, S. W. Nam, and G. J. Pryde, Nat. Photonics **11**, 700 (2017).

[22] A. Ourjoumtsev, H. Jeong, R. Tualle-Brouri, and P. Grangier, Nature (London) **448**, 784 (2007).

[23] Y. Yamamoto and H. A. Haus, Rev. Mod. Phys. **58**, 1001 (1986).

[24] F. W. Cummings and A. K. Rajagopal, Phys. Rev. A **39**, 3414 (1989).

[25] B. T. H. Varcoe, S. Brattke, M. Weidinger, and H. Walther, Nature (London) **403**, 743 (2000).

[26] X. Zhou, I. Dotsenko, B. Peaudecerf, T. Rybarczyk, C. Sayrin, S. Gleyzes, J. M. Raimond, M. Brune, and S. Haroche, Phys. Rev. Lett. **108**, 243602 (2012).

[27] M. Hofheinz, E. M. Weig, M. Ansmann, R. C. Bialczak, E. Lucero, M. Neeley, A. D. O'Connell, H. Wang, J. M. Martinis, and A. N. Cleland, Nature (London) **454**, 310 (2008).

[28] J. Tiedau, T. J. Bartley, G. Harder, A. E. Lita, S. W. Nam, T. Gerrits, and C. Silberhorn, Phys. Rev. A **100**, 041802(R) (2019).

[29] L. Besombes, K. Kheng, L. Marsal, and H. Mariette, Phys. Rev. B **63**, 155307 (2001).

[30] P. Borri, W. Langbein, S. Schneider, U. Woggon, R. L. Sellin, D. Ouyang, and D. Bimberg, Phys. Rev. Lett. **87**, 157401 (2001).

[31] B. Krummheuer, V. M. Axt, and T. Kuhn, Phys. Rev. B **65**, 195313 (2002).

[32] V. M. Axt, T. Kuhn, A. Vagov, and F. M. Peeters, Phys. Rev. B **72**, 125309 (2005).

[33] D. E. Reiter, T. Kuhn, and V. M. Axt, Adv. Phys.: X **4**, 1655478 (2019).

[34] R. J. Young, R. M. Stevenson, P. Atkinson, K. Cooper, D. A. Ritchie, and A. J. Shields, New J. Phys. **8**, 29 (2006).

[35] R. M. Stevenson, R. J. Young, P. See, D. G. Gevaux, K. Cooper, P. Atkinson, I. Farrer, D. A. Ritchie, and A. J. Shields, Phys. Rev. B **73**, 033306 (2006).

[36] J. Zhang, J. S. Wildmann, F. Ding, R. Trotta, Y. Huo, E. Zallo, D. Huber, A. Rastelli, and O. G. Schmidt, Nat. Commun. **6**, 10067 (2015).

[37] M. Cygorek, M. Korkusinski, and P. Hawrylak, Phys. Rev. B **101**, 075307 (2020).

[38] A. Mukherjee, A. Widhalm, D. Siebert, S. Krehs, N. Sharma, A. Thiede, D. Reuter, J. Förstner, and A. Zrenner, Appl. Phys. Lett. **116**, 251103 (2020).

[39] A. Vagov, M. D. Croitoru, M. Glässl, V. M. Axt, and T. Kuhn, Phys. Rev. B **83**, 094303 (2011).

[40] A. M. Barth, A. Vagov, and V. M. Axt, Phys. Rev. B **94**, 125439 (2016).

[41] M. Cygorek, A. M. Barth, F. Ungar, A. Vagov, and V. M. Axt, Phys. Rev. B **96**, 201201(R) (2017).

[42] C. Schneider, T. Heindel, A. Huggenberger, P. Weinmann, C. Kistner, M. Kamp, S. Reitzenstein, S. Höfling, and A. Forchel, Appl. Phys. Lett. **94**, 111111 (2009).

[43] S. Reitzenstein and A. Forchel, J. Phys. D: Appl. Phys. **43**, 033001 (2010).

[44] R. Jozsa, J. Mod. Opt. **41**, 2315 (1994).

[45] T. Kaldewey, S. Lüker, A. V. Kuhlmann, S. R. Valentin, J.-M. Chauveau, A. Ludwig, A. D. Wieck, D. E. Reiter, T. Kuhn, and R. J. Warburton, Phys. Rev. B **95**, 241306(R) (2017).

[46] M. Bayer, A. Kuther, A. Forchel, A. Gorbunov, V. B. Timofeev, F. Schäfer, J. P. Reithmaier, T. L. Reinecke, and S. N. Walck, Phys. Rev. Lett. **82**, 1748 (1999).

[47] A. Högele, S. Seidl, M. Kroner, K. Karrai, R. J. Warburton, B. D. Gerardot, and P. M. Petroff, Phys. Rev. Lett. **93**, 217401 (2004).

[48] B. Patton, W. Langbein, and U. Woggon, Phys. Rev. B **68**, 125316 (2003).

[49] D. Gammon, E. S. Snow, B. V. Shanabrook, D. S. Katzer, and D. Park, Phys. Rev. Lett. **76**, 3005 (1996).

[50] A. Vagov, V. M. Axt, T. Kuhn, W. Langbein, P. Borri, and U. Woggon, Phys. Rev. B **70**, 201305(R) (2004).

[51] C. Gustin and S. Hughes, Phys. Rev. B **98**, 045309 (2018).

[52] K. Gawarecki, S. Lüker, D. E. Reiter, T. Kuhn, M. Glässl, V. M. Axt, A. Grodecka-Grad, and P. Machnikowski, Phys. Rev. B **86**, 235301 (2012).

[53] P. Chen, C. Piermarocchi, and L. J. Sham, Phys. Rev. Lett. **87**, 067401 (2001).

[54] G. E. Dialynas, C. Xenogianni, E. Trichas, P. G. Savvidis, G. Constantinidis, Z. Hatzopoulos, and N. T. Pelekanos, in *Proceedings of the 2007 Quantum Electronics and Laser Science Conference, Baltimore, MD* (IEEE, Piscataway, NJ, 2007), pp. 1–2.

[55] F. Ding, R. Singh, J. D. Plumhof, T. Zander, V. Křápek, Y. H. Chen, M. Benyoucef, V. Zwiller, K. Dörr, G. Bester, A. Rastelli, and O. G. Schmidt, Phys. Rev. Lett. **104**, 067405 (2010).

[56] R. Trotta, P. Atkinson, J. D. Plumhof, E. Zallo, R. O. Rezaev, S. Kumar, S. Baunack, J. R. Schröter, A. Rastelli, and O. G. Schmidt, Adv. Mater. **24**, 2668 (2012).
[57] R. Trotta, E. Zallo, E. Magerl, O. G. Schmidt, and A. Rastelli, Phys. Rev. B **88**, 155312 (2013).
[58] A. M. Barth, S. Lüker, A. Vagov, D. E. Reiter, T. Kuhn, and V. M. Axt, Phys. Rev. B **94**, 045306 (2016).
[59] M. Glässl, A. M. Barth, and V. M. Axt, Phys. Rev. Lett. **110**, 147401 (2013).
[60] D. E. Reiter, T. Kuhn, M. Glässl, and V. M. Axt, J. Phys.: Condens. Matter **26**, 423203 (2014).
[61] P.-L. Ardelt, L. Hanschke, K. A. Fischer, K. Müller, A. Kleinkauf, M. Koller, A. Bechtold, T. Simmet, J. Wierzbowski, H. Riedl, G. Abstreiter, and J. J. Finley, Phys. Rev. B **90**, 241404(R) (2014).
[62] S. Bounouar, M. Müller, A. M. Barth, M. Glässl, V. M. Axt, and P. Michler, Phys. Rev. B **91**, 161302(R) (2015).
[63] J. H. Quilter, A. J. Brash, F. Liu, M. Glässl, A. M. Barth, V. M. Axt, A. J. Ramsay, M. S. Skolnick, and A. M. Fox, Phys. Rev. Lett. **114**, 137401 (2015).
[64] M. Reindl, K. D. Jöns, D. Huber, C. Schimpf, Y. Huo, V. Zwiller, A. Rastelli, and R. Trotta, Nano Lett. **17**, 4090 (2017).
[65] S. Ates, S. M. Ulrich, A. Ulhaq, S. Reitzenstein, A. Löffler, S. Höfling, A. Forchel, and P. Michler, Nat. Photonics **3**, 724 (2009).
[66] A. Naesby, T. Suhr, P. T. Kristensen, and J. Mørk, Phys. Rev. A **78**, 045802 (2008).
[67] U. Hohenester, A. Laucht, M. Kaniber, N. Hauke, A. Neumann, A. Mohtashami, M. Seliger, M. Bichler, and J. J. Finley, Phys. Rev. B **80**, 201311(R) (2009).
[68] U. Hohenester, Phys. Rev. B **81**, 155303 (2010).
[69] A. Majumdar, E. D. Kim, Y. Gong, M. Bajcsy, and J. Vučković, Phys. Rev. B **84**, 085309 (2011).
[70] S. Hughes, P. Yao, F. Milde, A. Knorr, D. Dalacu, K. Mnaymneh, V. Sazonova, P. J. Poole, G. C. Aers, J. Lapointe, R. Cheriton, and R. L. Williams, Phys. Rev. B **83**, 165313 (2011).
[71] M. Florian, P. Gartner, C. Gies, and F. Jahnke, New J. Phys. **15**, 035019 (2013).
[72] M. Calic, P. Gallo, M. Felici, K. A. Atlasov, B. Dwir, A. Rudra, G. Biasiol, L. Sorba, G. Tarel, V. Savona, and E. Kapon, Phys. Rev. Lett. **106**, 227402 (2011).
[73] A. Laucht, N. Hauke, A. Neumann, T. Günthner, F. Hofbauer, A. Mohtashami, K. Müller, G. Böhm, M. Bichler, M.-C. Amann, M. Kaniber, and J. J. Finley, J. Appl. Phys. **109**, 102404 (2011).
[74] N. Makri and D. E. Makarov, J. Chem. Phys. **102**, 4600 (1995).
[75] N. Makri and D. E. Makarov, J. Chem. Phys. **102**, 4611 (1995).
[76] B. Krummheuer, V. M. Axt, T. Kuhn, I. D'Amico, and F. Rossi, Phys. Rev. B **71**, 235329 (2005).
[77] C. Schneider, P. Gold, S. Reitzenstein, S. Höfling, and M. Kamp, Appl. Phys. B **122**, 19 (2016).

Publication 7

Suitability of solid-state platforms as sources of N-photon bundles.

M. Cosacchi, A. Mielnik-Pyszczorski, T. Seidelmann, M. Cygorek, A. Vagov, D. E. Reiter, V. M. Axt.

arXiv:2108.03967 (2021), under review at *Quantum*.

arXiv:2108.03967 (2021)

Author contributions

The author has designed the concept of this study, in particular, he has performed the data generation and analysis, has provided the interpretation of the results, and has written the first draft of the paper. He proposed superconducting qubits in microwave resonators as an alternative solid-state system, where pure dephasing is negligible. He has moderated all discussions and revision requests of the draft and has organized the correspondence with the editor.

A. Mielnik-Pyszczorski has discussed the results in detail with the author, thus contributing to the interpretation. He has redesigned and optimized all figures and has contributed to revisions of the draft.

T. Seidelmann has discussed the results in detail with the author, thus contributing to the interpretation. In particular, he has proposed the interpretation of the bundle physics in terms of laser-dressed states. He has contributed to revisions of the draft.

M. Cygorek, A. Vagov, and D. E. Reiter have cosupervised this work, in particular, they have participated in the discussion and interpretation of the results. They have contributed to revisions of the draft and optimized the presentation.

V. M. Axt has advised the author throughout his work as the main supervisor. He has obtained the funding for this work and has participated in the discussion and interpretation of the results and has contributed to revisions of the draft and the optimization of the presentation.

Suitability of solid-state platforms as sources of N-photon bundles

M. Cosacchi[1], A. Mielnik-Pyszczorski[1,2], T. Seidelmann[1], M. Cygorek[3], A. Vagov[1,4], D. E. Reiter[5], and V. M. Axt[1]

[1]Theoretische Physik III, Universität Bayreuth, 95440 Bayreuth, Germany
[2]Department of Theoretical Physics, Wrocław University of Science and Technology, 50-370 Wrocław, Poland
[3]Heriot-Watt University, Edinburgh EH14 4AS, United Kingdom
[4]ITMO University, St. Petersburg, 197101, Russia
[5]Institut für Festkörpertheorie, Universität Münster, 48149 Münster, Germany

N-photon bundles constitute a class of highly nonclassical quantum states of light. They are a specific type of photon emission, where light quanta are released from a cavity only in groups of N particles with a characteristic photon number statistics that may be taken as their fingerprint. We consider two solid-state cavity quantum electrodynamics (cQED) systems in terms of their suitability as emitters of N-photon bundles. As one example, we consider a semiconductor quantum-dot–microcavity system coupled to longitudinal acoustic phonons. There, we find the environmental influence to be detrimental to the emission of N-photon bundles. The other example is a superconducting qubit inside a microwave resonator. In these systems, pure dephasing is not important and an experimentally feasible parameter regime is found, where bundle emission can be observed.

1 Introduction

Many innovative applications of the quantum realm rely on the on-demand preparation of specific, highly nonclassical target states. Cavity quantum electrodynamics (cQED) is a machinery well suited for this purpose. On numerous different platforms, e.g., atoms in resonators [1, 2, 3], superconducting qubits in microwave resonators [4, 5], or semiconductor quantum dots in microcavities [6, 7, 8, 9, 10, 11, 12, 13, 14, 15, 16, 17, 18, 19, 20, 21, 22, 23, 24, 25, 26], preparation of single photons, entangled photon pairs, Fock states, and Schrödinger or Voodoo cat states has been proposed or achieved. Recently, a new class of emitters of N-photon bundles has been proposed [27], where the photon emission takes place only in groups of the integer bundle number N. They are characterized by a specific temporal spacing between their constituent photons, see sketch in Fig. 1. In contrast to the ordinary Fock state $|N\rangle$, a bundle is emitted as a cascade over successive Fock states $|n\rangle$, where $0 \leq n \leq N$, which is a direct result of the outcoupling via resonator losses. In a resonator with loss rate κ, the Fock state $|n\rangle$ effectively decays with the rate $n\kappa$, explaining the temporal spacing between the photons constituting the bundle. This is also reflected in the photon statistics of the resonator photons, which is

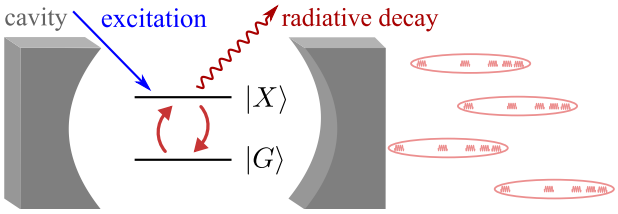

Figure 1: Sketch of a two-level system (2LS) embedded in a cavity resulting in the coupling to one cavity mode. The 2LS is driven by a continuous external excitation. It can decay radiatively, while the cavity is lossy. For particular sets of parameters, N-photon bundles leave the cavity. They are characterized by the specific temporal spacing between the constituent photons and their specific photon number statistics. Exemplary, four 5-photon bundles are depicted.

$$P_N(n) = \begin{cases} 1 - \frac{\langle n \rangle}{N} \sum_{j=1}^{N} \frac{1}{j} & n = 0 \\ \frac{\langle n \rangle}{N} \frac{1}{n} & 1 \leq n \leq N \\ 0 & n > N \end{cases} \quad (1)$$

in the ideal case of an N-photon bundle emission [27] with $\langle n \rangle$ being the average photon number in the resonator. Considering this from a detection point of view means the following: When a Poissonian source emits photons, their arrival times at the detector are distributed randomly; in the case of an N-photon bundle emission, the bundles arrive randomly, but the photons contained in each bundle obey the temporal order as sketched in Fig. 1. Therefore, there is a Poissonian distribution over bundles. In this sense, N-photon bundles can be considered as an alternative to Fock states as building blocks for more complex quantum states of light. Furthermore, N-photon bundles have the property to herald a Fock state. Finally, on timescales longer than the size of the bundle, Planck's constant is effectively renormalized in the relationship between frequency and energy, $E = N\hbar\omega$. Therefore, N-photon bundles are even discussed for medical applications due to a greater penetration depth and increased resolution [27].

In this work, we study the suitability of solid-state platforms as sources of such N-photon bundles. We consider two platforms: (i) semiconductor quantum dots (QDs) in microcavities and (ii) superconducting qubits in microwave resonators.

In QDs, where the coupling to longitudinal acoustic phonons is known as the main source of decoherence, the pure dephasing interaction is the most important loss channel. We analyze a QD–cavity system coupled to a phonon environment modeled by a microscopic phonon Hamiltonian. This full many-body problem is solved in a numerically exact way by employing a path-integral formalism. We compare these results with those found in a model accounting for phonons only via a phenomenological pure dephasing rate. For realistic parameters that are currently achievable, we find that the bundle emission is completely destroyed by phonons.

In superconducting qubit–microwave resonator systems, pure dephasing is negligible. For these systems, we propose a set of parameters experimentally well within reach, where bundle emission with $N = 2$ can be observed. We show that for a bundle emission a resonator with a mediocre Q-factor is optimal.

2 Model and methods

2.1 cQED model

Both example systems can be described by a strongly driven Jaynes–Cummings model with the Hamiltonian in a frame co-rotating with the frequency of the external excitation ω_L in the usual dipole and rotating-wave approximations

$$\begin{aligned} H = &-\hbar\Delta\omega_\mathrm{LX}|X\rangle\langle X| + \hbar\Delta\omega_\mathrm{CL}a^\dagger a \\ &+ \hbar g\left(|X\rangle\langle G|a + |G\rangle\langle X|a^\dagger\right) \\ &+ \hbar f\left(|X\rangle\langle G| + |G\rangle\langle X|\right) . \end{aligned} \tag{2}$$

The two-level system (2LS) has an excited state $|X\rangle$ at energy $\hbar\omega_\mathrm{X}$ and a ground state $|G\rangle$ at energy zero. a ($a^\dagger$) is the annihilation (creation) operator of a photon in the single resonator mode at energy $\hbar\omega_\mathrm{C}$ coupled to the 2LS by g. The detuning between the external excitation with strength f and the upper state $|X\rangle$ is denoted by $\Delta\omega_\mathrm{LX} = \omega_\mathrm{L} - \omega_\mathrm{X}$ and the detuning between resonator and external excitation $\Delta\omega_\mathrm{CL} = \omega_\mathrm{C} - \omega_\mathrm{L}$ is defined analogously. The detuning between resonator and the upper state $|X\rangle$, $\Delta\omega_\mathrm{CX} = \omega_\mathrm{C} - \omega_\mathrm{X}$, is fixed by the growth process of the structure. Hence, we keep it constant in our analysis.

When the 2LS is strongly driven ($f \gg g$) and it is in the dispersive regime ($\Delta\omega_\mathrm{CX} \gg g$), a sharp N-photon resonance emerges with N being an integer. It corresponds to a polariton of the type $(|G,0\rangle \pm |X,N\rangle)/\sqrt{2}$, where $|\chi,n\rangle$ denotes the product state of the 2LS state $|\chi\rangle$ and the photon number state $|n\rangle$. When dissipative channels are included by introducing the excited state's radiative decay with rate γ and resonator losses with rate κ, this resonance becomes a source of N-photon bundles, when the stationary state is reached [27].

We include these dissipative effects by accounting for the Lindblad superoperators $\mathcal{L}_{|G\rangle\langle X|,\gamma}$ and $\mathcal{L}_{a,\kappa}$ acting on the density matrix ρ as

$$\mathcal{L}_{O,\Gamma}\rho = \Gamma\left(O\rho O^\dagger - \frac{1}{2}\left\{\rho, O^\dagger O\right\}_+\right) , \tag{3}$$

describing loss processes with rate Γ on a dissipation channel O, where $\{A,B\}_+$ is the anti-commutator of operators A and B.

2.1.1 QD model

At first, we consider a self-assembled GaAs QD system in a single-mode microcavity. In these systems, additionally the pure-dephasing coupling of the electronic states to an environment of longitudinal acoustic phonons is important [28, 29]. It is described by the Hamiltonian [30, 31, 32, 33]

$$H_{\mathrm{Ph}} = \hbar \sum_{\boldsymbol{q}} \omega_{\boldsymbol{q}} b_{\boldsymbol{q}}^{\dagger} b_{\boldsymbol{q}} + \hbar \sum_{\boldsymbol{q}} \left(\gamma_{\boldsymbol{q}}^{\mathrm{X}} b_{\boldsymbol{q}}^{\dagger} + \gamma_{\boldsymbol{q}}^{\mathrm{X}*} b_{\boldsymbol{q}} \right) |X\rangle\langle X| \,, \quad (4)$$

where $b_{\boldsymbol{q}}$ ($b_{\boldsymbol{q}}^{\dagger}$) annihilates (creates) a phonon of energy $\hbar\omega_{\boldsymbol{q}}$ in mode $\boldsymbol{q}$ with the coupling strength $\gamma_{\boldsymbol{q}}^{\mathrm{X}}$. The phonons are assumed to be initially in thermal equilibrium at temperature T.

This coupling to phonons is the source of many well-known effects in QDs, like the phonon sideband in the QD emission spectrum [30, 34], the renormalization of the Rabi frequency [35, 36], and the damping of Rabi oscillations [37, 38, 39]. To discuss resonances, the most important effect is the polaron shift of the excited state $|X\rangle$. Whenever we refer to the excited state energy when phonons are taken into account, we mean the polaron-shifted excited state energy.

To treat this full many-body Hamiltonian in a numerically exact way, we employ an iterative real-time path-integral formalism [40, 41] to solve the Liouville–von Neumann equation (details are explained in Refs. [42, 43, 44]). Within this approach, all effects mentioned above are thus taken into account.

Unless noted otherwise, we take $\hbar g = 0.02\,\mathrm{meV}$ [45], $\gamma = 1\,\mathrm{ns}^{-1}$, and $\kappa = 8.5\,\mathrm{ns}^{-1}$ [46]. These values, in particular, the cavity loss rate κ are realistically achievable [46]. The record in cavity quality so far is around $\kappa \approx 4\,\mathrm{ns}^{-1}$ to $6\,\mathrm{ns}^{-1}$ [45], which means that it should be possible to achieve the value of κ chosen here with current state-of-the-art equipment with reasonable effort. Further, following Ref. [27], we set $\hbar\Delta\omega_{\mathrm{CX}} = -60\hbar g = -1.2\,\mathrm{meV}$ and $\hbar f = 32\hbar g = 0.64\,\mathrm{meV}$. For the phonon coupling, standard GaAs parameters [47, 44] are chosen for a QD with a radius of 3 nm.

2.1.2 Superconducting qubit model

As a second example, we consider a superconducting qubit in a microwave resonator. Here, pure dephasing is negligible. Therefore, no addition to the model in Sec. 2.1 is necessary.

We use the parameter set $\hbar g = 0.079\,\mu\mathrm{eV}$, $\gamma = 1.54\,\mu\mathrm{s}^{-1}$, $\kappa = 0.29\,\mu\mathrm{s}^{-1}$, i.e. $\kappa \ll \gamma$, taken from Ref. [5]. Again, following Ref. [27], we choose $\hbar\Delta\omega_{\mathrm{CX}} = -60\hbar g = -4.71\,\mu\mathrm{eV}$ and $\hbar f = 32\hbar g = 2.51\,\mu\mathrm{eV}$.

3 Results: QD–cavity system

3.1 Resonance landscape and N=2

The resonance corresponding to an N-photon bundle are found at [48, 27]

$$\Delta\omega_{\mathrm{LX}} = \frac{\sqrt{4\left(N^2-1\right) f^2 + N^2 \Delta\omega_{\mathrm{CX}}^2} + \Delta\omega_{\mathrm{CX}}}{N^2-1} + \Delta\omega_{\mathrm{CX}} \,. \quad (5)$$

In this work, we focus mostly on the case $N = 2$. For the QD–cavity system, this results in a detuning value of $\hbar\Delta\omega_{\mathrm{LX}} = -0.51\,\mathrm{meV}$. Higher-order bundles with $N > 2$ can be reached by tuning the excitation to the corresponding resonance according to Eq. (5), however for the realistic set of parameters assumed here they are negligible.

To illustrate the appearing resonances, we scan the stationary photon number occupation with the laser frequency ω_{L}. Figure 2 shows the corresponding results for the photon numbers $n = 1$, 2, and 3 in the QD–cavity system. Three resonance peaks emerge in the vicinity of the bundle resonance [presented in Fig. 2(a)], which itself is shown on a magnified scale in the inset.

The most prominent peaks are found for the limiting cases $N \to \infty$ and $N = 1$. For $N \to \infty$ a double-peaked structure emerges at $\hbar\Delta\omega_{\mathrm{LX}} = \hbar\Delta\omega_{\mathrm{CX}} = -1.2\,\mathrm{meV}$ (cf., Fig 7 for a zoom-in). At its center the photon statistics is Poissonian and is hardly influenced by phonons [cf., Figs. 2(a) and (b)]. In contrast, the peak at $\hbar\Delta\omega_{\mathrm{LX}} \approx 0.08\,\mathrm{meV}$ corresponds to the resonance for $N = 1$. Here, Fock states with $n > 1$ are not occupied due to a photon blockade effect [cf., Fig. 2(a)], which is spoiled once phonons are considered: then, the system can climb up the Jaynes-Cummings ladder [cf., Fig. 2(b)]. The different physical mechanisms giving rise to these

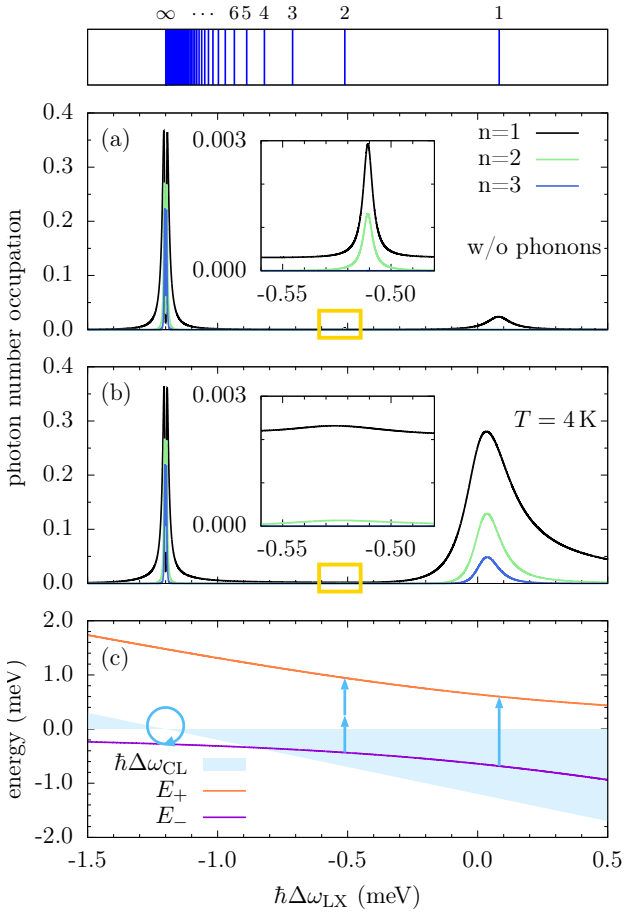

Figure 2: Stationary photon number occupation in the QD–cavity system as a function of the laser–exciton detuning $\Delta\omega_{\mathrm{LX}}$ (a) without taking phonon effects into account, (b) including phonons initially at $T = 4\,\mathrm{K}$ (the insets show the region marked by yellow boxes on a larger scale), (c) the corresponding energies of the laser-dressed states $|+\rangle$ and $|-\rangle$. The energy of a photon in the rotating frame is given by the cavity–laser detuning $\hbar\Delta\omega_{\mathrm{CL}}$, which is plotted as a shaded area to illustrate its modulus. Arrows indicate the number of photons involved in the processes leading to the various resonance peaks, while their length corresponds to their energy $\hbar\Delta\omega_{\mathrm{CL}}$. The circular arrow indicates a 1-photon process with a photon energy (in the rotating frame) of $\hbar\Delta\omega_{\mathrm{CL}} = 0$. The blue lines above panel (a) mark the energetic positions of the bundle resonances, starting for $N = 1$ and quickly converging to $\hbar\Delta\omega_{\mathrm{CX}}$ for larger N. Since the bundle resonance is derived from the condition that N cavity photons energetically fit between the two dressed states, an equation analogous to Eq. (5) can be found for the trivial case $N = 1$.

two limiting cases and the phonon influence on them is discussed in detail in Appendix A.

We now consider the range of bundle physics for $1 < N < \infty$ and focus on $N = 2$. The characteristic feature of N-photon bundles reflected in their statistics as denoted in Eq. (1) is well visible for the 2-photon bundle shown in the inset of Fig. 2(a), in particular, the 3-photon occupation is zero.

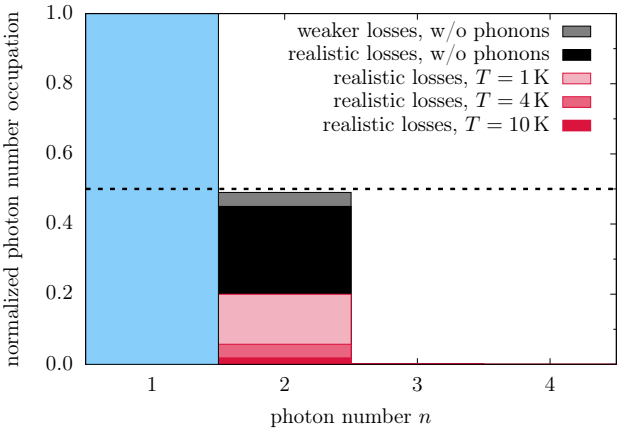

Figure 3: The stationary photon number occupation normalized to its value at $n = 1$ for the QD–cavity system. While the data labeled 'realistic losses' is obtained using the parameters listed in Sec. 2.1.1, weaker losses of $\gamma = 0.01g$ and $\kappa = 0.1g$ were chosen following Ref. [27] for the calculation shown in gray. Note that in the phonon-free case, the absolute values of the Fock state with $n = 1$ are 0.016 for the weaker losses and 0.003 for the realistic parameter set.

To understand all the resonances, we diagonalize the Hamiltonian of the laser-driven 2LS neglecting the cavity (since $f \gg g$). As a result, we obtain the dressed states $|+\rangle$ and $|-\rangle$. Their energies in the laser-rotating frame are plotted in Fig. 2(c) along with the energy of a cavity photon given by $\hbar\Delta\omega_{\mathrm{CL}}$ in this frame.

The analysis in terms of laser-dressed states reveals the fact that the 2-photon bundle resonance at $\hbar\Delta\omega_{\mathrm{LX}} = -0.51\,\mathrm{meV}$ originates from a 2-photon process [27], in this case a transition from $|-,0\rangle$ to $|+,2\rangle$. The study of the influence of the phonons on this resonance shows that already at 4 K [inset of Fig. 2(b)], it is strongly suppressed. The occupation of $n = 1$ strongly rises around the resonance peak. Apparently, phonon-assisted 1-photon transitions are favored against the 2-photon process creating the bundle. In particular, the characteristic $1/n$ feature [cf., Eq. (1)] of the number distribution is destroyed.

To illustrate this point in more detail, the stationary photon number distribution normalized to its value at $n = 1$ is shown in Fig. 3. First of all, it is interesting to note that the ideal bundle statistics $\propto 1/n$ is only observed for loss parameters weaker than the realistic, state-of-the-art

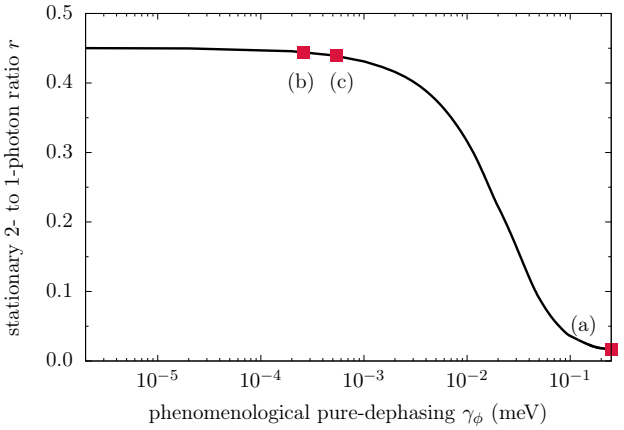

Figure 4: The stationary ratio between the 2- and the 1-photon occupation in the QD–cavity system with the phonon influence approximated by an Lindblad operator with a phenomenological pure dephasing rate γ_ϕ instead of the microscopic Hamiltonian H_{Ph} in Eq. (4), cf. main text. (a) γ_ϕ corresponding to the full driven Jaynes–Cummings model at $T = 4\,\mathrm{K}$. (b) γ_ϕ corresponding to a Jaynes–Cummings dynamics with $n = 1$. (c) γ_ϕ corresponding to a Jaynes–Cummings dynamics with $n = 2$.

values (cf. gray data in Fig. 3). This parameter set consists of $\gamma = 0.01g = 0.3\,\mathrm{ns}^{-1}$ and $\kappa = 0.1g = 3\,\mathrm{ns}^{-1}$, following the values chosen in Ref. [27]. Already the slightly higher values chosen in our work (cf. Sec. 2.1.1) lead to a ratio of the stationary 2- to the 1-photon occupation

$$r := \lim_{t\to\infty} \frac{\langle|2\rangle\langle 2|\rangle(t)}{\langle|1\rangle\langle 1|\rangle(t)} \tag{6}$$

equal to 0.45. Thus, the ratio deviates from the target of 0.50, which is a necessary indicator for an $N = 2$ bundle state. The phonon coupling pushes this value down to $r = 0.20$ already at $T = 1\,\mathrm{K}$. For higher temperatures up to $10\,\mathrm{K}$, r swiftly approaches zero and the 2-photon bundle is completely destroyed. QD–cavity systems are therefore not a suitable platform to design an emitter of N-photon bundles ($1 < N < \infty$).

3.2 Comparison with a phenomenological dephasing model

The phonon environment has a drastic influence on the emission of an N-photon bundle as shown in the previous section for the case $N = 2$. Already at a low temperature of $T = 1\,\mathrm{K}$ the $1/n$-distribution characteristic for the bundle [cf., Eq. (1)] is not recognizable anymore (cf., Fig. 3). This result was obtained within a microscopic model of the phonon influence. In contrast, in Ref. [27], the dephasing has been analyzed using a phenomenological Lindblad operator $\mathcal{L}_{|X\rangle\langle X|,\gamma_\phi}$.

It is therefore instructive to compare the microscopic model with the phenomenological one to check whether the latter is valid. On first sight, we find a quite different behavior: for the phenomenological model taking values for the corresponding Lindblad rate γ_ϕ from the literature on semiconductor QD–cavity systems, the impact of pure dephasing is almost negligible [27].

To analyze this in more detail, we have plotted results of the phenomenological model in Fig. 4, which shows the stationary ratio r as a function of the phenomenological pure-dephasing rate γ_ϕ which is incorporated into the model by the addition of the Lindblad operator $\mathcal{L}_{|X\rangle\langle X|,\gamma_\phi}$ instead of the microscopic Hamiltonian model H_{Ph}. Indeed, in that approximation a large plateau range is found where the ratio stays essentially at its phonon-free value of $r = 0.45$ (cf., also Fig. 3).

To assess, what γ_ϕ should be chosen in the reduced model to best approximate the full phonon effect, we apply the following procedure: We compare the exciton dynamics resulting from the full calculation (where phonons are included by H_{Ph}) with the phenomenological model (where H_{Ph} is replaced by $\mathcal{L}_{|X\rangle\langle X|,\gamma_\phi}$) and vary γ_ϕ until the envelopes of the two dynamical results essentially match. Note that we set $\kappa = \gamma = 0$ for this procedure to extract the pure phonon influence on the dynamics. Furthermore, this comparison is conducted for the all-resonant case, i.e., $\Delta\omega_{\mathrm{LX}} = \Delta\omega_{\mathrm{CX}} = 0$. We perform this procedure at $T = 4\,\mathrm{K}$ for three different cases and mark the resulting rate γ_ϕ by red squares in Fig. 4: (a) Driven Jaynes–Cummings system with the initial state $|G, 0\rangle$, resembling the closest approximation to the full calculation, (b) Jaynes–Cummings system without driving ($f = 0$) for the initial state $|G, 1\rangle$, and (c) same as (b) but with $|G, 2\rangle$ as the initial state. The three extracted rates (cf., Fig. 4) indicate that a very large pure-dephasing rate of the order of $10^{-1}\,\mathrm{meV}$ is necessary to reproduce the dynamics of the full microscopic model [cf., red square labeled with (a)]. With such a large rate, the ratio r is close to zero, meaning that no 2-photon bundle emission takes place in accordance with the results of the full model at $T = 4\,\mathrm{K}$ (cf., Fig. 3).

The reason for such a significant increase in γ_ϕ lies in the impact of pure dephasing mechanism,

which gains in strength for larger Rabi frequencies related to the effective couplings present in the system. While in (b) and (c) the cavity Rabi frequency amounts to $2g\sqrt{n+1}$ with n the number of photons present in the cavity, the driving $f \gg g$ introduces the highest transition frequency in (a). In Fig. 4, it becomes clear that the pure-dephasing rate increases with larger effective coupling, in accordance with earlier observations in the case of a microscopic description of phonons [38, 49, 50]. The values of γ_ϕ in (b) and (c) are of the order of experimentally found pure-dephasing rates for strong QD–cavity coupling like the one studied here (cf., Sec. 2.1.1), but without external driving. Choosing such values for the rate indeed results in a marginal influence of pure dephasing, since both points lie well inside the plateau region.

Thus, the conclusion in Ref. [27] that dephasing does not significantly affect the N-photon bundle generation can be traced back to the fact that values for dephasing rates have been considered that are no longer applicable in the regime of very strong driving as required for this protocol. The physical reason lies in the fact that an optically driven system is influenced by the phonon Hamiltonian in a profoundly different way than its non-driven counterpart: while phonons cannot induce transitions between the two electronic states in the undriven case, they can lead to transitions between the laser-dressed states, which are the eigenstates of the driven two-level system. In essence, the dephasing rate depends on the driving strength. A quadratic dependence $\gamma_\phi \propto f^2$ can be derived in a weak-coupling limit [51].

In conclusion, a phenomenological pure dephasing model is also able to qualitatively predict the destruction of the N-photon bundle. The challenge is the choice of a proper rate, which has to be calibrated to the full phonon system.

4 Results: Superconducting qubit–microwave resonator systems

Superconducting qubit–microwave resonator systems have been successfully used to demonstrate the on-demand preparation of various highly nonclassical photon states, such as Fock states [4], superpositions thereof, and Voodoo cat states, i.e., coherent superpositions of three coherent states [5]. In none of these experiments, a significant impact of pure dephasing was reported.

For state-of-the-art superconducting systems [5], the resonator losses are much smaller than the decay of the qubit ($\kappa \ll \gamma$ as in Sec. 2.1.2). Again, the 2-photon bundle resonance is achieved by an external excitation tuned according to Eq. (5). The resulting photon number distribution is shown in Fig. 5, normalized to its value at $n = 1$ (light blue bars). Surprisingly, no bundle is emitted, as the photons are able to climb up the Jaynes–Cummings ladder instead. In particular, the characteristic cutoff for $n > N = 2$ is not observed. The reason lies in the fact that the radiative decay γ can induce transitions from $|+, n\rangle$ to $|-, n\rangle$. From the latter, additional photons can be emitted to break the cutoff and reach higher n.

The failure of the superconducting qubit to emit a bundle can be traced back to the lack of resonator losses κ in comparison to radiative decay γ. Indeed, if we consider a resonator loss rate much larger (following Ref. [27], $\kappa = 0.1g$ has been chosen, cf., also Fig. 3 for this specific choice), we can obtain a near-perfect 2-photon bundle. The resulting photon number distribution (cf., dark blue bars in Fig. 5) indeed shows a near-perfect 2-photon bundle, with $r = 0.49$ and no occupation for $n > 2$. This means that though much effort is usually invested into resonators of better quality, here the use of a bad resonator is mandatory when bundle generation is the target.

To analyze the impact of the losses in more detail, we study the quality of the emitted 2-photon bundle as a function of the resonator losses. To this end, the 2- to 1-photon ratio r is shown as a function of κ in Fig. 6 as well as the 3- to 1-photon ratio, which should vanish for an ideal 2-photon bundle emission due to the cutoff for $n > N = 2$. Indeed, these two quantities confirm that the chosen value of $\kappa = 0.1g = 7.76\gamma$ lies well within a plateau region of $r \approx 0.5$ and a vanishing occupation for $n > 2$. While resonator losses too low compared to the decay of the qubit results in the occupation of states with $n > 2$, using very low-quality resonators with $\kappa \gtrsim 20\gamma$ (cf., Fig. 6) leads to a drastic reduction of r and thus an emission, which has no bundle structure anymore. While constructing resonators of better quality is always an experimental challenge, creating a bad resonator should be

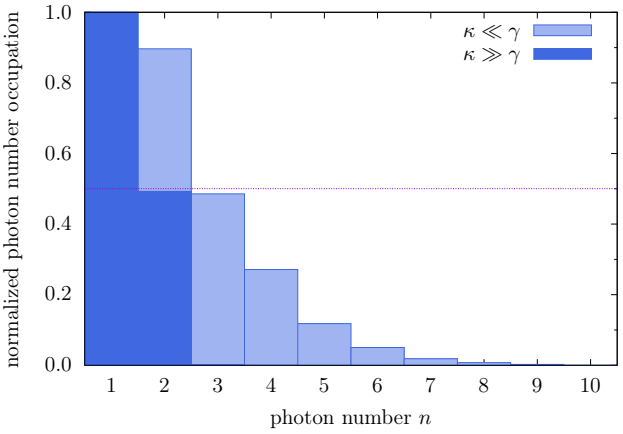

Figure 5: The stationary photon number occupation normalized to its value at $n = 1$ for the superconducting qubit–microwave system. The data labeled $\kappa \ll \gamma$ is obtained using the parameters from Sec. 2.1.2. In dark blue, the result of a calculation with a cavity loss rate two orders of magnitude larger than in Sec. 2.1.2 is shown, namely $\kappa = 0.1g = 7.76\gamma$, cf. Fig. 3.

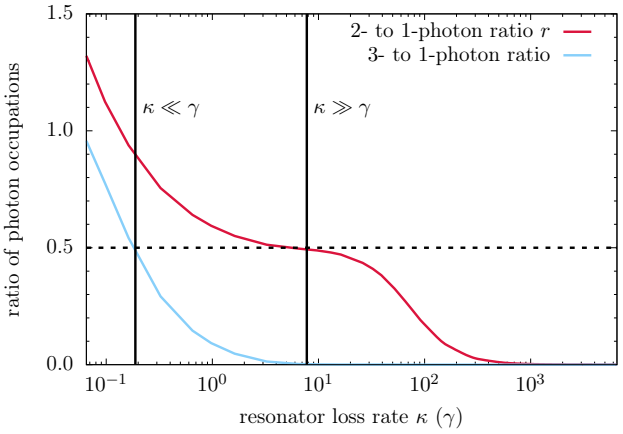

Figure 6: The stationary ratios of the 2- to 1-photon occupations r and of the 3- to 1-photon occupations as functions of the resonator loss rate κ (in units of γ) for the superconducting qubit–microwave system. The two vertical black lines mark those values of κ, which are used to obtain the corresponding data in Fig. 5. The dotted black line shows the target value of 0.5 for the ratio r.

a lesser problem. Thus, superconducting qubit–microwave resonator systems are indeed suitable candidates for sources of N-photon bundles.

5 Conclusion

We have studied two solid-state platforms as possible sources of N-photon bundles [27]: semiconductor quantum-dot–cavity systems and superconducting qubit–microwave resonator systems.

In quantum-dot–cavity systems, pure dephasing is induced by longitudinal acoustic phonons. We have found that even at low operating temperatures of a few kelvin, a 2-photon bundle is destroyed, thereby crushing the hopes for the emission of bundles with $N > 2$. The reason is the considered driving regime that is required to address the bundle resonance, which also favors the phonon activity in the electronic subsystem of the quantum dot.

In contrast, superconducting qubit–microwave resonator systems are suitable to generate N-photon bundles. Here, the pure dephasing does not play a notable role. However, the quality of the resonator should not be too high to facilitate the emission of photon bundles.

Acknowledgments

This work was funded by the Deutsche Forschungsgemeinschaft (DFG, German Research Foundation) – project No. 419036043.

A Resonance peaks for $N \to \infty$ and $N = 1$

Since the peaks at $\hbar\Delta\omega_{\mathrm{LX}} = -1.2\,\mathrm{meV}$ and $0.08\,\mathrm{meV}$ are the most striking features in Fig. 2, we shall discuss them in some detail in this appendix. This will give additional insights into the physics taking place in this parameter regime in general, although the analysis reveals that these peaks are not related to the bundles which are the main target of our paper. The most prominent peak in Fig. 2 at $\hbar\Delta\omega_{\mathrm{LX}} = \hbar\Delta\omega_{\mathrm{CX}} = -1.2\,\mathrm{meV}$ is obtained in the limit $N \to \infty$ and corresponds to a process where the photon energy in a frame rotating with the laser frequency is $\hbar\Delta\omega_{\mathrm{CL}} = 0$ and the system can climb up the photon ladder from $|-, n\rangle$ to $|-, n+1\rangle$, such that a Poissonian distribution with respect to n emerges. Note that one observes a double-peaked structure at this resonance in Fig. 2. At its center, the order of the photon occupations is reversed, i.e., the occupation of $n = 2$ is higher than that of $n = 1$, consistent with a Poissonian with an average photon number of $\langle n\rangle = 6.6$ and a maximum occupation of 0.15 at $n = 6$. A magnification of this peak, where the reversal of the photon order is visible, is replotted in Fig. 7. An analysis of the

corresponding Wigner function [5, 26] (not shown here) confirms that the corresponding state is a (Glauber) coherent state.

The peak at $\hbar\Delta\omega_{\mathrm{LX}} \approx 0.08\,\mathrm{meV}$ corresponds to a 1-photon bundle, i.e., a 1-photon Fock state, and also results from a one-photon process. But in contrast to the previously discussed case, the photon is emitted by the transition from $|-,0\rangle$ to $|+,1\rangle$. Due to an energy mismatch between the photon energy and the transition between $|+,1\rangle$ and $|\pm,2\rangle$, no further photons are put into the cavity, as can be seen in the stationary occupations of this peak in Fig. 2(a). This effect is commonly known as the photon blockade [52].

The phonon influence on the occupations at $T = 4\,\mathrm{K}$ as shown in Fig. 2(b) could not be more different for these two resonances. The first one for $N \to \infty$ at $\hbar\Delta\omega_{\mathrm{LX}} = -1.2\,\mathrm{meV}$ is hardly influenced by phonons at all. Indeed, the photon number distribution remains Poissonian with a slightly lower average photon number of $\langle n\rangle = 5.6$ and a similar maximum occupation of 0.16 at $n = 5$. The reason lies in the fact that the photons are emitted from transitions, where the electronic (laser-dressed) state remains $|-\rangle$ and does not change. Since this is the energetically lower dressed state and at temperatures below a few tens of kelvins phonon absorption is highly unlikely, phonons have only a slight influence on the stationary photon distribution.

On the other hand, the second peak at $\hbar\Delta\omega_{\mathrm{LX}} \approx 0.08\,\mathrm{meV}$ for $N = 1$ experiences strong phonon-enhancement, since the photon blockade is spoiled. The energy mismatch between $|+,n\rangle$ and $|-,n\rangle$ is now bridged by phonon emission, which is possible for all temperatures down to absolute zero, and a subsequent resonant transition to $|+,n+1\rangle$ can take place. Therefore, the phonon coupling drives the occupation of higher-order Fock states beyond $n = 1$ [44, 53].

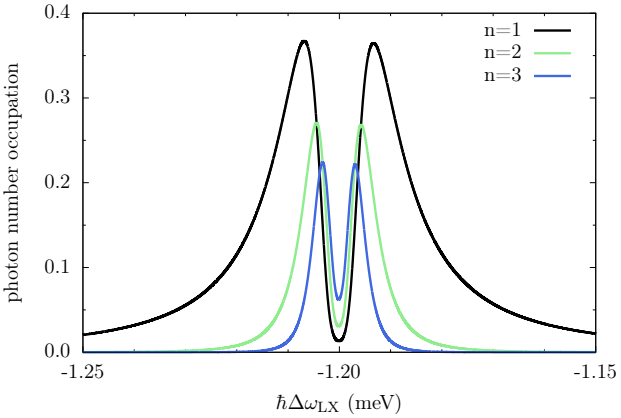

Figure 7: Stationary photon number occupation in the QD–cavity system as a function of the laser–exciton detuning $\Delta\omega_{\mathrm{LX}}$ without taking phonon effects into account. This is a magnification of the resonance peak for $N \to \infty$ in Fig. 2(a). On this scale, the double-peak structure and the reversal of the photon order at its center are well visible.

References

[1] F. W. Cummings, A. K. Rajagopal. 'Production of number states of the electomagnetic field'. *Phys. Rev. A* **39**, 3414 (1989). doi:10.1103/PhysRevA.39.3414.

[2] B. T. H. Varcoe, S. Brattke, M. Weidinger, H. Walther. 'Preparing pure photon number states of the radiation field'. *Nature* **403**, 743 (2000). doi:10.1038/35001526.

[3] X. Zhou, I. Dotsenko, B. Peaudecerf, T. Rybarczyk, C. Sayrin, S. Gleyzes, J. M. Raimond, M. Brune, S. Haroche. 'Field locked to a Fock state by quantum feedback with single photon corrections'. *Phys. Rev. Lett.* **108**, 243602 (2012). doi: 10.1103/PhysRevLett.108.243602.

[4] M. Hofheinz, E. M. Weig, M. Ansmann, R. C. Bialczak, E. Lucero, M. Neeley, A. D. O'Connell, H. Wang, J. M. Martinis, A. N. Cleland. 'Generation of Fock states in a superconducting quantum circuit'. *Nature* **454**, 310 (2008). doi:10.1038/nature07136.

[5] M. Hofheinz, H. Wang, M. Ansmann, R. C. Bialczak, E. Lucero, M. Neeley, A. D. O'Connell, D. Sank, J. Wenner, J. M. Martinis, A. N. Cleland. 'Synthesizing arbitrary quantum states in a superconducting resonator'. *Nature* **459**, 546 (2009). doi: 10.1038/nature08005.

[6] P. Michler, A. Kiraz, C. Becher, W. V. Schoenfeld, P. M. Petroff, L. Zhang, E. Hu, A. Imamoglu. 'A quantum dot single-photon turnstile device'. *Science* **290**, 2282 (2000). doi:10.1126/science.290.5500.2282.

[7] C. Santori, M. Pelton, G. Solomon, Y. Dale, Y. Yamamoto. 'Triggered single photons from a quantum dot'. *Phys. Rev. Lett.* **86**, 1502 (2001).

[8] C. Santori, D. Fattal, J. Vuckovic, G. S. Solomon, Y. Yamamoto. 'Indistinguishable photons from a single-photon device'. *Nature* **419**, 594 (2002).

[9] Y.-M. He, Y. He, Y.-J. Wei, D. Wu, M. Atatüre, C. Schneider, S. Höfling, M. Kamp, C.-Y. Lu, J.-W. Pan. 'On-demand semiconductor single-photon source with near-unity indistinguishability'. *Nat. Nanotechnol.* **8**, 213 (2013).

[10] Y.-J. Wei, Y.-M. He, M.-C. Chen, Y.-N. Hu, Y. He, D. Wu, C. Schneider, M. Kamp, S. Höfling, C.-Y. Lu, J.-W. Pan. 'Deterministic and robust generation of single photons from a single quantum dot with 99.5% indistinguishability using adiabatic rapid passage'. *Nano Lett.* **14**, 6515 (2014).

[11] X. Ding, Y. He, Z.-C. Duan, N. Gregersen, M.-C. Chen, S. Unsleber, S. Maier, C. Schneider, M. Kamp, S. Höfling, C.-Y. Lu, J.-W. Pan. 'On-demand single photons with high extraction efficiency and near-unity indistinguishability from a resonantly driven quantum dot in a micropillar'. *Phys. Rev. Lett.* **116**, 020401 (2016). doi:10.1103/PhysRevLett.116.020401.

[12] N. Somaschi, V. Giesz, L. De Santis, J. C. Loredo, M. P. Almeida, G. Hornecker, S. L. Portalupi, T. Grange, C. Antón, J. Demory, C. Gómez, I. Sagnes, N. D. Lanzillotti-Kimura, A. Lemaítre, A. Auffeves, A. G. White, L. Lanco, P. Senellart. 'Near-optimal single-photon sources in the solid state'. *Nat. Photonics* **10**, 340 (2016).

[13] L. Schweickert, K. D. Jöns, K. D. Zeuner, S. F. Covre da Silva, H. Huang, T. Lettner, M. Reindl, J. Zichi, R. Trotta, A. Rastelli, V. Zwiller. 'On-demand generation of background-free single photons from a solid-state source'. *Appl. Phys. Lett.* **112**, 093106 (2018). doi:10.1063/1.5020038.

[14] L. Hanschke, K. A. Fischer, S. Appel, D. Lukin, J. Wierzbowski, S. Sun, R. Trivedi, J. Vučković, J. J. Finley, K. Müller. 'Quantum dot single-photon sources with ultra-low multi-photon probability'. *npj Quantum Inf.* **4** (2018).

[15] M. Cosacchi, F. Ungar, M. Cygorek, A. Vagov, V. M. Axt. 'Emission-frequency separated high quality single-photon sources enabled by phonons'. *Phys. Rev. Lett.* **123**, 017403 (2019). doi: 10.1103/PhysRevLett.123.017403.

[16] N. Akopian, N. H. Lindner, E. Poem, Y. Berlatzky, J. Avron, D. Gershoni, B. D. Gerardot, P. M. Petroff. 'Entangled photon pairs from semiconductor quantum dots'. *Phys. Rev. Lett.* **96**, 130501 (2006). doi: 10.1103/PhysRevLett.96.130501.

[17] R. M. Stevenson, R. J. Young, P. Atkinson, K. Cooper, D. A. Ritchie, A. J. Shields. 'A semiconductor source of triggered entangled photon pairs'. *Nature* **439**, 179 (2006). doi: 10.1038/nature04446.

[18] R. Hafenbrak, S. M. Ulrich, P. Michler, L. Wang, A. Rastelli, O. G. Schmidt. 'Triggered polarization-entangled photon pairs from a single quantum dot up to 30 k'. *New J. Phys.* **9**, 315 (2007).

[19] A. Dousse, J. Suffczynski, A. Beveratos, O. Krebs, A. Lemaître, I. Sagnes, J. Bloch, P. Voisin, P. Senellart. 'Ultrabright source of entangled photon pairs'. *Nature* **466**, 217 (2010).

[20] E. del Valle. 'Distilling one, two and entangled pairs of photons from a quantum dot with cavity QED effects and spectral filtering'. *New J. Phys* **15**, 025019 (2013).

[21] M. Müller, S. Bounouar, K. D. Jöns, M. Glässl, P. Michler. 'On-demand generation of indistinguishable polarization-entangled photon pairs'. *Nat. Photonics* **8**, 224 (2014).

[22] A. Orieux, M. A. M. Versteegh, K. D. Jöns, S. Ducci. 'Semiconductor devices for entangled photon pair generation: a review'. *Rep. Prog. Phys.* **80**, 076001 (2017). doi: 10.1088/1361-6633/aa6955.

[23] T. Seidelmann, F. Ungar, A. M. Barth, A. Vagov, V. M. Axt, M. Cygorek, T. Kuhn. 'Phonon-induced enhancement of photon entanglement in quantum dot-cavity systems'. *Phys. Rev. Lett.* **123**, 137401 (2019). doi:10.1103/PhysRevLett.123.137401.

[24] M. Cosacchi, J. Wiercinski, T. Seidelmann, M. Cygorek, A. Vagov, D. E. Reiter, V. M. Axt. 'On-demand generation of higher-order Fock states in quantum-dot–cavity systems'.

Phys. Rev. Research **2**, 033489 (2020). doi: 10.1103/PhysRevResearch.2.033489.

[25] J. Gea-Banacloche. 'Collapse and revival of the state vector in the jaynes-cummings model: An example of state preparation by a quantum apparatus'. *Phys. Rev. Lett.* **65**, 3385 (1990). doi: 10.1103/PhysRevLett.65.3385.

[26] M. Cosacchi, T. Seidelmann, J. Wiercinski, M. Cygorek, A. Vagov, D. E. Reiter, V. M. Axt. 'Schrödinger cat states in quantum-dot-cavity systems'. *Phys. Rev. Research* **3**, 023088 (2021). doi: 10.1103/PhysRevResearch.3.023088.

[27] C. S. Muñoz, E. del Valle, A. G. Tudela, K. Müller, S. Lichtmannecker, M. Kaniber, C. Tejedor, J. J. Finley, F. P. Laussy. 'Emitters of n-photon bundles'. *Nat. Photonics* **8**, 550 (2014).

[28] D. E. Reiter, T. Kuhn, M. Glässl, V. M. Axt. 'The role of phonons for exciton and biexciton generation in an optically driven quantum dot'. *J. Phys.: Condens. Matter* **26**, 423203 (2014).

[29] D. E. Reiter, T. Kuhn, V. M. Axt. 'Distinctive characteristics of carrier-phonon interactions in optically driven semiconductor quantum dots'. *Advances in Physics: X* **4**, 1655478 (2019).

[30] L. Besombes, K. Kheng, L. Marsal, H. Mariette. 'Acoustic phonon broadening mechanism in single quantum dot emission'. *Phys. Rev. B* **63**, 155307 (2001). doi: 10.1103/PhysRevB.63.155307.

[31] P. Borri, W. Langbein, S. Schneider, U. Woggon, R. L. Sellin, D. Ouyang, D. Bimberg. 'Ultralong dephasing time in InGaAs quantum dots'. *Phys. Rev. Lett.* **87**, 157401 (2001). doi: 10.1103/PhysRevLett.87.157401.

[32] B. Krummheuer, V. M. Axt, T. Kuhn. 'Theory of pure dephasing and the resulting absorption line shape in semiconductor quantum dots'. *Phys. Rev. B* **65**, 195313 (2002). doi:10.1103/PhysRevB.65.195313.

[33] V. M. Axt, T. Kuhn, A. Vagov, F. M. Peeters. 'Phonon-induced pure dephasing in exciton-biexciton quantum dot systems driven by ultrafast laser pulse sequences'. *Phys. Rev. B* **72**, 125309 (2005). doi: 10.1103/PhysRevB.72.125309.

[34] D. P. S. McCutcheon. 'Optical signatures of non-Markovian behavior in open quantum systems'. *Phys. Rev. A* **93**, 022119 (2016). doi:10.1103/PhysRevA.93.022119.

[35] A. Krügel, V. M. Axt, T. Kuhn, P. Machnikowski, A. Vagov. 'The role of acoustic phonons for rabi oscillations in semiconductor quantum dots'. *Appl. Phys. B* **81**, 897 (2005). doi:10.1007/s00340-005-1984-1.

[36] A. J. Ramsay, T. M. Godden, S. J. Boyle, E. M. Gauger, A. Nazir, B. W. Lovett, A. M. Fox, M. S. Skolnick. 'Phonon-induced rabi-frequency renormalization of optically driven single InGaAs/GaAs quantum dots'. *Phys. Rev. Lett.* **105**, 177402 (2010). doi: 10.1103/PhysRevLett.105.177402.

[37] J. Förstner, C. Weber, J. Danckwerts, A. Knorr. 'Phonon-assisted damping of rabi oscillations in semiconductor quantum dots'. *Phys. Rev. Lett.* **91**, 127401 (2003). doi: 10.1103/PhysRevLett.91.127401.

[38] P. Machnikowski, L. Jacak. 'Resonant nature of phonon-induced damping of Rabi oscillations in quantum dots'. *Phys. Rev. B* **69**, 193302 (2004). doi: 10.1103/PhysRevB.69.193302.

[39] A. J. Ramsay, A. V. Gopal, E. M. Gauger, A. Nazir, B. W. Lovett, A. M. Fox, M. S. Skolnick. 'Damping of exciton Rabi rotations by acoustic phonons in optically excited InGaAs/GaAs quantum dots'. *Phys. Rev. Lett.* **104**, 017402 (2010). doi: 10.1103/PhysRevLett.104.017402.

[40] N. Makri, D. E. Makarov. 'Tensor propagator for iterative quantum time evolution of reduced density matrices. I. Theory'. *J. Chem. Phys.* **102**, 4600 (1995). doi: 10.1063/1.469508.

[41] N. Makri, D. E. Makarov. 'Tensor propagator for iterative quantum time evolution of reduced density matrices. II. Numerical methodology'. *J. Chem. Phys.* **102**, 4611 (1995). doi:10.1063/1.469509.

[42] A. Vagov, M. D. Croitoru, M. Glässl, V. M. Axt, T. Kuhn. 'Real-time path integrals

for quantum dots: Quantum dissipative dynamics with superohmic environment coupling'. *Phys. Rev. B* **83**, 094303 (2011). doi: 10.1103/PhysRevB.83.094303.

[43] A. M. Barth, A. Vagov, V. M. Axt. 'Path-integral description of combined Hamiltonian and non-Hamiltonian dynamics in quantum dissipative systems'. *Phys. Rev. B* **94**, 125439 (2016). doi: 10.1103/PhysRevB.94.125439.

[44] M. Cygorek, A. M. Barth, F. Ungar, A. Vagov, V. M. Axt. 'Nonlinear cavity feeding and unconventional photon statistics in solid-state cavity QED revealed by many-level real-time path-integral calculations'. *Phys. Rev. B* **96**, 201201(R) (2017). doi:10.1103/PhysRevB.96.201201.

[45] D. Najer, I. Söllner, P. Sekatski, V. Dolique, M. C. Löbl, D. Riedel, R. Schott, S. Starosielec, S. R. Valentin, A. D. Wieck, N. Sangouard, A. Ludwig, R. J. Warburton. 'A gated quantum dot strongly coupled to an optical microcavity'. *Nature* **575**, 622 (2019). doi:10.1038/s41586-019-1709-y.

[46] C. Schneider, P. Gold, S. Reitzenstein, S. Höfling, M. Kamp. 'Quantum dot micropillar cavities with quality factors exceeding 250,000'. *Applied Physics B* **122**, 19 (2016). doi:10.1007/s00340-015-6283-x.

[47] B. Krummheuer, V. M. Axt, T. Kuhn, I. D'Amico, F. Rossi. 'Pure dephasing and phonon dynamics in GaAs- and GaN-based quantum dot structures: Interplay between material parameters and geometry'. *Phys. Rev. B* **71**, 235329 (2005). doi: 10.1103/PhysRevB.71.235329.

[48] Y.-T. Chough, H.-J. Moon, H. Nha, K. An. 'Single-atom laser based on multiphoton resonances at far-off resonance in the jaynes-cummings ladder'. *Phys. Rev. A* **63**, 013804 (2000). doi:10.1103/PhysRevA.63.013804.

[49] A. Vagov, M. D. Croitoru, V. M. Axt, T. Kuhn, F. M. Peeters. 'Nonmonotonic field dependence of damping and reappearance of Rabi oscillations in quantum dots'. *Phys. Rev. Lett.* **98**, 227403 (2007). doi: 10.1103/PhysRevLett.98.227403.

[50] M. Glässl, L. Sörgel, A. Vagov, M. D. Croitoru, T. Kuhn, V. M. Axt. 'Interaction of a quantum-dot cavity system with acoustic phonons: Stronger light-matter coupling can reduce the visibility of strong coupling effects'. *Phys. Rev. B* **86**, 035319 (2012). doi:10.1103/PhysRevB.86.035319.

[51] A. Nazir, D. P. S. McCutcheon. 'Modelling exciton–phonon interactions in optically driven quantum dots'. *J. Phys.: Condens. Matter* **28**, 103002 (2016). doi: 10.1088/0953-8984/28/10/103002.

[52] K. M. Birnbaum, A. Boca, R. Miller, A. D. Boozer, T. E. Northup, H. J. Kimble. 'Photon blockade in an optical cavity with one trapped atom'. *Nature* **436**, 87 (2005). doi: 10.1038/nature03804.

[53] M. Cosacchi, T. Seidelmann, F. Ungar, M. Cygorek, A. Vagov, V. M. Axt. 'Transiently changing shape of the photon number distribution in a quantum-dot–cavity system driven by chirped laser pulses'. *Phys. Rev. B* **101**, 205304 (2020). doi: 10.1103/PhysRevB.101.205304.

Publication 8

Transiently changing shape of the photon number distribution in a quantum-dot–cavity system driven by chirped laser pulses.

M. Cosacchi, T. Seidelmann, F. Ungar, M. Cygorek, A. Vagov, V. M. Axt.

Phys. Rev. B **101**, 205304 (2020).

DOI: 10.1103/PhysRevB.101.205304

Author contributions

The author has designed the concept of this study, in particular, he has performed the data generation and analysis, has provided the interpretation of the results, and has written the first draft of the paper. He has moderated all discussions and revision requests of the draft, has organized the correspondence with the editor and referees, and has provided the first drafts of answers to the referees.

T. Seidelmann has discussed the results in detail with the author, thus contributing to the interpretation. In particular, he has contributed the interpretation in terms of laser- and cavity-dressed states. He has contributed to revisions of the draft and the answers to the referees.

F. Ungar has discussed the results in detail with the author, thus contributing to the interpretation. He has contributed to revisions of the draft and the answers to the referees.

M. Cygorek and A. Vagov have cosupervised this work, in particular, they have participated in the discussion and interpretation of the results. They have contributed to the optimization of the presentation as well as revisions of the draft and the answers to the referees.

V. M. Axt has advised the author throughout his work as the main supervisor. He has obtained the funding for this work and has participated in the discussion and interpretation of the results. He has contributed to the optimization of the presentation as well as revisions of the draft and the answers to the referees.

Transiently changing shape of the photon number distribution in a quantum-dot–cavity system driven by chirped laser pulses

M. Cosacchi,[1] T. Seidelmann,[1] F. Ungar,[1] M. Cygorek,[2] A. Vagov,[1,3] and V. M. Axt[1]
[1]*Theoretische Physik III, Universität Bayreuth, D-95440 Bayreuth, Germany*
[2]*Department of Physics, University of Ottawa, Ottawa, Ontario, Canada K1N 6N5*
[3]*ITMO University, St. Petersburg, 197101, Russia*

(Received 10 March 2020; revised manuscript received 24 April 2020; accepted 28 April 2020; published 13 May 2020)

We have simulated the time evolution of the photon number distribution in a semiconductor quantum-dot–microcavity system driven by chirped laser pulses and compare with unchirped results. When phonon interactions with the dot are disregarded—thus corresponding to the limit of atomic cavity systems—chirped pulses generate photon number distributions that change their shape drastically in the course of time. Phonons have a strong and qualitative impact on the photon statistics. The asymmetry between phonon absorption and emission destroys the symmetry of the photon distributions obtained for positive and negative chirps. While for negative chirps transient distributions resembling thermal ones are observed, for positive chirps the photon number distribution still resembles its phonon-free counterpart but with overall smoother shapes. In sharp contrast, using unchirped pulses of the same pulse area and duration wave packets are found that move up and down the Jaynes-Cummings ladder with a bell shape that changes little in time. For shorter pulses and lower driving strength Rabi-like oscillations occur between low photon number states. For all considered excitation conditions transitions between sub- and super-Poissonian statistics are found at certain times. For resonant driving with low intensity the Mandel parameter oscillates and is mostly negative, which indicates a nonclassical state in the cavity field. Finally, we show that it is possible that the Mandel parameter dynamically approaches zero and still the photon distribution exhibits two maxima and thus is far from being a Poissonian.

DOI: 10.1103/PhysRevB.101.205304

I. INTRODUCTION

Semiconductor quantum-dot–cavity (QDC) systems continue to raise attention as highly integrable on-demand emitters of nonclassical states of light. In particular, QDCs have proven to be rather successful providing, e.g., reliable on-demand high quality single photon sources [1–10] as well as sources for entangled photon pairs [11–18]. Clearly, QDCs support a much larger class of excitations when higher mean photon numbers are reached. The additional degrees of freedom provided by higher number photon states obviously allow for a rich variety of dynamical scenarios and may open the way to new kinds of applications such as, e.g., the encoding of quantum information in the photon number state distribution. These possibilities are, however, far from being explored.

Often, the first step to characterize systems with photon distributions ranging up to higher photon numbers is to record a few characteristic numbers such as the mean photon number [19] and/or the Mandel parameter [20]. In simple cases, the mean photon number is indeed enough to capture the whole information about the photon distribution even when the latter is time dependent. This applies in particular when photons are generated by classically driving an empty cavity without a quantum dot (QD) where the photonic system is at all times in a coherent state and thus the distribution is a Poissonian [21,22], i.e., in this case the photonic excitation is always as close as possible to a classical light field and thus nonclassical states cannot be reached. Moreover, although the mean photon number varies in time, the photon distribution keeps its shape at all times.

The situation is different when a system with few discrete levels near resonance to a cavity mode such as an atom or a quantum dot is placed inside the cavity. When driving transitions between these discrete levels deviations from the coherent state may occur as is evident, e.g., by monitoring the Mandel parameter,

$$Q(t) = (\langle \Delta n^2 \rangle - \langle n \rangle)/\langle n \rangle. \tag{1}$$

$Q(t)$ measures the deviation of the mean-square fluctuation from the mean photon number normalized to the latter. Therefore, Q vanishes for a Poisson distribution. A positive Q indicates a super-Poissonian distribution with larger fluctuations than in a coherent state with the same mean photon number while negative Q values correspond to the sub-Poissonian regime which is known to have no classical analog [23]. Indeed, deviations from the coherent state have been reported for the stationary distribution obtained in an atomic cavity with constant driving where different signs of Q have been found for different ratios between cavity loss and radiative decay rates [24]. In Ref. [25] it has been shown that the statistics of photons emitted from the exciton-biexciton system of a QD can be steered from sub- to the super-Poissonian by varying the biexciton binding energy, the pump strength or the temperature [26]. Although the experiments in

Ref. [25] have been performed on QDs without cavity, the number of modes in the theoretical modeling was restricted to two which corresponds to the situation in a QDC. Therefore, the results should also apply to QDCs. Simulations for a pulsed excitation of a QDC indicate that Q can exhibit oscillations and change its sign repeatedly in time [27].

It is clear, however, that in general the photon number distribution contains much more detailed information than captured by the mean photon number or the Mandel parameter. Recently, calculations of the stationary photon number distribution in a constantly driven QDC revealed a strong qualitative influence of phonons on the shape of the distribution [28,29]. While without phonons distributions with many different shapes were found for different detunings, the stationary distribution with phonons turned out to be close to a thermal state with a high effective temperature. Note that the case without phonons describes, e.g., a cavity with a trapped atom.

Advances in measuring techniques have demonstrated possibilities for observing directly the photon number resolved distributions in various systems without the necessity to perform quantum tomography to reconstruct the entire state [30], ranging from bimodal microlasers [31] over QDs [32,33] to exciton-polariton condensates [34]. Furthermore, a novel algorithm for data evaluation free of systematic errors to obtain number distributions has been successfully employed [35]. These achievements could pave the way to novel applications where easy access to information encoded in the photon number distribution is needed.

The focus of the present paper is on the transient behavior of the photon number distribution in a QDC system driven by chirped pulses in comparison to the unchirped case. Our most striking result is the finding that the shape of the number distribution changes dynamically when driving the QDC with chirped pulses. In sharp contrast, for sufficiently strong unchriped excitations a wave packet which keeps a bell shape for all times moves up and down the Jaynes-Cummings ladder. Phonons have noticeable effects on the photon statistics for all excitation conditions that we compare. Notably, for chirped excitation the phonon impact induces qualitative changes of the shape of the distribution in particular for negative chirps.

II. THEORY

A. Model and methods

We study a self-assembled QD, e.g., GaAs/In(Ga)As, with strong electronic confinement, such that only the lowest conduction and the highest valence band states need to be taken into account. Furthermore, we consider only situations where the system is well represented by a two-level model. The latter applies, e.g., for resonant driving of the exciton by circularly polarized light when the fine-structure splitting is negligible or when all other states such as the biexciton are sufficiently far from resonance. Then the Hamiltonian for the laser driven dot reads

$$H_{\mathrm{DL}} = -\hbar\Delta\omega_{\mathrm{LX}}|X\rangle\langle X| - \frac{\hbar}{2}f(t) \times \left(e^{-i\varphi(t)}|X\rangle\langle G| + e^{i\varphi(t)}|G\rangle\langle X|\right), \tag{2}$$

where the detuning between the exciton and central laser frequency $\Delta\omega_{\mathrm{LX}} := \omega_{\mathrm{L}} - \omega_{\mathrm{X}}$ is introduced. Here, the ground state $|G\rangle$ is chosen as the zero of the energy scale. Note that the usual dipole and rotating wave approximations are employed and the Hamiltonian is written down in a frame co-rotating with the laser frequency ω_{L}. The real amplitude $f(t)$ and the phase $\varphi(t)$ are related to the instantaneous Rabi frequency $\Omega(t)$ by

$$\Omega(t) := 2\mathbf{M_0}\cdot\mathbf{E}(t) = f(t)\,e^{-i(\omega_{\mathrm{L}}t+\varphi(t))}, \tag{3}$$

where $\mathbf{M_0}$ is the dipole matrix element of the transition between the QD ground $|G\rangle$ and exciton state $|X\rangle$ and $\mathbf{E}$ is the positive frequency part of the laser field.

To enhance the coupling between the QD and the electromagnetic field, the dot can be placed into a microcavity. We account for a single cavity mode with frequency ω_{C} far from the electromagnetic continuum and a QD coupled to that mode close to resonance via

$$H_{\mathrm{C}} = \hbar\Delta\omega_{\mathrm{CL}}a^\dagger a + \hbar g\left(a^\dagger|G\rangle\langle X| + a|X\rangle\langle G|\right), \tag{4}$$

where the cavity photons are created (annihilated) by the bosonic operator $a^\dagger$ (a) and are detuned by $\Delta\omega_{\mathrm{CL}} := \omega_{\mathrm{C}} - \omega_{\mathrm{L}}$ from the laser frequency. The QD is coupled to the cavity with a strength of $\hbar g$.

The subsystem of interest comprising the dot laser and the cavity Hamiltonian H_{DL} and H_{C}, respectively, is not an ideal few-level system, since it is embedded into the surrounding solid-state matrix. Even at cryogenic temperatures of a few Kelvin, the QD exciton is prone to the coupling to phonons. In strongly confined excitonic systems, the most important phononic contribution usually results from the deformation potential coupling to longitudinal acoustic (LA) phonons and is of the elastic pure dephasing type [36–39],

$$H_{\mathrm{Ph}} = \hbar\sum_{\mathbf{q}}\omega_{\mathbf{q}}b_{\mathbf{q}}^\dagger b_{\mathbf{q}} + \hbar\sum_{\mathbf{q}}\left(\gamma_{\mathbf{q}}^{\mathrm{X}}b_{\mathbf{q}}^\dagger + \gamma_{\mathbf{q}}^{\mathrm{X}*}b_{\mathbf{q}}\right)|X\rangle\langle X|, \tag{5}$$

where the bosonic operator $b_{\mathbf{q}}^\dagger$ ($b_{\mathbf{q}}$) creates (destroys) phonons with frequency $\omega_{\mathbf{q}}$. $\gamma_{\mathbf{q}}^{\mathrm{X}}$ denotes the coupling constant between the exciton state and the bosonic mode labeled by its wave vector $\mathbf{q}$ which is adequate for bulk phonons. Here, we use the fact that in GaAs/In(Ga)As the lattice properties of the dot and its surroundings are similar, such that phonon confinement is negligible. Other QD-phonon interaction mechanisms like, e.g., the piezoelectric coupling to LA and transverse acoustic (TA) phonons can become important in strongly polar crystals such as, e.g., GaN-based QDs [40,41], but are of minor importance for GaAs-type structures.

Finally, we account for Markovian loss processes by phenomenological decay rates for the radiative decay and cavity losses, respectively, that are incorporated into the model as Lindblad-type superoperators $\mathcal{L}_{|G\rangle\langle X|,\gamma}\bullet + \mathcal{L}_{a,\kappa}\bullet$ with

$$\mathcal{L}_{O,\Gamma}\bullet = \Gamma\left(O\bullet O^\dagger - \frac{1}{2}\{\bullet, O^\dagger O\}_+\right), \tag{6}$$

where $\{\cdot,\cdot\}_+$ denotes the anticommutator. O is a system operator and Γ the decay rate of the associated loss process, i.e., in our case γ stands for the radiative decay rate while κ is the cavity loss rate.

The dynamical equation to be solved is the Liouville-von Neumann equation for the density matrix,

$$\frac{\partial}{\partial t}\rho = -\frac{i}{\hbar}\{H, \rho\}_- + \mathcal{L}_{|G\rangle\langle X|,\gamma}\rho + \mathcal{L}_{a,\kappa}\rho, \tag{7}$$

with the total Hamiltonian $H = H_{\mathrm{DL}} + H_{\mathrm{C}} + H_{\mathrm{Ph}}$ and $\{\cdot,\cdot\}_-$ denotes the commutator.

We employ a path-integral formalism for simulating the dynamics in the above-defined model in a numerically complete fashion. By tracing out the phonon degrees of freedom analytically, a non-Markovian memory kernel decaying on a time scale of a few picoseconds is obtained that manifests in experiments as, e.g., non-Lorentzian line shapes in linear and nonlinear spectra [37,38,42,43] or in characteristic dependencies of the phonon-induced damping of Rabi rotations [44–47]. Therefore, this memory cannot be neglected in calculating the QD dynamics which takes place on a similar time scale. We call a numerical solution complete if a finer time discretization or a longer cutoff of the phonon-induced memory kernel does not change the results noticeably.

Most current implementations of the real-time path-integral approach are based on the pioneering work of Makri and Makarov [48,49], who introduced an iterative scheme for the augmented density matrix of the subsystem of interest. We are using an extension of this scheme that allows the inclusion of non-Hamiltonian Lindblad-type contributions into the path-integral algorithm without the loss of precision with respect to the phonon-induced part of the dynamics by formulating the iterative scheme not in a Hilbert, but a Liouville space [50]. In the present study, the system that couples to the phonons is represented by a large number of basis states of the form $|G, n\rangle$ and $|X, n\rangle$ where n denotes the photon number and G or X indicates whether the dot is in its ground or excited state. A numerically complete study of such systems is currently impossible with the Makri-Makarov algorithm due to the extreme growth of the numerical demand with rising number of system states. Nevertheless, we are able to present numerically complete results because we are using a recently developed reformulation of the algorithm that iterates a partially summed augmented density matrix [28]. Note that this reformulation of the path-integral algorithm does not introduce any additional approximations. For details on the methods, consider the supplement of Ref. [28]. The photon number distribution is obtained by taking the corresponding matrix element of the subsystem's reduced density operator $\bar{\rho} = \mathrm{Tr}_{\mathrm{Ph}}[\rho]$, with $\mathrm{Tr}_{\mathrm{Ph}}$ denoting the trace over the phonon degrees of freedom,

$$P_n(t) = \sum_{\nu=\mathrm{G,X}} \langle \nu, n|\bar{\rho}(t)|\nu, n\rangle. \tag{8}$$

B. Chirped pulses and laser-dressed states

In order to generate a chirped pulse one usually starts with a Gaussian pulse with an envelope and phase:

$$f_0(t) = \frac{\Theta}{\sqrt{2\pi}\sigma} e^{-\frac{(t-t_0)^2}{2\sigma^2}}, \tag{9}$$

$$\varphi(t) = \mathrm{const.}, \tag{10}$$

where Θ denotes the pulse area and σ determines the duration corresponding to a full width at half maximum (FWHM) of $\mathrm{FWHM} = 2\sqrt{2\ln(2)}\sigma$ and t_0 marks the time of the pulse maximum. We shall assume in the following a resonant excitation where $\varphi(t) = 0$ in Eq. (3) for an unchirped pulse. We note in passing that also other pulse shapes are possible as a starting point for the generation of chirped pulses. In particular, secant hyperbolic pulses may have advantages in certain circumstances [51].

Passing the initial pulse in Eq. (9) through a Gaussian chirp filter [52] yields a chirped pulse with envelope and phase:

$$f_{\mathrm{chirp}}(t) = \frac{\Theta_{\mathrm{chirp}}}{\sqrt{2\pi}\sigma_{\mathrm{chirp}}} e^{-\frac{(t-t_0)^2}{2\sigma_{\mathrm{chirp}}^2}}, \tag{11}$$

$$\varphi(t) = a\,(t-t_0)^2/2, \tag{12}$$

pulse area $\Theta_{\mathrm{chirp}} = \Theta\sqrt{\sigma_{\mathrm{chirp}}/\sigma}$ and duration $\sigma_{\mathrm{chirp}} = \sqrt{(\alpha^2/\sigma^2) + \sigma^2}$. The phase in Eq. (3) has acquired a quadratic time dependence, which corresponds to an instantaneous laser frequency $\omega_{\mathrm{L}} + \dot{\varphi} = \omega_{\mathrm{L}} + a\,(t - t_0)$ that changes linearly in time and for $\omega_{\mathrm{L}} = \omega_{\mathrm{X}}$ crosses the exciton resonance at the pulse maximum $t = t_0$. The strength of the chirp is commonly expressed in terms of the chirp parameter α which is related to the coefficient a in Eq. (12) by $a = \alpha/(\alpha^2 + \sigma^4)$. Note that the pulse area and in particular the pulse length increases drastically when chirps are introduced (cf. the definition of σ_{chirp}).

III. NUMERICAL RESULTS ON TRANSIENT PHOTON STATISTICS

For the numerical calculations, we assume a QD with 6-nm diameter and standard GaAs parameters [28,41]. The cavity is coupled to the QD exciton with a strength of $\hbar g = 0.1\,\mathrm{meV}$ while it is on resonance, i.e., $\Delta\omega_{\mathrm{CX}} := \omega_{\mathrm{C}} - \omega_{\mathrm{X}} = 0$. The cavity losses are taken to be $\hbar\kappa = 6.6\,\mu\mathrm{eV}$, which corresponds to a quality factor $\approx 10^5$ assuming a mode frequency of $\hbar\omega_{\mathrm{C}} = 1.5\,\mathrm{eV}$. The radiative decay rate of the QD exciton is set to $\hbar\gamma = 2\,\mu\mathrm{eV}$.

A. The chirp-free situation

Let us first concentrate on the chirp-free case. Figures 1(a) and 1(c) display photon number distributions at different times for a QDC driven by an unchirped Gaussian pulse with a pulse area of 5π and a duration of 2.4 ps FWHM. Figure 1(a) shows results without phonons while in Fig. 1(c) the corresponding simulations with phonons are depicted assuming the phonons before the pulse to be in thermal equilibrium at a temperature of $\mathrm{T} = 4\,\mathrm{K}$. The initial state for the cavity photons is taken to be the vacuum, i.e., the $n = 0$ Fock state and the QD is initially in the ground state.

As expected the photons stay in the vacuum state until the arrival of the pulse. At the end of the 5π pulse (cf. black markers in Fig. 1) the QD is in the exciton state and the resonant coupling to the cavity initiates vacuum Rabi oscillations [53–57], i.e., oscillations between the $|X, n = 0\rangle$ and the $|G, n = 1\rangle$ states. This is reflected in the photon distribution as oscillations between the $n = 0$ and $n = 1$ Fock states and results in damped oscillations of the mean photon number

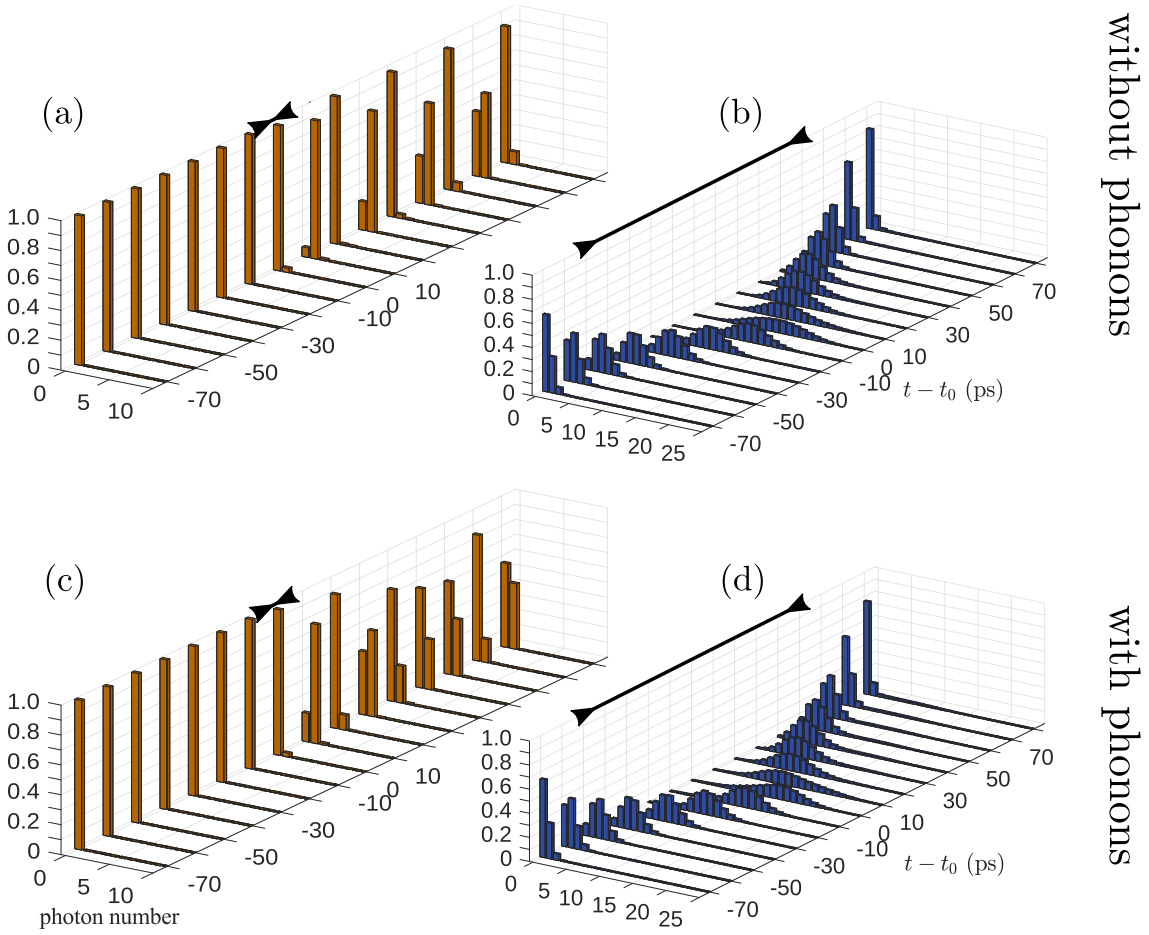

FIG. 1. Transient photon number distributions for laser excitations with unchirped pulses with (a) and (c) pulse area $\Theta = 5\pi$ and duration FWHM=2.4 ps, (b) and (d) pulse area $\Theta = 31.63\pi$ and duration FWHM $= 94.22$ ps. Panels (c) and (d) display results accounting for phonons that are initially at equilibrium at a temperature of $T = 4$ K while the corresponding phonon-free results are shown in (a) and (b). The pulse has its maximum at $t = t_0$. Black markers indicate the FWHM of the pulse.

between zero and and a maximal amplitude that due to losses and phonon effects is below one [cf. orange curve in Fig. 3(a)]. Quantitatively, a small occupation of the two-photon state $|2\rangle$ is observed, seen, e.g., for $t - t_0 = 10$ ps in Figs. 1(a) and 1(c). The reason lies in the re-excitation of the QD during the same pulse, whereby effectively two photons can be put into the single cavity mode.

The phonon impact on Rabi-type oscillations in a two-level system has been extensively studied [29,44–47,58–64] and shall therefore not be analyzed here in detail. We just note that the main effects are a phonon-induced damping, which depends on the driving strength, and a renormalization of the Rabi frequency. The renormalization of g is reflected in Figs. 1(a) and 1(c) by slightly different oscillation frequencies. The damping seen in the orange curve in Fig. 3(a) is the result of the combined effects of phonons, cavity losses, and radiative decay.

For a fair comparison between unchirped and chirped pulses, recall that the application of a Gaussian chirp filter involves besides the time-dependent variation of the phase $\varphi(t)$ in Eq. (12) also a considerable increase of the pulse duration and of the pulse area. Therefore, we show in Figs. 1(b) and 1(d) the photon distribution with and without the influence of phonons for a pulse with pulse area $\Theta = 31.63\pi$ and duration FWHM $= 94.22$ ps, which corresponds to the application of a filter with an effective value of $|\alpha| = 40$ ps^2 in Eq. (11) but keeping the phase $\varphi(t) = 0$ constant. Most strikingly, with this driving there are no traces of vacuum Rabi oscillations visible. Instead, a wave-packet-type dynamics sets in, where a bell-shaped distribution is found for all times. The mean photon number rises monotonically in time to values $n \approx 12$ [note that the blue curve in Fig. 3(a) is scaled down by a factor of 5 for better visibility] and subsequently falls back to zero after the pulse has vanished.

B. Finite chirps

Figure 2 displays transient photon number distributions obtained for chirped pulses that are generated by passing the Gaussian pulse used in Figs. 1(a) and 1(c) through a chirp filter with $\alpha = \pm 40$ ps^2 [(a) and (c) $\alpha = -40$ ps^2, (b) and (d) $\alpha = +40$ ps^2]. The upper panels correspond to simulations without phonons while for the lower panels the interaction with phonons has been included. Note that the pulses used in Fig. 2 have the same pulse area and duration as the unchirped pulses used in Figs. 1(b) and 1(d) which allows us to compare excitation conditions where the only difference is the frequency modulation.

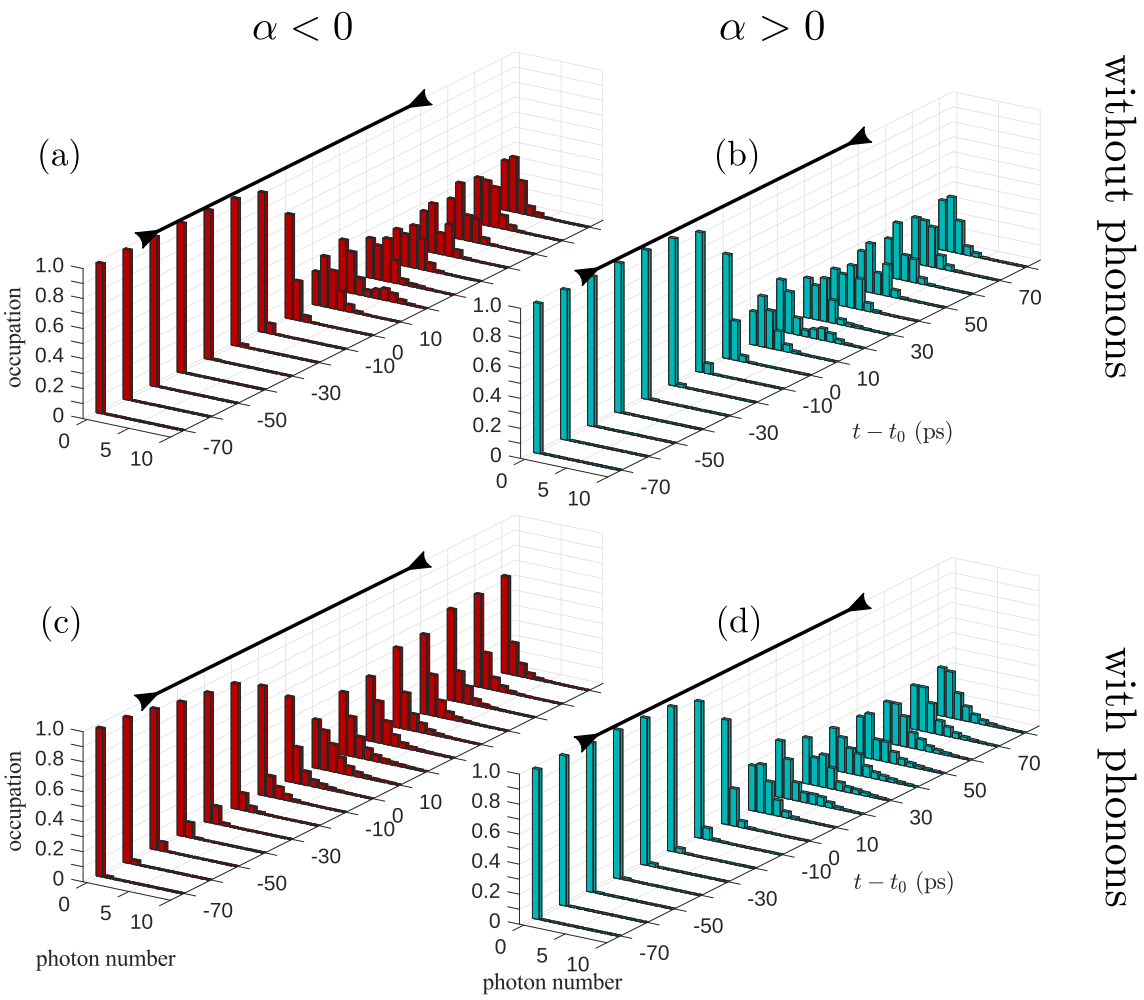

FIG. 2. Transient photon number distributions for laser excitations with chirped pulses with pulse area and FWHM before the chirp filter of $\Theta = 5\pi$ and FWHM=2.4 ps, i.e., $\Theta_{\text{chirp}} = 31.63\pi$ and duration $\text{FWHM}_{\text{chirp}} = 94.22$ ps for $|\alpha| = 40$ ps^2. (a) and (c) Calculated with chirp parameter $\alpha = -40$ ps^2, (b) and (d) $\alpha = +40$ ps^2. (c) and (d) Displayed are results accounting for phonons that are initially at equilibrium at a temperature of $T = 4$ K while the corresponding phonon-free results are shown in (a) and (b). The pulse has its maximum at $t = t_0$. Black markers indicate the FWHM of the pulse after the chirp filter.

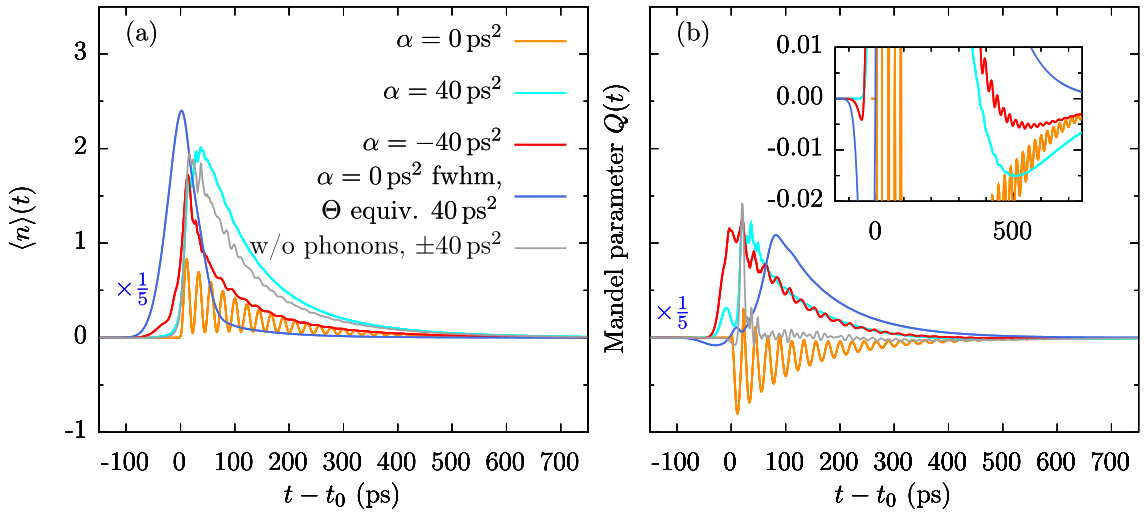

FIG. 3. The time-dependent (a) mean photon number and (b) Mandel parameter $Q(t) = (\langle \Delta n^2 \rangle - \langle n \rangle)/\langle n \rangle$ for the cases indicated by the labels. All curves are calculated with phonons initially at $T = 4$ K, except for the gray curves which correspond to the phonon-free case. The blue curve is scaled down by a factor of 5 for better visibility. The inset in (b) corresponds to a zoomed-in scale.

In the phonon-free case identical distributions are obtained for positive and negative chirp [cf. Figs. 2(a) and 2(b)]. This symmetry is removed when phonons are taken into account [cf. Figs. 2(c) and 2(d)]. In contrast to the unchirped case with the same pulse area and duration in Figs. 1(b) and 1(d), the photon number is close to zero until the pulse maximum is reached, which can be explained by noting that for chirped pulses the instantaneous laser frequency is strongly detuned from the QD resonance for times away from the pulse maximum. The most striking difference compared with Figs. 1(b) and 1(d) is, however, that the photon distributions in Fig. 2 significantly change their shape in time. The distributions found in the phonon free case have at early times after the pulse maximum a bell shape with a single maximum and transform into a bimodal distribution with two well-separated bell-shaped contributions at later times [cf. $t - t_0 = 20\,\mathrm{ps}$ in Fig. 2(a)]. Subsequently, at times $t - t_0 \approx 30-50\,\mathrm{ps}$ the distribution still has two peaks but looks rather jagged having little resemblance with bell-shaped distributions. Eventually, at later times only a single maximum is found which appears at a finite photon number or at zero, depending on time.

Phonons change the situation qualitatively for negative chirp [cf. Fig. 2(c)], where now the photon number distribution has a single maximum at $n = 0$ for all times. The shape of the transient distribution resembles thermal photon occupations, which due to mean photon numbers around $n = 2$ [cf. Fig. 3(a)] corresponds to an effective temperature above $T_{\mathrm{eff}} \approx 40\,000$ K for photon energies $\hbar\omega_{\mathrm{C}} \approx 1.5$ eV. A similar impact of phonons on the photon number distribution has been reported previously for the stationary distribution found at long times for permanent driving [28]. The phonon impact for positive chirp is less dramatic [cf. Fig. 2(d)]. As in the phonon-free case, there are still times where the distribution is bi-modal while at other times only a single maximum is found. Overall, the irregular looking shape appearing at certain times in Figs. 2(a) and 2(b) is smoothened. Moreover, there is a tendency to build up a maximum near $n = 0$.

Further differences between the number distributions in Figs. 1 and 2 are revealed by looking at the time evolution of the corresponding Mandel parameters $Q(t)$ in Fig. 3(b). For a Fock state the number fluctuation disappears, leading to a negative Mandel parameter, except for the $n = 0$ Fock state, where the Mandel parameter approaches an expression of the form zero divided by zero. We see from the orange curves in Fig. 3 that for weakly driven unchirped pulses the damped oscillation of the mean photon number between 0 and at most 1 is accompanied by damped oscillations of the Mandel parameter ranging down to almost -1 and up to essentially 0. The negative values of the minima correspond to times where the system is close to the $n = 1$ Fock state. If the dynamics would exclusively involve states with photon numbers 0 or 1 such that only P_0 and P_1 are different from zero, it is easy to show that for all times, where $P_1 \neq 0$, the Mandel parameter is $Q(t) = -\langle n \rangle$. Therefore, Q should approach 0 when the $n = 0$ Fock state is approached. We see, however, from the orange curve in Fig. 3(b) that the first maxima of the Mandel parameter Q are a bit above 0, indicating small admixtures of higher number states.

For higher pulse areas Q is positive for most of the time for chirped as well as for unchirped pulses. Interestingly, although the bell-shaped distributions in Figs. 1(b) and 1(d) at first glance resemble much more Poissonian distributions than the somehow irregular ones found for chirped pulses in Figs. 2(b) and 2(d) their deviation from a Poissonian as measured by the Mandel parameter is much larger than for chirped pulses [note that the blue curve in Fig. 3(b) is scaled down by a factor of 5]. But most remarkably, in the calculation with finite chirp without phonons [cf. the gray line in Fig. 3(b)] the Mandel parameter decays extremely fast after its initial rise to positive values compared with the other situations considered. Most notably, already at around $\sim$40 ps after the pulse maximum it has dropped close to zero. In sharp contrast to the common interpretation that a Mandel parameter near zero implies a distribution with a shape close to a Poissonian, Fig. 2(b) shows a jagged distribution with two maxima at $\sim$40 ps after the pulse maximum. Therefore, using the Mandel parameter as a measure for the deviation from a Poisonian is not valid in all physically relevant situations.

We further note that the Mandel parameter calculated for all excitation conditions studied in this paper changes its sign during the course of time. Without chirp and low intensities (orange curve) this happens near the first maxima of the Q oscillations, as discussed above, but also for higher driving strength (blue curve) a sign change occurs indicating that before the pulse maximum is reached the photon distribution is sub-Poissonian and switches at the pulse maximum to super-Poissonian. Also for the chirped excitations Q exhibits sign changes as revealed by the inset in Fig. 3(b). Actually, the Mandel parameter calculated for high pulse areas falls below zero before approaching its asymptotic value of zero from below for chirped as well as for unchirped excitations. Indeed, also the blue curve in Fig. 3(b) falls below zero at $t - t_0 = 1090\,\mathrm{ps}$ (not seen in the plotted range). This sign change of Q shortly before cavity losses have relaxed the photon distribution to the empty cavity, can be understood as follows. The maximal photon numbers that are transiently reached for high pulse areas are well above one. The cavity losses remove photons from the cavity such that eventually the limit of $n = 0$ with zero fluctuations is reached. However, since the cavity losses for a state with n photons scale like $\sim n$, the relaxation from states with $n > 1$ to lower states is faster than the final relaxation from the $n = 1$ to the $n = 0$ states. Therefore, before the final relaxation is completed the photons preferably occupy the $n = 1$ state which results in a negative Mandel parameter before the asymptotic value of zero is reached. Note that this effect presumes only $\kappa \neq 0$ and thus should be robust with respect to variations of this parameter.

Finally, we note that Q exhibits small amplitude oscillations for chirped pulses which are absent in the unchirped case. A similar but less pronounced tendency is seen in the mean photon number.

C. Interpretation in terms of laser-dressed states

A popular application of driving QDs with chirped laser pulses is the robust preparation of exciton or biexciton states by invoking an adiabatic rapid passage (ARP) process [65–75]. ARP exploits the adiabatic theorem of quantum mechanics which predicts a time evolution through instantaneous

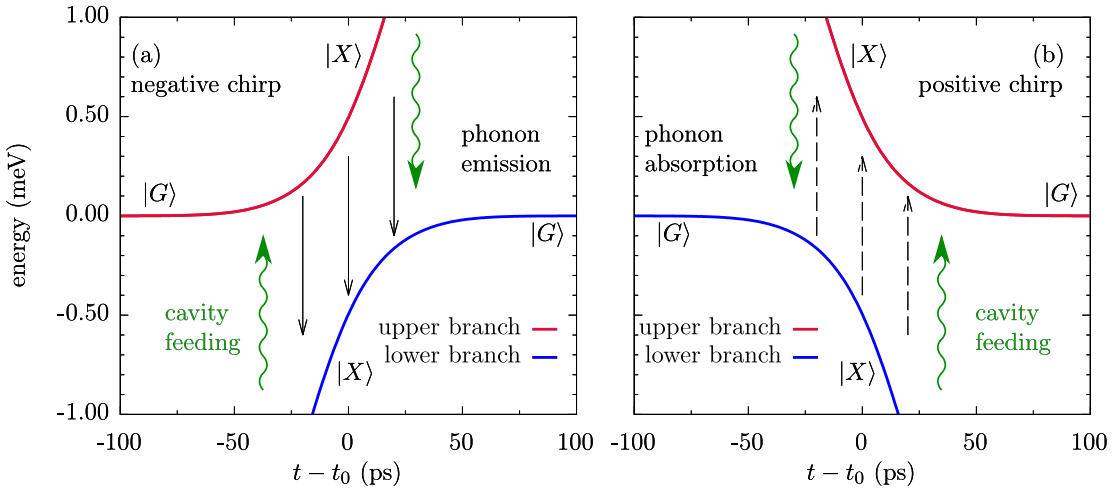

FIG. 4. Time evolution of the upper and lower laser-dressed state energies with respect to the excitation pulse maximum at $t = t_0$. While for negative chirps (a) phonon emission is probable (represented by black arrows), for positive chirps (b) phonon absorption is suppressed at low temperatures, which is indicated by the dashed arrows. Green curly arrows indicate transitions between laser-dressed states due to the QD cavity feeding.

eigenstates (dressed states) of the system provided the external driving fulfills the restrictions of the adiabatic regime [76]. In order to comply with these restrictions for a two-level system driven by Gaussian chirped pulses with a frequency modulation given by Eq. (12), it is advisable to transform the QD-laser Hamiltonian H_{DL} in Eq. (13) to a frame co-rotating with the phase φ to get rid of a possibly rapidly changing coupling. The transformed Hamiltonian reads

$$\begin{aligned}\widetilde{H}_{\mathrm{DL}} =& -\hbar(\Delta\omega_{\mathrm{LX}} + a\,(t - t_0))|X\rangle\langle X| \\ & - \frac{\hbar}{2} f(t)(|X\rangle\langle G| + |G\rangle\langle X|). \end{aligned} \tag{13}$$

The laser-dressed states can now be defined as the instantaneous eigenstates of $\widetilde{H}_{\mathrm{DL}}$. The corresponding eigenenergies are plotted in Fig. 4, where the left panel corresponds to a negative chirp while the result for positive chirp is shown in the right panel. The distinctive feature of ARP is that when the system is in the ground state $|G\rangle$ long before the pulse (i.e., for $t \to -\infty$) it will evolve adiabatically towards the exciton state $|X\rangle$ after the pulse (i.e., for $t \to +\infty$) independent of the sign of the chirp. However, it is important to note that the evolution proceeds along the lower (upper) branch for positive (negative) chirp. This affects in particular the impact of phonons. In general phonons can efficiently induce transitions between the two branches. However, at low temperatures phonon absorption is strongly suppressed and phonon emission can invoke only transitions from the upper to the lower branch (cf. the black arrows in Fig. 4). That is why phonons have little effects on the ARP dynamics for positive chirp while for negative chirp the ARP-based exciton preparation is strongly disturbed [68,70,73,74]. In order to preserve an efficient exciton preparation also at negative chirps, it has been recently demonstrated that high pulse areas can be used since this effectively decouples the phonons from the electronic system [29,75].

When also a cavity is coupled to the QD, then the coupling leads to Rabi-type rotations between states $|X, n\rangle$ and $|G, n+1\rangle$ with different numbers n of cavity photons. In particular for times when the laser is far off-resonant and the laser-dressed states are close to the undressed states, the effect of coupling the QD to a cavity can be understood as inducing a transition between the dressed states similar to the coupling to phonons. To be a bit more specific, when the system is in the exciton state the QD-cavity coupling leads to a feeding of the cavity by an additional photon accompanied by a transition from the $|X\rangle$-like branch to the $|G\rangle$-like branch (cf. the green curly arrows in Fig. 4). At early times, the reverse process, where one photon disappears from the cavity while transferring the system from the ground to the exciton state is suppressed since there are initially no photons in the cavity.

We shall now try to interpret the pertinent features of the photon dynamics in some more detail using the simplified picture where the system evolves adiabatically through the laser-dressed states in Fig. 4 while phonons and cavity feeding induce transitions between these states.

In the case of a negative chirp [cf. Fig. 4(a)] transitions form the upper branch to the lower branch of the laser-dressed states accompanied by phonon emission are possible before and after the pulse maximum at $t = t_0$. Thus, phonons should have a profound impact on the resulting photon statistics during the entire pulse. In fact, this explains why the distribution is close to a thermal one at all times [cf. Fig. 2(c)]. For times before the pulse reaches its maximum, cavity feeding can occur form the excitonlike lower branch to the upper branch, which has a large ground-state contribution. Subsequently, the system can again decay to the lower branch by phonon emission followed by another cavity feeding process back into the upper branch and so on. Because of this constructive interplay between phonon and cavity feeding processes, higher photon states can be reached compared with the phonon-free situation for $t \leqslant t_0$ [cf. Figs. 2(a) and 2(c)]. In the time interval shortly after the pulse maximum the upper branch becomes the state with the excitonlike characteristics and cavity feeding now takes place from the upper branch into the ground-state-like lower branch of the laser-dressed states. Thus, after the pulse

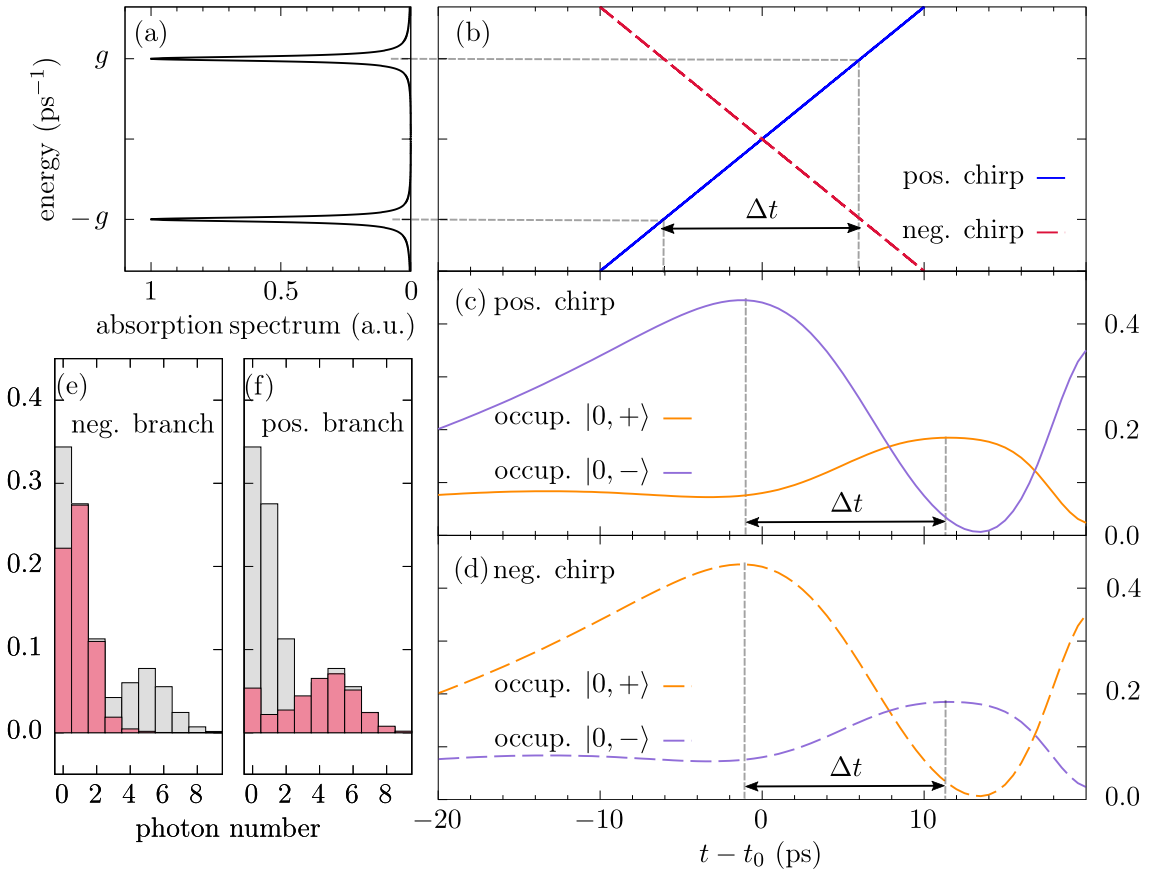

FIG. 5. (a) Linear absorption spectrum of the QDC system. (b) Time-dependent instantaneous frequency, blue (red) for positive (negative) chirp. Δt marks the time elapsed between the crossing of the two resonances. (c) and (d) Time evolution of the occupations of the lowest excited eigenstates of the QDC system [(c) for positive and (d) for negative chirp]. (e) and (f) Photon number distribution at $t - t_0 = 20\,\mathrm{ps}$ (gray); red, accounting only for $|n,+\rangle$ (e) or $|n,-\rangle$ (f) states. Here, only phonon-free results are shown.

maximum has appeared phonon and cavity feeding processes are now in direct competition with each other. Therefore, compared with the phonon-free situation, the mean photon number should be reduced. Altogether, for negative chirp, the phonon impact on the photon distributions is visible at all times leading to nearly thermal distributions. At times before the pulse maximum the interaction with phonons increases the mean photon number because of a constructive interplay between phonon and cavity feeding processes. This effect is reversed after the pulse maximum and the mean photon number is reduced compared with the phonon-free situation due to the phonon interaction, as can be seen comparing the red with the gray curve in Fig. 3(a).

The situation is different when the chirp is positive as seen in Figs. 2(b) and 2(d). Here, a phonon influence on the photon statistics can be hardly seen before the pulse maximum. This can again be explained by inspection of the branches of the laser-dressed states. Starting in the ground state the system evolves adiabatically alongside the lower branch. Since phonon absorption processes are suppressed at low temperatures, transitions to the excitonlike upper state are unlikely to occur. Also cavity feeding is hardly possible [cf. Fig. 4(b)] and, like in the phonon-free situation, the system remains essentially in the ground state without photons and phonons have almost no visible effect. This observation changes after the pulse maximum. Now, cavity feeding processes accompanied by transitions from the excitonlike lower branch to the upper branch appear. Subsequently, phonon emission processes take place, resulting in a transition back to the lower branch. Thus, now, a constructive interplay between phonon emission and cavity feeding is possible, leading to a thermalization of the photon distribution. Therefore, after a transition time of a few 10 ps the distribution resembles a thermal distribution. Because of the constructive interplay the mean photon number is increased compared with the phonon-free situation, as can be seen comparing the cyan with the gray curve in Fig. 3(a). Consequently, only for a finite time interval after the pulse maximum photon distributions can be detected which are similar to the distributions in the phonon-free situation and display irregular behavior or several maxima.

D. Interpretation in terms of cavity-dressed states

Finally, we would like to explain why chirped pulse excitation leads to photon number distributions where the number of maxima changes dynamically from one to two and back to one. To this end we have to go beyond the laser-dressed state picture and recall that the linear absorption of a QDC comprises two lines split by $\Delta\omega = 2g$ [cf. Fig. 5(a)]. Thus, the instantaneous frequency of a pulse with positive chirp first crosses the energetically lower resonance and then, delayed

by a time $\Delta t = 2g/a$, the higher one [cf. Fig. 5(b)]. Each crossing of these resonances initiates a wave packet climbing up the Jaynes-Cummings ladder. This behavior is efficiently described in the picture of the cavity-dressed states, i.e., the eigenstates of the dot-cavity Hamiltonian, which relate to the bare QD states by

$$|n,+\rangle = \frac{1}{\sqrt{2}}(+|X,n\rangle + |G,n+1\rangle),$$
$$|n,-\rangle = \frac{1}{\sqrt{2}}(-|X,n\rangle + |G,n+1\rangle), \tag{14}$$

in the case of a resonant cavity mode $\omega_X - \omega_C = 0$.

Starting from the state $|G,0\rangle$ only the two states $|0,\pm\rangle$ can be reached directly by the laser coupling and thus climbing up the Jaynes cummings ladder one has to pass these states. Since the corresponding eigenenergies are separated by $2g$, the transitions to these states are in resonance with the instantaneous frequency of a chirped pulse at different times. Indeed, Fig. 5(c) reveals that the occupation of the lowest excited eigenstate of the QDC system $|0,-\rangle$ rises before the upper state $|0,+\rangle$ acquires a noticeable occupation. The maximum occupation of $|0,-\rangle$ is reached ≈ 5 ps after the instantaneous frequency has crossed the lower resonance, revealing the reaction time of the system. $|0,+\rangle$ is maximally occupied delayed exactly by Δt from the maximal occupation of $|0,-\rangle$. The time ordering of the excitation of the $|0,\pm\rangle$ states is reversed when reversing the sign of the chirp [cf. Fig. 5(d)] since now the upper resonance is crossed first.

The laser driving couples $|n,+\rangle$ to $|n,-\rangle$ states. However, when the instantaneous frequency is in resonance with transitions between $|n,+\rangle$ states with adjacent n then the transitions to $|n,-\rangle$ states are off-resonant and vice versa. Thus, it can be expected that the packets running up the Jaynes-Cummings ladder are essentially composed either of $|n,+\rangle$ or $|n,-\rangle$ states. Indeed, this is confirmed by Figs. 5(e) and 5(f) which displays in gray the photon number distribution at time $t - t_0 = 20$ ps, i.e., the time where according to Fig. 2(b) the two maxima are most pronounced. Also shown in red are photon number distributions calculated according to

$$P_n^{(\pm)} = \begin{cases} \frac{1}{2}\left(\langle n,\pm|\rho|n,\pm\rangle + \langle n-1,\pm|\rho|n-1,\pm\rangle\right) \\ \quad \text{for } n > 0, \\ \frac{1}{2}\left(\langle 0,\pm|\rho|0,\pm\rangle + \langle G,0|\rho|G,0\rangle\right) \\ \quad \text{for } n = 0 \end{cases}. \tag{15}$$

Recalling that for a cavity in resonance with the QD transition the $|n,\pm\rangle$ states have a probability of $1/2$ for finding n or $n+1$ photons, Eq. (15) yields, for $n > 0$, the probability for having n photons when accounting only for either the $|n,+\rangle$ or the $|n,-\rangle$ states. For $n = 0$ the contribution from $|G,0\rangle$ is counted by $1/2$ for the plus and minus branch, since this state can be counted as lower or upper state. We note in passing that $P_n^{(-)}$ [red bars in Fig. 5(e)] does not add up with $P_n^{(+)}$ [red bars in Fig. 5(f)] to the total photon number P_n (gray bars in Fig. 5), because P_n comprises coherences between the $|n,+\rangle$ and the $|n,-\rangle$ states in addition to their occupations. Nevertheless, Fig. 5 reveals that the two peaks in the photon number distribution can be attributed unambiguously either to the upper or lower branch of the QDC states.

Altogether this explains the time evolution of the peaks in the photon number distribution. After crossing the first resonance the distribution has a single peak since at first only a single packet is climbing up the Jaynes-Cumming ladder. When the second resonance is crossed a second packet is initiated such that at $t - t_0 \approx 20$ ps two well-resolved packets are observed. Both packets move up and down the Jaynes-Cummings ladder similar to the single wave packet observed for the unchirped excitation in Figs. 1(b) and 1(d). Since the decline of the first packet starts while the second is still rising, at some time both packets overlap. Although the packets are no longer well resolved, two maxima are still found over an extended time period [$30\text{ ps} \lesssim t - t_0 \lesssim 50$ ps in Fig. 2(b)]. At later times the relaxation drives both packets to low photon numbers such that the maxima merge and a single-peaked distribution is recovered.

Finally, we note that for a cavity in resonance with the QD transition the energies of the QDC eigenstates $|n,\pm\rangle$ are found in the rotating frame at $\hbar\omega_{n,\pm} = \pm g\sqrt{n+1}$ such that the transition energies between states with adjacent n are all different and decrease with rising n. Therefore, the instantaneous frequency of a chirped pulse crosses all of these resonances at different times which is likely to contribute to the somewhat irregular looking time evolution of the photon number distribution found in particular in the intermediate time interval $30\text{ ps} \lesssim t - t_0 \lesssim 50$ ps in Fig. 2(b).

IV. CONCLUSION

We have studied transient photon number distributions generated in a microcavity by a pulsed excitation of an embedded quantum dot. We find qualitatively different photon distributions for chirped and unchirped pulses. Phonons have a noticeable influence on the photon distributions in particular for negative chirps, where the phonon coupling introduces qualitative changes of the shape of the distribution already at a temperature of $T = 4$ K. To be more specific, phonons lead in this case to almost thermalized photon distributions at high effective temperatures for all times. For positive chirp, the transient distributions are far away from a thermal one for times after the pulse maximum until about 80 ps afterwards.

For all investigated cases, we find that the Mandel parameter changes its sign during the time evolution of the system, indicating the ability to enter and leave a regime of genuine nonclassical photon statistics in the course of time. Moreover, cases were encountered where the Mandel parameter is zero, but the photon number distribution has two peaks and is definitely not a Poissonian. Therefore, one has to be careful when using the Mandel parameter as a measure for the deviation from a Poissonian distribution, as it is often done [24,77–80]. This finding underlines the necessity to carefully consider the definition of the Mandel parameter, which indeed yields zero for a Poissonian distribution. But the reverse implication is obviously not true for all cases.

Our most striking result is, however, that the shape of the photon number distribution changes significantly during the time evolution when the system is excited by chirped pulses. In fact, when the excitation starts to populate states with higher photon numbers, one observes at first bell-shaped distributions with a single maximum that increases in time.

Subsequently, two well-separated bell-shaped contributions develop which at later times first evolve into a single broad feature with two peaks and eventually merge into a distribution with a single peak. This is in sharp contrast to the unchirped case, where for the same high driving strengths the photon number distributions keep a bell shape with a single maximum for all times. Our analysis reveals that the transient changes of the shape of the photon distribution in the chirped case can be attributed to subsequent crossings of resonances of the quantum-dot–cavity system by the instantaneous frequency.

We believe that our findings deepen the understanding of the transient behavior of photon distributions in a driven quantum-dot–cavity system and its dependence on the driving conditions. This might pave the way to targeted manipulations of photon distributions which could result in new types of photonic applications in the future.

ACKNOWLEDGMENTS

M.Cy. thanks the Alexander-von-Humboldt foundation for support through a Feodor Lynen fellowship. A.V. acknowledges the support from the Russian Science Foundation under Project No. 18-12-00429 which was used to study dynamical processes nonlocal in time by the path-integral approach. This work was also funded by the Deutsche Forschungsgemeinschaft (DFG, German Research Foundation) Project No. 419036043.

[1] P. Michler, A. Kiraz, C. Becher, W. V. Schoenfeld, P. M. Petroff, L. Zhang, E. Hu, and A. Imamoglu, Science **290**, 2282 (2000).
[2] C. Santori, M. Pelton, G. Solomon, Y. Dale, and Y. Yamamoto, Phys. Rev. Lett. **86**, 1502 (2001).
[3] C. Santori, D. Fattal, J. Vuckovic, G. S. Solomon, and Y. Yamamoto, Nature (London) **419**, 594 (2002).
[4] Y.-M. He, Y. He, Y.-J. Wei, D. Wu, M. Atatüre, C. Schneider, S. Höfling, M. Kamp, C.-Y. Lu, and J.-W. Pan, Nat. Nanotechnol. **8**, 213 (2013).
[5] Y.-J. Wei, Y.-M. He, M.-C. Chen, Y.-N. Hu, Y. He, D. Wu, C. Schneider, M. Kamp, S. Höfling, C.-Y. Lu, and J.-W. Pan, Nano Lett. **14**, 6515 (2014).
[6] X. Ding, Y. He, Z.-C. Duan, N. Gregersen, M.-C. Chen, S. Unsleber, S. Maier, C. Schneider, M. Kamp, S. Höfling, C.-Y. Lu, and J.-W. Pan, Phys. Rev. Lett. **116**, 020401 (2016).
[7] N. Somaschi, V. Giesz, L. De Santis, J. C. Loredo, M. P. Almeida, G. Hornecker, S. L. Portalupi, T. Grange, C. Antón, J. Demory, C. Gómez, I. Sagnes, N. D. Lanzillotti-Kimura, A. Lemaítre, A. Auffeves, A. G. White, L. Lanco, and P. Senellart, Nat. Photonics **10**, 340 (2016).
[8] L. Schweickert, K. D. Jöns, K. D. Zeuner, S. F. Covre da Silva, H. Huang, T. Lettner, M. Reindl, J. Zichi, R. Trotta, A. Rastelli, and V. Zwiller, Appl. Phys. Lett. **112**, 093106 (2018).
[9] L. Hanschke, K. A. Fischer, S. Appel, D. Lukin, J. Wierzbowski, S. Sun, R. Trivedi, J. Vučković, J. J. Finley, and K. Müller, npj Quantum Inf. **4** (2018).
[10] M. Cosacchi, F. Ungar, M. Cygorek, A. Vagov, and V. M. Axt, Phys. Rev. Lett. **123**, 017403 (2019).
[11] N. Akopian, N. H. Lindner, E. Poem, Y. Berlatzky, J. Avron, D. Gershoni, B. D. Gerardot, and P. M. Petroff, Phys. Rev. Lett. **96**, 130501 (2006).
[12] R. M. Stevenson, R. J. Young, P. Atkinson, K. Cooper, D. A. Ritchie, and A. J. Shields, Nature (London) **439**, 179 (2006).
[13] R. Hafenbrak, S. M. Ulrich, P. Michler, L. Wang, A. Rastelli, and O. G. Schmidt, New J. Phys. **9**, 315 (2007).
[14] A. Dousse, J. Suffczynski, A. Beveratos, O. Krebs, A. Lemaître, I. Sagnes, J. Bloch, P. Voisin, and P. Senellart, Nature (London) **466**, 217 (2010).
[15] E. del Valle, New J. Phys. **15**, 025019 (2013).
[16] M. Müller, S. Bounouar, K. D. Jöns, M. Glässl, and P. Michler, Nat. Photonics **8**, 224 (2014).
[17] A. Orieux, M. A. M. Versteegh, K. D. Jöns, and S. Ducci, Rep. Prog. Phys. **80**, 076001 (2017).
[18] T. Seidelmann, F. Ungar, A. M. Barth, A. Vagov, V. M. Axt, M. Cygorek, and T. Kuhn, Phys. Rev. Lett. **123**, 137401 (2019).
[19] Y. T. Chough and H. J. Carmichael, Phys. Rev. A **54**, 1709 (1996).
[20] L. Mandel, Opt. Lett. **4**, 205 (1979).
[21] C. Gerry and P. L. Knight, *Introductory Quantum Optics* (Cambridge University Press, Cambridge, 2004).
[22] Note that fields produced by lasers in real experiments usually have some degree of amplitude noise. Therefore, the photon number distribution is always a bit wider than the Poissonian one.
[23] W. Vogel and D.-G. Welsch, *Quantum Optics* (Wiley-VCH, Weinheim, 2006).
[24] T. Quang and H. Freedhoff, Phys. Rev. A **47**, 2285 (1993).
[25] G. Callsen, A. Carmele, G. Hönig, C. Kindel, J. Brunnmeier, M. R. Wagner, E. Stock, J. S. Reparaz, A. Schliwa, S. Reitzenstein, A. Knorr, A. Hoffmann, S. Kako, and Y. Arakawa, Phys. Rev. B **87**, 245314 (2013).
[26] Although the experiments in Ref. [25] have been performed on QDs without cavity, the number of modes in the theoretical modeling was restricted to two which corresponds to the situation in a QDC. Therefore, the results should also apply to QDCs.
[27] M. Bagheri Harouni, R. Roknizadeh, and M. H. Naderi, Phys. Rev. B **79**, 165304 (2009).
[28] M. Cygorek, A. M. Barth, F. Ungar, A. Vagov, and V. M. Axt, Phys. Rev. B **96**, 201201(R) (2017).
[29] D. E. Reiter, T. Kuhn, and V. M. Axt, Adv. Phys.: X **4**, 1655478 (2019).
[30] A. I. Lvovsky and M. G. Raymer, Rev. Mod. Phys. **81**, 299 (2009).
[31] E. Schlottmann, M. von Helversen, H. A. M. Leymann, T. Lettau, F. Krüger, M. Schmidt, C. Schneider, M. Kamp, S. Höfling, J. Beyer, J. Wiersig, and S. Reitzenstein, Phys. Rev. Appl. **9**, 064030 (2018).
[32] M. Schmidt, M. von Helversen, M. López, F. Gericke, E. Schlottmann, T. Heindel, S. Kück, S. Reitzenstein, and J. Beyer, J. Low Temp. Phys. **193**, 1243 (2018).
[33] M. v. Helversen, J. Böhm, M. Schmidt, M. Gschrey, J.-H. Schulze, A. Strittmatter, S. Rodt, J. Beyer, T. Heindel, and S. Reitzenstein, New J. Phys. **21**, 035007 (2019).
[34] M. Klaas, E. Schlottmann, H. Flayac, F. Laussy, F. Gericke, M. Schmidt, M. Helversen, J. Beyer, S. Brodbeck, H. Suchomel,

S. Höfling, S. Reitzenstein, and C. Schneider, Phys. Rev. Lett. **121**, 047401 (2018).
[35] J. Hloušek, M. Dudka, I. Straka, and M. Ježek, Phys. Rev. Lett. **123**, 153604 (2019).
[36] L. Besombes, K. Kheng, L. Marsal, and H. Mariette, Phys. Rev. B **63**, 155307 (2001).
[37] P. Borri, W. Langbein, S. Schneider, U. Woggon, R. L. Sellin, D. Ouyang, and D. Bimberg, Phys. Rev. Lett. **87**, 157401 (2001).
[38] B. Krummheuer, V. M. Axt, and T. Kuhn, Phys. Rev. B **65**, 195313 (2002).
[39] V. M. Axt, T. Kuhn, A. Vagov, and F. M. Peeters, Phys. Rev. B **72**, 125309 (2005).
[40] I. A. Ostapenko, G. Hönig, S. Rodt, A. Schliwa, A. Hoffmann, D. Bimberg, M. R. Dachner, M. Richter, A. Knorr, S. Kako, Y. Arakawa, Phys. Rev. B **85**, 081303(R) (2012).
[41] B. Krummheuer, V. M. Axt, T. Kuhn, I. D'Amico, and F. Rossi, Phys. Rev. B **71**, 235329 (2005).
[42] A. Vagov, V. M. Axt, T. Kuhn, W. Langbein, P. Borri, and U. Woggon, Phys. Rev. B **70**, 201305(R) (2004).
[43] D. E. Reiter, Phys. Rev. B **95**, 125308 (2017).
[44] J. Förstner, C. Weber, J. Danckwerts, and A. Knorr, Phys. Rev. Lett. **91**, 127401 (2003).
[45] A. Krügel, V. M. Axt, T. Kuhn, P. Machnikowski, and A. Vagov, Appl. Phys. B **81**, 897 (2005).
[46] A. Vagov, M. D. Croitoru, V. M. Axt, T. Kuhn, and F. M. Peeters, Phys. Rev. Lett. **98**, 227403 (2007).
[47] A. J. Ramsay, A. V. Gopal, E. M. Gauger, A. Nazir, B. W. Lovett, A. M. Fox, and M. S. Skolnick, Phys. Rev. Lett. **104**, 017402 (2010).
[48] N. Makri and D. E. Makarov, J. Chem. Phys. **102**, 4600 (1995).
[49] N. Makri and D. E. Makarov, J. Chem. Phys. **102**, 4611 (1995).
[50] A. M. Barth, A. Vagov, and V. M. Axt, Phys. Rev. B **94**, 125439 (2016).
[51] J. S. Melinger, D. McMorrow, C. Hillegas, and W. S. Warren, Phys. Rev. A **51**, 3366 (1995).
[52] B. Saleh and M. Teich, *Fundamentals of Photonics, 2 Volume Set*, Wiley Series in Pure and Applied Optics (Wiley Interscience, New York, 2019).
[53] J. P. Reithmaier, G. Sęk, A. Löffler, C. Hofmann, S. Kuhn, S. Reitzenstein, L. V. Keldysh, V. D. Kulakovskii, T. L. Reinecke, and A. Forchel, Nature (London) **432**, 197 (2004).
[54] T. Yoshie, A. Scherer, J. Hendrickson, G. Khitrova, H. M. Gibbs, G. Rupper, C. Ell, O. B. Shchekin, and D. G. Deppe, Nature (London) **432**, 200 (2004).
[55] G. Khitrova, H. M. Gibbs, M. Kira, S. W. Koch, and A. Scherer, Nat. Phys. **2**, 81 (2006).
[56] D. G. Nahri, F. H. A. Mathkoor, and C. H. R. Ooi, J. Phys.: Condens. Matter **29**, 055701 (2017).
[57] K. Kuruma, Y. Ota, M. Kakuda, S. Iwamoto, and Y. Arakawa, Phys. Rev. B **97**, 235448 (2018).
[58] P. Machnikowski and L. Jacak, Phys. Rev. B **69**, 193302 (2004).
[59] A. Krügel, V. M. Axt, and T. Kuhn, Phys. Rev. B **73**, 035302 (2006).
[60] D. Mogilevtsev, A. P. Nisovtsev, S. Kilin, S. B. Cavalcanti, H. S. Brandi, and L. E. Oliveira, Phys. Rev. Lett. **100**, 017401 (2008).
[61] D. Mogilevtsev, A. P. Nisovtsev, S. Kilin, S. B. Cavalcanti, H. S. Brandi, and L. E. Oliveira, J. Phys.: Condens. Matter **21**, 055801 (2009).
[62] A. J. Ramsay, T. M. Godden, S. J. Boyle, E. M. Gauger, A. Nazir, B. W. Lovett, A. M. Fox, and M. S. Skolnick, Phys. Rev. Lett. **105**, 177402 (2010).
[63] D. P. S. McCutcheon and A. Nazir, New J. Phys. **12**, 113042 (2010).
[64] D. P. S. McCutcheon, N. S. Dattani, E. M. Gauger, B. W. Lovett, and A. Nazir, Phys. Rev. B **84**, 081305(R) (2011).
[65] E. R. Schmidgall, P. R. Eastham, and R. T. Phillips, Phys. Rev. B **81**, 195306 (2010).
[66] C.-M. Simon, T. Belhadj, B. Chatel, T. Amand, P. Renucci, A. Lemaitre, O. Krebs, P. A. Dalgarno, R. J. Warburton, X. Marie, and B. Urbaszek, Phys. Rev. Lett. **106**, 166801 (2011).
[67] Y. Wu, I. M. Piper, M. Ediger, P. Brereton, E. R. Schmidgall, P. R. Eastham, M. Hugues, M. Hopkinson, and R. T. Phillips, Phys. Rev. Lett. **106**, 067401 (2011).
[68] S. Lüker, K. Gawarecki, D. E. Reiter, A. Grodecka-Grad, V. M. Axt, P. Machnikowski, and T. Kuhn, Phys. Rev. B **85**, 121302(R) (2012).
[69] K. Gawarecki, S. Lüker, D. E. Reiter, T. Kuhn, M. Glässl, V. M. Axt, A. Grodecka-Grad, and P. Machnikowski, Phys. Rev. B **86**, 235301 (2012).
[70] A. Debnath, C. Meier, B. Chatel, and T. Amand, Phys. Rev. B **86**, 161304(R) (2012).
[71] A. Debnath, C. Meier, B. Chatel, and T. Amand, Phys. Rev. B **88**, 201305(R) (2013).
[72] M. Glässl, A. M. Barth, K. Gawarecki, P. Machnikowski, M. D. Croitoru, S. Lüker, D. E. Reiter, T. Kuhn, and V. M. Axt, Phys. Rev. B **87**, 085303 (2013).
[73] R. Mathew, E. Dilcher, A. Gamouras, A. Ramachandran, Hong Yi Shi Yang, S. Freisem, D. Deppe, and K. C. Hall, Phys. Rev. B **90**, 035316 (2014).
[74] D. E. Reiter, T. Kuhn, M. Glässl, and V. M. Axt, J. Phys.: Condens. Matter **26**, 423203 (2014).
[75] T. Kaldewey, S. Lüker, A. V. Kuhlmann, S. R. Valentin, A. Ludwig, A. D. Wieck, D. E. Reiter, T. Kuhn, and R. J. Warburton, Phys. Rev. B **95**, 161302(R) (2017).
[76] M. Born and V. Fock, Z. Phys. **51**, 165 (1928).
[77] W. M. Itano, J. C. Bergquist, and D. J. Wineland, Phys. Rev. A **38**, 559 (1988).
[78] I. S. Osad'ko, J. Exp. Theor. Phys. **101**, 64 (2005).
[79] X.-Z. Zhang, Z.-H. Wang, H. Li, Q. Wu, B.-Q. Tang, F. Gao, and J.-J. Xu, Chin. Phys. Lett. **25**, 3976 (2008).
[80] J. Sanders, M. Jonckheere, and S. Kokkelmans, Phys. Rev. Lett. **115**, 043002 (2015).

Publication 9

Schrödinger cat states in quantum-dot-cavity systems.

M. Cosacchi, T. Seidelmann, J. Wiercinski, M. Cygorek, A. Vagov, D. E. Reiter, V. M. Axt.

Phys. Rev. Research **3**, 023088 (2021).

DOI: 10.1103/PhysRevResearch.3.023088

Author contributions

The author has designed the concept of this study, in particular, he has performed the data generation and analysis, has provided the interpretation of the results, and has written the first draft of the paper. He has proposed to use the fidelity and the non-classicality measure δ as complementary quantities to characterize the Schrödinger cat states and has implemented their numerical extraction. He has moderated all discussions and revision requests of the draft, has organized the correspondence with the editor and referees, and has provided the first drafts of answers to the referees.

T. Seidelmann has assisted in the numerical implementation of the adaption of the Law & Eberly protocol to quantum-dot—cavity systems, has discussed the results in detail with the author, thus contributing to the interpretation, and has contributed to revisions of the draft and the answers to the referees.

J. Wiercinski has written the initial version of the code to extract photonic Wigner functions from the simulations. He has participated in the discussion and interpretation of the results and has contributed to revisions of the draft and the answers to the referees.

M. Cygorek, A. Vagov, and D. E. Reiter have cosupervised this work, in particular, they have participated in the discussion and interpretation of the results. They have contributed to the optimization of the presentation as well as revisions of the draft and the answers to the referees.

V. M. Axt has advised the author throughout his work as the main supervisor. He has obtained the funding for this work and has participated in the discussion and interpretation of the results. He has contributed to the optimization of the presentation as well as revisions of the draft and the answers to the referees.

Schrödinger cat states in quantum-dot-cavity systems

M. Cosacchi,[1,*] T. Seidelmann,[1] J. Wiercinski,[1] M. Cygorek,[2] A. Vagov,[1,3] D. E. Reiter,[4] and V. M. Axt[1]

[1]*Theoretische Physik III, Universität Bayreuth, 95440 Bayreuth, Germany*

[2]*Heriot-Watt University, Edinburgh EH14 4AS, United Kingdom*

[3]*ITMO University, St. Petersburg, 197101, Russia*

[4]*Institut für Festkörpertheorie, Universität Münster, 48149 Münster, Germany*

(Received 24 December 2020; accepted 5 April 2021; published 3 May 2021)

A Schrödinger-cat state is a coherent superposition of macroscopically distinguishable quantum states, in quantum optics usually realized as superposition of coherent states. Protocols to prepare photonic cats have been presented for atomic systems. Here we investigate in what manner and how well the preparation protocols can be transferred to a solid-state platform, namely, a semiconductor quantum-dot–cavity system. In quantum-dot–cavity systems there are many disruptive influences like cavity losses, the radiative decay of the quantum dot, and the coupling to longitudinal acoustic phonons. We show that for one of the protocols these influences kill the quantum coherence between the states forming the cat, while for a second protocol a parameter regime can be identified where the essential characteristics of Schrödinger-cat states survive the environmental influences under conditions that can be realized with current equipment.

DOI: 10.1103/PhysRevResearch.3.023088

I. INTRODUCTION

Schrödinger cats are probably the most popular example of highly nonclassical, purely quantum mechanical states. Realizing a coherent superposition of two macroscopically distinct states, where in analogy to Schrödinger's Gedankenexperiment [1] the cat is simultaneously dead and alive, remains a challenge due to the inevitable decoherence induced by the environmental coupling. A general Schrödinger-cat state with two macroscopically distinguishable states $|\text{alive}\rangle$ and $|\text{dead}\rangle$ can be written as

$$|\text{cat}\rangle = \mathcal{N}(|\text{alive}\rangle + e^{i\varphi}|\text{dead}\rangle) \tag{1}$$

with normalization $\mathcal{N}$ and phase φ. These states find numerous applications in advanced quantum metrology [2,3], quantum teleportation [4], quantum computation [5–7], and quantum error correction algorithms [8]. Cat states being a superposition of more than two states [9–11] as well as phononic cat states [12] have been investigated. Schrödinger-cat states are a suitable platform to study the decoherence between two superposed quantum objects, in other words, to observe the quantum-to-classical transition [13]. Therefore, Schrödinger-cat states are of fundamental interest in understanding the very foundations of quantum mechanics.

Schrödinger-cat states have to be sharply distinguished from incoherently superposed macroscopically distinct states, which are described by the density matrix

$$\rho_{\text{mixture}} = \tfrac{1}{2}(|\text{alive}\rangle\langle\text{alive}| + |\text{dead}\rangle\langle\text{dead}|), \tag{2}$$

where the interference terms are missing. This discrimination is best visible in the Wigner function. While in the cat state there are negative parts, which imply nonclassicality, the Wigner function of the classical incoherent mixture ρ_{mixture} is strictly positive.

Because of the fundamental and technological importance of Schrödinger-cat states, their preparation has long been a research target. Earlier efforts in this direction focused mostly on atom-based systems, where atoms are placed in an optical

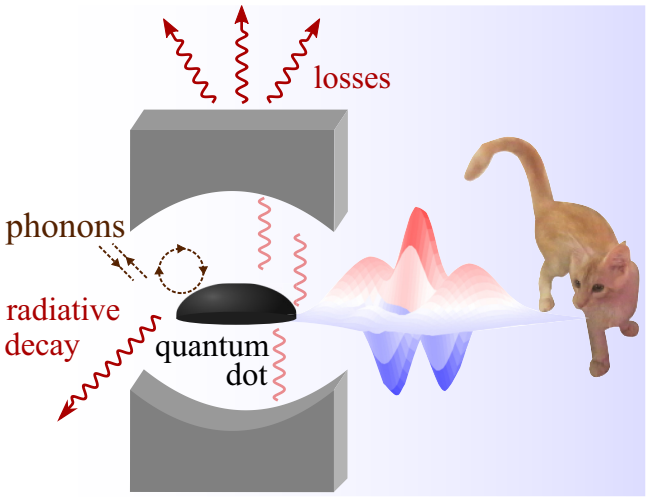

FIG. 1. A Schrödinger-cat state appearing in a QDC system. Photons are created by recombination of the QD exciton. The photoemission is controlled such that cats are created on demand.

*Corresponding author: michael.cosacchi@uni-bayreuth.de

cavity [14–16]. Recently, many concepts of atom quantum optics have been transferred to solid state systems, in particular to semiconductor quantum-dot–cavity systems (QDCs) giving rise to the field of semiconductor quantum electrodynamics. QDCs already have been shown to be highly integrable on-demand emitters of photons in nonclassical states including high-quality single photons [17–26] and entangled photon pairs [27–37]. QDC-based protocols for generating higher-order Fock states have also been developed [38]. An easy to use solid-state-based source of Schrödinger cats would be a highly attractive extension of these achievements.

As atomic systems, QDCs have loss channels, namely, the energetic loss channels provided by the radiative decay of a quantum dot (QD) and the finite cavity quality factor. The main difference between QDC and atomic systems is the presence of longitudinal acoustic phonons, which is a well-known source of decoherence even at cryogenic temperatures of $T = 4$ K [39,40]. Hence, it is an open question whether in the QDC platform as well the generation of Schrödinger-cat states is possible.

In this paper, we consider two protocols to prepare Schrödinger-cat states in a QDC. For both protocols we adapt existing preparation schemes and apply them to the QDC system. The first protocol is based on the proposal by Law and Eberly [15]. To use this protocol in the QDC we rely solely on driving the QD by external laser pulses. To create a Schrödinger-cat state we need a precise timing of the arrival time of the pulses steering the QD-cavity coupling. We call the protocol DOD, short for dot-driven protocol. The second protocol is adapted from Gea-Banacloche [16] and can be transferred to the QDC system by producing a coherent initial state. This can be achieved by driving the cavity, hence we call this protocol CAD, short for cavity-driven protocol.

For both protocols, we analyze the impact of losses and phonon coupling in detail using realistic parameters that have been realized in current experiments. For the DOD protocol we show that the losses are a detrimental influence on the sensitive coherence in a Schrödinger cat and the protocol can produce only mixed states [cf. Eq. (2)] under realistic conditions. In contrast, for the CAD protocol we find that even under realistic conditions it is possible to create a cat state, and we identify experimentally accessible parameter regimes favorable for generating photonic Schrödinger cats.

Our work demonstrates that also in QDCs the preparation of Schrödinger-cat states is possible, and we propose a protocol and specify a suitable parameter regime to prepare them.

II. THEORETICAL MODEL

The QDC system can be well modeled by a driven two-level QD coupled to a single photon mode [38,40]. The corresponding Hamiltonian then reads

$$H = H_{\mathrm{QDC}} + H_{\mathrm{driving}} + H_{\text{ac-Stark}}. \tag{3}$$

The QDC is described by the Jaynes-Cummings model

$$H_{\mathrm{QDC}} = \hbar\omega_X |X\rangle\langle X| + \hbar\omega_C a^\dagger a + \hbar g(a\sigma_X^\dagger + a^\dagger \sigma_X), \tag{4}$$

where $|X\rangle$ is the exciton state at energy $\hbar\omega_X$. $\sigma_X := |G\rangle\langle X|$ is the transition operator between the excited state $|X\rangle$ and the ground state $|G\rangle$. The energy of $|G\rangle$ is set to zero. a ($a^\dagger$) denotes the photonic annihilation (creation) operator. The cavity frequency is denoted by ω_C and its coupling to the QD by g. We consider two different forms of driving Hamiltonians for the two protocols:

$$H_{\mathrm{driving}} = \begin{cases} -\frac{\hbar}{2}\left[f_{\mathrm{p}}^*(t)\sigma_X + f_{\mathrm{p}}(t)\sigma_X^\dagger\right] & \text{DOD} \\ -\frac{\hbar}{2}\left[f_{\mathrm{p}}^*(t)a + f_{\mathrm{p}}(t)a^\dagger\right] & \text{CAD} \end{cases}. \tag{5}$$

Effectively decoupling the QD from the cavity can be achieved with an ac-Stark pulse driving the QD [38,41], described by

$$H_{\text{ac-Stark}} = -\frac{\hbar}{2}\left[f_{\text{ac-Stark}}^*(t)\sigma_X + f_{\text{ac-Stark}}(t)\sigma_X^\dagger\right]. \tag{6}$$

The exciting and Stark laser pulses are represented by the functions $f_{\mathrm{p}}(t)$ and $f_{\text{ac-Stark}}(t)$, which are specified in Appendix A.

We also account for the coupling to longitudinal acoustic (LA) phonons [40,42–45] (as detailed in Appendix A) as well as the radiative decay of the QD exciton and cavity losses. Whenever we consider phonon effects, the phonons are assumed to be initially in thermal equilibrium at a temperature of $T = 4$ K. A sketch of the QDC system is shown in Fig. 1. The corresponding Liouville equation is solved in a numerically complete manner by employing a path-integral formalism (for details see Refs. [46–48]). The parameters used in the calculations are given in Appendix C.

III. DOT-DRIVEN (DOD) PROTOCOL

In the optical realm, coherent states $|\alpha\rangle$ are the most classical states. A general coherent superposition of two coherent states of the form

$$\mathcal{N}(|\alpha\rangle + e^{i\varphi}|-\alpha\rangle) \tag{7}$$

with normalization $\mathcal{N}$ and phase φ is one of the most common realizations of Schrödinger-cat states in quantum optics [14]. Hence, we choose this realization as the target state for the DOD protocol and set $\alpha = \pi/2$ and $\varphi = 0$. This choice ensures that the corresponding coherent states are distinct, while their average photon number is low enough that we expect the influence of cavity losses to be limited.

To prepare this target state we adapt the protocol from Ref. [15], which is proposed to create arbitrary photonic states in a single-mode microcavity. However, the originally proposed protocol does not account for any loss channels. The requirements are a driven Jaynes-Cummings model with controllable driving $f(t)$ and coupling $g(t)$ between the two-level system and the cavity. To transfer the proposal to QDCs, a few obstacles have to be overcome. While time-dependent driving of a QDC is possible by applying appropriate laser pulses, controlling the QD-cavity coupling time dependently remains a challenge. In particular, the protocol in Ref. [15] relies on a stepwise switching between $f(t)$ and $g(t)$; i.e., one has to be off, whenever the other one is on.

Accordingly, the challenge of implementing this protocol in a QDC protocol is twofold: (1) the magnitude of the QD-cavity coupling has to be varied and (2) the QD and cavity are supposed to be decoupled during the time the driving is on. In Ref. [15] the time intervals τ, when either $f(t)$ or $g(t)$ is

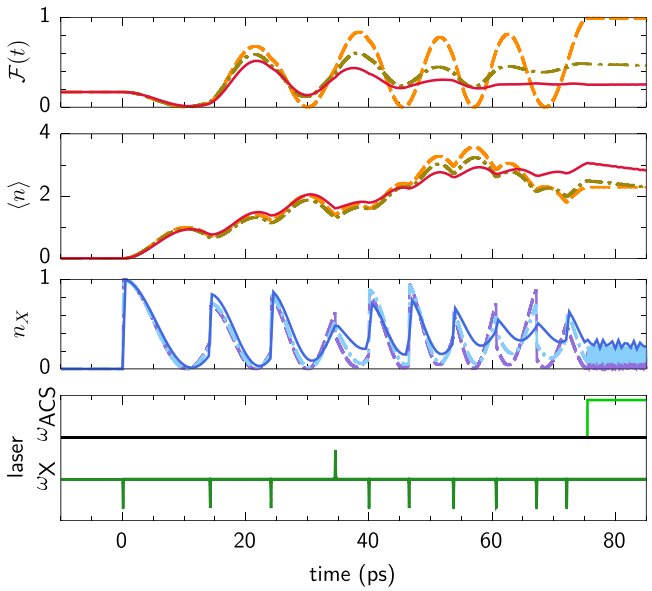

FIG. 2. Dynamics of the QDC in the DOD protocol. Panels from bottom to top: External pulses as well as the Stark pulse, exciton occupation n_X, average photon number $\langle n \rangle$, and time-dependent fidelity $\mathcal{F}(t)$ to the target Schrödinger-cat state in Eq. (7). Dashed lines: ideal case without phonons and losses. Dashed-dotted lines: without phonons but with losses. Solid lines: with phonons and losses.

on, are kept constant. Only the products $f_i\tau$ and $g_i\tau$ in the ith interval are relevant for the success of the protocol. Therefore, problem (1) can be solved by varying the time interval while keeping the coupling constant, i.e., we use $g\tau_i$. Concerning problem (2), the decoupling suggested in Ref. [15] can in principle be realized by inducing suitable Stark shifts, which is, however, highly demanding experimentally. As demonstrated for protocols to prepare higher-order Fock states [38], it can be advantageous to avoid the decoupling provided the desired goal can be achieved by short enough pulses. Indeed, when the switching induced by the laser driving $f(t)$ takes place on timescales shorter than the dynamics induced by the cavity, the action of the latter cannot interfere noticeably with the switching, even though the QD and the cavity are coupled. Furthermore, on such fast timescales, the precise shape of the pulse becomes irrelevant (see, e.g., Appendix A 1 of Ref. [38]). Therefore, a Gaussian pulse with the same area as the rectangular $f_i\tau$ can be used, which vastly reduces the experimental demand. Its full width at half maximum (FWHM) is chosen to be 100 fs. Note that the corresponding spectral width of the pulse is quite large. Nonetheless, for typical energetic spacings to higher lying exciton states [49] the two-level approximation to the QD still holds well [38].

A. The ideal case

Figure 2 shows the dynamics of the QDC in the DOD protocol. The lowest panel displays the sequence of laser pulses proposed to prepare the Schrödinger-cat state in Eq. (7). The pulse sequence is derived by solving the set of equations determining the protocol to prepare arbitrary states in Ref. [15]. After adapting the solution to pulses as explained above, one obtains the pulse areas and central peak times necessary to prepare the target state. In total, a series of ten π pulses is applied. Note that relative phases of π of the pulses are absorbed into the definition of the pulse areas and that the time difference between two subsequent pulses is the time τ_i where the cavity coupling g takes effect. The arrival times and pulse areas are listed in Table I. After reaching the target state, the cavity needs to be decoupled from the QD in order to preserve the preparation, which is achieved by an ac-Stark pulse as shown in the lower panel of Fig. 2 .

TABLE I. Pulse sequence for the DOD protocol in Sec. III. The times t_c of their maxima and their pulse areas Θ are given.

Number of the pulse	t_c (ps)	Θ (π)
1	0.1	−1
2	14.2	−1
3	24.1	−1
4	34.6	1
5	40.0	−1
6	46.5	−1
7	53.7	−1
8	60.7	−1
9	67.2	−1
10	72.1	−1

The resulting time evolution of the exciton occupation n_X is shown in blue in Fig. 2, where the dashed lines correspond to the ideal case without phonons and losses. Each laser pulse partially excites the exciton, which then decays by photon creation. Accordingly, the average photon number $\langle n \rangle$, as shown in the second panel from top in Fig. 2, increases after each pulse.

To see whether we have created a Schrödinger-cat state, we consider the fidelity defined as

$$\mathcal{F}(\rho_1, \rho_2) = \left[\mathrm{Tr}\left(\sqrt{\sqrt{\rho_1}\rho_2\sqrt{\rho_1}}\right)\right]^2 \tag{8}$$

for two arbitrary density matrices ρ_1 and ρ_2 [50]. Setting one density matrix to the target Schrödinger-cat state in Eq. (7), we get a measure how close we are to this specific cat state. The results are shown in the topmost panel of Fig. 2. We see that after the pulse sequence the fidelity reaches unity, implying that in the purely Hamiltonian ideal case without losses and phonons, this protocol is able to perfectly prepare the target state.

This is confirmed by looking at the Wigner function (definition in Appendix B) in Fig. 3(a). We see all relevant features of a Schrödinger cat where the two Gaussians indicate the two macroscopically distinct states, here, coherent states, and the oscillations between them point to a coherent character of their superposition.

An important property of a cat state is its nonclassicality. In general, the nonclassicality δ of a state can be measured by considering the negative part of its Wigner function $W(\alpha)$, since all Wigner functions corresponding to classical states are positive. The doubled volume of the integrated negative part of the Wigner function was introduced in Ref. [51] as such a

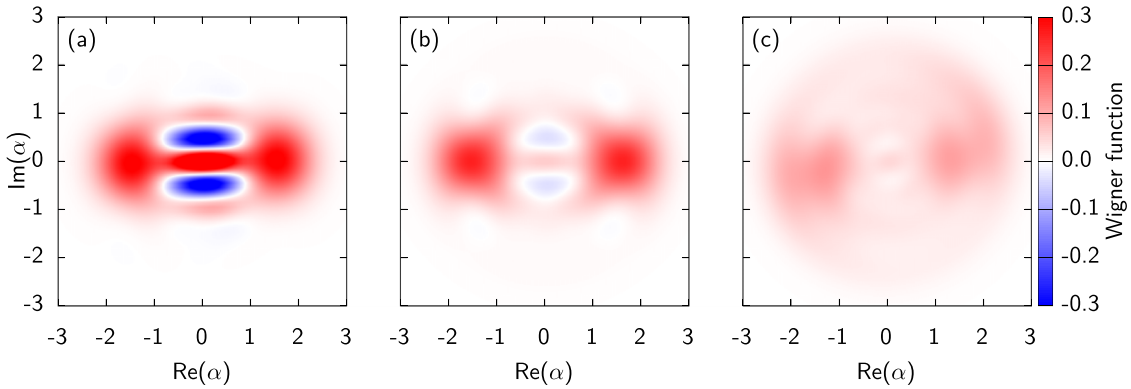

FIG. 3. Wigner functions of the photonic states prepared by the DOD protocol (a) for the ideal case, (b) including losses, and (c) taking both phonons and losses into account. The Wigner functions are calculated at the start time of the decoupling Stark pulse, $t = 75.5$ ps.

nonclassicality measure:

$$\delta = \frac{\int [|W(\alpha)| - W(\alpha)]\, d\alpha}{\int W(\alpha)\, d\alpha}, \tag{9}$$

where $\delta = 0$ implies a classical state. For the DOD protocol we obtain $\delta = 0.51$ for this Schrödinger cat, thus, indeed implying quantum features of the state.

The results in Figs. 2 and 3 as well as the value of δ indicate that the adaption of the protocol in Ref. [15] to ideal QDCs with constant cavity coupling g is accomplished successfully.

B. Loss and phonon effects

Next, we account for the loss channels. When taking the radiative decay of the QD and the cavity losses into account, the preparation fidelity drops to $\mathcal{F} = 48.7\,\%$ (cf. dashed-dotted lines in Fig. 2). Interestingly, the nonclassicality measure δ drops to 0.03. Looking at the corresponding Wigner function in Fig. 3(b) reveals that the domains of negative values of the Wigner function have practically disappeared.

Phonons destroy even the remaining nonclassicality. While the fidelity in the case including all loss and phonon effects still yields $\mathcal{F} = 25.0\,\%$ (see solid lines in Fig. 2), δ is identically zero, thus indicating a classical state. Indeed, the Wigner function in Fig. 3(c) shows two blurred macroscopically distinct states, here again coherent states, but no oscillations between them. Thus, they are superimposed incoherently and, therefore, closely resemble the statistical mixture in Eq. (2).

The reason for this behavior lies in the nature of a Schrödinger-cat state, which involves the formation of a quantum mechanical superposition of distinct states with a well-defined relative phase. All processes diminishing this phase relation lead to a degradation of the cat state. For typical QDCs, the cavity loss rate is much larger than the radiative decay rate, thus having greater impact on the preparation scheme. Furthermore, the effective cavity loss rate is proportional to the photon occupation, thus degrading especially states with large multiphoton contribution, such as cat states. The phonons then destroy any nonclassicality left after taking the other two processes into account.

From the analysis in this section it becomes clear that the fidelity alone is not sufficient to characterize a Schrödinger-cat state, since it may miss the essential feature of oscillations of the Wigner function to negative values. Therefore, it is necessary to simultaneously consider a nonclassicality measure like δ.

In summary, the DOD protocol is not suitable to prepare the Schrödinger-cat state in a QDC under realistic conditions, because the interference terms of a cat state do not survive the environmental coupling. Even at $T = 4$ K, phonon effects destroy the coherent superposition of the two macroscopically distinct states. Note that it is interesting from a fundamental point of view that the phonons provide sufficiently strong environmental coupling necessary to facilitate the quantum-to-classical transition, which in this case is a transition from a Schrödinger cat as in Eq. (7) to an incoherent mixture as in Eq. (2).

IV. CAVITY-DRIVEN (CAD) PROTOCOL

The CAD protocol is based on the ideas of Refs. [16,52], which showed that the textbook collapse-and-revival example in the Jaynes-Cummings model has two additional very striking features: (1) at half the revival time the QD and photonic subspaces factorize and (2) at precisely this time a Schrödinger-cat state appears in the cavity mode.

The main requirement for this cat state preparation scheme is a coherent state in the cavity mode as the initial state of the Jaynes-Cummings dynamics [16]. The photonic state prepared at half the revival time is [52]

$$\mathcal{N}(|\Phi_+\rangle + |\Phi_-\rangle), \tag{10}$$

which is another realization of a Schrödinger-cat state as defined in Eq. (1). Here $\mathcal{N}$ is a normalization constant and

$$|\Phi_\pm\rangle = e^{-\frac{1}{2}\langle n\rangle} \sum_{n=0}^{\infty} \frac{\langle n\rangle^{n/2}}{\sqrt{n!}} e^{-in\phi} e^{\mp i\pi\sqrt{\langle n\rangle n}} |n\rangle \tag{11}$$

with $\langle n\rangle = |\alpha|^2$ the average photon number of the initial coherent state and ϕ the phase of α. When using a real envelope Gaussian pulse as in our case, this phase is determined to be $3\pi/2$ as a short analytical calculation shows (cf. Appendix D). These two states are macroscopically distinguishable, but they are not coherent states as in Eq. (7) because of the $\langle n\rangle$- and n-dependent phase in Eq. (11). However, it should be noted that $|\Phi_\pm\rangle$ approaches in the limit $\langle n\rangle \to \infty$ the coherent

state $|\Phi_\pm\rangle \to e^{\mp i\langle n\rangle\pi/2}|\mp i\alpha\rangle$ (cf. Ref. [52]), and therefore the state in Eq. (10) becomes $\mathcal{N}(|i\alpha\rangle + e^{-i\langle n\rangle\pi}|-i\alpha\rangle)$, which has the form given in Eq. (7). The fidelity with which the state in Eq. (10) is reached in the Jaynes-Cummings dynamics at half the revival time is unity only in the limit $\langle n\rangle \to \infty$ [52]. Thus, in the ideal phonon and loss-free case higher average photon numbers are favorable in this scheme. However, since the revival time is longer for higher mean photon numbers, the preparation time rises with increasing mean photon numbers. The system is thus exposed a longer time to losses before the end of the protocol. As a result of this trade-off situation, there is an optimal photon number when losses are accounted for.

Using this idea for a preparation protocol of Schrödinger-cat states in the microcavity mode, we have to face two tasks: (1) preparing a suitable initial state in the cavity and (2) finding a suitable $\langle n\rangle$ to achieve maximum fidelity to the cat state in Eq. (10). Task (1) is solved easily, since it is textbook knowledge [14] that driving an empty cavity with a classical laser yields a coherent state in the cavity. Now, the cavity in a QDC is not empty, but as long as the laser pulse driving the cavity mode is short enough compared with the dynamics induced by the coupling g, it may be approximated as such. We use a 1 ps Gaussian pulse (cf. bottom panel of Fig. 4) to drive the cavity mode and vary its pulse area Θ to analyze the success of the protocol depending on $\langle n\rangle$ to tackle task (2). Note that the average photon number of the prepared coherent state is connected to the laser pulse area via $\langle n\rangle = |\alpha|^2 = (\Theta/2)^2$.

A. The ideal case

Figure 4 shows the dynamics of the QDC in the CAD protocol when driving the cavity with a pulse of area 1.2π. As we show later this is the optimal pulse area when losses are taken into account. The dashed lines in Fig. 4 correspond to the ideal case.

For the chosen pulse area the average photon number, as shown in the middle panel in Fig. 4, is about 3. While this is not high enough to lead to a clear-cut collapse-and-revival signature, the exciton dynamics (blue curves) shows hints of this feature with a revival at about 80 ps. The fidelity $\mathcal{F}$ shows oscillations within a bell-like envelope to reach its maximum of $\mathcal{F} = 88.1\,\%$ at 39.5 ps after the pulse. At the same time, the photonic subsystem is close to a pure state as indicated by the near-unity value of the trace of the squared photonic density matrix. Thus, the QD and photon subspaces factorize. To preserve the Schrödinger-cat state as it appears at this point in time, an additional QD-driving pulse is needed to effectively decouple the QD from the cavity. This is in analogy to the ac-Stark pulse shown for the DOD protocol in Sec. III.

Figure 5(a) shows the corresponding Wigner function evaluated at the time of maximum fidelity when the decoupling is evoked by a Stark pulse for the ideal case. Two macroscopically distinct states are clearly visible as elongated Gaussians corresponding to the states $|\Phi_\pm\rangle$ in Eq. (11). Oscillations to negative values between these two structures indicate a coherent superposition. Therefore, this state is clearly a Schrödinger-cat state.

As the CAD protocol depends sensitively on the pulse areas, we plot in Fig. 6(b) the maximum fidelity to the

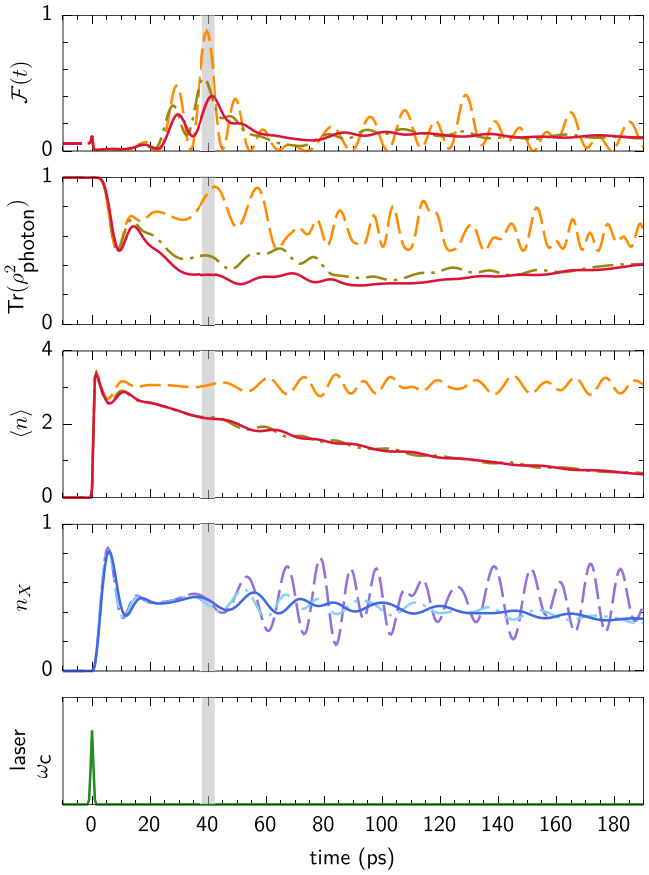

FIG. 4. Dynamics of the QDC in the CAD protocol. Panels from bottom to top: the exciting laser pulse, the occupation of the exciton n_X, the average photon number $\langle n\rangle$, $\mathrm{Tr}(\rho^2_{\mathrm{photon}})$ which indicates how close the photonic system is to a pure state, and the fidelity to the Schrödinger-cat state in Eq. (10). Dashed lines: ideal case without phonons and losses. Dashed-dotted lines: without phonons but with losses. Solid lines: with phonons and losses. The temporal range where the fidelity reaches its maximum value in all three considered cases is shaded in gray.

Schrödinger-cat state in Eq. (10) during the time evolution after the cavity preparation pulse as a function of the pulse area, i.e., the average photon number of the initial state. Having seen that the fidelity is not sufficient as a measure for obtaining a nonclassical photon state as the cat state, we additionally show in Fig. 6(a) the nonclassicality measure δ at the time of maximum fidelity.

For the ideal case (black lines in Fig. 6) the nonmonotonic behavior of the fidelity is prominent. In contrast to the naive expectation that it rises monotonically with Θ, i.e., $\langle n\rangle$, it increases for $\langle n\rangle \to 0$ and shows an oscillatory behavior for higher $\langle n\rangle$. For decreasing $\langle n\rangle$, the prepared state contains a larger contribution of the vacuum, while the target state in Eq. (10) itself shows more vacuum characteristics. Therefore, the fidelity approaches unity, while the nonclassicality measure δ decreases [cf. Fig. 6(a)]. Thus, the state for low $\langle n\rangle$ cannot be considered to be a genuine Schrödinger cat, since the target state in Eq. (10) ceases to be a superposition of two macroscopically distinct states.

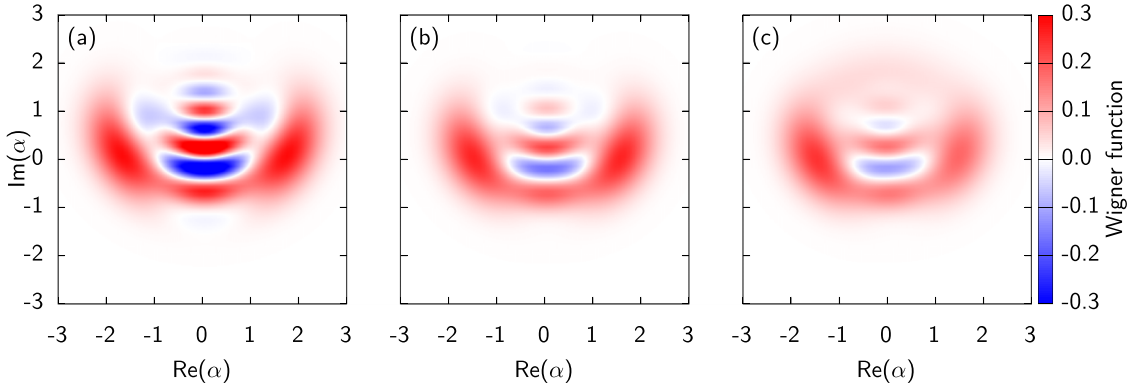

FIG. 5. Wigner functions of the photonic states prepared by the CAD protocol (a) for the ideal case, (b) including losses, and (c) taking both phonons and losses into account. The Wigner functions are calculated at the respective times of maximum fidelity (cf. Fig. 4): $t = 39.5$ ps (ideal case), $t = 38.5$ ps (including losses), and $t = 41.0$ ps (including losses and phonons).

The nonmonotonic behavior of the maximum fidelity in Fig. 6(b) starting at $\Theta = \pi$ has its origin in the dynamics of the fidelity as shown exemplary in Fig. 4. The oscillation frequency within the bell-like envelope increases with rising Θ (not shown in the figure), while the maximum of the oscillation need not coincide with the maximum of the envelope. Therefore, $\max_t \mathcal{F}(t)$ does not rise monotonically with Θ, contrary to the naive expectation.

The proposal in Ref. [16] is based on the assumption of a coherent state in the cavity mode as an initial state of the dynamics. The orange line in Fig. 6(b) shows the fidelity corresponding to the solution of the initial value problem

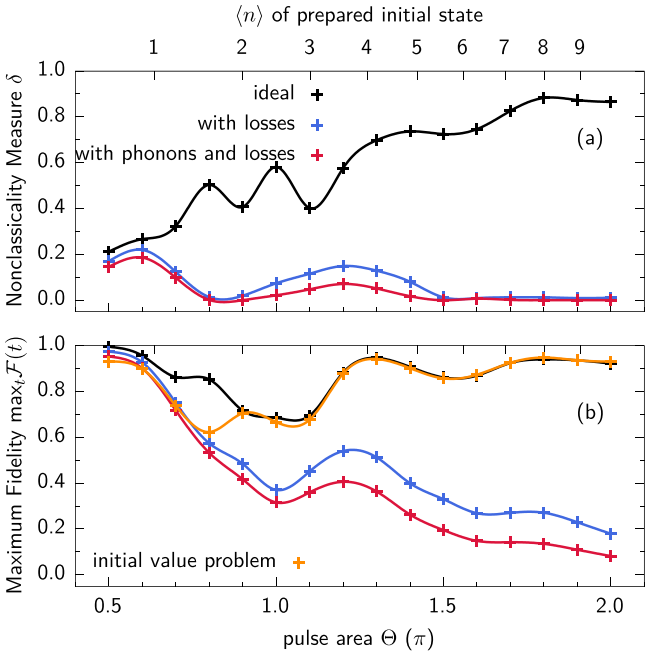

FIG. 6. (a) Nonclassicality measure δ at the time of maximum fidelity and (b) maximum fidelity during the time evolution as a function of the pulse area, i.e., the average photon number of the initial state. Black: ideal case, blue: including losses but without phonons, red: with losses and phonons, orange: solution of the initial value problem.

posed in Ref. [16], i.e., without first preparing the initial state with a laser pulse. If such a coherent state is to be prepared in a cavity mode, an external laser pulse is necessary [cf. task (1) in Sec. IV]. For pulse areas greater than π, the maximum fidelity obtained after solving the initial value problem perfectly coincides with the result obtained in the ideal case of the preparation. This implies that indeed a coherent state is prepared in the cavity mode by the external driving. The deviations seen at smaller pulse areas have their origin in the finite length of the preparation pulse.

The overall rise of the nonclassicality measure δ with $\langle n \rangle$, on the other hand, and its oscillations [cf. black line in Fig. 6(a)] are a known feature [51]. In particular, the oscillation is a signature of a nonzero phase due to a finite momentum of the cat state in (q, p) representation that distinguishes "standing" and "moving" cats [51]. Note that the Wigner function in (q, p) and $(\mathrm{Re}(\alpha), \mathrm{Im}(\alpha))$ representation are connected by a factor of $2\pi\hbar$ [53–55]. Since the nonclassicality measure δ is a ratio of volumes of the Wigner function, it is independent of the representation.

B. Loss and phonon effects

The influence of cavity losses and radiative decay on the preparation using the CAD protocol is very strong. The dynamics of all photonic variables shown in Fig. 4 are damped (orange dashed-dotted line). The effect is even more pronounced when looking at the protocol as a function of $\langle n \rangle$ in Fig. 6 (blue lines). In particular, at high $\langle n \rangle$, where the highest fidelity in the ideal case is achieved, the losses have the greatest impact and the fidelity drops to almost zero. This is due to the fact that the effective loss rate for a Fock state $|n\rangle$ is proportional to the photon number n, i.e., $n\kappa$. Likewise, the nonclassicality measure δ becomes identically zero when the pulse area exceeds 1.5π. Thus, in stark contrast to the ideal case, the limit $\langle n \rangle \to \infty$ yields no Schrödinger cat at all.

Considering phonon effects on top of the loss influence further smooths out the dynamics (cf. solid lines in Fig. 4) and lowers both the fidelity and the nonclassicality of the target state (cf. red lines in Fig. 6), while showing qualitatively the same behavior as in the case with losses but without phonons. These findings depend on the considered temperature, the

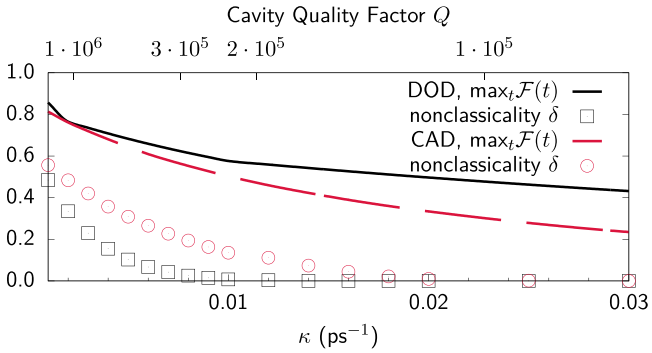

FIG. 7. The maximum fidelity to the Schrödinger-cat states in Eqs. (7) and (10) in the case of the DOD protocol (black solid line) and the CAD protocol (red dashed line), respectively, and the nonclassicality measure δ (open rectangles and circles) as a function of the cavity loss rate κ. The cavity quality factor assuming a mode frequency of $\hbar\omega_C = 1.5$ meV is displayed as a second axis.

GaAs material parameters, and the QD geometry and might differ for other parameter sets. In the case considered in this work, however, the loss effects have the most detrimental influence on the preparation of the target Schrödinger-cat state.

This is further underscored by considering the dependence of the protocols' success on the cavity loss rate, as shown in Fig. 7 for the case without phonons. For both the DOD and the CAD protocols, the preparation fidelity rises monotonically with the quality factor, as does the nonclassicality measure δ. The latter rises faster for the case of controlling the cavity, implying a comparatively higher robustness of this scheme with respect to cavity losses. This is due to the fact that the total length of the DOD protocol of about 80 ps is roughly twice the length of the CAD protocol of about 40 ps. Therefore, loss processes have less time to take effect in the CAD protocol. Furthermore, the DOD protocol presumes 10 operations, i.e., pulses which need to be timed exactly, whereas the CAD protocol relies only on one pulse. This also makes the CAD protocol more stable against environmental influences and more attractive for experiments.

Note that it has been shown experimentally that a system with a Purcell factor roughly three orders of magnitude larger than in our case is well suited for the preparation of exotic photonic states. Hofheinz *et al.* showed [56] that a so-called voodoo-cat state, a superposition of three coherent states, can be prepared in a system consisting of a superconducting qubit in a microwave resonator with a fidelity of 83 %. While such a setup has drawbacks, such as the wavelength of the emitted photonic state and the temperature in the mK-regime needed for the qubit to operate, this amazing result underscores the necessity of a high-quality resonator, both concerning the quality factor and the Purcell enhancement for the preparation of Schrödinger-cat or even more complicated voodoo-cat states.

Strikingly, in our QD-cavity system there is still a window of pulse areas, where the fidelity and the nonclassicality measure are rather high. The optimum pulse area yielding the maximum preparation fidelity under loss and phonon influence for our parameters is at $\Theta = 1.2\pi$, where both the fidelity and the nonclassicality measure have a maximum. This is due to a competition between the rising fidelity for $\langle n\rangle \to \infty$ as predicted in Ref. [52] and the inclusion of losses, which also become stronger for increasing $\langle n\rangle$. As a check, whether we indeed have created a cat state at $\Theta = 1.2\pi$, we have a look at the Wigner function in Fig. 5(c). The Wigner function clearly shows two macroscopically distinct states and oscillations between them, thus indicating a Schrödinger-cat state even when losses and phonons are accounted for under realistic conditions.

V. CONCLUSION

We have investigated two protocols for the preparation of photonic Schrödinger-cat states in the light field mode of a quantum-dot–cavity system (QDC). While in atomic systems Schrödinger cats have been already prepared, we here adapted the protocols used in the atomic case to a solid state system. In the calculations, we considered realistic values for the cavity losses as have been reported in QDCs, which showed that the radiative decay and cavity losses can be quite detrimental to the preparation scheme. In contrast to atoms, in QDC devices phonons also play a role, which have a great impact on the Schrödinger-cat preparation. Therefore, a theoretical guidance on the feasibility to prepare cat states is of high importance.

The first scheme relies on controlling the quantum dot with external laser pulses (DOD protocol) by adapting Ref. [15]. We developed a multipulse protocol for the QDC, where both the precise timing of the pulses and their mutual phases are of utmost importance. Most detrimental to the fidelity to the Schrödinger-cat state are cavity and radiative losses. The environmental coupling to longitudinal acoustic phonons further reduces drastically the fidelity and completely destroys the coherence between the two states. Only an incoherent mixture of the two macroscopically distinct states with zero nonclassicality remains, such that this scheme is not suitable to prepare Schrödinger cats in realistic QDCs. We mention that this is different for superconducting qubits in microwave cavities, where similar protocols have been successfully employed [56], because the quality factor of microwave cavities relative to the coupling strength is higher than in QDCs. A similar boost of the quality factor would be needed to enable a Schrödinger-cat preparation with this protocol also in QDCs.

The second protocol exploits the internal dynamics of the Jaynes-Cummings model, where a Schrödinger-cat state can be found naturally in the time evolution of the system [16,52]. Only one pulse driving the cavity is necessary to prepare a single coherent state in the field mode (CAD protocol), which serves as an initial state for the subsequent Jaynes-Cummings dynamics. While this protocol in the ideal case works best for high-pulse areas, the losses also increase in this case such that no preparation is possible. Again, the losses are the main cause of destroying the cat, while the phonon effects are less dramatic than in the first protocol. Remarkably, for intermediate pulse areas between π and 1.5π, the coherences as well as the nonclassicality of the Schrödinger cats survive even under the influence of both losses and phonons. Also in the CAD protocol, a boost of the cavity quality factor would improve the characteristics of the prepared cat state.

Our results show that Schrödinger cats in QDCs can be prepared under realistic conditions with an easy to use protocol.

ACKNOWLEDGMENT

This work was funded by the Deutsche Forschungsgemeinschaft (DFG, German Research Foundation), Project No. 419036043 and the University of Bayreuth in the funding program Open Access Publishing.

APPENDIX A: COUPLING HAMILTONIAN

The external laser pulses are described by

$$f_{\mathrm{p}}(t) = \sum_m f_m^{\mathrm{p}}(t - t_m) e^{-i\omega_{\mathrm{p}}(t-t_m)}. \tag{A1}$$

$f_m^{\mathrm{p}}(t)$ are the envelope functions of the pump fields and ω_{p} the corresponding laser frequencies. The product $\omega_{\mathrm{P}} t_m$ is chosen as an integer multiple of 2π. The pump fields are Gaussian pulses with area Θ_j,

$$f_j^{\mathrm{p}}(t) = \frac{\Theta_j}{\sqrt{2\pi}\sigma} e^{-\frac{t^2}{2\sigma^2}}, \tag{A2}$$

where σ denotes the standard deviation. It is connected to the full width at half maximum (FWHM) by $\mathrm{FWHM} = 2\sqrt{2\ln 2}\sigma$. Throughout this work, $\omega_{\mathrm{p}} = \omega_X$ is assumed. The ac-Stark pulses are assumed to be of rectangular shape:

$$f_{\text{ac-Stark}}(t) = e^{-i\omega_{\mathrm{ACS}} t} \begin{cases} 0 & t < -\frac{\tau_{\mathrm{length}}}{2} \\ f_s & -\frac{\tau_{\mathrm{length}}}{2} \leqslant t \leqslant \frac{\tau_{\mathrm{length}}}{2} \\ 0 & t > \frac{\tau_{\mathrm{length}}}{2} \end{cases}, \tag{A3}$$

where f_s denotes the field strength, i.e., the plateau height of the rectangular pulse, and τ_{length} its duration.

The ac-Stark pulses are tuned below the exciton line by $\omega_{\mathrm{ACS,X}} := \omega_{\mathrm{ACS}} - \omega_{\mathrm{X}}$, which is chosen within the range of validity of the RWA. The resulting shift of the exciton line can be calculated from the energies of the laser-dressed states.

The QD is coupled to LA phonons [40,42–45,57].

$$H_{\mathrm{Ph}} = \sum_{\mathbf{q}} \hbar\omega_{\mathbf{q}} b_{\mathbf{q}}^\dagger b_{\mathbf{q}} + \sum_{\mathbf{q}} (\gamma_{\mathbf{q}} b_{\mathbf{q}}^\dagger + \gamma_{\mathbf{q}}^* b_{\mathbf{q}}) |X\rangle\langle X|, \tag{A4}$$

where $b_{\mathbf{q}}^\dagger$ and $b_{\mathbf{q}}$ are the (bulk) phonon operators with wave vector $\mathbf{q}$ and energy $\hbar\omega_{\mathbf{q}}$. The deformation potential-type coupling to the electronic state is denoted by $\gamma_{\mathbf{q}}$. This Hamiltonian is of the so-called pure dephasing type [44,58]. Many well-known phenomena emerge from the interaction described by this Hamiltonian, e.g., the phonon sideband in the QD emission spectrum [42,59], the damping of the Rabi oscillations [39,60], as well as the renormalization of their frequency [61,62]. Since our treatment of this Hamiltonian is numerically complete, all of these phenomena are included in our results.

Finally, we take radiative recombination of the excitons with rate γ and cavity loss processes with rate κ into account by introducing Markovian Lindblad-type operators

$$\mathcal{L}_{O,\Gamma}\bullet = \Gamma\left(O \bullet O^\dagger - \frac{1}{2}\{\bullet, O^\dagger O\}_+\right), \tag{A5}$$

where $\{\cdot,\cdot\}_+$ denotes the anticommutator. O is a system operator and Γ the decay rate of the associated loss process.

The full Hamiltonian then reads as

$$H_{\mathrm{full}} = H + H_{\mathrm{Ph}} \tag{A6}$$

with the system Hamiltonian H as defined in Sec. II. The dynamics of these systems are then described by the Liouville–von Neumann equation

$$\frac{\partial}{\partial t}\rho = -\frac{i}{\hbar}\{H_{\mathrm{full}}, \rho\}_- + \mathcal{L}_{a,\kappa}\rho + \mathcal{L}_{\sigma_X,\gamma}\rho, \tag{A7}$$

where $\{\cdot,\cdot\}_-$ denotes the commutator.

A path-integral formalism [46,47,63,64] is used to solve Eq. (A7) in a numerically complete manner. Tracing out the phonon degrees of freedom analytically yields a phonon-induced memory kernel for the subsystem of interest H in Eq. (A6). We call a solution "numerically complete" if a finer time discretization and considering a longer memory do not change the result noticeably. Since the states considered in this paper are product states of the QD and number states of the cavity mode and therefore quite numerous, no solution within the path-integral framework could be obtained without the advances presented in Ref. [48].

TABLE II. Relevant system parameters.

QD-cavity coupling (meV)	$\hbar g$	0.1
Cavity loss rate (ps^{-1})	κ	0.0085
QD radiative decay rate (ps^{-1})	γ	0.001

APPENDIX B: DEFINITION OF THE OPTICAL WIGNER FUNCTION

The optical Wigner function, which is a function of the complex coherent amplitude α, can be obtained as [53–55]

$$W(\alpha) = 2\mathrm{Tr}[\rho_{\mathrm{photon}} D(\alpha)(-1)^{a^\dagger a} D(-\alpha)], \tag{B1}$$

where ρ_{photon} is the photonic density matrix of the system and $D(\alpha)$ the coherent displacement operator. The photonic density matrix is obtained by tracing out the phonon and QD degrees of freedom:

$$\rho_{\mathrm{photon}} = \mathrm{Tr}_{\mathrm{QD}}[\mathrm{Tr}_{\mathrm{Ph}}(\rho)]. \tag{B2}$$

Using the Fock basis and introducing $\rho'_{\mathrm{photon}}(\alpha) := D(-\alpha)\rho_{\mathrm{photon}} D(\alpha)$, this expression simplifies to

$$W(\alpha) = 2\sum_n [\rho'_{\mathrm{photon}}(\alpha)]_{nn}(-1)^n. \tag{B3}$$

APPENDIX C: PARAMETERS

For the numerical calculations we use typical parameters for self-assembled strongly confined GaAs/In(Ga)As QDs [48,65]. Other relevant parameters are summarized in Table II. Assuming a mode frequency of $\hbar\omega_{\mathrm{C}} = 1.5$ eV, the cavity loss rate κ corresponds to a quality factor $Q \approx 268\,000$, which has been reported in the experiments in Ref. [66]. The phonons are assumed to be initially in thermal equilibrium at a temperature of $T = 4$ K, whenever phonon effects are considered in this work.

On a timescale of $\approx$3 ps, the phonon-induced memory kernel for GaAs/In(Ga)As QDs of 6 nm diameter at $T = 4$ K decays to zero [46–48]. To obtain numerically complete converged results, a two-grid strategy is employed for the time discretization. Details can be found in Appendix A 3 of Ref. [38].

APPENDIX D: CALCULATION OF THE PHASE IN THE CAD PROTOCOL

The phase ϕ in Eq. (11) is the phase of the coherent state which is prepared in the cavity mode by the initial laser pulse driving the cavity. Since the pulse used to prepare the coherent state is short compared with the scale of the dynamics induced by the coupling to the QD, we can neglect the latter in the analysis of the preparation. In a frame corotating with the laser frequency, the Hamiltonian thus reduces to

$$H_{\text{driving}}(t) = -\frac{\hbar}{2}\left[f_{\text{p}}^{*}(t)a + f_{\text{p}}(t)a^{\dagger}\right]. \tag{D1}$$

Up to second order in the time increment Δt, the time evolution operator reads

$$\begin{aligned} U(t+\Delta t, t) &= e^{-\frac{i}{\hbar}H_{\text{driving}}(t)\Delta t} \\ &= D[u(t)\Delta t] \end{aligned} \tag{D2}$$

with $u(t) := \frac{i}{2}f_{\text{p}}(t)$ and the coherent displacement operator D. Using the relation $D(\alpha)D(\beta) = \exp\left[\text{Im}(\alpha\beta^{*})\right]D(\alpha+\beta)$ and noting that the phase vanishes since $u(t)$ is purely imaginary for real pulse envelopes, one obtains for a pulse with center t_c that is chosen such that at 0 and τ_{max} the envelope is essentially zero (again up to second order in Δt)

$$U(\tau_{\text{max}}, 0) = D[\alpha(\tau_{\text{max}})], \tag{D3}$$

with

$$\begin{aligned} \alpha(\tau_{\text{max}}) &= \int_0^{\tau_{\text{max}}} u(t)\,dt \\ &= \frac{i}{2}\int_0^{\tau_{\text{max}}} \frac{\Theta}{\sqrt{2\pi}\sigma} e^{-\frac{(t-t_c)^2}{2\sigma^2}} dt \approx \frac{i}{2}\Theta = \frac{\Theta}{2}e^{-i\phi} \end{aligned} \tag{D4}$$

with $\phi = 3\pi/2$.

[1] E. Schrödinger, Die gegenwärtige Situation in der Quantenmechanik, Naturwissenschaften **23**, 807 (1935).

[2] J. Joo, W. J. Munro, and T. P. Spiller, Quantum Metrology with Entangled Coherent States, Phys. Rev. Lett. **107**, 083601 (2011).

[3] A. Facon, E.-K. Dietsche, D. Grosso, S. Haroche, J.-M. Raimond, M. Brune, and S. Gleyzes, A sensitive electrometer based on a Rydberg atom in a Schrödinger-cat state, Nature (London) **535**, 262 (2016).

[4] S. J. van Enk and O. Hirota, Entangled coherent states: Teleportation and decoherence, Phys. Rev. A **64**, 022313 (2001).

[5] T. C. Ralph, A. Gilchrist, G. J. Milburn, W. J. Munro, and S. Glancy, Quantum computation with optical coherent states, Phys. Rev. A **68**, 042319 (2003).

[6] A. P. Lund, T. C. Ralph, and H. L. Haselgrove, Fault-Tolerant Linear Optical Quantum Computing with Small-Amplitude Coherent States, Phys. Rev. Lett. **100**, 030503 (2008).

[7] M. Mirrahimi, Z. Leghtas, V. V. Albert, S. Touzard, R. J. Schoelkopf, L. Jiang, and M. H. Devoret, Dynamically protected cat-qubits: A new paradigm for universal quantum computation, New J. Phys. **16**, 045014 (2014).

[8] N. Ofek, A. Petrenko, R. Heeres, P. Reinhold, Z. Leghtas, B. Vlastakis, Y. Liu, L. Frunzio, S. M. Girvin, L. Jiang, *et al.*, Extending the lifetime of a quantum bit with error correction in superconducting circuits, Nature (London) **536**, 441 (2016).

[9] D. Leibfried, E. Knill, S. Seidelin, J. Britton, R. B. Blakestad, J. Chiaverini, D. B. Hume, W. M. Itano, J. D. Jost, C. Langer, *et al.*, Creation of a six-atom 'Schrödinger cat' state, Nature (London) **438**, 639 (2005).

[10] W.-B. Gao, C.-Y. Lu, X.-C. Yao, P. Xu, O. Gühne, A. Goebel, Y.-A. Chen, C.-Z. Peng, Z.-B. Chen, and J.-W. Pan, Experimental demonstration of a hyper-entangled ten-qubit Schrödinger cat state, Nat. Phys. **6**, 331 (2010).

[11] D. D. Sedov, V. K. Kozin, and I. V. Iorsh, Chiral Waveguide Optomechanics: First Order Quantum Phase Transitions with $\mathbb{Z}_3$ Symmetry Breaking, Phys. Rev. Lett. **125**, 263606 (2020).

[12] D. E. Reiter, D. Wigger, V. M. Axt, and T. Kuhn, Generation and dynamics of phononic cat states after optical excitation of a quantum dot, Phys. Rev. B **84**, 195327 (2011).

[13] M. Brune, E. Hagley, J. Dreyer, X. Maître, A. Maali, C. Wunderlich, J. M. Raimond, and S. Haroche, Observing the Progressive Decoherence of the "Meter" in a Quantum Measurement, Phys. Rev. Lett. **77**, 4887 (1996).

[14] C. Gerry and P. L. Knight, *Introductory Quantum Optics* (Cambridge University Press, Cambridge, 2004).

[15] C. K. Law and J. H. Eberly, Arbitrary Control of a Quantum Electromagnetic Field, Phys. Rev. Lett. **76**, 1055 (1996).

[16] J. Gea-Banacloche, Collapse and Revival of the State Vector in the Jaynes-Cummings Model: An Example of State Preparation by a Quantum Apparatus, Phys. Rev. Lett. **65**, 3385 (1990).

[17] P. Michler, A. Kiraz, C. Becher, W. V. Schoenfeld, P. M. Petroff, L. Zhang, E. Hu, and A. Imamoglu, A quantum dot single-photon turnstile device, Science **290**, 2282 (2000).

[18] C. Santori, M. Pelton, G. Solomon, Y. Dale, and Y. Yamamoto, Triggered Single Photons from a Quantum Dot, Phys. Rev. Lett. **86**, 1502 (2001).

[19] C. Santori, D. Fattal, J. Vuckovic, and G. S. Solomon, Y. Yamamoto, Indistinguishable photons from a single-photon device, Nature (London) **419**, 594 (2002).

[20] Y.-M. He, Y. He, Y.-J. Wei, D. Wu, M. Atatüre, C. Schneider, S. Höfling, M. Kamp, C.-Y. Lu, and J.-W. Pan, On-demand semiconductor single-photon source with near-unity indistinguishability, Nat. Nanotechnol. **8**, 213 (2013).

[21] Y.-J. Wei, Y.-M. He, M.-C. Chen, Y.-N. Hu, Y. He, D. Wu, C. Schneider, M. Kamp, S. Höfling, C.-Y. Lu, and J.-W. Pan, Deterministic and robust generation of single photons from a single quantum dot with 99.5% indistinguishability using adiabatic rapid passage, Nano Lett. **14**, 6515 (2014).

[22] X. Ding, Y. He, Z.-C. Duan, N. Gregersen, M.-C. Chen, S. Unsleber, S. Maier, C. Schneider, M. Kamp, S. Höfling, *et al.*, On-Demand Single Photons with High Extraction Efficiency and Near-Unity Indistinguishability from a Resonantly Driven Quantum Dot in a Micropillar, Phys. Rev. Lett. **116**, 020401 (2016).

[23] N. Somaschi, V. Giesz, L. De Santis, J. C. Loredo, M. P. Almeida, G. Hornecker, S. L. Portalupi, T. Grange, C. Antón, J. Demory, *et al.*, Near-optimal single-photon sources in the solid state, Nat. Photonics **10**, 340 (2016).

[24] L. Schweickert, K. D. Jöns, K. D. Zeuner, S. F. Covre da Silva, H. Huang, T. Lettner, M. Reindl, J. Zichi, R. Trotta, A. Rastelli, and V. Zwiller, On-demand generation of background-free single photons from a solid-state source, Appl. Phys. Lett. **112**, 093106 (2018).

[25] L. Hanschke, K. A. Fischer, S. Appel, D. Lukin, J. Wierzbowski, S. Sun, R. Trivedi, J. Vučković, J. J. Finley, and K. Müller, Quantum dot single-photon sources with ultra-low multi-photon probability, npj Quantum Inf. **4**, 43 (2018).

[26] M. Cosacchi, F. Ungar, M. Cygorek, A. Vagov, and V. M. Axt, Emission-Frequency Separated High Quality Single-Photon Sources Enabled by Phonons, Phys. Rev. Lett. **123**, 017403 (2019).

[27] N. Akopian, N. H. Lindner, E. Poem, Y. Berlatzky, J. Avron, D. Gershoni, B. D. Gerardot, and P. M. Petroff, Entangled Photon Pairs from Semiconductor Quantum Dots, Phys. Rev. Lett. **96**, 130501 (2006).

[28] R. M. Stevenson, R. J. Young, P. Atkinson, K. Cooper, D. A. Ritchie, and A. J. Shields, A semiconductor source of triggered entangled photon pairs, Nature (London) **439**, 179 (2006).

[29] R. Hafenbrak, S. M. Ulrich, P. Michler, L. Wang, A. Rastelli, and O. G. Schmidt, Triggered polarization-entangled photon pairs from a single quantum dot up to 30K, New J. Phys. **9**, 315 (2007).

[30] A. Dousse, J. Suffczynski, A. Beveratos, O. Krebs, A. Lemaître, I. Sagnes, J. Bloch, P. Voisin, and P. Senellart, Ultrabright source of entangled photon pairs, Nature (London) **466**, 217 (2010).

[31] S. Schumacher, J. Förstner, A. Zrenner, M. Florian, C. Gies, P. Gartner, and F. Jahnke, Cavity-assisted emission of polarization-entangled photons from biexcitons in quantum dots with fine-structure splitting, Opt. Express **20**, 5335 (2012).

[32] E. del Valle, Distilling one, two and entangled pairs of photons from a quantum dot with cavity QED effects and spectral filtering, New J. Phys **15**, 025019 (2013).

[33] M. Müller, S. Bounouar, K. D. Jöns, M. Glässl, and P. Michler, On-demand generation of indistinguishable polarization-entangled photon pairs, Nat. Photonics **8**, 224 (2014).

[34] C. S. Muñoz, F. P. Laussy, C. Tejedor, and E. del Valle, Enhanced two-photon emission from a dressed biexciton, New J. Phys. **17**, 123021 (2015).

[35] D. Heinze, A. Zrenner, and S. Schumacher, Polarization-entangled twin photons from two-photon quantum-dot emission, Phys. Rev. B **95**, 245306 (2017).

[36] A. Orieux, M. A. M. Versteegh, K. D. Jöns, and S. Ducci, Semiconductor devices for entangled photon pair generation: A review, Rep. Prog. Phys. **80**, 076001 (2017).

[37] T. Seidelmann, F. Ungar, A. M. Barth, A. Vagov, V. M. Axt, M. Cygorek, and T. Kuhn, Phonon-Induced Enhancement of Photon Entanglement in Quantum Dot-Cavity Systems, Phys. Rev. Lett. **123**, 137401 (2019).

[38] M. Cosacchi, J. Wiercinski, T. Seidelmann, M. Cygorek, A. Vagov, D. E. Reiter, and V. M. Axt, On-demand generation of higher-order Fock states in quantum-dot–cavity systems, Phys. Rev. Res. **2**, 033489 (2020).

[39] A. J. Ramsay, A. V. Gopal, E. M. Gauger, A. Nazir, B. W. Lovett, A. M. Fox, and M. S. Skolnick, Damping of Exciton Rabi Rotations by Acoustic Phonons in Optically Excited InGaAs/GaAs Quantum Dots, Phys. Rev. Lett. **104**, 017402 (2010).

[40] D. E. Reiter, T. Kuhn, and V. M. Axt, Distinctive characteristics of carrier-phonon interactions in optically driven semiconductor quantum dots, Adv. Phys. X **4**, 1655478 (2019).

[41] T. Unold, K. Mueller, C. Lienau, T. Elsaesser, and A. D. Wieck, Optical Stark Effect in a Quantum Dot: Ultrafast Control of Single Exciton Polarizations, Phys. Rev. Lett. **92**, 157401 (2004).

[42] L. Besombes, K. Kheng, L. Marsal, and H. Mariette, Acoustic phonon broadening mechanism in single quantum dot emission, Phys. Rev. B **63**, 155307 (2001).

[43] P. Borri, W. Langbein, S. Schneider, U. Woggon, R. L. Sellin, D. Ouyang, and D. Bimberg, Ultralong Dephasing Time in InGaAs Quantum Dots, Phys. Rev. Lett. **87**, 157401 (2001).

[44] B. Krummheuer, V. M. Axt, and T. Kuhn, Theory of pure dephasing and the resulting absorption line shape in semiconductor quantum dots, Phys. Rev. B **65**, 195313 (2002).

[45] V. M. Axt, T. Kuhn, A. Vagov, and F. M. Peeters, Phonon-induced pure dephasing in exciton-biexciton quantum dot systems driven by ultrafast laser pulse sequences, Phys. Rev. B **72**, 125309 (2005).

[46] A. Vagov, M. D. Croitoru, M. Glässl, V. M. Axt, and T. Kuhn, Real-time path integrals for quantum dots: Quantum dissipative dynamics with superohmic environment coupling, Phys. Rev. B **83**, 094303 (2011).

[47] A. M. Barth, A. Vagov, and V. M. Axt, Path-integral description of combined Hamiltonian and non-Hamiltonian dynamics in quantum dissipative systems, Phys. Rev. B **94**, 125439 (2016).

[48] M. Cygorek, A. M. Barth, F. Ungar, A. Vagov, and V. M. Axt, Nonlinear cavity feeding and unconventional photon statistics in solid-state cavity QED revealed by many-level real-time path-integral calculations, Phys. Rev. B **96**, 201201(R) (2017).

[49] A. Vagov, V. M. Axt, T. Kuhn, W. Langbein, P. Borri, and U. Woggon, Nonmonotonous temperature dependence of the initial decoherence in quantum dots, Phys. Rev. B **70**, 201305(R) (2004).

[50] R. Jozsa, Fidelity for mixed quantum states, J. Mod. Opt. **41**, 2315 (1994).

[51] A. Kenfack and K. Życzkowski, Negativity of the Wigner function as an indicator of non-classicality, J. Opt. B **6**, 396 (2004).

[52] J. Gea-Banacloche, Atom- and field-state evolution in the Jaynes-Cummings model for large initial fields, Phys. Rev. A **44**, 5913 (1991).

[53] W. H. Louisell, *Quantum Statistical Properties of Radiation* (Wiley, New York, 1973).

[54] K. E. Cahill and R. J. Glauber, Density operators and quasiprobability distributions, Phys. Rev. **177**, 1882 (1969).

[55] K. E. Cahill and R. J. Glauber, Ordered expansions in boson amplitude operators, Phys. Rev. **177**, 1857 (1969).

[56] M. Hofheinz, H. Wang, M. Ansmann, R. C. Bialczak, E. Lucero, M. Neeley, A. D. O'Connell, D. Sank, J. Wenner, J. M. Martinis, and A. N. Cleland, Synthesizing arbitrary quantum states in a superconducting resonator, Nature (London) **459**, 546 (2009).

[57] D. E. Reiter, T. Kuhn, M. Glässl, and V. M. Axt, The role of phonons for exciton and biexciton generation in an optically

driven quantum dot, J. Phys.: Condens. Matter **26**, 423203 (2014).

[58] S. Mukamel, *Principles of Nonlinear Optics and Spectroscopy* (Oxford University Press, Oxford, 1995).

[59] D. P. S. McCutcheon, Optical signatures of non-Markovian behavior in open quantum systems, Phys. Rev. A **93**, 022119 (2016).

[60] P. Machnikowski and L. Jacak, Resonant nature of phonon-induced damping of Rabi oscillations in quantum dots, Phys. Rev. B **69**, 193302 (2004).

[61] A. Krügel, V. M. Axt, T. Kuhn, P. Machnikowski, and A. Vagov, The role of acoustic phonons for Rabi oscillations in semiconductor quantum dots, Appl. Phys. B **81**, 897 (2005).

[62] A. J. Ramsay, T. M. Godden, S. J. Boyle, E. M. Gauger, A. Nazir, B. W. Lovett, A. M. Fox, and M. S. Skolnick, Phonon-Induced Rabi-Frequency Renormalization of Optically Driven Single InGaAs/GaAs Quantum Dots, Phys. Rev. Lett. **105**, 177402 (2010).

[63] N. Makri and D. E. Makarov, Tensor propagator for iterative quantum time evolution of reduced density matrices. I. Theory, J. Chem. Phys. **102**, 4600 (1995).

[64] N. Makri and D. E. Makarov, Tensor propagator for iterative quantum time evolution of reduced density matrices. II. Numerical methodology, J. Chem. Phys. **102**, 4611 (1995).

[65] B. Krummheuer, V. M. Axt, T. Kuhn, I. D'Amico, and F. Rossi, Pure dephasing and phonon dynamics in GaAs- and GaN-based quantum dot structures: Interplay between material parameters and geometry, Phys. Rev. B **71**, 235329 (2005).

[66] C. Schneider, P. Gold, S. Reitzenstein, S. Höfling, and M. Kamp, Quantum dot micropillar cavities with quality factors exceeding 250,000, Appl. Phys. B **122**, 19 (2016).

Publication 10

Numerically exact open quantum systems simulations for arbitrary environments using automated compression of environments.

M. Cygorek, **M. Cosacchi**, A. Vagov, V. M. Axt, B. W. Lovett, J. Keeling, E. M. Gauger.

arXiv:2101.01653 (2021), under review at *Nature Physics*.

arXiv:2101.01653 (2021)

Author contributions

M. Cygorek had the original idea to generalize the real-time path-integral method for diagonal coupling to an environment to the explicit construction of the process tensor to simulate arbitrary open quantum systems. He is responsible for the details of the algorithm, its implementation in a C++ library, the generation of the data, the design of the figures, and the first draft of the paper. He has moderated all discussions and revision requests of the draft, has organized the correspondence with the editor and referees, and has provided the first drafts of answers to the referees.

The author has addressed the question, how to incorporate the off-diagonal coupling of a quantum few-level system to an environment of photons into the path-integral framework under supervision of and in discussion with M. Cygorek, A. Vagov, and V. M. Axt. During these studies, it turned out that no closed expression of a generalized influence functional can be obtained analytically.

M. Cygorek, B. W. Lovett, J. Keeling, and E. M. Gauger have found a numerically efficient representation of the process tensor in terms of matrix product operators based upon the preliminary work conducted by M. Cygorek, A. Vagov, V. M. Axt, and the author.

All authors have participated in the discussion and interpretation of the results and have contributed to revisions of the draft and the answers to the referees.

Numerically exact open quantum systems simulations for arbitrary environments using automated compression of environments

Moritz Cygorek,[1] Michael Cosacchi,[2] Alexei Vagov,[2] Vollrath Martin Axt,[2]
Brendon W. Lovett,[3] Jonathan Keeling,[3] and Erik M. Gauger[1]

[1] *SUPA, Institute of Photonics and Quantum Sciences, Heriot-Watt University, Edinburgh, EH14 4AS, United Kingdom*
[2] *Theoretische Physik III, Universität Bayreuth, 95440 Bayreuth, Germany*
[3] *SUPA, School of Physics and Astronomy, University of St Andrews, St Andrews, KY16 9SS, United Kingdom*

The central challenge for describing the dynamics in open quantum systems is that the Hilbert space of typical environments is too large to be treated exactly. In some cases, such as when the environment has a short memory time or only interacts weakly with the system, approximate descriptions of the system are possible. Beyond these, numerically exact methods exist, but these are typically restricted to baths with Gaussian correlations, such as non-interacting bosons. Here we present a numerically exact method for simulating open quantum systems with arbitrary environments which consist of a set of independent degrees of freedom. Our approach automatically reduces the large number of environmental degrees of freedom to those which are most relevant. Specifically, we show how the process tensor—which describes the effect of the environment—can be iteratively constructed and compressed using matrix product state techniques. We demonstrate the power of this method by applying it to problems with bosonic, fermionic, and spin environments: electron transport, phonon effects and radiative decay in quantum dots, central spin dynamics, anharmonic environments, dispersive coupling to time-dependent lossy cavity modes, and superradiance. The versatility and efficiency of our automated compression of environments (ACE) method provides a practical general-purpose tool for open quantum systems.

An inevitable property of quantum technologies is that quantum devices interact with their environment [1]. This interaction gives rise to dephasing and dissipation but, if understood, it can be exploited for example in environment-assisted quantum transport [2–4], or even quantum information processing [5, 6]. Because of the exponential growth of Hilbert space dimension, and the large number of environmental degrees of freedom, the direct solution of Schrödinger's equation for system and environment is usually infeasible. As such, one requires practical methods that allow simulation of the dynamics of the system, while accounting for effects of the environment [1, 7–9].

Among such approaches, those most frequently used rely on the Born and Markov approximations, which enable one to derive time-local equations of motion for the reduced system density matrix [1, 10]. The Born approximation implies that the environment does not change significantly with time—i.e. that system-environment correlations are weak and transient. While valid for weakly coupled open quantum systems, other environments lead to strong system-environment correlations [11]. The Markov approximation depends on the memory time of the environment being short compared to the time evolution of the system. This fails if the spectral density is highly structured, or if there is a long memory time [12]. Given these widespread limitations, approaches beyond the Born–Markov approximation are clearly necessary.

Numerically exact methods—where tuning convergence parameters allows one to trade off precision against computation time—do exist for some non-Markovian problems: those where the environments have Gaussian correlations, such as non-interacting bosonic modes. Such methods include hierarchical equations of motion (HEOM) [13, 14], chain mapping through orthogonal polynomials [15–17], or the Feynman-Vernon real-time path integral formalism [18]. In particular, the iterative form of the path integral [19–21] and its reformulation with matrix product operators [22] have been used successfully, e.g., to simulate phonon effects on spectra [23, 24], to devise robust and high-fidelity protocols for the emission of nonclassical light [25–27], and to model concrete experiments on optically driven quantum dots [28–30]. Such approaches have been extended to systems with multiple environments [31], to multi-level systems [21], and to special types of non-Gaussian baths such as quadratic coupling to bosons or fermions [32]. Some methods for general environments do exist, such as correlation expansion [33], but it is complicated to derive these equations at higher expansion order. As such, a challenge remains: to provide general and efficient numerically exact methods which can also model non-Gaussian non-Markovian environments.

Here we provide such a method, which can be used to simulate open quantum systems coupled to arbitrary environments (see Fig. 1a). We demonstrate its practical application with a variety of forms of environment—bosonic, fermionic, and spins. Because the derivation is general the same code can be used to simulate the dynamics of a large variety of different physical systems. At the core of our *automated compression of environments* (ACE) method is the explicit microscopic construction of the process tensor (PT) [34, 35]—an object originally conceived as a way to conceptualize correlations for a general non-Markovian environment—and a route to efficiently compress this object using matrix product operator (MPO) techniques [36, 37]. Specifically, we provide a general and efficient algorithm to directly construct an

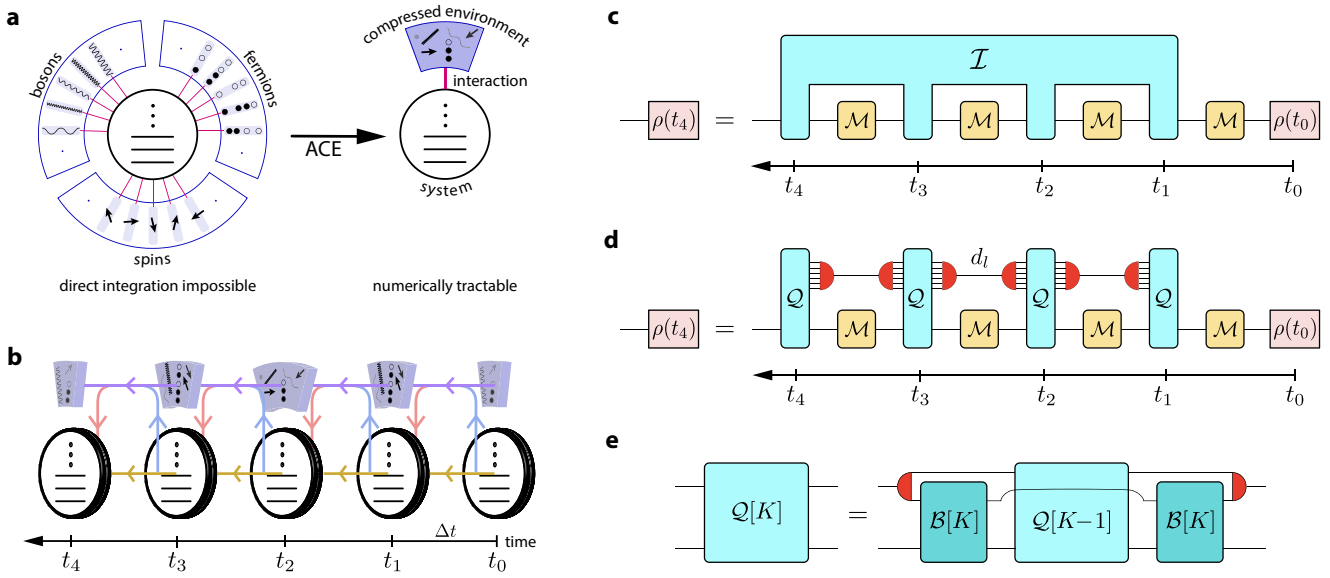

FIG. 1. **Depiction of the automated compression of environments approach. a,** The identification of an efficient representation is fully automatic and does not rely on any a priori approximations or assumptions. **b,** The time evolution of system plus its compressed environment proceeds in discrete time steps. Information flow is indicated by the coloured arrows. **c,** Formally, the general propagation of a quantum system can be expressed with a process tensor $\mathcal{I}$. **d,** Propagation with a process tensor in MPO form: this corresponds to the schematic situation depicted in panel b. **e,** Combination of the influence of environment mode K with the process tensor containing the influences of modes $1, 2, \ldots, K-1$. Red semicircles indicate the effects of the MPO compression (as depicted schematically in panels a and b).

MPO representation of the PT, corresponding to an automated projection of the environment onto its most relevant degrees of freedom.

Results

Automated compression of environments. The working principle of ACE is to represent the environment efficiently by concentrating on its most relevant degrees of freedom (cf. Fig. 1a). These are selected automatically using MPO compression techniques and may differ from one time step to another. This procedure guarantees fully capturing the non-Markovian information flow from past time steps to later time steps via the environment (cf. Fig. 1b). We now summarise the ACE method introduced in this paper; further details are provided in the Methods section. Our goal is to obtain the reduced system density matrix $\rho_{\nu\mu}(t)$ at a time t, accounting for coupling to a given environment. We discretise the time axis on a grid $t_l = l\Delta t$ with equal time steps Δt (Fig. 1b-d); then, for a single time step, the time evolution operator $U(\Delta t) = e^{-\frac{i}{\hbar}H\Delta t}$ of the total system can be factorised using the Trotter expansion $U(\Delta t) = e^{-\frac{i}{\hbar}H_E\Delta t}e^{-\frac{i}{\hbar}H_S\Delta t} + \mathcal{O}(\Delta t^2)$, where the total Hamiltonian $H = H_S + H_E$ is decomposed into the system Hamiltonian H_S and the environment Hamiltonian H_E including the system-environment coupling. Inserting a complete set of basis states for the system and the environment and tracing out the environment, the reduced system density matrix at time t_n can be written

$$\rho_{\alpha_n} = \sum_{\substack{\alpha_{n-1}\ldots\alpha_0 \\ \tilde{\alpha}_n\ldots\tilde{\alpha}_1}} \mathcal{I}^{(\alpha_n\tilde{\alpha}_n)\ldots(\alpha_1\tilde{\alpha}_1)} \left(\prod_{l=1}^{n} \mathcal{M}^{\tilde{\alpha}_l\alpha_{l-1}} \right) \rho_{\alpha_0}, \quad (1)$$

where we have defined $\alpha = (\nu, \mu)$ to combine two Hilbert space indices into a single Liouville space index. A visual representation of Eq. (1) is depicted in Fig. 1c. Here, $\mathcal{M}$ describes the free propagation of the system. This can be time-dependent, and can additionally include effects of Markovian baths. The effects of the general non-Markovian non-Gaussian environment are captured in the quantity $\mathcal{I}$, which we refer to as the process tensor (PT). This object differs slightly from the original definition of the PT [35], in that we have separated out the initial state and the free system evolution. When $\mathcal{I}$ is non-zero only for diagonal couplings $\alpha_l = \tilde{\alpha}_l$ this object becomes equivalent to the Feynman-Vernon influence functional [18]. The PT can thus be considered as a generalisation of this influence functional to the case of non-diagonal couplings. From the explicit expression for the PT we find that it automatically has the form of an MPO:

$$\mathcal{I}^{(\alpha_n,\tilde{\alpha}_n)(\alpha_{n-1},\tilde{\alpha}_{n-1})\ldots(\alpha_1,\tilde{\alpha}_1)} = \sum_{d_{n-1}\ldots d_1} \mathcal{Q}_{1d_{n-1}}^{(\alpha_n,\tilde{\alpha}_n)} \mathcal{Q}_{d_{n-1}d_{n-2}}^{(\alpha_{n-1},\tilde{\alpha}_{n-1})} \cdots \mathcal{Q}_{d_1 1}^{(\alpha_1,\tilde{\alpha}_1)}. \quad (2)$$

Here the dimension of the inner indices d_l is very large, corresponding to a complete basis of environment states

in Liouville space. This large dimension precludes the direct application of Eqs. (1) and (2) for typical environments. However, the MPO form of the PT means it is in principle amenable to standard MPO compression, based on singular value decomposition as described in the Methods [36, 37]. Such compression corresponds physically to reducing the environment to its most relevant degrees of freedom, which, as theoretical consideration of PTs suggest [38], may be few in number.

The key challenge is thus to find an efficient way to calculate the compressed form of the PT MPO, without first constructing the uncompressed PT. This can be achieved through the ACE approach, for any problem with an environment that can be decomposed into N_E different noninteracting degrees of freedom:

$$H = H_S + \sum_{k=1}^{N_E} H_E^k. \tag{3}$$

The label k can describe both the different degrees of freedom within a bath (e.g. different spins, or photon modes defined by their wave vector $\mathbf{q}$), but can also enumerate multiple environments coupled to the same system. In all of these cases, the PT can be constructed iteratively, by adding successively the contribution of each bath degree of freedom. The process of combining the influence of the K-th degree of freedom, $\mathcal{B}[K]$, with an existing PT MPO $Q[K-1]$ is shown in Fig. 1e. If the resulting MPOs are compressed after each step (red semicircles), the inner dimension remains manageable and exact diagonalisation can be used for the singular value decomposition. This is described in more detail in the Methods section.

Once one has the compressed PT in MPO representation, this can be substituted into Eq. (1). The calculation of the reduced system density matrix then amounts to the contraction of a network of the form shown in Fig. 1d. If the PT MPO has a sufficiently small inner dimension, this contraction is straightforward. Because this algorithm can be applied in principle to arbitrary environments simply by specifying the respective environment Hamiltonians H_E^k, ACE allows investigations of a huge variety of different open quantum systems. We next show how this method works in practice for a few paradigmatic example problems.

Resonant-level model. As a first test of ACE, we consider the archetypal problem of electron transport between a single localised electron state and other nearby environment states, described by the resonant-level model. The k-th environment state is described by

$$H_E^k = \hbar\omega_k c_k^\dagger c_k + \hbar g_k (c_k^\dagger c_S + c_S^\dagger c_k), \tag{4}$$

where $c_S^\dagger(c_S)$ and $c_k^\dagger(c_k)$ create (destroy) a fermion in the localised system state and the k-th environment state, respectively, $\hbar\omega_k$ is the energy of the k-th environment state with respect to the system state, and g_k is the coupling constant, which we assume to be independent of k, $g_k = g$. The free system Hamiltonian is $H_S = 0$. The Hamiltonian in Eq. (4) shows distinct behaviour depending on the number of environment modes: coherent oscillations for few modes, and irreversible decay for a broad continuum of modes. In the following we show that ACE can automatically capture both these limits, and interpolate between them.

For a few environment modes, the dynamics is described by coherent oscillations at the eigenfrequencies of the coupled system and environment. Here, we consider the situation depicted in the inset of Fig. 2a where a single initially empty site is connected to two sites at the same energy $\omega_k = 0$, which are initially occupied. In this scenario the time-dependent many-body state of the total system is

$$|\Psi(t)\rangle = \left[\cos(\sqrt{2}gt)\frac{c_1^\dagger + c_2^\dagger}{\sqrt{2}} - i\sin(\sqrt{2}gt)c_S^\dagger\right]\frac{c_1^\dagger - c_2^\dagger}{\sqrt{2}}|0\rangle. \tag{5}$$

In Figure 2a, we compare the occupation $n_S = \sin^2(\sqrt{2}gt)$ to the results of ACE simulations for convergence parameters $\Delta t = 0.01g$ and $\epsilon = 10^{-7}$ (see Methods). We see the results match perfectly. Since the oscillations are undamped, the memory time of the environment is infinite. Furthermore, whenever $n_S = \frac{1}{2}$, Eq. (5) describes a state with maximal entanglement between system and environment. This demonstrates that ACE can account for infinite memory times as well as strong system-environment correlations.

Different behaviour occurs for a quasi-continuum of environment states, e.g., metallic leads coupled to a quantum dot [39], as depicted in the top left inset of Fig. 2b. The oscillatory contributions of the different modes interfere destructively, suppressing oscillations. When the continuum is broad enough, there is a short memory time and weak system-bath correlations, so the situation is well described by Markovian master equations. These predict charge transfer to the localised state at a rate $\gamma = 2\pi\hbar g^2 D$, where $D = (N_E - 1)/(\hbar\omega_{BW})$ is the density of states and $\hbar\omega_{BW}$ is the bandwidth. Figure 2b shows the corresponding dynamics for different numbers of environment modes N_E with a fixed density of states $D = 1/(\hbar\gamma)$. As the number of environment modes (and therefore the bandwidth) increases, the simulations approach the Markovian analytic result $1 - \exp(-\gamma t)$. For intermediate $N_E = 10$, the finite bandwidth introduces a finite memory time $\sim 1/\omega_{BW}$. To check the validity of the ACE results in this more complicated crossover regime, we also plot the analytic short-time Taylor expansion, $n_S \approx \gamma\omega_{BW}t^2/(2\pi)$ for the case $N_E = 10$.

The inset in Fig. 2b shows the maximal inner dimension $d_{\max}$ of the PT MPO as a function of the number of modes N_E. We see this scales linearly with the number of modes, indicating a very efficient reduction, compared to the exponential scaling of the dimension of the full environment Liouville space of up to $4^{100} \approx 1.6 \times 10^{60}$ for $N_E = 100$. A more detailed analysis of numerical convergence is given in the Supplemental Material S.2. This

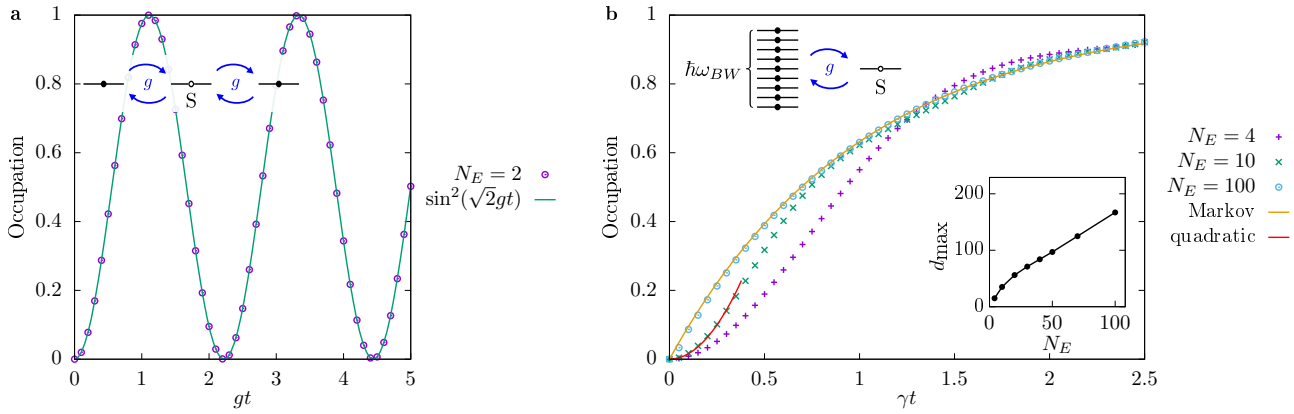

FIG. 2. **Resonant-level model application of ACE, spanning small to infinite bath memory time. a,** Dynamics of the occupations of a single localised quantum state (S) coupled to two resonant environment modes. **b,** Dynamics of a quantum state coupled to a quasi-continuum of modes. ACE simulations (points) are shown together with analytic solutions (lines). In b, the analytic result in the Markov limit corresponds to an exponential transfer with the rate obtained from Fermi's golden rule. The result of a quadratic Taylor expansion around $t = 0$ is depicted for the case $N_E = 10$. The top left insets depict the respective physical situations. The bottom right inset in b shows the maximal inner dimension $d_{\max}$ of the PT MPO as a function of the number of environment states N_E for constant density of states.

simple example demonstrates that ACE is able to reproduce analytic results in all regimes from infinite memories to Markovian environments and from strong to weak system-environment correlations.

Simultaneous coupling of quantum dots to phonons and electromagnetic field modes. Our second example involves a system coupled simultaneously to two structured baths, as exemplified by a semiconductor quantum dot, coupled both to acoustic phonons and an electromagnetic environment. The acoustic phonon modes couple via a pure-dephasing interaction:

$$H_{\text{ph}}^{\mathbf{q}} = \hbar\omega_{\mathbf{q}} b_{\mathbf{q}}^\dagger b_{\mathbf{q}} + \hbar\gamma_{\mathbf{q}}\big(b_{\mathbf{q}}^\dagger + b_{\mathbf{q}}\big)|X\rangle\langle X|, \tag{6}$$

where $b_{\mathbf{q}}^\dagger$ ($b_{\mathbf{q}}$) creates (annihilates) a phonon with wave vector $\mathbf{q}$ and $|X\rangle$ denotes the exciton state of the quantum dot. If this were the only interaction, its linear and diagonal structure would mean it could be treated within the iterative quasi-adiabatic path integral (iQUAPI) method [19, 21, 23]. We will use this below to compare the results of ACE to that of iQUAPI.

In addition to the bath of phonons, QDs also couple to the continuum of electromagnetic modes, which are responsible for radiative decay. Here the interaction with photon mode k takes the Jaynes-Cummings form:

$$H_{JC}^{k} = \hbar\omega_k a_k^\dagger a_k + \hbar g_k\big(a_k^\dagger|G\rangle\langle X| + a_k|X\rangle\langle G|\big), \tag{7}$$

where $a_k^\dagger$ (a_k) is the bosonic creation (annihilation) operator for a photon in mode k.

There are several ways of including both baths in simulations: First, for unstructured (i.e. Markovian) photon environments, the Born–Markov approximation holds, so we can account for the radiative decay as a Lindblad term, $\kappa\mathcal{L}\big[|G\rangle\langle X|, \rho\big]$ where

$$\mathcal{L}\big[|G\rangle\langle X|, \rho\big] \equiv |G\rangle\langle X|\rho|X\rangle\langle G| - \tfrac{1}{2}\big(|X\rangle\langle X|\rho + \rho|X\rangle\langle X|\big). \tag{8}$$

In both ACE and iQUAPI [40], such Markovian dissipation can be included into the free system Liouville propagator $\mathcal{M}$. Due to the flexibility of ACE, we can also describe the radiative decay microscopically by including both the phonon and electromagnetic environments in the PT. This has the advantage that it automatically captures possible non-additive effects of the simultaneous coupling to multiple baths [41–43], and also allows one to extend to structured electromagnetic environments.

In Fig. 3a, we show how the occupation of a QD responds to off-resonant excitation by a Gaussian laser pulse. This drive corresponds to the following time-dependent Hamiltonian in the rotating frame of the laser:

$$H_S = -\hbar\delta|X\rangle\langle X| + \tfrac{\hbar}{2}\Omega(t)\big(|X\rangle\langle G| + |G\rangle\langle X|\big), \tag{9}$$

where δ is the laser detuning and $\Omega(t)$ is a Gaussian envelope centred at $t_0 = 7$ ps with pulse duration $\tau_{\text{FWHM}} = 5$ ps. The QD simultaneously interacts with the phonon and photon baths, which are treated within different theoretical approaches. In this figure we assume a flat electromagnetic environment, so all approaches should work equally well. The simulation parameters are summarised in the Methods section.

In the absence of QD-phonon interactions, the exciton is only occupied transiently during the pulse, as absorption is suppressed by the detuning of the laser from the exciton energy. Including phonons within ACE but disregarding radiative decay entirely results in a nonzero stationary exciton occupation, as the detuning may be bridged by phonon emission. Including both

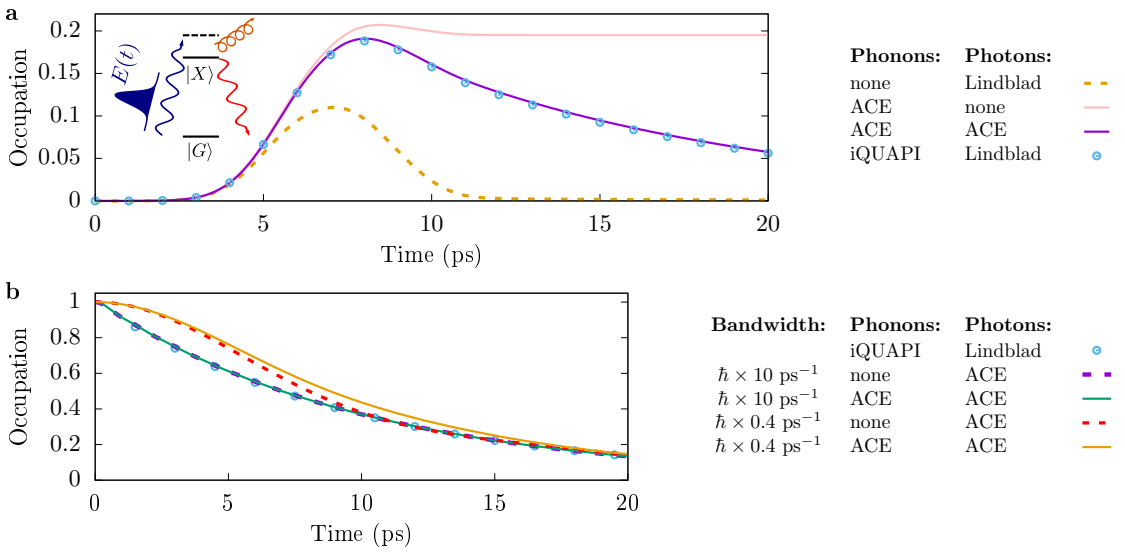

FIG. 3. **Dynamics of quantum dots embedded in (non-additive) photon and phonon environments. a,** Dynamics of the exciton occupation for phonon-assisted off-resonant excitation of a QD driven by a Gaussian laser pulse and subject to radiative decay according to different theoretical approaches: The QD-phonon interaction may be disregarded (none) or treated within ACE or iQUAPI. The coupling between the QD and the photonic modes may be disregarded (none), included explicitly in ACE via its Hamiltonian, or replaced by a Lindblad term for radiative decay. **b,** Radiative decay of an initially occupied exciton state with and without interactions with phonons for model photon densities of states with different bandwidths $\hbar\omega_{BZ}$.

phonons and photons, one sees absorption followed by radiative decay. Identical results are found for this case for both ACE—treating the electromagnetic environment microscopically—and for iQUAPI with photon decay $\kappa\mathcal{L}\big[|G\rangle\langle X|,\rho\big]$. As such, we both further confirm the capabilities of ACE, and see that—as may be anticipated—for an unstructured photon environment, no cross-action between the coupling to photon and phonon baths can be identified.

As already noted, ACE is also able to treat situations with non-additive environments, as is relevant for structured photonic environments like waveguides or microcavities [44, 45]. Figure 3b shows the decay of an initially occupied exciton state (with $H_S = 0$) where, in addition to the non-Markovian phonon bath, we use a photon bath with a finite bandwidth $\hbar\omega_{BW}$. For large bandwidths, no cross-interaction between the couplings to the two baths is found (and so the results again match iQUAPI with Lindbladian photon loss). For small bandwidths $\omega_{BW} = 0.4$ ps^{-1}, the photon environment obtains a memory time $\tau \sim 1/\omega_{BW}$ of the same order of magnitude as the phonon environment. As a result the two baths couple non-additively, as can be seen by the fact that the coupling to phonons significantly influences the decay of excitations into the electromagnetic modes.

Spin dynamics. Our third example concerns the spin dynamics in the presence of a spin environment [46, 47]. Besides demonstrating the applicability of ACE to non-Gaussian spin environments, this example also identifies the limits on efficient environment compression. We consider a central spin coupled to a bath of environment spins by a Heisenberg interaction

$$H_E^k = \frac{J_k}{\hbar^2}\,\hat{\mathbf{S}}\cdot\hat{\mathbf{s}}_k, \tag{10}$$

where $\hat{\mathbf{S}}$ and $\hat{\mathbf{s}}_k$ are the spin-$\frac{1}{2}$ operators of the central spin and the k-th environment spin, respectively—see inset of Fig. 4. In the following we choose the coupling constants $J_k = J/N$, where N is the number of environment spins and J defines the energy scale of the coupling. We set $H_S = 0$ and initially prepare the system spin in the state with maximal $\langle S_x\rangle$. We then explore how the initial degree of polarisation of the environment affects the system dynamics, and the ability to efficiently compress the environment.

First, we focus on the situation where the environment spins are completely polarised along the z-axis. The respective dynamics of $\langle S_x\rangle$ is depicted in Fig. 4a for different numbers of environment spins $N = 10$, $N = 100$, and $N = 1000$ and for convergence parameters $\Delta t = 0.01\hbar/J$ and $\epsilon = 10^{-10}$. The Heisenberg coupling leads to a coherent precession of the system and environment spins about each other. In the limit $N \to \infty$, there is no back-action on the environment so the environment remains in its initial state. The dynamics is then equivalent to a precession about a constant effective magnetic field, for which $\langle S_x\rangle = (\hbar/2)\cos\big[(tJ)/(2\hbar)\big]$. We see the ACE simulations for $N = 1000$ approach this limit. It is noteworthy that for all N the inner dimension of the PT MPO remains 4, corresponding to the Liouville space dimension of a single spin $\frac{1}{2}$. This is because all environ-

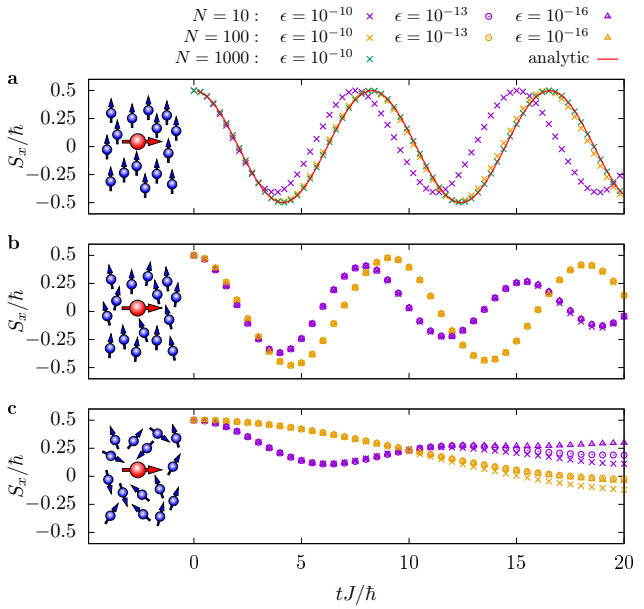

FIG. 4. **Central spin model for different degrees of spin bath polarisation.** Dynamics of a central spin (red) initially prepared along the x-axis in a bath of N spins (blue) as depicted in the insets. The x-component of a central spin is shown for situations where the bath spins are fully polarised **a,** partially polarised **b,** or unpolarised **c**. The number of environment spins N is varied keeping the sum of the couplings $\sum_k J_k = J$ constant. Colours correspond to different numbers of environment spins N while point types correspond to different values of the MPO compression threshold ϵ.

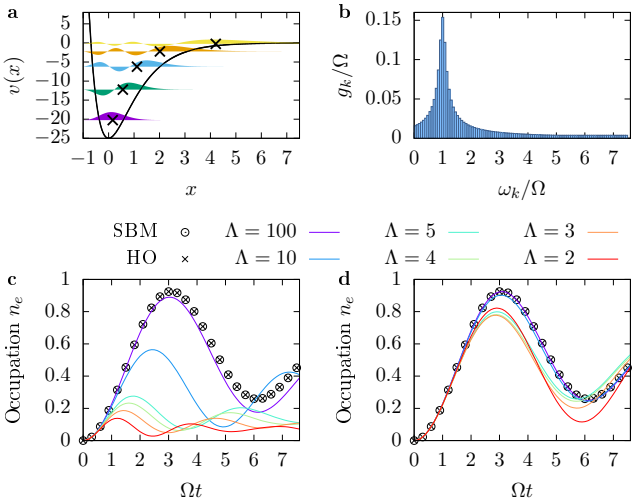

FIG. 5. **Two-level system coupled to a bath of anharmonic modes.** **a**: Morse potential, Eq. (11), with parameter $\Lambda = 5$ and its bound eigenstates obtained numerically. Crosses mark the average position $\langle i|\hat{x}|i\rangle$ for each eigenstate. **b**: Coupling coefficients g_k corresponding to a Lorentzian spectral density of environment modes. **c**: ACE simulations with $M = \min\{5, \Lambda\}$ environment levels for: the spin-boson model (SBM), harmonic oscillator (HO) modes obtained by the finite differences method, and finite differences solutions of the Morse potential for different Λ. **d**: Analogous calculations to **c** but where energy shifts due to non-zero $\langle i|\hat{x}|i\rangle$ have been subtracted.

ment spins behave identically, so the environment can be replaced by a single effective spin.

We next explore the limitations of compression of the environment, by considering randomised initial conditions for the environment spins. In Fig. 4b and c we present ACE simulations with $N = 10$ and $N = 100$ environment spins for different values of the MPO truncation threshold ϵ. In Fig. 4b the bath is partially polarised: we randomly select pure spin states from an isotropic distribution and filter these with a rejection probability $1 - \exp\left[b\left(s_k^z/\hbar - \frac{1}{2}\right)\right]$. Here, $b = (g\mu_B B)/(k_B T)$ is a Boltzmann factor, taken as $b = 20$ for Fig. 4b. In Fig. 4c we instead use a uniform distribution (i.e. $b = 0$). In both cases a dephasing of the central spin is visible. However, for the unpolarised case, the spin dynamics for different ϵ start to diverge at long times. The slow convergence with ϵ in this situation is a consequence of the intrinsic incompressibility of the environment degrees of freedom. That is, because each environment spin reacts differently to the system spin, the joint PT cannot be compressed efficiently. Furthermore, environment spins can become correlated via an effective interaction mediated by the system, and without an external magnetic field the environment states are highly degenerate. Consequently, there is no clear physical constraint on the accessible environment Hilbert space. In the partially polarised case, the environment can be compressed more efficiently, so that the ACE simulations show a better convergence.

Anharmonic environments. While a bath of harmonic oscillators forms a Gaussian environment, which can be addressed by a multitude of existing numerically exact methods, anharmonic environment modes have so far been out of reach. Anharmonicities are found in practice, e.g., in vibrational modes of molecules with a finite number of bound vibrational states, commonly modelled by a Morse potential [48]

$$v(x) = \Lambda^2\left(e^{-2x} - 2e^{-x}\right), \tag{11}$$

where Λ controls the depth of the potential and number of bound states. Here, we use the Morse potential as a demonstration of simulating environment modes with arbitrary potentials $v(x)$.

As described in more detail in the Supplementary Material S.4, we first use a finite differences method to numerically find the eigenstates of a single uncoupled environment mode, before introducing coupling to the system. For example, the bound eigenstates of the Morse potential for $\Lambda = 5$ are depicted in Fig. 5**a**. Keeping only the M lowest energy eigenstates and choosing a system-environment coupling proportional to the environment

position operator, we find that for environment mode k

$$H_E^k = \sum_{j=0}^{M-1} \hbar\omega_k \tilde{E}_j \sigma_{jj}^k + \hbar g_k \sum_{i,j=0}^{M-1} \sqrt{2}\langle i|\tilde{x}|j\rangle \sigma_{ij}^k \, |e\rangle\langle e|, \quad (12)$$

where $\tilde{E}_j$ and $\langle i|\tilde{x}|j\rangle$ are scaled so that the spin-boson model Hamiltonian is recovered when $v(x)$ is the harmonic oscillator potential.

ACE simulations are performed for $H_S = \frac{\hbar}{2}\Omega\big(|e\rangle\langle g| + |g\rangle\langle e|\big)$, describing a continuously driven system performing Rabi oscillations damped by the anharmonic environment. We choose a set of ω_k and g_k that correspond to a Lorentzian spectral density as shown in Fig. 5**b**; for other parameters see Supplementary Material S.4. The resulting excited state occupations n_e are shown in Fig. 5**c**.

As a validity check, we first apply the above method to a harmonic potential, and recover exactly the dynamics of the spin-boson model. On moving to Morse potential environments, we find significant differences, especially for small Λ. Much of the difference is due to the asymmetry of the Morse potential, leading to an average position $\langle i|\tilde{x}|i\rangle$ that increases for higher excited states, indicated as crosses in Fig. 5**a**. This enters in H_E via the system-environment coupling and results in an energy shift of the $|e\rangle$ system state. To better identify intrinsic effects of anharmonicity, Fig. 5**d** shows ACE results where this shift has been subtracted. For small Λ, one sees effects of the anharmonicity of the Morse potential, while for large Λ the anharmonicity becomes negligible and the result of the Gaussian simulations is recovered.

Discussion

We have presented a novel, numerically exact, efficient, and versatile method: *automated compression of environments* (ACE), which makes it possible to simulate the dynamics of N-level quantum systems coupled to arbitrary environments directly from the microscopic system-environment coupling Hamiltonian. We have illustrated the power of this method with examples of electron transport, the simultaneous interaction of a QD with phonon and photon modes, spin dynamics, and anharmonic environments. In the Supplementary Material S.5, we provide an example exploring superradiant decay, illustrating that ACE can handle higher-dimensional system Hilbert spaces. Supplementary Material S.6 further contains an example of simulations of dispersive system-environment couplings as well as time-dependent driving and non-Hamiltonian loss terms acting directly on the environment. We have shown that ACE reproduces exact results in limiting cases, and can interpolate between infinite and short memory scenarios within the same algorithm. In particular, non-Markovian effects, system-environment correlations, and non-Gaussian baths are fully accounted for.

A fundamental restriction of ACE is that the environment must decompose into a set of separate modes without interactions between these modes. However, most typical models of open system environments satisfy this requirement. Moreover, recent work by [49] shows that, adapting a method of [50], one can extend tensor network methods to models where bath modes have nearest-neighbour interactions. Some environments have particular features that enable more specialised methods to be used, and these can be more efficient than the general method ACE. For example, Gaussian baths with a broad continuum of modes have short memory times at high temperature, and then iQUAPI [19] extremely efficient. In contrast, for environments consisting of only a few discrete modes, ACE outperforms methods based on Gaussian path integrals (see Supplementary Material S.3). For spectral densities with several peaks on top of a broad background, the construction of a PT for Gaussian environments in Ref. 34 can be readily combined with ACE to enable a hybrid approach within the common process tensor framework.

However, the unique feature of ACE is its generality. It can be used in situations where no specialised methods are available, and no new derivations or modifications of the algorithm are required when a new system or environment are considered. Due to its numerical exactness, ACE can serve as a benchmark for approximate methods which may provide a more tangible interpretation of physical processes, or serve a "turnkey solution" to simulate concrete experiments. These features make ACE a valuable general-purpose tool for open quantum systems.

[1] H.-P. Breuer and F. Petruccione, *The Theory of Open Quantum Systems* (Oxford University Press, Oxford, 2002).

[2] M. B. Plenio and S. F. Huelga, Dephasing-assisted transport: quantum networks and biomolecules, New J. Phys. **10**, 113019 (2008).

[3] P. Rebentrost, M. Mohseni, I. Kassal, S. Lloyd, and A. Aspuru-Guzik, Environment-assisted quantum transport, New J. Phys. **11**, 033003 (2009).

[4] A. W. Chin, A. Datta, F. Caruso, S. F. Huelga, and M. B. Plenio, Noise-assisted energy transfer in quantum networks and light-harvesting complexes, New J. Phys. **12**, 065002 (2010).

[5] A. Beige, D. Braun, B. Tregenna, and P. L. Knight, Quantum computing using dissipation to remain in a decoherence-free subspace, Phys. Rev. Lett. **85**, 1762 (2000).

[6] F. Verstraete, M. M. Wolf, and J. I. Cirac, Quantum computation and quantum-state engineering driven by dissipation, Nat. Phys. **5**, 633 (2009).

[7] I. de Vega and D. Alonso, Dynamics of non-markovian open quantum systems, Rev. Mod. Phys. **89**, 015001 (2017).

[8] Y. Tanimura, Stochastic Liouville, Langevin,

Fokker–Planck, and Master Equation Approaches to Quantum Dissipative Systems, J. Phys. Soc. Jpn. **75**, 082001 (2006).
[9] M. B. Plenio and P. L. Knight, The quantum-jump approach to dissipative dynamics in quantum optics, Rev. Mod. Phys. **70**, 101 (1998).
[10] A. G. Redfield, The theory of relaxation processes, in *Advances in Magnetic Resonance*, Advances in Magnetic and Optical Resonance, Vol. 1, edited by J. S. Waugh (Academic Press, 1965) pp. 1 – 32.
[11] A. Nazir and D. P. S. McCutcheon, Modelling exciton–phonon interactions in optically driven quantum dots, J. Phys.: Condens. Matter **28**, 103002 (2016).
[12] H.-P. Breuer, E.-M. Laine, J. Piilo, and B. Vacchini, Colloquium: Non-markovian dynamics in open quantum systems, Rev. Mod. Phys. **88**, 021002 (2016).
[13] Y. Tanimura and R. Kubo, Time evolution of a quantum system in contact with a nearly Gaussian-Markoffian noise bath, J. Phys. Soc. Jpn. **58**, 101 (1989).
[14] Y. Tanimura, Numerically "exact" approach to open quantum dynamics: The hierarchical equations of motion (HEOM), J. Chem. Phys. **153**, 020901 (2020).
[15] J. Prior, A. W. Chin, S. F. Huelga, and M. B. Plenio, Efficient simulation of strong system-environment interactions, Phys. Rev. Lett. **105**, 050404 (2010).
[16] A. D. Somoza, O. Marty, J. Lim, S. F. Huelga, and M. B. Plenio, Dissipation-assisted matrix product factorization, Phys. Rev. Lett. **123**, 100502 (2019).
[17] A. Nüßeler, I. Dhand, S. F. Huelga, and M. B. Plenio, Efficient simulation of open quantum systems coupled to a fermionic bath, Phys. Rev. B **101**, 155134 (2020).
[18] R. Feynman and F. Vernon, The theory of a general quantum system interacting with a linear dissipative system, Ann. Phys. (N.Y.) **24**, 118 (1963).
[19] N. Makri and D. E. Makarov, Tensor propagator for iterative quantum time evolution of reduced density matrices. I. Theory, J. Chem. Phys. **102**, 4600 (1995).
[20] N. Makri and D. E. Makarov, Tensor propagator for iterative quantum time evolution of reduced density matrices. II. Numerical methodology, J. Chem. Phys. **102**, 4611 (1995).
[21] M. Cygorek, A. M. Barth, F. Ungar, A. Vagov, and V. M. Axt, Nonlinear cavity feeding and unconventional photon statistics in solid-state cavity qed revealed by many-level real-time path-integral calculations, Phys. Rev. B **96**, 201201 (2017).
[22] A. Strathearn, P. Kirton, D. Kilda, J. Keeling, and B. W. Lovett, Efficient non-markovian quantum dynamics using time-evolving matrix product operators, Nat. Commun. **9**, 3322 (2018).
[23] M. Cosacchi, M. Cygorek, F. Ungar, A. M. Barth, A. Vagov, and V. M. Axt, Path-integral approach for nonequilibrium multitime correlation functions of open quantum systems coupled to markovian and non-markovian environments, Phys. Rev. B **98**, 125302 (2018).
[24] E. V. Denning, M. Bundgaard-Nielsen, and J. Mørk, Electron-phonon decoupling due to strong light-matter interactions, 2007.14719 (2020), preprint.
[25] M. Cosacchi, F. Ungar, M. Cygorek, A. Vagov, and V. M. Axt, Emission-frequency separated high quality single-photon sources enabled by phonons, Phys. Rev. Lett. **123**, 017403 (2019).
[26] T. Seidelmann, F. Ungar, A. M. Barth, A. Vagov, V. M. Axt, M. Cygorek, and T. Kuhn, Phonon-induced enhancement of photon entanglement in quantum dot-cavity systems, Phys. Rev. Lett. **123**, 137401 (2019).
[27] O. Kaestle, R. Finsterhoelzl, A. Knorr, and A. Carmele, Protected quantum correlations in multiple non-Markovian system-reservoir dynamics (2020), preprint, 2011.05071.
[28] A. Vagov, M. D. Croitoru, M. Glässl, V. M. Axt, and T. Kuhn, Real-time path integrals for quantum dots: Quantum dissipative dynamics with superohmic environment coupling, Phys. Rev. B **83**, 094303 (2011).
[29] J. H. Quilter, A. J. Brash, F. Liu, M. Glässl, A. M. Barth, V. M. Axt, A. J. Ramsay, M. S. Skolnick, and A. M. Fox, Phonon-assisted population inversion of a single InGaAs/GaAs quantum dot by pulsed laser excitation, Phys. Rev. Lett. **114**, 137401 (2015).
[30] Z. X. Koong, E. Scerri, M. Rambach, M. Cygorek, M. Brotons-Gisbert, R. Picard, Y. Ma, S. I. Park, J. D. Song, E. M. Gauger, and B. D. Gerardot, Coherent dynamics in quantum emitters under dichromatic excitation, 2009.02121 (2020), preprint.
[31] T. Palm and P. Nalbach, Quasi-adiabatic path integral approach for quantum systems under the influence of multiple non-commuting fluctuations, The Journal of Chemical Physics **149**, 214103 (2018).
[32] L. Simine and D. Segal, Path-integral simulations with fermionic and bosonic reservoirs: Transport and dissipation in molecular electronic junctions, The Journal of Chemical Physics **138**, 214111 (2013).
[33] F. Rossi and T. Kuhn, Theory of ultrafast phenomena in photoexcited semiconductors, Rev. Mod. Phys. **74**, 895 (2002).
[34] M. R. Jørgensen and F. A. Pollock, Exploiting the causal tensor network structure of quantum processes to efficiently simulate non-markovian path integrals, Phys. Rev. Lett. **123**, 240602 (2019).
[35] F. A. Pollock, C. Rodríguez-Rosario, T. Frauenheim, M. Paternostro, and K. Modi, Non-markovian quantum processes: Complete framework and efficient characterization, Phys. Rev. A **97**, 012127 (2018).
[36] U. Schollwöck, The density-matrix renormalization group in the age of matrix product states, Ann. Phys. (N.Y.) **326**, 96 (2011).
[37] R. Orús, A practical introduction to tensor networks: Matrix product states and projected entangled pair states, Ann. Phys. (N.Y.) **349**, 117 (2014).
[38] I. A. Luchnikov, S. V. Vintskevich, H. Ouerdane, and S. N. Filippov, Simulation complexity of open quantum dynamics: Connection with tensor networks, Phys. Rev. Lett. **122**, 160401 (2019).
[39] T. Brandes and B. Kramer, Spontaneous emission of phonons by coupled quantum dots, Phys. Rev. Lett. **83**, 3021 (1999).
[40] A. M. Barth, A. Vagov, and V. M. Axt, Path-integral description of combined Hamiltonian and non-Hamiltonian dynamics in quantum dissipative systems, Phys. Rev. B **94**, 125439 (2016).
[41] D. Nagy, G. Szirmai, and P. Domokos, Critical exponent of a quantum-noise-driven phase transition: The open-system dicke model, Phys. Rev. A **84**, 043637 (2011).
[42] M. T. Mitchison and M. B. Plenio, Non-additive dissipation in open quantum networks out of equilibrium, New J. Phys. **20**, 033005 (2018).
[43] H. Maguire, J. Iles-Smith, and A. Nazir, Environmental

nonadditivity and Franck–Condon physics in nonequilibrium quantum systems, Phys. Rev. Lett. **123**, 093601 (2019).
[44] K. Roy-Choudhury and S. Hughes, Spontaneous emission from a quantum dot in a structured photonic reservoir: phonon-mediated breakdown of Fermi's golden rule, Optica **2**, 434 (2015).
[45] U. Hoeppe, C. Wolff, J. Küchenmeister, J. Niegemann, M. Drescher, H. Benner, and K. Busch, Direct observation of non-markovian radiation dynamics in 3d bulk photonic crystals, Phys. Rev. Lett. **108**, 043603 (2012).
[46] D. A. Gangloff, G. Éthier-Majcher, C. Lang, E. V. Denning, J. H. Bodey, D. M. Jackson, E. Clarke, M. Hugues, C. Le Gall, and M. Atatüre, Quantum interface of an electron and a nuclear ensemble, Science **364**, 62 (2019).
[47] J. Scheuer, I. Schwartz, S. Müller, Q. Chen, I. Dhand, M. B. Plenio, B. Naydenov, and F. Jelezko, Robust techniques for polarization and detection of nuclear spin ensembles, Phys. Rev. B **96**, 174436 (2017).
[48] M. Bramberger and I. De Vega, Dephasing dynamics of an impurity coupled to an anharmonic environment, Phys. Rev. A **101**, 012101 (2020).
[49] E. Ye and G. K.-L. Chan, Constructing tensor network influence functionals for general quantum dynamics, The Journal of Chemical Physics **155**, 044104 (2021).
[50] M. C. Bañuls, M. B. Hastings, F. Verstraete, and J. I. Cirac, Matrix product states for dynamical simulation of infinite chains, Phys. Rev. Lett. **102**, 240603 (2009).
[51] B. Krummheuer, V. M. Axt, T. Kuhn, I. D'Amico, and F. Rossi, Pure dephasing and phonon dynamics in gaas- and gan-based quantum dot structures: Interplay between material parameters and geometry, Phys. Rev. B **71**, 235329 (2005).

Methods

Derivation of the process tensor. We consider an arbitrary open quantum system specified by the Hamiltonian $H = H_S + H_E$, where H_S is the free system Hamiltonian without coupling to the environment. For simplicity of notation we assume a time-independent Hamiltonian in the following, but generalisation to the time-dependent case is straightforward. The time evolution of the system density operator $\hat{\rho}_S$ can be obtained from the time evolution operator $U(t)$ of the total system, including the environment, by tracing out the environment to give:

$$\hat{\rho}_S(t) = \mathrm{Tr}_E\Big[U(t)\big(\hat{\rho}_S(0)\otimes\hat{\rho}_E(0)\big)U^\dagger(t)\Big]. \tag{13}$$

We discretise the time evolution operator $U(t) = \prod_{l=1}^{n} U(\Delta t)$ on a time grid $t_l = l\Delta t$, $l = 1\dots n$ and apply a Trotter decomposition $U(\Delta t) = e^{-\frac{i}{\hbar}H_E\Delta t}\, e^{-\frac{i}{\hbar}H_S\Delta t} + \mathcal{O}(\Delta t^2)$. Next, we introduce a complete basis for the system (ν or μ) as well as for the full environment (ξ or η). We then introduce the matrix elements

$$A^{\nu_l\tilde{\nu}_l}_{\xi_l\xi_{l-1}} = \langle\nu_l,\xi_l|e^{-\frac{i}{\hbar}H_E\Delta t}|\tilde{\nu}_l,\xi_{l-1}\rangle, \tag{14}$$

$$M^{\tilde{\nu}_l\nu_{l-1}} = \langle\tilde{\nu}_l|e^{-\frac{i}{\hbar}H_S\Delta t}|\nu_{l-1}\rangle, \tag{15}$$

and, using calligraphic symbols, their counterparts in Liouville space:

$$\mathcal{A}^{(\nu_l,\mu_l),(\tilde{\nu}_l,\tilde{\mu}_l)}_{(\xi_l,\eta_l),(\xi_{l-1},\eta_{l-1})} := A^{\nu_l\tilde{\nu}_l}_{\xi_l\xi_{l-1}} A^{\mu_l\tilde{\mu}_l *}_{\eta_l\eta_{l-1}} \tag{16}$$

$$\mathcal{M}^{\tilde{\nu}_l\nu_{l-1}}_{\tilde{\mu}_l\mu_{l-1}} := M^{\tilde{\nu}_l\nu_{l-1}} M^{\tilde{\mu}_l\mu_{l-1}*}. \tag{17}$$

The reduced system density matrix at time step $t_n = n\Delta t$ can then be expressed as

$$\rho_{\nu_n\mu_n} = \sum_{\substack{\nu_{n-1}\dots\nu_0\\ \tilde{\nu}_n\dots\tilde{\nu}_1\\ \mu_{n-1}\dots\mu_0\\ \tilde{\mu}_n\dots\tilde{\mu}_1}} I^{(\nu_n\tilde{\nu}_n)\dots(\nu_1\tilde{\nu}_1)}_{(\mu_n\tilde{\mu}_n)\dots(\mu_1\tilde{\mu}_1)} \left(\prod_{l=1}^{n}\mathcal{M}^{\tilde{\nu}_l\nu_{l-1}}_{\tilde{\mu}_l\mu_{l-1}}\right)\rho_{\nu_0\mu_0}, \tag{18}$$

where

$$I^{(\nu_n\tilde{\nu}_n)\dots(\nu_1\tilde{\nu}_1)}_{(\mu_n\tilde{\mu}_n)\dots(\mu_1\tilde{\mu}_1)} = \sum_{\substack{\xi_n\dots\xi_0\\ \eta_n\dots\eta_0}} \delta_{\xi_n\eta_n}\left(\prod_{l=1}^{n}\mathcal{A}^{(\nu_l,\mu_l),(\tilde{\nu}_l,\tilde{\mu}_l)}_{(\xi_l,\eta_l),(\xi_{l-1},\eta_{l-1})}\right)\rho^E_{\xi_0\eta_0}. \tag{19}$$

Here, $\rho_{\nu_0\mu_0}$ and $\rho^E_{\xi_0\eta_0}$ are the initial system and environment states, respectively. The implicit assumption of a factorisation of the initial state into system and environment parts, i.e., uncorrelated initial states, does not restrict the generality, because initial states with finite system-environment correlations can always be rewritten as sums of product states using Schmidt decomposition.

By combining pairs of Hilbert space indices into Liouville space indices $\alpha_l = (\nu_l,\mu_l)$, $\tilde{\alpha}_l = (\tilde{\nu}_l,\tilde{\mu}_l)$ and $d_l = (\xi_l,\eta_l)$, Eq. (18) becomes Eq. (1) and Eq. (19) takes the form of Eq. (2). The matrices $\mathcal{Q}$ can be obtained by comparison with Eq. (19) as

$$\mathcal{Q}^{(\alpha_l,\tilde{\alpha}_l)}_{d_l d_{l-1}} = \begin{cases} \delta_{d_0,1}\sum_{d'_0}\mathcal{A}^{\alpha_1,\tilde{\alpha}_l}_{d_1,d'_0}\rho^E_{d'_0} & l=1,\\ \mathcal{A}^{\alpha_l,\tilde{\alpha}_l}_{d_l,d_{l-1}} & 1<l<n,\\ \delta_{d_n,1}\sum_{d'_n}\mathfrak{I}_{d'_n}\mathcal{A}^{\alpha_n,\tilde{\alpha}_n}_{d'_n,d_{n-1}} & l=n. \end{cases} \tag{20}$$

where $\mathfrak{I}_{d'_n=(\xi,\eta)} = \delta_{\xi,\eta}$.

Network summation. The network structure determining the reduced system density matrix, visualised in Fig. 1d, can be most easily evaluated by propagating the quantity $\mathcal{R}_{\alpha_l d_l}$ defined recursively via

$$\mathcal{R}_{\alpha_0 1} = \rho_{\alpha_0} = \rho_{\nu_0\mu_0}, \tag{21a}$$

$$\mathcal{R}_{\alpha_l d_l} = \sum_{\tilde{\alpha}_l\alpha_{l-1}}\sum_{d_{l-1}}\mathcal{Q}^{(\alpha_l,\tilde{\alpha}_l)}_{d_l d_{l-1}}\mathcal{M}^{\tilde{\alpha}_l\alpha_{l-1}}\mathcal{R}_{\alpha_{l-1}d_{l-1}}. \tag{21b}$$

Comparing with Eqs. (1) and (2), it can be seen that the density matrix at the last time step is given by $\rho_{\alpha_n} = \mathcal{R}_{\alpha_n 1}$.

When the environment time evolution operator is unitary, the reduced density matrix ρ_{α_l} at intermediate time steps t_l can be easily obtained from $\mathcal{R}_{\alpha_l d_l}$ as

$$\rho_{\alpha_l} = \sum_{d_l} q_{d_l} \mathcal{R}_{\alpha_l d_l} \tag{22}$$

using the closures q_{d_l} defined by the recursion (cf. Supplementary Material S.1 for a detailed derivation)

$$q_{d_n=1} = 1 \tag{23}$$

$$q_{d_{l-1}} = \sum_{d_l} q_{d_l} \sum_{\alpha_l} \mathfrak{I}_{\alpha_l} \mathcal{Q}^{(\alpha_l 0)}_{d_l d_{l-1}}. \tag{24}$$

Thus, in practice one needs to calculate only a single PT MPO with n time steps, where $n\Delta t = t_{\text{final}}$ is the final time one is interested in, and obtains the density matrix at all intermediate time steps $l\Delta t$ at marginal numerical extra cost.

PT combination rule. In order to combine the influences of multiple environments or of independent environments into a single PT, consider a system coupled to multiple environmental degrees of freedom (which we henceforth call modes) via

$$H_E = \sum_{k=1}^{N_E} H_E^k. \tag{25}$$

We define the partial sum of the Hamiltonians from modes $1, 2, \dots K$ as

$$H_E[K] = \sum_{k=1}^{K} H_E^k \tag{26}$$

and denote by $\mathcal{Q}^{(\alpha_l, \tilde{\alpha}_l)}_{d_l d_{l-1}}[K]$ the l-th MPO matrix of the PT including the influences of the modes $1, 2, \dots K$. Then, by means of the symmetric Trotter decomposition

$$\begin{aligned} e^{-\frac{i}{\hbar} H_E[K]\Delta t} &= e^{-\frac{i}{\hbar}\left(H_E[K-1] + H_E^K\right)\Delta t} \\ &= e^{-\frac{i}{\hbar} H_E^K \frac{\Delta t}{2}} e^{-\frac{i}{\hbar} H_E[K-1]\Delta t} e^{-\frac{i}{\hbar} H_E^K \frac{\Delta t}{2}} + \mathcal{O}(\Delta t^3) \end{aligned} \tag{27}$$

the influence of mode K can be combined with the PT containing already the influences of the first $K-1$ modes by

$$\begin{aligned} &\mathcal{Q}^{(\alpha_l, \tilde{\alpha}_l)}_{(d'_l, d_l)(d'_{l-1}, d_{l-1})}[K] \\ &\approx \sum_{\gamma_l, \tilde{\gamma}_l, \tilde{d}_l} \mathcal{B}^{(\alpha_l, \gamma_l)}_{d_l \tilde{d}_l}(K)\ \mathcal{Q}^{(\gamma_l, \tilde{\gamma}_l)}_{d'_l d'_{l-1}}[K-1]\ \mathcal{B}^{(\tilde{\gamma}_l, \tilde{\alpha}_l)}_{\tilde{d}_l d_{l-1}}(K), \end{aligned} \tag{28}$$

where

$$\begin{aligned} &\mathcal{B}^{((\nu_l, \mu_l), (\tilde{\nu}_l, \tilde{\mu}_l))}_{(\xi_l, \eta_l), (\xi_{l-1}, \eta_{l-1})}(K) \\ &= \langle \nu_l, \xi_l | e^{-\frac{i}{\hbar} H_E^K \frac{\Delta t}{2}} | \tilde{\nu}_l, \xi_{l-1} \rangle \langle \tilde{\mu}_l, \eta_{l-1} | e^{\frac{i}{\hbar} H_E^K \frac{\Delta t}{2}} | \mu_l, \eta_l \rangle. \end{aligned} \tag{29}$$

This step is visualised in Fig. 1e.

In practice, we start with the trivial PT MPO with matrices $\mathcal{Q}^{(\alpha_l, \tilde{\alpha}_l)}_{d_l d_{l-1}}[0] = \delta_{d_l,1}\delta_{d_{l-1},1}\delta_{\alpha_l, \tilde{\alpha}_l}$ and add the influence of all environment modes by recursively applying Eq. (28) until $K = N_E$. After each combination step, the PT MPO is compressed using the SVD-based compression as described in the next section.

MPO Compression. In order to reduce the inner dimension of the MPO representing the PT, we perform sweeps of singular value decompositions (SVDs) across the MPO chain. Any matrix $A \in \mathbb{C}^{n \times m}$ can be factorised into a product

$$A = U \Sigma V^\dagger, \tag{30}$$

where $U \in \mathbb{C}^{n \times k}$ and $V \in \mathbb{C}^{m \times k}$ are matrices with orthogonal column vectors and Σ is a diagonal matrix containing the $k = \min(n, m)$ real and non-negative singular values σ_i in descending order. Here, we start with the first MPO matrix, we define

$$A_{d_1, (\alpha_1, \tilde{\alpha}_1)} = \mathcal{Q}^{(\alpha_1, \tilde{\alpha}_1)}_{d_1 1}, \tag{31}$$

and we calculate a SVD of the matrix A. In order to reduce the inner dimension, we truncate the matrices U, Σ, and V, keeping only the $k_{\text{eff}} \leq k$ singular values with $\sigma_i > \epsilon \sigma_1$, where σ_1 is the largest singular value of A and ϵ is a predefined threshold. Then, we replace $\mathcal{Q}^{(\alpha_1, \tilde{\alpha}_1)}_{d_1 1}$ by $\left(V^\dagger\right)_{k_{\text{eff}}(\alpha_1, \tilde{\alpha}_1)}$ and multiply the next matrix $\mathcal{Q}^{(\alpha_2, \tilde{\alpha}_2)}_{d_2 d_1}$ from the right by $U_{d_1 k_{\text{eff}}} \sigma_{k_{\text{eff}}}$ and perform a SVD of

$$A_{d_2, (\alpha_2, \tilde{\alpha}_2, k_{\text{eff}})} = \sum_{d_1} \mathcal{Q}^{(\alpha_2, \tilde{\alpha}_2)}_{d_2 d_1} U_{d_1 k_{\text{eff}}} \sigma_{k_{\text{eff}}}. \tag{32}$$

The reduction is continued until the end of the MPO is reached. Then, another line sweep is performed in the opposite direction. Note that sweeps along the whole chain are required between each PT combination step, because information necessary to effectively compress the MPO, such as the initial environment state, needs to be propagated from the ends throughout the whole MPO.

In the overall process, the inner dimensions d_i are reduced to the respective effective ranks k_{eff}, where the latter are controlled by the threshold ϵ.

Parameters for QD, QD-phonon, and QD-photon Hamiltonians. The effects of the dot-phonon coupling are completely defined by the phonon spectral density

$$J(\omega) = \sum_{\mathbf{q}} \gamma_{\mathbf{q}}^2 \delta(\omega - \omega_{\mathbf{q}}). \tag{33}$$

Using established parameters [51] for a GaAs quantum dot with electron radius $a_e = 3.0$ nm and hole radius $a_h = a_e / 1.15$

$$J(\omega) = \frac{\omega^3}{4\pi^2 \rho \hbar c_s^5} \left(D_e e^{-\omega^2 a_e^2/(4c_s^2)} - D_h e^{-\omega^2 a_h^2/(4c_s^2)} \right)^2 \tag{34}$$

with mass density $\rho = 5370$ kg/m^3, speed of sound $c_s = 5110$ m/s and electron and hole deformation potential constants $D_e = 7.0$ eV and $D_h = -3.5$ eV. We discretise the phonon continuum using steps of equal width, so that $\omega_q = qd\omega$ with $d\omega = \omega_{\max}/N_E$, $N_E = 100$ and $\omega_{\max} = 5$ meV$/\hbar$ and we obtain the coupings γ_q from the phonon density of states using $\gamma_q = \sqrt{J(\omega_q)d\omega}$. The phonon modes are initially assumed to be in thermal equilibrium with temperature $T = 4$ K. We have checked that for these parameters it is enough to consider up to two excitations per mode.

We use a radiative decay rate of $\kappa = 0.1$ ps^{-1}. When the electromagnetic environment is treated microscopically we assume a constant density of states with bandwidth $\omega_{BW} = 10$ ps^{-1}, discretised using $N_E = 100$ equally spaced modes. The coupling constants g_k are taken to be constant and the value is chosen such that Fermi's golden rule reproduces the radiative decay rate κ. The PTs for the phonon and photon environments are calculated separately and combined using Eq. (28) without performing a final SVD sweep. For both baths, we use time steps $\Delta t = 0.1$ ps and an MPO compression threshold $\epsilon = 5 \times 10^{-8}$.

The Gaussian excitation pulse is detuned $\hbar\delta = 1.5$ meV above the quantum dot resonance and the envelope is described by

$$\Omega(t) = \frac{A}{\sqrt{2\pi}\sigma} \exp\left(-\frac{(t-t_0)^2}{2\sigma^2} \right), \tag{35}$$

where we use the pulse area $A = 3\pi$, pulse centre $t_0 = 7$ ps, and $\sigma = \tau_{\mathrm{FWHM}}/\left(2\sqrt{2\ln 2}\right)$ with $\tau_{\mathrm{FWHM}} = 5$ ps.

Numerical implementation. We have implemented ACE in a C++ code using the Eigen library to calculate matrix exponentials and singular value decompositions. All calculations have been performed on a conventional laptop computer with Intel Core i5-8265U processor and 16 GB of RAM. The computation times for the presented examples are listed in the Supplementary Material S.3.

Data availability

The data presented in the figures as well as the computer code including documentation is available online at https://doi.org/10.5281/zenodo.5214128

Acknowledgement

M. Co. and V. M. A. are grateful for funding by the Deutsche Forschungsgemeinschaft (DFG, German Research Foundation) under project No. 419036043. A. V. acknowledges the support from the Russian Science Foundation under the Project 18-12-00429. M. Cy. and E. M. G. acknowledge funding from EPSRC grant no. EP/T01377X/1. B. W. L. and J. K. were supported by EPSRC grant no. EP/T014032/1.

Author contributions

M. Cy., M. Co., A. V., and V. M. A. developed the concept of explicitly constructing the PT to simulate open quantum systems with arbitrary system-environment couplings. M. Cy., B. W. L., J. K. and E. M. G. contributed the idea of using MPO representations for efficient storage and evaluation of the PT. M. Cy. is responsible for the details of the algorithm, the implementation in the form of the C++-code, and the generation of data. All authors analysed and discussed the results and contributed to writing the article.

Competing interests

The authors declare no competing interests.

Additional information

Supplementary information. is available for this article at ...

Supplementary material: Numerically exact open quantum systems simulations for arbitrary environments using automated compression of environments

S.1. CALCULATION OF INTERMEDIATE-TIME CLOSURES

In Eq. (18) we gave an expression for the reduced system density matrix at time t_n using the process tensor (PT) for n time steps. In practical applications, it is desirable to also be able to calculate the reduced system density matrix at intermediate times t_l to extract the full dynamics of the system. Here we show how this can be extracted. As a reminder, in the following we use the symbols ν or μ to enumerate system states, and ξ or η for environment states.

The calculation of ρ_{α_l} for $l < n$ requires the knowledge of a PT for l time steps. From Eq. (19) it is clear that, before any matrix product operator (MPO) compression, the PT for l time steps can be obtained from the PT for $n > l$ time steps by tracing over the environment at that step, $\sum_{\xi_l,\eta_l} \delta_{\xi_l,\eta_l}$. After compression, it is less clear how this trace is to be executed on the inner indices d_l. In principle, it is possible to track how the trace operation transforms under the individual MPO compression steps. A more practical alternative is to make use of the unitarity of the environment evolution and recursively obtain the PT for $n-1$ time steps from the PT for n time steps.

Consider the terms corresponding to the last time step in Eq. (19):

$$\sum_{\xi_n\eta_n} \delta_{\xi_n\eta_n} A^{\nu_n\tilde{\nu}_n}_{\xi_n\xi_{n-1}} A^{\mu_n\tilde{\mu}_n *}_{\eta_n\eta_{n-1}} = \sum_{\xi} \langle\tilde{\mu}_n, \eta_{n-1}| e^{\frac{i}{\hbar}H_E\Delta t}|\mu_n,\xi\rangle\langle\nu_n,\xi| e^{-\frac{i}{\hbar}H_E\Delta t}|\tilde{\nu}_n,\xi_{n-1}\rangle. \tag{S.1.1}$$

Performing the trace over the system states $\sum_{\nu_n,\mu_n} \delta_{\nu_n\mu_n}$ in addition to the trace over the environment states yields

$$\begin{aligned}\sum_{\nu_n\mu_n} \delta_{\nu_n\mu_n} \sum_{\xi_n\eta_n} \delta_{\xi_n\eta_n} A^{\nu_n\tilde{\nu}_n}_{\xi_n\xi_{n-1}} A^{\mu_n\tilde{\mu}_n *}_{\eta_n\eta_{n-1}} =& \langle\tilde{\mu}_n, \eta_{n-1}| e^{\frac{i}{\hbar}H_E\Delta t}\left[\sum_{\nu,\xi} |\nu,\xi\rangle\langle\nu,\xi|\right] e^{-\frac{i}{\hbar}H_E\Delta t}|\tilde{\nu}_n,\xi_{n-1}\rangle \\ =& \langle\tilde{\mu}_n, \eta_{n-1}| e^{\frac{i}{\hbar}H_E(\Delta t-\Delta t)}|\tilde{\nu}_n,\xi_{n-1}\rangle = \langle\tilde{\mu}_n, \eta_{n-1}|\tilde{\nu}_n,\xi_{n-1}\rangle = \delta_{\tilde{\mu}_n\tilde{\nu}_n}\delta_{\eta_{n-1}\xi_{n-1}}.\end{aligned} \tag{S.1.2}$$

Together with the sum over the η_{n-1} and ξ_{n-1} in the $(n-1)$-th time step in the PT, the term $\delta_{\eta_{n-1}\xi_{n-1}}$ again becomes equivalent to calculating the trace over the environment modes, but at time step $n-1$. Therefore, the PT for $n-1$ time steps can be related to the PT for n time steps by

$$I^{(\nu_{n-1}\tilde{\nu}_{n-1})\ldots(\nu_1\tilde{\nu}_1)}_{(\mu_{n-1}\tilde{\mu}_{n-1})\ldots(\mu_1\tilde{\mu}_1)} = \sum_{\nu_n\mu_n} \delta_{\nu_n\mu_n} I^{(\nu_n\tilde{\nu})(\nu_{n-1}\tilde{\nu}_{n-1})\ldots(\nu_1\tilde{\nu}_1)}_{(\mu_n\tilde{\nu})(\mu_{n-1}\tilde{\mu}_{n-1})\ldots(\mu_1\tilde{\mu}_1)}, \tag{S.1.3}$$

where $\tilde{\nu}$ is an arbitrary system state, which we choose as $\tilde{\nu} = 0$. As this expression only involves outer indices and is independent of the inner indices, it applies equally to the PT after MPO compression. Thus, given the PT for n time steps in MPO form in Liouville space

$$\mathcal{I}^{(\alpha_n,\tilde{\alpha}_n)(\alpha_{n-1},\tilde{\alpha}_{n-1})\ldots(\alpha_1,\tilde{\alpha}_1)} = \sum_{d_{n-1}\ldots d_1} \mathcal{Q}^{(\alpha_n,\tilde{\alpha}_n)}_{1d_{n-1}} \mathcal{Q}^{(\alpha_{n-1},\tilde{\alpha}_{n-1})}_{d_{n-1}d_{n-2}} \ldots \mathcal{Q}^{(\alpha_1,\tilde{\alpha}_1)}_{d_11}, \tag{S.1.4}$$

we can obtain the PT for l time steps as

$$\mathcal{I}^{(\alpha_l,\tilde{\alpha}_l)(\alpha_{l-1},\tilde{\alpha}_{l-1})\ldots(\alpha_1,\tilde{\alpha}_1)} = \sum_{d_l\ldots d_1} q_{d_l} \mathcal{Q}^{(\alpha_l,\tilde{\alpha}_l)}_{d_ld_{l-1}} \mathcal{Q}^{(\alpha_{l-1},\tilde{\alpha}_{l-1})}_{d_{l-1}d_{l-2}} \ldots \mathcal{Q}^{(\alpha_1,\tilde{\alpha}_1)}_{d_11}, \tag{S.1.5}$$

where the closures q_{d_l} are calculated recursively via

$$q_{d_n=1} = 1 \tag{S.1.6}$$

$$q_{d_{l-1}} = \sum_{d_l} q_{d_l} \sum_{\alpha_l\nu_l} \delta_{\alpha_l,(\nu_l,\nu_l)} \mathcal{Q}^{(\alpha_l 0)}_{d_ld_{l-1}}. \tag{S.1.7}$$

With the closures q_{d_l} the reduced system density matrix ρ_{α_l} at time step t_l can be extracted from the propagated quantities $\mathcal{R}_{\alpha_l d_l}$ defined in Eq. (19) as

$$\rho_{\alpha_l} = \sum_{d_l} q_{d_l} \mathcal{R}_{\alpha_l d_l}. \tag{S.1.8}$$

S.2. NUMERICAL CONVERGENCE OF THE ACE ALGORITHM

The ACE algorithm, as described in the main text, is numerically exact in the following sense: Every step in the derivation that involves an approximation is controlled by convergence parameters, such that in principle the error can be made arbitrarily small as the corresponding convergence parameters are taken to zero or infinity as appropriate. Thus, in principle, exact results can be approximated to arbitrary precision given enough computational resources. In this section we first review the sources of numerical error that exist—time discretisation, MPO compression, and discretisation of a continuum of environment modes. We then present a study of the tradeoff between accuracy and the computational cost of a calculation.

A. Sources of numerical error

1. Time discretization

The starting point of the derivation of ACE is the introduction of an equidistant time grid $t_n = n\Delta t$, defined by a time step width Δt. The maximal number of time steps $n_{\max}$ then determines the simulation end time $t_e = n_{\max}\Delta t$. Decomposing the total time evolution operator into system and environment parts for a time step Δt introduces numerical Trotter errors. For the system–environment decomposition we use a first-order expansion

$$e^{-\frac{i}{\hbar}(H_S+H_E)\Delta t} = e^{-\frac{i}{\hbar}H_E\Delta t}e^{-\frac{i}{\hbar}H_S\Delta t} + \mathcal{E}^{SE}_{\text{Trotter}} \tag{S.2.1}$$

while between different environment modes we use a second-order expansion

$$e^{-\frac{i}{\hbar}\left(H_E[K-1]+H_E^K\right)\Delta t} = e^{-\frac{i}{\hbar}H_E[K-1]\frac{\Delta t}{2}}e^{-\frac{i}{\hbar}H_E^K\Delta t}e^{-\frac{i}{\hbar}H_E[K-1]\frac{\Delta t}{2}} + \mathcal{E}^{K}_{\text{Trotter}}. \tag{S.2.2}$$

While there has been considerable work on finding rigorous bounds for Trotter errors (see e.g. Childs *et al.* [1] and references therein), here we limit our discussion to a simple analysis in terms of a Taylor expansion orders. This yields single-step error terms of the order $\mathcal{E}^{SE}_{\text{Trotter}} = \mathcal{O}(\Delta t^2)$ and $\mathcal{E}^{K}_{\text{Trotter}} = \mathcal{O}(\Delta t^3)$, respectively. Regarding the system–environment decoupling we may note however, that when the full time evolution up to the final time t_e is considered, the product

$$P_1 := \left(e^{-\frac{i}{\hbar}H_E\Delta t}e^{-\frac{i}{\hbar}H_S\Delta t}\right)\left(e^{-\frac{i}{\hbar}H_E\Delta t}e^{-\frac{i}{\hbar}H_S\Delta t}\right)\dots\left(e^{-\frac{i}{\hbar}H_E\Delta t}e^{-\frac{i}{\hbar}H_S\Delta t}\right) \tag{S.2.3}$$

is related to the product obtained by symmetric Trotter decomposition

$$P_2 := \left(e^{-\frac{i}{\hbar}H_S\frac{\Delta t}{2}}e^{-\frac{i}{\hbar}H_E\Delta t}e^{-\frac{i}{\hbar}H_S\frac{\Delta t}{2}}\right)\left(e^{-\frac{i}{\hbar}H_S\frac{\Delta t}{2}}e^{-\frac{i}{\hbar}H_E\Delta t}e^{-\frac{i}{\hbar}H_S\frac{\Delta t}{2}}\right)\dots\left(e^{-\frac{i}{\hbar}H_S\frac{\Delta t}{2}}e^{-\frac{i}{\hbar}H_E\Delta t}e^{-\frac{i}{\hbar}H_S\frac{\Delta t}{2}}\right), \tag{S.2.4}$$

by the relation $P_2 = e^{-\frac{i}{\hbar}H_S\frac{\Delta t}{2}}P_1e^{+\frac{i}{\hbar}H_S\frac{\Delta t}{2}}$. Thus, the results obtained by first-order Trotter decomposition converge identically to those obtained by a second-order Trotter decomposition, up to evolving the initial and final states by a half time step.

By keeping the final time t_e fixed and expressing the time step width $\Delta t = t_e/n_{\max}$, the total error accumulated can be written in terms of the total number of time steps $n_{\max}$. For the second-order Trotter decomposition the total error is $\left|e^{-\frac{i}{\hbar}(H_S+H_E)t} - P_2\right| = n_{\max}\,\mathcal{O}(1/n^3_{\max}) = \mathcal{O}(1/n^2_{\max})$. As the environment propagator $e^{-\frac{i}{\hbar}H_E\Delta t}$ itself is also approximated up to an error $\mathcal{O}(1/n^3_{\max})$— arising from decomposing it into different modes— the overall Trotter error accumulated during the simulation scales as $\mathcal{O}(1/n^2_{\max})$. This error can thus be made arbitrarily small by choosing a fine enough time discretisation.

2. MPO compression

A second source of numerical error occurs when the MPO representing the process tensor is compressed. This compression is done using a singular value decomposition (SVD), and truncation by neglecting singular values below a given threshold. A sequential sweep of SVDs is performed across the MPO.

For a single SVD step the Eckart–Young–Mirsky theorem [2] provides concrete error bounds: Given the SVD of a matrix A, we define

$$A = U\Sigma V^\dagger = \sum_{i=1}^{n}\sigma_i u_i v_i^\dagger = \underbrace{\sum_{i=1}^{k}\sigma_i u_i v_i^\dagger}_{=:\tilde{A}} + \underbrace{\sum_{i=k+1}^{n}\sigma_i u_i v_i^\dagger}_{=:\delta A}, \tag{S.2.5}$$

where σ_i are the singular values in descending order, u_i, v_i the corresponding singular vectors, and k is the smallest number such that $\sigma_i < \epsilon\sigma_1$ for all $i > k$. $\tilde{A}$ represents the relevant part of the matrix A, whereas δA is considered irrelevant and is therefore neglected. The Eckart–Young–Mirsky theorem states that the matrix $\tilde{A}$ provides the best approximation to A of all matrices with rank k. In particular, the error in the spectral norm is $\|A - \tilde{A}\|_2 = \sigma_{k+1}$ while for the Frobenius norm $\|A - \tilde{A}\|_F = \sqrt{\sigma_{k+1}^2 + \sigma_{k+2}^2 + \cdots + \sigma_n^2}$. In any case, for $\epsilon \to 0$ one finds $\|A - \tilde{A}\| \to 0$ and the low-rank approximation $\tilde{A} \to A$ becomes exact.

Exact bounds for the accumulated error of a full line sweep are more difficult to assess. This is because, e.g., in a sweep from right to left, the next matrix is multiplied with vectors $\sigma_i u_i$ $(i = 1, 2, \ldots, k)$ from the SVD of the previous matrix, so the result depends on the overlap between u_i and the row vectors of the next matrix. Furthermore, it is a priori not clear how strongly a given matrix element of the PT MPO contributes to the reduced system density matrix at a given point in time, in particular because this also depends on the concrete system Hamiltonian H_S. It also remains an open question how numerical errors propagate, e.g., if small deviations from Hermitianity and positivity of the density matrices grow exponentially or behave more advantageously.

A rigorous mathematical analysis of the error bounds for tensor network methods is beyond the scope of the present article. Yet, it is clear that the MPO compressed object turns into an exact reformulation of the original uncompressed PT in the limit $\epsilon \to 0$. As such, in this work, we restrict further analysis to numerical convergence tests.

3. Continuum discretisation

While some open quantum systems, such as the example of spin baths in the main text, contain a finite number of environment modes, others involve a continuum of modes that require discretisation in order to apply the ACE algorithm. For this discretisation to converge numerically, one has to additionally demand piecewise continuity of the environment initial state as well as the environment Hamiltonian with respect to the index $\mathbf{k}$ describing the continuum.

B. Numerical convergence and computational cost

To numerically test the convergence of ACE with respect to different convergence parameters, we consider again the example of the resonant level model (first example in the main text). In particular, we focus on the case of band width $\omega_{BW} = 10\gamma$, where visible deviations from the Markovian result can be seen.

First, using $N_E = 10$ modes to discretise the continuum and fixed final time $\gamma t_e = 2.5$, we investigate the numerical error for different time step widths Δt and MPO compression thresholds ϵ. Here, we define the error as

$$\text{Error} = \max_i \left| n_S\big(t_i, \{\Delta t, \epsilon\}\big) - n_S\big(t_i, \{\Delta t, \epsilon_{\min}\}\big) \right|, \tag{S.2.6}$$

where $n_S\big(t_i, \{\Delta t, \epsilon\}\big)$ is the system site occupation at time $t_i = i\Delta t$ calculated using the set of convergence parameters $\{\Delta t, \epsilon\}$. Because the computation time and the convergence with respect to the threshold ϵ differ vastly for different time discretisations Δt, we use reference calculations with different $\epsilon_{\min}$ for each Δt. Specifically we use $\epsilon_{\min}(\gamma\Delta t = 0.1) = 3 \times 10^{-9}$, $\epsilon_{\min}(\gamma\Delta t = 0.05) = 3 \times 10^{-10}$, and $\epsilon_{\min}(\gamma\Delta t = 0.01) = \epsilon_{\min}(\gamma\Delta t = 0.005) = \epsilon_{\min}(\gamma\Delta t = 0.001) = 10^{-11}$.

These numerical errors vs compression threshold ϵ are depicted in Fig. S.2.1**a** on a double logarithmic scale. As expected, the numerical error generally decreases as the threshold is reduced. The threshold needed to obtain a given numerical accuracy is found to depend strongly on the time step width Δt. Furthermore, a common feature in all curves is that there exists a plateau where for a broad range of thresholds no significant gain in accuracy is observed.

These facts can be explained by the distribution of singular values: The uncompressed PT MPO matrices are directly related to the environment propagator, which for very small time steps can be approximated as $e^{-\frac{i}{\hbar}H_E\Delta t} \approx 1 - \frac{i}{\hbar}H_E\Delta t$ and therefore possesses matrix elements (diagonals) of order 1 as well as contributions (off-diagonals) of order $\|H_E\|\Delta t/\hbar$, but hardly any elements in the intermediate range. Matrix elements of vastly different orders of magnitude translate into singular values of different orders of magnitude, leading to a corresponding gap in the SVD spectrum. This analysis also demonstrates that smaller time steps require smaller convergence thresholds to produce the same level of accuracy, to avoid terms of the order $\|H_E\|\Delta t/\hbar \lesssim \epsilon$ being disregarded.

Figure S.2.1**b** depicts the results of the same calculations plotted against the maximal inner dimension $d_{\max}$ of the PT. Displayed in this way, the curves calculated for different time step widths Δt all nearly overlap, suggesting that the maximal inner dimension is a more reliable measure of the numerical accuracy than the compression threshold ϵ itself. Note, however, that in our fixed-precision algorithm, $d_{\max}$ is not known a priori.

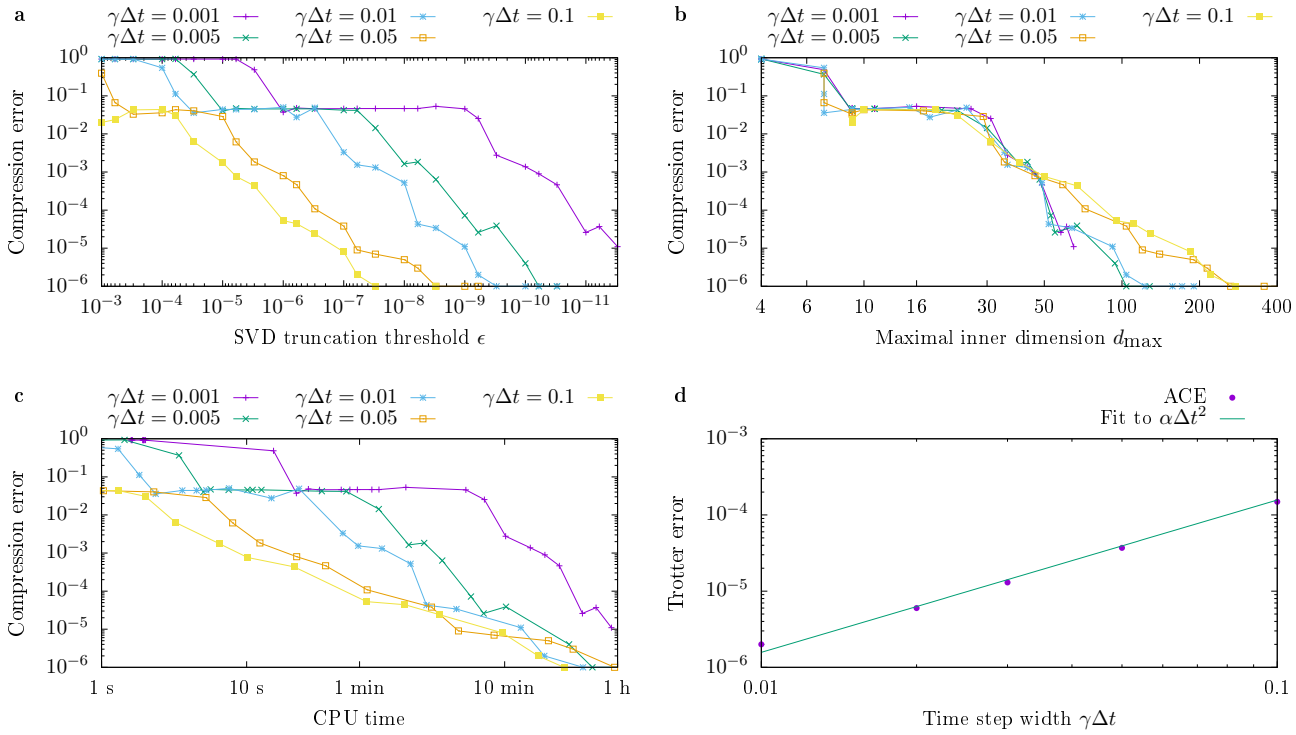

FIG. S.2.1. Convergence of ACE simulations with respect to SVD truncation threshold ϵ (panel **a**). Note the horizontal axis goes from largest ϵ to smallest. The same results are also plotted as a function of the maximal inner dimension $d_{\max}$ (panel **b**) and the total CPU time (panel **c**) needed for the calculations on a conventional laptop computer with Intel Core i5-8265U. The error associated with the time discretisation (Trotter error) is depicted in panel **d**.

For practical applications it is important to relate these parameters controlling precision to the computation time needed to perform ACE simulations. We therefore also present the numerical error of the above calculations as a function of the CPU time in Fig. S.2.1**c**. These were obtained on a conventional laptop computer with Intel Core i5-8265U processor. For a given accuracy, the fastest computation is achieved for the largest time steps because the PT MPO has fewer sites and, thus, fewer SVDs to perform. In particular, for this problem, we find that very accurate results are achievable within minutes of computation time.

Figure S.2.1**d**, shows the Trotter error $\max_i \left| n_S\big(t_i, \{\Delta t, \epsilon_{\min}\}\big) - n_S\big(t_i, \{\Delta t_{\min}, \epsilon_{\min}\}\big)\right|$ defined as the difference with respect to reference calculations with time step width $\gamma\Delta t_{\min} = 0.005$, where for given Δt the corresponding best converged results with smallest threshold $\epsilon_{\min}$ is used. The theoretical expectation that the accumulated Trotter error is proportional to Δt^2 (or $1/n_{\max}^2$) is corroborated by a fit of the data points to this trend.

Finally, we numerically investigate the convergence of the PT with respect to the mode discretisation of a continuum of environment modes. Figure S.2.2**a** shows the time evolution of the system occupation for the same Fermionic open quantum system as discussed above. Results are shown up to final time $\gamma t_e = 5$ using a fixed compression threshold $\epsilon = 10^{-6}$ and a fixed time step width $\gamma\Delta t = 0.05$, comparing the results for different numbers of environment modes N_E spanning the total band with $\omega_{BW} = 10\gamma$. For a large number of modes $N_E = 100$ the results shown in the main text are reproduced, i.e. system occupation grows roughly as predicted by the Markovian limit $1 - e^{-\gamma t}$, albeit with visible deviations. However, if the continuum discretisation is too coarse as in the case $N_E = 2$, the description is only accurate for a short time, after which strong deviations occur. For small N_E this is inevitable, because there is a limited set of degrees of freedom, corresponding to a limited set of frequencies controlling the dynamics of the system. With increasing number of modes N_E, the time at which these strong deviations appear becomes later. Here, for $N_E = 8$ this point is almost beyond the final time t_e, so a good description of environment effects is retained for the full simulation.

The mode discretisation has a significant impact on the structure of the process tensor. In Fig. S.2.2**b**, the inner dimension d_i at every time step t_i is depicted. The typical shape of the d_i distribution is roughly trapezoidal; this reflects the constraint in the bond dimension near the ends of the MPO, so that the maximum inner dimension $d_{\max}$ occurs near the centre of the MPO. Notably, we find that increasing the number of modes leads first to an increase

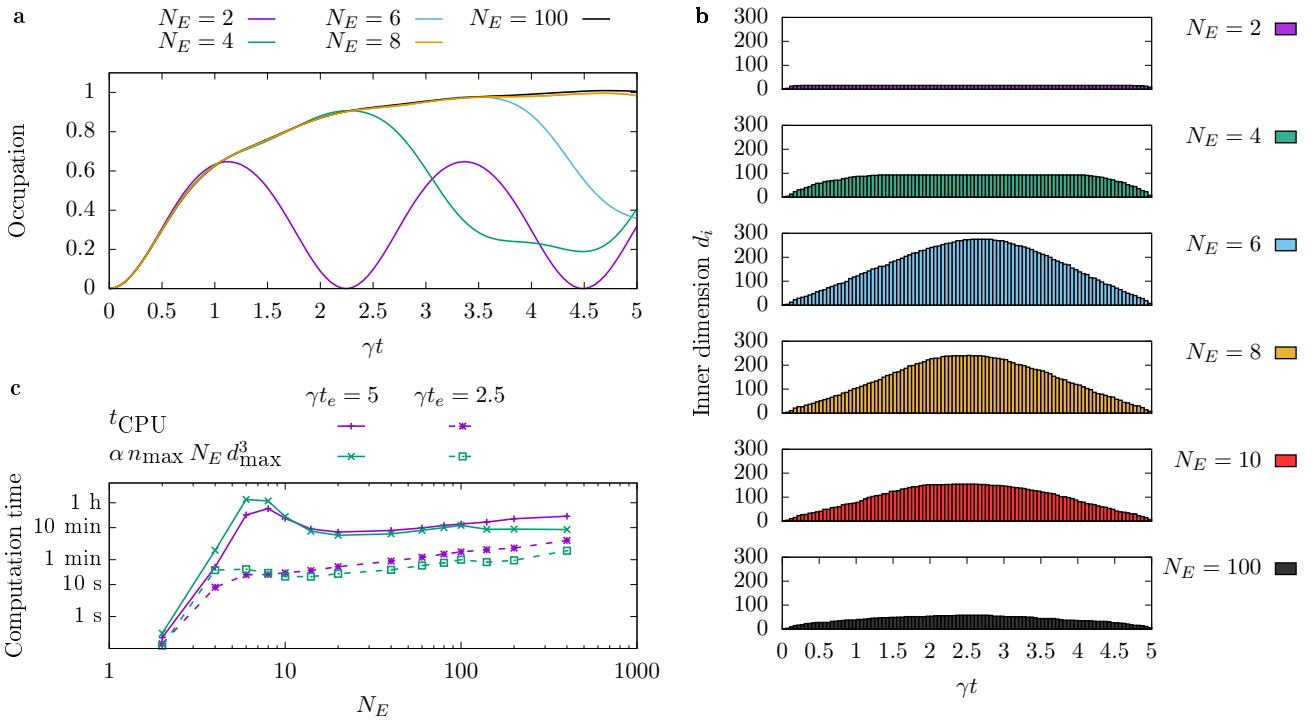

FIG. S.2.2. Convergence of ACE simulations with respect to the number of modes N_E used to discretise a continuum. Panel **(a)** compares the time dependence of occupation for different values of N_E. Panel **(b)** shows how N_E affects the inner dimensions of the MPO, while panel **(c)** shows how this affects the computation time required.

in $d_{\max}$ up to a certain N_E after which $d_{\max}$ begins to decrease. The initial increase can be explained by the PT including more and more degrees of freedom. The eventual decrease is due to dephasing between modes with similar frequencies. This result is consistent with recent results by Ye and Chan [3]. The largest values of $d_{\max}$ are found at similar values of N_E to the conditions where convergence of the result with N_E is first reached, as seen in Fig. S.2.2**a**.

The dependence of the inner dimensions of the PT on the mode discretisation has a significant impact on the computational resources required for the ACE method. Figure S.2.2**c** shows the CPU time needed for carrying out the ACE simulation for two different final times $\gamma t_e = 5$ and $\gamma t_e = 2.5$. The computation time is found to increase rapidly with N_E when N_E is small, but then reach an approximate plateau at large N_E. (The required computation time can even have a minimum, as seen around $N_E = 20$ in the case $\gamma t_e = 5$.) These trends can be explained by a simple scaling argument: Exact SVD routines scale as d^3 where d is the matrix dimension. The number of SVDs performed in total is proportional to the number of time steps $n_{\max}$ times the number of environment modes N_E. Using the maximal inner dimension $d_{\max}$ as a proxy for the typical dimension, one expects the computation time to scale as $t_{\mathrm{estimate}} = \alpha\, n_{\max} N_E d_{\max}^3$. With $d_{\max}$ extracted from the simulations, t_{estimate} is fit against the CPU times of the curve for $\gamma t_e = 5$. This is depicted in Fig. S.2.2**c**. We find that this formula, with a constant α, indeed captures the trends in the computation time well.

S.3. RUN TIMES AND COMPARISON TO GAUSSIAN METHODS

A. Run time for examples provided

Example	Run time
Resonant level model:	
$N_E = 2$	< 1 s
$N_E = 4$	4 s
$N_E = 10$	56 s
$N_E = 100$	13 h 3 min
Phonons & photons:	
Construct PT phonons	1 h 14 min
Construct PT photons, $\omega_{BW} = 10$ ps^{-1}	10 h 47 min
Construct PT photons, $\omega_{BW} = 0.4$ ps^{-1}	17 s
Contraction of PT (combined)	40 s
[iQUAPI: phonons]	[1 min 0 s]
Spins, fully polarised:	
$N = 10$, $\epsilon = 10^{-10}$	1 min 10 s
$N = 100$, $\epsilon = 10^{-10}$	4 min 09 s
$N = 1000$, $\epsilon = 10^{-10}$	13 min 50 s
Spins, partially polarised:	
$N = 10$, $\epsilon = 10^{-10}$	3 min 32 s
$N = 10$, $\epsilon = 10^{-13}$	19 min 59 s
$N = 10$, $\epsilon = 10^{-16}$	1 h 45 min
$N = 100$, $\epsilon = 10^{-10}$	5 min 30 s
$N = 100$, $\epsilon = 10^{-13}$	33 min 12 s
$N = 100$, $\epsilon = 10^{-16}$	2 h 28 min
Spins, unpolarised:	
$N = 10$, $\epsilon = 10^{-10}$	5 min 21 s
$N = 10$, $\epsilon = 10^{-13}$	34 min 2 s
$N = 10$, $\epsilon = 10^{-16}$	4 h 40 min
$N = 100$, $\epsilon = 10^{-10}$	8 min 27 s
$N = 100$, $\epsilon = 10^{-13}$	40 min 52 s
$N = 100$, $\epsilon = 10^{-16}$	3 h 8 min

Example	Run time
Morse potential:	
SBM, $M = 5$	20 min 17 s
HO, $M = 5$	23 min 30 s
$\Lambda = 2$, $M = 2$	3 min 39 s
$\Lambda = 2$, $M = 2$, renorm.	3 min 48 s
$\Lambda = 3$, $M = 3$	22 min 39 s
$\Lambda = 3$, $M = 3$, renorm.	21 min 58 s
$\Lambda = 4$, $M = 4$	1 h 37 min
$\Lambda = 4$, $M = 4$, renorm.	1 h 36 min
$\Lambda = 5$, $M = 5$	4 h 4 min
$\Lambda = 5$, $M = 5$, renorm.	3 h 48 min
$\Lambda = 10$, $M = 5$	1 h 6 min
$\Lambda = 10$, $M = 5$, renorm.	1 h 7 min
$\Lambda = 100$, $M = 5$	33 min 15 s
$\Lambda = 100$, $M = 5$, renorm.	32 min 15 s
Superradiance:	
Construct PT	31 min 39 s
Contraction of PT	2 s
Dispersive coupling:	
single mode	7 s
instant. Fock	2 s
pulsed, no losses	23 min 36 s
pulsed, with losses	13 min 2 s

TABLE S.3.1. Run times for the examples discussed in the main text and the Supplementary Material. In some examples ("phonons & photons" and "superradiance"), we use the fact that the construction of the process tensor ("Construct PT") using ACE and the subsequent contraction to determine time evolution can be separated. This separation is useful when one environment is used multiple times with different system Hamiltonians.

The simulations for this article are performed on a conventional laptop computer with Intel i5-8265U processor and 16 GB of RAM. The ACE code is available at Ref. [4]. The numerically most demanding part, the MPO compression using SVDs, is done using the `JacobiSVD` routine provided by the Eigen library (version 3.4-rc1), which calls the corresponding LAPACK routines when compiled and linked appropriately. Here, we use the LAPACK implementation provided by the Intel MKL (version 2021.3.0). The C++ code is compiled and linked using the GCC compiler (version 9.3.0).

The run times of the simulations for the examples discussed in the main text as well as in other sections of the Supplemental Material are listed in Tab. S.3.1. As can be seen, typical calculation times for these examples range between minutes to several hours, demonstrating the efficiency and practicability of ACE over a broad range of different physical systems. The challenging simulations of spin baths with tiny thresholds $\epsilon = 10^{-16}$ require more than the physical 16 GB of RAM, and so the times observed here are affected by swapping to disk. Note that swapping is efficient for ACE simulations because a single MPO compression step only modifies a single MPO matrix at a time.

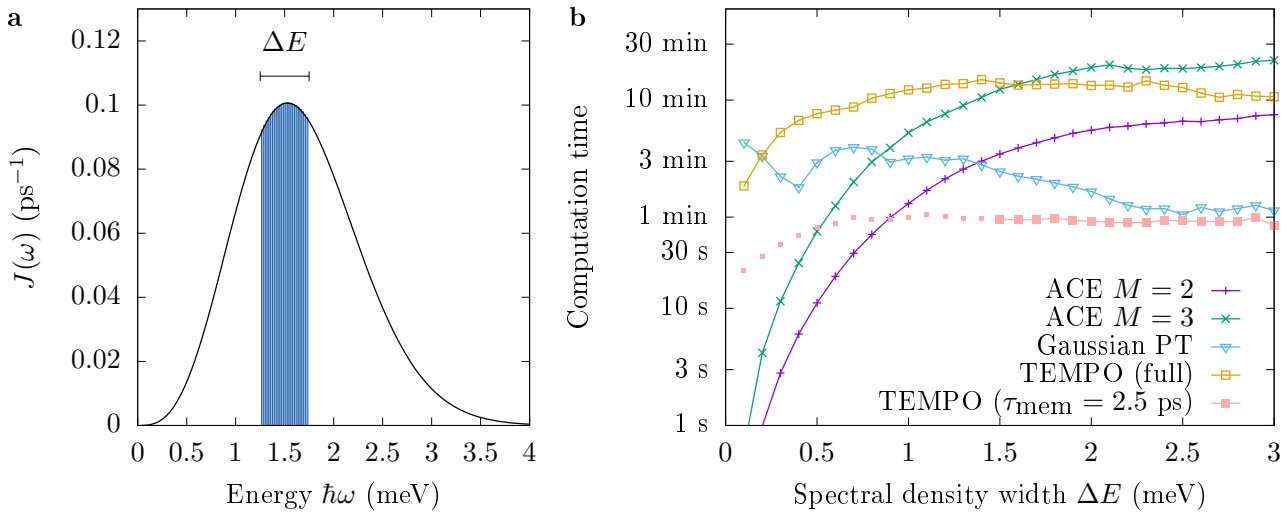

FIG. S.3.1. Comparison of different numerically exact methods for Gaussian environments: ACE, Gaussian PT calculation, and TEMPO for the example of an off-resonantly driven quantum dot coupled to a bath of phonons. To control the non-Markovianity of the bath, the spectral density is manually restricted to a finite spectral range ΔE centred around the energy $\hbar\delta = 1.5$ meV corresponding to the detuning of the excitation, as depicted in panel **a**. The corresponding computation times are shown in panel **b**.

B. Comparison with numerically exact methods for Gaussian baths

In the special case of Gaussian environments, other numerically exact methods have been established such as the calculation of PTs for Gaussian baths devised by Jørgensen and Pollock [5] building on the TEMPO algorithm [6], which itself is a reformulation of the iterative path integral approach iQUAPI [7]. In such methods, the augmented density matrix is presented, compressed, and propagated in MPO representation. An implementation of these two methods is incorporated into our ACE computer code [4].

These methods rely on the fact that for Gaussian baths, the path integral over the environment can be solved analytically, giving explicit expressions for the Feynman-Vernon influence functional. As all these methods are numerically exact, it is an interesting question which method performs best (requires least computation time) in which situation—restricting to Gaussian cases where all methods are available. To this end, we consider again the example of the quantum dot coupled to phonons and subject to radiative losses discussed in the main text, focusing on the numerically exact modelling of phonon effects while losses are accounted for by Lindblad terms. Anticipating that the performance of the different methods strongly depends on the memory time of the environment, we perform calculations for various widths of the spectral density. As depicted in Fig. S.3.1**a**, we use the envelope of the spectral density as in the main text, but restrict it to a finite support of ΔE centred around $\hbar\delta = 1.5$ meV, corresponding to the detuning of the excitation from the quantum dot transition. For large values of $\Delta E \approx 3$ meV, the memory time of the environment is shortest, while in the limiting case for small widths $\Delta E \to 0$ only a single environment mode energy exists and the memory time becomes infinite.

In all methods, we use a time step width of $\Delta t = 0.1$ ps, compression threshold $\epsilon = 10^{-7}$ and initial bath temperature $T = 0$ K. For ACE, we discretise the continuum ΔE on N_E intervals with a density of states $N_E/\Delta E = 20$ meV^{-1} and we truncate the environment Hilbert space per Boson mode to dimension $M = 2$ or $M = 3$. For this set of parameters, the typical relative difference between exciton populations in the different methods is $\approx 2 \times 10^{-3}$.

In Fig. S.3.1**b**, the computation times needed for the different methods are depicted as a function of the spectral density width ΔE. For large widths $\Delta E \gtrsim 1.4$ meV, we find the Gaussian PT calculation to be faster than both ACE and TEMPO without memory truncation. Note, however, that TEMPO can benefit significantly from memory truncation, as this reduces the length of the MPO chain to be compressed and propagated. Fixing the memory time to $\tau_{\mathrm{mem}} = 2.5$ ps in TEMPO leads to the fastest results of all considered methods in the regime of large ΔE. Yet, for smaller widths $\Delta E \lesssim 1.5$ meV, the bath memory time starts to exceed 2.5 ps, which leads to visible deviations in the occupations (not shown). The smaller (disconnected) pink dots in Fig. S.3.1**b** indicate data points where the relative error with respect to Gaussian PT calculations exceeds 1%. For narrow spectral densities, we observe a cross-over rendering ACE faster than all other methods. As shown, the required dimension M per boson mode has a large influence on the run time for ACE.

To summarize, in the special case of Gaussian baths, alternative methods can benefit from the existence of analytical expressions for the influence functional describing the environment, and therefore perform faster than ACE in cases where broad spectral densities lead to short memory times. On the other hand, for narrowly peaked spectral densities that can be well described in terms of a few environment modes, the general method ACE can even outperform specialised methods for Gaussian baths. Finally, it is noteworthy that our computer code produces Gaussian PTs that are completely compatible with the PTs utilised by ACE, paving the way for prospective hybrid approaches for spectral densities with sharp peaks on top of broad continua.

S.4. ENVIRONMENT MODES WITH ANHARMONIC POTENTIALS

In the main text, we present ACE simulations for an open quantum system coupled to a bath of anharmonic environment modes whose free evolution is governed by the Morse potential. Here, we lay out the full numerical treatment starting from the Schrödinger equation of a single environment mode for an arbitrary potential $V(r)$ directly from a numerical representation of the potential on a real space grid.

A. Finite differences to find environment states

We start from the one-dimensional Schrödinger equation for a given potential $V(r)$:

$$H = -\frac{\hbar^2}{2m}\frac{\partial^2}{\partial r^2} + V(r). \tag{S.4.1}$$

We first map this onto a dimensionless ordinary differential equation by introducing a characteristic length scale a_0 and energy scale $\epsilon = \hbar^2/(2ma_0^2)$, and defining the dimensionless coordinate $x = r/a_0$. We then define the dimensionless Hamiltonian

$$h := \frac{1}{\epsilon}H = -\frac{\partial^2}{\partial x^2} + v(x), \tag{S.4.2}$$

$$v(x) := \frac{1}{\epsilon}V(a_0 x), \tag{S.4.3}$$

where $v(x)$ is the dimensionless potential. The dimensionless problem is solved by a finite differences method, where a real space grid $x_j = x_0 + j\Delta x$ with width Δx and N_x sample points is introduced and the second derivative is approximated by

$$\frac{\partial^2}{\partial x^2}f(x_i) = \frac{f(x_{i-1}) - 2f(x_i) + f(x_{i+1})}{\Delta x^2}. \tag{S.4.4}$$

The ODE in Eq. (S.4.2) then takes the form of a symmetric tridiagonal matrix, which is diagonalized numerically.

For simulations in ACE, we work in the truncated energy eigenbasis accounting for only the M lowest energy eigenstates of a given mode. The energy eigenvalues E_i of the original problem are obtained by multiplying the eigenvalues of h with ϵ. The operators describing the system-environment coupling are evaluated in the truncated basis depending on the concrete details of the model. For example, if the system couples to the environment modes via the position operator $\hat{r}$, one has to numerically evaluate matrix elements $\langle i|\hat{r}|j\rangle = a_0\langle i|\hat{x}|j\rangle$ with $i, j \in 0, 1, \ldots, M-1$.

B. Example: Harmonic oscillator

As a reference, we first consider the example of the harmonic oscillator potential $V(r) = \frac{m\omega^2}{2}r^2$. Defining length and energy scales $a_0 = \sqrt{\frac{\hbar}{m\omega}}$ and $\epsilon = \frac{\hbar\omega}{2}$, the corresponding dimensionless Schrödinger equation is

$$h := -\frac{\partial^2}{\partial x^2} + x^2. \tag{S.4.5}$$

Back-transforming the numerically obtained eigenvalues of $h : 1, 3, 5, \ldots$, by multiplying with ϵ, one recovers the series $E_n = \hbar\omega\left(n + \frac{1}{2}\right)$ with $n = 0, 1, 2, \ldots$. From the conventional definition of the harmonic oscillator climbing operators it follows that $a_0\hat{x} = \hat{r} = \sqrt{\frac{\hbar}{2m\omega}}\left(a^\dagger + a\right) = \frac{a_0}{\sqrt{2}}\left(a^\dagger + a\right)$. Consequently, to enable a comparison with the spin Boson model, we consider an environment Hamiltonian for ACE simulations of the form

$$\begin{aligned} H_E =& \sum_k \hbar\omega_k \left(a_k^\dagger a_k + \frac{1}{2}\right) + \sum_k \hbar g_k (a_k^\dagger + a_k)|e\rangle\langle e| \\ =& \sum_k \sum_{j=0}^{M-1} \hbar\omega_k \frac{E_j}{2\epsilon}\sigma_{jj}^k + \sum_k \hbar g_k \sum_{i,j=0}^{M-1} \left(\sqrt{2}\langle i|\hat{x}|j\rangle\right)\sigma_{ij}^k\,|e\rangle\langle e|, \end{aligned} \tag{S.4.6}$$

where σ_{ij}^k describes the effect of the single-particle operator $|i\rangle\langle j|$ for the k-th environment mode. As shown in Fig. 5 of the main text, this procedure perfectly reproduces the results of the spin Boson model.

C. Example: Morse potential

The Morse potential [8] is an asymmetric anharmonic potential with a finite number of bound states below a continuum of unconfined states. It is often used to describe molecular vibrations with a finite dissociation energy [9]. It takes the form

$$V(r) = D_e\Big(e^{-2(r-r_e)/a_0} - 2e^{-(r-r_e)/a_0}\Big), \tag{S.4.7}$$

where D_e is the well depth, r_e is the position of the minimum of the potential, and a_0 defines its spatial extent. Here, we use a_0 as the length scale and shift the coordinate system such that $r_e = 0$. The Morse potential is made dimensionless

$$v(x) = \Lambda^2\Big(e^{-2x} - 2e^{-x}\Big) \tag{S.4.8}$$

by introducing the parameter $\Lambda = \sqrt{D_e/\epsilon} = \sqrt{2ma_0^2 D_e/\hbar^2}$. The Morse potential is known to have M bound states [8], where M is the largest integer smaller than $\Lambda + \frac{1}{2}$, with energies

$$E_n = -\epsilon\Big(\Lambda - n - \frac{1}{2}\Big)^2 = \epsilon\Big[-\Lambda^2 + 2\Lambda\Big(n + \frac{1}{2}\Big) - \Big(n + \frac{1}{2}\Big)^2\Big]. \tag{S.4.9}$$

For deep potentials $\Lambda \to \infty$, the spectrum of the lowest states becomes equivalent to that of a harmonic oscillator with $\hbar\omega = 2\epsilon\Lambda$, which is consistent with the second-order Taylor expansion around $r = r_e$ being $V(r) \approx -D_e + \frac{m\omega^2}{2}(r - r_e)^2$. For general Λ, the level spacings between confined states are

$$\Delta E_n = E_{n+1} - E_n = \hbar\omega\Big(1 - \frac{n+1}{\Lambda}\Big). \tag{S.4.10}$$

The energy difference between first excited state and ground state is $\Delta E_g = \hbar\omega\big(1 - \Lambda^{-1}\big) = \sqrt{\frac{2\hbar^2 D_e}{ma_0^2}} - \frac{\hbar^2}{ma_0^2}$.

In Fig. 5**a** in the main article, the five bound eigenstates of the Morse potential with $\Lambda = 5$ obtained from numerical finite-differences calculations are depicted. In contrast to harmonic oscillator wave functions, the anharmonicity of the Morse potential manifests itself in the decreasing level spacings for higher states. Furthermore, the wavefunctions are strongly asymmetric leading to nonzero values of the average position operator $\langle i|\hat{x}|i\rangle$ for the i-th state. This non-zero expectation has a significant impact on the system-environment coupling.

Note that the matrix element of the dimensionless position operator $\hat{x}$ between subsequent eigenstates of the Morse potential behaves as $\langle i+1|\hat{x}|i\rangle \to \sqrt{i+1}/\sqrt{2\Lambda}$ for $\Lambda \to \infty$, so that a situation comparable with the independent-boson model in this limit requires an environment Hamiltonian of the form

$$H_E = \sum_k \sum_j \hbar\omega_k \tilde{E}_j \sigma_{jj}^k + \sum_k \hbar g_k \sum_{i,j=0}^{M-1} \Big(\sqrt{2}\langle i|\tilde{x}|j\rangle\Big)\sigma_{ij}^k\, |e\rangle\langle e|, \tag{S.4.11}$$

with $\tilde{E}_j = E_j/\Delta E_g$ and $\langle i|\tilde{x}|j\rangle = \sqrt{\Lambda}\langle i|\hat{x}|j\rangle$.

With nonzero diagonals $\langle i|\hat{x}|i\rangle$ for finite Λ, the asymmetry of the potential leads to the additional effect of a renormalisation of the system excited state energy by a value of $\Delta E = \sum_k \hbar g_k \sqrt{2\Lambda}\, \langle\hat{x}\rangle_E^k = \sum_k \hbar g_k \sqrt{2\Lambda}\, \mathrm{Tr}\big(\hat{x}\rho_E^k\big)$, which depends on the state of the environment.

D. Details of the calculation and parameters

For the ACE simulation depicted in Fig. 5 in the main article, we consider a continuously driven two-level system with system Hamiltonian $H_S = \frac{\hbar}{2}\Omega\big(|e\rangle\langle g| + |g\rangle\langle e|\big)$. The environment is described by the Hamiltonian H_E in Eq. (S.4.11) with parameters ω_k and g_k sampling a Lorentzian spectral density

$$J(\omega) = C\frac{1}{\pi}\frac{\gamma}{(\omega - \omega_c)^2 + \gamma^2}. \tag{S.4.12}$$

We do this by discretising ω_k/Ω equidistantly in the range $[0, 7.5]$ with $N_E = 100$ modes, and setting $g_k = \sqrt{J(\omega_k)\Delta\omega}$, where $\Delta\omega$ is the distance between subsequent ω_k sample points. Here, we set $\hbar = 1$, and fix the parameters of the spectral density to $C = 0.1\Omega^2$, $\gamma = 0.1\Omega$, and $\omega_c = \Omega$. The corresponding values g_k/Ω are plotted in Fig. 5**b** in the main article. The environment modes are initialised with thermal states at temperature $k_B T = 0.5\Omega$.

S.5. SUPERRADIANCE OF TWO QUANTUM EMITTERS

In this section we present an additional illustration of the potential of ACE. We consider the radiative decay of two quantum emitters coherently coupled to the same radiation field as depicted in Fig. S.5.1a. If the distance d between the emitters is much smaller than the wavelength λ associated with the fundamental transitions of the emitters, both emitters couple with the same phase to the radiation field. This gives the Hamiltonian of photon mode k as

$$H_E^k = \hbar\omega_k a_k^\dagger a_k + \hbar g_k \Big[a_k^\dagger \big(|g_1\rangle\langle e_1| + |g_2\rangle\langle e_2| \big) + h.c. \Big], \tag{S.5.1}$$

where $|g_i\rangle$ and $|e_i\rangle$ denote the ground and excited state of emitter $i = 1, 2$ and $a_k^\dagger$ creates a photon in mode k. In analogy to the first example in the main article, our environment is a discretised quasi-continuum of electromagnetic modes with a density of states which would correspond to keeping the Fermi's golden rule rate for the decay of a single emitter, κ, fixed. We admit in general a detuning δ between the transitions of the two emitters, which enters the system Hamiltonian $H_S = \frac{\hbar\delta}{2}\big(|e_1\rangle\langle e_1| - |e_2\rangle\langle e_2|\big)$. The initial conditions are chosen such that both emitters are excited at time $t = 0$.

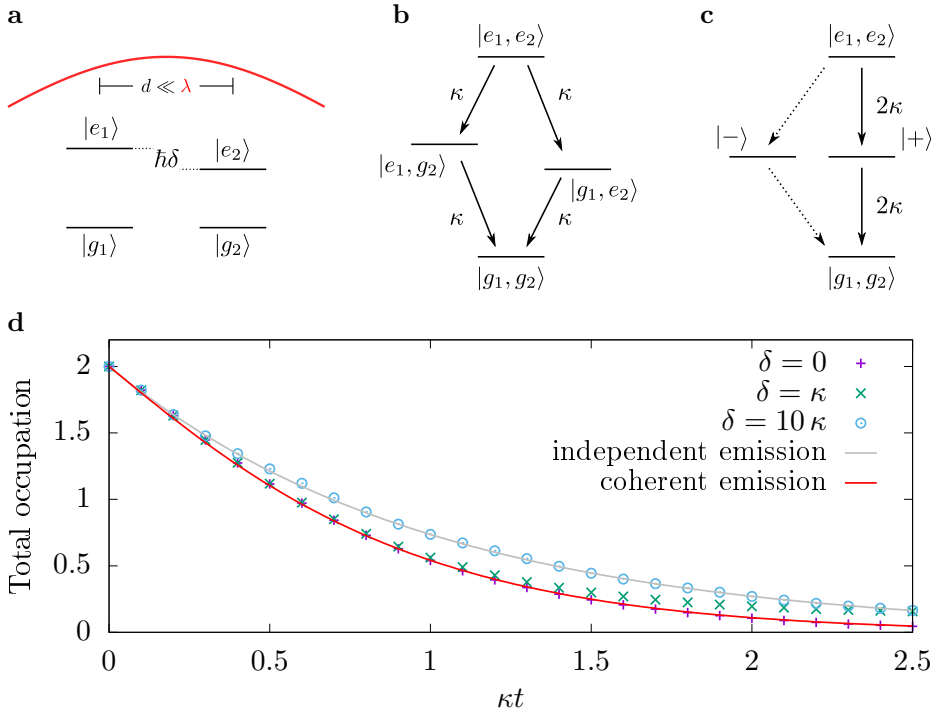

FIG. S.5.1. **Transition between independent and superradiant emission of two proximal optical dipoles. a,** Two quantum emitters detuned by an energy $\hbar\delta$ and separated by a distance d much smaller than the wavelength λ corresponding to the emitter transitions. **b,** Radiative decay of two independent emitters. **c,** Superradiance of two coherently coupled emitters. The transition through the symmetric state $|+\rangle$ has twice the rate compared to that of independent emitters whereas the transition through the antisymmetric state $|-\rangle$ is forbidden. **d,** ACE simulations for different detunings δ and analytic results for independent emission and for coherent emission in the superradiant regime of two emitters.

This situation is interesting as it constitutes a minimal setup for superradiance: If the emitters are distinguishable, e.g., if the detuning δ is large, both emitters radiatively decay with a rate κ, as depicted in Fig. S.5.1b, so that the sum of the occupations decays as $2\exp(-\kappa t)$. If, however, the emitters are indistinguishable $\delta = 0$, the coherent coupling makes it necessary to derive the respective decay rates in the symmetrised basis including the states $|\pm\rangle = \big(|e_1, g_2\rangle \pm |g_1, e_2\rangle\big)/\sqrt{2}$. The dipole for transitions involving the symmetrised state $|+\rangle$ is larger than that of a single emitter, whereas it is zero of the antisymmetrised state $|-\rangle$. Consequently, $|-\rangle$ is dark and the decay takes place from $|e_1, e_2\rangle$ to $|+\rangle$ and from $|+\rangle$ to $|g_1, g_2\rangle$ with the rate 2κ, as depicted in Fig. S.5.1c. Taking into account the dynamics of the intermediate state occupations, the total occupation of the two indistinguishable emitters is $n_{\mathrm{tot}} = 2(1 + \kappa t)\exp(-2\kappa t)$ [10].

Figure S.5.1d shows the total occupation of the two emitters for $\delta = 0$, $\delta = \kappa$, and $\delta = 10\kappa$ obtained using the ACE method as well as the analytic results corresponding to the case of distinguishable and indistinguishable emitters.

For $\delta = 10\kappa$, the ACE simulation agrees with the exact result for independent emitters, while for $\delta = 0$ the result for coherently coupled indistinguishable emitters is reproduced. In the intermediate regime $\delta = \kappa$, the dynamics can be understood qualitatively by interpreting δ as a perturbation facilitating a rotation from the symmetric $|+\rangle$ to the antisymmetric $|-\rangle$ state. As the latter is dark, the total occupation at long times is found to be even slower than the decay of independent emitters.

This example demonstrates that in a situation where rate equations crucially depend on the basis in which they are derived, the ACE reproduces correct results independent of the basis. Thus, even in Markovian scenarios, ACE simulations can have an advantage over conventional techniques in that it can be applied straightforwardly in an arbitrary basis.

On the technical side, we have solved the dynamics of a four-level system, showing that the method is not restricted two-level systems. To achieve this, we have made use of the fact that the matrices $\mathcal{Q}^{(\alpha_l,\tilde{\alpha}_l)}_{d_l d_{l-1}}$ are identical for some combinations of $(\alpha_l, \tilde{\alpha}_l)$. This can be done by analogy with the method devised for iQUAPI [11], using a decomposition into groups with identical couplings. With this, we only compute non-redundant values, which reduces the 256 possible combinations of $(\alpha_l, \tilde{\alpha}_l)$ to 18. These groups can be identified numerically from the specified environment Hamiltonians H^k_E, so that this step is also automated.

S.6. DISPERSIVE COUPLING

Here, we consider a toy model of a TLS dispersively coupled to a multi-mode microcavity, in order to demonstrate several remaining aspects of the generality of ACE that were not covered in previous examples. Specifically: non-Gaussian interactions due to non-linear system-environment coupling, time-dependent driving of the environment, and non-unitary evolution of the environment modes.

A common situation in which non-Gaussian environments emerge is when the coupling to the environment is non-linear in environment mode creation and annihilation operators. The simplest case is that of quadratic system-environment coupling, as in the case of dispersive coupling described by an interaction Hamiltonian $H_I = \sum_k \hbar g_k a_k^\dagger a_k \sigma_z$. Such a coupling arises, e.g., in an effective description of a two-level system (TLS) coupled to a microcavity in the limit where the detuning between TLS and cavity is much larger than the coupling strength [12]. The main effect of dispersive coupling is that the TLS transition energy experiences a shift depending on the cavity photon number and, vice versa, the cavity mode energy is modified by the excited state population n_e of the TLS. The former paves the way for quantum non-demolition measurement of the cavity photons by probing the TLS [12].

We consider the setting depicted in Fig. S.6.1**a**: A TLS is coupled to a microcavity that supports multiple discrete photon modes which can be individually addressed by external driving. The cavity modes are assumed to be detuned far enough from the fundamental TLS transition that the TLS-cavity coupling is well described by a dispersive interaction. The initially empty cavity modes are then driven one-by-one by short external pulses centred around times τ_k, $k = 1, 2, 3, 4$. As a result of the dispersive coupling, this leads to a shift of the TLS transition energy, which is probed by driving the TLS directly and continuously with a driving field (driving strength Ω) that is resonant with the bare TLS transition frequency.

To this end, we apply ACE to the Hamiltonian $H = H_S + \sum_k H_E^k$ with

$$H_S = \frac{\hbar}{2}\Omega\big(|e\rangle\langle g| + |g\rangle\langle e|\big), \tag{S.6.1}$$

$$H_E^k = \hbar g a_k^\dagger a_k \sigma_z + \hbar\omega_k a_k^\dagger a_k + \frac{\hbar}{2} G_k(t)\big(a_k^\dagger e^{-i\omega_k t} + a_k e^{i\omega_k t}\big), \tag{S.6.2}$$

using model parameters $\Omega/g = 8.5\pi/10$, and $\omega_k/g = 10 + k$, as well as convergence parameters $g\Delta t = 0.01$ and $\epsilon = 10^{-9}$ accounting for up to four bosons per cavity mode.

In a first step, to aid understanding of the general case, instead of modelling the cavity mode excitation explicitly by pulses with envelope $G_k(t)$, we consider the instantaneous preparation of one-photon Fock states. This corresponds to applying creation operators $a_k^\dagger$ to the forward propagating part of the environment mode Liouville propagator, and the annihilation operators a_k to the backward propagating part at time $g\tau_k = 10k$ for the k-th mode. The results are depicted in Fig. S.6.1**b** and indeed show that whenever a photon is added to a cavity mode, the observed Rabi oscillations of the TLS become more and more off-resonant as indicated by their decreasing amplitude and increasing frequency.

Next, we consider explicit time-dependent driving of the cavity modes by Gaussian pulses with

$$G_k(t) = \frac{A_k}{\sqrt{2\pi}\sigma} \exp\left[-\frac{(t-\tau_k)^2}{2\sigma^2}\right], \tag{S.6.3}$$

with $\sigma = \tau_{\mathrm{FWHM}}/(2\sqrt{2\ln 2})$, $g\tau_{\mathrm{FWHM}} = 0.2$, and $A_k = 2$. These parameters are chosen such that after the k-th pulse the cavity photon number $\langle a_k^\dagger a_k\rangle \approx 1$. As can be seen in Fig. S.6.1**c**, the TLS dynamics is now more complicated. As seen for instantaneous Fock state preparation, the oscillation amplitudes are reduced when another cavity mode is excited, however the signal now involves more than a single frequency. This is due to the fact that the external driving as described by H_E^k induces coherent states as opposed to one-photon Fock states, so that now contributions corresponding to Fock states with $n = 0$, $n = 2$, $n = 3$, and $n = 4$ are also excited with a finite probability. The joint state of TLS and cavity is therefore best discussed in terms of sectors with fixed photon and excitation numbers n and n_e, respectively. This can be illustrated by considering a single cavity mode, where the total system plus environment is tractable without compression, so that the total system can be propagated as a single, closed quantum system. This provides access to the full state including photon-number-resolved TLS populations $|e, n\rangle$, where $|e\rangle$ refers to the excited state of the TLS and n is the cavity photon number. These are shown in Fig. S.6.1**d**. This calculation agrees with the ACE simulations in Fig. S.6.1**c** up to time τ_2, when a second mode becomes involved. This demonstrates that the complicated evolution of the TLS occupation is just a sum of contributions from individual n-photon sectors, each evolving with a single, well-defined frequency.

Finally, because the starting point of ACE are the propagators of the environment modes in Liouville space, it is straightforward to include non-unitary evolution of the environment, such as loss terms that directly affect the

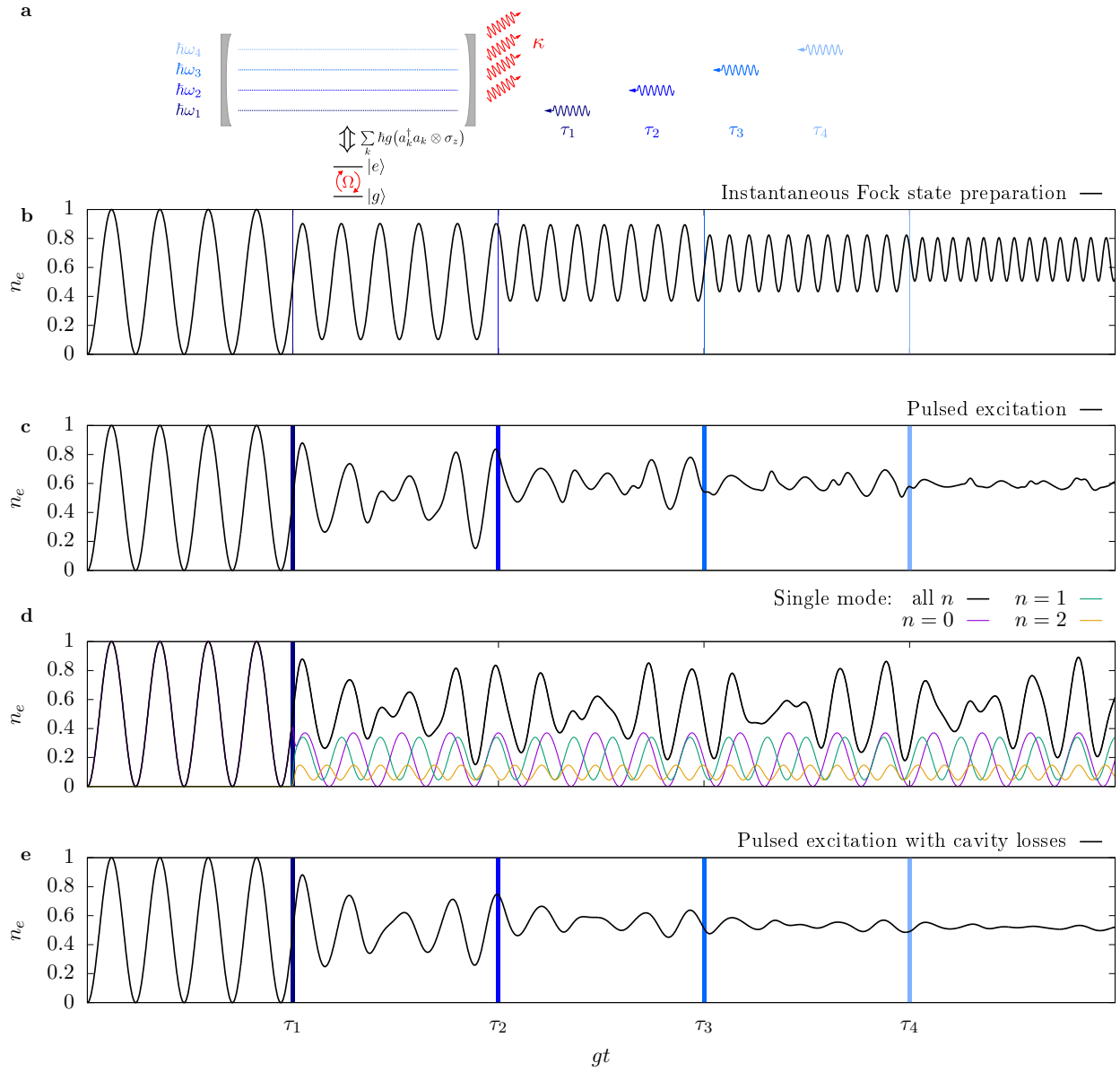

FIG. S.6.1. **a**: Sketch of a TLS dispersively coupled to a multi-mode microcavity, resulting in changes of the effective transition frequency of the TLS when the cavity modes are driven externally by pulses arriving at times τ_k. The TLS itself is continuously driven with bare Rabi frequency Ω, allowing one to detect signatures brought about by changes of the transition frequency. Photons are lost from the cavity modes with rate κ (but $\kappa = 0$ for panels **b**-**d**) **b**: Evolution of the excited state population n_e when the pulses exciting the cavity modes are replaced by an instantaneous change of the state of the i-th cavity mode from the vacuum to the one-photon Fock state at time τ_i indicated by blue vertical lines. **c**: Excited state population when the cavity modes are excited by Gaussian pulses. **d**: Numerical simulation accounting for a single cavity mode as part of the system. The total TLS excitation is presented as well as the photon-number-resolved TLS excitations. **e**: Like **c** but additionally accounting for non-zero photon loss rate $\kappa = 0.1g$.

dynamics of the environment modes. Including Lindblad terms

$$\kappa\left[a_k\rho a_k^\dagger - \frac{1}{2}\left(a_k^\dagger a_k\rho + \rho a_k^\dagger a_k\right)\right] \tag{S.6.4}$$

describing the loss of photons with rate $\kappa = 0.1g$ to the environment propagator, one obtains the results depicted in Fig. S.6.1**e**. While generally very similar to the behaviour in the case without losses shown in Fig. S.6.1**c**, losses with

a finite rate κ are found to lead to more efficient dephasing as they intermix sectors with different photon numbers.

[1] A. M. Childs, Y. Su, M. C. Tran, N. Wiebe, and S. Zhu, Theory of trotter error with commutator scaling, Phys. Rev. X **11**, 011020 (2021).
[2] C. Eckart and G. Young, The approximation of one matrix by another of lower rank, Psychometrika **1**, 211 (1936).
[3] E. Ye and G. K.-L. Chan, Constructing tensor network influence functionals for general quantum dynamics, The Journal of Chemical Physics **155**, 044104 (2021).
[4] M. Cygorek, Automated Compression of Environments (ACE), http://dx.doi.org/10.5281/zenodo.5214128 (2021).
[5] M. R. Jørgensen and F. A. Pollock, Exploiting the causal tensor network structure of quantum processes to efficiently simulate non-markovian path integrals, Phys. Rev. Lett. **123**, 240602 (2019).
[6] A. Strathearn, P. Kirton, D. Kilda, J. Keeling, and B. W. Lovett, Efficient non-markovian quantum dynamics using time-evolving matrix product operators, Nat. Commun. **9**, 3322 (2018).
[7] N. Makri and D. E. Makarov, Tensor propagator for iterative quantum time evolution of reduced density matrices. I. Theory, J. Chem. Phys. **102**, 4600 (1995).
[8] P. M. Morse, Diatomic molecules according to the wave mechanics. ii. vibrational levels, Phys. Rev. **34**, 57 (1929).
[9] M. Bramberger and I. De Vega, Dephasing dynamics of an impurity coupled to an anharmonic environment, Phys. Rev. A **101**, 012101 (2020).
[10] M. Gross and S. Haroche, Superradiance: An essay on the theory of collective spontaneous emission, Physics Reports **93**, 301 (1982).
[11] M. Cygorek, A. M. Barth, F. Ungar, A. Vagov, and V. M. Axt, Nonlinear cavity feeding and unconventional photon statistics in solid-state cavity qed revealed by many-level real-time path-integral calculations, Phys. Rev. B **96**, 201201 (2017).
[12] A. Blais, R.-S. Huang, A. Wallraff, S. M. Girvin, and R. J. Schoelkopf, Cavity quantum electrodynamics for superconducting electrical circuits: An architecture for quantum computation, Phys. Rev. A **69**, 062320 (2004).

Eidesstattliche Versicherung

Hiermit versichere ich an Eides statt, dass ich die vorliegende Arbeit selbstständig verfasst und keine anderen als die von mir angegebenen Quellen und Hilfsmittel verwendet habe.

Weiterhin erkläre ich, dass ich die Hilfe von gewerblichen Promotionsberatern bzw. -vermittlern oder ähnlichen Dienstleistern weder bisher in Anspruch genommen habe noch künftig in Anspruch nehmen werde.

Zusätzlich erkläre ich hiermit, dass ich keinerlei frühere Promotionsversuche unternommen habe.

Bayreuth, den 20. Dezember 2021

_____

Michael Cosacchi